2

NUREG/CR-0497
TREE-1280
for U.S. Nuclear Regulatory Commission

MASTER

MATPRO — VERSION 11
A HANDBOOK OF MATERIALS PROPERTIES FOR USE IN THE ANALYSIS OF LIGHT WATER REACTOR FUEL ROD BEHAVIOR

February 1979

EG&G Idaho, Inc.

IDAHO NATIONAL ENGINEERING LABORATORY

DEPARTMENT OF ENERGY

IDAHO OPERATIONS OFFICE UNDER CONTRACT EY-76-C-07-1570

DISCLAIMER

NUREG/CR-0497
TREE-1280
R3

MATPRO-VERSION 11

A HANDBOOK OF MATERIALS PROPERTIES

FOR USE IN THE ANALYSIS OF LIGHT WATER REACTOR FUEL ROD BEHAVIOR

Compiled and Edited by

Donald L. Hagrman
Gregory A. Reymann

EG&G Idaho, Inc.
Idaho Falls, Idaho

Date Published February 1979

PREPARED FOR THE
U.S. NUCLEAR REGULATORY COMMISSION
AND THE U.S. DEPARTMENT OF ENERGY
IDAHO OPERATIONS OFFICE
UNDER CONTRACT NO. EY-76-C-07-1570
NRC FIN NO. A6046

ACKNOWLEDGMENTS

The editors would like to extend thanks to B. W. Burnham and M. A. Morgan for their invaluable assistance in maintaining the MATPRO library. Mrs. Morgan's contributions in making computer plots and analyzing data are also gratefully acknowledged. We also extend thanks to S. B. Letson for his technical editorial expertise.

Blank Page

FIGURES

TABLES

MATPRO-VERSION 11

A HANDBOOK OF MATERIALS PROPERTIES

FOR USE IN THE ANALYSIS OF LIGHT WATER REACTOR FUEL ROD BEHAVIOR

I. INTRODUCTION

Understanding the performance of light water reactor (LWR) fuel under accident conditions is a major objective of the Reactor Safety Research Program being conducted by the U.S. Nuclear Regulatory Commission (NRC). An extensive program has been defined – centered upon out-of-pile and in-pile experiments and their analyses – with the goal of verifying analytical models. These models are designed to predict fuel transient performance during a wide range of accident types and conditions, and at any time during the operating life of a fuel rod.

These models are based on the materials properties correlations which define the physical condition of LWR fuel and cladding under changing thermal, nuclear, and physical load conditions. The NRC and the nuclear industry have accumulated a large amount of data on these properties. This handbook describes the materials properties correlations and computer subcodes developed for use with various LWR fuel rod behavior analytical models at the Idaho National Engineering Laboratory (INEL).

II. DESCRIPTION OF MATPRO

This handbook is a computer library of 44 subcodes dealing with uranium dioxide and mixed uranium-plutonium dioxide fuels, zircaloy cladding, and gas mixture material properties. Each property is programmed in MATPRO as a separate unit so that individual parts may be changed without necessitating changes elsewhere. This modular format is consistent with the structure of other INEL light water reactor safety analysis programs.

MATPRO-11 is an update of MATPRO-10[1]. Ten new models have been added; seventeen models have been completely rewritten to incorporate new experimental data and to describe an effect more accurately; two models have been revised slightly in their descriptions but not their computer subcodes; and the remaining fifteen descriptions have not been changed. Table I is a list of the specific material properties documented in MATPRO-11. New models and models completely rewritten since MATPRO-10 are denoted.

The fuel, cladding, and gas material properties are in Appendices A, B, and C, respectively. Appendix D contains various supporting material, such as a physical properties subcode (PHYPRO), a linear interpolation subcode (POLATE), and a list of useful International System of Units (SI) with conversion factors.

Each material property description in the appendices contains a review and evaluation of the data in the literature, the development of a mathematical model based upon theory and experiment, a FORTRAN subcode, and comparisons of the model predictions with data. References are provided in each section. The current developer of each code is named under the heading of each section and the originator is named in the computer listing at the end of each section.

Many of the subcodes have been assigned a local index, designated by the acronym LOCIDX, which has a unique value for each subcode. When the MATPRO subroutine is used in conjunction with a fuel rod analysis code such as FRAP-S[2] or FRAP-T[3], this index is used as an identifier allowing specific material property subcodes to be replaced with alternative codes specified by the user.

TABLE I

PROPERTIES INCLUDED IN MATPRO

	Property	Subcode
	Fuel Material Properties (Appendix A)	
1.	Specific Heat Capacity[b]	FCP
2.	Thermal Conductivity[b]	FTHCON
3.	Emissivity	FEMISS
4.	Thermal Expansion	FTHEXP
5.	Elastic Moduli[b]	FELMOD,FPOIR
6.	Creep Rate[b]	FCREEP
7.	Densification[b]	FUDENS
8.	Swelling[b]	FSWELL
9.	Pressure Sintering[a]	FHOTPS
10.	Restructuring	FRESTR
11.	Fracture Strength	FFRACS
12.	Fission Gas Release[b]	FGASRL
13.	Cesium and Iodine Release	CESIOD
	Cladding Material Properties (Appendix B)	
1.	Specific Heat Capacity and the Effect of Hydride Solution on the Specific Heat	CCP, CHSCP
2.	Zircaloy Thermal Conductivity[c] and ZrO_2 Thermal Conductivity	CTHCON,ZOTCON
3.	Zirconium Dioxide Emissivity	ZOEMIS
4.	Thermal Expansion[c]	CTHEXP
5.	Elastic Moduli	
	Young's Modulus for Isotropic Cladding[b]	CELMOD
	Shear Modulus for Isotropic Cladding[a]	CSHEAR
	Cladding Elastic Modulus[a]	CELAST
6.	Axial Growth	CAGROW
7.	Creep Rate[b]	CCRPR
8.	Stress versus Strain	

TABLE I (continued)

	Cladding Material Properties (Appendix B)	Subcode
	Plastic Deformation Parameters [a]	CKMN
	Cold Work and Irradiation Annealing [a]	CANEAL
	Cladding Stress versus Strain [b]	CSTRES
	Flow Stress [b]	CSIGMA
9.	Strain versus Stress [b]	CSTRAN
	Strain versus Stress Integrated [a]	CSTRNI
10.	Texture Factors [a]	CTXTUR
11.	Mechanical Limits	
	Cladding Mechanical Limits [b]	CMLIMT
	Rupture Strain [b]	CSRUPT
	Local Strains to Rupture [b]	CLOCRP
	Wall Thinning [a]	CTHIN
12.	Cyclic Fatigue	CFATIG
13.	Collapse Pressure [a]	CCLAPS
14.	Low and High [a] Temperature Oxidation	CORROS, COBILD
15.	Hydrogen Uptake [b]	CHUPTK
16.	Meyer Hardness [b]	CMHARD
	Gas Material Properties (Appendix C)	
1.	Thermal Conductivity	GTHCON
2.	Viscosity	GVISCO

[a] Model is completely new.

[b] Model has been completely rewritten for MATPRO-11.

[c] Model has been rewritten somewhat for MATPRO-11 without change in the correlations used.

III. REFERENCES

1. G. A. Reymann and D. L. Hagrman (eds.), *MATPRO-Version 10, A Handbook of Materials Properties For Use in the Analysis of Light Water Reactor Fuel Rod Behavior*, TREE-NUREG-1180 (February 1978).

2. J. A. Dearien et al, *FRAP-S2: A Computer Code for the Steady State Analysis of Oxide Fuel Rods, Report 1, Analytical Models and Input Manual*, TREE-NUREG-1107 (July 1977).

3. J. A. Dearien et al, *FRAP-T2: A Computer Code for the Transient Analysis of Oxide Fuel Rods, Report 1, Analytical Models and Input Manual*, TREE-NUREG-1040 (August 1977).

APPENDIX A

FUEL MATERIAL PROPERTIES

APPENDIX A

FUEL MATERIAL PROPERTIES

Fourteen materials properties of light water reactor fuel have been modeled for inclusion in MATPRO-Version 11. The approaches range from: (a) a least-squares fit to available data using a polynomial or other function having little or no theoretical basis to (b) a semiempirical correlation employing an analytical expression suggested by theory with constants determined by comparison with data. The intent of current and future work is to take the second approach whenever possible.

Each material property description includes a listing of a FORTRAN subcode which may be used to calculate the value of the property for various input conditions. All 14 MATPRO fuel subcodes have temperature as an argument. In addition, many are functions of burnup, plutonia content, density, time, and other variables.

Several of the subcodes use a physical properties subcode (PHYPRO, Appendix D, Section 1) to get fuel melting temperatures and heats of fusion. These and other commonly used material parameters are placed in a common block by this separate routine and are thus available to all other subprograms in MATPRO.

1. FUEL SPECIFIC HEAT CAPACITY (FCP)

(G. A. Reymann)

The specific heat capacity of nuclear fuel is needed for temperature calculations in time dependent problems. The stored energy, or enthalpy, is calculated from the specific heat capacity. It has special importance in the analysis of problems involving coolant loss or coolant flow restriction, because the severity of these transients is greatly affected by the initial stored energy.

1.1 Summary

The specific heat capacity of nuclear fuel is modeled as a function of four parameters: temperature, composition, molten fraction, and oxygen to metal ratio. Since UO_2 and PuO_2 are the principal LWR fuels, these are the constituents considered. The correlations cover temperatures from 300 K to more than 4000 K.

The equations for the specific heat capacity (FCP) of solid UO_2 and PuO_2 are assumed to have the same form, but with different constants. The basic equation is

$$FCP = \frac{K_1 \theta^2 \exp(\theta/T)}{T^2 [\exp(\theta/T) - 1]^2} + K_2 T + \left(\frac{O/M}{2}\right) \frac{K_3 E_D}{RT^2} \exp(-E_D/RT) \qquad \text{(A-1.1)}$$

where

FCP = specific heat capacity (J/kg·K)

T = temperature (K)

O/M = oxygen to metal ratio

R = 8.3143 (J/mol·K)

θ = the Einstein temperature (K)

and the constants are given in Table A-1.I.

TABLE A-1.I

CONSTANTS USED IN UO_2 AND PuO_2 SPECIFIC HEAT CAPACITY CORRELATIONS

Constant	UO_2	PuO_2	Units
K_1	296.7	347.4	J/kg·K
K_2	2.43×10^{-2}	3.95×10^{-4}	J/kg·K^2
K_3	8.745×10^{7}	3.860×10^{7}	J/kg
θ	535.285	571.000	K
E_D	1.577×10^{5}	1.967×10^{5}	J/mol

The specific capacities of both UO_2 and PuO_2 in the liquid state are given by

$$FCP = 503 \text{ J/kg·K}. \quad \text{(A-1.2)}$$

For a mixture of UO_2 and PuO_2, the specific heat capacity of the solid is found by combining the contribution from each constituent in proportion to its weight fraction. When the material is partially molten, the FCP is found similarly with a weighted sum. The standard error of the UO_2 correlation is ±3 J/kg·K, and for the mixed oxide correlation it is 6 to 10 J/kg·K, depending on the fraction of PuO_2. For nonstoichiometric fuels, these uncertainties are approximately doubled.

Section 1.2 is a review of the surveyed literature. The model development is presented in Section 1.3, which also includes comparisons of model predictions and data. The effects of departures from stoichiometry are analyzed in Section 1.4. An uncertainty analysis is given in Section 1.5, the FORTRAN subcode listing is given in Section 1.6, and the references are given in Section 1.7.

1.2 Review of Literature

An important source for this report is the extensive review by Kerrisk and Clifton[A-1.1]. Additional data from Kruger and Savage[A-1.2] are used to find the parameters for PuO_2 in Equation (A-1.1). The heat capacity of liquid fuel is taken from Leibowitz et al[A-1.3].

1.2.1 Limitations of the Data Sources. While the data sources used by Kerrisk and Clifton cover a wide range of temperatures (483 to 3107 K), their data are restricted to nearly stoichiometric material ($2.00 \lesssim O/U \lesssim 2.015$) and the oxygen to metal ratio has been shown to be significant by Grønvold et al[A-1.4] and by Affortit and Marcon[A-1.5]. The data of Kruger and Savage are limited in that the highest temperature was only 1400 K, which is well below the melting point of about 2600 K for PuO_2. They also restricted themselves to approximately stoichiometric PuO_2. The specific heat capacity of liquid fuel taken from Leibowitz et al is only for UO_2. The assumption is made that the same value is also valid for liquid PuO_2. Although departures from stoichiometry were found to be significant for solid fuel, no experimental effort has been made to assess the importance of this parameter in the liquid state.

1.2.2 Other Data Sources. Several other data sources are used to estimate the uncertainty of the model, but not in its development. These sources will be cited in Section 1.5 where the uncertainty is analyzed.

1.3 Development of the Model

The most common technique for finding the specific heat capacity is to measure the enthalpy of a sample by drop calorimetry and deduce the heat capacity by finding the rate of enthalpy change with temperature. Generally, the enthalpy data is fitted with an empirical function, often a simple polynomial. While the accuracy of this approach is quite good, a function based on first principles would be preferable because it would allow identification of the physical processes involved and could be extrapolated beyond its temperature base with more confidence. This was the approach used by Kerrisk and Clifton and adopted here.

1.3.1 Specific Heat Capacity of a Typical Solid. The lattice specific heat capacity of solids at constant volume can be characterized theoretically quite well using the Debye model of specific heat. Except at low temperatures, a similar but simpler theory developed earlier by Einstein is also adequate. These theories are described in most basic solid state textbooks such as Kittel[A-1.6]. The Einstein formulation is used because of its simplicity. This formulation is

$$C_v = \frac{K_1 \theta^2 \exp(\theta/T)}{T^2 [\exp(\theta/T) - 1]^2} \quad \text{(A-1.3)}$$

where

C_v = specific heat capacity (J/kg·K)

K_1 = a constant to be determined (J/kg·K).

Equation (A-1.3) gives the specific heat capacity at constant volume. In most reactor situations, the specific heat capacity at constant pressure, C_p, is more appropriate. The relationship between the two is[A-1.7]

$$C_p = C_v + \left(\frac{\alpha^2 V}{\beta}\right) T \quad \text{(A-1.4)}$$

where

α = the coefficient of thermal expansion (K^{-1})

β = the coefficient of compressibility (Pa^{-1})

V = the molar volume (m^3).

The temperature dependence of the term in parentheses in Equation (A-1.4) is complicated. The compressibility of a liquid or a solid is nearly constant, but the molar volume and the coefficient of thermal expansion change with temperature. However, a function with $(C_p - C_v)$ = (constant) x temperature yields results which are within the scatter of the data. Therefore, C_p is expressed as

$$C_p = C_v + K_2 T \quad \text{(A-1.5)}$$

where C_v is given by Equation (A-1.3) and K_2 is a constant to be determined by comparison with data.

1.3.2 Defect Energy Contribution to the Specific Heat Capacity. Above about 1500 K, the specific heat capacity data show a rapid increase not described by Equation (A-1.5). This increase is generally attributed to the energy necessary to form Frenkel defects[A-1.7, A-1.8, A-1.9], which is the assumption made here. However, some investigators[A-1.4, A-1.8] have suggested that Schottky defects may also contribute. The

functional form of the extra term which should be added to the specific heat capacity correlation may be found from the defect energy contribution to the enthalpy given by[A-1.6]

$$H_D = K_3 \exp(-E_D/RT) \tag{A-1.6}$$

where

H_D = defect energy contribution to the enthalpy (J)

E_D = activation energy for Frenkel defects (J/mol)

K_3 = constant to be determined (J).

R and T were previously defined in Equation (A-1.1). To find the defect contribution to the specific heat capacity, the derivative of H_D with respect to temperature (C_D) is

$$C_D = \frac{K_3 E_D}{RT^2} \exp(-E_D/RT). \tag{A-1.7}$$

Combining Equations (A-1.3), (A-1.5), and (A-1.7) gives the general expression

$$FCP = \frac{K_1 \theta^2 \exp(\theta/T)}{T^2 [\exp(\theta/T) - 1]^2} + K_2 T + \frac{K_3 E_D}{RT^2} \exp\left(-\frac{E_D}{RT}\right) \tag{A-1.8}$$

which is used in this model for the specific heat capacity of both UO_2 and PuO_2.

1.3.3 Determination of the Constants in the Model. For UO_2, the values of the five constants, K_1, K_2, K_3, θ, and E_D are taken from Kerrisk and Clifton, and for PuO_2, they are determined by fitting the data of Kruger and Savage. In both cases, the fuel was nearly stoichiometric. Data sources for pure PuO_2 are scarce. One potential source is the work of Affortit and Marcon. However, they give only correlations fit to data and not the actual data, nor do they present an uncertainty analysis. Without knowing the number or accuracy of the data on which their correlations are based, one cannot estimate what weight to give to their results. Therefore, their correlations were not used to determine the constants of Equation (A-1.8). Their work was useful for the assessment of the effects of departures from stoichiometry.

1.3.4 Comparisons of the Model with Data. Figure A-1.1 shows the correlation for UO_2 along with data from three sources[A-1.4, A-1.13, A-1.14]. These data are all taken from stoichiometric UO_2. At the high end of the temperature range, a few hundred kelvins before melting, the data fall below the model predictions. This is probably the result of partial melting due to a nonuniform temperature distribution within the sample. In such a

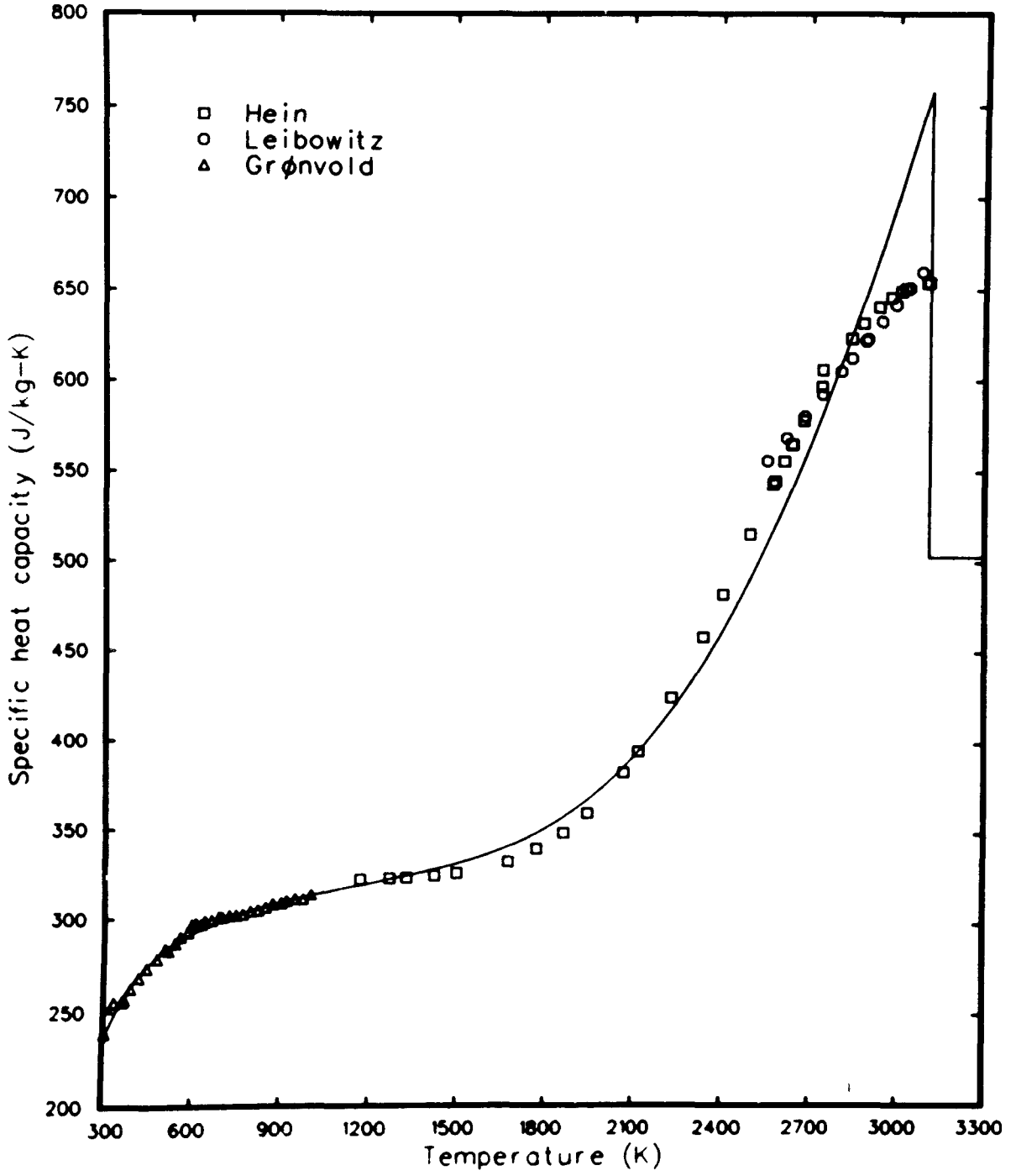

Fig. A-1.1 Specific heat capacity of UO_2 from three experimenters compared with the FCP correlation (solid line) for UO_2.

case, the measured specific heat capacity would be smaller because in a liquid it is considerably lower than in a solid. A similar comparison is shown in Figure A-1.2 for PuO_2. In this instance, the fit is better because the correlation is compared with its own data base. This was necessary due to the lack of a broad data base for this fuel. A better test of the accuracy of the model is found by comparing its predictions with mixed oxide

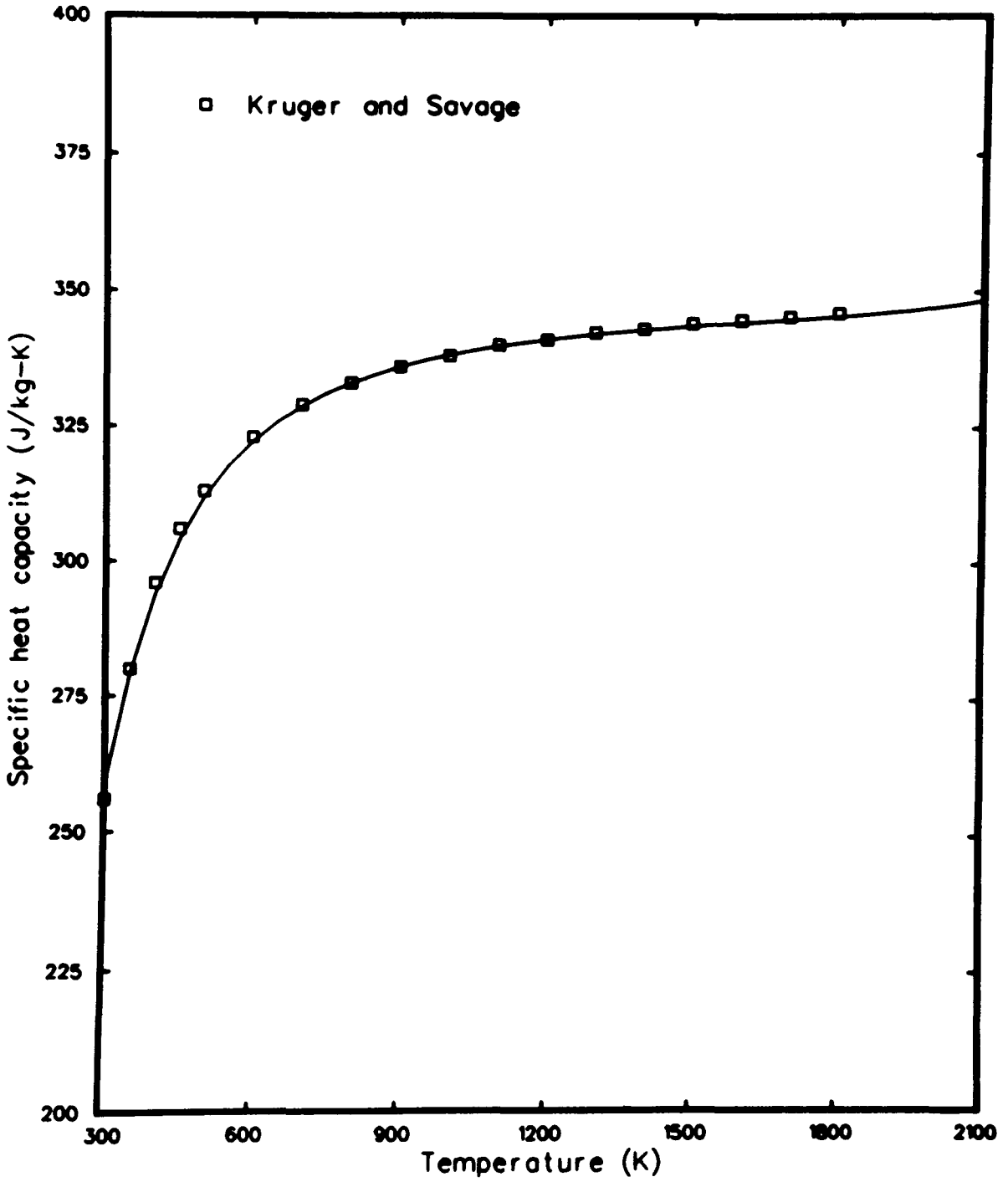

Fig. A-1.2 Specific heat capacity of PuO_2 from Kruger and Savage compared to FCP correlation (solid line) for PuO_2.

data[A-1.5, A-1.10, A-1.12], as is done in Figure A-1.3. None of the data shown on this figure were used in the development of the model. The agreement is relatively good except for the low values reported by Affortit and Marcon. Other experimenters[A-1.3, A-1.10] have pointed out that the results of Affortit and Marcon are generally low when compared with their own data, and have been excluded from their data bases, although no one has

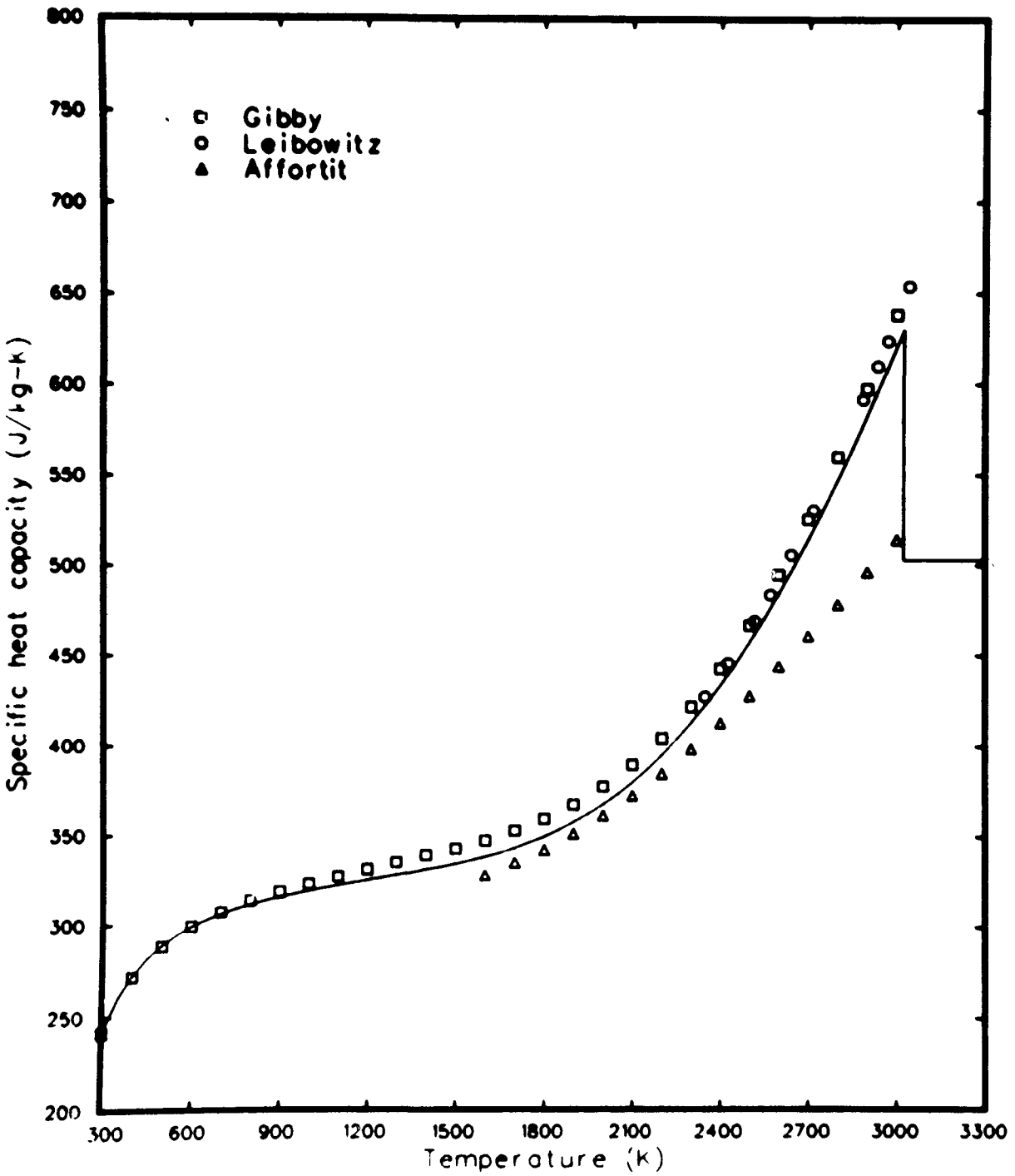

Fig. A-1.3 Specific heat capacity of $(U_{0.8}\,Pu_{0.2})O_2$ from three experimenters compared with the FCP correlation (solid line) for mixed oxides.

proposed an adequate explanation for the discrepancy. On the other hand, at least one investigator[A-1.9] has given considerable weight to the work done by Affortit and Marcon. Herein their results are used in the following section which contains an analysis of the effect of departures from stoichiometry on the specific heat capacity.

1.4 Effect of Nonstoichiometry

Several investigators have found the oxygen to metal ratio of fuel to influence the specific heat capacity[A-1.1, A-1.5, A-1.8, A-1.10]. At temperatures above 1300 K, departures from stoichiometry, typical of those found in LWR fuel, have caused changes in the specific heat capacity greater than the data scatter. The most complete analysis of this effect has been done by Affortit and Marcon. Even though their results are quantitatively different from the sources used to develop this model, they illustrate well the qualitative aspects of this effect. Therefore, Figures A-1.4 and A-1.5, made by computer from their correlations, are presented. Figure A-1.4 is for UO_2 and Figure A-1.5 for mixed oxide fuels. It is clear from these figures that the specific heat capacity increases as the oxygen to metal ratio increases.

Very hyperstoichiometric materials such as U_4O_9 and U_3O_8 have specific heat capacities considerably larger than that of UO_2[A-1.4, A-1.11]. In addition, these materials exhibit specific heat capacity peaks at certain temperatures which are associated with phase transitions. The incidence of these states in light water reactor fuel is small; however, their influence is neglected in this model.

In reactor fuel, nonstoichiometry is believed to be due to oxygen interstitials for hyperstoichiometric fuel, and oxygen vacancies for hypostoichiometric fuel[A-1.8]. Excess oxygen tends to increase, and oxygen deficiency to decrease, the probability of formation of Frenkel and Schottky defects, thereby changing the specific heat capacity. Thus the logical place to make an adjustment to Equation (A-1.8) is in its last term, which includes the effect of defect formation. By multiplying the term by the oxygen to metal ratio divided by 2.0,

(1) The correlation is unaffected for stoichiometric fuel

(2) The proper temperature dependence is obtained

(3) The specific heat capacity is increased for hyperstoichiometry and decreased for hypostoichiometry, in accordance with the data.

Therefore, this correction has been made as a first approximation.

1.5 Uncertainty of the Model

As would be expected, the accuracy of these models when compared with their own data bases it quite good. A better test is found by comparing the correlations with data not used in their development. The UO_2 and mixed oxide fuel correlations are analyzed separately in this section.

1.5.1 Uncertainty in UO_2 Model. Kerrisk and Clifton report an accuracy of ±3% for their correlation over the temperature range 300 to 3000 K, with an approximately uniform

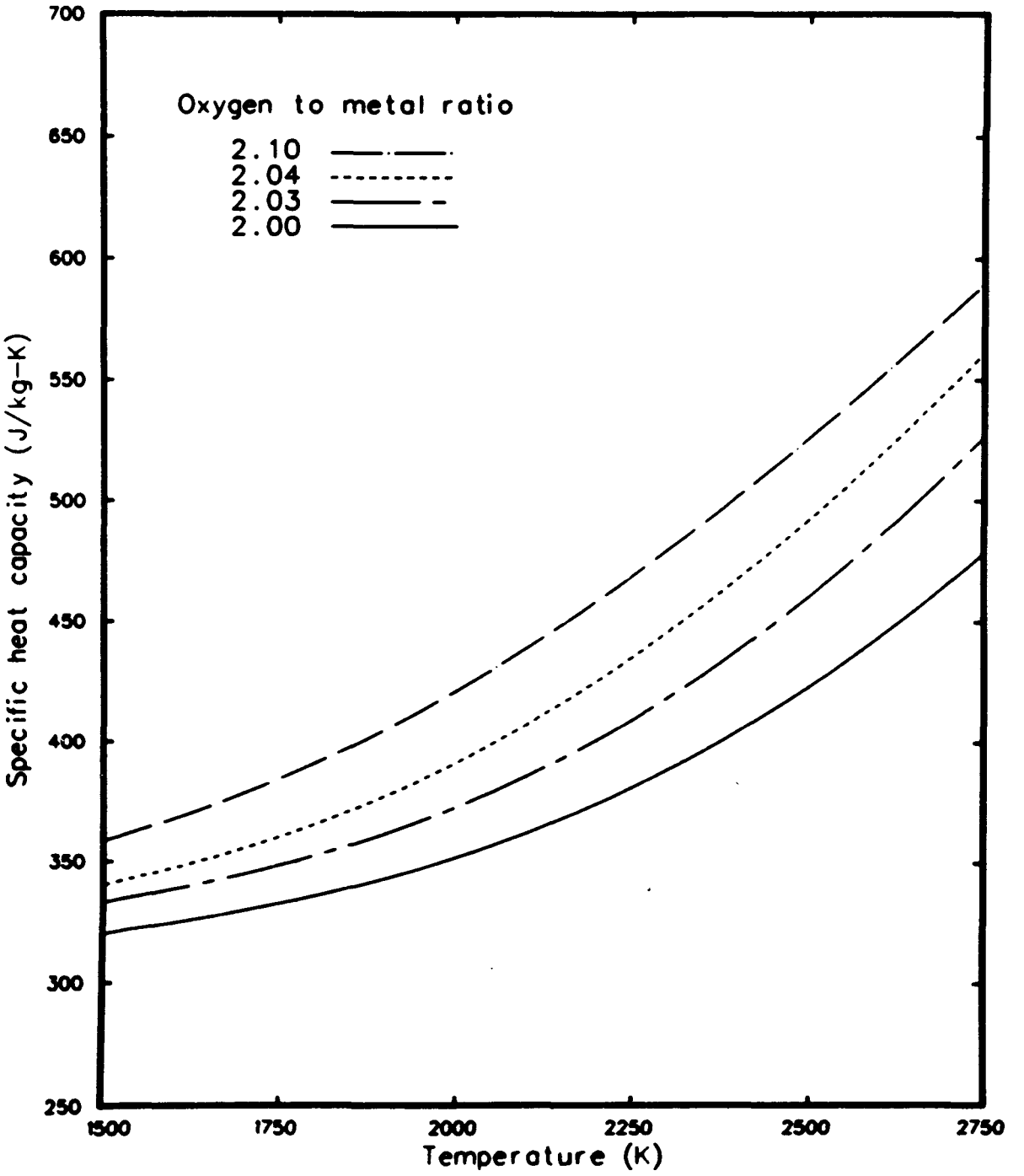

Fig. A-1.4 Specific heat capacity as a function of temperature and oxygen to metal ratio for UO_2.

distribution relative to temperature. When the predictions of the correlation are compared with the data of Grønvold et al for stoichiometric oxide the agreement is even better, having a standard error of only 2.0 J/kg·K. This is a good test of the model, since these data were not used to develop the correlation. The paper by Affortit and Marcon gives correlations fit to their data. Arbitrarily taking 200 K intervals over their range from 1600 to 3000 K and

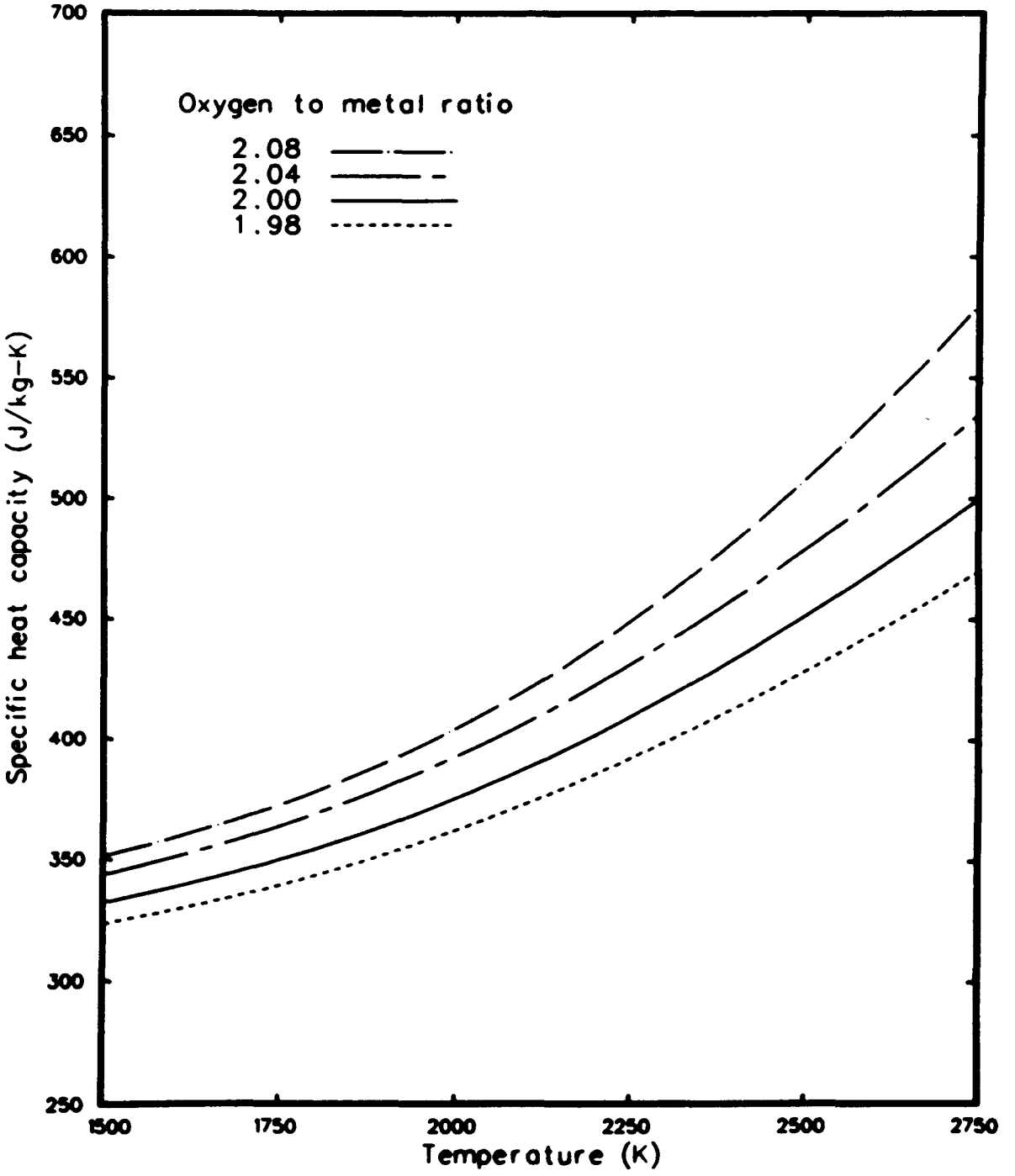

Fig. A-1.5 Specific heat capacity as a function of temperature and oxygen to metal ratio for $(U_{0.8}\,Pu_{0.2})O_{2+x}$.

using their correlations, the standard error is 46 J/kg·K, with Affortit and Marcon's predictions being smaller at all temperatures and the residuals increasing with temperature.

1.5.2 Uncertainty in the Mixed Oxide Model. Because of the limited number of data for PuO_2, the accuracy of the correlation for mixed oxide was used as a test for this correlation. Data were taken from Leibowitz et al[A-1.12], Gibby et al[A-1.10], and Affortit and Marcon. The model presented in this paper, using a weighted sum of the UO_2 and PuO_2 results, predicts specific heat capacities slightly larger than all but two of the 55 data reported by Gibby and Leibowitz. At the highest and lowest temperatures (3000 and 300 K) the differences are negligible, less than 1.0 J/kg·K, while at intermediate temperatures around 1600 K the residuals are about 10.0 J/kg·K, falling off smoothly from this temperature. The standard error relative to the model of these three data sets is 5.6 J/kg·K. This is equivalent to a maximum percentage error of less than 2.5%. Since these residuals are smaller than the scatter in the data, the model represents these data sets adequately. When the model is compared with that of Affortit and Marcon, again taking 200 K steps from 1600 K to melting, the standard error is 46 J/kg·K. Affortit and Marcon always have the smaller value and the residuals increase with temperature, as with the UO_2 results. Because of the lack of actual data, the results of Affortit and Marcon are not included in the standard error estimates in the computer subcode listed in Section 1.6.

1.6 Fuel Specific Heat Capacity Subcode FCP Listing

A listing of the FCP subcode is given in Table A-1.II. The expected standard error is computed within the subcode, but is not returned.

TABLE A-1.II

LISTING OF THE FCP SUBCODE

```
C
C
      FUNCTION FCP(FTEMP,FACMOT,FOTMTL)
C
C     THE FUNCTION FCP IS USED TO CALCULATE THE SPECIFIC HEAT CAPACITY
C     OF UO2, PUO2, AND (U,PU)O2 FUELS AS A FUNCTION OF TEMPERATURE,
C     FRACTION OF FUEL WHICH IS MOLTEN, PUO2 CONTENT, AND OXYGEN-TO-
C     METAL RATIO.
C
C     FCP    = OUTPUT FUEL SPECIFIC HEAT CAPACITY (J/(KG*K))
C
C     FTEMP  = INPUT FUEL MESHPOINT TEMPERATURE (K)
C     FACMOT = INPUT FUEL FRACTION MOLTEN (UNITLESS)
C              FACMOT = 1.0 - FUEL IS ALL MOLTEN
C              FACMOT = 0.0 - FUEL IS ALL SOLID
C     FOTMTL = INPUT OXYGEN TO METAL RATIO (UNITLESS)
C              FOTMTL = (ATOMS OXYGEN)/(ATOMS METAL) IF NOT KNOWN,
C                       ENTER 2.0
C     UFCP   = ESTIMATED STANDARD ERROR FOR UO2 (J/(KG*K))
C              (NOT CURRENTLY RETURNED)
C     PLFCP  = ESTIMATED STANDARD ERROR FOR PUO2 (J/(KG*K))
C              (NOT CURRENTLY RETURNED)
C
C     THE EQUATIONS USED IN THIS FUNCTION ARE BASED ON DATA FROM;
C       (1) J.KERRISK AND D.CLIFTON, NUCLEAR TECHNOLOGY,16 (1972).
C       (2) O.KRUGER AND H.SAVAGE, JOURNAL OF CHEMICAL PHYSICS,45
C           (1968).
C     THE EFFECT OF OXYGEN-TO-METAL RATIO WAS ESTIMATED FROM
C     EQUATIONS PUBLISHED BY;
```

TABLE A-1.II (continued)

```
C         (3) C.AFFORTIT AND J.MARCON, REVUE INTERNATIONALE DES HAUTES
C             TEMPERATURES ET DES REFRACTAIRES,7 (1970).
C       THE SPECIFIC HEAT CAPACITY OF MOLTEN UO2 WAS TAKEN FROM
C         (4) L.LEIBOWITZ ET AL, JOURNAL OF NUCLEAR MATERIALS,39 (1970)
C
C       FCP WAS ORIGINALLY CODED BY V.F.BASTON IN MARCH 1974.
C       LAST MODIFIED BY G.A.REYMANN IN MAY 1978.
C
C
        COMMON  / PHYPRO / FTMELT,FHEFUS,CTMELT,CHEFUS,CTRANB,
     #                     CTRANE,CTRANZ,FDELTA,BU    ,COMP
C
C           THE PHYPRO COMMON BLOCK IS SET BY CALL TO THE SUBROUTINE
C           PHYPRO WHICH IS PART OF THE MATERIALS PROPERTIES PACKAGE
C           USED AT THE INEL.
C           QUANTITIES CONTAINED IN IT USED IN THIS SUBCODE ARE;
C              FTMELT = FUEL MELTING TEMPERATURE (K)
C              FDELTA = LIQUID-SOLID COEXISTENCE TEMPERATURE (K)
C              COMP   = PUO2 CONTENT (WT.%)
C           WHEN THE FUNCTION FCP IS USED ALONE, NOT AS PART OF THE
C           INEL CODE, VALUES FOR FTMELT, FDELTA, AND COMP MUST BE
C           INPUT.
C
        DATA C1U ,C2U ,C3U ,THU ,EDU / 296.7   , 2.43E-02, 8.745E07,
     #                                 535.285, 1.577E05 /
        DATA C1PU,C2PU,C3PU,THPU,EDPU/ 347.4   , 3.95E-04, 3.860E07,
     #                                 571.0   , 1.967E05 /
C
        CP(C1,C2,C3,TH,ED,T,FOTMTL) =
     #          C1*(TH**2)*EXP(TH/T)/((T**2)*((EXP(TH/T)-1.)**2)) + C2*T
     #        + (FOTMTL/2.1)*(C3*ED/(8.314*(T**2)))*EXP(-ED/(8.314*T))
C
        T      = FTEMP
        R      = FACMOT
        TM     = FTMELT
        COMP   = COMP/100.0
        FCPMOL = 503.0
C       FCPMOL = SPECIFIC HEAT CAPACITY OF MOLTEN FUEL (J/(KG*K))
C
        IF (T .GT. (TM+FDELTA)) GO TO 50
C
        FCP    = CP(C1U ,C2U ,C3U ,THU ,EDU ,T,FOTMTL)*(1.0 - COMP) +
     #           CP(C1PU,C2PU,C3PU,THPU,EDPU,T,FOTMTL)*COMP
C
        IF (T .LT. (TM-0.1)) GO TO 100
        FCP    = (1.0 - R)*FCP + R*FCPMOL
        GO TO 100
C
   50   FCP    = FCPMOL
        UFCP   = 2.0
        PUFCP  = 5.6
C
  100   RETURN
        END
```

1.7 References

A-1.1. J. F. Kerrisk and D. G. Clifton, "Smoothed Values of the Enthalpy and Heat Capacity of UO_2," *Nuclear Technology, 16* (December 1972) pp 531-535.

A-1.2. O. L. Kruger and H. Savage, "Heat Capacity and Thermodynamic Properties of Plutonium Dioxide," *The Journal of Chemical Physics, 45* (November 1968) pp 4540-4544.

A-1.3. L. Leibowitz, M. G. Chasanov, L. W. Mishler, D. F. Fischer, "Enthalpy of Liquid Uranium Dioxide to 3500 K," *Journal Nuclear Materials, 39* (1971) pp 115-116.

A-1.4. F. Grønvold, N. J. Kveseth, A. Sveen, J. Tichy, "Thermodynamics of the UO_{2+x} Phase I. Heat Capacities of $UO_{2.017}$ and $UO_{2.254}$ from 300 to 1000 K and Electronic Contributions," *Journal of Chemical Thermodynamics, 2* (1970) pp 665-679.

A-1.5. C. Affortit and J. Marcon, "Chaleur Specifique a Haute Temperature Des Oxydes D'Uranium et de Plutonium," *Revue Internationale des Hautes Temperatures et des Refractaires, 7* (1970) pp 236-241.

A-1.6. C. Kittel, *Introduction to Solid State Physics*, 3rd Edition, New York: John Wiley and Sons, Inc., 1966.

A-1.7. D. R. Olander, *Fundamental Aspects of Nuclear Reactor Fuel Elements,* Technical Information Center, Energy Research and Development Administration, TID-26711-P1 (1976).

A-1.8. R. Szwarc, "The Defect Contribution to the Excess Enthalpy of Uranium Dioxide – Calculation of the Frenkel Energy," *Journal of Chemistry and Physics of Solids, 30* (1969) pp 705-711.

A-1.9. E. A. Fischer, P. R. Kinsman, R. W. Ohse, "Critical Assessment of Equations of State for UO_2," *Journal of Nuclear Materials, 59* (1976) pp 125-136.

A-1.10. R. L. Gibby, L. Leibowitz, J. Kerrisk, D. G. Clifton, "Analytical Expressions for Enthalpy and Heat Capacity for Uranium – Plutonium Oxide," *Journal of Nuclear Materials, 50* (1974) pp 155-161.

A-1.11. H. Inaba, H. Shimizu, K. Naito, "Lambda – Type Heat Capacity Anomalies in U_3O_8," *Journal of Nuclear Materials, 64* (1977) pp 66-70.

A-1.12. L. Leibowitz, D. F. Fischer, M. G. Chasanov, "Enthalpy of Uranium – Plutonium Oxides $(U_{0.8}Pu_{0.2})\ O_{1.97}$ from 2350 to 3000 K," *Journal of Nuclear Materials, 42* (1972) pp 113-116.

A-1.13. R. A. Hein, L. H. Sjodahl, R. Szwarc, "Heat Content of Uranium Dioxide from 1200 to 3100 K," *Journal of Nuclear Materials, 25* (1968) pp 99-102.

A-1.14. L. Leibowitz, L. W. Mischler, M. G. Chasanov, "Enthalpy of Solid Uranium Dioxide from 2500 K to its Melting Point," *Journal of Nuclear Materials, 29* (1969) pp 356-358.

1.8 Bibliography

The following data sources were used in previous EG&G Idaho, Inc., reports dealing with fuel specific heat models, but are not quoted in this version. They are included here for completeness.

(1) C. E. Wicks and F. E. Block, *Thermodynamics of 65 Elements – Their Oxides, Halides, Carbides, and Nitrides,* Bureau of Mines Bulletin No. 605 (1963).

(2) M. L. Bleiberg, R. M. Berman, B. Lustman, *Effects of High Burnup on Oxide Ceramic Fuels,* WAPD-T-1455 (1962).

(3) A. E. Ogard and J. A. Leary, in *Thermodynamics of Nuclear Materials,* IAEA, Vienna (1968) p 651.

(4) R. L. Gibby, *Enthalpy and Heat Capacity of* $U_{0.75}Pu_{0.25}O_{2-x}$ *(25 – 1490°C),* HEDL-TME-73-19 (1973).

(5) L. Leibowitz, D. F. Fischer, M. G. Chasanov, *Enthalpy of Molten Uranium – Plutonium Oxides,* ANL-8042 (1974).

2. FUEL THERMAL CONDUCTIVITY (FTHCON)

(G. A. Reymann)

In this section a correlation is presented for the thermal conductivity of UO_2 and $(U,Pu)O_2$ fuels based on the pooled data from ten sources in the former case and six sources in the latter. The uncertainty in these correlations is also evaluated. FTHCON calculates the fuel thermal conductivity with respect to temperature as a function of temperature, fractional density, and composition of the fuel.

2.1 Summary

The thermal conductivity of unirradiated UO_2 and $(U,Pu)O_2$ is well documented, especially in the temperature range below 1400°C. The correlations used to fit the data are:

for $0 < T \leq 1650$°C:

$$k = P\left[\frac{K_1}{K_2 + T} + K_3 \exp\,(K_4 T)\right] \qquad \text{(A-2.1a)}$$

for $1650 \leq T < 2840$°C:

$$k = P\left[K_5 + K_3 \exp\,(K_4 T)\right] \qquad \text{(A-2.1b)}$$

where

k = thermal conductivity in [W/(cm·K)]

D = fraction of theoretical density

P = porosity correction factor

T = temperature (^{o}C).

The values of the constants K_1 through K_5 are given in Table A-2.I for UO_2 and $(U,Pu)O_2$. For mixed oxide fuel the break between the low and high temperature regions is taken at 1550^{o}C rather than at 1650^{o}C.

TABLE A-2.I

VALUES OF THE CONSTANTS USED IN EQUATION (A-2.1) FOR UO_2 AND $(U,Pu)O_2$ THERMAL CONDUCTIVITY

	K_1	K_2	K_3	K_4	K_5
UO_2	40.4	464	1.216×10^{-4}	1.867×10^{-3}	0.0191
$(U,Pu)O_2$	33.0	375	1.540×10^{-4}	1.710×10^{-3}	0.0171

The thermal conductivity of UO_2 given by Equations (A-2.1a) and (A-2.1b) is compared with the available experimental data (normalized to 95% theoretical density) in Figure A-2.1. The mixed oxide results (normalized to 96% theoretical density) calculated using the same equations but with a different porosity correction factor are shown in Figure A-2.2. Computer-generated curves, without the obscuring data, are presented in Figure A-2.3 showing the UO_2 and $(U,Pu)O_2$ curves on a single graph for comparison. The one-standard deviation uncertainties are virtually independent of temperature and are of the magnitude:

$$\sigma_K = 3.5 \times 10^{-3} \text{ W/(cm·K) for } UO_2 \qquad \text{(A-2.2a)}$$

and

$$\sigma_K = 4 \times 10^{-3} \text{ W/(cm·K) for } (U,Pu)O_2. \qquad \text{(A-2.2b)}$$

More precisely, the uncertainty for UO_2 below 1650^{o}C is 3.6×10^{-3} W/(cm·K) and above 1650^{o}C is 3.0×10^{-3} W/(cm·K) if the available data are weighted equally. The uncertainty for mixed oxides is given with only one significant figure due to a smaller data base, a variation of plutonia contents within the data base and a lack of data for temperatures above 2000^{o}C.

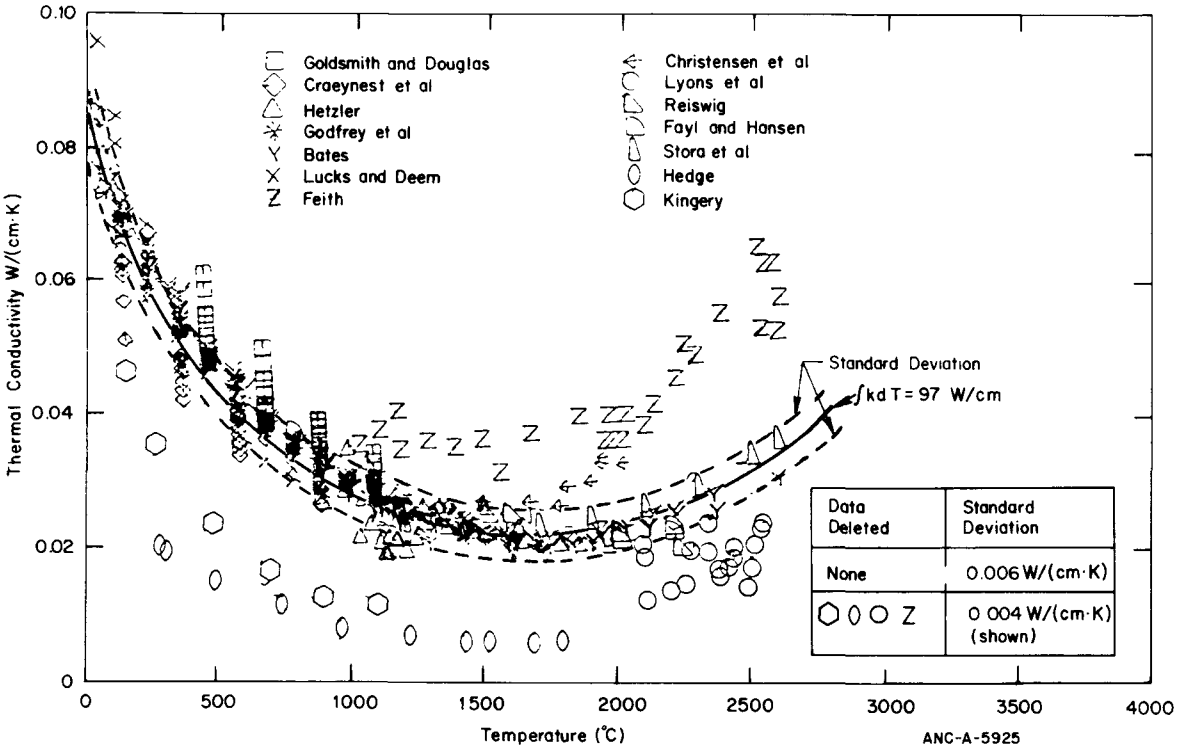

Fig. A-2.1 Comparison of measured and predicted values of the thermal conductivity of UO_2 for materials corrected to 95% TD and standard deviation of data from theoretical curve.

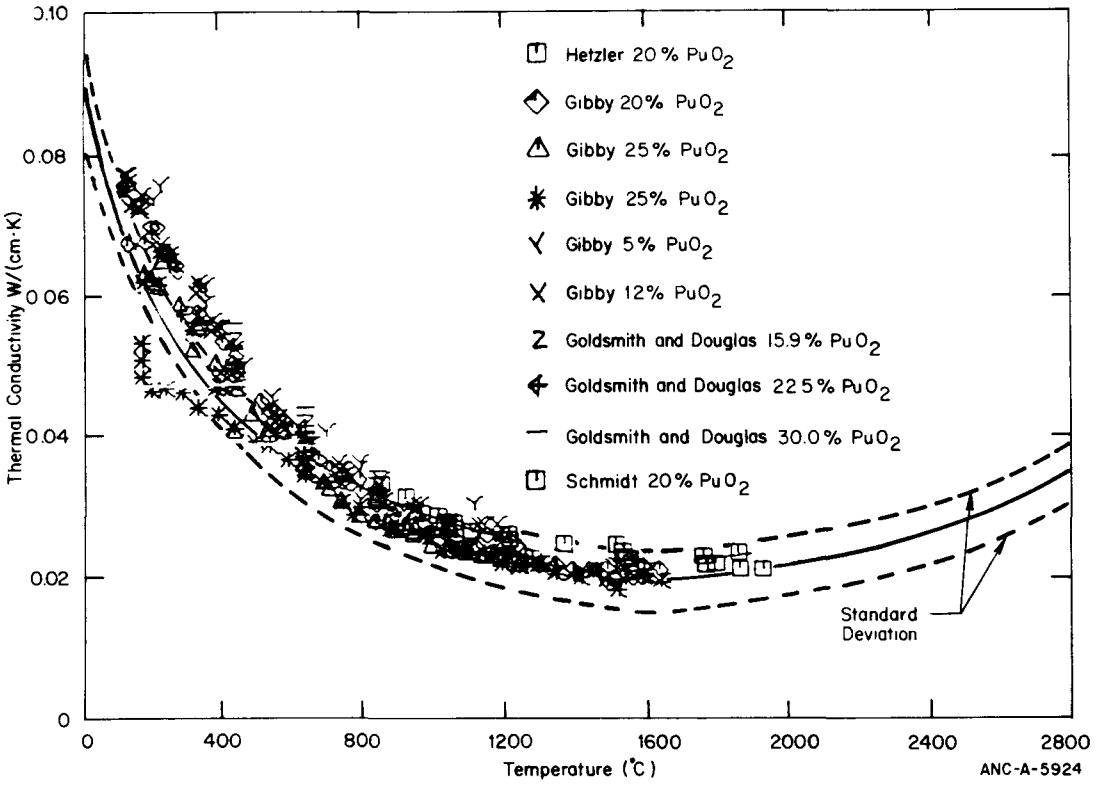

Fig. A-2.2 Comparison of measured and predicted values of the thermal conductivity of $(U,Pu)O_2$ for materials corrected to 96% TD and standard deviation of data from the theoretical curve.

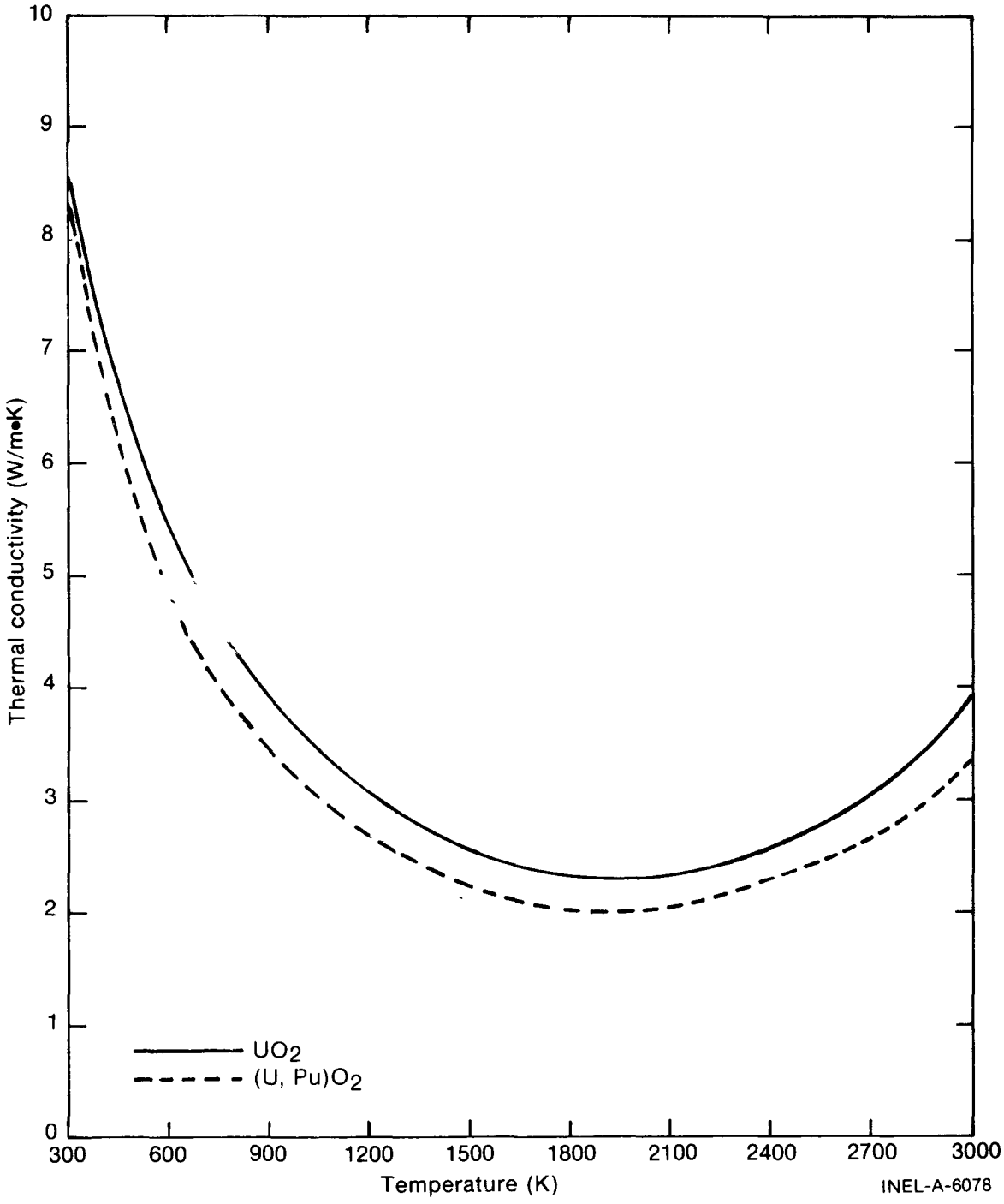

Fig. A-2.3 Calculated curves showing comparison between UO_2 and $(U,Pu)O_2$ thermal conductivity.

The integral of the UO_2 thermal conductivity between 0°C and the melting point (2840°C) was analytically determined. Assuming that the electronic contribution, K_3 exp (K_4 T), has the value 2×10^{-3} W/(cm·K) at 1500°C, a least-squares value of 97 W/cm is obtained for the integral of k from 0°C to the melting point.

2.2 Survey of Available Data

The available UO_2 data[A-2.1 – A-2.13] are presented in Figure A-2.1. The data of Hedge[A-2.1], Kingery[A-2.2], Feith (unpublished), Reiswig[A-2.11] and Lyons[A-2.10] were not used in the present analysis. Hedge and Kingery used samples having densities between 70 and 75% TD – far below those used in commercial fuel. Feith and Reiswig employed a radial heat flow method in which the electrically heated centerline wire was not insulated from the oxide sample, so that Joule heating of the oxide could result and indicate anomalously high conductivity. The data of Lyon et al were derived from observation of postirradiation grain growth and restructuring, a less reliable method than that used by other investigators. The remaining 476 data were fit to an equation including a temperature-dependent, modified Loeb porosity correction[A-2.4, A-2.14, A-2.15].

The thermal conductivity of mixed oxides as a function of temperature has been measured to determine the effect of plutonia content[A-2.16 – A-2.18] and the effect of porosity[A-2.4]. However, the only high temperature data ($T > 1650^{o}C$) available for stoichiometric mixed $(U,Pu)O_2$ is that of Hetzler et al[A-2.5], V. Craeynest et al[A-2.19], and Schmidt[A-2.20]. All these had a 20% plutonia content. Only ten points are available in this temperature range, with the maximum temperature from these sources being $2000^{o}C$. Due to this scarcity of data, the high temperature fit for the mixed oxides must be considered an interim curve pending the publication of additional data.

The causes of the data scatter seen in Figures A-2.1 and A-2.2 include pellet cracking, relocation, irradiation, and differences in oxygen to metal ratios. In fuel rods having a gap width greater than about one percent of the diameter, cracking and bulk relocation of the oxide may occur and result in apparent conductivities different from those shown in Figure A-2.1. Stoichiometry also affects the thermal conductivity. Most data indicate an enhancement[A-2.9, A-2.21, A-2.22] for hypostoichiometric samples and a degradation[A-2.23, A-2.24] for hyperstoichiometric samples.

2.3 Analytical Model

Expressions are derived in this section for the thermal conductivity of UO_2 and of mixed oxide fuels. Derivatives of the thermal conductivities are also derived for both types of fuel.

2.3.1 Thermal Conductivity Expressions. Expressions having the form of Equations (A-2.1a) and (A-2.1b) are employed for both UO_2 and $(U,Pu)O_2$. The optimum value of the integral of k with respect to temperature between $0^{o}C$ and the UO_2 melting point is also determined under certain simplifying assumptions.

(1) UO_2 Fuel. For UO_2 the porosity correction factor is given by

$$P = \frac{1-\beta(1-D)}{1-\beta(1-0.95)} \qquad \text{(A-2.3)}$$

where

P = porosity correction factor (unitless)

β = porosity coefficient ($2.58 - 0.58 \times 10^{-3}T$)

D = fraction of theoretical density (unitless)

T = temperature (^{o}C).

This is the Loeb porosity correction[A-2.14, A-2.15, A-2.19], employed here because it gives a better fit to the UO_2 data than the Maxwell-Euken factor used for PuO_2. Its purpose in Equation (A-2.1) is to normalize the data to 95% of theoretical density.

The constants K_1 and K_2 in Equation (A-2.1a) which yield the smallest standard deviation with respect to the data are 40.4 and 464, respectively. To obtain agreement between the high ($T > 1650^{o}C$) and low ($T < 1650^{o}C$) temperature portions of the curve, K_5 must then have a value of 0.0191 W/(cm·K). Only K_3 and K_4 then remain to be evaluated. However, K_3 and K_4 do have some effect on the low temperature curve, especially above $500^{o}C$. Therefore, the choice of these constants must not disturb the previously found good fit for $T < 1650^{o}C$ and must also give a good fit for $1650^{o}C < T < 2840^{o}C$. K_3 and K_4 may be evaluated by integrating Equations (A-2.1a) and (A-2.1b) from $0^{o}C$ to the melting point, T_m, by assuming a value for this integral and solving the resulting equation numerically. An outline of this procedure is:

$$INT \equiv \int_{0°C}^{T_m} k\,dT = \int_{0°C}^{1650°C} \frac{40.4}{464 + T}\,dT + \int_{1650°C}^{T_m} 0.0191\,dT + \int_{0°C}^{T_m} K_3 \exp K_4 T \qquad \text{(A-2.4a)}$$

or

$$\frac{K_3}{K_4}\left[\exp\left(K_4\ 2840\right) - 1\right] = INT - 83.99. \qquad \text{(A-2.4b)}$$

Even knowing the value of INT, Equation (A-2.4b) alone is not sufficient to solve for K_3 and K_4. The necessary second equation is obtained from the observation that for $T < 1650^{o}C$, the data show no significant deviation from the hyperbolic part of Equation (A-2.1a) $[K_1 (K_2 + T)^{-1}]$. Since these data are accurate to ±5% at $1500^{o}C$, the electronic contribution (k_e) to the thermal conductivity is ≤ 0.002 W/(cm·K). If

$k_e < 0.002$ W/(cm·K) at 1500°C, then the fit for $T < 1650$°C is disturbed, as shown in Figure A-2.4. This being inadmissable, 0.002 W/(cm·K) is chosen for k_e at 1500°C, and another equation in K_3 and K_4 is obtained:

$$0.002 \text{ W/(cm·K)} = K_3 \exp (K_4\ 1500). \qquad \text{(A-2.5)}$$

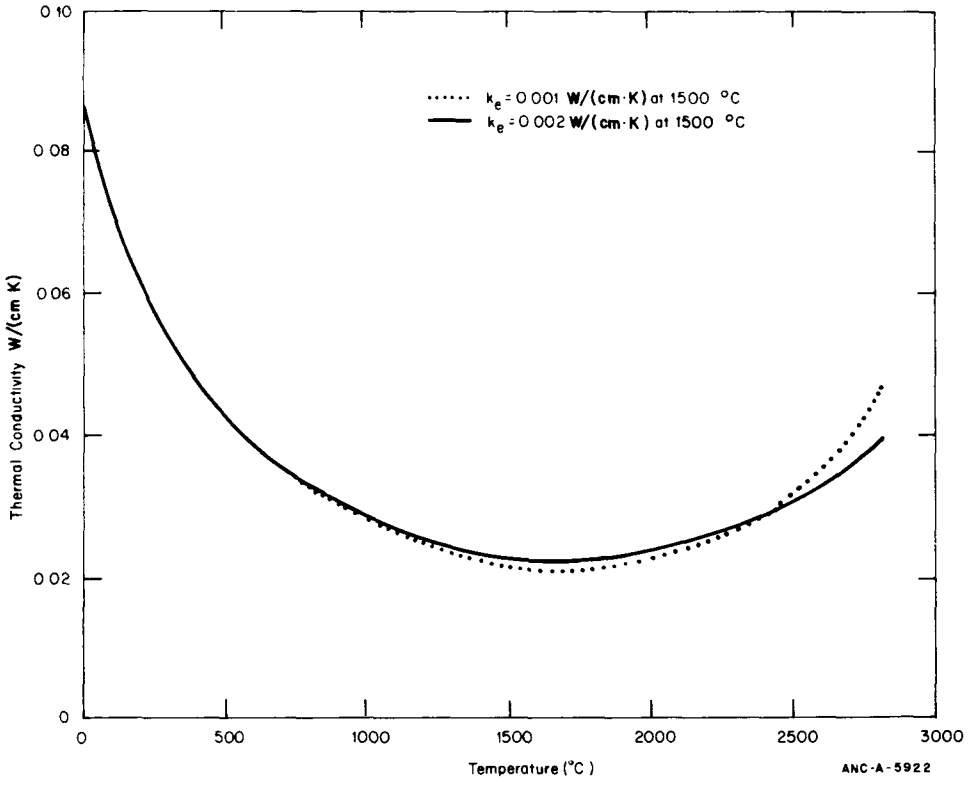

Fig. A-2.4 The effect of varying the assumed value for the electronic contribution, k_e, on the calculated thermal conductivity of 95% TD UO_2 with $\int k dt = 96$.

The exponential term in Equations (A-2.1) and (A-2.4) has been used in preference to other forms because it is of the same general form as the theoretical equation for the temperature dependence of the density of conduction band electrons, and the contribution to K from these electrons should become important at high temperatures.

The consequences of employing Equations (A-2.1), (A-2.4), and (A-2.5) for different values of $\int k dT$ are shown in Figures A-2.5 and A-2.6. Figure A-2.5 shows the sensitivity of k(T) under the above assumptions for values of the integral ranging from 93 to 98 W/cm. Figure A-2.6 indicates the standard deviation of such curves with respect to the experimental data shown in Figure A-2.1 for temperatures greater than 1650°C. The value of INT giving the smallest standard deviation is:

$$\int_{0^\circ C}^{T_m} k dT = 97 \text{ W/cm}. \qquad \text{(A-2.6)}$$

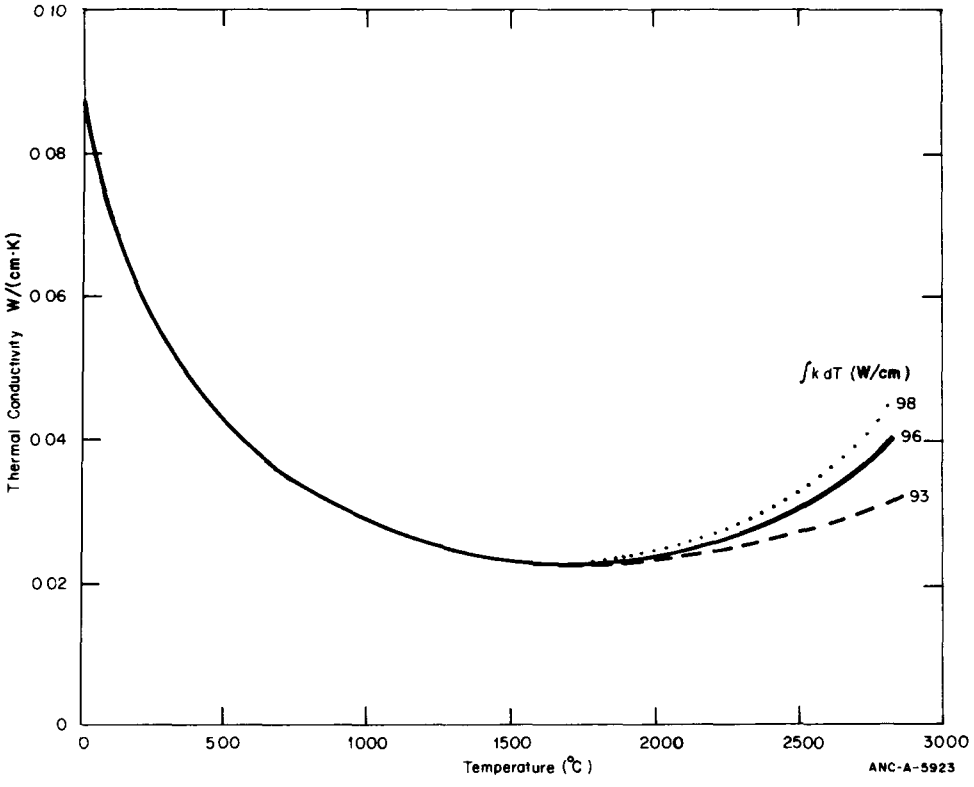

Fig. A-2.5 The effect of varying the assumed value for $\int_{0^o}^{T_m} k\,dt$ on the calculated thermal conductivity of 95% TD UO_2 with k_e held constant at 0.002 W/(cm·K).

The values of K_3 and K_4 resulting from different assumed values of the conductivity integral of the electronic contribution are shown in Table A-2.II.

(2) $\underline{(U,Pu)O_2}$ Fuel. Equations of the same form as Equations (A-2.1a) and (A-2.1b) can be employed to fit the data base for mixed oxides. The hyperbolic temperature dependence of k shown in Equation (A-2.7a) was reported to be valid to at least 1200°C by all the investigators except by Craeynest et al who reported an upper limit of 1000°C on Equation (A-2.7a). The thermal conductivity for mixed oxides can then be represented by Equations (A-2.7a) and (A-2.7b) for 96% TD using the Euken-Maxwell porosity correction factor:

for $0 < T \leq 1550^oC$:

$$k = \left(\frac{D}{1 + B\,(1-D)}\right)\left(\frac{1 + B \times 0.04}{0.96}\right)\left[\frac{33}{375 + T} + \left(1.54 \times 10^{-4} \exp(1.71 \times 10^{-3}\, T)\right)\right] \qquad \text{(A-2.7a)}$$

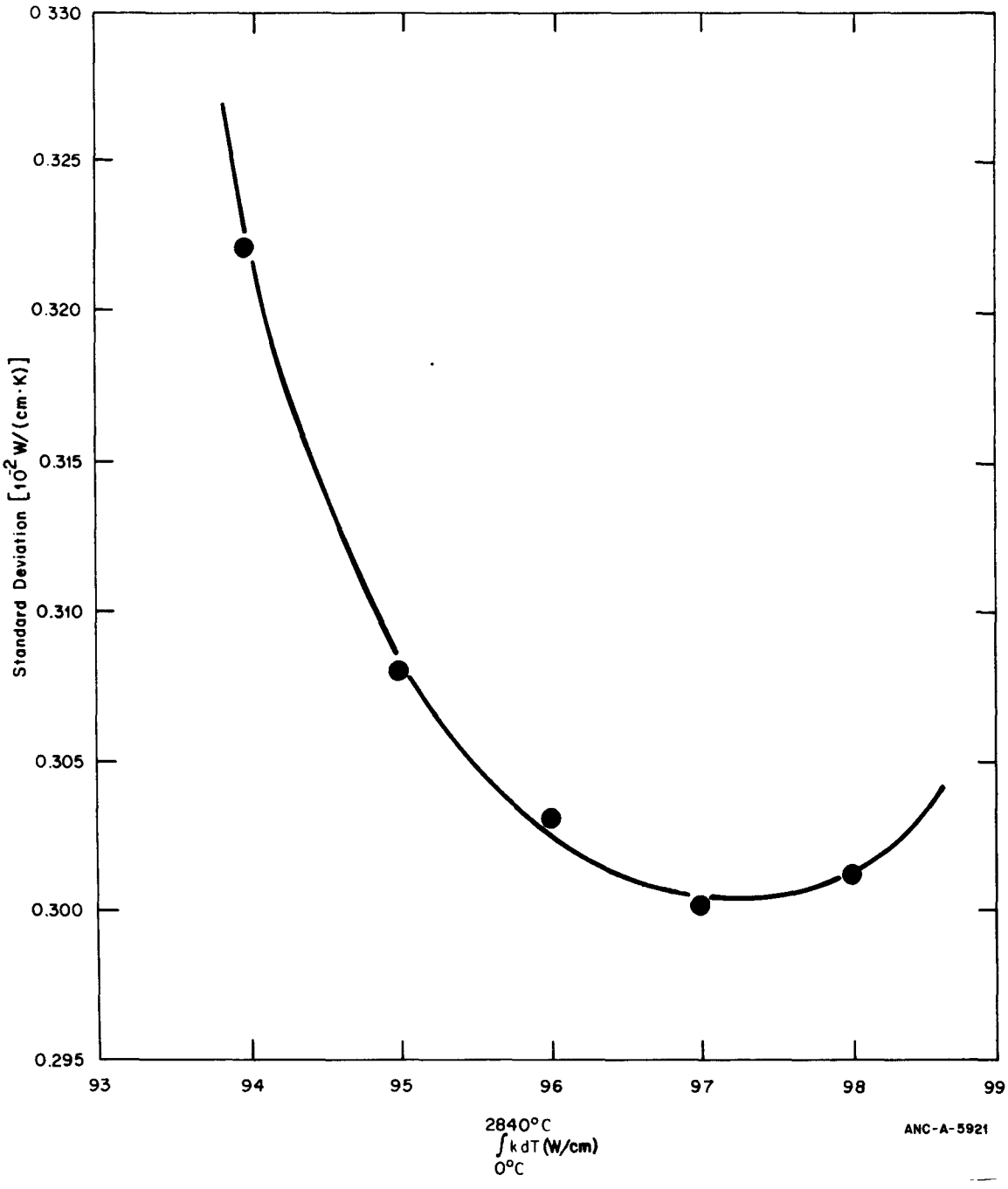

Fig. A-2.6 The standard deviation of the calculated UO_2 thermal conductivity from the data base as a function of the assumed value of the conductivity integral.

for $1550 < T < 2840^{\circ}C$:

$$k = \left(\frac{D}{1 + B\,(1-D)}\right)\left(\frac{1 + B \times 0.04}{0.96}\right)\left[0.0171 + \left(1.54 \times 10^{-4} \exp(1.71 \times 10^{-3}\,T)\right)\right] \qquad \text{(A-2.7b)}$$

TABLE A-2.II

THE EFFECT OF DIFFERENT ASSUMPTIONS ON
THE CALCULATED VALUES OF K_3 AND K_4 IN EQUATION (A-2.1) FOR UO_2

$\int k dT$	K_3	K_4	k_e at 1500°C W/(cm·K)
93	2.535×10^{-4}	1.377×10^{-3}	0.002
94	2.024×10^{-4}	1.627×10^{-3}	0.002
95	1.668×10^{-4}	1.656×10^{-3}	0.002
96	1.412×10^{-4}	1.767×10^{-3}	0.002
96	2.116×10^{-5}	2.555×10^{-3}	0.001
97	1.216×10^{-4}	1.867×10^{-3}	0.002
98	1.064×10^{-4}	1.956×10^{-3}	0.002

where

T = temperature (°C)

B = 1.43

D = the fraction of the theoretical density.

The experimental data, normalized to 96% TD and using the Eucken-Maxwell relation is compared with Equations (A-2.7a) and (A-2.7b) in Figure A-2.2. The data are from six sources[A-2.5, A-2.17, A-2.18, A-2.25 - A-2.27], comprising a total of 234 data. The standard deviation of the data from the curve, estimated on the basis of the number of points which should lie beyond one standard deviation on the graph, was 0.004 W/(cm·K). This is given to only one significant figure because of the widely varying plutonia contents in the data base and the scarcity of higher temperature data.

2.3.2 Derivatives of the Thermal Conductivity Expressions. In some fuel rod analyses, the derivative of the thermal conductivity with respect to temperature is required. These derivatives are presented in this section and calculated in the code.

(1) Porosity Correction Factor Derivative. The Loeb porosity factor used for UO_2 is temperature dependent, whereas the Euken-Maxwell factor used for $(U,Pu)O_2$ is not. The derivative of the Loeb factor is

$$\frac{dP}{dT} = \frac{0.58 \times 10^{-3}}{1-\beta(0.05)} \left[(1-D) - 0.05 \left(\frac{1-\beta(1-D)}{1-\beta(0.05)}\right)\right] \quad \text{(A-2.8)}$$

where P, β, and D are previously defined in Equation (A-2.3).

(2) Thermal Conductivity Derivatives. For UO_2 and PuO_2 the derivatives of the thermal conductivity have the same form

for UO_2, $0 < T < 1650^oC$

and for

PuO_2, $0 < T < 1550^oC$

$$\frac{dk}{dT} = k \frac{dP}{dT} + P \left[\frac{-K_1}{(K_2+T)^2} + K_3 K_4 \exp(K_4 T)\right] \quad \text{(A-2.9)}$$

and

for UO_2, $T > 1650^oC$

and for

PuO_2, $T > 1550^oC$

$$\frac{dk}{dT} = \frac{dP}{dT} k + P \left[K_3 K_4 \exp(K_4 T)\right] \quad \text{(A-2.10)}$$

where the constants K_1, K_2, K_3, and K_4 are given in Table A-2.I.

The derivative $\frac{dP}{dT}$ is defined by Equation (A-2.8) for UO_2 or $\frac{dP}{dT} = 0$ for $(U,Pu)O_2$. The porosity factors themselves are found in Equations (A-2.3) and (A-2.7).

2.4 Fuel Thermal Conductivity Subcode FTHCON Listing

A listing of the FORTRAN subcode FTHCON is presented in Table A-2.III.

TABLE A-2.III

LISTING OF THE FTHCON SUBCODE

```
C
C
      SUBROUTINE FTHCON(FTEMP, FRADEN, CON, DKDT)
C
C     FTHCON CALCULATES THE FUEL THERMAL CONDUCTIVITY AND ITS
C     DERIVATIVE WITH RESPECT TO TEMPERATURE AS A FUNCTION OF
C     TEMPERATURE,FRACTIONAL DENSITY, AND COMPOSITION.
C
C     CON    = OUTPUT FUEL THERMAL CONDUCTIVITY (W/M-K)
C     DKDT   = OUTPUT DERIVATIVE OF FUEL THERMAL CONDUCTIVITY WITH
C              RESPECT TO TEMPERATURE (W/(M*K*K))
C
C     FTEMP  = INPUT FUEL TEMPERATURE (K)
C     FRADEN = INPUT FRACTIONAL FUEL DENSITY
C                (RATIO OF ACTUAL DENSITY TO THEORETICAL DENSITY).
C
C     FTHCON WAS ORIGINALLY CODED BY C.S. OLSEN  FEB 1975
C     LAST MODIFIED BY G.A. REYMANN  AUGUST 1978.
C
      COMMON  /PHYPRO   / FTMELT,FHEFUS,CTMELT,CHEFUS,CTRANB,
     #                    CTRANE,CTRANZ,FDELTA,BU    ,COMP
C
      COMMON  /LACMDL/  MAXIDX,EMFLAG
      DIMENSION EMFLAG(1)
      DATA      ON      / 2HON    /,
     #          OFF     / 3HOFF   /,
     #          LOCIDX  / 12      /
C
      POROS1(D,B) = (1.0 - B*(1.0-D))/(1.0 - .05*B)
      UTCON1(T) = 40.47/(464. + T) + 1.216E-4* EXP(1.867E-3*T)
      UTCON2(T) = .0191 + 1.216E-4* EXP(1.867E-3*T)
C
      DPDT(D,T) = 0.56E-03*(1.-D)/(0.871+0.29E-04*T) - (1.-(1.-D)*
     #            (2.58 - .58E-03*T))*0.29E-04/(0.871+0.29E-04*T)**2
      DUKDT1(T) = 2.27E-07*EXP(1.867E-03*T) - 40.4/(464.+T)**2
      DUKDT2(T) = 2.27E-07*EXP(1.867E-03*T)
C        DPDT   = DERIVATIVE OF POROSITY FACTOR WITH RESPECT TO TEMP.
C        DUKDT1 = DERIVATIVE OF UTCON1 WITH RESPECT TO TEMPERATURE
C        DUKDT2 = DERIVATIVE OF UTCON2 WITH RESPECT TO TEMPERATURE
C
C     THE THERMAL CONDUCTIVITY CORRELATION  FOR MIXED OXIDES WAS BASED
C     ON STOICHIOMETRIC MIXED OXIDE DATA CONTAINING 5 TO 30% PUO2.
C
      POROS2(D,B) = D/(1.0 + B*(1.0-D))*(1.0 + .04*B)/0.96
      PTCON1(T) = 33./(375.+T) + 1.54E-4* EXP(1.71E-3*T)
      PTCON2(T) = 0.0171 + 1.54E-4* EXP(1.71E-3*T)
C
      DPKDT1(T) = 2.633E-07*EXP(1.71E-03*T) - 33./(375.+T)**2
      DPKDT2(T) = 2.633E-07*EXP(1.71E-03*T)
C        DPKDT1 = DERIVATIVE OF PTCON1 WITH RESPECT TO TEMPERATURE
C        DPKDT2 = DERIVATIVE OF PTCON2 WITH RESPECT TO TEMPERATURE
C
      IF(EMFLAG(LOCIDX).EQ.ON) GO TO 90
      TM1 = FTMELT
      T1  = FTEMP - 273.15
      D1  = FRADEN
C
      IF (T1 .GT. (TM1-273.15)) GO TO 30
   10 IF (COMP .GT. 0.0) GO TO 15
C
      B1 = 2.58 - 0.58E-3*T1
      IF (T1 .GT. 1650) GO TO  11
      CON = UTCON1(T1) *POROS1(D1,B1) * 100.0
      DKDT= (DPDT(D1,T1)*UTCON1(T1)+POROS1(D1,B1)*DUKDT1(T1))*100.
      GO TO 100
C
   11 CON = UTCON2(T1) *POROS1(D1,B1) * 100.0
      DKDT= (DPDT(D1,T1)*UTCON2(T1)+POROS1(D1,B1)*DUKDT2(T1))*100.
      GO TO 100
C
   15 B1 = 1.43
      IF (T1 .GT. 1550.) GO TO 16
      CON = PTCON1(T1) * POROS2(D1,B1) * 100.0
      DKDT= POROS2(D1,B1)*DPKDT1(T1)*100.
      GO TO 100
```

TABLE A-2.III (continued)

```
C
   16 CON = PTCON2(T1) * POROS2(D1,B1) * 100.0
      DKDT= POROS2(D1,B1)*DPKDT2(T1)*100.
      GO TO 100
C
   30 A2 = TM1 - 273.15
      IF (COMP .GT. 0.0) GO TO 31
      B1 = 2.4153
      CON = UTCON2(A2) * POROS1(9.124E-1,B1)* 100.0
      DKDT= POROS1(.9124,B1)*DUKDT2(A2)*100.
      GO TO 100
C
   31 B1 = 1.43
      CON = PTCON2(A2) * POROS2(9.124E-1,B1) * 100.0
      DKDT= POROS2(.9124,B1)*DPKDT2(A2)*100.
      GO TO 100
C
   90 CALL EMFTJN(FTEMP,FRADEN,FTMELT,CON,DKDT)
  100 CONTINUE
      RETURN
      END
```

2.5 References

A-2.1. J. C. Hedge, *Measurement of Thermal Conductivity of Uranium Oxide,* AECU-3881, Armour Research Foundation of Illinois Institute of Technology (September 20, 1956).

A-2.2. W. D. Kingery et al, "Thermal Conductivity X: Data for Several Pure Oxide Materials Corrected to Zero Porosity," *Journal of the American Ceramic Society, 37* (1954) p 107.

A-2.3. L. A. Goldsmith and J. A. M. Douglas, *Measurements of the Thermal Conductivity of Uranium Dioxide at 670-1,270°K,* TRG Department 2103 Reactor Development Laboratory Windscale (1971).

A-2.4. J. C. Van Craeynest and Jean Pierre Stora, "Effect de la Porosite sur la Variation de Conductibilite Thermique du Bioxyde d'Uranium en Fonction de la Temperature," *Journal of Nuclear Materials, 37* (1970) p 153.

A-2.5. F. J. Hetzler et al, *The Thermal Conductivity of Uranium and Uranium-Plutonium Oxides,* GEAP-4879 (August 1967).

A-2.6. T. G. Godfrey et al, *Thermal Conductivity of Uranium Dioxide and Armco Iron by an Improved Radial Heat Flow Technique,* ORNL-3556 (June 1964).

A-2.7. J. Lambert Bates, *High Temperature Thermal Conductivity of "Round Robin" Uranium Dioxide,* BNWL-1431 (July 1970).

A-2.8. C. F. Lucks and H. W. Deem, "Thermal Conductivity and Electrical Conductivity of UO_2," *Progress Relating to Civilian Applications During June 1960,* BMI-1448 (July 1, 1960).

A-2.9. J. A. Christensen et al, "Uranium Dioxide Thermal Conductivity," *Transactions of the American Nuclear Society, 7* (1964) p 391.

A-2.10. M. F. Lyons et al, *UO_2 Pellet Thermal Conductivity from Irradiations with Central Melting,* GEAP-4624 (July 1964).

A-2.11. R. D. Reiswig, "Thermal Conductivity of UO_2 to 2,100°C," *Journal of the American Ceramic Society, 44* (1961) p 48.

A-2.12. G. Fayl and K. Hansen, *In-Reactor Determination of the Thermal Conductivity of UO_2-Pellets up to 2,200°C,* RISO Department 269, Danish Atomic Energy Commission Research Establishment RISO, (July 1972).

A-2.13. J. Stora et al, *Thermal Conductivity of Sintered Uranium Oxide Under In-Pile Conditions,* EURAEC 1095 (CEA-R 2586) (August 1964).

A-2.14. A. L. Loeb, "Thermal Conductivity: A Theory of Thermal Conductivity of Porous Materials," *Journal of the American Ceramic Society, 37* (1954) p 96.

A-2.15. J. R. MacEwan, R. L. Stoute, M. F. Notley, "Effect of Porosity of the Thermal Conductivity of UO_2," *Journal of Nuclear Materials, 24* (1967) p 109.

A-2.16. M. Serizawa et al, "Thermal Diffusivity and Thermal Conductivity of Uranium-Plutonium Dioxide," *Journal of Nuclear Materials, 34* (1970) p 224.

A-2.17. R. L. Gibby, "The Effect of Plutonium Content on the Thermal Conductivity of $(U,Pu)O_2$ Solid Solutions," *Journal of Nuclear Materials, 38* (1971) pp 163-177.

A-2.18. L. A. Goldsmith and J. A. M. Douglas, "The Thermal Conductivity of Plutonium-Uranium Dioxide at Temperatures up to 1,273K," *Journal of Nuclear Materials, 43* (1972) p 225.

A-2.19. J. C. Van Craeynest and J. C. Weilbacher, "Etude de la Conductibility Thermique des Oxides Mixed d'Uranium et de Plutonium," *Journal of Nuclear Materials, 26* (1968) pp 132-136.

A-2.20. H. E. Schmidt, "Die Waermeleitfaehigkeit von Uran und Uran-Plutonium Dioxyd bei Hohen Temperaturen," *Forschung, Ingenieur-Wesen, 38* (1972) pp 149-151.

A-2.21. T. G. Kollie et al, "A Thermal Comparator Method for Thermal Conductivity Measurements from 50 to 400°C," *International Symposium Compounds of Interest, Nuclear Metallurgy, Volume X,* IMD Special Report Series 13.

A-2.22. A. D. Feith, "Thermal Conductivity of Several Ceramic Materials to 2,500°C," *Proceedings 4th Conference Thermal Conductivity (October 1964) IV-C1-IV-C-17.*

A-2.23. A. M. Ross, *The Dependence of the Thermal Conductivity of Uranium Dioxide on Density, Microstructure, Stoichiometry and Thermal Neutron Irradiation,* CRFD-817, AECL-1096 (1960).

A-2.24. V. C. Howard and T. F. Gulvin, *Thermal Conductivity Determinations on Uranium Dioxide by a Radial Flow Method,* U.K.A.E.A. IG Report 51 (Rd/c) (1960).

A-2.25. R. L. Gibby, *The Thermal Diffusivity and Thermal Conductivity of Stoichiometrics* $(U_{0.8}\,Pu_{0.2})\,O_2$, BNWL-704 (May 1968).

A-2.26. R. L. Gibby, *The Effect of Oxygen Stoichiometry on the Thermal Diffusivity and Conductivity of* $U_{0.75}\,Pu_{0.25}\,O_{2-x}$, BNWL-927 (January 1969).

A-2.27. H. E. Schmidt, "Die Waermeleitfaehigkeit von Uran and Uran-Plutonium Dioxyd bei Hohen Temperaturen," *High Temperatures – High Pressure, 3* (1971) p 345.

3. FUEL EMISSIVITY (FEMISS)

(R. E. Mason)

This function returns a value for the spectral emissivity of uranium dioxide at a given temperature. The only argument of the function is FTEMP, the fuel temperature at which the emissivity is required.

3.1 Summary

The spectral emissivity of light water reactor fuel is modeled as a linear function of temperature between 1000 and 2050 K. Outside this range, the emissivity is assumed to be independent of temperature.

The emissivity (e) is defined as follows:

$$T < 1000\ K, \qquad e = 0.8707$$

$$1000\ K \leq T \leq 2050\ K, \qquad e = 1.311 - 4.404 \times 10^{-4}\ T$$

$$T > 2050\ K, \qquad e = 0.4083$$

where

T = temperature of the fuel (K).

This representation is justified on the basis of a statistical evaluation of the measured values.

3.2 Experimental Data

The measured values of spectral emissivity using nonpolished UO_2 specimens obtained by Claudson[A-3.1] as reported by Belle[A-3.2] are shown in Table A-3.I.

TABLE A-3.I

SPECTRAL EMISSIVITY OF UO_2 AS MEASURED BY CLAUDSON[A-3.1]

Temperature (K)	Emissivity (unitless)
1000	0.850
1320	0.798
1593	0.628
1755	0.510
1795	0.515
1853	0.417
1920	0.402
1955	0.484
2053	0.446
2220	0.370

The one standard deviation uncertainty in Claudson's data is estimated to be about 10% based on the scatter in the values.

Ehlert and Margrave reported several values for the spectral emissivity at 650 nanometers of a polished solid UO_2 surface[A-3.3]. These results are given in Table A-3.II. The reported uncertainty is about 5%.

The following conclusions are relevant:

(1) The accuracy of the Claudson data is on the order of 10%

(2) Spectral emissivity monotonically decreases as temperature increases

TABLE A-3.II

SPECTRAL EMISSIVITY OF UO_2 AS MEASURED BY EHLERT AND MARGRAVE [A-3.3]

Temperature (K)	Emissivity
2073 - 2373	0.40 ± 0.02
3000 - 3100	0.416 ± 0.026

(3) The spectral emissivity of 0.4 in the temperature range $2073 < T < 2373$ K obtained by Ehlert and Margrave is consistent with the Claudson data.

3.3 Selection of Emissivity Values

The data of Claudson are used from 1000 K to approximately 2000 K. Above 2000 K the mean value of the Ehlert-Margrave data is used, namely 0.408. Also, since no data are available below 1000 K, where the spectral emissivity is difficult to measure, a constant value consistent with Claudson's data is chosen.

First, second, and third degree polynomials were generated by least-square fitting Claudson's data. These results are compared with the measured values in Figure A-3.1. The calculated standard deviation for each of the approximations is given in Table A-3.III.

These standard deviations indicate only how closely the fitting polynomial approximates the measured values and do not take into account the error associated with each data point. Recognizing the 10% error, the linear fit is statistically adequate. Any higher order fit attributes unrealistic accuracy to the data set.

The equation describing the data is of the form $y = a + bT$. The computed coefficients are

$$a = 1.31107$$

$$b = 4.40374 \times 10^{-4}.$$

This equation is used in the range $1000 \leqslant T \leqslant 2050$ K.

The lower temperature limit is taken as the lowest temperature at which a measured value was reported by Claudson. Below 1000 K, the emissivity is assumed to be independent of temperature. The constant value is the calculated value at 1000 K, namely 0.8707.

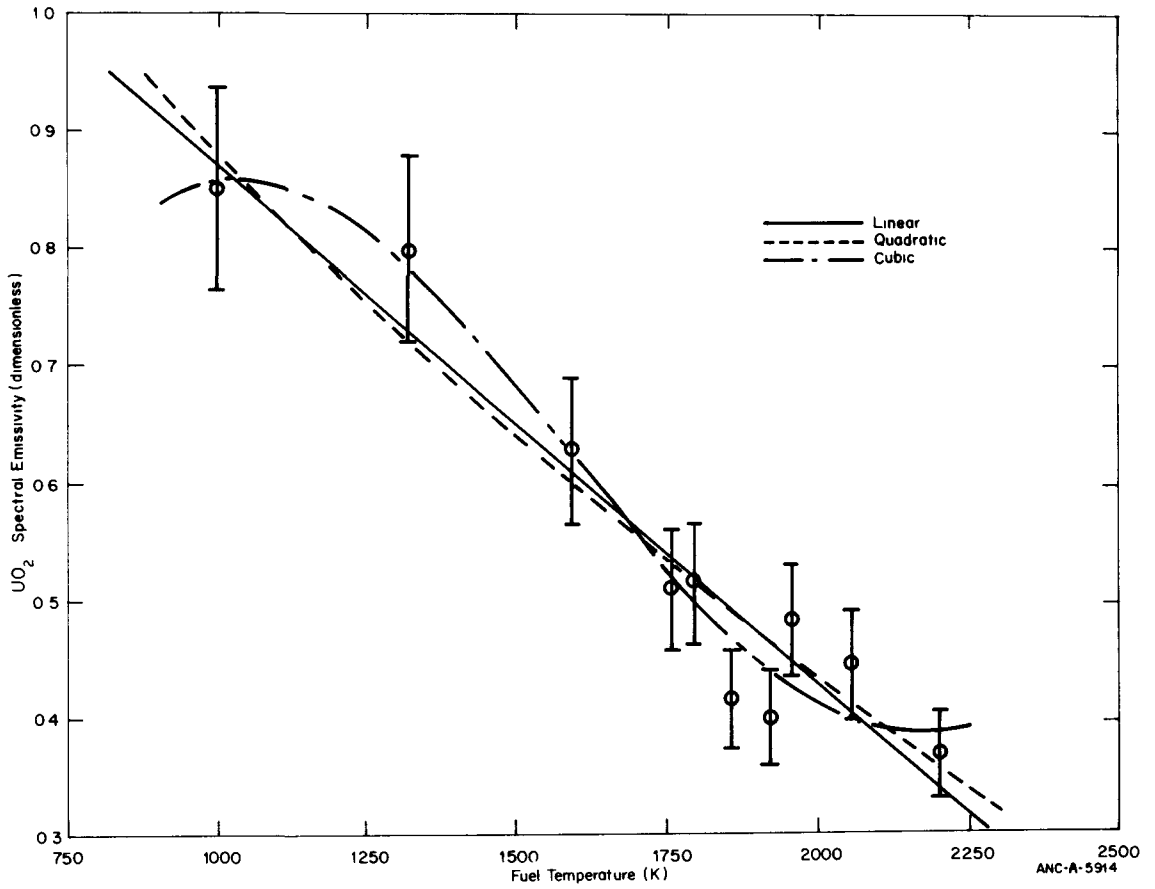

Fig. A-3.1 Comparison of fitting polynomials with emissivity data of Claudson.

TABLE A-3.III

STANDARD DEVIATION FOR THE LEAST-SQUARES APPROXIMATIONS TO CLAUDSON'S DATA

Degree	Standard Deviation
1	0.0505
2	0.0529
3	0.0432

The upper temperature limit was chosen as 2050 K since evaluation of the linear function at that temperature gives a value of 0.4083 for the emissivity, consistent with the Ehlert-Margrave high temperature data point as discussed previously. This value, 0.4083, is used for temperatures above 2050 K.

The emissivity is plotted as a function of temperature in Figure A-3.2 over the range $500 < T < 2300$ K. The importance of emissivity in fuel rod behavior analysis is to specify the radiant heat transfer contribution across the fuel-cladding gap. Typical calculated fuel surface temperatures, including those from transient analyses, fall in the range from 800 to 2000 K.

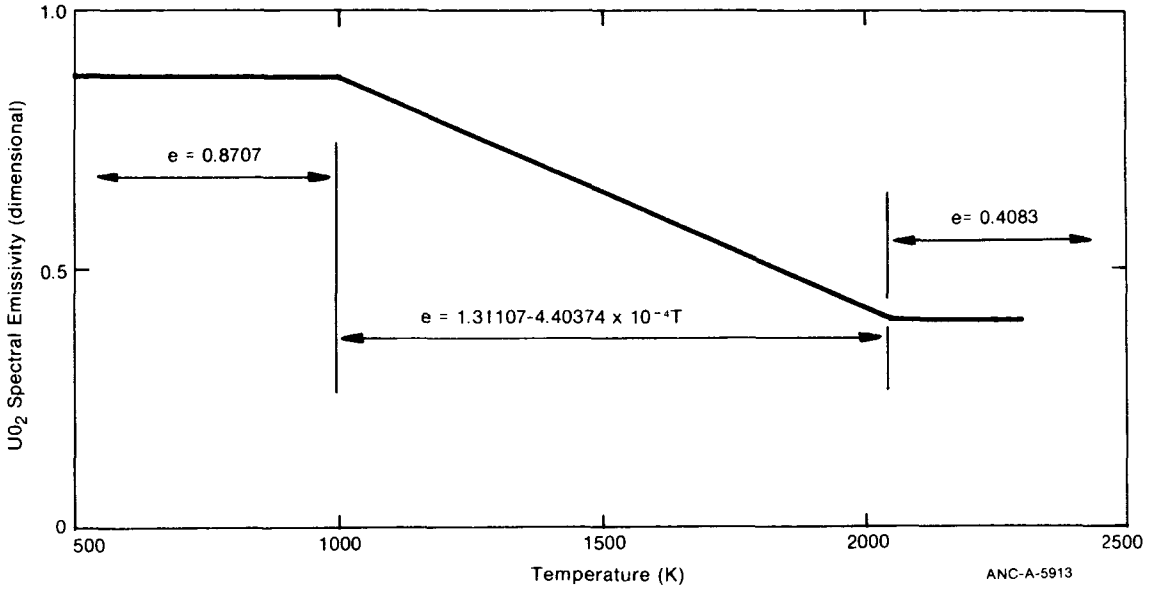

Fig. A-3.2 FEMISS representation of UO_2 emissivity.

3.4 Fuel Emissivity Subcode FEMISS Listing

A listing of the FEMISS subcode is given in Table A-3.IV.

3.5 References

A-3.1. T. T. Claudson, "Emissivity Data for Uranium Dioxide," HW-55414 (November 5, 1958).

A-3.2. J. Belle (ed.), *Uranium Dioxide: Properties and Nuclear Applications*, TID-7546, U.S. Government Printing Office, Washington, D.C. (1961).

A-3.3. T. C. Ehlert and J. L. Margrave, "Melting Point and Spectral Emissivity of Uranium Dioxide," *Journal of the American Ceramic Society, 41* (1958) p 330.

TABLE A-3.IV

LISTING OF THE FEMISS SUBCODE

```
C
C
      FUNCTION FEMISS(FTEMP)
C
C     FEMISS CALCULATES FUEL EMISSIVITY AS A FUNCTION OF TEMPERATURE.
C
C     FEMISS = OUTPUT FUEL EMISSIVITY (UNITLESS)
C     FTEMP  = INPUT FUEL TEMPERATURE (K)
C
C     THE EMISSIVITY IS GIVEN AS A LINEAR FUNCTION OF TEMPERATURE
C     IN DEGREES KELVIN BETWEEN 1000 AND 2050 K . THE COEFFICIENTS
C     WERE DETERMINED BY A LEAST SQUARE FIT TO THE DATA OF CLAUDSON
C     AS GIVEN IN "URANIUM DIOXIDE: PROPERTIES AND NUCLEAR
C     APPLICATIONS," J. BELLE, ED., USAEC, 1961, P 197
C     BELOW 1000 K AND ABOVE 2050 K THE EMISSIVITY IS ASSUMED CONSTANT.
C
C     FEMISS WAS CODED BY V.F. BASTON IN MARCH 1974.
C     LAST MODIFIED BY W.P. STEPHANY  FEB 1976.
C
      COMMON       / LACEMDL    / MAXIDX, EMFLAG
      DIMENSION EMFLAG(1)
      DATA          ON         / 2HON                /,
     #              OFF        / 3HOFF               /,
     #              LOCIDX     /  10                 /
C
      DATA            A        /  1.31107            /,
     #                B        / -4.4037E-4          /,
     #                E1       /  0.8707             /,
     #                E2       /  0.4083             /,
     #                T1       /    1000.0           /,
     #                T2       /    2050.0           /
C
       IF ( EMFLAG(LOCIDX) .EQ. ON ) GO TO 20
C
      T = FTEMP
      FEMISS = A + B*T
      IF(T .LT. T1) FEMISS = E1
      IF(T .GT. T2) FEMISS = E2
      GO TO 100
   20 FEMISS  = EMFESS ( FTEMP)
C
  100 RETURN
      END
```

4. FUEL THERMAL EXPANSION (FTHEXP)

(C. S. Olsen)

A fuel thermal expansion model is required to predict changes in pellet geometry due to changes in temperature. Linear thermal expansion models have been developed for both UO_2 and $(U,Pu)O_2$ fuel. The models used in FTHEXP include expansion in the solid phase, expansion due to the phase change at the melting point, and expansion in the liquid phase as a function of temperature and liquid fraction.

4.1 UO_2 Thermal Expansion

Linear thermal expansion data for unirradiated UO_2 have been published by Burdick and Parker[A-4.1], Conway et al[A-4.2, A-4.3], Christensen[A-4.4], and Hoch and Momin[A-4.5]. Belle[A-4.6] also reports data from Lambertson and Handwerk[A-4.7],

Bell and Makin[A-4.8], and Murray and Thackray[A-4.9]. These sets of data are generally consistent although Christensen reported slightly lower values at temperatures below 2000°C. The effect of irradiation on UO_2 thermal expansion is usually assumed to be negligible. However, no experimental data are available to support this assumption. In-pile fuel thermal expansion is uncertain because accurate descriptions of fuel cracking (resulting from thermal stresses) and healing are not available.

4.1.1 UO_2 Solid Phase. The data between 1000 and 2250°C presented by Conway et al[A-4.2] and the low temperature data of Burdick and Parker[A-4.1], Lambertson and Handwerk[A-4.7], Bell and Makin[A-4.8], and Murray and Thackray[A-4.9] for the solid phase are fitted by regression analysis to the third-order polynomial.

$$\frac{\Delta L}{L} = -4.972 \times 10^{-4} + 7.107 \times 10^{-6} T + 2.581 \times 10^{-9} T^2 + 1.140 \times 10^{-13} T^3 \quad \text{(A-4.1)}$$

for $0^{\circ}C < T < T_m$

where

$\frac{\Delta L}{L}$ = fractional linear thermal expansion

T = temperature (°C)

T_m = melting temperature of fuel (°C).

The melting point of the fuel is a function of burnup and plutonia content and is found using the subroutine PHYPRO (Appendix D, Section 1).

4.1.2 UO_2 Phase Change at Melting Point. The data of Christensen are used for the thermal expansion due to the phase change at the melting point. Uniform expansion is assumed. The resulting correlation is expressed by Equation (A-4.2).

$$\frac{\Delta L}{L} = \frac{\Delta L}{L}(T_m) + 3.096 \times 10^{-2} R \quad \text{(A-4.2)}$$

for $T > T_m$

where

$\frac{\Delta L}{L}(T_m)$ = the fractional linear thermal expansion given by Equation (A-4.1) with T equal to T_m

R = fraction of molten fuel.

4.1.3 UO_2 Liquid Phase. The coefficient of expansion presented by Christensen is used for the liquid phase. The resulting correlation is

$$\frac{\Delta L}{L} = \frac{\Delta L}{L}(T_m) + 3.096 \times 10^{-2} + 3.5 \times 10^{-5}(T - T_m) \qquad \text{(A-4.3)}$$

for $T > T_m$.

This correlation and those for the solid and phase change regimes are shown in Figure A-4.1, superimposed upon the data for the solid phase.

4.2 $(U,Pu)O_2$ Thermal Expansion

Linear thermal expansion data for solid unirradiated PuO_2 have been published by Tokar et al[A-4.10] and by Brett and Russell[A-4.11]. These data are fit to the third-order polynomial.

$$\frac{\Delta L}{L} = -3.9735 \times 10^{-4} + 8.4955 \times 10^{-6}T + 2.1513 \times 10^{-9}T^2 + 3.7143 \times 10^{-16}T^3 \qquad \text{(A-4.4)}$$

for $0 < T < T_m$

where $\frac{\Delta L}{L}$ and T are previously defined in Equation (A-4.1).

The expansion of solid mixed oxides is calculated from the weighted average of the expansion for UO_2 [Equation (A-4.1)] and the expansion of PuO_2 [Equation (A-4.4)].

The thermal expansion for the phase change and for the liquid phase of mixed oxides is assumed to be the same as that for UO_2 [Equations (A-4.2) and (A-4.3)] because of the similarity in structure of UO_2 and $(U,Pu)O_2$ mixed oxides.

Figure A-4.2 shows the linear expansion of PuO_2 as a function of temperature as based on the preceding correlations and the data of Tokar et al and Brett and Russell.

4.3 Fuel Thermal Expansion Subcode FTHEXP Listing

Table A-4.I is a listing of the FORTRAN subcode FTHEXP.

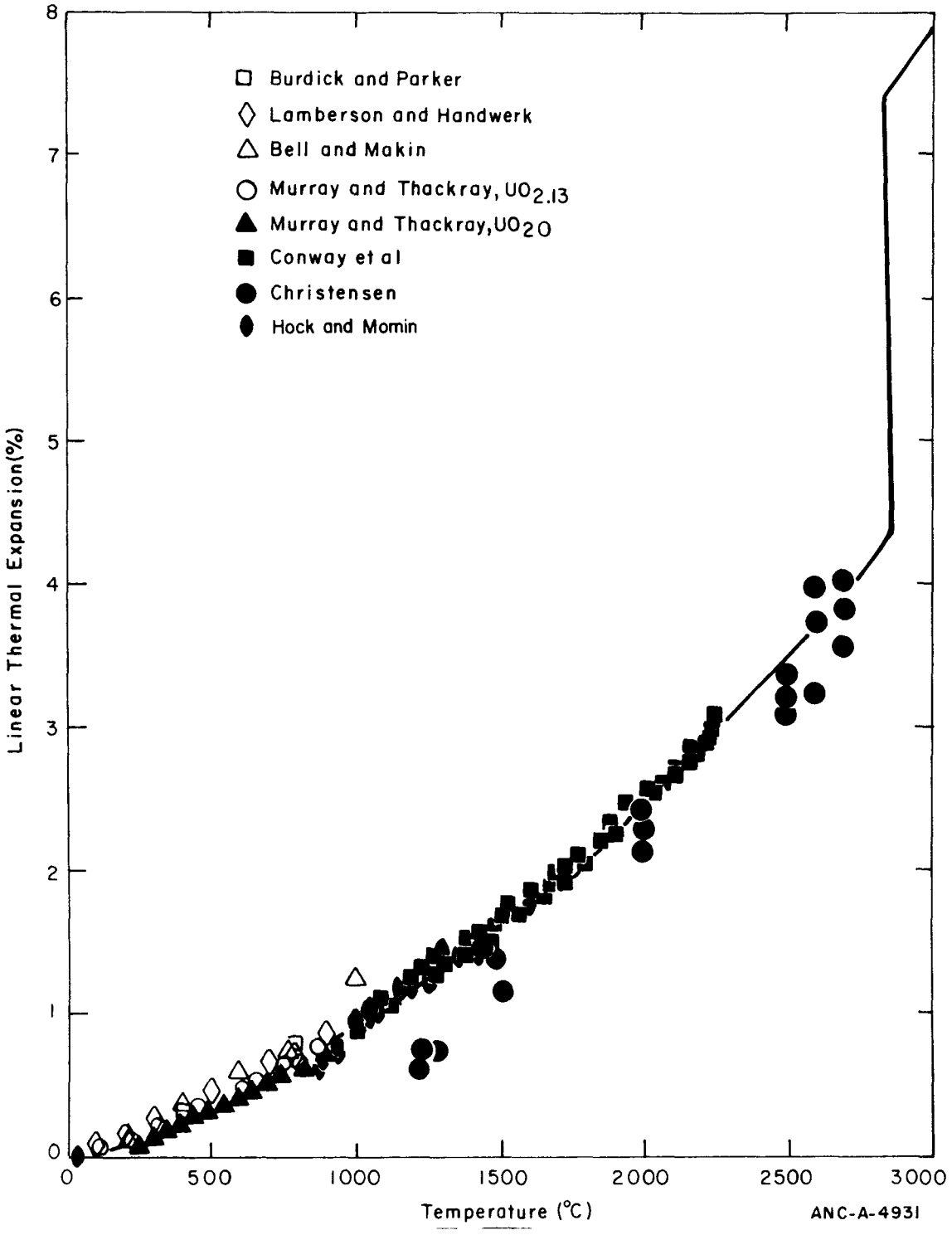

Fig. A-4.1 Comparison of UO_2 thermal expansion data with those calculated from FTHEXP subcode.

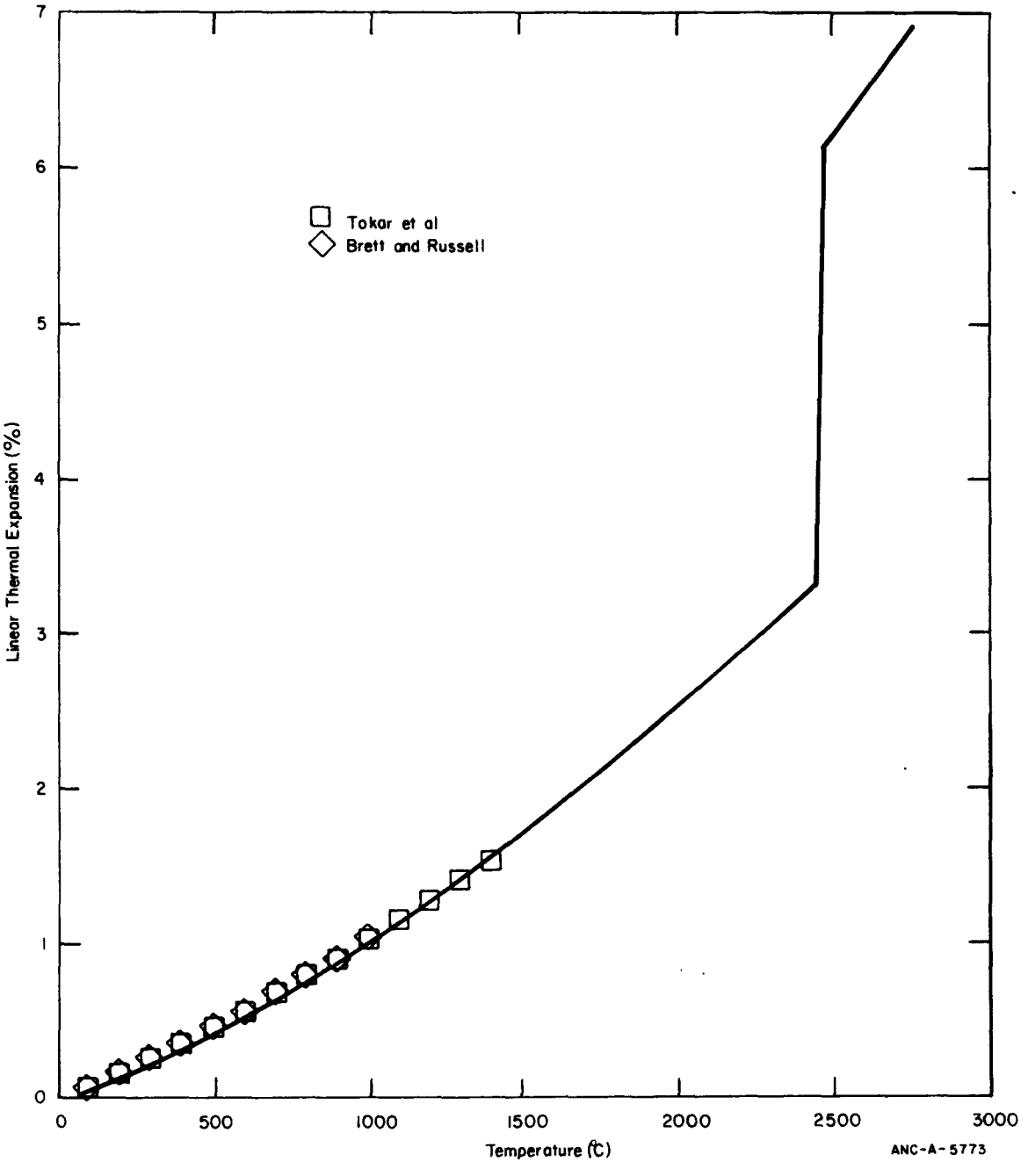

Fig. A-4.2 Comparison of PuO_2 thermal expansion data with those calculated from FTHEXP subcode.

TABLE A-4.I

LISTING OF THE FTHEXP SUBCODE

```
C
C
      FUNCTION FTHEXP(FTEMP, FACMOT)
C
C     FTHEXP CALCULATES FUEL LINEAR THERMAL EXPANSION FOR SOLID AND
C     LICUID PHASES AS A FUNCTION OF TEMPERATURE AND LIQUID FRACTION.
C
C     FTHEXP = OUTPUT FRACTIONAL FUEL THERMAL EXPANSION (UNITLESS RATIO)
C
C     FTEMP  = INPUT FUEL TEMPERATURE (K)
C     FACMOT = INPUT FUEL FRACTION MOLTEN.
C                FACMOT = 1   -   FUEL ALL MOLTEN
C                FACMOT = 0   -   FUEL ALL SOLID
C     BU     = INPUT BURNUP (MW-S/KG-U)
C     COMP   = INPUT PLUTONIA CONTENT (WEIGHT PERCENT)
C     FTMELT = FUEL MELTING TEMPERATURE (K)
C
C     THE THERMAL EXPANSION RELATIONSHIPS USED IN THIS FUNCTION ARE
C     (1) SOLID UO2 IS BASED ON DATA OF CONWAY ET AL, TRANS AMER NUCL
C     SOC, VOL 6 JUNE 1963, BELL AND MAKIN, BURDICK AND PARKER,
C     LAMBERTSON AND HANDWERK,  MURRAY AND THACKRAY, UO2 PROPERTIES,
C     EDITED BY J. BELLE.
C     CHRISTENSEN (MELTING TO 3200C), J.AMER.CERAM.SOC., 46 (DEC 1963)
C
C     THE THERMAL EXPANSION FOR SOLID PUO2 IS BASED ON DATA OF TOKAR
C     NUC. TECH., 17 (1973) P 147
C
C     FTHEXP WAS ORIGINALLY CODED BY V. F. BASTON IN MARCH 1974
C     MODIFIED BY C. S. OLSEN IN FEBRUARY 1975
C
C
      COMMON  /PHYPRO   / FTMELT,FHEFUS,CTMELT,CHEFUS,CTRANB,
     #                    CTRANE,CTRANZ,FDELTA,BU    ,COMP
C
C
      COMMON      / LACEMDL   / MAXIDX, EMFLAG
      DIMENSION EMFLAG(1)
      DATA        ON        / 2HON    /,
     #            OFF       / 3HOFF   /,
     #            LCCIDX    /   13    /
C
      DATA FDELTA / 1. /
      UEX(T) = -4.972E-4 + 7.107E-6*T + 2.581E-9*T*T + 1.140E-13*T**3
      PEX(T) = -3.9735E-4 + 8.4955E-6*T + 2.1513E-9*T*T +
     #         3.7143E-16*(T**3)
      T1 = FTEMP- 273.15
      R  = FACMOT
      C1 = COMP/100.0
C
      IF(EMFLAG(LCCIDX) .EQ. ON) GO TO 20
C
      TM = FTMELT - 273.15
      IF (T1 .LT. (TM-1.E-10)) GO TO 10
      IF (T1 .GE. (TM-1.E-10) .AND. T1 .LE. (TM+FDELTA)) GO TO 30
      IF (T1 .GE. (TM+FDELTA)) GO TO 50
   10 IF (COMP .GT. 0.0) GO TO 15
      FTHEXP = UEX(T1)
      GO TO 100
   15 FTHEXP = (1. - C1)*UEX(T1) + C1*PEX(T1)
      GO TO 100
   30 IF (COMP .GT. 0.0) GO TO 35
      FTHEXP = UEX(TM) + R*3.096E-2
      GO TO 100
   35 FTHEXP = (1. - C1)*UEX(TM) + C1*PEX(TM) + R*3.096E-2
      GO TO 100
   50 IF (COMP .GT. 0.0) GO TO 55
      FTHEXP = UEX(TM) + 3.096E-2 + (3.5E-5*(T1 - TM))
      GO TO 100
   55 FTHEXP = PEX(TM) + 3.096E-2 + (3.5E-5*(T1 - TM))
      GO TO 100
   20 FTHEXP = EMFTXP( FTEMP ,FACMOT,FTMELT)
C
  100 RETURN
      END
```

4.4 References

A-4.1. M. D. Burdick and H. S. Parker, "Effect of Particle Size on Bulk Density and Strength Properties of Uranium Dioxide Specimens," *Journal of the American Ceramic Society, 39,* (1956) p 181.

A-4.2. J. B. Conway, R. M. Fincel, Jr., R. A. Hein, "The Thermal Expansion and Heat Capacity of UO_2 to 2,200°C," *Transactions American Nuclear Society, 6,* 1 (June 1963).

A-4.3. J. B. Conway, R. M. Fincel, Jr., R. A. Hein, *The Thermal Expansion and Heat Capacity of UO_2 to 2,200°C,* TM-63-6-6, General Electric Company (1963).

A-4.4. J. A. Christensen, "Thermal Expansion and Change in Volume of Uranium Dioxide on Melting," *Journal of the American Ceramic Society, 46,* 12 (1963) p 607.

A-4.5. M. Hoch and A. C. Momin, "High Temperature Thermal Expansion of Uranium Dioxide and Thorium Dioxide," *High Temperatures – High Pressures, 1,* 4 (1969) p 401.

A-4.6. J. Belle (ed.), *Uranium Dioxide: Properties and Nuclear Applications,* TID-7546 USAEC (1961).

A-4.7. W. A. Lambertson and J. H. Handwerk, *The Fabrication and Physical Properties of Urania Bodies,* ANL-5053.(1956).

A-4.8. I. P. Bell and S. M. Makin, "Fast Reactor – Physical Properties of Materials of Construction," *Review of Progress from September 1, 1953 to April 1, 1954,* RDB(C)/TN-70 (1954).

A-4.9. P. Murray and R. W. Thackray, *The Thermal Expansion of Sintered UO_2,* AERE M/M 22 (undated).

A-4.10. M. Tokar, A. W. Nutt, T. K. Keenan, "Linear Thermal Expansion of Plutonium Dioxide," *Nuclear Technology, 17* (February 1973) p 147.

A-4.11. N. H. Brett and L. E. Russell, "The Thermal Expansion of PuO_2 and Some Other Actinide Oxides Between Room Temperature and 1,000°C," in *Plutonium 1960;* E. Grison, W. B. H. Lord, and R. D. Fowler (eds.), *Proceedings of the 2nd International Conference on Plutonium Metallurgy, Grenoble, France, April 19-22 1960,* p 397.

5. FUEL ELASTIC MODULI (FELMOD AND FPOIR)

(D. L. Hagrman, E. T. Laats, and C. S. Olsen)

The FELMOD subcode calculates values for Young's modulus for UO_2 and $(U,Pu)O_2$. An estimate of the standard error expected with FELMOD is also calculated. FELMOD and FPOIR are intended for use with mechanical codes like FRACAS[A-5.1] which predict pellet deformation.

The FELMOD code is discussed in Section 5.1 and the FPOIR code is discussed in Section 5.2. The code listings are given in Section 5.3 and the references are given in Section 5.4.

5.1 Fuel Young's Modulus (FELMOD)

The Young's modulus of ceramic fuels is affected by the temperature, density and, to a lesser extent, the oxygen to metal ratio (O/M) and burnup of the fuel. Although published $(U,Pu)O_2$ mixed oxide data are very limited, several authors indicate that the addition of PuO_2 to UO_2 causes an increase in Young's modulus which is at least as large as the standard error of the UO_2 correlation. The increase has therefore been included in the model.

5.1.1 Summary. The subcode was constructed by considering values of Young's modulus measured at high temperatures typical of normal and abnormal light water reactor operation. Extensive room temperature data were available but were used only to help evaluate the uncertainty of the model.

The correlation developed to model Young's modulus for stoichiometric UO_2 fuel below the melting temperature is

$$ES = 2.334 \times 10^{11} [1-2.752 (1-D)] [1-1.0915 \times 10^{-4} T] \quad \text{(A-5.1)}$$

where

ES = Young's modulus for stoichiometric UO_2 fuel (N/m^2)

D = fuel density (fraction of the theoretical density)

T = temperature (K).

For nonstoichiometric fuel or fuel which contains PuO_2 the Young's modulus below melting temperature is

$$E = ES \exp(-Bx) [1 + 0.05f] \quad \text{(A-5.2)}$$

where

E = Young's modulus (N/m^2)

ES = Young's modulus for stoichiometric UO_2 fuel (N/m^2)

B = 1.34 for hyperstoichiometric fuel or 1.75 for hypo-stoichiometric fuel

x = the magnitude of the deviation from stoichiometry in $MO_{2\pm X}$ fuel

f = PuO_2 content of the fuel (weight fraction).

The estimated standard error[a] of FELMOD for stoichiometric fuel is

(1) for temperatures between 450 and 1600 K

$$S_{ES} = 0.06 \times 10^{11} \qquad \text{(A-5.3a)}$$

(2) for temperatures between 1600 and 3113 K

$$S_{ES} = 0.06 \times 10^{11} + ES\ (T-1600)/6052.6 \qquad \text{(A-5.3b)}$$

where

S_{ES} = estimated standard error for stoichiometric UO_2 fuel (N/m^2)

and ES and T were previously defined.

For nonstoichiometric fuel or fuel which contains PuO_2 the estimated standard error is

$$S_E = \left[(S_{ES})^2 + (E-ES)^2\right]^{1/2} \qquad \text{(A-5.4)}$$

where

S_E = estimated standard error (N/m^2) for nonstoichiometric fuel

---

[a] The standard error is estimated with a set of data by the expression (sum of squared residuals/number of residuals minus the number of constants used to fit the data)$^{1/2}$.

and E, ES, and S_{ES} were previously defined.

The following subsection is a review of the available Young's modulus data for UO_2 and $(U,Pu)O_2$ fuel. Section 5.1.3 describes the approach used to formulate the model and Section 5.1.4 is a discussion of the uncertainty of the model.

5.1.2 Survery of Available Data on Young's Modulus for Reactor Fuels. Young's modulus for UO_2 and $(U,Pu)O_2$ fuel has been measured by bending techniques[A-5.2, A-5.3] and by resonant frequency methods. The bending techniques measure an isothermal Young's modulus which is more characteristic of reactor operating conditions than the adiabatic Young's modulus measured with resonant frequency methods. However, bending technique measurements are not as accurate as resonance frequency methods and will therefore not be used in the data base for this model. Also, the difference between adiabatic and isothermal Young's moduli is small, only about 0.1% of the measured value[A-5.4].

(1) Stoichiometric Fuels at Reactor Operating Temperatures. Data from Padel and de Novion[A-5.5], Belle and Lustman[A-5.6] and Hall[A-5.7] are most important because they include temperatures characteristic of reactors. Figure A-5.1 illustrates values of Young's modulus for stoichiometric UO_2 at several temperatures and densities. The modulus decreases with increasing temperature and decreasing density. Moreover, the temperature dependence of the modulus at each density is nearly linear.

Padel and de Novion have reported measurements of mixed oxide (with 20% PuO_2) moduli as a function of temperature and oxygen to metal ratio but their report includes only room temperature data and curves representing the fractional decrease in Young's modulus with increasing temperature on 95% dense fuel. Room temperature mixed oxide data from Padel and de Novion and from Boocock et al[A-5.8] as well as curves from Padel and de Novion are shown in Figure A-5.2. The effect of temperature on the $(U,Pu)O_2$ Young's modulus is similar to its effect on UO_2, but the stoichiometric mixed oxide samples have a larger Young's modulus than stoichiometric UO_2 samples.

Boocock's results suggest that Padel and de Novion have exaggerated the increase of Young's modulus in mixed oxides. Boocock's measurements are supported by the following observations: (a) Pu and U are transition elements with presumably similar atomic bonding, (b) more recent results which showed a 3% increase in Young's modulus due to addition of PuO_2 have been quoted elsewhere[A-5.9], and (c) Nutt et al[A-5.10] have published a correlation for the effect of porosity on $(U,Pu)O_2$ oxides which agrees with Boocock's measurements. The 3% increase due to an addition of 20% PuO_2 to UO_2 is probably the most reliable estimate since it is based on the most recent data of de Novion[A-5.11].

Recent in-reactor measurements of Young's modulus as a function of neutron fluence[A-5.12] have indicated that irradiation increases Young's modulus by about 2% at saturation. Since the effect is small and could be explained by in-reactor densification of the fuel, no separate model for such burnup related changes as fission product accumulation and fuel lattice damage appears necessary at this time.

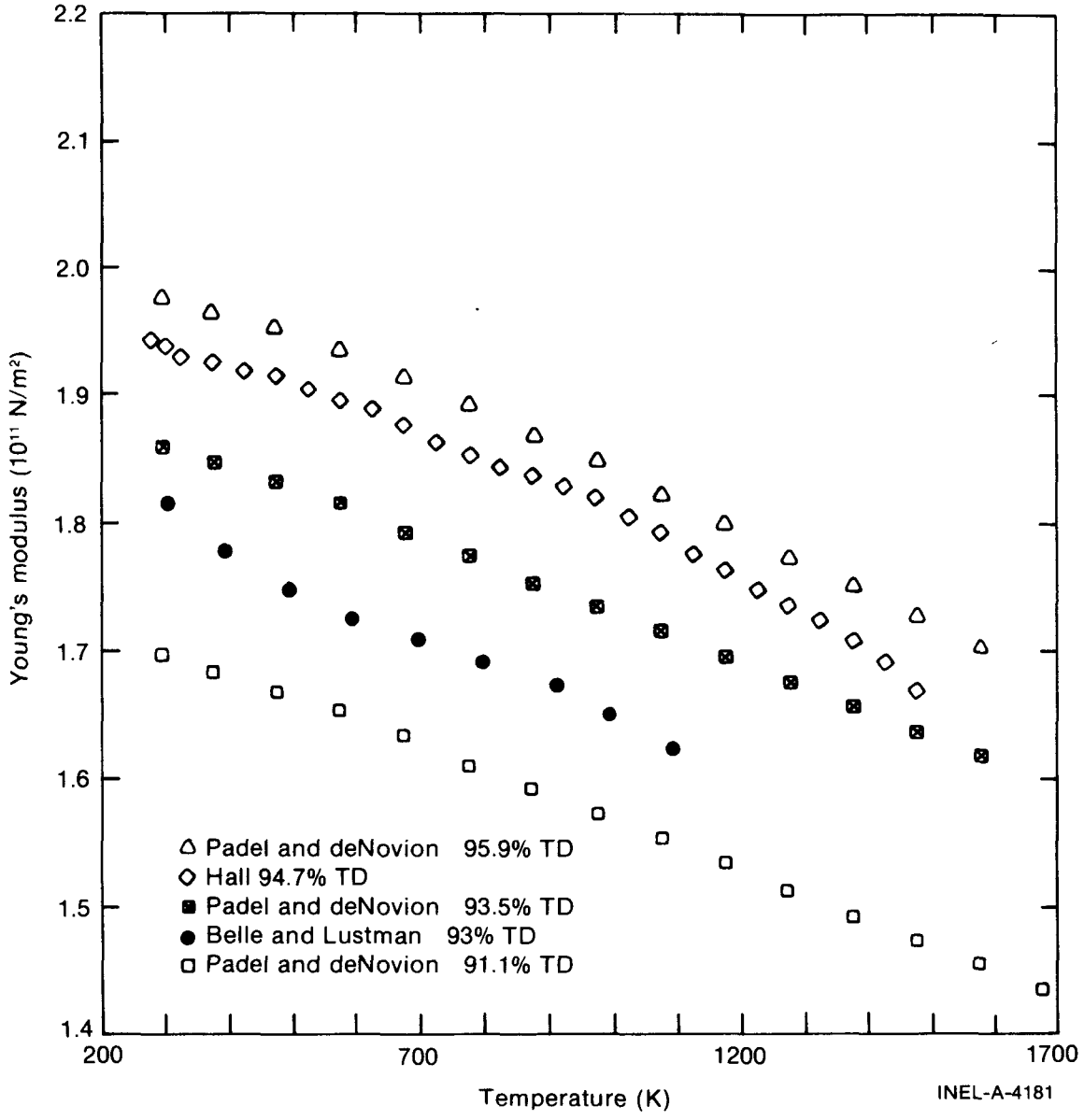

Fig. A-5.1 Young's modulus for stoichiometric UO_2 fuel at several temperatures and fractions of theoretical density.

(2) Room Temperature Measurements of UO_2 Young's Modulus. The effect of changes in fuel density shown in Figure A-5.1 is confirmed by room temperature measurements of Young's modulus as a function of density. Numerous data obtained with stoichiometric UO_2 fuels between 90% and 100% of theoretical density[A-5.5 – A-5.8 and A-5.13 – A-5.15] are reproduced in Figure A-5.3. The data are plotted both as a function of density and porosity (1 minus the density). The room temperature data for porosities between 0 and 0.1 can be described with the least-squares regression line also shown in Figure A-5.3. The equation represented by the line is

$$ES = 22.32 \times 10^{11} - 56.3 \times 10^{11} P \qquad \text{(A-5.5)}$$

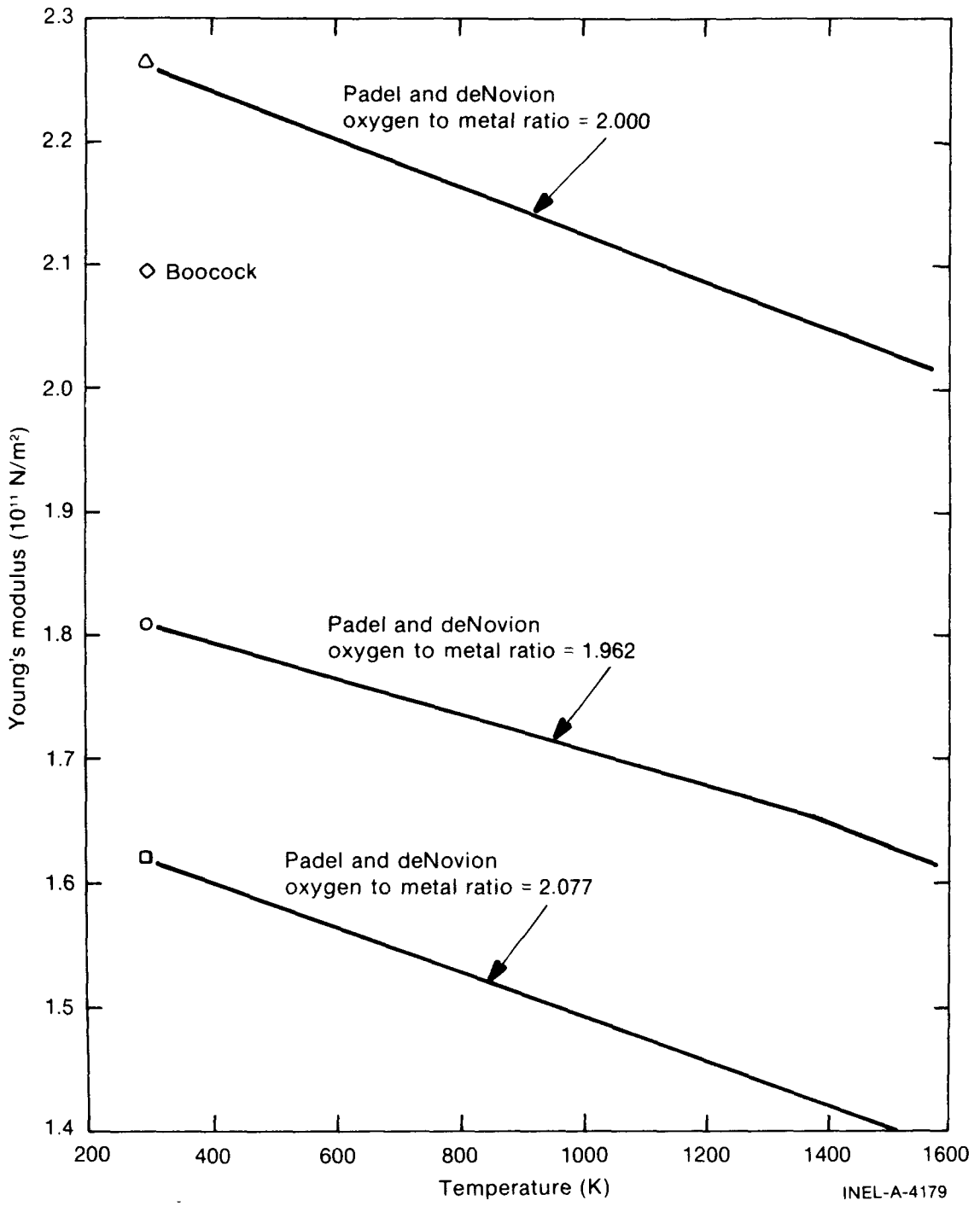

Fig. A-5.2 Young's modulus for $(U,Pu)O_2$ with various oxygen to metal ratios.

where

ES = Young's modulus for stoichiometric UO_2 fuel (N/m^2)

P = porosity (1-D).

The standard deviation of this fit is $\pm 0.6 \times 10^{11} N/m^2$.

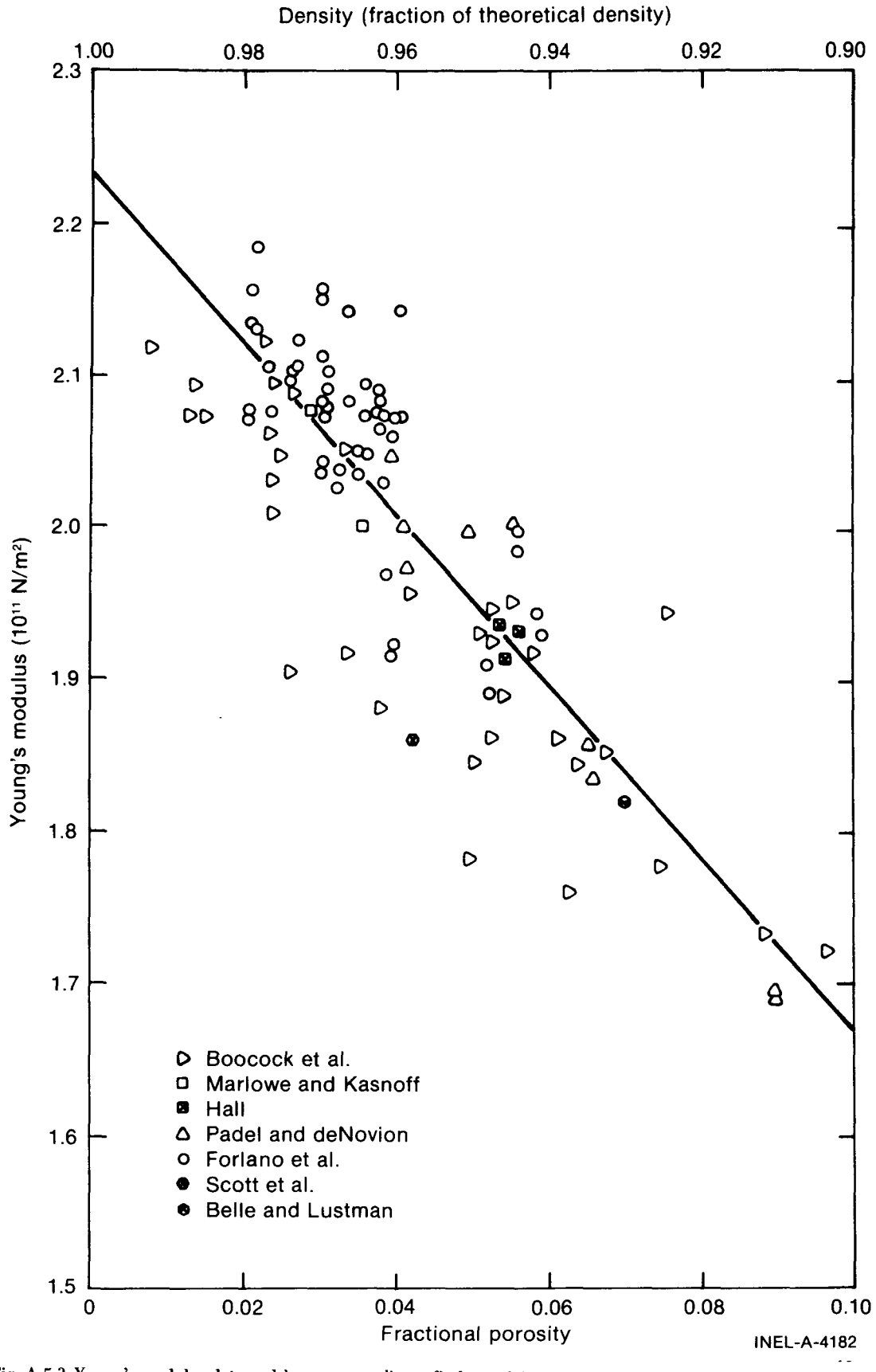

Fig. A-5.3 Young's modulus data and least-squares linear fit for stoichiometric UO_2 fuel at room temperature and several different densities.

(3) Nonstoichiometric Fuels. The data available to describe the effect of variations in the oxygen to metal (O/M) ratio on Young's modulus are difficult to interpret. For example, the significant variation of Young's modulus with changes in stoichiometry reported by Padel and de Novion (see Figure A-5.2) is not seen in low density fuel studied by Nutt et al[A-5.10]. Data attributed to de Novion et al by Matthews show an intermediate effect.

Table A-5.I summarizes relevant nonstoichiometric fuel data taken at room temperature.

TABLE A-5.I

SUMMARY OF YOUNG'S MODULI MEASURED IN NONSTOICHIOMETRIC FUEL AT ROOM TEMPERATURE

Reference	Composition	O/M Ratio	Porosity	Young's Modulus (10^{11} N/m^2)	Fraction of Stoichiometric Value
Padel and de Novion	20% $PuO_{2\pm X}$	1.962	0.051	1.808	0.798
Padel and de Novion	20% $PuO_{2\pm X}$	2.000	0.050	2.265	1.000
Padel and de Novion	20% $PuO_{2\pm X}$	2.077	0.050	1.620	0.715
Scott et al	$UO_{2\pm X}$	2.000	0.042	1.860	1.000
Scott et al	$UO_{2\pm X}$	2.160	0.042	1.240	0.666
de Novion et al as quoted by Matthews	20% $PuO_{2\pm X}$	2.000	--	--	1.000
de Novion et al as quoted by Matthews	20% $PuO_{2\pm X}$	1.967	--	--	0.926
de Novion et al as quoted by Matthews	20% $PuO_{2\pm X}$	1.963	--	--	0.919
de Novion et al as quoted by Matthews	20% $PuO_{2\pm X}$	1.926	--	--	0.873
de Novion et al as quoted by Matthews	20% $PuO_{2\pm X}$	1.911	--	--	0.848
de Novion et al as quoted by Matthews	20% $PuO_{2\pm X}$	1.904	--	--	0.871

TABLE A-5.I (continued)

Reference	Composition	O/M Ratio	Porosity	Young's Modulus (10^{11} N/m^2)	Fraction of Stoichiometric Value
de Novion et al as quoted by Matthews	20% $PuO_{2\pm X}$	1.900	--	--	0.876
de Novion et al as quoted by Matthews	20% $PuO_{2\pm X}$	2.022	--	--	0.960
de Novion et al as quoted by Matthews	20% $PuO_{2\pm X}$	2.050	--	--	0.929
de Novion et al as quoted by Matthews	20% $PuO_{2\pm X}$	2.052	--	--	0.915
de Novion et al as quoted by Matthews	20% $PuO_{2\pm X}$	2.089	--	--	0.903
de Novion et al as quoted by Matthews	20% $PuO_{2\pm X}$	2.111	--	--	0.895
de Novion et al as quoted by Matthews	20% $PuO_{2\pm X}$	2.142	--	--	0.816
de Novion et al as quoted by Matthews	20% $PuO_{2\pm X}$	2.168	--	--	0.812
Nutt et al	20% $PuO_{2\pm X}$	2.000	--	--	1.000
Nutt et al	20% $PuO_{2\pm X}$	1.968	--	--	0.996
Nutt et al	20% $PuO_{2\pm X}$	1.971	--	--	0.996
Nutt et al	20% $PuO_{2\pm X}$	1.982	--	--	0.998
Nutt et al	20% $PuO_{2\pm X}$	2.006	--	--	1.006
Nutt et al	20% $PuO_{2\pm X}$	2.008	--	--	1.002
Nutt et al	20% $PuO_{2\pm X}$	2.008	--	--	1.005

The ratio (Young's modulus in nonstoichiometric fuel / Young's modulus in stoichiometric fuel) is plotted as a function of the fuel's O/M ratio in Figure A-5.4. Most of the points show a decrease in Young's modulus when the fuel is either hypo- or hyperstoichiometric, but there is little agreement about the magnitude of the decrease.

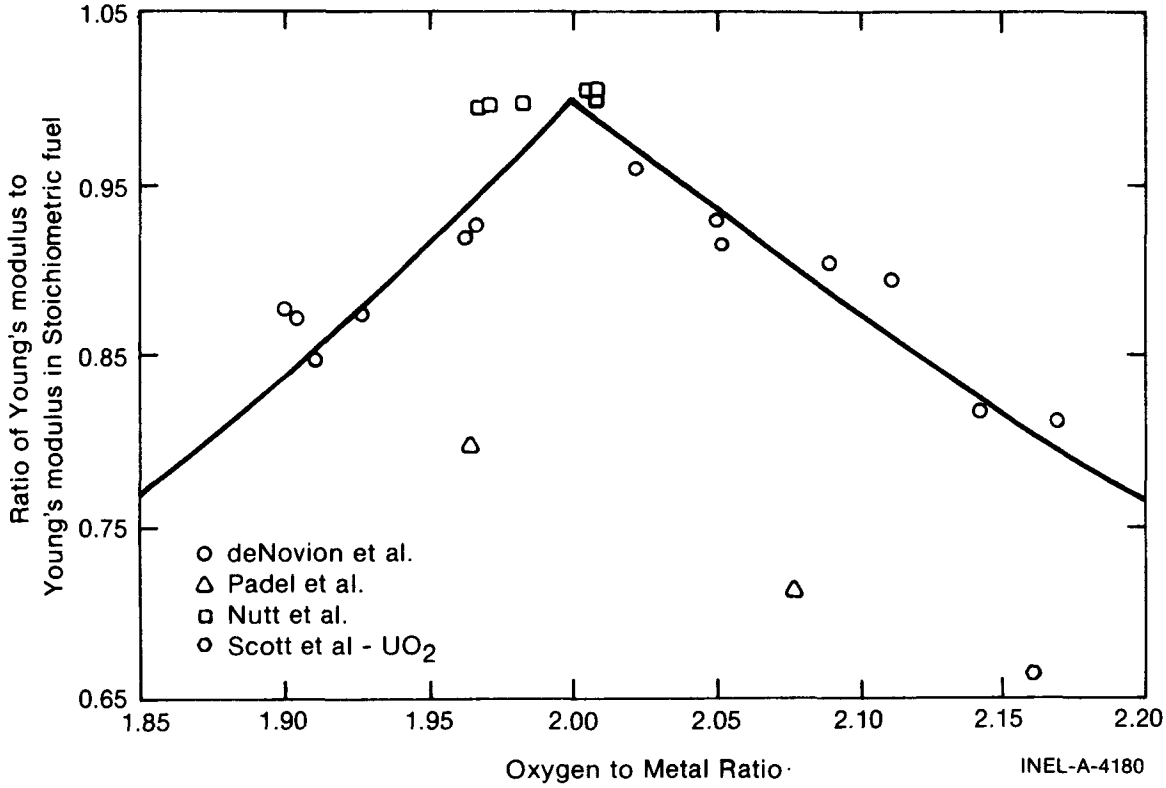

Fig. A-5.4 Ratio of Young's modulus for stoichiometric and nonstoichiometric fuels measured at room temperature compared to values predicted by de Novion's correlation.

It is possible that the fabrication history of the fuel is more significant than the O/M ratio in determining the Young's modulus. However, the inconsistent data of Nutt et al is from fuel of uncharacteristically low density (9.5 g/cm^3) and may not apply to more dense fuels. Therefore, the correlation selected for modeling the effects of nonstoichiometric fuel is that attributed to de Novion et al by Matthews.

$$E = ES \exp(-Bx) \qquad \text{(A-5-6)}$$

where the terms of the equation were previously defined.

Since typical in-reactor values of the O/M ratio are 1.96 to 2.04[A-5.16], the effect of nonstoichiometry is reduction of Young's modulus by 0 to 5%.

5.1.3 Development of the Model. The model for Young's modulus is based primarily on the available UO_2 fuel data. A correlation for the Young's modulus of stoichiometric UO_2 fuel in the temperature range 450 to 1600 K was developed first, then extrapolated to

the approximate melting temperature and modified to predict a slight increase proportional to the weight fraction of PuO_2. The rate of increase with PuO_2 was set to reproduce the factor of 1.03 which was estimated in Section 5.12 for 20% PuO_2. A second modification for the estimated effect of nonstoichiometric fuel was also included in the model. The section describes the development of the model for stoichiometric UO_2 fuel.

The most realistic correlation for the effect of temperature on Young's modulus is the exponential form proposed by Wachtman et al[A-5.17]. However, the data in the temperature range 300 to 1600 K shown in Figure A-5.1 of Section 5.1.2 can be described with an expression of the form

$$E = a\ (1 + b\ T) \tag{A-5.7}$$

where a and b are constants.

A similar approximation is possible to describe the effect of porosity on Young's modulus in the limited range of porosities of interest. The approximation is used because the information necessary to use detailed discussions of the effects of very large porosities[A-5.18, A-5.19] and pore shape variation[A-5.8, A-5.20] is most often not available. The room temperature data of Figure A-5.3 for porosities between 0 and 0.1 can be described with an expression of the form

$$E = c\ (1 + d\ P) \tag{A-5.8}$$

where c and d are constants.

Equation (A-5.8) was used to describe the effect of porosity on Young's modulus at temperatures above 450 K. However, the constants c and d were not evaluated with the room temperature data because (a) sufficient high temperature data exist to evaluate the effect of porosity in the temperature range of interest and (b) the room temperature data exhibit considerable scatter. The expression used to correlate the combined effects of porosity and temperature on Young's modulus is

$$E = e\ (1 + f\ T)\ (1 + g\ P) \tag{A-5.9}$$

where E, T, and P have been defined previously, and e, f, and g are constants.

The constants e, f, and g were evaluated using a two-step fitting procedure. In the first step, least-squares constants a and b of Equation (A-5.7) were determined for each UO_2 fuel sample shown in Figure A-5.1. The result of the fits is summarized in Table A-5.II.

The constant a is equivalent to the product of the factors e (1 + g P) in Equation (A-5.9) for each UO_2 fuel sample and the constant b is equivalent to the constant f in

TABLE A-5.II

LEAST-SQUARES CONSTANTS FOR DATA OF FIGURE A-5.1

Reference	Fraction of Theoretical Density	a (10^{10} N/m^2)	b (10^{-4}/K)
Padel and de Novion	0.911	17.605	-1.1053
Padel and de Novion	0.935	19.221	-1.0056
Padel and de Novion	0.959	20.549	-1.0665
Belle and Lustman	0.93	18.742	-1.1957
Hall	0.947	20.175	-1.0843

Equation (A-5.9). The second step of the fitting procedure was therefore the determination of a linear least-squares regression equation of a on P in order to find the best fit values of e and g. The least-squares fit produced values of e = 23.34 x 10^{10} N/m^2 and g = -2.752. These values were combined with the average of the values for f = b from Table A-5.II to produce the correlation

$$E = 23.34 \times 10^{10} (1-1.0915 \times 10^{-4}T) (1-2.752\ P) \qquad \text{(A-5.10)}$$

where the terms have been previously defined. The correlation is equivalent to Equation (A-5.1).

No data are available for solid UO_2 fuel above 1600 K. Equation (A-5.10) was simply extrapolated to estimate Young's modulus between 1600 K and the approximate melting temperature (3113 K).

5.1.4 Uncertainty of the Model. The standard error[a] of Equation (A-5.10) with respect to its own data base is 0.021 x 10^{11} N/m^2 (about 1% of the predicted value) and the standard error of the equation with respect to the room temperature data of Figure A-5.3 is 0.073 x 10^{11} N/m^2. These numbers represent lower and upper bounds for the standard error to be expected in applying the model to stoichiometric UO_2 fuel in the range 450 to 1600 K. The first number does not include possible variations to be expected

[a] Since three constants were used to fit the stoichiometric UO_2 fuel data base, the number of degrees of freedom is equal to number of measurements minus three.

with samples not in the data base and the second number was obtained using data taken at a low temperature where the linear expression for the effect of temperature systematically overpredicts Young's modulus. The best estimate for the standard error to be expected with this model is the standard deviation of Equation (A-5.5). The value, 0.06×10^{11} N/m^2, includes the effect of sample-to-sample variation but does not include the artificial error due to the extrapolation of the temperature coefficient.

For temperatures above 1600 K there are no data and no rigorous ways to test the model. In Equation (A-5.3b), the standard error estimate for 400 to 1600 K has been increased by an additive term which is zero at 1600 K and increases to one fourth of the predicted value at the approximate melting temperature (3113 K).

The modifications to the basic UO_2 fuel correlation to predict the effects of nonstoichiometry and PuO_2 additions are based on limited data and are therefore uncertain. The standard error estimate expressed in Equation (A-5.4) assumes an independent error equal to the change produced by the models for nonstoichiometry and PuO_2 addition. That is, the net estimated standard error is taken to be the square root of the sum of the square of the standard error of the prediction for the stoichiometric UO_2 fuel elastic modulus and the square of the net change produced by the models for nonstoichiometric and PuO_2 fuels.

5.2 Fuel Poisson's Ratio (FPOIR)

Poisson's ratio for both UO_2 and $(U,Pu)O_2$ fuels is calculated by the routine FPOIR as a function of fuel temperature and composition.

Poisson's ratio can be related to Young's modulus and the shear modulus as follows[A-5.21]:

$$\mu = \frac{E}{2G} - 1 \qquad \text{(A-5.11)}$$

where

μ = Poisson's ratio (unitless)

E = Young's modulus (N/m^2)

G = shear modulus (N/m^2).

Wachtman et al[A-5.22] report mean values for the Young's modulus and shear modulus of UO_2 from two experiments as $E = 2.30 \times 10^{11}$ N/m^2 and $G = 0.874 \times 10^{11}$ N/m^2. Consequently, the value of Poisson's ratio is 0.316 and the routine FPOIR returns this value for UO_2. The Wachtman et al paper only considers single crystal UO_2 data at 25°C. However, Padel and de Novion have reported values of 0.314 and 0.306 for the Poisson's ratio of polycrystalline UO_2. These values are in reasonable agreement with Wachtman's value of 0.316.

Nutt et al determined Poisson's ratio for $U_{0.8}$ $Pu_{0.2}$ O_{2-x} at room temperature by determining the Young's modulus and the shear modulus and calculating Poisson's ratio using Equation (A-5.11). Nutt and Allen's room temperature Poisson's ratio for $(U,Pu)O_2$ fuel of 0.276 ± 0.094 was found to be independent of density and is returned by FPOIR for mixed oxides.

Poisson's ratio for the fuel is shown in Figure A-5.5 as a function of temperature and fuel composition as can be seen from the figure, any plutonia content is assumed to reduce Poisson's ratio, which is independent of temperature.

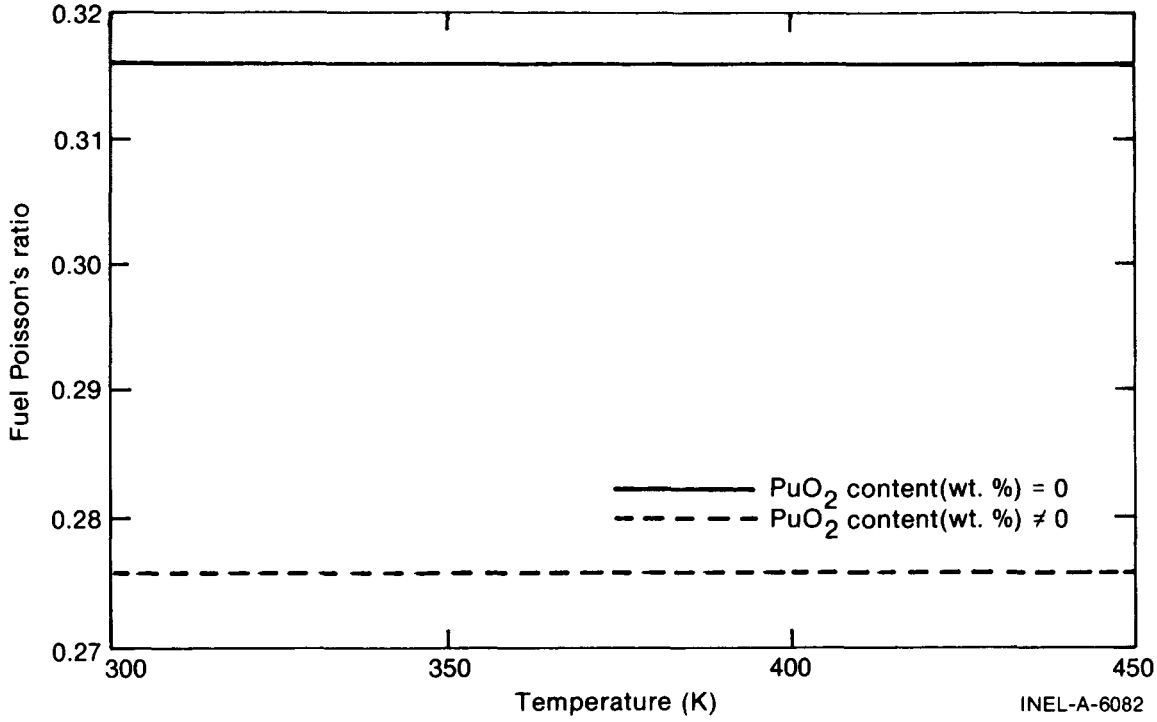

Fig. A-5.5 Poisson's ratio as a function of temperature.

5.3 Fuel Elastic Moduli Subcodes FELMOD and FPOIR Listings

FORTRAN listings of the FELMOD and FPOIR subcodes are given in Tables A-5.III and A-5.IV, respectively.

5.4 References

A-5.1. M. P. Bohn, *FRACAS – A Subcode for the Analysis of Fuel Pellet-Cladding Mechanical Interaction,* TREE-NUREG-1028 (April 1977).

A-5.2. W. A. Lambertson and J. H. Handwerk, *The Fabrication and Physical Properties of Urania Bodies,* ANL-5053 (February 1956).

TABLE A-5.III

LISTING OF THE FELMOD SUBCODE

```
C
C
C     FUNCTION FELMOD(FTEMP,FRADEN,FOTMTL,FCOMP)
C
CCC   FELMOD CALCULATES FUEL ELASTIC MODULUS AS A FUNCTION OF
CCC   TEMPERATURE, FRACTIONAL DENSITY, OXYGEN TO METAL RATIO AND
CCC   PUO2 CONTENT
CCC
CCC   FTEMP  = INPUT FUEL TEMPERATURE (K)
CCC   FRADEN = INPUT FRACTIONAL FUEL DENSITY -- RATIO
CCC            OF ACTUAL DENSITY TO THEORETICAL DENSITY
CCC   FOTMTL = INPUT OXYGEN TO METAL RATIO OF FUEL (ATOMS OXYGEN/
CCC            ATOMS METAL)
CCC   FCOMP  = INPUT PUO2 CONTENT OF FUEL -- WEIGHT FRACTION
CCC
CCC   FELMOD = OUTPUT FUEL YOUNG'S MODULUS (N/M**2)
CCC   UFELMD = OUTPUT STANDARD ERROR EXPECTED IN FELMOD (N/M**2)
CCC              (NOT CURRENTLY RETURNED)
CCC
CCC   THE EQUATIONS USED IN THIS FUNCTION ARE BASED ON DATA FROM
CCC   (1) A. PADEL AND C. DE NOVION, J. NUCL. MAT. 33 (1969)
CCC       PP 40 - 51
CCC   (2) J. BELLE AND B. LUSTMAN, FUEL ELEMENTS CONFERENCE,
CCC       TID-7546 (1958) PP 480-481
CCC   (3) A. R. HALL, J. NUCL. MAT. 37 (1970) PP 314 - 323
CCC
CCC   FELMOD CODED BY V. F. BASTON MARCH 1974
CCC   MODIFIED BY C. S. OLSEN IN FEBRUARY AND JULY 1975
CCC   MODIFIED BY D. L. HAGRMAN, E. T. LAATS, AND M. A. MORGAN
CCC   JUNE 1977
C
      YS = 23.34E10 * (1. - (2.752*(1. - FRADEN)))*(1. -1.0915E-04*
     #     FTEMP)
      UFELMD = 6.0E09
      IF (FTEMP .LT. 1.6E03) GO TO 10
      UFELMD = UFELMD + YS * (FTEMP - 1.6E03)/6.0526E03
      IF (FTEMP .LT. 3113.15) GO TO 10
      YS = 0.0
      UFELMD = 0.0
      GO TO 80
   10 UNSTOC = ABS(FOTMTL - 2.0)
      IF (UNSTOC .GT. 1.0E-03) GO TO 20
      IF (FCOMP .LT. 1.0E-03) GO TO 80
   20 B = 1.34
      IF (FOTMTL .LT. 2.0) B = 1.75
      Y = YS * EXP(-B*UNSTOC) * (1. + 0.15 * FCOMP)
      UFELMD = (UFELMD**2 + (Y - YS)**2)**0.5
      YS = Y
   80 FELMOD = YS
C
      RETURN
      END
```


A-5.3. J. T. A. Roberts and Y. Ueda, "Influence of Porosity and Deformation and Fracture of UO_2," *Journal of the American Ceramic Society, 55,* (1972) pp 117-124.

A-5.4. I. J. Fritz, "Elastic Properties of UO_2 at High Pressure," *Journal of Applied Physics, 47* (1976) pp 4353-4358.

A-5.5. A. Padel and C. de Novion, "Constants Elastiques des Carbures, Nitures et Oxydes d'Uranium et de Plutonium," *Journal of Nuclear Materials, 33* (1969) pp 40-51.

A-5.6. J. Belle and B. Lustman, "Properties of UO_2," *Fuel Elements Conference, Paris, France, November 18-23, 1957,* TID-7546, (March 1958) pp 480-481.

TABLE A-5.IV

LISTING OF THE FPOIR SUBCODE

```
C
C
      FUNCTION FPOIR(FTEMP, COMP)
C
C     FPOIR RETURNS POISSON'S RATIO FOR UO2 AND MIXED OXIDES
C
C     FPOIR = OUTPUT POISSON'S RATIO FOR UO2
C
C     FTEMP = INPUT FUEL TEMPERATURE (K)
C     COMP  = INPUT PLUTONIA CONTENT (WEIGHT PERCENT)
C
C      POISSON'S  RATIO FOR UO2 USED IN THIS ROUTINE WAS EVALUATED
C     FROM THE MEAN OF THE DATA PRESENTED BY WACHTMAN ET AL., J. NUC.
C     MAT. 16 (1965) PP 39-41
C     POISSON'S RATIO FOR MIXED OXIDES IS THE VALUE DETERMINED BY NUTT
C     AND ALLEN, J. AMER. CERAM. SOC., 53 (1970) P 205
C
C     FPOIR WAS ORIGINALLY CODED BY V.F. BASTON IN MARCH 1974.
C     FPOIR WAS MODIFIED BY C.S. OLSEN IN FEB 1975.
C
      COMMON      / LACEMOL   / MAXIDX, EMFLAG
      DIMENSION EMFLAG(1)
      DATA        ON          / 2HON    /,
     #            OFF         / 3HOFF   /,
     #            LOCIDX      /   11    /
C
      IF ( EMFLAG(LOCIDX) .EQ. ON ) GO TO 20
C
      T = FTEMP
      FPOIR = 0.316
      IF (COMP .GT. 0.0) FPOIR = 0.276
      GO TO 15
   20 FPOIR = EMFPIR( FTEMP)
   15 CONTINUE
      RETURN
      END
```


A-5.7. A. R. Hall, "Elastic Moduli and Internal Friction of Some Uranium Ceramics," *Journal of Nuclear Materials, 37* (1970) pp 314-323. Also AERE-R 5650 (1967).

A-5.8. J. Boocock, A. S. Furzer, J. R. Matthews, *The Effect of Porosity on the Elastic Moduli of UO_2 as Measured by an Ultrasonic Technique,* AERE-M 2565 (September 1972).

A-5.9. J. R. Matthews, *Mechanical Properties and Diffusion Data for Carbide and Oxide Fuels. Ceramics Data Manual Contribution,* AERE-M 2643 (1974).

A-5.10. A. W. Nutt, Jr., A. W. Allen, J. H. Handwerk, "Elastic and Anelastic Response of Polycrystalline UO_2-PuO_2," *Journal of the American Ceramic Society, 53* (1970) p 205.

A-5.11. C. de Novion et al, "Mechanical Properties of Uranium-Plutonium Based Ceramics," *Nuclear Metallurgy, 17* (1970) pp 509-517.

A-5.12. V. M. Baranov et al, "In-Reactor Measurements of the Modulus of Elasticity of Uranium Dioxide," *Soviet Atomic Energy, 40* (1976) pp 37-39.

A-5.13. M. O. Marlowe and A. I. Kaznoff, "Elastic Behavior of Uranium Dioxide," *Journal of the American Ceramic Society, 53* (1970) pp 90-99.

A-5.14. R. J. Forlano et al, "Elasticity and Anelasticity of Uranium Oxides at Room Temperature:I Stoichiometric Oxide," *Journal of the American Ceramic Society, 50* (1967) pp 92-96.

A-5.15. R. Scott et al, "The Plastic Deformation of Uranium Oxides Above 800°C," *Journal of Nuclear Materials, 1,* (1959) pp 39-48.

A-5.16. D. R. Olander, *Fundamental Aspects of Nuclear Reactor Fuel Elements,* TID-26711-P1 (1976) pp 160-166.

A-5.17. J. B. Wachtman et al, "Exponential Temperature Dependence of Young's Modulus for Several Oxides," *Physics Review, 122,* 6 (1961) pp 1754-1759.

A-5.18. M. O. Marlowe and D. R. Wilder, "Elasticity and Internal Friction of Polycrystalline Yttrium Oxide," *Journal of the American Ceramic Society, 48* (1965) pp 227-233.

A-5.19. N. Igata and K. Domoto, "Fracture Stress and Elastic Modulus of Uranium Dioxide Including Excess Oxygen," *Journal of Nuclear Materials, 45* (1972/73) pp 317-322.

A-5.20. D. P. H. Hasselman and R. M. Fulrath, "Effect of Cylindrical Porosity on Young's Modulus of Polycrystalline Brittle Materials," *Journal of the American Ceramic Society, 48* (1965) p 545.

A-5.21. I. S. Sokolnikoff and R. D. Specht, *Mathematical Theory of Elasticity,* 2nd Edition, New York: McGraw-Hill Book Company, Inc., 1956.

A-5.22. J. B. Wachtman, Jr., M. L. Wheat, H. J. Anderson, J. L. Bates, "Elastic Constants of Single Crystal UO_2 at 25°C," *Journal of Nuclear Materials, 16,* 1 (1965) p 39.

6. FUEL CREEP (FCREEP)

(R. E. Mason)

The fuel creep model, FCREEP, calculates creep rate of UO_2 and $(U,Pu)O_2$ fuels. Fuel creep affects the width of the gap between fuel pellets and cladding and hence the temperature gradient in the fuel rod. FCREEP was developed through use of both out-of-pile and in-pile data. The samples were high density (generally above 96% theoretically dense) and were irradiated to burnups too low for swelling to be a major factor. Therefore, the fuel dimensional changes calculated with the FCREEP subcode should simply be added to the dimensional changes calculated using other MATPRO correlations.

6.1 Summary

The FCREEP model calculates creep deformation of UO_2 or mixed oxide fuels. The model includes a time dependent creep rate for UO_2, valid for both steady state and transient reactor conditions. Fuel creep is modeled as a function of time, temperature, grain size, density, fission rate, oxygen to metal ratio, and external stress.

At a transition stress (σ_t), the creep rate changes from a linear stress dependence to a creep rate proportional to stress to a power n. The transition stress is defined by

$$\sigma_t = 1.6547 \times 10^7 / G^{0.5714} \qquad \text{(A-6.1)}$$

where

σ_t = transition stress (Pa)

G = fuel grain size (μ).

The creep function is dependent on an Arrhenius type activation energy. This energy is found to be a function of the fuel oxygen to metal ratio (O/M). Increasing the O/M ratio increases the creep rate, all other things being constant. The activation energy below the transition stress is given by

$$Q_1 = 17884.8 \left\{ \exp \left[\frac{-20}{\ln(x-2.0)} - 8 \right] + 1 \right\}^{-1} + 72124.23 \qquad \text{(A-6.2)}$$

where

Q_1 = activation energy (J/mol)

x = oxygen to metal ratio.

The activation energy of UO_2 above the transition stress is

$$Q_2 = 19872.0 \left\{ \exp \left[\frac{-20.0}{\log (x-2)} - 8.0 \right] + 1.0 \right\}^{-1} + 111543.5 \qquad \text{(A-6.3)}$$

where

Q_2 = activation energy (J/mol).

The steady state creep rate of UO_2 is determined using

$$\dot{\varepsilon}_s = \frac{(A_1 + A_2 \dot{F})\, \sigma \exp(-Q_1/RT)}{(A_3 + D)\, G^2} + \frac{(A_4 + A_8 \dot{F})\, \sigma^{4.5} \exp(-Q_2/RT)}{A_6 + D}$$

$$+ A_7\, \sigma\, \dot{F} \exp(Q_3/RT) \qquad \text{(A-6.4)}$$

where

$\dot{\varepsilon}_s$ = steady state creep rate (S^{-1})

A_1 = 0.3919

A_2 = 1.3100×10^{-19}

A_3 = -87.7

A_4 = 2.0391×10^{-25}

A_6 = -90.5

A_7 = 3.72264×10^{-35}

A_8 = 0.0

$\dot{F}$ = fission rate (fissions/m^3)/s

σ = stress (Pa)

T = temperature (K)

D = density (percent of theoretical density)

G = grain size (μm)

Q_3 = 2.6167×10^3 (J/mol)

R = universal gas constant (J/mol·K).

For mixed oxides, the steady state creep rate is found using the equation

$$\dot{\varepsilon}_s = \frac{(B_1 + B_2 F)\sigma}{G^2} \exp\left[-Q_3/RT + B_3 (1 - D) + B_4 C\right] +$$

$$(B_5 + B_6 \dot{F})\sigma^{4.5} \exp\left[-Q_4/RT + B_7 (1 - D) + B_4 C\right] \qquad \text{(A-6.5)}$$

where

B_1 = 0.1007

B_2 = 7.57×10^{-20}

B_3 = 33.3

B_4 = 3.56

B_5 = 6.469×10^{-25}

B_6 = 0.0

B_7 = 10.3

Q_3 = 55354.0

Q_4 = 70451.0

C = PuO_2 concentration (weight percent)

and the other terms have been previously defined.

When the applied stress (σ) is less than the transition stress (σ_t), the applied stress is used in the first term of Equation (A-6.4) or (A-6.5). For stresses greater than σ_t, the transition stress is used in the first term and the external stress in the second term of both equations.

When the fuel first experiences stress, usually during initial irradiation, or when a higher stress than in any other time step is applied, the strain rate is time dependent and is calculated using the equation

$$\dot{\varepsilon}_T = \dot{\varepsilon}_s \left[2.5 \exp(-1.40 \times 10^{-6} t) + 1\right] \qquad \text{(A-6.6)}$$

where

$\dot{\epsilon}_T$ = the total strain rate (s^{-1})

$\dot{\epsilon}_s$ = steady state strain rate defined by Equation (A-6.4) (s^{-1})

t = time since the largest stress was applied (s).

Equation (A-6.6) is the total creep rate function prescribed by the subcode FCREEP.

6.2 Model Development

Fuel deforms through a number of creep mechanisms depending on the stress, density, temperature, O/M ratio, irradiation level and grain size. The FCREEP model is based on vacancy diffusion at low stress, dislocation climb at high stress and a time dependent creep rate at all stresses at times less than 300 hours after a stress increase. The time dependent creep increases the creep rate over the steady state value for times less than 300 hours, but contributes little at longer times. Only constant volume creep is modeled in FCREEP, whereas hot pressing processes are being considered separately.

This subcode incorporates the UO_2 steady state creep model proposed by Bohaboy[A-6.1] with modifications suggested by Solomon[A-6.2] for fission-enhanced and fission-induced creep. The subcode also incorporates the $(U,Pu)O_2$ creep equation proposed by Evans et al[A-6.3], but modified in a similar manner to include fission enhanced creep. The constants proposed by Bohaboy and Solomon for UO_2 creep and by Evans for $(U,Pu)O_2$ creep were fit to the data base.

6.2.1 Steady State Creep. Steady state creep for ceramic fuel can be modeled as a two process phenomenon: (a) low stress creep based on vacancy diffusion and (b) power law creep based on dislocation climb.

The theoretical model[A-6.4 – A-6.6] for viscous creep is based upon diffusion of vacancies from grain boundaries in tension to grain boundaries in compression. This model results in a creep rate that is (a) proportional to the vacancy diffusion coefficient, (b) inversely proportional to the square of the grain size, and (c) proportional to stress. Low stress creep can be written as

$$\dot{\epsilon}_s = \left(\frac{A_1}{G^2}\right) \sigma \exp \quad (-Q_1/RT) \qquad \text{(A-6.7)}$$

where the terms of the equation have been previously defined.

Equation (A-6.7) is based upon the assumption that volume diffusion controls the creep rate. Therefore, the creep rate is inversely proportional to the square of the grain size with an activation energy determined for volume diffusion. However, Coble[A-6.7] has shown that if the diffusion path is along grain boundaries, the creep rate should be inversely

proportional to the cube of the grain size with an associated activation energy that corresponds to grain boundary diffusion. Equation (A-6.7) is derived solely for diffusion of vacancies, but grain boundary sliding has been observed during low stress creep deformation of UO_2[A-6.8,A-6.9]. Both grain boundary sliding and diffusional creep have the characteristics of linear stress dependence and an activation energy nearly that of self diffusion. Therefore, it is not possible to distinguish between mechanisms of grain boundary sliding and diffusion. Regardless of which mechanism predominates, the form of Equation (A-6.7) is still applicable.

At high stresses, the movement of dislocations due to external shear stresses within the crystal structure results in a macroscopic movement of material. At high temperatures, dislocation climb can occur which results in an increase in deformation rate by allowing dislocations to surmount barriers which normally would restrict movement. Weertman[A-6.10] has proposed a model based upon dislocation climb which results in a creep rate proportional to stress raised to the 4.5 power. In this case, creep rate is not a function of grain size. This power law model for steady state creep rate is

$$\dot{\varepsilon}_s = A_2 \sigma^{4.5} \exp(-Q_2/RT) \qquad \text{(A-6.8)}$$

where the terms of the equation have been previously defined.

6.2.2 Irradiated Fuel Creep. Equations (A-6.3) and (A-6.4) were modified to model enhanced creep rate due to irradiation following the method suggested by Solomon. Solomon concluded that in-reactor creep of UO_2 is composed of (a) an elevated temperature regime, in which normal thermal creep mechanisms are enhanced and (b) a low temperature regime, in which the fission process induces fuel creep. At temperatures less than 1173 K the creep rate is linearly proportional to fission rate and to stress. All the data appeared to lie within a broad scatter band that is insensitive to temperature. Evidence was insufficient to determine whether scatter is due primarily to variations of material properties (density, grain size, stoichiometry, and impurity concentration), or test conditions (temperature, stress, and fission rate).

Solomon consolidated the results of Perrin[A-6.11] and used Bohaboy's equation to arrive at the following expression.

$$\dot{\varepsilon}_s = \frac{(A_4 + A_8 \dot{F})}{(A_6 + D)} \sigma^{4.5} \exp(Q_2/RT) + \frac{(A_1 + A_2 \dot{F})}{(A_3 + D)\, G^2} \sigma \exp(Q_1/RT) + A_9 \sigma \dot{F} \qquad \text{(A-6.9)}$$

where A_1, A_2, A_3, A_4, A_6, A_8, A_9 are constants and the other terms of the equation have been previously defined. This equation assumes a fivefold increase in creep rate instead of the fourfold increase reported by Perrin at a fission rate of 1.2×10^{19} (fission/m^3)/s. The fivefold increase is also assumed at higher stresses where dislocation creep occurs but where no experimental data are available.

Brucklacher et al[A-6.12] reported an equation for the fission induced creep up to 2.5% burnup of

$$\dot{\varepsilon} = 5.6 \exp(-2616.8/T)\, \dot{F} \qquad \text{(A-6.10)}$$

where

$\dot{\epsilon}$ = creep rate (s^{-1}).

Equation (A-6.10) is used in place of the last term of Equation (A-6.9) resulting in the final form of the UO_2 steady state creep Equation (A-6.4).

For the creep of mixed oxides, the equation suggested by Evans et al is adopted with similar modifications for fission enhanced creep. The steady state mixed oxide creep rate equation is

$$\dot{\varepsilon}_s = \frac{(B_1 + B_2\dot{F})}{G^2}\,\sigma \exp\left[-Q_1/RT + B_3(1-D) + B_4C\right] + (B_5 + B_6\dot{F})\,\sigma^{4.5} \exp\left[-Q_2/RT + B_7(1-D) + B_4C\right]. \qquad \text{(A-6.11)}$$

where B_1, B_2, B_3, B_4, B_5, B_6, B_7 are constants and the other terms of the equation have been previously defined.

6.2.3 Transition Stress. Wolfe and Kaufman[A-6.13] pointed out that the stress at which the transition from viscous creep to power law creep occurs is only mildly dependent upon temperature, but more strongly affected by grain size. Seltzer et al[A-6.14,A-6.15] performed an analysis of the transition stress that presents circumstantial evidence for a power law creep rate with a 4.5 stress coefficient and a viscous creep rate with an inverse dependence on the square of the grain size. At the transition, Equations (A-6.7) and (A-6.8) can be equated:

$$\left(\frac{A_1\sigma}{G^2}\right)\exp(-Q_1/RT) = A_2\,\sigma^{4.5}\exp(-Q_2/RT) \qquad \text{(A-6.12)}$$

where the terms of the equation have been previously defined.

Solving Equation (A-6.12) for the stress at the transition (σ_t):

$$\sigma_t = \left(\frac{A_1}{A_2}\right)^{\frac{1}{3.5}} G^{-0.57} \exp\left[(Q_2-Q_1)/3.5RT\right]. \quad \text{(A-6.13)}$$

If the activation energies, Q_2 and Q_1, are about the same magnitude, then the temperature dependence of σ_t should be minimal and the resulting transition stress is calculated using

$$\sigma_t = A\, G^{-0.57} \quad \text{(A-6.14)}$$

6.2.4 Time Dependent Creep. The time dependent creep rate is based on an anelastic creep equation and is used in FCREEP to calculate the creep rate of water reactor fuel during the first 300 hours after the stress on the fuel has been increased. The strain resulting from this time dependent stress can be a major portion of the total creep deformation[A-6.16]. A number of time dependent creep functions were compared with transient creep data. In particular, time to a power used by other authors to describe UO_2 transient creep[A-6.17] was tried, but the function found to best predict the transient creep data was the exponential function.

$$\dot{\varepsilon}_t = 2.5\,[1 + \exp(-at)] \quad \text{(A-6.15)}$$

where

$\dot{\epsilon}_t$ = time dependent creep rate (s^{-1})

a = constant

t = time(s).

Since this subcode is to be used to calculate both steady state and transient reactor conditions, the anelastic form of time dependent creep was used because it better predicted the creep data for all times. The anelastic equation is multiplied by the steady state creep rate to obtain the total creep rate.

$$\dot{\varepsilon}_T = [1 + 2.5\exp(-at)]\,\dot{\varepsilon}_s \quad \text{(A-6.16)}$$

where

$\dot{\epsilon}_T$ = total creep rate (s^{-1})

and the other terms of the equation have been previously defined.

6.3 Evaluation of Constants and Data Comparison

Data selection for code development use was based on the requirements as follows:

(1) The data result from compressive creep tests

(2) The initial oxygen to metal ratio was measured and documented

(3) The temperature was measured and documented

(4) The grain size was measured and documented.

Requirement (2) prevented the use of some data in determining the constants of FCREEP. These data were used after the creep model was developed (with an assumed O/M ratio) as an extra data comparison and no significant deviation was noted.

6.3.1 Evaluation of Steady State Creep Constants UO_2. The basic form of the steady state equations of Solomon and Evans et al was retained but some of the constants were refit to include the effect of the fuel O/M ratio. The activation energies of Equation (A-6.2) and (A-6.3) were determined by calculating the creep rate using the data reported by Burton and Reynolds[A-6.18,A-6.19], Seltzer et al[A-6.15] and Bohaboy et al[A-6.1]. These were data of UO_2 under different stresses, temperatures and O/M ratios. Fitting the equations to the available data gave effective activation energies which changed less as the O/M ratio increased than is reported in the literature[A-6.15].

Other creep data considered while developing the subcode are Bohaboy and Asamto[A-6.20], Speight[A-6.21], Brucklacher and Dienst[A-6.22], Solomon[A-6.23], Scott et al[A-6.24] and Armstrong and Irvine[A-6.25].

The activation energies found to give the best fit to the base data were

(1) for low stresses

$$Q_1 = 17884.8 \left\{ \exp \left[\frac{-20.0}{\log(x-2.0)} - 8.0 \right] + 1.0 \right\}^{-1} + 72124.23 \qquad \text{(A-6.17)}$$

(2) for high stresses

$$Q_2 = 19872.0 \left\{ \exp \left[\frac{-20.0}{\log(x-2.0)} - 8.0 \right] + 1 \right\}^{-1} + 112142.4. \qquad \text{(A-6.18)}$$

After the approximate activation energies were determined, the equations were further evaluated against the data of Bohaboy et al[A-6.1] to refine the constants. Figure A-6.1 shows the calculated creep rates plotted against experimental data. Those data

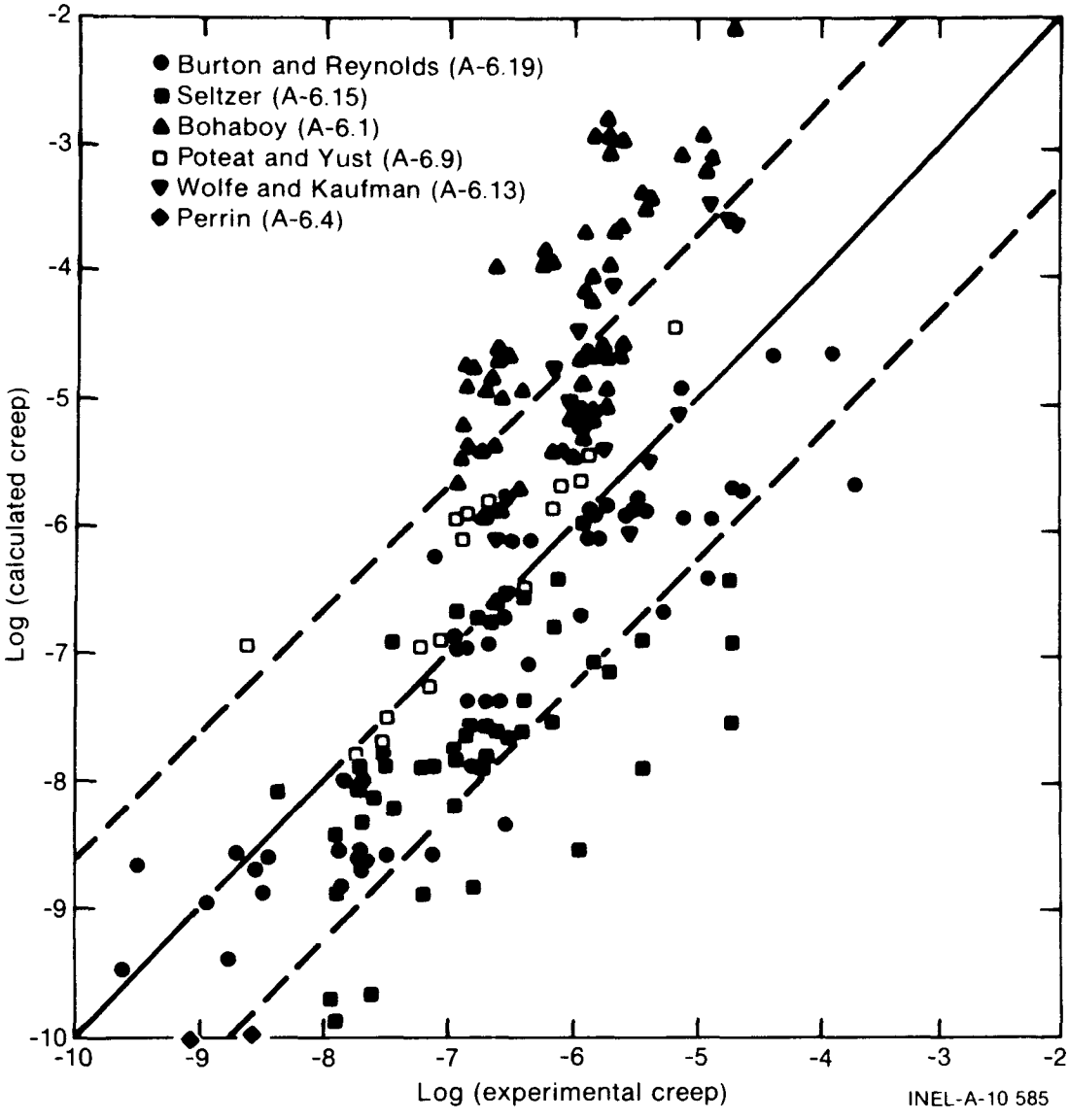

Fig. A-6.1 Comparison of unirradiated UO_2 experimental data with corresponding calculated values from FCREEP.

which did not have a documented O/M ratio are shown along with the data used to develop the code. Figure A-6.2 shows the calculated creep rates for irradiated fuel compared to the experimental data base. The uncertainty of the FCREEP calculations was determined as the standard deviation of the log of the calculated creep rate compared with the log of the corresponding creep rate. The uncertainty range is shown as dashed lines in Figures A-6.1 and A-6.2. The uncertainty creep rates can be calculated using the equation:

$$\dot{\varepsilon}_u = \dot{\varepsilon} \cdot 10^U \qquad \text{(A-6.19)}$$

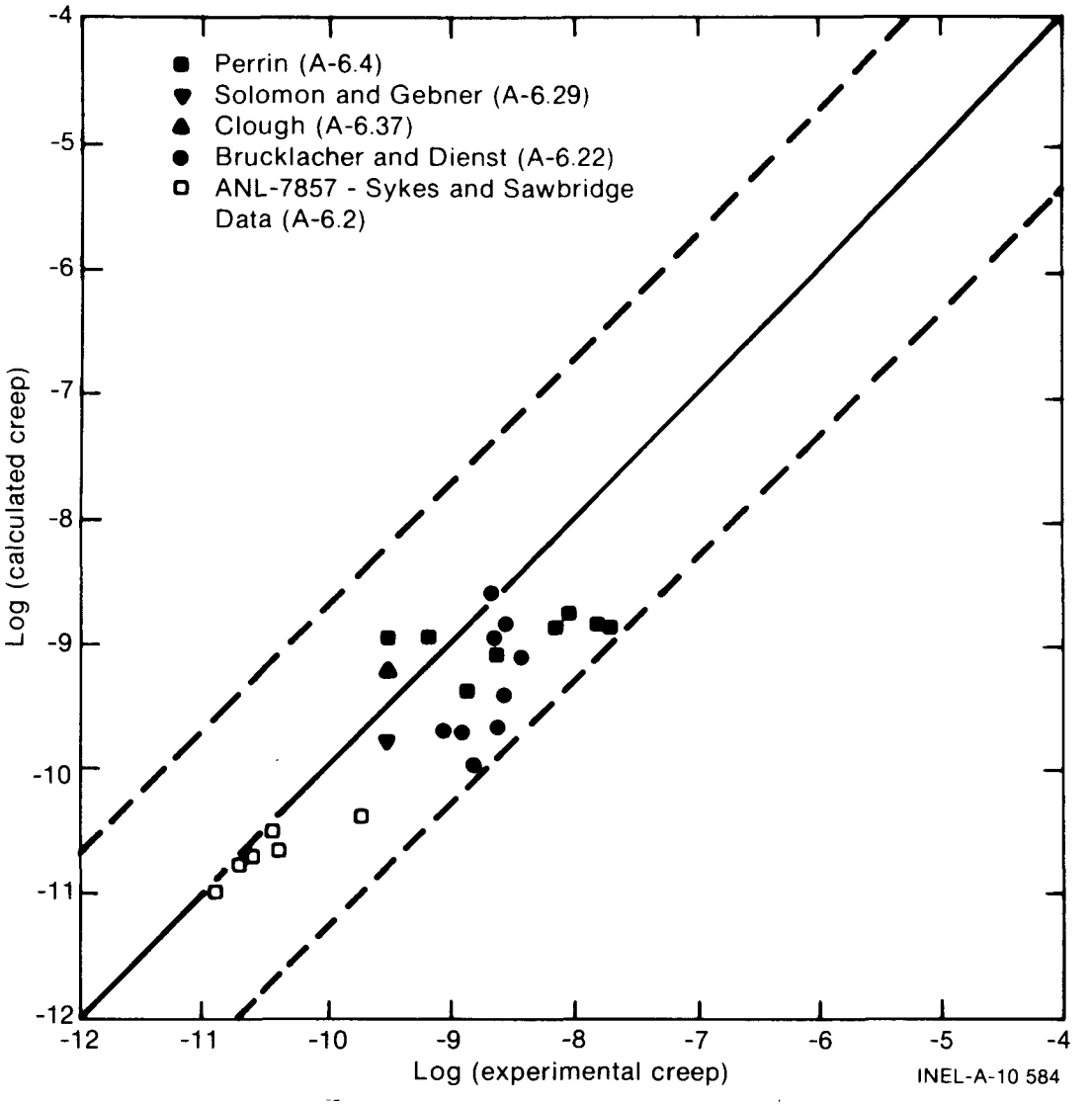

Fig. A-6.2 Comparison of irradiated UO_2 experimental data with corresponding calculated values from FCREEP.

where

$\dot{\epsilon}_u$ = upper and lower bounds of creep rate (s^{-1})

$\dot{\epsilon}$ = FCREEP calculated creep rate (s^{-1})

U = ±1.25.

6.3.2 Evaluation of Constants for Irradiation Enhanced Creep. The data sources used to evaluate the constants for the last term of Equation (A-6.4) are the fission induced creep tests of Sykes and Sawbridge[A-6.26], Clough[A-6.27], Brucklacher and Dienst[A-6.28] and Solomon and Gebner[A-6.29] and in-pile creep measurements of Perrin[A-6.11], D. Vollath[A-6.30] and O. D. Slagle[A-6.31]. These data were considered by Solomon[A-6.2] who developed Equation (A-6.4) except for the last term which was proposed by Brucklacher et al[A-6.12].

In Figure A-6.3 the predictions of FCREEP are compared with mixed oxide creep data selected from compressive experiments with O/M ratios between 1.95 and 1.98. This comparison includes data from Evans et al[A-6.3], Routbort et al[A-6.32], and Perrin[A-6.33]. Good agreement is obtained for O/M ratios between 1.95 and 1.96 and grain sizes between 18 and 23 μm. However, measured values for the 4-μm material used by Evans et al[A-6.3] are one to two orders of magnitude higher than the corresponding values calculated by FCREEP. Also, the high stress data of Routbort[A-6.32] (in the dislocation controlled creep regime) compare favorably with FCREEP calculations even though the oxygen to metal ratio is slightly higher than 1.95. The low stress data lie about an order of

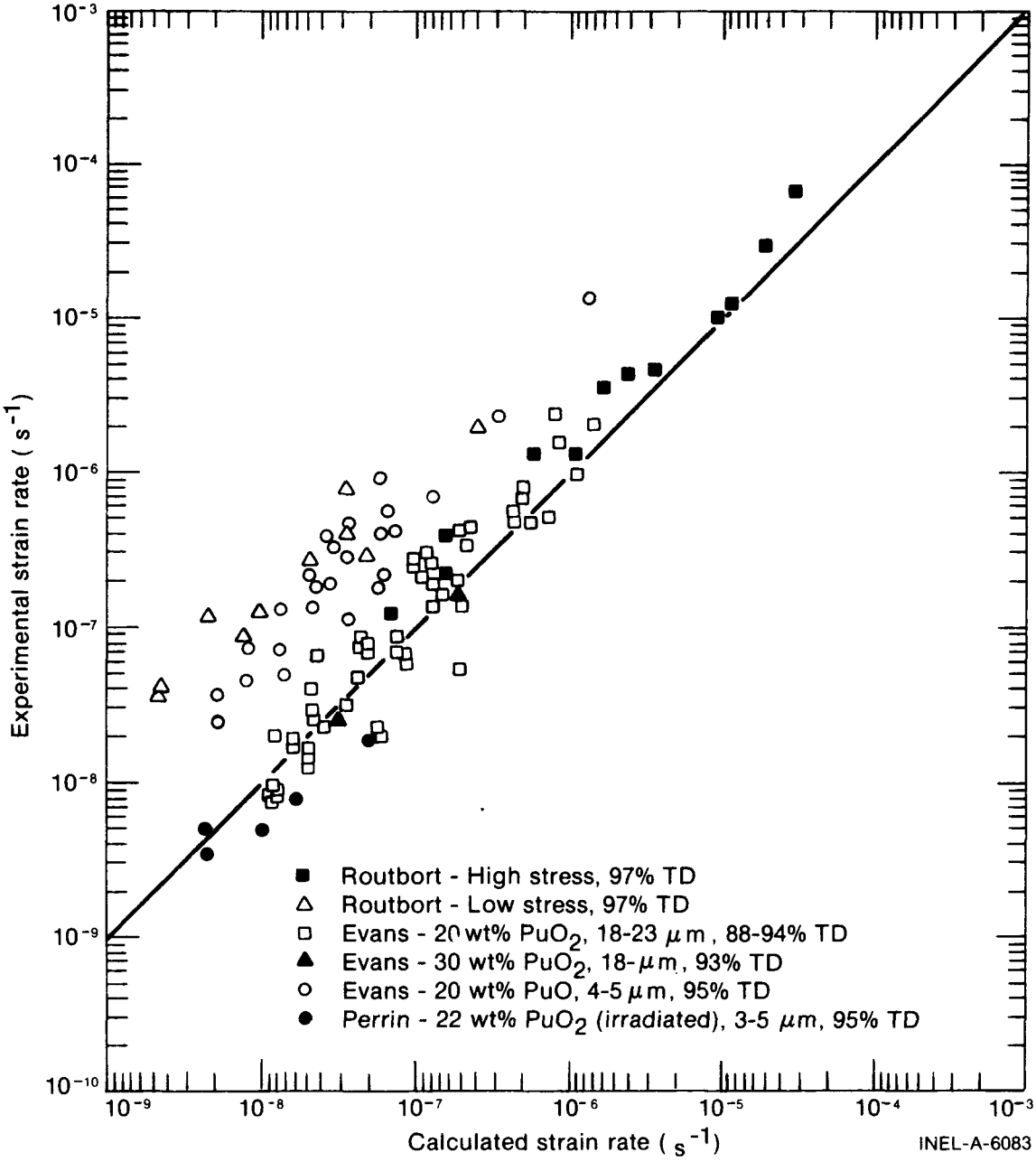

Fig. A-6.3 Comparison of (U,Pu)O_2 experimental data with corresponding calculated values from FCREEP.

magnitude higher than calculated by the FCREEP model indicating the significance of the stoichiometry on the diffusion mechanism in the viscous creep regime. Perrin's[A-6.33] data were used to determine the constants for fission enhanced creep in the linear stress creep of Equation (A-6.11). Reasonably good agreement is achieved for the irradiated material but the calculated values for unirradiated material are about an order of magnitude less than experimental values. The solid line represents perfect agreement between experimental and calculated values.

6.3.3 Evaluation of Constants for Time Dependent Creep. Much of the reported creep rate data do not include the time dependent creep contribution and the reported steady state data probably include those contributions, making an accurate analysis difficult. Some excellent creep studies reporting both time dependent and steady state creep have been reported. A comprehensive study was conducted by Battelle Columbus Laboratories[A-6.11,A-6.34,A-6.35]. They evaluated creep of UO_2 under both irradiated and unirradiated conditions. These data were used as the data base along with the data reported by Solomon[A-6.29,A-6.36], Clough[A-6.37], Dienst[A-6.38], and Brucklacher and Dienst[A-6.22].

Evaluation of the time dependent creep equation was carried out using the reported steady state creep rate and then determining the appropriate function to follow the curve and have the appropriate magnitude after a number of iterations. The best estimate equation is

$$\dot{\varepsilon}_t = 2.5 \exp(-1.4 \times 10^{-6} t)\ \dot{\varepsilon}_s \qquad \text{(A-6.20)}$$

where the terms of the equation have been previously defined.

Examples of the strain determined using the final strain rate equation

$$\dot{\varepsilon}_t = (2.5 \exp(-1.4 \times 10^{-6} t) + 1)\ \dot{\varepsilon}_s \qquad \text{(A-6.21)}$$

are shown in Figures A-6.4 and A-6.5. They show the FCREEP calculated strain compared with the base data and show a reasonably good fit.

6.4 Fuel Creep Subcode FCREEP Listing

A listing of the subcode FCREEP used for calculation of UO_2 and mixed oxide fuels is presented in Table A-6.I.

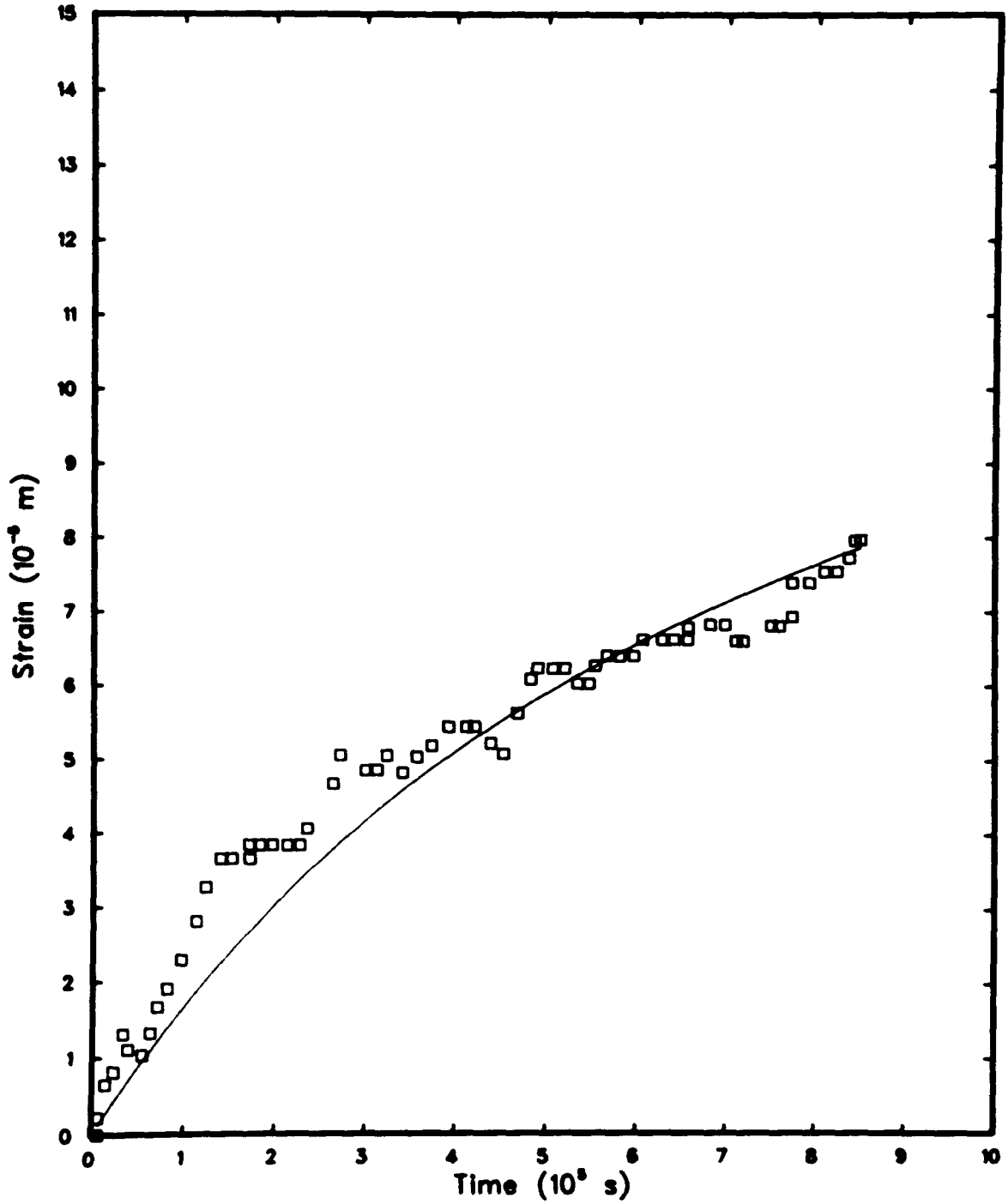

Fig. A-6.4 Comparison of UO_2 strain data of Rod 3C with corresponding FCREEP calculations.

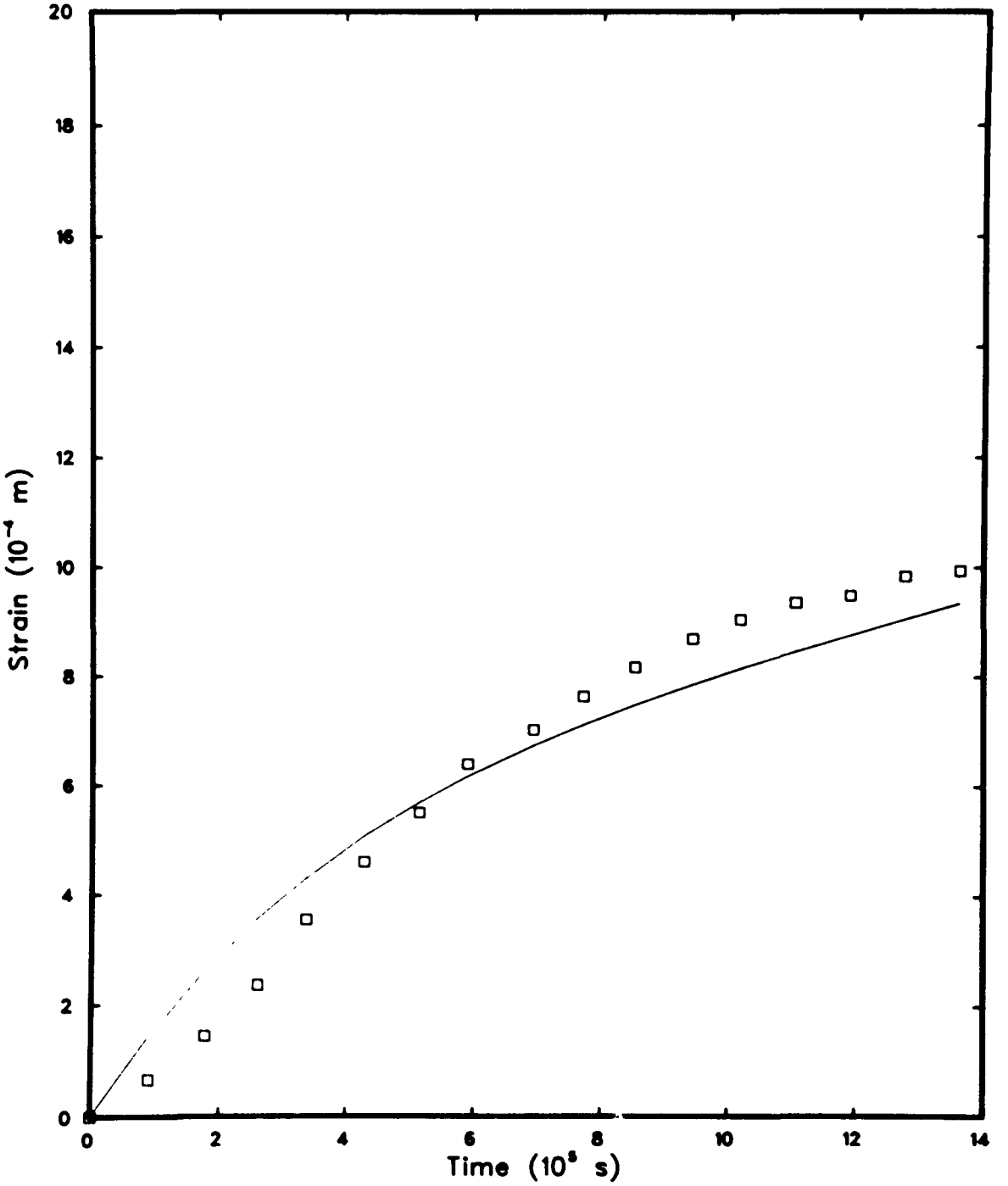

Fig. A-6.5 Comparison of UO_2 strain data of Capsule 2 with corresponding FCREEP calculations.

TABLE A-6.I

LISTING OF THE FCREEP SUBCODE

```
C
C
      FUNCTION FCREEP(FTEMP,FSTRES,FDENS,FGRN,FIS,COMP,FOM,TIME,IT,
     *                TLAST,PSTRES)
C
CCCCCC  THIS FUNCTION CALCULATES THE TOTAL CREEP FOR UO2 OR (U,PU)O2
CCCCCC  FUEL
CCCCCC
CCCCCC  FTEMP  = INPUT TEMPERATURE OF THE FUEL RING (K)
CCCCCC  FSTRES = INPUT STRESS (PA)
CCCCCC  FDENS  = INPUT INITIAL DENSITY OF THE FUEL (KG/M**3)
CCCCCC  FGRN   = INPUT GRAIN SIZE (MICRONS)
CCCCCC  FIS    = INPUT FISSION RATE ((FISSIONS/M**3)/S)
CCCCCC  COMP   = INPUT PLUTONIA CONTENT (WEIGHT PERCENT)
CCCCCC  FOM    = INPUT FUEL OXYGEN TO METAL RATIO
CCCCCC  TIME   = INPUT TIME TO END OF TIME STEP (S)
CCCCCC  TLAST  = INPUT TIME TO END OF LAST TIME STEP (S)
CCCCCC  PSTRES = INPUT STRESS ON FUEL DURING PREVIOUS TIME STEP (PA)
CCCCCC  L      = INPUT FUEL RING INDEX (1 - 10)
CCCCCC  IT     = INPUT TIME STEP NUMBER
CCCCCC
CCCCCC  FCREEP = OUTPUT STRAIN RATE ((M/M)/S)
CCCCCC
CCCCCC  FCREEP WAS DEVELOPED USING THE FOLLOWING DATA
CCCCCC      BURTON AND REYNOLDS ACTA METALLURGICA 21 (1973)
CCCCCC      SELTZER  JOURNAL OF NUCLEAR MATERIALS 34 (1970)
CCCCCC      PERRIN BMI - 1899 (1971)
CCCCCC      POTEAT AND YUST  ORNL-P-2371
CCCCCC      WOLFE AND KAUFMAN   WAPD - TM - 587 (1967)
CCCCCC      BOHABOY ET AL  GEAP - 10054 (1969)
CCCCCC
CCCCCC   FCREEP WAS DEVELOPED AND CODED BY C. S. OLSEN (NOVEMBER 1974).
CCCCCC   FCREEP WAS MODIFIED BY R. E. MASON (NOVEMBER 1978).
C
      STRANS = 16547416.8/(FGRN**0.5714)
      ROTH   = 11.45 * COMP/100. + (1. - COMP/100.) * 10.97
      D      = 0.1 * FDENS / ROTH
      IF (IT .LE. 1) XTIME = 0.0
      IF (COMP .GT. 0.0) GO TO 50
      IF(FOM .LT. 2.0) FOM = 2.0
      XLFOM  = - ALOG10(FOM - 1.99999) / 2.5
      QU1    = 9000.0
      QU2    = 10000.0
      Q1     = QU1 / (EXP(8.0 * (1.0 - XLFOM)/XLFOM) + 1.0) + 36294.4
      Q2     = QU2 / (EXP(8.0 * (1.0 - XLFOM)/XLFOM) + 1.0) + 56431.8
C
      IF (FSTRES .GT. PSTRES) XTIME = TLAST
      TTIME  = TIME - XTIME
      UPRURY = 2.5 * EXP(-1.2E-06 * TTIME) + 1.0
      ERUF   = 3.72264E-35 * FIS * FSTRES * EXP(-2617.0/FTEMP)
      IF (COMP .GT. 0.0) GO TO 50
C
C     LOW STRESS UO2 CREEP CALCULATION
C
      IF (FSTRES .GT. STRANS) GO TO 30
      UCREPL = (0.391924 + 1.31E-19 * FIS) * FSTRES * EXP(-Q1/FTEMP) /
     #         ((-87.7 + D) * FGRN * FGRN)
C
      FCREEP = UPRURY * (UCREPL + ERUF)
      GO TO 1000
   30 CONTINUE
C
C     HIGH STRESS UO2 CALCULATIONS
C
      UCREPL = (0.391924 + 1.31E-19 *  FIS) * STRANS * EXP(-Q1/FTEMP) /
     #         ((-87.7 + D) * FGRN * FGRN)
      UCREPH = 2.0391 E-25 * (FSTRES ** 4.5) * EXP(-Q2/FTEMP)/(-90.5+D)
C
      FCREEP = UPRURY * (UCREPL + UCREPH + ERUF)
      GO TO 1000
C
   50 CONTINUE
C     CALCULATION OF MIXED OXIDE CREEP
C
C     LOW STRESS (U,PU)O2 CALCULATIONS
```

TABLE A-6.I (continued)

```
C
      IF (FSTRES .GT. STRANS) GO TO 70
      PCREPL = (0.1007 + 7.57E-20 * FIS) *  FSTRES/(FGRN * FGRN)  *
     #          EXP(-50327.1/FTEMP + 33.3*(1. - .01*D) + .014 * COMP)
C
      FCREEP = PCREPL
C
      GO TO 1000
   70 CONTINUE
C
C     HIGH STRESS (U,PU)O2 CALCULATIONS
C
      PCREPH = 6.46916E-25 * (FSTRES ** 4.5) * EXP(-70458.0/FTEMP  +
     #          10.3 * (1. - 0.01 * D) + 0.014 * COMP)
      PCREPL = (0.1007 + 7.57E-20 * FIS) *  STRANS / (FGRN * FGRN)  *
     #          EXP(-50327.1/FTEMP + 33.3*(1. - .01*D) + .014 * COMP)
C
      FCREEP = PCREPL + PCREPH
C
C     THE FOLLOWING CALCULATIONS PROVIDE THE UPPER AND LOWER BOUNDS
C     TO THE CREEP RATE EQUATIONS AND ARE NOT AN OUTPUT OF THE
C     FUNCTION FCREEP UNLESS THE USER DESIRES TO MODIFY THE
C     SUBCODE APPROPRIATELY.
C
C     UCREPH IS THE UPPER BOUND
      UCREPH = FCREEP * 17.78
C     UCREPL IS THE LOWER BOUND
      UCREPL = FCREEP * 0.0562
C
 1000 CONTINUE
      RETURN
      END
```

6.5 References

A-6.1. P. E. Bohaboy, R. R. Asamoto, A. E. Conti, *Compressive Creep Characteristics of Stoichiometric Uranium Dioxide,* GEAP-10054 (May 1969).

A-6.2. A. A. Solomon, J. L. Routbort, J. C. Voglewede, *Fission-Induced Creep of UO_2 and Its Significance to Fuel-Element Performance,* ANL-7857 (September 1971).

A-6.3. S. K. Evans, P. E. Bohaboy, R. A. Laskiewicz, *Compressive Creep of Urania-Plutonia Fuels,* GEAP-13732 (August 1971).

A-6.4. J. S. Perrin and W. R. D. Wilson, *Effect of Irradiation on the Creep of Uranium Dioxide,* BMI-1899 (March 1971).

A-6.5. F. R. N. Nabarro, *Report of a Conference on the Strength of Solids,* Physical Society, London 1949, p 75.

A-6.6. C. Herring, "Diffusional Viscosity of Poly-Crystalline Solid," *Journal of Applied Physics, 21* (1950) p 437.

A-6.7. R. L. Coble, "A Model for Boundary Diffusion Controlled Creep in Poly-Crystalline Materials," *Journal of Applied Physics, 34* (1963) p 1679.

A-6.8. W. M. Armstrong, W. R. Irvine, R. H. Martinson, "Creep Deformation of Stoichiometric Uranium Dioxide," *Journal of Nuclear Materials, 7,* No. 2 (1962) pp 133-141.

A-6.9. L. E. Poteat and C. S. Yust, *Grain Boundary Reactions During Deformation,* ORNL-P-2371 (1965).

A-6.10. J. Weertman, "Steady-State Creep Based Through Dislocation Climb," *Journal of Applied Physics, 28* (1957) p 362.

A-6.11. J. S. Perrin, "Irradiation-Induced Creep of Uranium Dioxide," *Journal of Nuclear Materials, 39* (1971) pp 175-182.

A-6.12. D. Brucklacher, W. Dienst, F. Thümmler, *Creep Behavior of Oxide Fuels Under Neutron Irradiation,* Translated from German by J. L. Routbort, Argonne National Laboratory, ANL-Trans-942 (May 1973).

A-6.13. R. A. Wolfe and S. F. Kaufman, *Mechanical Properties of Oxide Fuels,* WAPD-TM-587 (October 1967).

A-6.14. M. S. Seltzer, A. H. Clauer, B. A. Wilcox, "The Stress Dependence for High Temperature Creep of Polycrystalline Uranium Dioxide," *Journal of Nuclear Materials, 34* (1970) pp 351-353.

A-6.15. M. S. Seltzer, J. S. Perrin, A. H. Clauer, B. A. Wilcox, "A Review of Creep Behavior of Ceramic Nuclear Fuels," *Reactor Technology, 14,* No. 2 (January 1971) pp 99-135.

A-6.16. J. R. Matthews, *Mechanical Properties and Diffusion Data for Carbide and Oxide Fuels,* AERE-M-2643 (September 1974).

A-6.17. R. G. Sachs, *Reactor Development Program Progress Report,* ANL-RDP-16 (April-May 1973).

A-6.18. B. Burton and G. L. Reynolds, "The Diffusional Creep of Uranium Dioxide: Its Limitation by Interfacial Processes," *Acta Metallurgica, 21* (August 1973) pp 1073-1078.

A-6.19. B. Burton and G. L. Reynolds, "The Influence of Deviations from Stoichiometric Composition on the Diffusional Creep of Uranium Dioxide," *Acta Metallurgica, 21* (December 1973) pp 1641-1647.

A-6.20. P. E. Bohaboy and R. R. Asamoto, "Compressive Creep Characteristics of Ceramic Oxide Nuclear Fuels: Part I: Uranium Dioxide," *Presented at American Ceramic Society Nuclear Division, Pittsburgh, Pennsylvania* (October 6-8, 1968).

A-6.21. M. V. Speight, *Enhancement of Diffusion Creep Under Irradiation,* Central Electricity Generating Board, RD/B/N-2402 (August 1972).

A-6.22. D. Brucklacher and W. Dienst, "Creep Behavior of Ceramic Nuclear Fuels Under Irradiation," *Journal of Nuclear Materials, 42* (1972) pp 285-296.

A-6.23. A. A. Solomon, "Effect of γ-Radiation on the Deformation of UO_2," *Journal of Nuclear Materials, 47* (1973) pp 345-346.

A-6.24. R. Scott, A. R. Hall, J. Williams, "The Plastic Deformation of Uranium Oxides above 800°C," *Journal of Nuclear Materials, 1* (1959) pp 39-48.

A-6.25. W. M. Armstrong and W. R. Irvine, "Creep Deformation on Nonstoichiometric Uranium Dioxide," *Journal of Nuclear Materials, 9,* No. 2 (1963) pp 121-127.

A-6.26. E. C. Sykes and P. T. Sawbridge, *The Irradiation Creep of Uranium Dioxide,* Central Electricity Generating Board, RD/BN/1489 (November 1969).

A-6.27. D. J. Clough, "Irradiation Induced Creep of Ceramic Fuels," *Proceedings on Fast Reactor Fuel and Fuel Elements,* GFK Karlsruhe (1970) p 321.

A-6.28. D. Brucklacher and W. Dienst, "Kontinuierliche Messung Des Kriechens von UO_2 Unter Bestrahlung," *Journal of Nuclear Materials, 36* (1970) pp 244-247.

A-6.29. A. A. Solomon and R. H. Gebner, "Instrumented Capsule for Measuring Fission-Induced Creep of Oxide Fuels," *Nuclear Technology, 13,* (February 1972) p 177.

A-6.30. D. Vollath, *Thermisches Kriechen von Plutonium-Haltigen Oxidischen Kernbrennstoffen,* Reactor Meeting, Bonn, Germany (March 30, 1971) pp 558-561.

A-6.31. O. D. Slagle, *High Temperature Creep of UO_2-20 wt% PuO_2,* HEDL-TME-71-28 (August 1971).

A-6.32. J. L. Routbort, N. A. Javed, J. C. Voglewede, "Compressive Creep of Mixed-Oxide Fuel Pellets," *Journal of Nuclear Materials, 44* (1972) pp 247-259.

A-6.33. J. S. Perrin, "Effect of Irradiation on Creep of UO_2-PuO_2," *Journal of Nuclear Materials, 42* (1972) pp 101-104.

A-6.34. J. S. Wilson and R. D. William, *Effect of Irradiation on the Creep of Uranium Dioxide,* BMI-1899 (March 1971).

A-6.35. W. R. D. Wilson and J. S. Perrin, "Anisothermal Effects During In-Pile Creep Testing of Uranium Dioxide," *Nuclear Science and Engineering, 45* (1971).

A-6.36. A. A. Solomon, "Radiation-Induced Creep of UO_2," *Journal of the American Ceramic Society, 56* (March 1973).

A-6.37. D. J. Clough, "Creep Properties of Oxide and Carbide Fuels Under Irradiation," *Journal of Nuclear Materials, 65* (1977).

A-6.38. W. Dienst, "Irradiation Induced Creep of Ceramic Nuclear Fuels," *Journal of Nuclear Materials, 65* (1977).

7. FUEL DENSIFICATION (FUDENS)

(R. E. Mason)

The subcode FUDENS calculates fuel dimensional changes due to irradiation induced densification of UO_2 and $(U,Pu)O_2$ fuels during the first few thousand hours of water reactor operation. Densification is calculated as a function of fuel burnup, temperature, and initial density. This subcode is based on data of fuel that had small amounts of hydrostatic stress applied. Densification can result from hydrostatic stress on the fuel due to contact with the cladding and is considered in Section 9 of Appendix A. Both models describe the same physical process, but the model which calculates the greater densification should be used.

The data used to develop FUDENS were taken from irradiated fuel which was also swelling. If fuel densification is much greater than swelling during the first thousand hours of irradiation, then to a first approximation, swelling can be neglected during this period. That was done for the development of FUDENS model. A suggested calculation procedure combining calculations of models given in this appendix is discussed in Section 8.

7.1 Summary

The subcode FUDENS uses one of two methods to calculate the maximum density change during irradiation. The density change observed during a resintering test (1973 K for more than 24 hours) in a laboratory furnace is the preferred input for the calculation. If a resintering density change is not input, the code uses the initial unirradiated density of the fuel and the fuel fabrication sintering temperature for the calculations. These inputs are used in the following equations to calculate the maximum densification length change during irradiation.

If a nonzero value for the resintering density change is input:

$$\left(\frac{\Delta L}{L}\right)_m = -(0.0015)\ \text{RSNTR, when FTEMP} < 1000\ \text{K} \qquad \text{(A-7.1)}$$

$$\left(\frac{\Delta L}{L}\right)_m = -(0.00285)\ \text{RSNTR, when FTEMP} \geq 1000\ \text{K.} \qquad \text{(A-7.2)}$$

If zero is input for the resintering density change:

$$\left(\frac{\Delta L}{L}\right)_m = \frac{-22.2\ (100 - \text{DENS})}{(\text{TSINT} - 1453)}, \text{ when FTEMP} < 1000\ \text{K} \qquad \text{(A-7.3)}$$

$$\left(\frac{\Delta L}{L}\right)_m = \frac{-66.6\ (100 - \text{DENS})}{(\text{TSINT} - 1453)}, \text{ when FTEMP} \geq 1000\ \text{K} \qquad \text{(A-7.4)}$$

where

$\left(\frac{\Delta L}{L}\right)_m$ = maximum possible dimension change of fuel due to irradiation (percent)

DENS = theoretical density (percent)

FTEMP = fuel temperature (K)

TSINT = sintering temperature (K)

RSNTR = resintered fuel density change (kg/m^3).

Densification as a function of burnup is calculated using

$$\frac{\Delta L}{L} = \left(\frac{\Delta L}{L}\right)_m + \exp\left[-3(\text{FBU} + B)\right] + 2.0 \exp\left[-35(\text{FBU} + B)\right] \qquad \text{(A-7.5)}$$

where

$\frac{\Delta L}{L}$ = dimension change (percent)

FBU = fuel burnup (MWd/kgU)

B = a constant determined by the subcode to fit the boundary condition: $\Delta L/L = 0$ when FBU = 0.

The FUDENS subcode uses Equation (A-7.5) to calculate total densification and then subtracts densification from the previous time step to obtain the incremental densification. The incremental densification for the time step being considered is the output of the FORTRAN function FUDENS.

7.2 UO_2 and Mixed Oxide Densification Data and Models

The sintering of cold pressed UO_2 powder compacts may be divided usefully into three regimes: (a) the formation of necks between particles, (b) the decrease of interconnected porosity, and (c) the subsequent volume reduction of isolated pores[A-7.1]. The last stage begins when 92 to 95% theoretical density (TD) is reached. The porosity in fuels less than 92% TD, which have been sintered at low temperatures, is open and located along grain edges. The closed porosity in low density materials sintered at low temperatures is also located along grain boundaries. However, at higher sintering temperatures, accelerated grain growth occurs and closed porosity may be found inside the grains even in low density compacts[A-7.2]. In-reactor densification involves the third sintering regime in which fine, isolated, closed, porosity (located either at grain boundaries or within the grains) is annihilated.

7.2.1 UO_2 and Mixed Oxide Densification Data. Edison Electric Institute/Electric Power Research Institute (EEI/EPRI)[A-7.3,A-7.4] recently concluded a comprehensive study of UO_2 fuel densification. The fuel was tested in the RAFT (Radially Adjustable Facility Tubes) of the General Electric Test Reactor (GETR)[a]. Pre- and postirradiation physical properties are reported on fuel subjected to burnups of up to 3.5 MWd/kgU. They concluded that irradiation induced densification can be correlated with fuel microstructure, that is, the largest in-reactor density changes occurred for fuel types having a combination of the smallest pore size, the largest volume percent of porosity less than 1 μm in diameter, the smallest initial grain size, and the lowest initial density. The volume fraction of porosity less than 1 μm in diameter contributed significantly to densification of the fuel types studied; density increases were accompanied by a significant decrease in volume fraction of pores in this size range. The volume fraction of pores ranging in diameter from 1 to 10 μm initially increased with densification; but decreased with continued densification. Significant density increases occurred during irradiation with only minimal increases in grain size.

Analysis of the EPRI data also shows that pellets in low burnup, low fission rate regions densify less than pellets irradiated to the same burnup but in higher fission rate and temperature positions as shown in Figure A-7.1. At higher fission rates and temperatures, densification occurs rapidly and pellets approach maximum densities at a burnup of 1 MWd/kgU. At lower fission rates, densification appears to be increasing with burnups of 2 MWd/kgU.

[a] Located in Pleasanton, California.

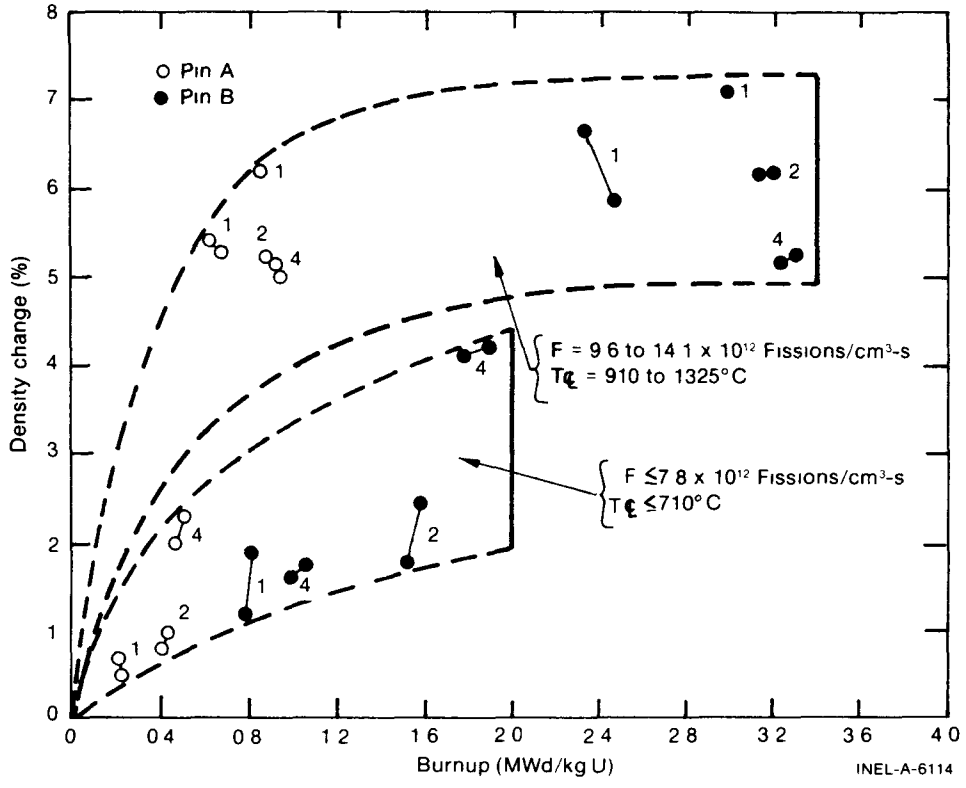

Fig. A-7.1 The effect of burnup and fission rate on the fuel density change for EPRI fuel types 1, 2, and 4.

Rolstad et al[A-7.5] measured the fuel stack length change of UO_2 in the Halden HBWR reactor[a]. Fuel densities (87, 92, and 95% TD), fabrication sintering temperatures, irradiation power levels, and fuel-cladding gap sizes were used to study irradiation induced densification. Rolstad found that fuel sintered at the highest temperature densified the least (stable fuel) and fuel sintered at the lowest temperature densified the most (unstable fuel). The axial length change was measured during irradiation and as a function of burnup (Figure A-7.2) for different power levels, did not depend on reactor power levels or fuel temperatures. Hanevik et al[A-7.6] proposed that this may be attributed to the fact that the outer edges (shoulders) of the pellet would be within 200 to 300 K of each other at both power levels. Since the shoulders of the pellet are much colder than its center, the axial in-reactor length change measurements are probably a measurement of the shrinkage in these regions (that is, low temperature irradiation densification). The amount of fuel stack length change of the Halden fuel was found to depend mainly on out-of-pile thermal fuel stability, initial density, and burnup.

Collins and Hargreaves[A-7.7] compared measurements of out-of-pile sintering rates at temperatures greater than 1600 K with the sintering rates of fuel irradiated in the Windscale Advanced Gas-Cooled Reactor (WAGR)[b]. The observed out-of-pile

[a] Test reactor located in Halden, Norway.

[b] A prototypic, power-productive reactor in Windscale, Cumberland, England.

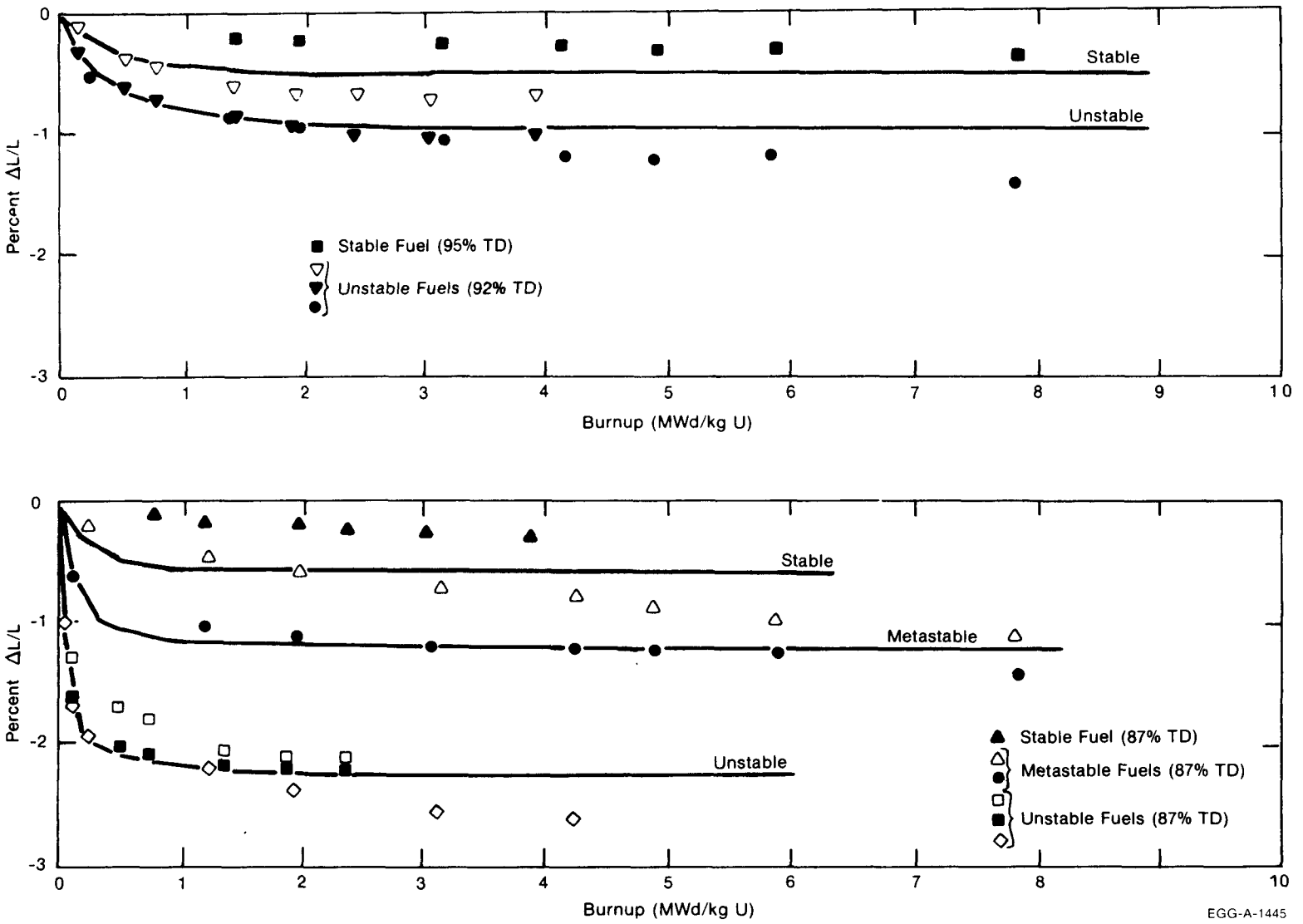

Fig. A-7.2 Change in fuel stack length of Halden fuel as a function of burnup.

densification was attributed to the sintering of grain boundary porosity and was characterized by an activation energy of 2.9×10^5 J/mol for grain boundary diffusion. Extrapolation of these results to the approximate 1000 K temperatures of the in-pile material indicated that negligible thermal sintering would be expected after a few hundred hours at this temperature. In addition, no evidence of sintering was observed in out-of-pile annealing tests at 1173 K and a pressure of 2.06 MPa. However, fuel irradiated to less than 0.3% burnup at temperatures between 1000 and 1100 K experienced significant reduction in diameter. This shrinkage was attributed to irradiation induced sintering which decreased the initial fuel porosity volume. Pores with diameters less than 3 μm were reported by Collins and Hargreaves to be the major source of increased density. Pores larger than 100 μm were reported stable during irradiation at temperatures below 1500 K.

Ferrari et al[A-7.8] measured UO_2 fuel pellet densification in commercial reactors; using both movable in-core flux detectors and postirradiation examination of selected test rods. The densification rate of the fuel was reported to occur rapidly during the early stages of irradiation and then slow or even stop after about 6 to 10 MWd/kgU, as shown in Figure A-7.3. These results are consistent with the measurements of Rolstad et al. For the given density (92% TD), the extent of densification was reported to vary significantly with microstructure, but no details of the microstructure were reported. Ferrari et al reported that power levels between 4.9 and 55.8 kW/m did not significantly affect densification. This result is in agreement with Rolstad et al. The axial shrinkage was suggested to be controlled

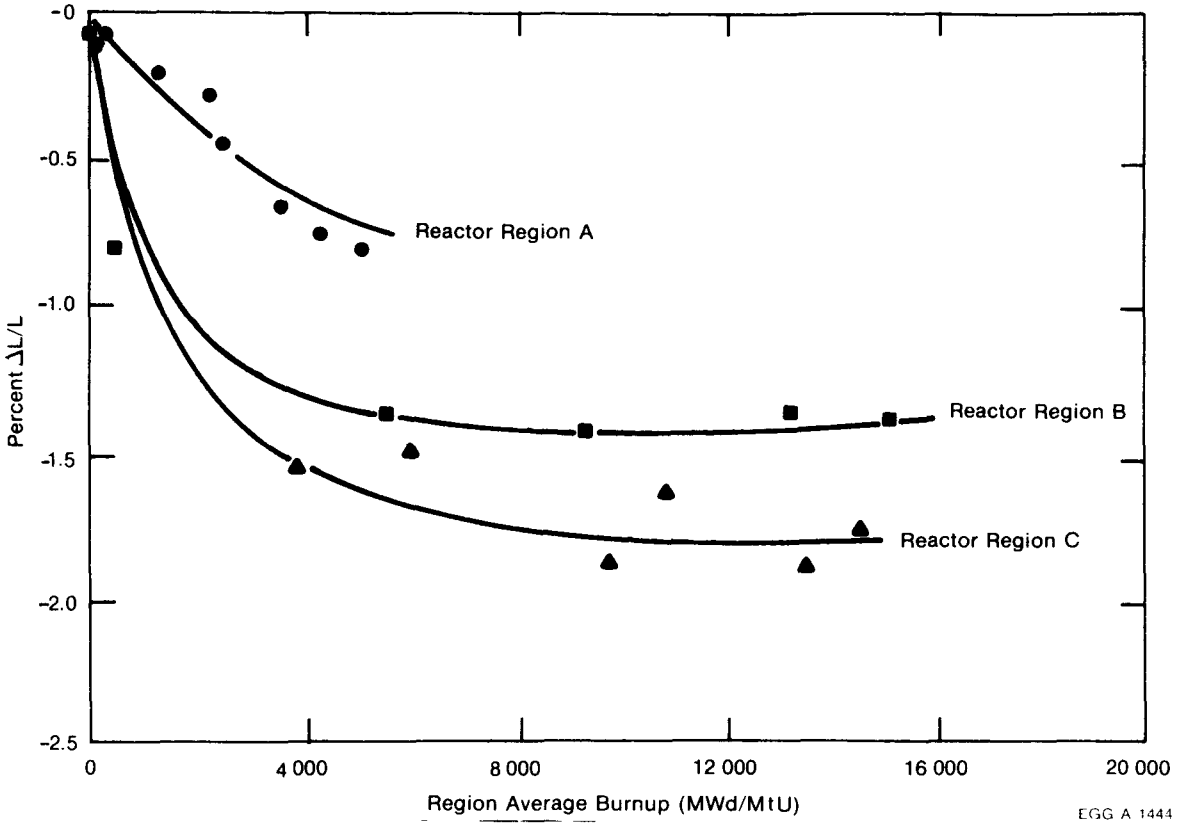

Fig. A-7.3 Fuel stack length changes for 92% TD UO_2 processed by different techniques.

by densification in the shoulder of the fuel pellets, a region of the fuel pellets generally below 1073 K. This temperature is too low for in-pile densification to be attributed to thermal mechanisms. Ferrari et al proposed that the kinetics of densification are compatible with irradiation enhanced diffusion processes.

Metallographic measurements on the fuel by Ferrari et al indicated that the irradiation enhanced densification was associated with the disappearance of fine pores and that pore shrinkage significantly decreased with increasing pore size. These results correspond to the EPRI findings. Ferrari et al suggested that densification could be reduced through both microstructural control of the fuel pellet and a reduction of the fine porosity content. Both of these factors are influenced by the fabrication process, especially sintering temperature and the use of so-called "pore formers". Ferrari et al reported that experimental fuel of 89% theoretical density has been made and demonstrated to be relatively stable in the Saxton reactor[a].

Heal et al[A-7.9] reported that by controlling the pore size they have developed UO_2 fuel which does not densify significantly. They assumed that shrinkage of the pores would continue until the internal pressure of trapped gas in the pores matched the surface tension forces causing shrinkage. Their calculations show shrinkage in pores of diameters greater than 20 μm and that pores of 10 μm shrink only to 6 to 7 μm before gas stabilization occurs, whereas voids of 1.0 μm or less shrink to 0.2 μm or less before gas stabilization occurs, causing considerable densification. Fuel pellets fabricated with porosity sizes greater than 25 μm were irradiated by Heal et al to 1.4×10^{26} fissions/m^3 with center temperatures up to 1873 K. Postirradiation examination of these pellets showed significantly less than 1% volume densification.

Ross[A-7.10] has shown that fuel after an irradiation of 2×10^{25} fissions/m^3 has lost most pores with radii less than 0.5 μm. He found that fuels with burnups even as low as 2×10^{24} fissions/m^3 had lost most pores with radii less than 0.3 μm.

Burton and Reynolds[A-7.11] measured the shrinkage of three fuel pellets during the final stage of out-of-pile sintering of 96.5% TD UO_2 with isolated porosity at grain boundaries. The densification rate was initially large but decreased greatly at longer times. The shapes of their curves are very similar to those for the in-pile densification of UO_2; however, in-pile densification occurs at much lower temperatures. This reduction in the sintering rate with time can arise for several reasons: (a) grain boundaries may migrate away from cavities during annealing, thus removing short diffusion paths of vacancies away from cavities, (b) when significant entrapped gas is present, cavities may shrink until they become stabilized as the internal gas pressure becomes equal to the surface tension of the cavity as proposed by Heal et al, and (c) the number of cavities can progressively decrease as densification proceeds. The first and second reasons were rejected by Burton and Reynolds because the majority of the cavities in their samples remained on grain boundaries during

---

[a] Experimental reactor in Saxton, Pennsylvania.

sintering, and smaller cavities sintered to closure. Therefore, Burton and Reynolds suggested that the reduction in the sintering rate with time is only due to the progressive reduction in the number of cavities.

The reported irradiation induced densification data indicate that it is affected by porosity and pore size distribution, fuel density, and irradiation temperature. The lack of a temperature dependence of the fuel densification data by Ferrari et al and Rolstad et al is probably a result of the measurement technique (that is, measurement of the length change in the low temperature pellet edges).

7.2.2 Survey of Densification Models. Densification models proposed by Rolstad, Meyer[A-7.12], Collins and Hargreaves, Voglewede and Dochwat[A-7.13], Stehle and Assmann[A-7.14], Marlowe[A-7.15], Hull and Kimmer[A-7.16], and MacEwen and Hastings[A-7.17] are reviewed in this section.

Rolstad et al[A-7.5] used two equations to correlate their data. In the first, the shortening $\left(\frac{\Delta L}{L}\right)_m$ is a function of the current theoretical density (DENS) and sintering temperature in degrees centigrade (TSINT) at a burnup of 5000 MWd/tUO_2:

$$\left(\frac{\Delta L}{L}\right)_m = -22.2\frac{(100 - DENS)}{(TSINT - 1453)}. \qquad \text{(A-7.6)}$$

The effect of burnup was introduced through the use of a master curve created by shifting all curves vertically to agreement at 5000 MWd/tU and then horizontally to achieve the best agreement at the low burnup portion of the curves. The master curve is

$$\frac{\Delta L}{L} = -3.0 + 0.93\ \exp(-BU) + 2.07\ \exp(-35BU) \qquad \text{(A-7.7)}$$

where

$\frac{\Delta L}{L}$ = the percent shrinkage of the fuel

BU = the burnup (MWd/kgU).

This equation results in a rapid length change at low burnups (<1.0 MWd/kgU) and small length change at higher burnup levels. Very little additional densification is calculated after a burnup of 5000 to 6000 MWd/kgU.

Meyer developed a conservative model based on resintering of fuel at 1973 K for 24 hours. The change in density of fuel after a resintering test was used as an upper limit. Two equations were used to calculate densification, one for fuels which resintered less than 4% and one for fuels which resintered more than 4%. Meyer's model was based on a log

function of burnup and the resintering density change. Meyer reports that his model adequately bounds all in-reactor densification data at his disposal.

Collins and Hargreaves developed an empirical densification expression based on the initial porosity and an exponential burnup function. They suggested that a complete description of the densification rate of uranium dioxide under irradiation demands a knowledge of the initial size distribution of the as-manufactured porosity in addition to the total volume of porosity because of the differing sintering rates of different pore sizes. However, the pore morphology of their fuel was not determined.

J. C. Voglewede and S. C. Dochwat developed an equation for final stage densification of mixed oxide fuels based on EBR-II[a] reactor data. It is a semiempirical approach based on porosity, stress, and temperature.

Stehle and Assmann proposed a vacancy controlled densification model as a function of initial fuel porosity, fission rate, initial pore radius, fuel temperature, and vacancy diffusion. Their equation considers pores of only one diameter; therefore, application of this equation to practical engineering problems requires that the equation be integrated over all pore sizes existing in the fuel. Their approach predicts that irradiation induced densification is temperature dependent because of the dependence of the volume diffusion coefficient, (D_V) on temperature. The authors used approximate values for D_V and found that the densification rate should change at approximately 1023 K. This corresponds very well with the experimental results found in the EPRI densification study.

Marlowe proposed a model for diffusion controlled densification and modified the model to include fuel swelling contributions to the density changes as well as an irradiation induced diffusivity which provides atomic mobility for grain growth densification. Their model is based on densification and grain growth rate, which must be determined experimentally for any particular fuel. These strongly affect the predicted in-reactor densification behavior through grain size modification. Because the model allows complete pore elimination and, in fact, densities greater than theoretical for the matrix material, an upper limit to the density must be calculated to limit the densification change.

Hull and Rimmer developed an empirical densification equation based on grain boundary diffusion and temperature. They report reasonably good agreement with the Burton and Reynolds data despite the approximations required to evaluate this equation and the errors in determining the porosity distribution of the samples. Both the shape of the predicted curve and the absolute magnitude of the values were reported to be in good agreement, demonstrating that the decrease in sintering rate with time is associated only with the progressive reduction in the number of cavities. However, the calculation assumed a constant cavity spacing for each time step in changing from one volume size to the next. The similarity between the out-of-pile and in-pile densification strongly suggests the importance of pore size distribution and volume for in-reactor densification.

---

[a] The Experimental Breeder Reactor, located at INEL, Idaho Falls, Idaho.

MacEwen and Hastings developed a model describing the rate change of pore diameter based on the time dependence of vacancy and interstitial concentrations, fission gas concentrations, and internal pore pressures. Two equations were used. One describes the diametral change of pores on the grain boundaries and the other describes intergranular pore shrinkage. Use of their model also requires vacancy jump frequencies. The model is thus difficult to use in engineering applications with the present in-reactor fuel data base.

Fuel densification models proposed in References A-7.11 and A-7.13 through A-7.17 attempted to correlate fuel densification with fundamental material properties. These theoretical or semiempirical approaches will eventually be the preferred modeling techniques but current versions of these models must be based on estimates of such material properties as diffusion coefficients, void concentrations, jump frequencies, etc., which are not sufficiently well defined to be used to predict in-reactor densification. As R. O. Meyer pointed out in his review, the use of complicated theoretical approaches is not justified unless they can be supported with material property data which allow significantly better predictions than fully empirical correlations. An empirical approach similar to the Meyer model is best for modeling densification.

7.3 FUDENS Model Development

The relation between densification and burnup suggested by Rolstad et al [Equation (A-7.7)] has been adopted to the FUDENS code. Densification is assumed to consist of a rapidly varying component, represented by the term 2.0 exp [-35 (FBU + B)] in Equation (A-7.5), and a slowly varying component, represented by the term exp [-3 (FBU + B)] in Equation (A-7.5). The expression was adopted because it successfully describes the burnup dependence of both the original Rolstad et al data and recent EPRI data.

The Rolstad et al model[A-7.5], as originally proposed, is solved graphically as indicated in Figure A-7.4. The curves in Figure A-7.4a are defined by Equation (A-7.6) for various sintering temperatures and the curve in Figure A-7.4b is defined by Equation (A-7.7).

The use of these equations to find the length change as a function of burnup is shown in Figure A-7.4. For an initial density of 91% TD and sintering temperature of 1,500°C, the left scale of Figure A-7.4 shows that the eventual length change will be about 0.6%. To determine the change as a function of burnup, new axes are drawn in Figure A-7.4b as shown by the dashed lines. With the (x,y) origin of these new axes interpreted to be zero burnup and zero length change, the solid curve in Figure A-7.4b then gives $\Delta L/L$ as a function of burnup. The 0.6% fractional length change is then seen to require about 5000 MWd/tU burnup.

The numerical equivalent to this graphical solution is incorporated into the subroutine FUDENS. Newton's method[A-7.18] was selected for the iterative determination of the new origin because of its rapid convergence. Between four and ten iterations are typically required to determine the position of the new axes with a 0.0002% convergence criterion defined by

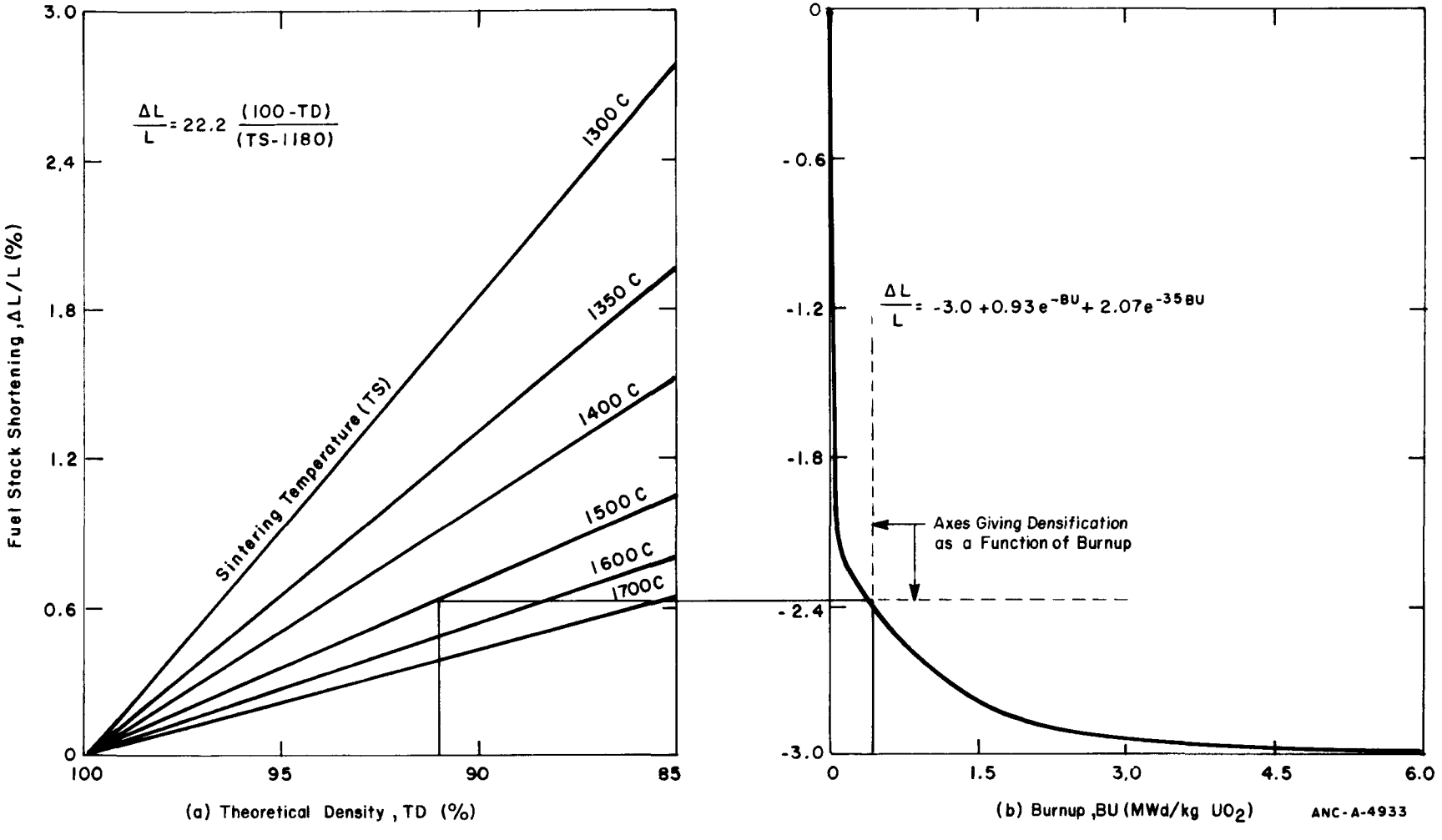

Fig. A-7.4 Graphical solution of Rolstad's model, where TD is percent of theoretical density, TS is sintering temperature (°C), and BU is burnup.

$$E = 100\ (X - X_1)/X \qquad \text{(A-7.8)}$$

where

E = calculated convergence

X = current value of burnup in Equation (A-7.8)

X_1 = preceding value of burnup in Equation (A-7.8).

The maximum densification term, $\left(\frac{\Delta L}{L}\right)_m$ in Equation (A-7.5), determines the in-reactor densification limit. Four different expressions, Equations (A-7.1) through (A-7.4), are used by the FUDENS code to determine a number for this term. When a measurement of fuel densification during a resintering test at 1973 K is available, this measurement is the basis of the model's prediction for the maximum in-pile shrinkage. The resintering density change found during a resintering test at 1973 K for at least 24 hours is the most appropriate basis to use in calculating the maximum in-pile densification because in-pile densification and thermal resintering are both dependent on porosity removal. However, Meyer's assumption that the change in length during a resintering test is equal to the maximum in-pile densification is too conservative for a best estimate code. The maximum irradiation induced densification calculated by FUDENS is therefore a fraction of the density change found during a resintering test. If resintering test data are not available, the FUDENS model defaults to the expression suggested by Rolstad et al, Equation (A-7.3). This provides a reasonable estimate of in-pile densification, but unlike resintering tests, it cannot account for variations in pore size distribution.

Constants in the expressions used by FUDENS for maximum in-pile shrinkage were determined separately for high (> 1000 K) and low temperatures. The separate expressions were used because a temperature dependence was found in the EPRI data and because of the irregular relation between the Halden and the EPRI data sets. The Rolstad et al model, which predicts the Halden data well, fits the EPRI low temperature data but not the high temperature EPRI data. Hanevik et al suggested the Halden data was probably a measurement of the densification of fuel pellet edges, that is, the cooler regions of the pellet. The Rolstad et al model is assumed by the FUDENS code to apply to low temperature densification, and the high temperature densification is assumed to be three times as large.

The constants in Equations (A-7.1) through (A-7.4) were determined by inspection to provide the best fit to the maximum density change of the EPRI data. Model predictions and the data base are shown in Figures A-7.2 and A-7.5. Mixed oxide fuel is assumed to densify in the same manner as UO_2 due to lack of data to show otherwise.

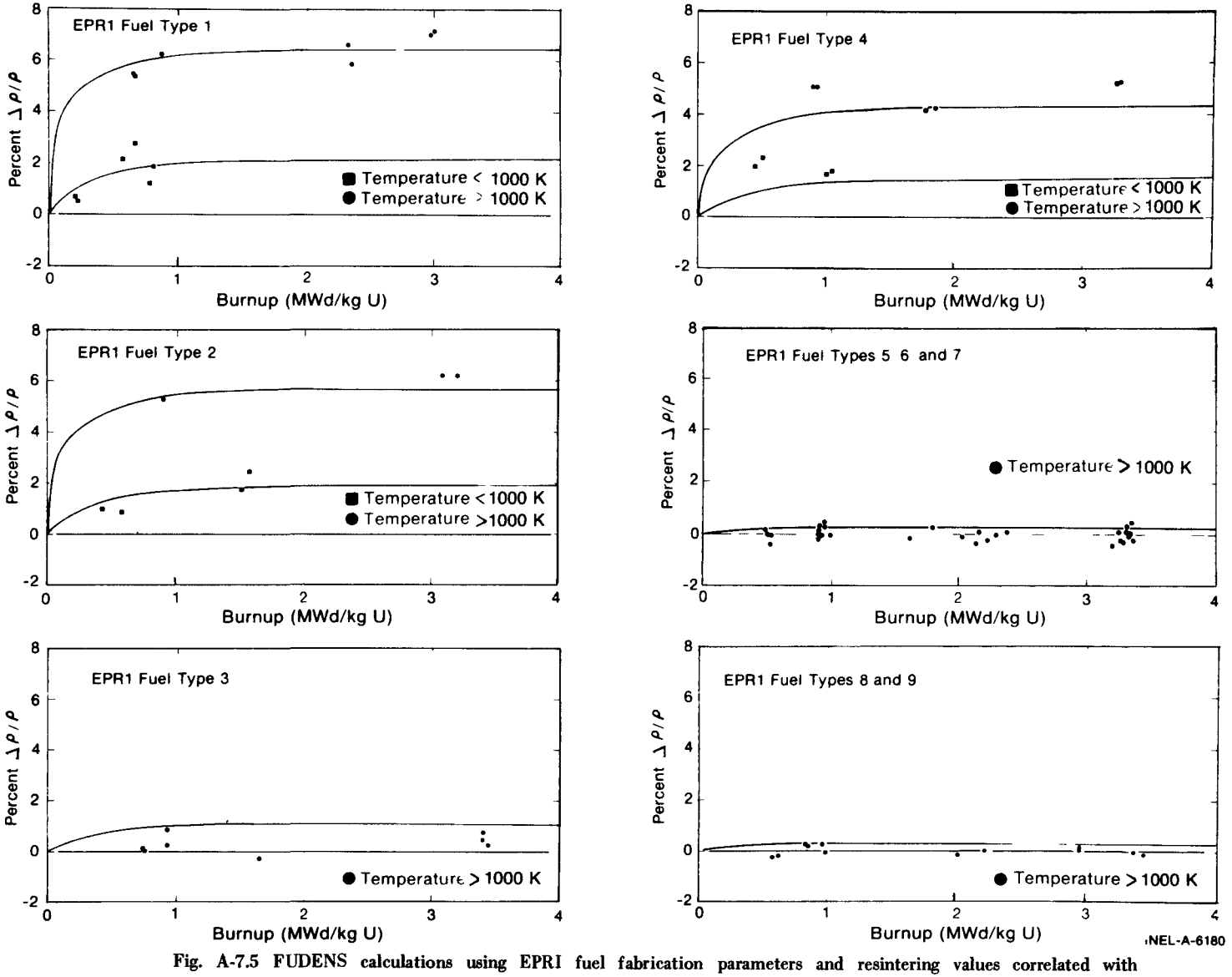

Fig. A-7.5 FUDENS calculations using EPRI fuel fabrication parameters and resintering values correlated with experimental EPRI in-pile data.

7.4 Fuel Densification Subcode FUDENS Listing

A FORTRAN listing of the subcode FUDENS is presented in Table A-7.I.

7.5 References

A-7.1. W. Beere, "The Sintering and Morphology of Interconnected Porosity in UO_2 Powder Compacts," *Journal of Materials Science, 5* (1973) pp 1717-1724.

A-7.2. W. M. Armstrong, W. R. Irvine, R. H. Martinson, "Creep Deformation of Stoichiometric Uranium Dioxide," *Journal of Nuclear Materials, 7* (1962) pp 133-141.

A-7.3. D. W. Brite et al, *EEI/EPRI Fuel Densification Project, Research Project 131 Final Report* (Revised June 1975).

A-7.4. M. D. Freshley et al, "The Effect of Pellet Characteristics and Irradiation Conditions on UO_2 Fuel Densification," *ANS/CNA Topical Meeting on Commercial Nuclear Fuel-Current Technology,* Toronto, Canada, April 1975.

A-7.5. E. Rolstad et al, "Measurements of the Length Changes of UO_2 Fuel Pellets During Irradiation," *Enlarged HPG Meeting on Computer Control and Fuel Research,* June 4-7, 1974.

A-7.6. A. Hanevik et al, "In-Reactor Measurements of Fuel Stack Shortening," *BNES Nuclear Fuel Performance Conference,* London, October 15-19, 1973, paper no. 89.

A-7.7. D. A. Collins and R. Hargreaves, "Performance-Limiting Phenomena in Irradiated UO_2," *BNES Nuclear Fuel Performance Conference,* London, October 15-19, 1973, paper no. 50.

A-7.8. H. M. Ferrari et al, "Fuel Densification Experience in Westinghouse Pressurized Water Reactors," *BNES Nuclear Fuel Performance Conference,* London, October 15-19, 1973, paper no. 54.

A-7.9. T. J. Heal et al, "Development of Stable Density UO_2 Fuel," *BNES Nuclear Fuel Performance Conference,* London, October 15-19, 1973, paper no. 52.

A-7.10. A. M. Ross, "Irradiation Behavior of Fission Gas Bubbles and Sintering Pores in UO_2," *Journal of Nuclear Materials, 30* (April 1969) pp 134-142.

A-7.11. B. Burton and G. L. Reynolds, "The Sintering of Grain Boundary Cavities in Uranium Dioxide," *Journal of Nuclear Materials, 45* (1972/73) pp 10-14.

A-7.12. R. O. Meyer, *The Analysis of Fuel Densification,* Office of Nuclear Reactor Regulation. U. S. Nuclear Regulatory Commission NUREG-0085 (July 1976).

TABLE A-7.I

LISTING OF THE FUDENS SUBCODE

```
C
C
      FUNCTION FUDENS(FTEMP, BU, FDENS, RSNTR, TSINT, COMP, PRVDEN)
C
C     FUDENS CALCULATES IRRADIATION-INDUCED DENSIFICATION.
C
C     FUDENS = OUTPUT FUEL DIMENSIONAL CHANGE (%)
C
C     FTEMP  = INPUT FUEL TEMPERATURE (K)
C     BU     = INPUT BURNUP (MW-S/KG-U)
C     FDENS  = INPUT FUEL DENSITY (KG/M**3)
C     RSNTR  = INPUT MAXIMUM DENSITY CHANGE DETERMINED BY A RESINTERING
C              TEST OF 1973K FOR 24 HOURS (KG/M**3)
C     TSINT  = INPUT FUEL SINTERING TEMPERATURE (K)
C     COMP   = INPUT PLUTONIA CONTENT (WEIGHT PERCENT)
C     PRVDEN = INPUT TOTAL DENSIFICATION FROM PREVIOUS TIME STEP (%)
C
C     FUDENS WAS DEVELOPED AND PROGRAMMED BY C. S. OLSEN (JANUARY 1975).
C     UPDATED AND CORRECTED BY B. W. BURNHAM (OCTOBER 1975).
C     FUDENS WAS MODIFIED BY R. E. MASON (NOVEMBER 1978).
C
      DIMENSION C(2),B(5)
      DATA C/10.97,11.46/
      DATA B/3.0,1.00,3.0,2.00,35.00/
C
      DLEN2(ALEN,BU,ABU) = -B(1) + ALEN + B(2)* EXP(-B(3)*(BU + ABU))
     #                   + B(4)* EXP(-B(5)*(BU + ABU))
      DLEN3(BU) = -B(2)*B(3)* EXP(-B(3)*BU) - B(4)*B(5)* EXP(-B(5)*BU)
      FBU = BU * 1.0202E-05
      TS  = TSINT - 2.7315E02
C     IF RSNTR OR TSINT IS NOT DEFINED BY USER, THE DEFAULT VALUE IS
C     TSINT = 1873 K.
      IF (TSINT .LE. 0.0) TS = 1600.0
      ROTH = C(1)*C(2)/(0.01*COMP*C(1) + (1.0 - 0.01*COMP)*C(2))
      DE = FDENS/(ROTH*10.0)
C
      IF((FTEMP .GE. 1000.) .AND. (RSNTR .GT. 0.))DLEN1 = 0.00285*RSNTR
      IF((FTEMP .LT. 1000.) .AND. (RSNTR .GT. 0.))DLEN1 = 0.00150*RSNTR
      IF((FTEMP .GE. 1000.) .AND. (RSNTR .LE. 0.))
     #     DLEN1 = 66.6*(100.0 - DE)/(TS - 1180.0)
      IF((FTEMP .LT. 1000.) .AND. (RSNTR .LE. 0.))
     #     DLEN1 = 22.2*(100.0 - DE)/(TS - 1180.0)
C
      X3  = 0.0
      X4  = 1.0
      AL1 = DLEN1
      AL3 = 3.0 - AL1
      AL4 = 0.0
      IF (AL3 .LE. 4.27E-03) GO TO 30
C
      DO 15 I = 1,6
      Y2 = DLEN2(AL3,X4,AL4)
      Y1 = DLEN2(AL3,X3,AL4)
      IF (Y1*Y2 .LE. 0.) GO TO 20
      X3 = X4
      X4 = X4 + 1.0
      IF (I .EQ. 6) GO TO 45
   15 CONTINUE
C
   20 CONTINUE
      X1  = X3
C
      DO 25 J = 1,50
      X   = X1 - DLEN2(AL3,X1,AL4)/DLEN3(X1)
      ERR =  ABS((X - X1)*100.0/X)
      IF (ERR .LE. 2.0E-04) GO TO 35
      X1  = X
   25 CONTINUE
C
   30 AL3 = 2.996
      AL2 = 5.384
      GO TO 40
C
   35 AL2 = X
   40 CONTINUE
      FUDEN  = DLEN2(AL3,FBU,AL2)
      IF (BU .LT. 1728) FUDEN  = 0.0
      GO TO 50
```

TABLE A-7.I (continued)

```
C
   45 PRINT 100
  100 FORMAT (1X,/45H NO ROOTS FOUND BETWEEN 0 AND 6000 MWS/MT UO2)
      FUDEN = 0.0
   50 CONTINUE
      IF (ABS(FUDEN) .LE. ABS(PRVDEN))  FUDENS = 0.0
      IF (ABS(FUDEN) .GT. ABS(PRVDEN))  FUDENS = FUDEN - PRVDEN
C
      RETURN
      END
```

A-7.13. J. C. Voglewede and S. C. Dochwat, *Reactor Development Program Progress Report*, ANL-RDP-33 (December 1974) pp 5-1 through 5-2.

A-7.14. H. Stehle and H. Assmann, "The Dependence of In-Reactor UO_2 Densification on Temperature and Microstructure," *Journal of Nuclear Materials, 52* (1974) pp 303-308.

A-7.15. M. O. Marlowe, "Predicting In-Reactor Densification Behavior of UO_2," *Transactions of the American Nuclear Society, 17* (November 1973) pp 166-169.

A-7.16. D. Hull and D. E. Rimmer, "The Growth of Grain-Boundary Voids Under Stress," *Philosophical Magazine, 4* (1959) p 673.

A-7.17. S. R. MacEwen and I. J. Hastings, "A Model for In-Reactor Densification of UO_2," *The Philosophical Magazine, 31*, 1 (January 1975) pp 135-143.

A-7.18. R. W. Hamming, *Introduction to Applied Numerical Analysis*, New York: McGraw-Hill Book Company, Inc. (1971).

8. FUEL SWELLING (FSWELL)

(R. E. Mason)

The computer subcode FSWELL calculates the swelling of fuel resulting from the increased volume fission products must occupy. Fuel swelling is defined as a positive volume change resulting from different solubilities, chemical states, lattice parameters, numbers of atoms, and chemical valancies of the atoms resulting from the nuclear fission process.

8.1 Summary

The subcode FSWELL calculates the positive volume change (S) resulting from the buildup of fission products in nuclear fuels. Swelling is a positive volume increase caused by solid and gaseous fission products. The correlation for swelling due to solid fission products is

$$S_s = 2.5 \times 10^{-29} B_s \quad \text{(A-8.1)}$$

where

S_s = fractional volume change due to solid fission products

B_s = burnup during a time step (fissions/m^3).

The correlation for swelling due to gaseous fission products for $T < 2800$ K is

$$S_g = 8.8 \times 10^{-56} (2800-T)^{11.73} \exp [-0.0162 (2800-T)]$$
$$\exp(-8.0 \times 10^{-27} B) B_s \quad \text{(A-8.2)}$$

where

S_g = fractional volume change/burnup [m^3/(fissions/m^3)]

T = temperature (K)

B = total burnup of fuel (fissions/m^3)

and for $T \geqslant 2800$ K

S_g = 0.0.

Development of the FSWELL subcode is divided into the following sections. Section 8.2 is a description of a calculation method to combine fuel densification, fuel swelling, fission gas release, and fuel creep. Section 8.3 is a description of solid fission product swelling data and Section 8.4 is a description of the solid fission product swelling model. Section 8.5 describes fission gas swelling data and Section 8.6 describes the fission gas swelling model. Section 8.7 is the subcode listing and Section 8.8 contains the references.

8.2 Combined Effects Analysis

The behavior of light water reactor fuel being irradiated or undergoing fission is controlled by a number of physical mechanisms operating simultaneously. These must be considered when evaluating in-pile fuel swelling. A method (subcode FDIMCH) is presented to combine the effects of fuel densification due to pressure sintering (FHOTPS) and irradiation enhancement (FUDENS) with the swelling calculations (FSWELL) so that the swelling calculations can be compared with in-pile data.

Fuel swelling and densification are often simply combined to obtain fuel dimensional changes from these effects. For example, Chubb et al[A-8.1] assumed that swelling was a linear function of burnup at any given temperature, and that swelling occurs whether or not pore removal is occurring. Stehle and Assmann[A-8.2] suggested that swelling and densification are additive and that the swelling rate per unit exposure time is constant. Their model differs from Chubb's in that it assumed no external dimensional changes of the fuel until the pores and the fuel pellet dish volumes are filled.

Fuel porosity is used in the subcode FDIMCH to determine when swelling or densification is the controlling mechanism. As long as sufficient porosity is available, swelling is accommodated by fuel pore spaces and there is a net reduction of pellet dimensions due to densification. Since fission gases are also reducing the porosity and the pore size and gas pressure equilibrium is reached before all the porosity is removed, the fuel can never become 100% dense. Based on a fit to available data, the maximum porosity that can be taken up by swelling and densification is

$$P_f = 1/P_0 - 9.425 \times 10^{-5} \qquad \text{(A-8.3)}$$

where

P_f = pore volume per gram available to be filled by densification and fuel swelling (kg/m^3)

P_0 = fabricated density of the fuel (kg/m^3).

This implies that if the fuel density is greater than 1.061×10^4 kg/m^3 (96.7% of theoretical density) the fuel will not densify but will begin swelling. The maximum porosity that can be filled by swelling and densification is determined using the Brite et al[A-8.3] and Banks[A-8.4] data. The fuel types 1 and 2 reported by Brite et al are used for the initial calculations. These showed rapid densification which reached maximum density between 1 and 3.5 GWd/tM. The Rolstad et al data[A-8.5] showed maximum densification before 8 MWd/kg. The Banks data also indicated that outward swelling begins by at least 10 MWd/kg. Using the fuel type 1 data reported by Brite et al, the constant in Equation (A-8.3) is chosen so that the FDIMCH calculations predict the density or length changes of other Brite et al fuel types and the Rolstad et al data.

At higher burnups the porosity is increased by release of fission gas from grain boundary bubbles and tunnels. The additional pore volume associated with fission gas release is obtained from the expression

$$\Delta P_f = 1.5 \times 10^{-32} (F) \cdot T \cdot Buf/P_0 \qquad \text{(A-8.4)}$$

where

ΔP_f = pore volume per gram opened to plenum region due to fission gas release from the fuel (kg/m^3)

F = fraction of gas released (unitless)

T = fuel temperature (K)

Buf = burnup during the time step ($fissions/m^3$).

Equation (A-8.4) is based on the assumption that only those pores (bubbles void of gas), tunnels, and bubbles which connect with the fuel rod plenum are affected by stresses on the fuel. It is also assumed that all bubbles in the fuel matrix, grain edges, and grain boundaries are at equilibrium with the fission gases. These assumptions imply that the only swelling volume which can be affected by external stresses (pressure sintering) is that increased porosity created by released gases. This open porosity is found by calculating a volume occupied by the gas released during a time step FDIMCH calculation subcode. Since an average bubble pressure is not calculated in FDIMCH, the pressure in the ideal gas law is assumed to be a constant. The constant is chosen such that the fractional open porosity created by fission gas being released is approximately the same as the fraction of gas released. That is, if 50% of the gas were released, approximately 50% of the calculated volume change due to fission gases would be considered open porosity. The moles of gas released and the constant pressure are then used in the ideal gas law which results in Equation (A-8.4), the change in open porosity per time step.

The point at which outward swelling begins and densification ceases is given by P=0, where

$$P = P_f - P_s - P_d \qquad \text{(A-8.5)}$$

where

P = pore volume per kilogram not filled by densification and swelling but potentially fillable without causing outward swelling (m^3/kg)

P_f = pore volume per kilogram available for filling by densification and swelling (m^3/kg)

P_s = pore volume per kilogram filled by swelling and is equal to the net change in volume calculated by FSWELL (m^3/kg)

P_d = pore volume per kilogram filled by densification and is equal to the net change in volume calculated by FUDENS or FHOTPS (m^3/kg).

When P is greater than zero according to Equation (A-8.4), densification may occur and the net volume change is negative and is calculated by the FUDENS model alone. If P is zero or negative, densification is not possible and the fuel swells. The change in volume (relative to the original fuel dimensions) is given by FDIMCH.

For $P > 0$

$$\frac{\Delta V}{V} = \left(\frac{\Delta V}{V}\right)^{DENS} . \tag{A-8.6}$$

for $P \leq 0$

$$\frac{\Delta V}{V} = \left(\frac{\Delta V}{V}\right)^{DENS}_{p=0} + \left(\frac{\Delta V}{V}\right)^{FSWELL} - \left(\frac{\Delta V}{V}\right)^{FSWELL}_{p=0} \tag{A-8.7}$$

where

$\frac{\Delta V}{V}$ = percent change in fuel volume for total irradiation time

$\left(\frac{\Delta V}{V}\right)^{DENS}$ = percent change in fuel volume calculated by FUDENS or FHOTPS for total irradiation time

$\left(\frac{\Delta V}{V}\right)^{FSWELL}$ = percent change in fuel volume calculated by FSWELL for total irradiation time

$\left(\frac{\Delta V}{V}\right)^{DENS}_{p=0}$ = percent change in fuel volume calculated by FUDENS or FHOTPS when P = 0

$\left(\frac{\Delta V}{V}\right)^{FSWELL}_{p=0}$ = percent change in fuel volume calculated by FSWELL when P = 0.

Data of Banks are emphasized in formulating the FDIMCH subcode. These are used because density changes of the fuel were measured and enough experimental parameters were given by Banks or could be found in the open literature. Banks' data also represent volume change in fuel which has been irradiated under normal LWR reactor conditions. The fuel volume changes determined by Banks and the corresponding calculations are summarized in Figure A-8.1.

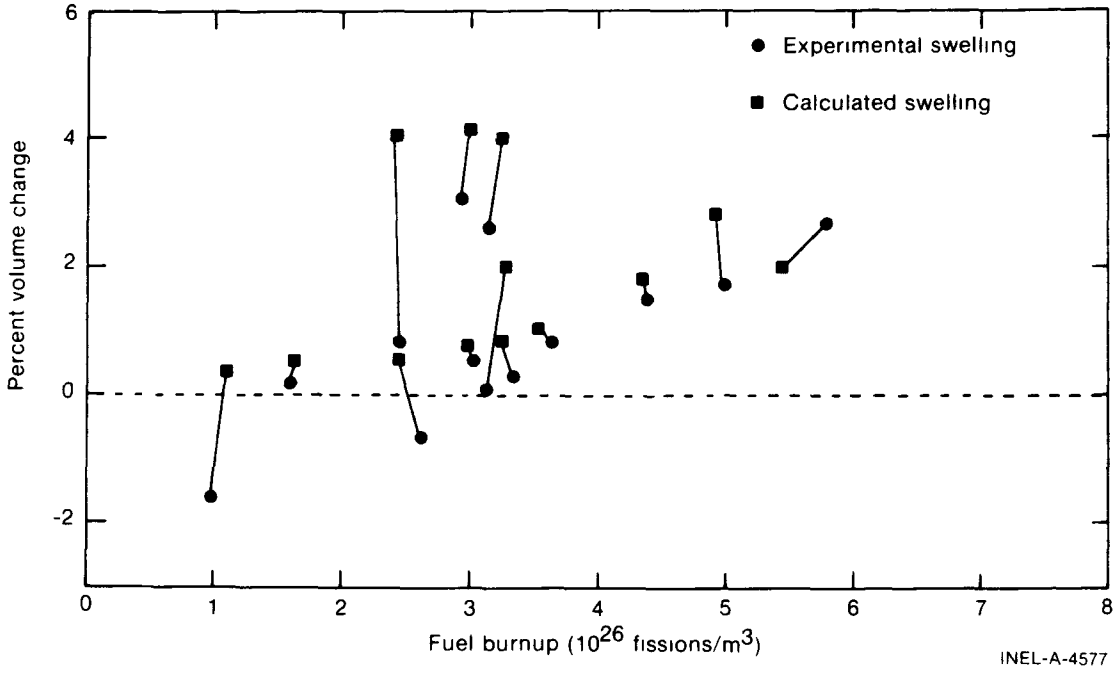

Fig. A-8.1 Fuel volume changes calculated by FDIMCH compared with experimental swelling data.

The FDIMCH calculations were compared with the Bettis flat plate data[A-8.2] in spite of the fact that these data represent burnups which are very high for normal LWR fuels. Figure A-8.2 shows the comparison. The code comparison was performed assuming the fuel did not densify during the initial burnup as calculated by FUDENS. The FDIMCH subcode using the above calculation procedure is listed in Table A-8.I.

8.3 Solid Fission Product Swelling Data

Measurement of volume increases resulting from nongaseous atoms is difficult. However, a number of studies have been undertaken to determine the relative amounts of fission product elements and compounds, their chemical states, and locations. These include studies of Bradbury and Frost[A-8.6], Bradbury et al[A-8.7,A-8.8], Jeffrey[A-8.9], Bates[A-8.10], O'Boyle et al[A-8.11], and many others[A-8.12 – A-8.20].

Anselin[A-8.13] and Anselin and Baily[A-8.14] used some of the experimental results in the literature just cited to calculate the approximate volume contribution of each fission product as a function of burnup. After considering volume loss due to fissioned atoms, volume loss due to migration of oxygen, reduction of the lattice parameter and the volume increase due to fission product atoms, Anselin found a maximum solid fission product swelling rate of 0.13% $\Delta V/\dot{V}$ ($\frac{\Delta V}{V} = 0.0013$) per 10^{26} fissions/m^3 if the fuel completely utilizes the vacancies created or 0.54% $\Delta V/V$ per 10^{26} fissions/m^3 if none of the vacancies are utilized. Anselin also proposed an average of 0.35% $\Delta V/V$ per 10^{26} fissions/m^3 for all conditions. He cautions that there is no unique number, since the contribution to swelling

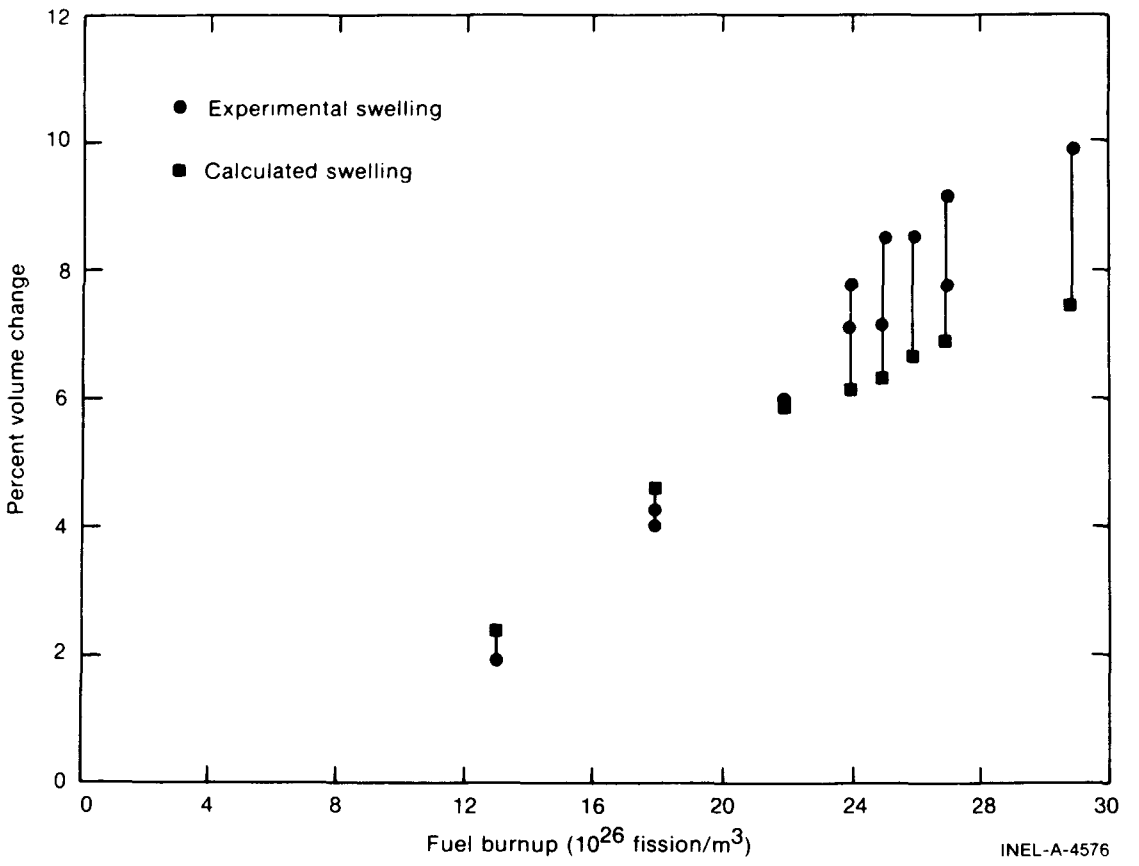

Fig. A-8.2 Fuel volume changes calculated by FDIMCH compared with experimental swelling data.

depends on irradiation conditions, fuel pin design, and the properties of the fuel. Anselin also assumed a fission product yield and chemical state for each element. Moreover, the calculations were carried out using room temperature data.

Harrison and Davies[A-8.15] calculated solid fission product swelling as a function of thermal neutron flux. They concluded that the swelling contribution monotonically decreases as the flux increases. Swelling contributions of 0.45% $\Delta V/V$ per 10^{26} fissions/m^3 and 0.39% $\Delta V/V$ per 10^{26} fissions/m^3 were calculated for thermal neutron fluxes of 10^{18} and 10^{21} (neutrons/m^2)/s, respectively.

Lyons et al[A-8.21] summarized the solid fission product swelling results of several authors, including those of Anselin. Frost[A-8.22] obtained 0.21% $\Delta V/V$ per 10^{26} fissions/m^3. Whapman and Sheldon[A-8.23] obtained 0.20% $\Delta V/V$ per 10^{26} fissions/m^3.

Olander[A-8.24] calculated the solid fission product swelling contribution. He obtained 0.32% $\Delta V/V$ per atom % burnup, which corresponds closely to Anselin's average value of 0.35% $\Delta V/V$ per 10^{26} fissions/m^3. Olander points out that this value does not account for fission product migration and is influenced by uncertainties in the physical and

TABLE A-8.I

LISTING OF THE FDIMCH SUBCODE

```
      SUBROUTINE FDIMCH
C     FDIMCH COMBINES THE CALCULATIONS OF FUDENS, FSWELL, FHOTPS
C     FCREEP AND FGRASRL TO OBTAIN AN ESTIMATE OF FUEL
C     DIMENSIONAL CHANGES DURING IRRADIATION.
C
C     FUMASS = INPUT MASS OF THE FUEL IN KILOGRAMS
C     FGASRR = INPUT FRACTIONAL GAS RELEASE IN FUEL RING L
C     DELRO  = INPUT/OUTPUT FRACTIONAL CHANGE IN FUEL DENSITY
C     FAXIAL = OUTPUT FRACTIONAL AXIAL LENGTH GHANGE
C     FRADIL = OUTPUT FRACTIONAL PELLET RADIUS CHANGE
C     POROPN = TOTAL FRACTIONAL VOLUME OPENED TO THE PLENUM BY
C              FISSION GAS RELEASE
C     SINPOR = FRACTIONAL POROSITY WHICH CAN BE SINTERED
C     GASSWL = TOTAL FRACTIONAL VOLUME CHANGE FROM GAS SWELLING
C     VCHANG = OUTPUT FUEL VOLUME CHANGE (FRACTION)
C
C     VARIABLES NOT LISTED HERE ARE DESCRIBED IN THE APPROIATE
C     CALLED SUBROUTINE.
C
      COMMON/MAIN/ FTEMP      , TFR(18)    , BP         , BUF        ,
     A FDENS      , RSNTR     , TSINT      , COMP       , FOM        ,
     B TNOW       , TLAST     , TIME       , DELRO      , L          ,
     C TC         , TS        , CC2(20)    , FMGR       , GBBG(12)   ,
     D FMGP       , FPOWER(10), GRNSIZ(11) , FMGPR(20)  , FMA(20)    ,
     E FIS        , HSTRES    , FSTRES     , BU         , NTSTEP     ,
     I PELTOI     , FUMASS    , LSTART     , BUL        , TOTOCH     ,
     J TFGFR      , FAXIAL(11), FRADIL(11) , CC1        , SGAPF      ,
     K FENGTH     , PINVV
C
      DIMENSION PRVDEN(11), SINP(11)   , POROP(11) , GASSW(11)
      DIMENSION RON(11)   , REMVO(11)  , FULDI(11) , VDEN(11)
      DIMENSION VCHANG(11)
      ROTH   = 125.72/ (0.1097*COMP + (1. - 0.01 * COMP) * 11.46)
      FGRN   = GRNSIZ(L)
      FGASRR = TFGFR
C
      IF (LSTART .GT. 1.) GO TO 10
      PSTRES = 0.0
      DELRO  = 0.0
      DELVOL = 0.0
      BUL    = 0.0
      VDEN(L)   = 0.0
      VCHANG(L) = 0.0
      PRVDEN(L) = 0.0
      SINP(L)   = 0.9672 - 0.001 * FDENS / ROTH
      POROP(L)  = 0.0
      GASSW(L)  = 0.0
      RON(L)    = FDENS * 1.0 E-03
      REMVO(L)  = 10970. / FDENS
      FULDI(L)  = 0.0
   10 CONTINUE
      SINPOR = SINP(L)
      POROPN = POROP(L)
      GASSWL = GASSW(L)
      RO     = RON(L)
      REMVOL = REMVO(L)
      FULDIM = FULDI(L)
C
   20 CONTINUE
C
C     CALCULATION OF NEW POROSITY DERIVED FROM BUBBLES WHICH HAVE
C     RELEASED FISSION GAS.
C
      PORNEW = FTEMP * BUF * FGASRR* 1.50E-26
      IF (POROPN .GE. GASSWL) PORNEW = 0.0
      POROPN = POROPN + PORNEW
      SINPOR = SINPOR + PORNEW
      IF (SINPOR .GT. 1. - RO/ROTH) SINPOR = 1. - RO/ROTH
C
      CALL       FSWELL(FDENS, COMP, BU, BUL, FTEMP, GASWL, SOLDSW)
      GASSWL = GASWL + GASSWL
      FULDIM = SOLDSW + GASWL + FULDIM
C
C     CALCULATION OF FUEL DENSIFICATION.
C     DENSIFICATION IS DEFINED AS POSITIVE DENSITY CHANGE AND A
C     NEGATIVE VOLUME CHANGE.
C
```

TABLE A-8.I (continued)

```
      CALL        FHOTPS (COMP,FOM,HSTRES,TIME,FTEMP,TLAST,SINPOR,FVC)
C
      IF (BU .GE. 864000.) GO TO 25
      FUD     = FUDENS(FTEMP,BU,FDENS,RSNTR,TSINT,COMP,PRVDEN(L)) *
     #          0.03/RO
   25 CONTINUE
      IF (BU .GE. 864000.) FUD = 0.0
      IF (FUD .LT. FVC) FVC = 0.0
      IF (FVC .LE. FUD) FUD = 0.0
      SINPOR = SINPOR + FUD + FVC/RO
C
C     CALCULATION OF FUEL VOLUME CHANGE.
      IF (REMVOL .LE. 0.0) GO TO 30
      VDEN(L)  = VDEN(L) + FUD + FVC/RO
      VPOROS = 1000. / FDENS - 0.09425
      VSWELL = FULDIM/RO
      REMVOL = VPOROS - VSWELL + VDEN(L)
      DELVOL = FVC + FUD * RO
      GO TO 40
C
   30 CONTINUE
C
      DELVOL = SOLDSW + GASWL + FVC
C
   40 CONTINUE
      DELRO  = - DELVOL
      SINP(L)  = SINPOR
      POROP(L) = POROPN
      GASSW(L) = GASSWL
      RON(L)   = RO + DELRO * RO
      REMVO(L) = REMVOL
      FULDI(L) = FULDIM
      PRVDEN(L) = PRVDEN(L) + FUD * RO / 0.03 + FVC / 0.03
      PAXIAL =          FCREEP(FTEMP,FSTRES,FDENS,FGRN,FIS,COMP,FOM,
     *                         TIME, LSTART, TLAST, PSTRES)
C
C     PELLET DIMENSIONAL CHANGE CALCULATIONS.
C     DIANIS IS THE DENSIFICATION ANISOTROPIC FACTOR.
      DIANIS = 1.0
      VCHANG(L) = VCHANG(L) + DELVOL
      FAXIAL(L) = VCHANG(L) / 3. + PAXIAL
      FRADIL(L) = VCHANG(L) * DIANIS / 3. + PAXIAL
C     TOTDCH IS THE TOTAL ACCUMULATIVE VOLUME CHANGE (FRACTION).
      TOTDCH = DELRO * 0.1 + TOTDCH
      WRITE(6,99)
      WRITE(6,98) SOLDSW, GASWL, FVC, PAXIAL, FUD, VCHANG (L), TOTDCH
   98 FORMAT(7E15.4)
   99 FORMAT(7X,*SOLDSW*,11X,*GASWL*,9X,*FVC*,7X,*PAXIAL*,15X,*FUD*,10X
     A,*VCHANG*,9X,*TOTDCH*)
      PSTRES = FSTRES
      RETURN
      END
```

chemical states of the fission products, leading to an error of ±50% in the calculated value. He found a minimum swelling rate of $0.16\% \frac{\Delta V}{V}$ per atom % burnup for initially hypostoichiometric UO_2 and a maximum of $0.48\% \frac{\Delta V}{V}$ per atom % burnup for initially hyperstoichiometric fuel or fuel irradiated to high burnups. Olander also presented a solid fission product swelling correlation which summed the swelling contribution of each fission product. Janks[A-8.25] also proposed a solid fission product swelling model for fission products in metallic fuels. These models are more complex than the present open literature data can support so a simpler model was used.

General Electric[A-8.26] conducted an extensive study of oxide fuel swelling and found the maximum total swelling of both solid and gaseous fission products to be 0.4% $\frac{\Delta V}{V}$ per 10^{26} fissions/m^3.

The literature data cited in this section present only calculated average swelling rates not measured directly from experiment. These swelling rates range from ∿0.1 to ∿0.6% $\frac{\Delta V}{V}$ per 10^{26} fissions/m^3. The results of the these authors are summarized in Table A-8.II.

TABLE A-8.II

SUMMARY OF SOLID FISSION PRODUCT SWELLING VALUES

Source	Values, % ΔV/V per 10^{26} fissions/m^3
Anselin [A-8.13]	0.13 to 0.54, calculated average 0.35
Frost [A-8.22]	0.21
Whapham & Sheldon [A-8.23]	0.20
Harrison & Davies [A-8.15]	0.46 to 0.39, flux dependent
Olander [A-8.24]	0.12 ± 0.06

8.4 Solid Fission Product Swelling Model Development

The solid fission product swelling model is developed by choosing a fission rate between the General Electric maximum swelling rate and Anselin's minimum rate. This rate is adjusted between 0.12% and 0.4% $\frac{\Delta V}{V}$ per 10^{26} fissions/m^3 to fit reactor fuel swelling data. The conclusion is that the best solid fission product swelling rate at both low burnups and high burnups (where much of the fission gas is released and solid fission product swelling dominates) is 0.25% $\frac{\Delta V}{V}$ per 10^{26} fissions/m^3.

8.5 Fission Gas Swelling Data

The fission gas swelling model is based on two types of swelling data; isothermal-unrestrained, that is, fuel not in hard contact with the cladding, and normal power reactor data which has a large temperature gradient and is generally in contact with the cladding.

8.5.1 Fission Gas Swelling Data – Isothermal-Unrestrained Swelling. Experimental conditions and parameters of a Battelle Columbus Laboratories study[A-8.27], are summarized in Table A-8.III. The swelling data were obtained using W26Re clad UO_2 and

TABLE A-8.III

CONDITIONS AND PARAMETERS FOR BATTELLE SWELLING EXPERIMENTS

Parameter/Condition	Value
Cladding Surface Temperature	1475 to 2173 K
Fuel Centerline Temperature	1723 to 2523 K
Maximum Linear Power	12 kW/m
Fission Rate Density	2×10^{19} (fissions/m^3)/s
Burnup	0.4 to 20 x 10^{26} fissions/m^3
Fuel Characteristics [UO_2 and $(U,Pu)O_2$]:	
density	91 to 97% TD
diameter	0.0053 m
length	0.0250 m
centerhole diameter	0.0014 to 0.0028 m
Cladding Thickness (W26Re)	0.0005 to 0.0015 m
Swelling Measurement Technique	Dimensions from radiographs

$(U,Pu)O_2$. The experimental conditions were unique in that the cladding surface temperatures ranged from 1473 to 2173 K, compared with typical BWR and PWR cladding surface temperatures of 553 to 623 K. Temperature gradients in the fuel were reported to be less than 300 K and the fuel surface temperature was estimated to be only 50 K higher than the cladding temperature. The data are, therefore, excellent to use as a basis for calculating the fuel swelling rate as a function of temperature. Other Battelle Columbus data are in References A-8.27 through A-8.31.

The data showed the swelling rate to have an Arrhenius dependence on the cladding surface temperature for fuel temperatures above 50% of the melting point[A-8.27]. Also, the swelling was observed to be a linear function of burnup, the rate being determined by the fuel temperature. The volumetric swelling rates were calculated from external dimensional changes of the fuel determined by radiography. The swelling rates varied from 3 to 15% $\Delta V/V$ per 10^{26} fissions/m^3 when cladding surface temperature varied from 1600 to 2173 K.

Turnbull[A-8.32,A-8.33] and Turnbull and Tucker[A-8.34] studied fission gas release and swelling of UO_2 under essentially isothermal conditions. Small cylindrical specimens 10 and 3 mm in diameter were sealed in TZC molybdenum alloy[a] capsules and irradiated in a flux of 2.2 - 2.6 x 10^{17} (thermal neutrons/m^2)/s for periods of 2, 4, and 6 months. During irradiation, a temperature of 2023 ± 50 K was maintained by electrical heating and fission of the fuel. Fission produced a temperature gradient of 100 K from centerline to fuel pellet surface. Table A-8.IV lists parameters and conditions of the data reported by Turnbull.

TABLE A-8.IV

CONDITIONS AND PARAMETERS FOR THE TURNBULL DATA

Parameter/Conditions	Value
Fuel Surface Temperature	2023 ± 25 K
Fuel Centerline Temperature	~2123 K
Thermal Neutron Flux	2.4 to 2.6 x 10^{17} neutrons/(m^2·s)
Burnup	1 x 10^{26} fission/m^3, maximum
Fuel Characteristics:	
density	near theoretical
diameter	0.003 m
length	0.010 m
Cladding	TZC molybdenum alloy
Restraint	small

A United Nuclear Corporation program on the swelling and gas release of fast reactor fuels reported by Grando et al[A-8.35], supports the hypothesis that unrestrained swelling rates are considerably higher than swelling rates of fuels restrained by cladding. The unrestrained swelling fuel specimens consisted of 0.00152-m diameter by 0.00127-m long free-standing pins in helium, held at the ends by tantalum carbide supports with space provided for axial expansion. The small diameter of the specimens was chosen to obtain isothermal conditions. Test capsules were designed to operate at 1273, 1573, and 1873 K controlled to ±25 K with a fuel ΔT of less than 50 K. Two specimens of $(U_{0.85}, Pu_{0.15})O_2$

[a] An alloy consisting of 1.25% Titanium, 0.30% Zirconium, 0.15% Carbon, and the balance Molybdenum.

were irradiated at temperatures of 1638 and 1853 K, respectively, to a burnup of 4.9×10^{26} fissions/m^3. The lower temperature specimen was observed to have a swelling rate of 1.5% $\Delta V/V$ per 10^{26} fissions/m^3. The higher temperature specimen swelled at a rate of 2.6% $\Delta V/V$ per 10^{26} fissions/m^3. The swelling results reported by Grando et al at 1573 K agree well with those reported by the Battelle Columbus Laboratories but the higher temperature swelling is lower than that obtained at the Battelle Columbus Laboratories.

Kuz'min and Lebedev[A-8.36] examined fuel swelling of both UO_2 and $(U,Pu)O_2$ with temperature gradients similar to in-reactor values. They analyzed the fuel optically (determined size and number of bubbles) and reported the swelling of three temperature regions along the pellets radius (1273 to 1773 K, 1773 to 1973 K, and 1973 to 2773 K). They found that the bubble population and size differed greatly in the different temperature regions. Kuz'min and Lebedev also concluded that in the temperature range of 1773 to 1973 K the porosity did not depend on the burnup or original porosity but only on the temperature and temperature gradient.

8.5.2 Fission Gas Swelling Data – Restrained and Nonisothermal. The unrestrained and isothermal swelling of UO_2 discussed in the previous subsection will usually not be found in light water reactors. This subsection discusses the effects of restraint and temperature gradients in the fuel based on the oxide swelling values of Banks, Baroch and Rigdon[A-8.37], Daniel et al[A-8.38], Meieran[A-8.39] and Rowland et al[A-8.40].

Banks reported pre- and postirradiation density measurements of fuel used both in England's SGHWR reactor and fuels used in the Halden BWR reactor. Density measurements were made on fuel irradiated to burnups of up to 24 000 MWd/tM. Both densification and swelling of the fuel were observed in the fuels studied so their data are excellent for code-data comparison. However, his report did not include all of the reactor conditions experienced by the fuel. Those experimental parameters and conditions which were reported are reproduced in Table A-8.V. Banks also reported an average swelling rate of $0.43\% \frac{\Delta V}{V}$ per 10^{26} fissions/m^3.

Bettis Laboratories[a] completed a fuel swelling study of UO_2 plates which were reported by Daniel et al and Meieran. These data indicate that UO_2 undergoes a volume increase at a rate of $0.16\% \frac{\Delta V}{V}$ per 10^{26} fissions/m^3 up to a "threshold" burnup. Above the threshold burnup, the swelling rate in 0.5 to 0.7% $\Delta V/V$ per 10^{26} fissions/m^3. Daniel et al concluded that the true swelling rate of UO_2, independent of burnup, was 0.7% $\Delta V/V$ per 10^{26} fissions/m^3. This true rate is observed only after the internal pores are sealed. Thus, this rate is masked during the initial exposure period until the as-fabricated porosity is reduced by fission products.

The experimental conditions and parameters of the Westinghouse program are summarized in Table A-8.VI.

---

[a] Operated by Westinghouse, Inc.

TABLE A-8.V

CONDITIONS AND PARAMETERS FOR SWELLING AND DENSIFICATION DATA REPORTED BY BANKS

Parameter/Condition	Value
Fuel Surface Temperature	~673 K
Fuel Centerline Temperature	673 to 2473 K
Maximum Power	1 to 5.6 x 10^5 kW/m
Swelling Measurement Technique	Pycnometer

TABLE A-8.VI

CONDITIONS AND PARAMETERS FOR BETTIS SWELLING EXPERIMENTS

Parameter/Condition	Value
Cladding Surface Temperature	563 to 588 K
Fuel Centerline Temperature	1158 to 2423 K
Maximum Linear Power	16 kW/m
Burnup	1 to 36 x 10^{26} fissions/m^3
Fuel Characteristics (UO_2):	
density	87 to 95% TD
thickness	7.62 x 10^{-4} to 4.06 x 10^{-4} m
width	3.175 x 10^{-3} to 1.27 x 10^{-2} m
length	3.81 x 10^{-2} to 15.24 x 10^{-2} m
Cladding Thickness	3.81 x 10^{-4} to 6.35 x 10^{-4} m

Westinghouse[A-8.41] also conducted a swelling study of fuel rods containing UO_2 dished-end pellets. The swelling rate was estimated as 0.82% $\Delta V/V$ per 10^{26} fissions/m^3. This is consistent with the Bettis flat plate value to 0.7% $\Delta V/V$ per 10^{26} fissions/m^3 on the basis of higher rod temperatures. The total swelling rate of 0.82% $\Delta V/V$ per 10^{26} fissions was divided into three components:

(1) 35% accommodated in pellet dishes

(2) 49% filled internal porosity

(3) 16% caused diametral expansion.

Baroch and Rigdon conducted a high burnup irradiation program to determine performance characteristics of typical PWR fuel. The fuel rods were designed to operate at 59 to 70.5 kW/m linear power, the maximum normal and peak overpower PWR heat rates, respectively. Conditions and parameters experienced by the fuel are listed in Table A-8.VII. The fuel volume changes and swelling fail to account for the cladding dimensional changes as discussed by Cox[A-8.42] and Bellamy and Rich[A-8.43]. Baroch and Rigdon assumed that the peak diameter change occurred over the entire length of the fuel column, an assumption considered valid for most fuel rod calculations. The average swelling rate determined for UO_2 pellets was 1.10% $\Delta V/V$ per 10^{26} fissions/m^3.

An extensive General Electric BWR fuel rod evaluation program showed very small amounts of swelling[A-8.21,A-8.26,A-8.44]. They concluded that fuel pins with diametral clearances typical of BWR design, 2.286×10^{-4} to 3.048×10^{-4}m, did not show any significant positive diameter changes due to the combined effects of differential thermal expansion and fission product swelling up to a burnup of 25.7×10^{26} fissions/m^3. Since actual cladding diameter changes were observed, the maximum swelling rate is that inferred by assuming all the internal volume of the fuel rod is filled by fission products, including

TABLE A-8.VII

CONDITIONS AND PARAMETERS FOR
BAROCH & RIGDON PWR DATA

Parameter/Condition	Value
Fuel Surface Temperature	984 to 1324 K
Fuel Centerline Temperature	2061 to 3088 K
Linear Power	44.6 to 86.3 kW/m
Burnup	8 to 65 GWd/tU
Fuel Density	93.5% TD

fuel pellet dishes and the as-fabricated pores. This assumption leads to a maximum swelling rate of 0.4% $\Delta V/V$ per 10^{26} fissions/m^3. Pins with smaller diametral clearances did exhibit real, positive diameter increases. However, the measured expansion of high exposure pins in this group falls within the data scatter of similar clearance, low exposure pins. General Electric concluded that all of these observed diameter increases can be attributed to early life, thermal expansion induced strain.

Collins and Hargreaves[A-8.45] summarized swelling results from several sources. They reported swelling rates from 0.17 to 0.33% $\Delta V/V$ per 10^{26} fissions/m^3 for "low temperature" fuel, that is, fuel at a maximum temperature below 1398 K. They found a swelling rate of 0.33% $\Delta V/V$ per 10^{26} fissions/m^3 to be conservative for describing low temperature swelling. This value corresponds to solid fission product swelling rates although it includes some effects of gaseous fission products. Bubble formation and interconnected pores are insignificant at this low temperature. Above 1398 K they state that gas bubble swelling becomes important. Fuel porosity increases at approximately 0.5% per 100 K as fuel centerline temperature increases.

Nelson and Zebroski[A-8.46] studied the effect of temperature on the swelling rates of $(U,Pu)O_2$ fuel. The irradiation capsules were designed to provide strong radial constraint so that any swelling resulted in axial elongation of the fuel. The fuel pellets were approximately 0.0762 m in length and 0.0025 m in diameter. The cladding was 0.0103-m thick, 304 stainless steel. Linear heat rates were 26.2 and 39.4 kW/m and cladding surface temperatures were between 563 and 693 K, values typical of commercial LWR conditions. Other data not discussed are listed in Section 8.9 numbers (1) through (39).

8.6 Fission Gas Swelling Model Development

Fuel swelling is primarily a result of the increase in fission gas bubbles within the fuel pellets. The physical mechanisms causing the fuel to swell are complex and are not modeled from first principles in the FSWELL subcode. Swelling due to fission gas is modeled using a relatively simple correlation for unrestrained swelling as a function of temperature and burnup. This is based on the unrestrained data of Battelle Columbus Laboratories[A-8.27 – A-8.31] Turnbull[A-8.34], Kuz'min and Lebedev[A-8.36] and Grando et al[A-8.35]. This swelling is caused by the growth of intergranular gas bubbles and tunnels on the grain boundaries, edges, and corners between the temperatures 1373 to 1973 K. At temperatures greater than 1573 K, macropores begin to grow and significantly increase the swelling of the fuel. At very high temperatures (1973 K to the melting point) columnar grains form, bubble concentration decreases, fission gas is released, and swelling reduced.

There are a number of fission gas swelling models in the literature. Some use a mechanistic approach; others use a mechanical-statistical approach, like the GRASS code[A-8.47]. Still, others use an empirical or semiempirical approach like the COMETHE code[A-8.48]. FSWELL was developed as a simple code and should be used when short computation times are desired. See Section 8.9, numbers (40) through (51) for these uncited references.

The fuel volume changes listed by Chubb et al[A-8.27] and Turnbull[A-8.34] are used to correlate the unrestrained isothermal swelling rate. The fission gas swelling rate equation is determined by comparing the calculated swelling curve with the data and adjusting the equation until a close match between the code values and the mean curve of each data set is achieved. The shape of the "unrestrained-isothermal" curve is chosen by assuming (a) at temperatures below ∿1000 K, the gases remain in very small bubbles and/or in the matrix as single atoms so that little swelling occurs, (b) between 1000 and 2000 K bubbles grow at the grain boundaries, edges, and corners creating volume changes and (c) above 2000 K, swelling is due only to solid fission product growth, because columnar grains form. These grains are dense (∿98% TD) and as they form the gas is removed from the grains making fission gas swelling insignificant compared to solid fission product swelling.

The equation for fission gas swelling which resulted from the process described above is

$$S_g = 8.8 \times 10^{-36} (2800-T)^{11.73} \exp [-0.0162(2800-T)] \qquad \text{(A-8.8)}$$

where

S_g = fractional swelling

T = absolute temperature (K).

Figure A-8.3 illustrates the predictions of Equation (A-8.8). The values shown in Figure A-8.3 may seem to be large but one must remember that Equation (A-8.8) describes swelling at one temperature in fuel under no physical restraint. When Equation (A-8.8) is used in a code that uses incremental radial temperature regions to calculate dimensional changes and when the effect of cladding restraint on the fuel is taken into account, the swelling rate reduces to 0.2 to 1.9% $\frac{\Delta V}{V}$ per 10^{26} fissions/m^3, values consistent with experimental swelling found by many authors.

Figure A-8.4 compares the data of Turnbull[A-8.27] and Chubbs et al[A-8.34] with the values calculated by FSWELL (solid lines). These data were the unrestrained points used to develop the unrestrained swelling rates.

Fission gas swelling must also be modeled as a function of burnup. The COMETHE III J code[A-8.47], for example, uses an exponential burnup function to calculate fission gas swelling. Other more complex codes such as the GRASS code[A-8.48] determine the number of fission gas atoms created during the life of the fuel to calculate fuel swelling. The approach used in the FSWELL subcode is to assume a linear function of burnup multiplied by an exponential burnup function. The exponential burnup function in the FSWELL subcode models the swelling saturation observed by a number of investigators. The Battelle Columbus Laboratories UO_2 swelling data[A-8.27 – A-8.31], for example, saturate at relatively low burnups (<10^{26} fissions/m^3) and at different porosities. The same trend was

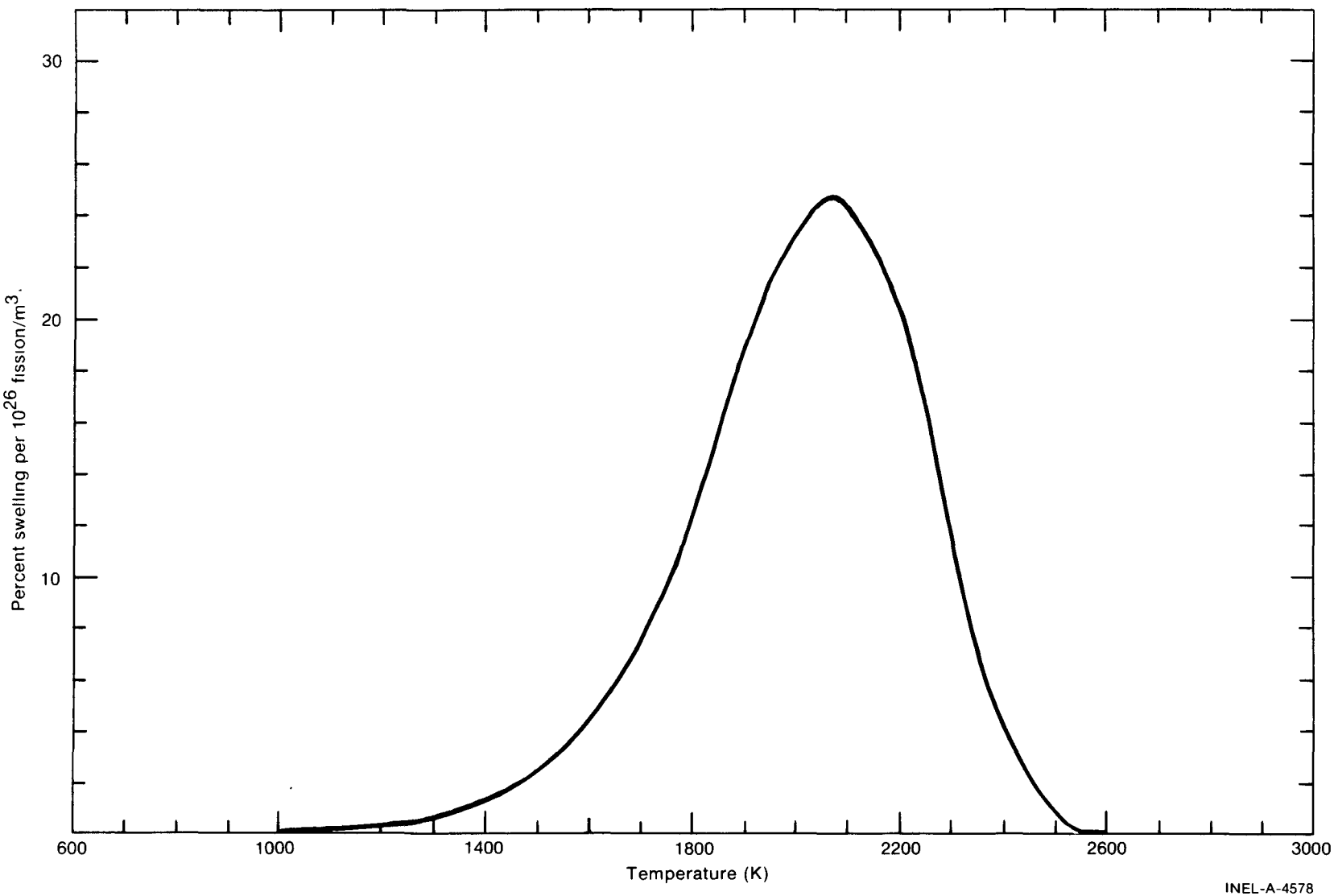

Fig. A-8.3 Unrestrained fission gas swelling.

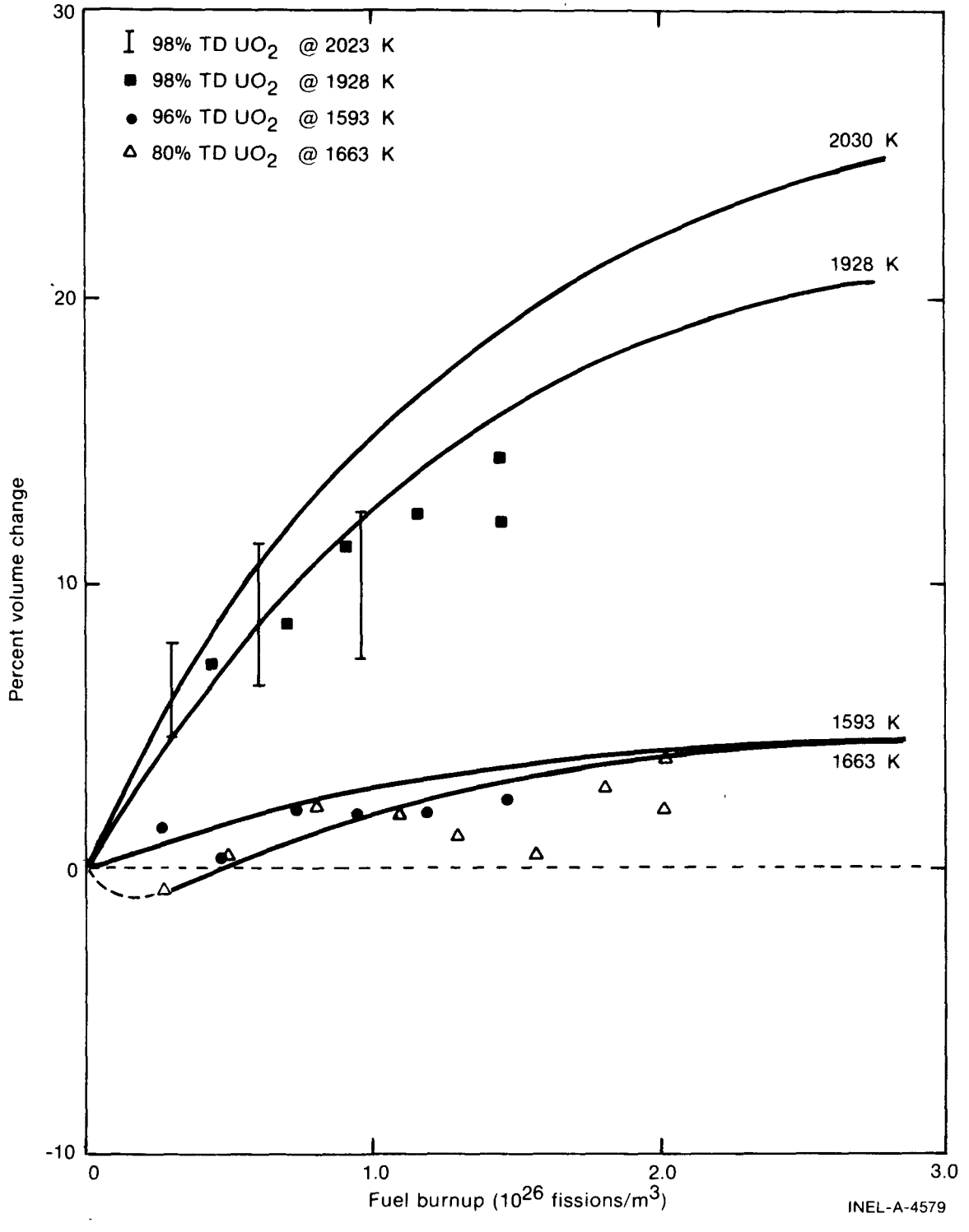

Fig. A-8.4 Fuel volume changes calculated by FSWELL compared with experimental fuel swelling data.

observed by Turnbull[A-8.32] and Kuz'min and Lebedev[A-8.36]. Thus swelling saturation is included in the swelling subcode FSWELL by determining the burnup exponential in Equation (A-8.2). The swelling dependence on burnup is

$$\left(\frac{\Delta V}{V}\right)_g = S_g \quad B_s \quad \exp(-8.0 \times 10^{-27} \quad B) \tag{A-8.9}$$

where

$\left(\frac{\Delta V}{V}\right)_g$ = fractional swelling of fuel per 10^{26} fissions/m^3

S_g = temperature dependent swelling rate of Equation (A-8.8)

B_s = burnup from beginning to end of time step (fissions/m^3)

B = total burnup of the fuel (fissions/m^3).

8.7 Fuel Swelling Subcode FSWELL Listing

A listing of the FSWELL subcode is presented in Table A-8.VIII.

8.8 References

A-8.1. W. Chubb, A. C. Hott, B. M. Argall, G. R. Kiop, "The Influence of Fuel Micro-Structure on In-Pile Densification," *Nuclear Technology, 26* (August 1975) pp 486-495.

A-8.2. H. Stehle and H. Assmann, "The Dependence of In-Reactor UO_2 Densification on Temperature and Microstructure," *Journal of Nuclear Materials, 52* (1974) pp 303-308.

A-8.3. D. W. Brite, J. L. Daniel, N. C. Davis, M. D. Freshley, P. E. Hart, R. K. Marshall, *EEI/EPRI Fuel Densification Project, Research Project 131 Final Report – June 1975*, pp 0-76.

A-8.4. D. A. Banks, "Some Observations of Density and Porosity Changes in UO_2 Fuel Irradiated in Water Cooled Reactors," *Journal of Nuclear Materials, 54* (1974) pp 97-107.

A-8.5. E. Rolstad, A. Hanevik, K. K. Knudsen, *Measurements of the Length Changes of UO_2 Fuel Pellets During Irradiation,* Presented at the Enlarged HPG Meeting on Computer Control and Fuel Research, June 4-7, 1974.

TABLE A-8.VIII

LISTING OF THE FSWELL SUBCODE

```
C
C
      SUBROUTINE FSWELL(FDENS, COMP, BU, BUL, FTEMP, GASWL, SOLDSW)
C
C     CCMP   = INPUT PLUTONIA CONTENT (WEIGHT PERCENT)
C     FDENS  = INPUT INITIAL DENSITY OF THE FUEL (KG/M**3)
C     FTEMP  = INPUT TEMPERATURE OF THE FUEL RING (K)
C     BL     = INPUT BURNUP TO END OF TIME STEP (MW-S/KG-U)
C     BLL    = INPUT BURNUP TO END OF LAST TIME STEP (MW-S/KG-U)
C
C     GASWL  = OUTPUT FUEL SWELLING DUE TO GAS FISSION PRODUCTS
C                     (FRACTION)
C     SCLDSW = OUTPUT FUEL SWELLING DUE TO SOLID FISSION PRODUCTS
C                     (FRACTION)
C
C     FSWFLL WAS DEVELOPED AND PROGRAMMED BY R. E. MASON - JUNE 1978.
C
C     THE UO2 SWELLING CORRELATION IS BASED ON THE FOLLOWING DATA
C             CHUBB,ET AL., NUCLEAR TECHNOLOGY 18(1973)
C             TURNBULL, JOURN. NUCL. MATER., 50(1974)
C             BANKS, JOURN. NUCL. MATER., 54(1974)
C             DANIEL ET AL., WAPD - 263
C
C                 - PRUGRAM -
C
      BUS    = FDENS * 2.974E+10 * (BU - BUL)
      SCLDSW = BUS * 2.5 E-23
      IF (FTEMP .LT. 2800.) GO TO 25
      GASWL  = 0.0
      GC TO 50
   25 CCNTINUE
      GASWL  = (6.60E-50*((2800.-FTEMP)**11.73)*EXP(-2.4E-10*BU*FDENS)
     #          *EXP(-0.0162 * (2800. - FTEMP))) * BUS
   50 CCNTINUE
      RETURN
      END
```

A-8.6. B. T. Bradbury and B. R. T. Frost, *Studies in Radiation Effects on Solids,* (ed.) G. J. Dienes, Gordon and Breach, New York, 1967.

A-8.7. B. T. Bradbury, J. T. Demant, P. M. Martin, D. M. Poole, *Journal of Nuclear Materials, 17* (1965).

A-8.8. B. T. Bradbury, J. T. Demant, P. M. Martin, *UKAEA Report,* AERE-R-5149 (1966).

A-8.9. G. M. Jeffery, *Journal of Nuclear Materials, 22* (1964).

A-8.10. J. L. Bates, *Metallic Uranium in Irradiated* UO_2, Hanford (USA) Report HW-82263 (1964).

A-8.11. D. R. O'Boyle, F. L. Brown, J. E. Saneck, "Solid Fission Product Behavior in Uranium – Plutonium Oxide Fuel Irradiated in a Fast Neutron Flux," *Journal of Nuclear Materials, 29* (1969) pp 27-42.

A-8.12. I. J. Hastings, D. H. Rose, J. Barid, "Identification of Precipitates Associated with Intergranular Fission Gas Bubbles in Irradiated UO_2 Fuel," *Journal of Nuclear Materials, 61* (1976) pp 229-231.

A-8.13. F. Anselin, *The Role of Fission Products in the Swelling of Irradiated UO_2 and $(U,Pu)O_2$ Fuel,* GEAP-5583 (January 1969).

A-8.14. F. Anselin and W. E. Baily, "The Role of Fission Products in the Swelling of Irradiated UO_2 and $(U,Pu)O_2$ Fuels," *Transactions of the American Nuclear Society, 10* (1967).

A-8.15. J. W. Harrison and L. M. Davies, "The Variation of Solid Fission Product and Gas Swelling in Uranium Compounds with Thermal Neutron Dose Rate," *Journal of Nuclear Materials, 27* (1968).

A-8.16. B. Lustman, *Technical Progress Report, PWR Project,* WAPD MRP 11 (October 1964 – January 1965).

A-8.17. J. H. Davies, R. F. Boyle, D. Weidenbaum, J. Hanson, "On the Composition of Metallic Ingots Formed in High Performance Ceramic Fuel Elements," *Transactions of the American Nuclear Society, 9*, 63 (1966).

A-8.18. J. H. Davies, *Some Considerations Regarding the Behavior of Fission Products in the Fast Ceramic Reactor,* GEAP-4872.

A-8.19. M. L. Bleiberg, R. M. Berman, B. Lustman, *Effect of High Burnup on Oxide Ceramic Fuels,* WAPD-T-1455 (1962).

A-8.20. I. G. Lebedev, V. I. Kuz'min, A. S. Piskum, "Swelling of Hot Oxide Fuel," *Soviet Journal of Atomic Energy, 28* (1970).

A-8.21. M. F. Lyons, R. F. Boyle, J. H. Davies, V. E. Hazel, T. C. Rowland, "UO_2 Properties Affecting Performance," *Nuclear Engineering and Design, 21* (1972) pp 167-199.

A-8.22. B. R. T. Frost, "Studies of Irradiation Effects in Ceramic Fuel at Harwell," Ceramic Nuclear Fuels, *Journal of the American Ceramic Society* (1969).

A-8.23. A. D. Whapham and B. E. Sheldon, *Electron Microscope Observation of the Fission Gas Bubble Distribution in UO_2,* AERE-R-4970 (April 1966).

A-8.24. D. R. Olander, *Fundamental Aspects of Nuclear Reactor Fuel Elements,* TID-26711-P1, Technical Information Center Energy Research and Development Administration, 1967.

A-8.25. V. Z. Janks, *BEMOD, A Code for the Lifetime of Metallic Fuel Elements,* ANL-7586 (July 1969) p 91.

A-8.26. T. C. Rowland, M. O. Marlowe, R. B. Elkins, *Fission Product Swelling BWR Fuels,* NEDP-20702 (November 1974).

A-8.27. W. Chubb, V. W. Storhok, D. L. Keller, "Observations Relating to the Mechanisms of Swelling and Gas Release in Uranium Dioxide of High Temperatures," *Journal of Nuclear Materials, 44* (1972) pp 136-152.

A-8.28. W. Chubb, V. W. Storhok, D. L. Keller, "Factors Affecting the Swelling of Nuclear Fuel at High Temperatures," *Nuclear Technology, 18* (June 1973) pp 231-255.

A-8.29. W. Chubb and D. L. Keller, *Implication of High Temperature Irradiation Data for Low Temperature Reactor Design,* BMI-1918 (July 1971) pp B98-B112.

A-8.30. R. F. Hilbert, W. J. Zielenbach, D. E. Lozier, R. B. Clark, V. W. Storhok, *Irradiation Behavior of Oxide Fuels at High Temperatures,* BMI-1918 (July 1971) pp B2-B43.

A-8.31. R. F. Hilbert, V. W. Storhok, W. Chubb, D. L. Keller, "Mechanisms of Swelling and Gas Release in Uranium Dioxide," *Journal of Nuclear Materials, 38* (1971) pp 26-34.

A-8.32. J. A. Turnbull, "The Effect of Grain Size on the Swelling and Gas Release Properties of UO_2 During Irradiation," *Journal of Nuclear Materials, 50* (1974) pp 62-68.

A-8.33. J. A. Turnbull, "The Mobility of Intragranular Bubbles in Uranium Dioxide During Irradiation," *Journal of Nuclear Materials, 62* (1976) pp 325-328.

A-8.34. J. A. Turnbull and M. O. Tucker, "Swelling in UO_2 under Conditions of Gas Release," *The Philosophical Magazine, 30* (July 1974) pp 47-64.

A-8.35. C. Grando, M. Montgomery, A. Strasser, "Unrestrained Swelling and Fission Gas Release of Fast Reactor Fuels," *Proceeding of the Conference on Fast Reactor Fuel Element Technology,* April 13-15, 1971, New Orleans. Ruth Farmakes (ed.) pp 771-784.

A-8.36. V. I. Kuz'min and I. G. Lebedev, "Effect of Temperature Distribution on the Swelling of UO_2 and UO_2-PuO_2 Cores," *Power Atomic Energy, 28* (January 1975).

A-8.37. C. J. Baroch and M. A. Rigdon, "Irradiation Behavior of UO_2 Burnups from 10 to 80 GWd/tonne U," Paper No. 58, *Proceedings of the BNES International Conference on Nuclear Fuel Performance,* October 15-19, 1973, London (CONF-731004).

A-8.38. R. C. Daniel, M. L. Bleigerg, H. B. Meieran, W. Yeniscavich, *Effects of High Burnup on Zircaloy Clad Bulk UO_2,* WAPD-263 (September 1962).

A-8.39. H. B. Meieran, *History of the NRX Reactor X-1-q and X-3-n Tests and the Nondestructive Post Irradiation Examination of Their Plate Type Ceramic Fuel Elements,* WAPD-TM-455 (March 1966).

A-8.40. T. C. Rowland, M. O. Marlowe, R. B. Elkins, *American Nuclear Society* (1974 annual meeting) p 124.

A-8.41. R. M. Berman, H. B. Meieran, P. W. Patterson, *Irradiation Behavior of Zircaloy-Clad Fuels Rods Containing Dished-End UO_2 Pellets,* WAPD-TM-629 (July 1967).

A-8.42. C. M. Cox, "The Irradiation Performance of Uranium-Plutonium Oxide Fuel Pins," *Nuclear Safety, 10* 5 (September – October 1969) pp 380-391.

A-8.43. R. G. Bellamy and J. B. Rich, "Grain-Boundary Gas Release and Swelling in High Burnup Uranium Dioxide," *Journal of Nuclear Materials, 33* (1969) pp 64-76.

A-8.44. R. C. Nelson, J. H. Baumgartner, K. J. Perry, E. L. Zebroski, *Irradiation Induced Swelling Rates of PuO_2 – UO_2 Fuel with Strong Radial Restraint,* GEAP-13686 (1971).

A-8.45. D. A. Collins and R. Hargreaves, "Performance-Limiting Phenomena in Irradiated UO_2," Paper No. 50, *Proceedings of the BNES International Conference on Nuclear Fuel Performance, October 15-19, 1973,* London (CONF-731004).

A-8.46. R. C. Nelson and E. L. Zebroski, "Irradiation – Induced Swelling Rates of PuO_2 with Strong Radial Restraint," *Transactions of the American Nuclear Society, 9* (1966) pp 412-413.

A-8.47. R. B. Poeppel, "An Advanced Gas Release and Swelling Subroutine," *Proceedings of the ANS Conference on Fast Reactor Fuel Element Technology, New Orleans, April 13-15, 1971,* Ruth Farmakes (ed.) pp 311-326.

A-8.48. P. Verbeck and N. Hoppe, *COMETHE III J – A Computer Code for Predicting Mechanical and Thermal Behavior of a Fuel Pin,* BN-7609-01.

8.9 Bibliography

The following list of reference material is pertinent to a literature review and was consulted by the FSWELL code developer.

(1) R. S. Barnes, "A Theory of Swelling and Gas Release for Reactor Materials," *Journal of Nuclear Materials, 11,* 2 (1964) pp 135-148.

(2) C. Ronchi and C. Sari, "Swelling Analysis of Highly Rated MX-Type LMBR Fuels. I. Restructuring and Porosity Behavior," *Journal of Nuclear Materials, 58* (1975) pp 140-152.

(3) C. Ronchi and H. J. Matzke, "Calculations and Estimates of Contributions of Different Transport Mechanisms to Fission-Gas Behavior in Fast Breeder Oxide Fuels," *Fuel and Fuel Elements for Fast Reactors Vol. 1*, Omtermatopma; Atomic Energy Agency, Vienna, 1974.

(4) Y. Sun and D. Okrent, *A Simplified Method of Computing Clad and Fuel Strain and Stress During Irradiation,* UCLA-ENG-7591 (October 1975).

(5) S. S. Bupara and R. L. Jentgen, *Mechanical Model of Swelling of Nuclear Fuels,* BMI-1918 (July 1971) pp B85-B98.

(6) A. A. Bauer, "A Model for the High Temperature Swelling of Clad Oxide Fuel," *Nuclear Technology, 13* (April 1972) pp 65-70.

(7) F. A. Nichols and H. R. Warner, "Swelling and Gas-Release Models for Oxide Fuel Rods (LWBR Development Program)," *Proceeding of the Conference on Fast Reactor Fuel Element Technology,* April 13-15, 1971, New Orleans, Ruth Farmakes (ed.) pp 267-289.

(8) H. R. Warner and F. A. Nichols, "A Statistical Fuel Swelling and Fission Gas Release Model," *Nuclear Applications and Technology, 9* (August 1970) pp 148-166.

(9) H. Zimmermann, "Fission Gas Behavior in Oxide Fuel Elements of Fast Breeder Reactors," *Nuclear Technology, 28* (1976).

(10) R. N. Duncan, D. A. Cantley, K. J. Perry, R. C. Nelson, "Fuel Swelling-Fast Reactor Mixed Oxide Fuels," *Proceedings of the Conference on Fast Reactor Fuel Element Technology,* April 13-15, 1971, New Orleans, Ruth Farmakes (ed.).

(11) W. B. Lewis, J. R. MacEwan, W. H. Stevens, R. G. Hart, "Fission-Gas Behavior in UO_2 Fuel," *Geneva Conference, Volume II* (1965) pp 405-415.

(12) M. V. Speight and J. A. Turnbull, "Enhanced Fission Product Release by Grain Boundary Diffusion," *Journal of Nuclear Materials, 68* (1977).

(13) G. L. Kulcinski and R. D. Leggett, "Reversibility of Fission Gas Swelling Uranium," *Journal of Nuclear Materials, 31* (1969) pp 279-287.

(14) T. D. Anderson, "Effects of High Burnup on Bulk UO_2 Fuel Elements," *Nuclear Safety, 6,* 2 (1964-65) pp 164-182.

(15) D. A. Collins, R. Hargreaves, H. Hughes, "UO_2 Fuel Performance Modeling and Predictive Methods," Paper No. 49, *Proceedings of the BNES International Conference on Nuclear Fuel Performance,* October 15-19, 1973, London (CONF-721004).

(16) G. W. Greenwood, H. J. E. Foreman, D. E. Rimmer, "The Role of Vacancies and Dislocations in the Nucleation and Growth of Gas Bubbles in Irradiated Fissile Material," *Journal of Nuclear Materials, 4* (1959) pp 305-324.

(17) S. H. Chien, A. R. Wazzan, D. Okrent, "The Effect of Solid Fission Products and Dislocations on Swelling and Fission Gas Release in Oxides During a Fast Overpower Transient," *Transactions of the American Nuclear Society, 26* (1977 annual meeting).

(18) W. G. Steele and D. Okrent, "Equation-of-State and Nonequilibrium Bubble Behavior During Fast Transients," *Transactions of the American Nuclear Society, 26* (1977 annual meeting).

(19) P. Chenebault and R. Delmas, "Fission Gas Emission by Uranium Oxide in Fuel Elements," Paper No. 19C, *Panel on the Behavior and Chemical State of Fission Products in Irradiated Fuel,* Vienna, August 1972.

(20) B. R. T. Frost, "Theories of Swelling and Gas Release in Ceramic Fuels," *Nuclear Applications and Technology, 9* (August 1970).

(21) H. Blank, "On the Driving Forces for Bubble Growth and Swelling in MX-Type Fast Breeder Fuels," *Journal of Nuclear Materials, 58* (1975) pp 123-139.

(22) C. C. Dollins and H. Ocken, "Re-Solution Effects and Fission Gas Swelling in UO_2," *Journal of Nuclear Materials, 45* (1972/73) pp 150-162.

(23) J. F. Bates and E. R. Gilbert, "Experiment Evidence for Stress Enhanced Swelling," *Journal of Nuclear Materials, 59* (1976) pp 95-102.

(24) R. E. Skaudahl, G. N. Spalaris, E. L. Zebroski, "U.S. Experience on Irradiation Performance of $UO_2 - PuO_2$ Fast Reactor Fuel," *American Institute of Mining, Metallurgical and Petroleum Engineers. Institute of Metals Division. Nuclear Metallurgy Symposium U.* 13, 1968.

(25) R. A. Weinger and A. Boltax, "Microstructural Modeling of Irradiation Creep and Swelling," *Journal of Nuclear Materials, 66* (1977) pp 1-16.

(26) W. Oldfield and J. B. Brown, Jr., "Bubble Migration in UO_2 – A Study Using a Laser Image Furnace," *Material Science and Engineering, 6* (1970) pp 361-370.

(27) W. Oldfield and A. J. Markworth, "The Theory of Bubble Migration Applied to Irradiated Materials," *Materials Science and Engineering, 4* (1969) pp 353-366.

(28) A. P. Malinauskas, R. A. Lorenz, M. F. Osborne, J. L. Collins, S. R. Manning, *Quarterly Progress Report on Fission Product Release from LWR Fuel for the Period July – September 1975,* ORNL-TM-5143.

(29) Y. Iwano. H. Kojima, N. Oi, *Studies on Swelling of Fast Reactor Fuel Due to Gaseous Fission Products 1 Out-of-Pile Experiment on Gaseous Fission Product Precipitation,* JAPFNR-23 (1971).

(30) M. J. F. Notely, R. Deshaies, J. R. MacEwan, *Measurements of the Fission Product Gas Pressure Developed in UO_2 Fuel Elements During Operation,* AECL-2662 (1966).

(31) D. Stahik and T. J. Partician, *Fission – Gas Behavior During A Mild Over-Power Transient,* ANL-8069 (February 1974) pp 1-24.

(32) H. Stehle, H. Assmann, F. Wunderlich, "Uranium Dioxide Properties for LWR Fuel Rods," *Nuclear Engineering and Design, 33* (1975) pp 230-260.

(33) R. M. Carroll, "Fission-Gas Behavior in Fuels," *Nuclear Safety, 10* 3 (May-June 1969).

(34) W. Beere, *An In Situ Observation of the Grain Boundary/Bubble Interaction,* (February 1975) RD/B/N3304.

(35) H. Blank and H. J. Matzke, "The Effect of Fission Spikes on Fission Gas Re-solution," *Radiation Effects, 17* (1973) pp 57-64.

(36) C. Ronchi and H. J. Matzke, "Calculations on the In-Pile Behavior of Fission Gas in Oxide Fuels," *Journal of Nuclear Materials, 45* (1972/73) pp 15-28.

(37) A. D. Brailsford and R. Bullough, "The Stress Dependence of High Temperature Swelling," *Journal of Nuclear Materials, 48* (1973) pp 87-106.

(38) M. F. Lyons, T. C. Rowland, D. T. Weiss, "BWR Fuel Testing at General Electric – An Overview," Paper No. 68 in *Proceedings of the BNES International Conference on Nuclear Fuel Performance,* October 15-19, 1973, London (CONF-731004).

(39) F. N. Rhines et al, *Quantitative Determination of the Structure – Property Relationship in Nuclear Fuel Elements Materials,* ORO-4212-13 (July-September 1972).

(40) C. C. Dollins and H. Ocken, "A Fission Gas Swelling Model Incorporating Re-Solution Effects," *Nuclear Applications and Technology, 9* (August 1970) pp 141-147.

(41) C. C. Dollins, "Fission Gas Swelling and Long Range Migration at Low Temperature," *Journal of Nuclear Materials, 49* (1973/74) pp 10-20.

(42) C. C. Dollins, "On Fission Gas Swelling Below $\sim$1200°C," *Journal of Nuclear Materials, 60* (1976) pp 107-110.

(43) C. C. Dollins and F. A. Nichols, "Swelling and Gas Release in UO_2 at Low and Intermediate Temperatures," *Journal of Nuclear Materials, 66* (1977) pp 43-157.

(44) E. E. Gruber, "Calculated Size Distribution for Gas Bubble Migration and Coalescence in Solids," *Journal of Applied Physics, 38* (1967) pp 243-250.

(45) J. Rest, M. G. Seitz, S. M. Gehl, L. R. Kelman, "Development and Experimental Verification of SST-GRASS: A Steady-State and Transient Fuel Response and Fission-Product Release Code," *OECD-CSNI Meeting on the Behavior of Water Reactor Fuel Elements under Accident Conditions held in Norway,* September 13-16, 1976.

(46) J. W. Dias and R. B. Poeppel, *Transient Swelling Studies with the GRASS Code,* ANL-7992 (March 1973).

(47) J. Rest, "Behavior of Fission Gas in LWR Fuel During Steady-State Operating Conditions," *Transactions of the American Nuclear Society, 23* (June 1976).

(48) F. A. Nichols, *Behavior of Gaseous Fission Products in Oxide Fuel Elements,* WAPD-TD-570 (October 1966).

(49) G. W. Greenwood and M. V. Speight, "An Analysis of the Diffusion of Fission Gas Bubbles and Its Effect on the Behavior of Reactor Fuels," *Journal of Nuclear Materials, 10* (1963) pp 140-144.

(50) E. Duncombe, J. E. Meyer, W. A. Coffman, *Comparisons with Experiment of Calculated Dimensional Changes and Failure Analysis of Irradiated Bulk Oxide Fuel Test Rods Using the CYGRO-1 Computer Program,* WAPD-TD-583 (September 1966).

(51) I. Goldberg, L. L. Lynn, C. D. Sphar, *FIGRO-FORTRAN IV Digital Computer Program for the Analysis of Fuel Swelling and Calculation of Temperature in Bulk Oxide Cylindrical Fuel Elements,* WAPD-TD-618 (December 1966).

9. PRESSURE SINTERING (FHOTPS)

(R. E. Mason)

Densification of light water reactor fuel during reactor operation results from a number of different driving forces such as irradiation, pore surface tension, and external pressure. This section describes a fuel densification model to calculate pressure (stress) related densification. Stress on the fuel is typically due to cladding constraints.

This model complements the irradiation induced densification model, FUDENS, and is to be used instead of the FUDENS model when applied stress and temperature make the densification calculated by FHOTPS larger than that calculated by FUDENS. At burnups above approximately 4.32×10^5 MWs/kgU, where the as-fabricated pores have been sintered closed, the FHOTPS subcode should be used to calculate sintering of pores and bubbles from which fission gas has escaped. Section A-8 presents a more detailed discussion of how this subcode should be used with other MATPRO subcodes.

9.1 Summary

The pressure sintering subcode, FHOTPS, calculates the negative fractional volume change (densification) due to stresses on the fuel pellet. If the fuel is in contact with the cladding, the hydrostatic stress of the cladding on the fuel must be input to FHOTPS. If the fuel is not in contact with the cladding, the plenum pressure should be input. FHOTPS uses an integral expression to calculate volume change rather than a constant rate correlation because the densification rate is not constant during a calculation time step. The expression is

$$\frac{1}{V}\int_{V_0}^{V_2}\left(\frac{V_T}{V-V_T}\right)^{2.4} \Delta V = 30\ \sigma^{4/3}\ \Delta t\ \exp\ (-Q/RT) \qquad \text{(A-9.1)}$$

where

V = fuel volume (m^3)

V_2 = volume of the fuel at the end of the time interval (m^3)

V_0 = volume of the fuel at the start of a time interval (m^3)

V_T = volume of the fuel at theoretical density (m^3)

σ = applied stress (Pa)

Q = activation energy (MJ/mol)

R = universal gas constant (MJ/K·mol)

T = absolute temperature (K)

t = time from beginning to end of time step (s).

Equation (A-9.1) is used in an iteration routine to find V_2. A trial value is assumed for V_2 and the left-hand side of Equation (A-9.1) is integrated using Simpson's rule. The right-hand side of Equation (A-9.1) is assumed independent of time. The trial value of V_2 is adjusted until both sides of Equation (A-9.1) differ by less than ±0.01. The activation energy, Q, used in the right-hand size of Equation (A-9.1) is determined using the equation

$$Q = 0.3363\ \left\{\exp\left(\frac{20}{|\log x|} - 8\right) + 1\right\}^{-1} + 0.021628 \qquad \text{(A-9.2)}$$

where

Q = activation energy (MJ/mol)

x = oxygen to metal ratio -1.9999.

If the oxygen to metal ratio of the fuel is not known, 2.006 should be input.

9.2 Pressure Sintering Models and Data

Pressure sintering data are scarce and most describe fabrication sintering (sintering from ∿50 to 60% TD to ∿95% TD) rather than final stage sintering (90 to 95% TD to ∿96 to 98% TD) which is the regime appropriate for FHOTPS calculations. Voglewede and Dochwat[A-9.1] proposed a pressure sintering model based on final stage sintering data. These data form the base used to develop the FHOTPS model.

The pressure sintering data reported by Voglewede[A-9.2,A-9.3] describe mixed oxide fuel preannealed at the testing temperature (1473 to 1773 K) before stress was applied. The mixed oxide densification rate determined by Voglewede[A-9.4] and the FHOTPS calculation are plotted in Figure A-9.1. It shows how the densification rate decreases as the density of the fuel approaches theoretical density. Using data generated at Argonne National Laboratories, Voglewede and Dochwat derived the semiempirical pressure sintering expression

$$\frac{1}{V}\frac{dV}{dt} = K\left(\frac{P}{1-P}\right)^m \sigma^n \exp\left(-Q/RT\right) \qquad \text{(A-9.3)}$$

where

$\frac{1}{V}\frac{dV}{dt}$ = fractional rate of volume change (S^{-1})

K = 5.5×10^{17}

m = 2.4

n = 4/3

σ = stress (kgf/cm^2)

Q = 0.4605 MJ/mol

P = fractional porosity.

Wolfe and Kaufman[A-9.5] found pressure sintering of UO_2 to be proportional to $\sigma^{4.5}$ where σ is the applied stress. Using the UO_2 pressure sintering results listed in

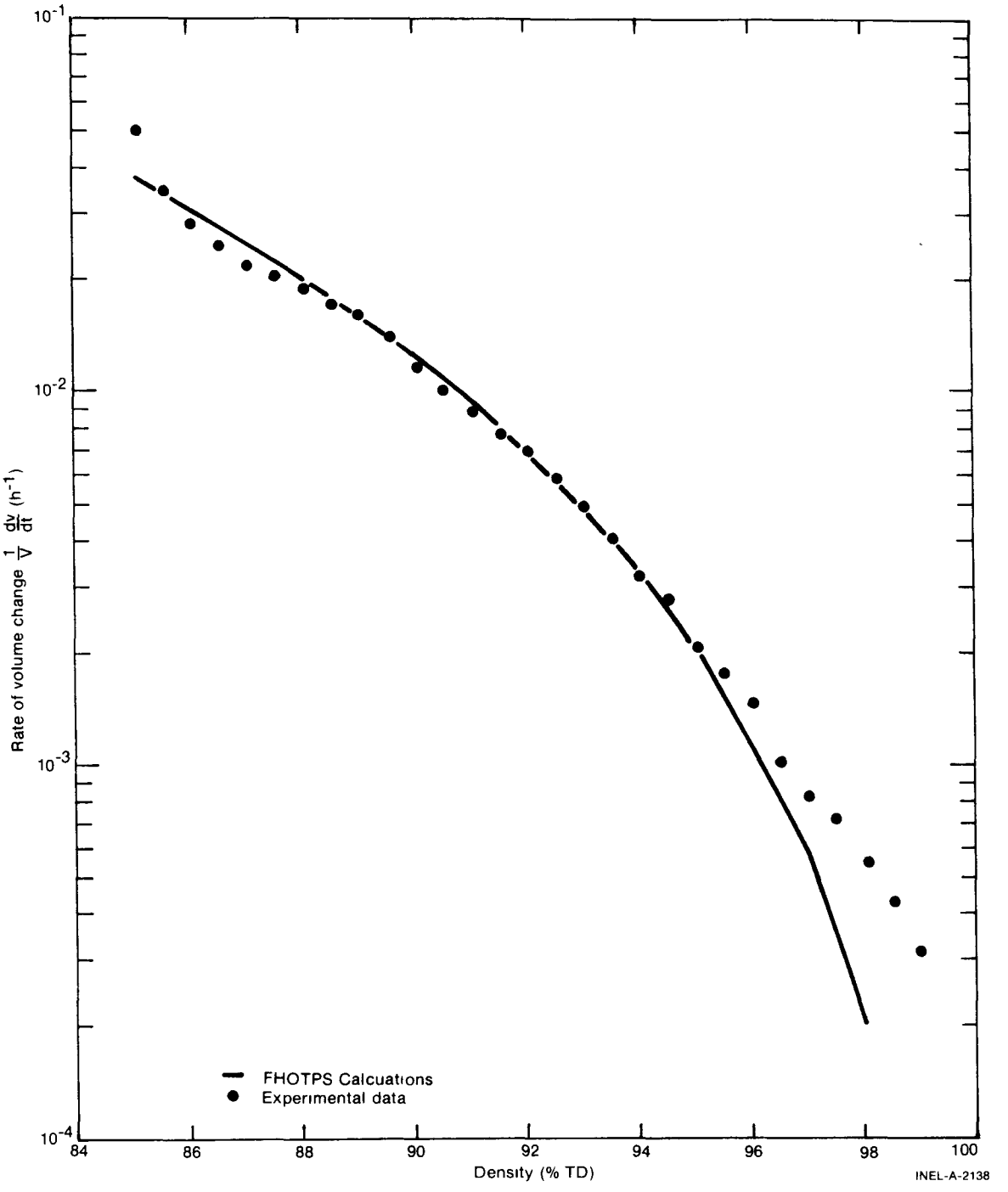

Fig. A-9.1 Comparison of experimental pressure sintering data of Voglewede and FHOTPS calculations for mixed oxide fuel pellets.

Table A-9.I, they developed a densification equation based on fuel temperature, porosity and stress. Wilkinson and Ashby[A-9.6], using theoretical considerations, derived an equation very similar to that developed by Wolfe and Kaufman.

TABLE A-9.I

PRESSURE SINTERING RESULTS REPORTED BY WOLFE AND KAUFMAN[a]

Initial Porosity	Time (s)	Final Porosity	FHOTPS Calculated Final Porosity
0.1763	299	0.1396	0.1668
0.1722	299	0.1537	0.1655
0.1742	1019	0.1405	0.1458
0.1537	1800	0.1276	0.1221
0.1738	1800	0.1391	0.1326
0.1722	2099	0.1276	0.1270
0.1751	2099	0.1220	0.1286
0.1745[b]	6779	0.0844	0.0985

[a] For fuel pressed at 38.61 MPa and 2123 K. FHOTPS calculations used an activation energy of 0.44 MJ/mol (an oxygen to metal ratio of 2.0019).

[b] Pressed at 39.61 MPa.

Other models and data are based on UO_2 fabrication data, theoretical considerations, or ceramic pressure sintering data. Rhines et al[A-9.7] suggested that the stress exponent depends on the external pressure. Hart[A-9.8] found that the stress exponent of UO_2 and $(U,Pu)O_2$ pressure sintering was not constant at stresses between 13.79 and 41.37 MPa and between 1173 and 1373 K. He discussed data of Fryer[A-9.9] and Warren and Chaklader[A-9.10] and found the densification rates at constant porosity and temperature were best expressed by stress exponents between 2 to 3.

Pressure sintering is also a function of fuel porosity. This has been considered by a number of authors, for example, Rossi and Fulrath[A-9.11] proposed pressure sintering calculations be made using an effective stress (σ_e) of the form $\sigma_e = \sigma (1\text{-}bP)$ where σ is the external stress, b is the stress concentration factor and P is the external stress.

McClelland[A-9.12] multiplied the stress by $(1-P^{2/3})^{-1}$ to obtain an effective stress whereas Fryer proposed that multiplying stress by P/ρ gives the effective stress. Fryer also developed a pressure sintering model, based on aluminum dioxide data, that was linearly proportional to the stress.

Warren and Chaklader applied the Fryer equation to their UO_2 reactive sintering (uranium compond reacting during pressing to form the oxide) data and reported that the densification rate was adequately predicted by the equation. Hart, on the other hand, found that the densification rate of Warren and Chaklader was better predicted by a nonlinear stress dependence. The fuel had an O/M ratio of 2.15 or greater. The calculations used by Warren and Chaklader were made using an activation energy of 0.22 MJ/mol. Pressure sintering data reported by Warren and Chaklader are shown in Figure A-9.2 along with FHOTPS predictions.

9.3 FHOTPS Model Development

FHOTPS is based on a modification of the densification proposed by Voglewede and Dochwat which agrees with Hart, Voglewede[A-9.3], and Wolfe and Kaufman who found pressure sintering to be a nonlinear function of stress. The equation proposed by Voglewede and Dochwat, Equation (A-9.3), is modified to include UO_2 pressure sintering data resulting in Equation (A-9.1). Voglewede and Dochwat determined the numerical exponents n and m in Equation (A-9.3) from their mixed oxide pressure sintering data. Rhines et al suggested correlating the stress exponent with pressure, but they and others reporting UO_2 pressure sintering data did not provide enough data to permit development of such a correlation. The data reported by Voglewede and Dochwat are especially applicable to our modeling requirements because the fabricated pellets were annealed at the sintering temperature before stress was applied.

The activation energies are based on the values determined by Voglewede[A-9.4] and on comparisons with the data reported by Wolfe and Kaufman, and Warren and Chaklader. The UO_2 pressure sintering data reported by Warren and Chaklader are used to correlate densification rates of fuel with $O/M > 2.08$. The activation energy (0.4395 MJ/mol) used to correlate Wolfe and Kaufman's data is chosen assuming that their UO_2 had an $O/M = 2.0019$. Activation energy magnitudes are not well defined. Seltzer et al[A-9.13] have a fairly complete table of activation energies for UO_2 creep. Activation energies reported by Seltzer et al have an uncertainty of ±0.02 MJ/mol. This can alter the calculated volume change by a factor of 2 to 10. The scatter of reported activation energies by different experimenters is also very large, 0.2344 to 0.8372 MJ/mol for approximately the same O/M ratio. Since the scatter is so large, approximate activation energies as a function of O/M ratio are calculated using Equation (A-3.2).

The value of B is found by fitting Equation (A-9.3) by inspection to the data shown in Figure A-9.2 and in Table A-9.I. All the variables of the right-hand side of Equation (A-9.3) are assumed independent of time. The fractional porosity of the equation is related to the fuel volume by the equation

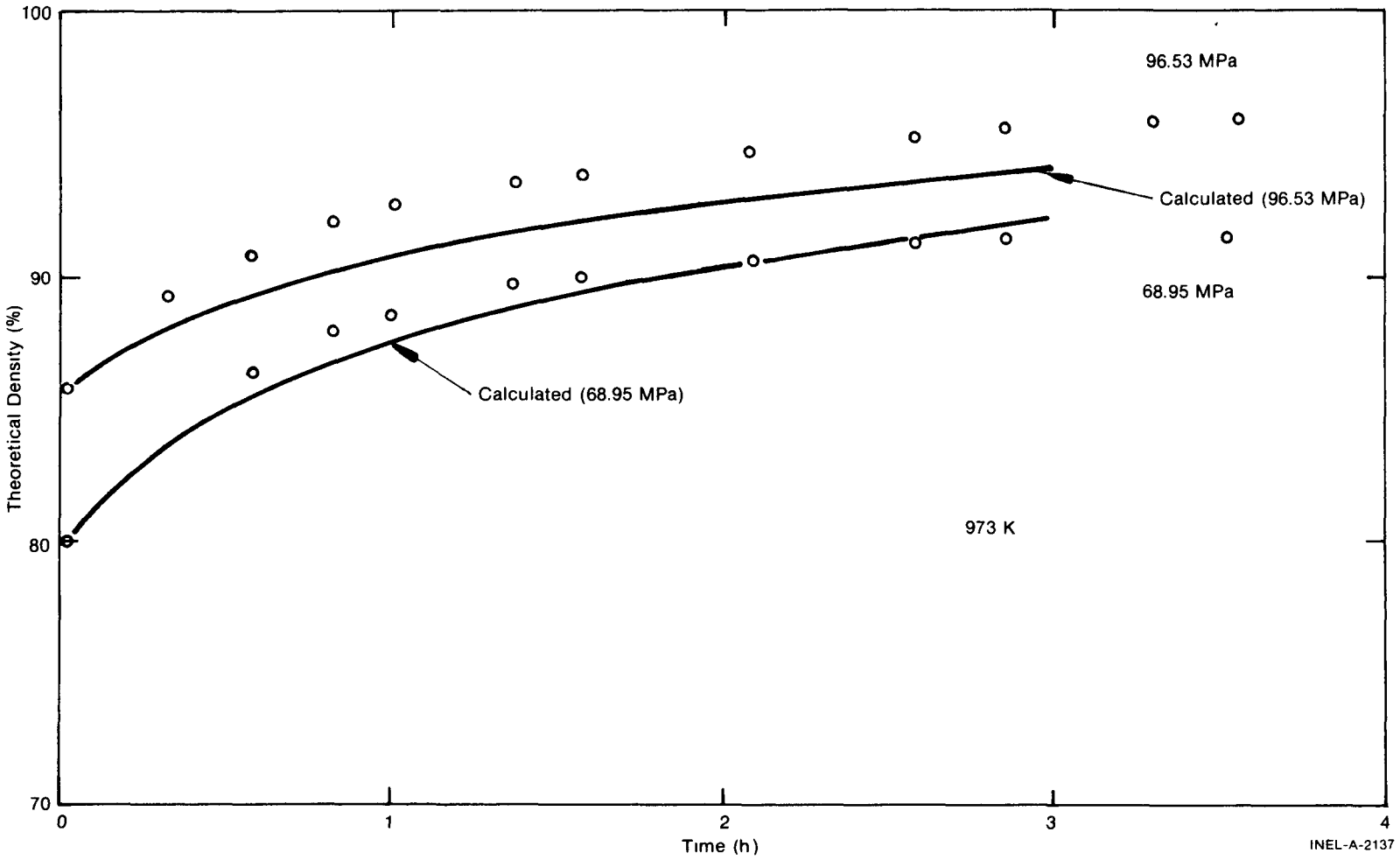

Fig. A-9.2 Reactive pressure sintering data versus FHOTPS density calculations for UO_2 with an O/M ratio greater than 2.08.

$$P = \frac{V - V_T}{V} \tag{A-9.4}$$

where

P = fractional porosity

V = fuel volume (m^3)

V_T = volume of theoretically dense fuel (m^3).

Since the time required for fuel to densify is short (a few hours) relative to time steps of 500 to 1000 hours, numerical integration of the equation within the program is necessary. This avoids calculating fuel densities greater than theoretical density, a result that could be obtained if the initial rate of volume change was simply multiplied by a time step of 500 hours or greater. Simpson's numerical integration rule is used to integrate

$$A_L = \int_{V_0}^{V_2} \frac{1}{V} \left(\frac{V_T}{V - V_T} \right)^{2.4} dV \tag{A-9.5}$$

where

A_L = left-hand side of Equation (A-9.1).

V_2 is adjusted by the computer routine until the results of A_L and A_r of the following equation

$$A_r = 30\ \sigma^{4/3}\ \Delta t\ B \exp\ (-Q/RT) \tag{A-9.6}$$

where

A_r = right-hand side of Equation (A-9.1)

agree within ±0.01. After each iteration, a new value of V_2 is assigned which is halfway between the last volume which made A_r smaller than A_L and the last volume which made Equation (A-9.5) larger than A_L. When A_r and A_L are within 0.01 of each other (this usually requires fewer than 7 iterations), the fuel volume change (FVC) is calculated by the expression

$$FVC = \frac{V_2 - V_0}{V_0} . \tag{A-9.7}$$

V_2 is the new fuel volume per gram. The calculation gives a volume change accurate to within ± 0.05%.

9.4 Pressure Sintering End Point

An effect completely ignored in the preceding formulations and data correlations is that of gas entrapped in the pores during final stage densification. Warren and Chaklader found definite end point densities during reactive pressure sintering. The effect of gas on the densification end point must also be greatly amplified in in-pile fuel because of the fission gases. The author has seen no data to evaluate the effect of atmospheric gases, plenum gases, or fission gases on the final fuel density. This area should be studied if pressure sintering effects are to be properly utilized as a part of in-pile fuel analysis.

9.5 Fuel Pressure Sintering Subcode FHOTPS Listing

A listing of the FHOTPS subcode is given in Table A-9.II.

9.6 References

A-9.1. J. C. Voglewede and S. C. Dochwat, *Reactor Development Program Progress Report,* ANL-RDP-33 (December 1974).

A-9.2. J. C. Voglewede, *Reactor Development Program Progress Report,* ANL-RDP-29 (June 1974).

A-9.3. J. C. Voglewede, *Reactor Development Program Progress Report,* ANL-RDP-22 (January 1974).

A-9.4. J. C. Voglewede, *Reactor Development Program Progress Report,* ANL-RDP-26 (March 1974).

A-9.5. R. A. Wolfe and S. F. Kaufman, *Mechanical Properties of Oxide Fuels (LSBR/LWB Development Program),* WAPD-TM-587 (October 1967).

A-9.6. D. S. Wilkinson and M. F. Ashby, "Pressure Sintering by Power Law Creep," *Acta Metallurgica, 23* (November 1975) pp 1277-1285.

A-9.7. F. N. Rhines et al, *Quantitative Determination of the Structure-Property Relationship in Nuclear Fuel Element Materials,* ORO-4212-13 (July – September 1972).

A-9.8. P. E. Hart, "Fabrication of High-Density UO_2 and $(U_{0.75}Pu_{0.25})O_2$ by Hot Pressing," *Journal of Nuclear Materials, 51* (1974) pp 199-202.

A-9.9. G. M. Fryer, "Hot Pressing of Alumina: A New Treatment of Final Densification," *Transactions of the British Ceramic Society, 66* (1977) pp 127-134.

A-9.10. I. H. Warren and A. C. D. Chaklader, "Reactive Hot Pressing of Nonstoichiometric Uranium Dioxide," *Metallurgical Transactions, 1* (1970) pp 199-205.

TABLE A-9.II

LISTING OF THE FHOTPS SUBCODE

```
C
C
      SUBROUTINE FHOTPS(COMP,FOM,HSTRES,TIME,FTEMP,TLAST,SINPOR,FVC)
C
C      FHOTPS RETURNS THE FRACTIONAL VOLUME CHANGE FOR UO2 AND
C             MIXED OXIDES
C
C      COMP   = INPUT PLUTONIA CONTENT (WEIGHT PERCENT)
C      FOM    = INPUT FUEL OXYGEN TO METAL RATIO
C      HSTRES = INPUT HYDROSTATIC STRESS ON THE FUEL PELLET (PA)
C      TIME   = INPUT TIME TO END OF TIME STEP (S)
C      TLAST  = INPUT TIME TO END OF LAST TIME STEP (S)
C      FTEMP  = INPUT TEMPERATURE OF THE FUEL RING (K)
C      SINPOR = INPUT FRACTIONAL POROSITY WHICH CAN BE SINTERED
C
C      FVC    = OUTPUT FRACTIONAL VOLUME CHANGE
C
C      THE UO2 PRESSURE SINTERING CORRELATION IS BASED ON THE FOLLOWING
C      DATA
C             WOLFE AND KAUFMAN, WAPD-TM-587(1967)
C             WARREN AND CHAKLADER, METALLURGICAL TRANSACTIONS 1(1970)
C
C      THE (U,PU)O2 PRESSURE SINTERING CORRELATION IS BASED ON THE
C      FOLLOWING DATA
C             VOGLEWEDE, ANL-RDP-22
C
C      FHOTPS WAS DEVELOPED AND PROGRAMMED BY R. E. MASON - AUGUST 1977
C
C      IF HSTRES IS NOT DETERMINED IN THE CODE USING THIS SUBCODE
C      THEN SET HSTRES EQUAL TO A DEFAULT VALUE OF 1.0E+06
C
C                    - PROGRAM -
C
      DIMENSION C(7)
      Y(V,VT)  =   ((VT/(V - VT))**2.4)/V
      ROTH     = 11.45 * COMP/100. + (1. - COMP/100.) * 10.97
C
      IF (HSTRES .EQ. 0.0) GO TO 700
      B        = 30.0
      M        = 0.0
C
      IF (COMP .GT. 0.0) GO TO 10
      IF(FOM .LT. 2.0) FOM = 2.0
      XX       = ABS(ALOG10(FOM - 1.9999) / 2.5)
      Q        = 40431.8/(EXP(8 * (1. - XX)/XX) + 1.) + 26000.
      GO TO 20
   10 CONTINUE
      B        = 22.0
      Q        = 9.0E 04
   20 CONTINUE
      H        = 4.0/3.0
      TCHG     = TIME - TLAST
      Z        = B*TCHG*(HSTRES**H)*(EXP(-Q/FTEMP))
C
      IF(Z .EQ. 0.0) GO TO 700
      VT       = (0.1097*COMP + (1.0 - 0.01*COMP)*11.46)/125.72
      IF(SINPOR .LE. 0.0) GO TO 700
      V1       = 1.0/(ROTH * (1.0 - SINPOR))
      VF       = V1
      V2       = VT + 1.0E-07
      A        = ABS(VF - V2)
      C(1)     = Y(VF,VT)
      C(7)     = Y(V2,VT)
      V        = VF
C
      DO 100     I = 2,6
      V        = V - A/6
      IF(V .LT. VT) GO TO 700
      C(I)     = Y(V,VT)
  100 CONTINUE
C
      SIM      = A*(C(1)+4.0*(C(2)+C(4)+C(6))+2.0*(C(3)+C(5))+C(7))/18.0
      IF(SIM/Z .LE. 1.0) GO TO 900
      V2       = - (ABS(V1 - VT)) * 0.5 + V1
      A        = ABS(VF - V2)
      C(1)     = Y(VF,VT)
      C(7)     = Y(V2,VT)
      V        = VF
```

TABLE A-9.II (continued)

```
C
      DO 150   I = 2,6
      V        = V - A/6
      C(I)     = Y(V,VT)
  150 CONTINUE
C
      SIM      = A*(C(1)+4.0*(C(2)+C(4)+C(6))+2.0*(C(3)+C(5))+C(7))/18.0
      IF(SIM/Z .GE. 0.990   .AND.  SIM/Z .LE. 1.011) GO TO 800
      IF(SIM/Z .LT. 1.0) GO TO 300
C
  200 CONTINUE
      V3       = V2
      V2       = ((ABS(V1 - V2))/2.0) + V2
      GO TO 500
C
  300 CONTINUE
      V1       = V2
      V2       = ((ABS(V2 - VT)) * 0.5) + VT
      V3       = VT
C
  500 CONTINUE
      IF(M .GE. 15) GO TO 800
      M        = M + 1
      A        = ABS(VF - V2)
      C(1)     = Y(VF,VT)
      C(7)     = Y(V2,VT)
      V        = VF
      DO 220   I = 2,6
      V        = V - A/6
      IF (V - VT .LE. 0.0) GO TO 800
      C(I)     = Y(V,VT)
C
  220 CONTINUE
      SIM      = A*(C(1)+4.0*(C(2)+C(4)+C(6))+2.0*(C(3)+C(5))+C(7))/18.0
      IF(SIM/Z .GE. 0.990   .AND.  SIM/Z .LE. 1.011) GO TO 800
      IF(SIM/Z .GT. 1.0) GO TO 510
      IF(SIM/Z .LT. 1.0) GO TO 520
C
  510 CONTINUE
      V3       = V2
      V2       = ((ABS(V1 - V2))/2.0) + V2
      GO TO 500
  520 CONTINUE
      V1       = V2
      V2       = ((ABS(V2 - V3))/2.0) + V3
      GO TO 500
C
  700 CONTINUE
      FVC      = 0.0
      GO TO 1000
  800 CONTINUE
      FVC      = (V2 - VF)/VF
      GO TO 1000
  900 CONTINUE
      FVC      = (VT - V1)/V1
 1000 CONTINUE
      IF(ABS(FVC) .GE. SINPOR) FVC = - SINPOR
C
      RETURN
      END
```

A-9.11. R. C. Rossi and R. M. Fulrath, "Final Stage Densification in Vacuum Hot-Pressing of Alumina," *Journal of the American Ceramic Society, 48* (1965) pp 558-564.

A-9.12. J. D. McClelland, *Kinetics of Hot Pressing,* NAA-SR-5591 (1961).

A-9.13. M. S. Seltzer, J. S. Perrin, A. H. Claver, B. A. Wilcox, *Review of Out-of-Pile and In-Pile Creep of Ceramic Nuclear Fuel,* DMI-1906 (July 1971) p 72.

10. FUEL RESTRUCTURING (FRESTR)

(C. S. Olsen)

During the irradiation of light water reactor fuels at relatively high powers, equiaxed grain growth occurs near the outer periphery of the fuel, and columnar grains form near the center of the fuel[A-10.1]. At the periphery the temperatures are lower than those necessary for noticeable equiaxed grain growth to occur and the as-sintered structure remains. The subroutine FRESTR calculates the equiaxed grain growth as a function of temperature, initial grain size, and time and also calculates a time-dependent threshold temperature necessary for the formation of columnar grains.

10.1 Summary

The FRESTR subroutine consists of the following equations. Equiaxed grain growth is expressed by:

$$D^4 - D_o^4 = 1.717 \times 10^{10} \exp(-3.87 \times 10^5/RT)\, t \qquad \text{(A-10.1)}$$

where

D = grain size (μm)

D_o = initial grain size (μm)

R = 8.314 J/mol·K

T = temperature (K)

t = time (s).

The columnar grain formation is characterized by a threshold temperature, FTCRIT. If the fuel temperature at a particular location exceeds the threshold temperature, columnar grains with a density of 98% TD are assumed to form instantaneously. FTCRIT is defined by the following equation:

$$1/FTCRIT = 3.435 \times 10^{-5} \log_{10} t + 3.47 \times 10^{-4} \qquad \text{(A-10.2)}$$

where

FRCRIT = threshold temperature (K).

Equiaxed grain growth will be discussed in the next section and columnar grain formation is discussed in Section A-10.3. An integrated restructuring model for UO_2 and $(U,Pu)O_2$ equiaxed grain growth and columnar grain formation is presented in Section A-10.4.

10.2 UO_2 and $(U,Pu)O_2$ Equiaxed Grain Growth

Several models for equiaxed grain growth have been developed to predict grain growth as a function of time and temperature. These different models correspond to different mass transport mechanisms. The theoretical models will be discussed first, followed by a review of the experimental data and comparisons of the data with these models and with an empirical model which was developed to explain grain growth in α-brass.

10.2.1 Theoretical Models for Equiaxed Grain Growth. The driving force for equiaxed grain growth is the decrease in surface free energy brought about by the decrease in the number of grains and, consequently, the total surface area. The pressure drop (or chemical potential) within a grain (analogous to a soap bubble) is given by $2\gamma/r$ where γ is the surface free energy and r is the radius of the bubble ($1/r$ is the curvature). The grain boundaries move outward from the center of curvature; the larger grains consuming the smaller grains or the grains with fewer than six sides. If the grain growth rate is assumed to be inversely proportional to the curvature and the curvature is defined by the grain diameter, then:

$$\frac{dD}{dt} = \frac{k}{D} \qquad \text{(A-10.3)}$$

where

k = a proportionality constant which contains the diffusion coefficient for the material

and the other terms are previously defined.

Using an Arrhenius equation for the diffusion coefficient and the boundary condition that at $t = 0$, the initial grain size is D_o, Equation (A-10.3) becomes upon integration:

$$D^2 - D_o^2 = k_o \exp(-Q/RT)\, t \qquad \text{(A-10-4)}$$

where

k_o = $2k$

Q = the activation energy (J/mol)

R = the gas constant

other terms are previously defined.

Equation (A-10.4) has been used successfully to predict the grain growth of metals at high temperatures, but with considerable deviations at low temperatures. The presence of inclusions at the fuel grain boundaries may explain why Equation (A-10.4) does not make a good prediction of low temperature grain growth in metals[A-10.2]. In ceramic materials

such as UO_2 or $(U,Pu)O_2$ a large fraction of the porosity is located at the grain boundaries. Speight and Greenwood[A-10.3] performed an analysis that showed bubbles could not prevent the movement of grain boundaries, but their effect was to reduce the velocity of movement as long as they remain attached to the boundary, whereas larger bubbles move more slowly, and for a given spacing, have the greatest effect in retarding boundary movement. In this way, the effect of voids is markedly different from that of solid precipitates which remain relatively stationary and permit only local boundary movement or complete boundary breakaway.

Kingery and Francois[A-10.4] developed a model that considers the retarding effect of pores on grain boundaries or more commonly at grain intersections. For grain boundary movement, the pores on these boundaries have to migrate at a rate inversely proportional to the pore diameter, D_p. When, as usually found, the grain (and pore) growth is more rapid than other changes, the pore-grain geometry remains about the same and thus the pore size remains nearly proportional to the grain size, D. For the ideal case, Equation (A-10.3) is modified by the retardation effects of the pore

$$\frac{dD}{dt} = \frac{K}{D}\left(\frac{K'}{D_p}\right) = \left(\frac{K}{D}\right)\left(\frac{K''}{D}\right) \qquad \text{(A-10.5a)}$$

where

K = proportionality constant

K′ = a constant which contains the diffusion constant for the pores

K″ = K′ divided by the constant of proportionality relating the pore size to the grain size

and upon integration

$$D^3 - D_o^3 = 3KK''t = kt\exp(-Q/RT) \qquad \text{(A-10.5b)}$$

where

k = a single empirical constant of the material.

Thus when pores restrict grain boundary movement, a cubic relationship between grain size and time results rather than the square of grain size with time relationship expressed in Equation (A-10.4).

Nichols[A-10.2] extended the analysis of Kingery and Francois[A-10.4] and showed that their results implicitly assumed a vapor transport mechanism with the pressure in the

pore remaining equal to the equilibrium pressure drop $2\gamma/r$ where γ is the surface tension and r is the pore radius. Nichols[A-10.2] also showed that for a constant pore pressure (which is not a function of pore radius), equiaxed grain growth due to a vapor-transport mechanism can be expressed by:

$$D^4 - D_o^4 = kt \exp(-Q/RT). \quad \text{(A-10.6)}$$

10.2.2 Model Comparisons with Experimental Data. Lyons et al[A-10.5] compared available grain growth data[A-10.6 – A-10.11] with the cubic model represented by Equation (A-10.5). He obtained a reasonable fit to the data with this equation except for Padden's data[A-10.7] at 1500 and 1700°C during the initial grain growth period, and most of the Hausner data[A-10.9]. The problems with the Hausner data were attributed to UO_2 evaporation during annealing in an open system. A rerun of Hausner's experiments with encapsulation of the UO_2 specimens resulted in a constant time dependence at all temperatures and values equal to that initially obtained at 1950°C. However, the rerun values were still different than the third order time dependence predicted by Equation (A-10.3). This behavior, as well as Padden's data[A-10.7] from the initial grain growth period, may represent discontinuous grain growth where the pores are not at the grain boundaries and therefore are not hindering the rate of boundary migration.

Nichols[A-10.2] reevaluated the MacEwan data[A-10.6] and calculated an activation energy of 5.19×10^5 J/mol which compares favorably with the value of 5.77×10^5 J/mol for the heat of vaporization of UO_2. Using this value of 5.19×10^5 J/mol rather than the 4.98×10^5 J/mol value from Lyons et al and a constant k of 8.57×10^{14} from Lyons et al, the cubic grain growth equation becomes:

$$D^3 - D_o^3 = 8.57 \times 10^{14}\ t \exp\left(-5.19 \times 10^5/RT\right). \quad \text{(A-10.7)}$$

Equation (A-10.7) was compared with all the experimental data[A-10.6, A-10.8, A-10.10, A-10.12] except those from Hausner[A-10.9], Runfors[A-10.11], and Padden data[A-10.7] which were questioned by Lyon[A-10.5]. The results of this comparison are shown in Figure A-10.1.

Ainscough et al[A-10.12] performed measurements of equiaxed grain growth at temperatures between 1300 to 1500°C over fairly long periods (up to 24 weeks). They rejected the cubic relationship of Equation (A-10.5). In its place, Ainscough et al proposed a limiting grain size, D_m, which is only a function of temperature. The grain growth kinetics for UO_2, then become:

$$\frac{dD}{dt} = k\left(\frac{1}{D} - \frac{1}{D_m}\right) \quad \text{(A-10.8a)}$$

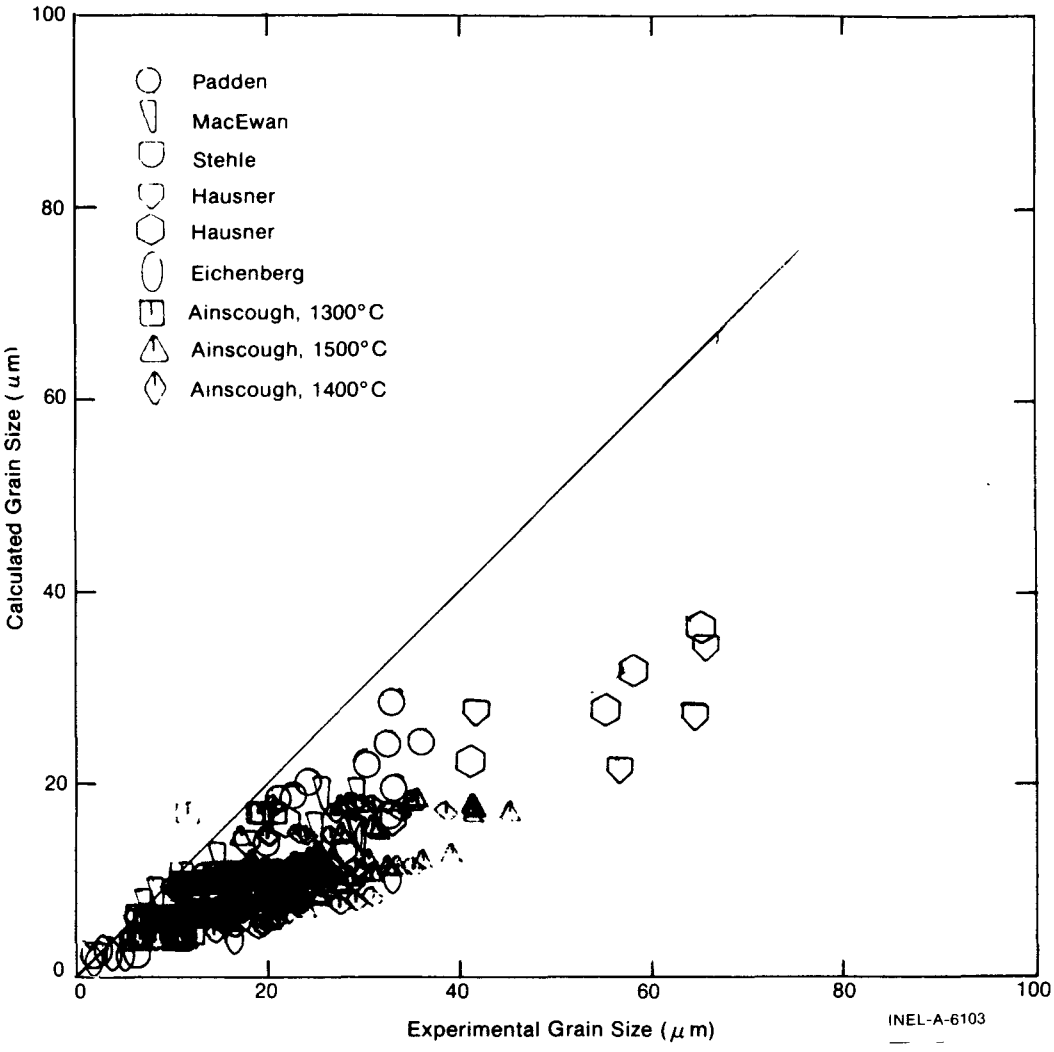

Fig. A-10.1 Comparison of Equation (A-10.7) with experimental data for UO_2 grain growth.

and upon integration:

$$D_m (D_o - D) + D_m^2 \ln \frac{(D_m - D_o)}{(D_m - D)} = kt. \qquad \text{(A-10.8b)}$$

Burke[A-10.13] successfully used this expression to correlate grain growth data for α-brass specimens containing a stable array of inclusions. A comparison of Equation (A-10.8b) with the higher temperature grain growth studies reported by other workers showed the rate constants calculated with this equation to be, in general, higher than those calculated by this author by extrapolating the results of Ainscough et al. However, most of the measurements made on UO_2, where the O/U ratio was close to 2.0, gave rate constants within a factor of four of the predicted values. A comparison of the Ainscough correlation with the experimental data used in Figure A-10.1 is shown in Figure A-10.2.

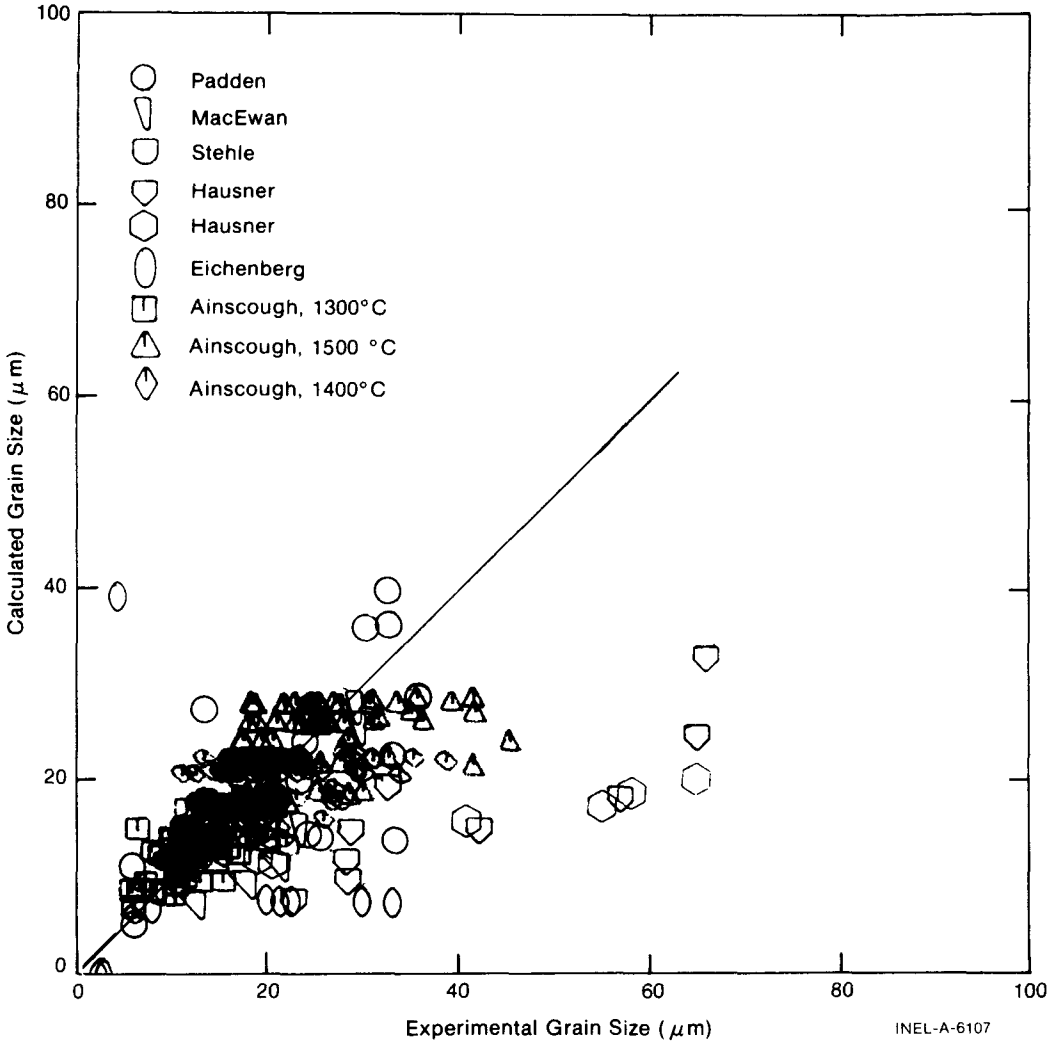

Fig. A-10.2 Comparison of Ainscough et al correlation with experimental data for UO_2 grain growth.

The fourth order Equation (A-10.6) developed by Nichols was also evaluated using the same experimental data for UO_2 grain growth as shown in Figures A-10.1 and A-10.2 to determine the constants k and Q. The average value of Q was 3.87×10^5 J/mol and the resultant expression is

$$D^4 - D_o^4 = 1.717 \times 10^{10} \exp(-3.87 \times 10^5/RT)\, t. \qquad \text{(A-10.9)}$$

The activation energy of 3.87×10^5 J/mol is less than the 5.77×10^5 J/mol expected for the heat of vaporization. However, reevaluation of the activation energy using the cubic relation [Equation (A-10.5)] resulted in an even lower value of about 3.64×10^5 J/mol. Even though the activation energies do not compare with the expected value for the heat of vaporization, Equation (A-10.9) is the best representation of the present grain growth data with a standard deviation of ±4.8 μm.

10.3 Columnar Grain Growth

Most sources[A-10.2,A-10.14 – A-10.17] attribute the formation of columnar grains in UO_2 or $(U,Pu)O_2$ mixed oxide fuels to the migration of lenticular pores up a temperature gradient. Various theoretical models[A-10.18 – A-10.23] for the rates of pore migration have been proposed which depend upon a particular mechanism of mass transfer: surface diffusion, volume diffusion, or vaporization-condensation mechanisms with either pore pressure held constant or pore pressure in equilibrium with the surface tension. These models will be discussed first, followed by an evaluation of the experimental data on UO_2 pore migration rates.

10.3.1 Theoretical Models. From irreversible thermodynamics, the diffusion of gas bubbles, or voids, up a temperature gradient implies a corresponding transfer of mass down the gradient proportional to the temperature gradient[A-10.24]. The mass flux is given by

$$J_M = \frac{D_i}{kT} C_i \left(- \frac{Q_I}{T} \nabla T \right) \qquad \text{(A-10.10)}$$

where

J_M = mass flux

D_i = diffusion coefficient

C_i = concentration of diffusing species

Q_i = heat of transport

k = Boltzmann's constant.

The diffusion coefficient and heat of transport are intimately related to the detailed mechanisms of both mass and heat transfer such as volume diffusion, surface diffusion, or vaporization-condensation mechanisms. Unfortunately, Q_i for migration in condensed phases cannot be calculated with any degree of confidence, even as to sign. Q_i is viewed as a process heat of transport which may include certain specific parameters if one considers specific migration mechanisms[A-10.18]. For example, with a vacancy volume diffusion mechanism, it will involve the enthalpy of vacancy formation. For a vaporization-condensation mechanism, it is simply the heat of vaporization since no activated jump process is involved.

The migration rate of spherical pores along a thermal gradient, assuming that they migrate without distortion, has been treated by various authors for different mechanisms and may be written[A-10.20, A-10.21]:

for surface diffusion

$$V = \frac{2D_s \nu \Omega Q_s}{r k T^2} \cdot \frac{dT}{dx} \qquad \text{(A-10.11)}$$

for volume diffusion

$$V = \frac{2D Q_v}{f k T^2} \cdot \frac{dT}{dx} \qquad \text{(A-10.12)}$$

for vapor transport
with P = constant

$$V = A(T) P \Delta H_v \cdot \frac{dT}{dx} \qquad \text{(A-10.13)}$$

for vapor transport
with $P = 2\lambda/r$

$$V = B(T) r P_v \Delta H_v \cdot \frac{dT}{dx} \qquad \text{(A-10.14)}$$

where

D_s	=	surface diffusion coefficient
ν	=	number of diffusing species per unit area
Ω	=	atomic volume
Q_s	=	heat of transport for surface diffusion
r	=	pore radius
$\frac{dT}{dx}$	=	thermal gradient in pore
D_v	=	volume diffusion coefficient
Q_v	=	heat of transport for volume diffusion
f	=	correlation factor

P_v = matrix vapor pressure

ΔH_v = heat of vaporization

P = vapor pressure in pore

k = Boltzmann's constant

A(T),B(T) = constants.

Analysis by Gruber[A-10.21] of a spherical pore moving by surface diffusion showed that a spherical pore would not be distorted during migration. Similarly, Nichols[A-10.22, A-10.23] analyzed the case for the vapor transport mechanism and showed that the spherical pore would essentially remain spherical but would tend to elongate in the direction of the temperature gradient. No mechanism is described to explain the formation of the often observed lenticular pores perpendicular to the temperature gradient.

The relative importance of the various mechanisms of mass transport should depend upon the pore size and temperature. Surface diffusion should dominate at small pore sizes for all temperatures and its relative importance may sometimes increase with lower temperature. For larger pore sizes, vapor transport or volume diffusion may dominate. The critical radius between surface diffusion and vapor transport ($P = 2\gamma/r$) has been evaluated by Speight[A-10.25] to be about 1 μm at 2000 K. Bubbles with radii larger than 1 μm would migrate by vapor transport with $P = \frac{2\gamma}{r}$ and surface diffusion would dominate at smaller radii.

Oldfield and Markworth[A-10.26] developed a model for the formation of columnar grains based upon pore migration by vapor transport and the formation of steps by layer nucleation or by the development of screw dislocations. This process is analogous to a zone-melting situation in which the hot surface of the bubble is evaporating into a gaseous solution and then crystallizing upon the cool surface. The atoms of vapor attach to the solid at favorable low energy sites, usually provided by a kink in a layer edge or reentrance in the lattice. Atoms reach the surface and migrate along it until they reach a suitable site. The driving force to cause attachment is a function of the concentration gradient of atoms at the surface. Thus all growth takes place at layer edges so that eventually one might expect them to grow out, leaving a close-packed surface in contact with the vapor. This behavior can be expressed by the Bravais law which states that a crystal is bounded by its slowest growing surfaces.

Oldfield and Markworth consider the variation of surface angle, and hence the variation in number of growth steps around the crystal surface. Their model is expressed by

$$V = B \frac{\tanh\left(\frac{\lambda L}{2}\right)}{L} \Delta T \qquad \text{(A-10.15)}$$

where

$B = \frac{PQ}{RT^2 \lambda 2\pi RT} b_o$

$\lambda^2 = \frac{\nu}{D} \exp(\phi/RT)$

V = growth velocity associated with a layer

P = partial pressure of vapor in the bubble

ϕ = heat of crystallization (or with vapor transport, the heat of sublimation)

D = surface diffusion coefficient

ν = atomic vibration frequency

L = is related directly to the angle between the surface and the migration direction

b_o = molar volume.

Oldfield and Markworth used this equation to compute the shape of a migrating bubble, assuming fixed velocity, over the entire surface, matching the ΔT in Equation (A-10.15) to the corresponding total available ΔT, and solving for L. Repetition of this calculation around the bubble surface yielded the bubble shape. When ΔT was assumed to be equal at the top and bottom, the calculated bubble was flattened and had a lenticular shape as has been observed.

The equations for migration rates [Equations (A-10.11) to (A-10.14)] do not predict the proper shape of the bubbles. However, the analyses by Oldfield and Markworth predicts the general shape of the bubble when a process of crystallization is factored into the analysis of pore migration. The fact that this model does predict observed bubble shapes suggests that the rate controlling step for columnar grain formation may be the recrystallization process rather than diffusion through the pore. Under these circumstances, measurements of migration rates of pores at grain boundaries would not be governed by Equations (A-10.11) to (A-10.14). Instead, these equations would be applicable only to pore migration in single crystals or within grains. Equation (A-10.15) predicts the rate of formation of columnar grains.

Lenticular pores contain impurities so that the smooth surface bounding the pore becomes unstable beyond a certain growth velocity or impurity concentration and steep-walled grooves develop into which the impurities are rejected. These grooves form at the end of the lenticular void and leave a trail of spherical bubbles in the boundary between two adjacent columnar grains. This rejection of bubbles into the grain boundaries has been experimentally observed (Figure A-10.3)[A-10.18, A-10.22].

The association of crystal growth with the movement of lenticular voids also accounts for the observed orientation of the <111> crystallographic direction in the radial direction of the fuel[A-10.14].

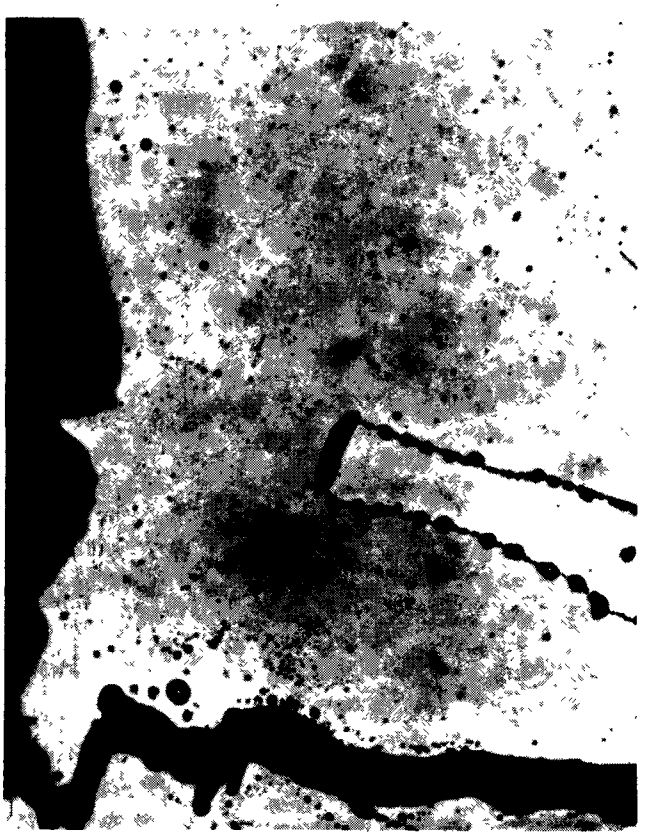

Fig. A-10.3 Lenticular void in ThO_2 - 5% UO_2 fuel showing injection of spherical bubbles into grain boundaries.

10.3.2. Experimental Pore Migration Rates. Based on the preceding discussion of pore migration rates, the experimental data were separated into two categories: (a) pore migration in single crystals and (b) pore migration at grain boundaries. The initial migration of pores at grain boundaries leads directly to the formation of columnar grains. Whereas after the formation of columnar grains, pore migration through the columnar grains results in fission gas release and fuel swelling.

Williamson and Cornell[A-10.27] measured pore migration rates in UO_2 single crystals at temperatures between 1250 and 1450°C. They attributed the pore migration to surface diffusion since small bubbles were observed to move faster than larger ones. Pore sizes were less then 0.5 μm.

Gulden[A-10.28] measured the migration of fission gas bubbles in UO_2 between 1400 and 1500°C and for pore sizes between 2.5 and 14 nm. From the effect of the diffusion coefficient upon the bubble radius, a volume diffusion mechanism was attributed to be the rate controlling mechanism for a pore radius greater than 3.7 nm. These results conflict with the expectation that volume diffusion occurs only in very large pores.

Oldfield and Brown[A-10.29] measured the migration rate of bubbles at columnar grain boundaries in UO_2. The measured rates were much lower than corresponding values predicted by vapor transport. This experimental result supports the theoretical contention that the migration rates of pores at grain boundaries should be different from the migration rates of pores within grains. Migration rates of columnar grains ranged between 0.01 and 1 μm/s for temperatures between 1900 and 2450°C.

Michels and Poeppel[A-10.30] measured the migration rates of fission gas bubbles in $(U,Pu)O_2$ oxide fuel for pore sizes from 2.5 to 6.5 μm. Large scatter in the pore migration rates precluded an exact determination of the effect of pore size upon the migration rate.

However, they selected the surface diffusion mechanism because it gave more reasonable predicted values than a vapor transport mechanism. Michels and Poeppel stated that a vapor transport mechanism was also possible.

Ronchi and Sari[A-10.31] measured the out-of-pile migration rates for pores located at columnar grain boundaries in UO_2. Based upon a measured activation energy of 4.85×10^5 J/mol (slightly below the evaporation enthalpy of UO_2) and using a constant pore pressure, they deduced that the pores in their samples migrated by a vapor transport mechanism with a constant pore pressure. Their migration rates were higher than those of Oldfield and Brown but their values were in agreement with those predicted by a vapor transport model. They concluded that the pore pressure could not be in equilibrium with the surface tension.

Buescher and Meyer[A-10.32] measured pore migration rates in single crystal UO_2 for pore radii between 0.01 and 1.0 μm. The migration velocities were found to be independent of pore size. The observed values were found to be substantially larger than those predicted by mechanisms of volume diffusion and vapor transport ($P = 2\gamma/r$) but smaller than those predicted by surface diffusion models. They proposed a model based upon nonlocalized surface diffusion that is affected by collisions between diffusing species and gas atoms within the bubble. In ruling out the vapor transport mechanism, they ignored the constant pore pressure model which predicts the migration rates to be independent of the pore size, as observed in their results. The absolute values for pore migration rates, of course, depend upon the assumed pore pressure. In other words, vapor transport with constant pore pressure is a possible mechanism in their experiments.

The results from experimental measurements of pore migration rates are summarized in Table A-10.I. As a whole, the conclusions reached by various authors are mixed and leave no concensus as to the mechanism of pore migration. Factors contributing to this lack of concensus include (a) different pore sizes, (b) imprecise estimates of temperature gradients, (c) inaccurate temperature measurements, (d) mutual interaction of grain boundaries and pores in retarding pore migration, and (e) assumption of pore pressure and size relation migration rates.

However, in considering these data some general conclusions can be drawn. The measurements of Williamson and Cornell clearly indicate a surface diffusion mechanism when the pore sizes are less than about 0.5 μm. For pore sizes larger than about 1 μm, Ronchi and Sari suggest a vapor transport mechanism with a constant pore pressure as the rate controlling mechanism, and the results from Michels and Poeppel and Buescher and Meyer do not preclude this mechanism. At very small pore sizes (2.5 to 14 nm), volume diffusion appears to be the rate controlling mechanism.

Large uncertainties still exist in the absolute values of pore migration rates, of pores both at grain boundaries and within grains. Also, one must distinguish between the initial formation of columnar grains probably by the movement of pores located at grain boundaries and the subsequent pore migration within or through essentially single crystal columnar grains.

TABLE A-10.I

SUMMARY OF PORE MIGRATION RATE EXPERIMENTS

Investigation	Material Type	Temperature	Pore Size	Comments on Mechanism
Williamson and Cornell[A-10.27]	UO_2 single crystal	1250 to 1450°C	2.5 to 5.0 nm	Inferred surface diffusion mechanism
Gulden[A-10.28]	Polycrystalline UO_2	1400 to 1500°C	2.5 to 14.0 nm	Volume diffusion for $r > 3.7$ nm, unknown for $r < 3.7$ nm
Oldfield and Brown[A-10.29]	Polycrystalline UO_2	1955 to 2410°C	0.2 to 0.2 μm	Ledge nucleation impeded motion
Michels and Poeppel[A-10.30]	Polycrystalline $(U,Pu)O_2$	1585 to 1850°C	1 to 10 μm	Size dependence undetermined but authors indicated surface diffusion with a possibility of vapor transport
Ronchi and Sari[A-10.31]	Polycrystalline UO_2 and $(U,Pu)O_2$	1600 to 2600°C	not given	Vapor transport mechanism
Buescher and Meyer[A-10.32]	UO_2 single crystal	1940 to 2020°C	0.01 to 1.0 μm	Rates independent of pore size; authors proposed an impeded surface diffusion mechanism but results could fit vapor transport with constant pore pressure

10.4 Fuel Restructuring Model

A number of theoretical models have been proposed for equiaxed grain growth in UO_2. Since pores located at grain boundaries apparently restrict grain boundary movement, either a third or fourth order relationship between grain size and time is theoretically expected, depending upon whether the pore pressure is in equilibrium with the surface tension or is constant. The models were compared with the available data, as discussed in Subsection A-10.2.2, and the grain growth rates predicted with the fourth order Equation (A-10.9) gave the smallest standard deviation of the models tested. This result suggests that the vapor transport mechanism operates with a constant pore pressure and is independent of the pore size. Moreover, examination of pore migration rates as a function of pore size shows the rates to be independent of size. Therefore, equiaxed grain growth in UO_2 and $(U,Pu)O_2$ fuels is represented in the FRESTR subcode by

$$D^4 - D_o^4 = 1.717 \times 10^{10} \exp(-3.87 \times 10^5/RT)\, t \qquad \text{(A-10.16)}$$

where the terms have been previously defined. A comparison of this equation with experimental data (Figure A-10.4) shows a standard deviation of ±4.8 μm.

Columnar grains apparently form by pore migration due to vapor transport and subsequent crystal growth where the rate controlling mechanism is the crystal growth. Conservatively low measurements of the columnar grain boundary velocity show the rates to be between 0.01 to 1 μm/s for temperatures between 1900 and 2450°C[A-10.29]. For a fuel radius of 0.51 cm, a time between 1.4 and 141 hours would be required for columnar grain formation, corresponding to the fastest and slowest rates of columnar grain formation. Thus the formation of columnar grains occurs very rapidly once the threshold temperature is exceeded.

Since the rates of columnar grain movement are very ill-defined and the constants in the various published models are difficult to evaluate, a theoretical model is not very useful. However, the published equations do show that a threshold temperature should exist for the formation of columnar grains and that this temperature should be a function of time, decreasing with an increase in time. Christensen[A-10.33] measured threshold temperature as a function of time and derived the following relationship:

$$1/T = 3.435 \times 10^{-5} \log_{10} t + 3.47 \times 10^{-4} \qquad \text{(A-10.17)}$$

where the terms of the equation have been previously defined.

This is the model chosen for the FRESTR subcode.

In the formation of columnar grains, most of the sintering porosity moves toward the fuel center, but some of this porosity is left in boundaries between columnar grains. Based on postirradiation examinations of pellet microstructures, a density of 98% TD is assumed for the density of the columnar grain zone[A-10.34]. Therefore, the model for the

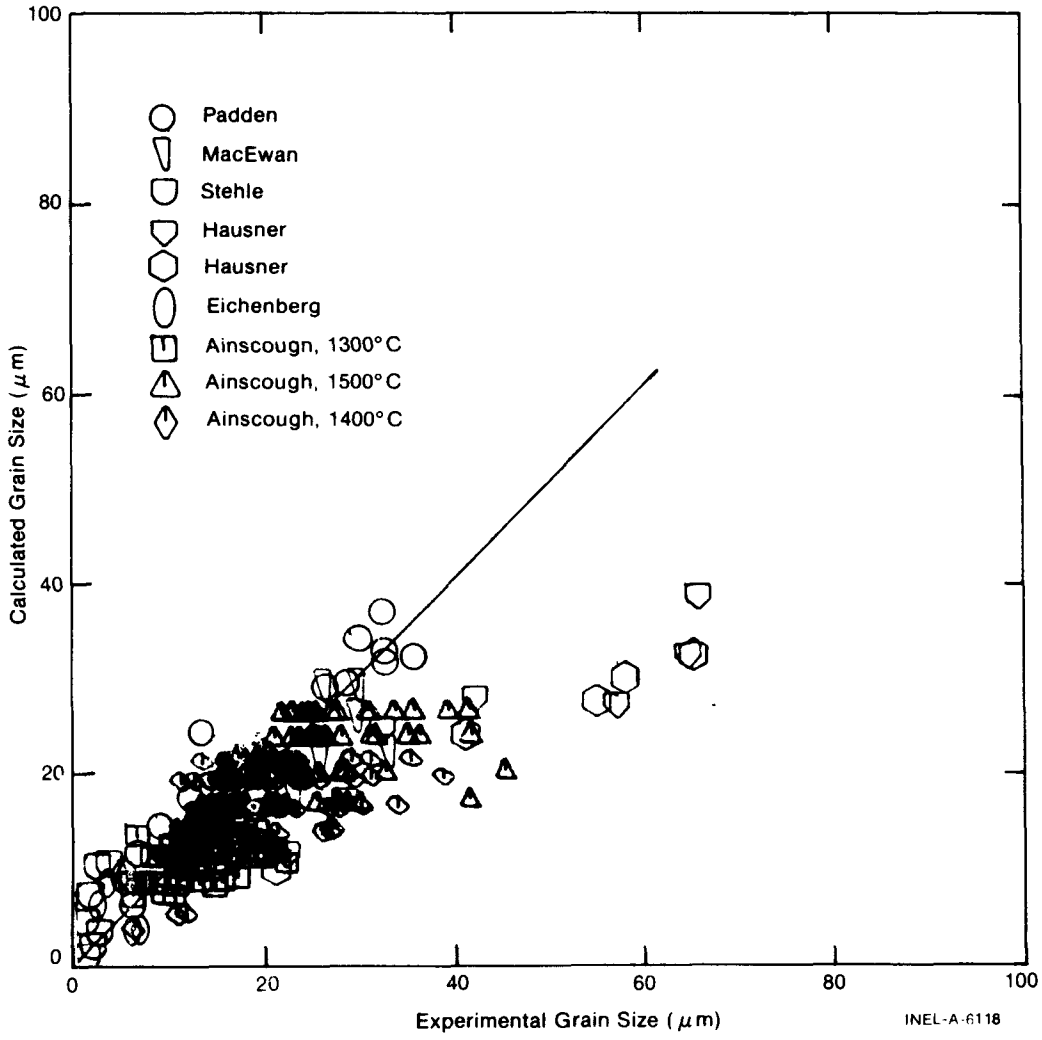

Fig. A-10.4 Comparison of Equation (A-10.16) with experimental data for UO_2 grain growth.

formation of columnar grains consists of an estimate of the threshold temperature for the formation of columnar grains as a function of time. Then, for areas of the fuel that exceed this threshold temperature, the density is assumed to be 98% TD. The porosity corresponding to the difference between the 98% density value and the initial density of the fuel is placed instantaneously in the central hole of the fuel.

The equiaxed grain growth equation is assumed to apply over the entire fuel region from the fuel surface to the radius of column grain formation. However, in regions of low fuel temperature, such as near the pellet surface, essentially no change in grain structure will be calculated.

10.5 Fuel Restructuring Subcode FRESTR Listing

A FORTRAN listing of the FRESTR subroutine is shown in Table A-10.II.

TABLE A-10.II

LISTING OF THE FRESTR SUBCODE

```
C
C
      SUBROUTINE FRESTR(FTEMP,TTIME,DO,DSIZE,FTCRIT,FDENS,FRACS)
C
CCC   FRESTR CALCULATES FUEL RESTRUCTURING INCLUDING EQUIAXED GRAIN
CCC   GROWTH AND COLUMNAR GRAIN FORMATION.
CCC   EQUIAXED GRAIN GROWTH IS CALCULATED AS A FUNCTION OF TEMPERATURE
CCC   AND TIME.
CCC   THE FORMATION OF COLUMNAR GRAINS IS CHARACTERIZED BY A THRESHOLD
CCC   TEMPERATURE WHICH IS A FUNCTION OF TIME. WHEN THE TEMPERATURE OF
CCC   THE FUEL EXCEEDS THE THRESHOLD TEMPERATURE THE FUEL DENSITY IS
CCC   SET AT 98% OF THE THEORETICAL DENSITY.
CCC
CCC   DSIZE = OUTPUT GRAIN SIZE AT TIME, TTIME (MICROMETERS)
CCC   FTCRIT= OUTPUT THRESHOLD TEMPERATURE FOR COLUMNAR GRAIN
CCC           FORMATION (K)
CCC   FDENS = OUTPUT DENSITY OF COLUMNAR GRAIN ZONE (UNITLESS FRACTION)
CCC
CCC   FTEMP = INPUT FUEL TEMPERATURE (K)
CCC   TTIME = INPUT TIME (S)
CCC   DO    = INPUT GRAIN SIZE (MICROMETERS)
CCC   FRACS = INPUT INITIAL AS-SINTERED FUEL DENSITY (UNITLESS FRACTION)
CCC
CCC   THE EQUIAXED GRAIN GROWTH EQUATION IS BASED ON PORE RETARDATION
CCC   OF GRAIN BOUNDARIES AND PORE MIGRATION BY VAPOR TRANSPORT WITH
CCC   CONSTANT PORE PRESSURE.
CCC   THE EQUATION FOR THE THRESHOLD TEMPERATURE IS OBTAINED FROM J.
CCC   CHRISTENSEN, ANS TRANSACTIONS, VOL 15 (1972) PP 214-215
CCC
CCC   FRESTR WAS CODED BY C.S. OLSEN  NOV 1975
CCC
CCC   THE DENSITY OF THE COLUMNAR GRAIN ZONE IS ASSUMED TO BE 98% OF
CCC   THEORETICAL DENSITY.
CCC
C
      DATA A1,Q1,B1,B2 /6.16E 13, 9.24E 04, 3.435E-05, 4.69E-04/
      TIME1 = TTIME/3600.0
      FDENS = FRACS
      IF (TIME1 .GT. 0.) GO TO 10
C
      DSIZE = DO
      FTCRIT= 2132.20
      GO TO 20
C
   10 DSIZE = (DO**4 + A1*EXP(-Q1/(1.987*FTEMP)) * TIME1)**0.25
      FTCRIT= 1.0/(B1*ALOG10(TIME1) + B2)
      IF (FTEMP .GE. FTCRIT) FDENS = 0.98
C
   20 RETURN
      END
```

10.6 References

A-10.1. D. R. DeHalas and G. R. Horn, "Evolution of Uranium Dioxide Structure During Irradiation of Fuel Rods," *Journal of Nuclear Materials, 8* (1963) pp 207-220.

A-10.2. F. A. Nichols, "Theory of Grain Growth in Porous Compacts," *Journal of Applied Physics, 37* (1966) pp 4599-4602.

A-10.3. M. V. Speight and G. W. Greenwood, "Grain Boundary Mobility and Its Effects in Materials Containing Inert Gases," *Philosophical Magazine, 9* (1964) pp 683-688.

A-10.4. W. D. Kingery and B. Francois, "Grain Growth in Porous Compacts," *Journal of the American Ceramic Society, 48* (1965) pp 546-547.

A-10.5. M. F. Lyons et al, *Analysis of UO_2 Grain Growth Data from Out-of-Pile Experiments,* GEAP-4411 (November 1963).

A-10.6. J. R. MacEwan, *Grain Growth in Sintered Uranium Dioxide,* AECL-1184 (CRFD-999), Atomic Energy Commission of Canada Limited (January 1961).

A-10.7. T. R. Padden, "Behavior of Uranium Oxide as a Reactor Fuel," *Proceedings of 2nd International Conference on Peaceful Uses of Atomic Energy, Volume 6, Paper P/2404,* (September 1958) pp 569-586.

A-10.8. H. Stehle, Paper Presentation at *Joint Meeting of the Deutsche Gesellschaft für Metallkunde and the Deutsche Keramische Gesellschaft, November 8-9, 1962.*

A-10.9. H. Hausner, *UO_2 Grain Growth and Melting Studies,* High Performance UO_2 Program Quarterly Progress Reports, GEAP-3771-5, 3771-6, 3771-7 (1962-1963).

A-10.10. J. D. Eichenberg, et al, *Effects of Irradiation on Bulk UO_2,* WAPD-183 (October 1957).

A-10.11. U. Runfors et al, "Sintering of Uranium Dioxide," *Proceedings of 2nd International Conference on Peaceful Uses of Atomic Energy, Volume 6, Paper P/142, September 1958* p 605.

A-10.12. J. B. Ainscough et al, "Isothermal Grain Growth Kinetics in Sintered UO_2 Pellets," *Journal of Nuclear Materials, 49* (1973/1974) pp 117-128.

A-10.13. J. E. Burke, "Some Factors Affecting the Rate of Grain Growth in Metals," *Transactions of the American Institute of Metallurgical Engineers, 180* (1949) pp 73-91.

A-10.14. J. P. MacEwan and V. B. Lawson, "Grain Growth in Sintered Uranium Dioxide: II, Columnar Grain Growth," *Journal of the American Ceramic Society, 45* (1962) pp 42-46.

A-10.15. J. A. Christensen, "In-Pile Void Migration in Uranium Dioxide," *Transactions of the American Nuclear Society, 8* (1965) pp 44-45.

A-10.16. J. A. Christensen, "Columnar Grain Growth in Oxide Fuels," *Transactions of the American Nuclear Society, 15* (1972) pp 214-215.

A-10.17. P. F. Sens, "The Kinetics of Pore Movement in UO_2 Fuel Rods," *Journal of Nuclear Materials, 43* (1972) pp 293-307.

A-10.18. F. A. Nichols, "Movement of Pores in Solids," *Journal of Metals* (1969) pp 19-27.

A-10.19. P. G. Shewmon, "The Movement of Small Inclusions in Solids, by a Temperature Gradient," *Transactions of the American Institute of Metallurgical Engineers, 230* (1964) pp 1134-1137.

A-10.20. F. A. Nichols, "Kinetics of Diffusional Motion of Pores in Solids," *Journal of Nuclear Materials, 30* (1969) pp 143-165.

A-10.21. E. E. Gruber, "Calculated Size Distributions for Gas Bubble Migration and Coalescence in Solids," *Journal of Applied Physics, 38* (1967) pp 243-250.

A-10.22. F. A. Nichols, "Pore Migration in Ceramic Fuel Elements," *Journal of Nuclear Materials, 27* (1968) pp 137-146.

A-10.23. F. A. Nichols, "Pore Migration in Ceramic Fuel Elements," *Journal of Nuclear Materials, 22* (1967) pp 214-222.

A-10.24. G. N. Lewis et al, *Thermodynamics,* Second Edition, New York: McGraw Hill Book Co., 1961.

A-10.25. M. V. Speight, "The Migration of Gas Bubbles in Material Subject to a Temperature Gradient," *Journal of Nuclear Materials, 13* (1964) pp 207-209.

A-10.26. W. Oldfield and A. J. Markworth, "The Theory of Bubble Migration Applied to Irradiated Materials," *Material Science and Engineering, 4* (1969) pp 353-366.

A-10.27. G. K. Williamson and R. M. Cornell, "The Behavior of Fission Product Gases in Uranium Dioxide," *Journal of Nuclear Materials, 13* (1964) pp 278-280.

A-10.28. M. E. Gulden, "Migration of Gas Bubbles in Irradiated Uranium Dioxide," *Journal of Nuclear Materials, 23* (1967) pp 30-36.

A-10.29. W. Oldfield and J. B. Brown Jr., "Bubble Migration in UO_2 – A Study Using a Laser Image Furnace," *Materials Science and Engineering, 6* (1970) pp 361-370.

A-10.30. L. C. Michels and R. B. Poeppel, "In-Pile Migration of Fission Product Inclusions in Mixed-Oxide Fuels," *Journal of Applied Physics, 44* (1973) pp 1003-1008.

A-10.31. C. Ronchi and C. Sari, "Properties of Lenticular Pores in UO_2, (U, Pu)O_2 and PuO_2," *Journal of Nuclear Materials, 50* (1974) pp 91-97.

A-10.32. B. J. Buescher and R. O. Meyer, "Thermal Gradient Migration of Helium Bubbles in Uranium Dioxide," *Journal of Nuclear Materials, 48* (1973) pp 143-156.

A-10.33. J. A. Christensen, "Columnar Grain Growth in Oxide Fuels," *Transactions of the American Nuclear Society, 15* (1972) pp 214-215.

A-10.34. R. D. Leggett et al, "Central Void Size in Irradiated Mixed-Oxide Fuel Pins," *Transactions of the American Nuclear Society,* (1973) pp 175-176.

11. FUEL FRACTURE STRENGTH (FFRACS)

(C. S. Olsen)

FFRACS calculates the UO_2 fracture strength as a function of fuel temperature and fractional fuel density.

11.1 Summary

FFRACS calculates the fracture strength of UO_2 as a function of fractional fuel density and temperature up to 1000 K, the lowest temperature at which plasticity has been observed in-pile. For temperatures above 1000 K, a constant value is used for the in-pile fracture strength of plastic UO_2. The UO_2 fracture model is given by the following equations

for $273 < T \leq 1000$ K:

$$\sigma_F = 1.7 \times 10^8 [1 - 2.62 (1 - D)]^{1/2} \exp(-1590/8.314\ T) \quad \text{(A-11.1a)}$$

for $T > 1000$ K

$$\sigma_F = \sigma_F (1000\ K) \quad \text{(A-11.1b)}$$

where

σ_F	=	fracture strength (Pa)
D	=	fraction of theoretical density
T	=	temperature (K)
$\sigma_F(1000\ K)$	=	fracture strength found with T = 1000 K.

Equation (A-11.1a) is based upon out-of-pile UO_2 data and describes the behavior of brittle UO_2. Because no in-pile measurements of fracture strength have been made, Equation (A-11.1b) is based upon theoretical considerations and fragmentary out-of-pile data and applies to plastic UO_2. The transition from brittle to ductile material is accompanied by a discontinuity in fracture strength and occurs at temperatures below the usual out-of-pile

brittle-ductile transition temperature due to fission induced plasticity. Equation (A-11.1a) has a standard deviation with respect to experimental data of 0.19×10^8 Pa. The uncertainty in Equation (A-11.1b) is not estimated because of lack of in-pile data.

11.2 Out-of-Pile UO_2 Deformation

The out-of-pile deformation of UO_2 exhibits either elastic or elastic-plastic behavior. Elastic behavior is characterized by stress being linearly proportional to strain up to the fracture point[A-11.1 – A-11.5]. Elastic-plastic behavior is characterized by the stress-strain curve which is initially elastic (to the elastic proportional limit), and which then exhibits plastic behavior[A-11.1 –A-11.5].

11.2.1 Review of Out-of-Pile UO_2 Elastic Behavior Data and Theory.

At temperatures below a ductile-brittle transition temperature, T_c, UO_2 deforms elastically up to the fracture point[A-11.1 – A-11.5]. In such cases the fracture strength, σ_F, is much less than the yield strength, σ_y, so that no yielding occurs prior to fracture. The fracture topography of near-theoretically dense UO_2 exhibits the cleavage fracture mode of a brittle material. However, this fracture mode is affected by the amount of porosity and grain size, where, in general, the relative proportion of brittle to ductile fracture decreases with an increase in porosity and a decrease in grain size[A-11.6].

The crack initiator[A-11.1,A-11.2,A-11.4,A-11.6] has been suggested as the largest pore. The Griffith fracture theory[A-11.7] can be applied to theoretically examine the parameters which affect the fracture strength. Griffith showed that the fracture stress or critical stress required to propagate an elliptical crack of length 2c with an "infinitely" small radius of curvature is given by Equation (A-11.2):

$$\sigma_F = \sqrt{\frac{2 E \gamma}{\pi c (1 - \nu^2)}} \qquad \text{(A-11.2)}$$

where

E = elastic modulus (Pa)

γ = surface energy (J/m^2)

c = crack length (m)

ν = Poisson's ratio (unitless).

This equation applies to plane strain conditions and to an infinitely thick section of purely elastic material.

In Equation (A-11.2), the fracture strength is proportional to the square root of the elastic modulus, which in turn linearly decreases with porosity and temperature as discussed in Section 5.1 of this appendix. Therefore, the fracture strength should decrease with increasing temperature. However, the fracture strength of UO_2 has been observed to increase slightly with temperature[A-11.2,A-11.4]. These measurements can be explained by the fact that γ in Equation (A-11.2) probably increases with temperature[A-11.4] at a faster rate than the rate of decrease of E with temperature.

Hasselman[A-11.8] has shown that when a material contains numerous elliptical cracks of length 2c spaced a distance 2h from each other, Equation (A-11.2) becomes for plane strain conditions

$$\sigma_F = \sqrt{\frac{E\,\gamma}{2\,(1-\nu^2)\,h}}\;\cot\left(\frac{\pi\,c}{2h}\right) \qquad \text{(A-11.3)}$$

where the terms are previously defined.

Equation (A-11.3) and Equation (A-11.2) both predict a UO_2 fracture strength which is dependent on porosity because of the effect of porosity on the elastic modulus. Equation (A-11.3) also predicts a crack spacing effect upon fracture strength, which in turn depends upon both the pore size and volume of porosity. A fracture strength dependence upon the pore morphology (size, shape, and distribution) has also been observed by Roberts and Ueda[A-11.1].

11.2.2 Out-of-Pile Elastic Models. Experimental data[A-11.1,A-11.2,A-11.6,A-11.9, A-11.10] for fracture strength in the brittle region were fit to Equation (A-11.4) using a linear least-squares regression analysis [after reducing Equation (A-11.4) to a linear form] to determine the coefficients A, m, and Q

$$\sigma_F = A\,[1 - 2.62\,(1 - D)]^{1/2}\,G^{-m}\exp(-Q/RT) \qquad \text{(A-11.4)}$$

where

G = grain size (μm)

R = gas constant (8.314 J/mol·K)

and the other terms of the equation have been previously defined.

The following values of A, m, and Q were determined:

A = 1.70×10^8 Pa

m = 0.047

Q = 1590 J/mol.

The expression $[1 - 2.62\ (1 - D)]^{1/2}$ arises from the proportionality between σ_F and $\sqrt{E}$ in Equation (A-11.2) and (A-11.3) and the relation between E and D (see Section 5.1 of this appendix). The expression between fracture strength and grain size was based upon the suggestion of Orowan[A-11.11] and Petch[A-11.12] and the data of Igata and Domoto[A-11.13] which relate the strength of a material to $G^{-1/2}$. In general terms, this factor is written G^{-m}. The Boltzmann factor was selected to represent the temperature dependence. The effects of pore morphology have been ignored because of a lack of appropriate data. In Figure A-11.1, Equation (A-11.4) is compared with experimental data normalized to a 10-μm grain size and to 95% TD using Equation (A-11.4).

Knudsen[A-11.14] proposed the following empirical equation relating fracture strength to grain size and porosity

$$\sigma_F = AG^{-m} \exp[-b(1-D)] \qquad \text{(A-11.5)}$$

where

1-D = porosity

b = constant

the other terms have been previously defined and constants are given below.

Knudsen suggested that this relation describes the strength of chromium carbide and thoria reasonably well. This expression was fit to UO_2 fracture strength data, except that the Arrhenius term from Equation (A-11.4) was added to provide a temperature dependence. The resultant expression was reduced to a linear form and a linear, multiple variable regression analysis was used to determine the coefficients A, m, b, and Q. The results are:

A = 1.7108×10^8 Pa

m = 0.05136

b = 2.412

Q = 1649 J/mol.

Equation (A-11.5) is compared with experimental data in Figure A-11.2.

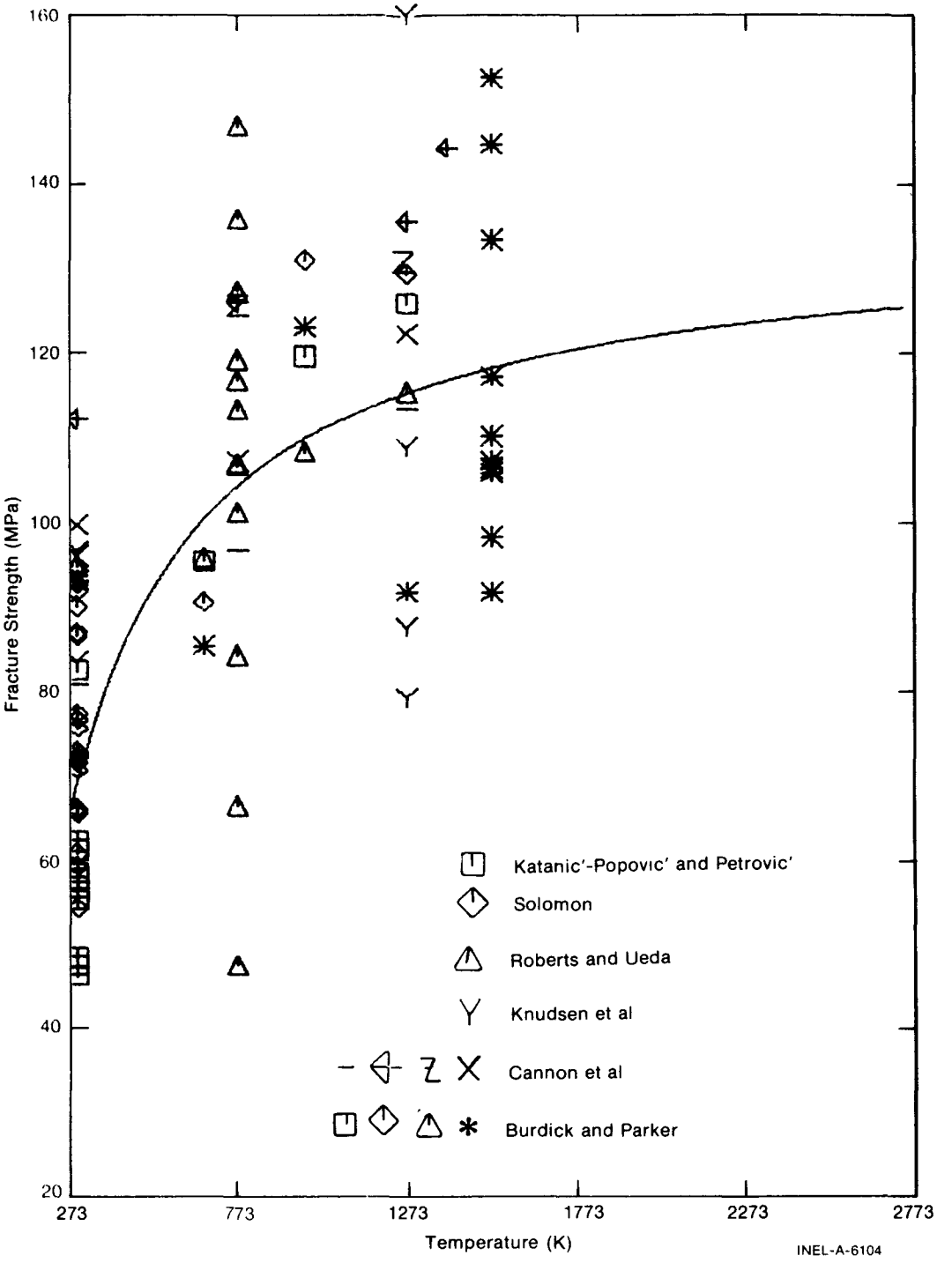

Fig. A-11.1 Comparison of Equation (A-11.4) in the elastic behavior regime with out-of-pile UO_2 fracture strength data normalized to 10-μm grain size and 95% TD.

Both Equations (A-11.4) and (A-11.5) indicate a very small effect of grain size upon the fracture strength. Values of m on the order of 0.5 are expected theoretically[A-11.11,A-11.12] but values of 0.05 were obtained, indicating a very insignificant effect of grain size on UO_2 fracture strength. Much scatter exists in the data with respect to Equations (A-11.4) and (A-11.5) and is attributed to differences in pore morphology not accounted for in these equations and also not reported with the data.

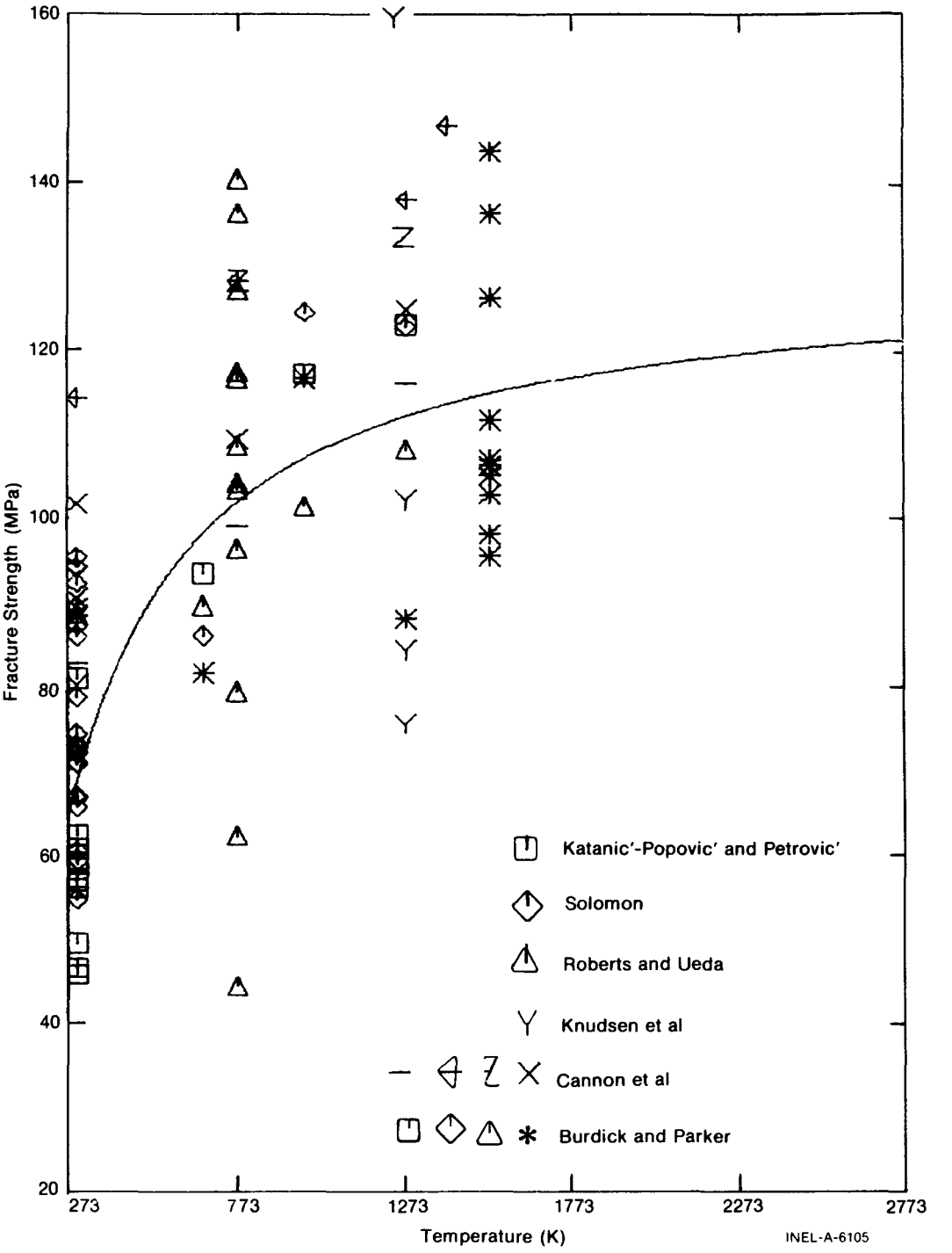

Fig. A-11.2 Comparison of Equation (A-11.5) in the elastic behavior regime with out-of-pile UO_2 fracture strength data normalized to 10-μm grain size and 95% TD.

In some cases, porosity has not been the initiator of cracks in UO_2. Instead, silica or alumina[A-11.15] precipitated at grain boundaries has considerably reduced the fracture strength, whereas small additions of titania increased the fracture strength of UO_2[A-11.9]. These additions are not normally part of the fabrication process and were not considered in the UO_2 fracture strength model.

11.2.3 Out-of-Pile Transition Temperature. The transition temperature, T_c, is defined to be the temperature at which the stress-strain curve departs from (linear) elastic to plastic behavior. Density, grain size, and strain rate are expected to affect this transition temperature, but data are insufficient to obtain a precise relationship.

Cannon et al[A-11.2] reported out-of-pile transitions at 1100, 1375, and 1450°C for strain rates of 0.092, 0.93, and 9.2/h, respectively, in material with an 8-μm average grain size. Transitions at 1050 and 1100°C occurred for a strain rate of 0.092/h in material with 15- and 31-μm average grain sizes, respectively. Evans and Davidge[A-11.4] reported transition temperatures of 1200 and 1300°C for 8- and 25-μm materials. A transition temperature of 1250°C is assumed for FFRACS since that is the midpoint of the 1050 to 1450°C range.

11.2.4 Out-of-Pile UO_2 Elastic-Plastic Behavior. At temperatures above the transition temperature, the deformation of UO_2 exhibits plastic behavior after some elastic deformation has occurred. The fracture mode is mostly intergranular, and a significant contribution to the deformation arises from grain boundary sliding. Figure A-11.3 shows the fracture strength of UO_2 as a function of temperature. At temperatures above T_c the ultimate tensile strength decreases with increasing temperature. The effect of strain rate is significant but the effect of grain size is negligible for grain sizes up to about 30 μm. Strain rate effects and grain boundary sliding strongly suggest that creep plays a dominant role at these temperatures. When the creep rate for a given temperature is nearly the same order of magnitude as the strain rate, stress relaxation reduces the fracture stress. This effect is shown in Figure A-11.3 by the increase in fracture strength with the increase in strain rate.

11.3 UO_2 Fracture Strength Model

Irradiation substantially reduces the ductile-brittle transition temperature. As discussed in Section 6, Appendix A, in-pile creep measurements show plasticity exists in UO_2 at temperatures as low as 1000 K. UO_2 is assumed to be brittle below this temperature, and Equation (A-11.4) (without the grain size term) is selected for the low temperature fracture strength model for UO_2. Equations (A-11.4) and (A-11.5), each with a standard deviation of about 1.9×10^7 Pa, predict the experimental out-of-pile fracture strength about equally well but Equation (A-11.4) has more theoretical foundation.

Above 1000 K, irradiation and thermal effects enhance the plasticity of UO_2 so that a decrease in fracture strength with increasing temperature may not occur. A strain rate effect may also exist, but the experimental data available are not sufficient to quantify a strain rate effect. Therefore, the in-pile fracture strength for plastic UO_2 at temperatures higher than 1000 K is taken to be that found with the low temperature correlation at 1000 K. This ensures calculational continuity between the two correlations.

The in-pile UO_2 fracture strength model is summarized by the following equations:

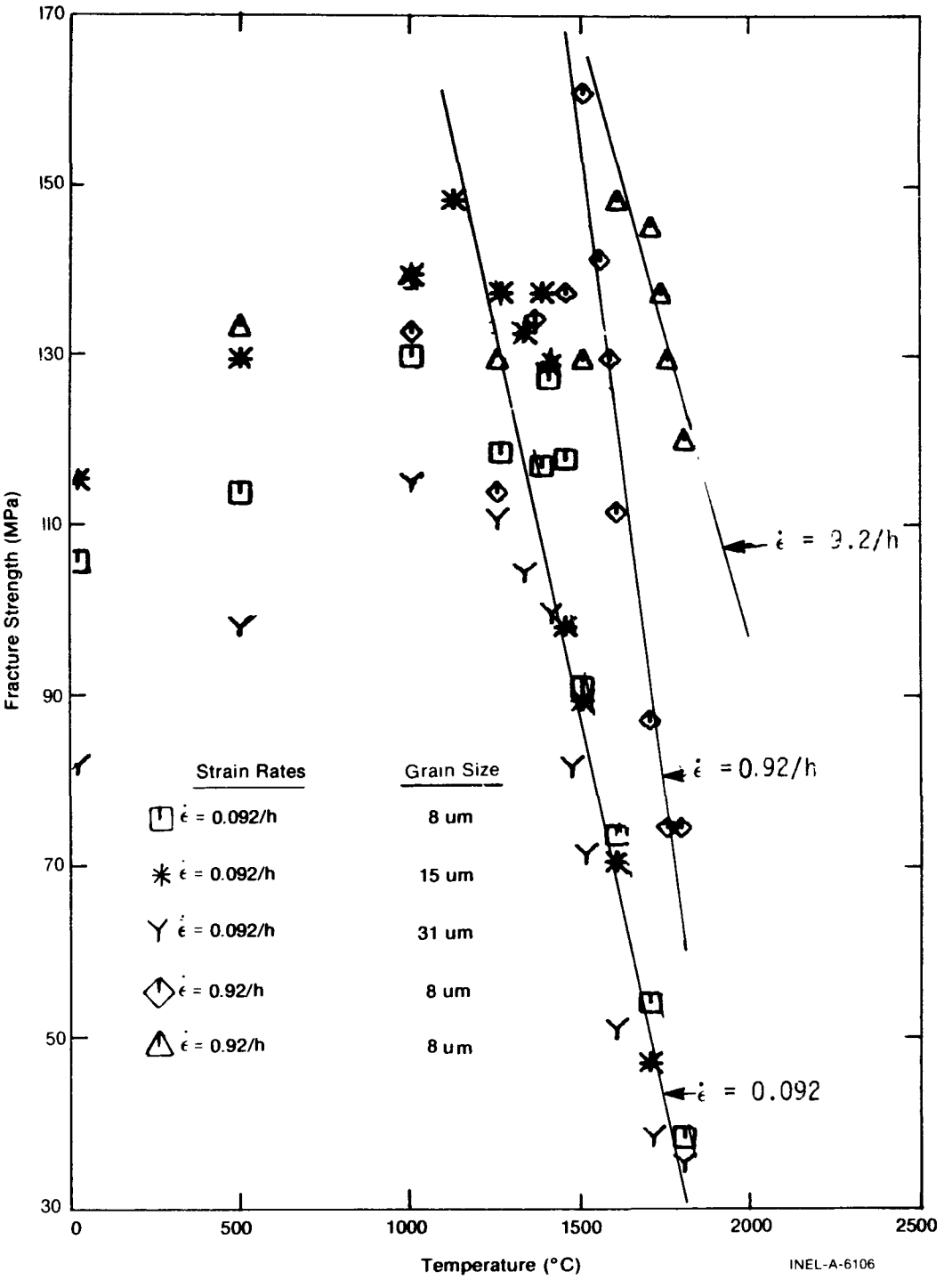

Fig. A-11.3 Least-squares regression fit of UO_2 fracture strength in the elastic-plastic regime to out-of-pile data of Cannon et al.

for 273 < T 1000 K

$$\sigma_F = 1.7 \times 10^8 [1 - 2.62 (1 - D)]^{1/2} \exp(-1590/8.314\ T) \quad \text{(A-11.6a)}$$

for $T > 1000$ K

$$\sigma_F = \sigma_F \ (1000 \ K) \qquad \text{(A-11.6b)}$$

where the terms have been defined in Equation (A-11.1).

Equation (A-11.6a) can be used for temperatures up to about (1323 K) for out-of-pile use. The predictions of FFRACS for two different fuel densities as a function of temperature are shown in Figure A-11.4.

11.4 Fuel Fracture Strength Subcode FFRACS Listing

The FORTRAN listing of the FFRACS subcode is presented in Table A-11.I.

11.5 References

A-11.1. J. T. A. Roberts and Y. Ueda, "Influence of Porosity on Deformation and Fracture of UO_2," *Journal of the American Ceramic Society, 55,* 3 (1972) pp 117-124.

A-11.2. R. F. Cannon, J. T. A. Roberts, R. J. Beals, "Deformation of UO_2 at High Temperatures," *Journal of the American Ceramic Society, 54* (1971) pp 105-112.

A-11.3. Y. Guerin, "Etude par Compression a'Hautes Temperatures de la Deformation Plastique du Bioxyde d'Uranium Polycristallin," *Journal of Nuclear Materials, 56,* (1975) pp 61-75.

A-11.4. A. G. Evans and R. W. Davidge, "The Strength and Fracture of Stoichiometric Polycrystalline UO_2," *Journal of Nuclear Materials, 33* (1969) pp 249-260.

A-11.5 C. R. Tottle, *Mechanical Properties of Uranium Compounds,* ANL-7070 (November 1965).

A-11.6. J. Katanic'-Popovic' and V. Petrovic', "Strength Dependence on Microstructure Characteristics of Sintered UO_2," *Physics Sintering, 5,* 2 (1973) pp 95-105.

A-11.7. A. Tetelman and A. McEvily, Jr., *Fracture of Structural Materials,* New York: John Wiley and Sons (1967) p 53.

A-11.8. D. Hasselman, "Analysis of the Strain at Fracture of Brittle Solids with High Densities of Microcracks," *Journal of the American Ceramic Society, 52* (1969) pp 458-459.

A-11.9. F. P. Knudsen, H. S. Parker, and M. D. Burdick, "Flexural Strength of Specimens Prepared from Several Uranium Dioxide Powders; Its Dependence on Porosity and Grain Size and the Influence of Additions of Titania," *Journal of the American Ceramic Society, 43* (1960) pp 641-647.

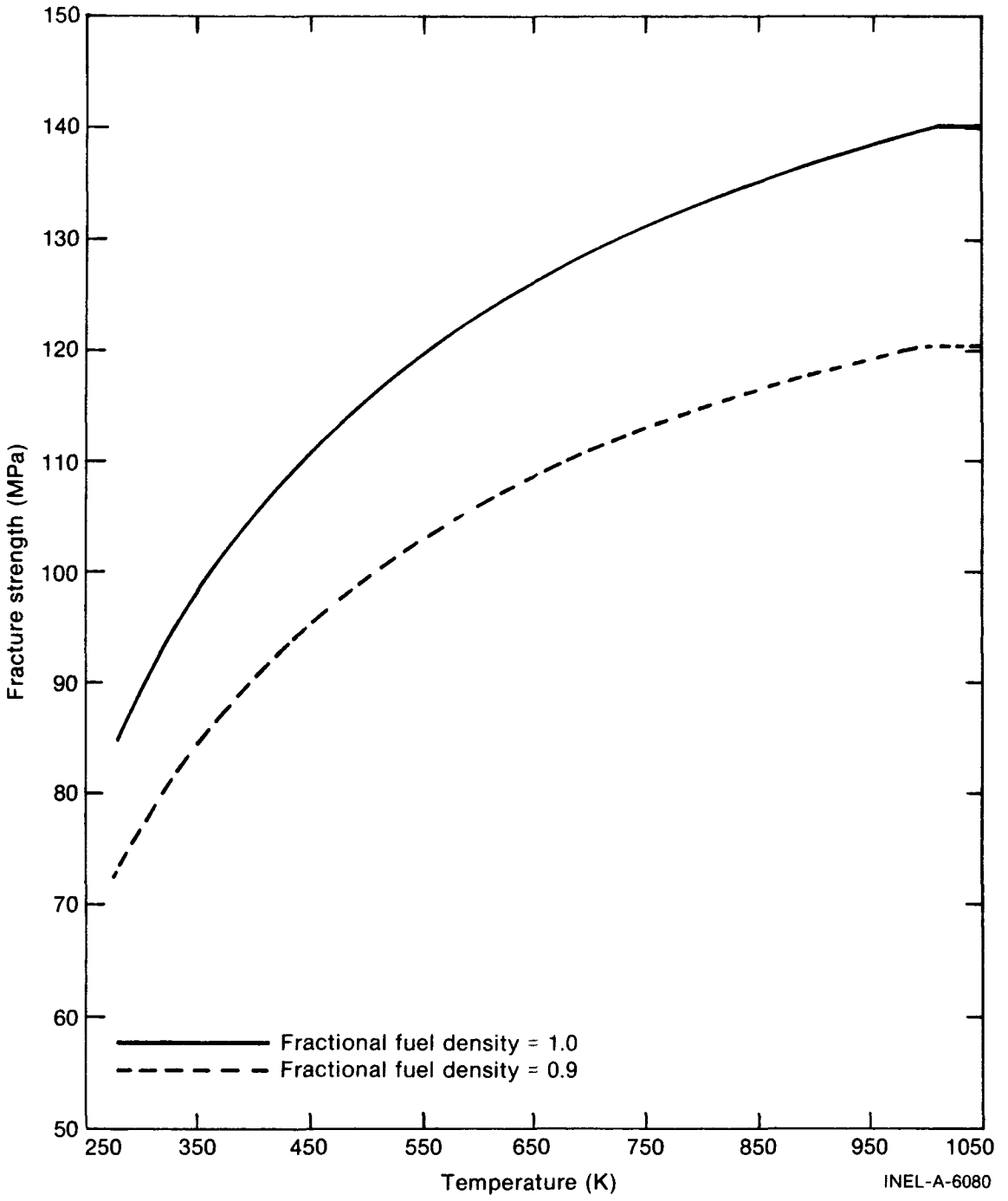

Fig. A-11.4 Calculated curves showing the predictions of FFRACS as a function of temperature for two fuel densities.

A-11.10. M. C. Burdick and H. S. Parker, "Effect of Particle Size on Bulk Density and Strength Properties of Uranium Dioxide Specimens," *Journal of the American Ceramic Society, 39* (1956) pp 181-187.

A-11.11. E. Orowan, "Die Erhöhte Festigkeit Dünner Faden, die Joffe-Effekt, und Verwandte Erscheinungen vom Standpunkt der Griffithschen Bruchtheorie," *Zeitschrift Fuer Physik,* (3/4) pp 195-213.

TABLE A-11.I

LISTNG OF THE FFRACS SUBCODE

```
C
C
      FUNCTION FFRACS(FTEMP, FRADEN)
C
C     FFRACS CALCULATES THE UO2 FRACTURE STRESS AS A FUNCTION OF
C     TEMPERATURE AND FRACTIONAL DENSITY.
C
C     FFRACS = OUTPUT UO2 FRACTURE STRENGTH (PA)
C
C     FTEMP  = INPUT FUEL TEMPERATURE (K)
C     FRADEN = INPUT FRACTIONAL FUEL DENSITY (RATIO OF ACTUAL DENSITY TO
C              THEORETICAL DENSITY).
C
C     THE CORRELATION FOR UO2 FRACTURE STRENGTH IS BASED ON THE
C     FOLLOWING DATA:
C          J. T. A. ROBERTS AND Y. UEDA, J. AMER. CER. SOC. 55 117(1972)
C          R. F. CANNON ET AL, J. AMER. CERAM. SOC. 54 105(1971).
C          J. KATANIC-POPOVIC AND PETROVIC, PHYS. SINTERING 5 95(1973).
C          F. KNUDSEN ET AL, J. AMER. CER. SOC. 43 641(1960).
C          M. BURDICK AND H. PARKER, J. AMER. CER. SOC. 39 181(1956).
C
C     FFRACS WAS PROGRAMMED BY C. S. OLSEN IN SEPTEMBER 1975
C     MODIFIED BY G. A. REYMANN IN SEPTEMBER 1977.
C
      STRU(T,F,A,B,C,Q) = A * (1. - B*(1. - F))**C * EXP(-Q/(1.987*T))
      DATA A1,B1,C1,Q1/1.70E08,2.62,0.5,380./
      T1 = FTEMP
      F1 = FRADEN
      IF(T1 .GT. 1000.0) T1 = 1000.
C
      FFRACS = STRU(T1,F1,A1,B1,C1,Q1)
      RETURN
      END
```

A-11.12. N. J. Petch, "Cleavage Strength of Polycrystals," *Journal of the Iron Steel Institute, 174* Part I (1953) pp 25-28.

A-11.13. N. Igata and K. Domoto, "Fracture Stress and Elastic Modulus of Uranium Dioxide Including Excess Oxygen," *Journal of Nuclear Materials, 45* (1972/73) pp 317-322.

A-11.14. F. P. Knudsen, "Dependence of Mechanical Strength of Brittle Polycrystalline Specimen on Porosity and Grain Size," *Journal of the American Ceramic Society, 42* (1959) pp 376-387.

A-11.15. A. A. Solomon, "Influence of Impurity Particles on the Fracture of UO_2," *Journal of the American Ceramic Society, 55* (1972) pp 622-627.

12. FISSION GAS RELEASE (FGASRL)

(R. E. Mason)

During irradiation of light water reactor fuel rods, gaseous fission products are produced in the fuel and slowly released to various void volumes in the fuel rods. The released gases degrade the thermal conductivity of the fill gas and thus change the thermal response of the fuel rods. Moreover, fuel rod internal pressure is increased thereby affecting cladding mechanical response.

12.1 Summary

The fission gas release subcode, FGASRL, uses a two-step gas release process: (a) release from fuel grains to the grain boundaries and, (b) release from the grain boundaries to internal free volume of the fuel. The fission gas reaching the fuel free volume is a fraction (F) times the sum of the fission gas stored at the grain boundaries (S) and the fission gas that reaches the grain boundaries (Δn) during a time increment

$$R = F\ (S + \Delta n) \qquad \text{(A-12.1)}$$

where

R = fission gas released to the fuel free volume (mol)

F = fraction of fission gas released from the grain boundaries to the fuel free volume

S = fission gas stored at the grain boundaries during previous time steps (mol)

Δn = fission gas released from fuel grains to the grain boundaries during a time increment (mol).

The fraction of grain boundary gas released to the fuel free volume is a function of fuel density and grain size and is calculated in FGASRL.

For $T \leqslant 2100$ K

$$F = 1 - \mathrm{erf}(\rho) + \exp(-1.25 \times 10^{14}/B^3) \qquad \text{(A-12.2a)}$$

for $T > 2100$ K

$$F = 1 - [\mathrm{erf}(\rho)/(T - 2099)] + [\exp(-1.25 \times 10^{14}/B^3)] \qquad \text{(A-12.2b)}$$

where

B = burnup (MWd/t)

T = fuel temperature (K)

$\text{erf}(\rho)$ = error function $\left(\frac{2}{\pi}\int_0^{\rho} e^{-t^2} dt\right)$

ρ = $[1.0 + 10^5 (X^{-1} - 1.0)\, g^{-3}]^{-1}$

X = fractional fuel porosity

g = average grain diameter (μm).

The fission gas reaching the grain boundaries from the fuel grains is calculated using the equation

$$\Delta n = \beta \left[t - \frac{[1 - \exp(k' k'' t)]\ (1 - k')}{k' k''} \right] + C\ [1 - \exp(k' k'' t)] \qquad \text{(A-12.3)}$$

where

β = fission gas production rate (mol/s)

t = time step (s)

C = fission gas trapped at defect sites in the grain matrix at the beginning of the step (mol)

k' = $9 \times 10^7 \exp(-45\,289.9/T) + 0.0005$

k'' = $0.0005 \left\{ 1 - \left[\exp\left(\frac{T - 1900}{40}\right) + 1 \right]^{-1} + \exp\left(1.24 \times 10^{14}/B^3\right) \right\}$.

Equations (A-12.1), (A-12.2), and (A-12.3) describe the subcode calculation of fission gas release from light water reactor fuel. The resulting correlation is a function of temperature, time, burnup, grain size, and fuel density. Time steps of 7.9×10^6 s or less are to be used with FGASRL calculations. FGASRL fractional gas release predictions (fraction of total fission gas produced which is released) using fuel rod operation histories are within ±60% of the experimental fractional gas release experienced by the fuel rods.

Section 12.2 describes the development of the subcode. In Section 12.3 a comparison of subcode predictions with gas release data is discussed. Section 12.4 contains the FGASRL computer subcode and Section 12.5 lists the references.

12.2 Model Development

Fission gas release from nuclear fuels results from many physical processes. These were condensed into two major steps, shown schematically in Figure A-12.1. The shaded

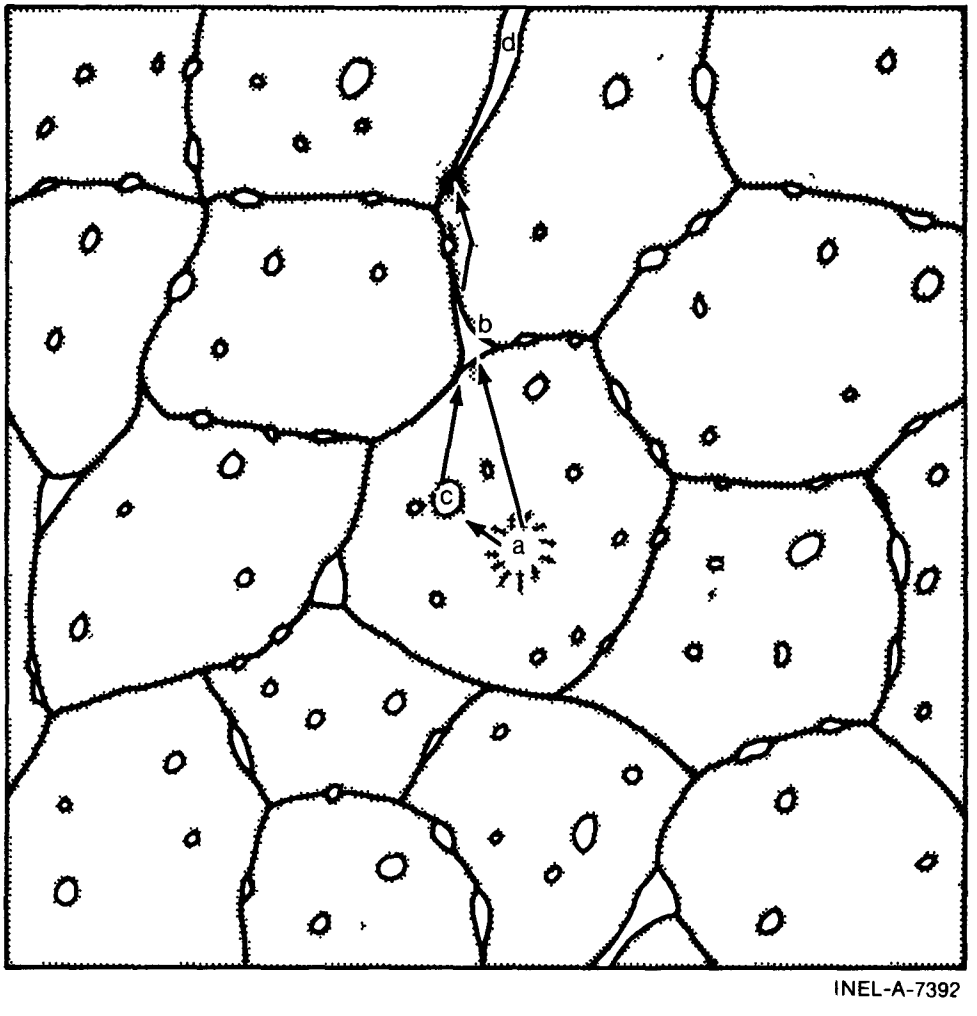

Fig A-12.1 Schematic of the mechanisms modeled in the FGASRL fission gas release model.

areas represent fuel grains and the open areas represent pores or gas bubbles. Fission gas is created in a grain matrix (a) and then migrates to the grain boundaries (b) or to defect traps (c). Trapped atoms are eventually released back into the grain matrix and diffuse to the grain boundaries (b). Fission gas is trapped at the grain boundaries until it is released through fissures or cracks (d) communicating with the fuel rod free volume. These processes are assumed to occur in series. The fission gas created in a grain either migrates to the grain boundary or is trapped in the grain interior by defect traps until it is released and migrates to the grain boundaries. Fission gas reaching the grain boundaries is either stored or released directly to the fuel free volume.

12.2.1 Analytical Model Development. Following Weisman et al[A-12.1], the various mechanisms for gas release from the grains to the grain boundaries [that is, recoil or knockout by fission fragments or both passing through the grains[A-12.2], random motion[A-12.3], biased movement[A-12.4] (due to temperature gradient), ...] are represented simply as a single mechanism of gas movement through the grain. This representation corresponds to the escape of gas from the fuel grains to the grain boundaries. Two probabilities in evaluating fission gas release from grains are defined. The first, k', is the probability of direct release from the fuel grains to the grain boundaries, and the second, k'', is the probability of release per unit time of fission gases from grain defect traps such as dislocations or large bubbles[A-12.4,A-12.5].

If β is the gas production rate, then the rate of direct gas release to the grain boundaries of gas created during a time step, t, is $\beta k'$. If C is the number of gas moles trapped in the grain matrix, the rate of release from these traps is Ck''. The gas released from the traps escapes from the interior of the grain to the grain boundary by the same process as the newly created gas. The total rate of fission gas release from the interior of the grain to the grain surface is

$$\frac{dn}{dt} = k' (\beta + k''C) \qquad \text{(A-12.4)}$$

where

n = fission gas released from the grain interior to the grain surfaces (mol)

β = fission gas production rate (mol/s)

C = fission gases trapped in the grain matrix (mol)

t = time (s)

k' = probability of direct release from the fuel grains

k'' = probability per unit time of release of fission gases from grain defect traps.

The rate of fission gas production in the fuel matrix during reactor steady state operation is equal to the sum of the rate of loss from the matrix to the grain surfaces plus the loss to the interior grain defect traps.

$$\beta = \frac{dn}{dt} + \frac{dC}{dt} . \qquad \text{(A-12.5)}$$

For any period of time in which β, k', and k'' are constant, Equations (A-12.3) and (A-12.4) may be solved simultaneously[a] to show:

$$n - n_o = \beta \left[t - \frac{(1 - k')[1 - \exp(-k' k'' t)]}{k' k''} \right] + C [1 - \exp(-k' k'' t)] \quad \text{(A-12.6)}$$

where

n = fission gas released from the grain during the time step interval, t (mol)

n_o = fission gas released from the grain at t = 0 (mol)

t = time interval (s)

k', k'' = values of k' and k'' during the time interval

C = trapped fission gases at the start of the time interval (mol).

k' is assumed to have an Arrhenius temperature dependence. This functional form is reasonable because the probability of escape by diffusion without being trapped is quite small at low temperatures but rises rapidly at high temperatures[A-12.2,A-12.6,A-12.7]. An additional constant term (H) is included in the expression for k' to represent the temperature independent contribution of knockout and recoil.

$$k' = A \exp(-Q/T) + H \quad \text{(A-12.7)}$$

where

T = temperature (K)

A,Q,H = constants.

The constants A, Q, and H are determined by fitting the model to gas release data as explained in Section 12.2.2.

The probability function k'' simulates fission gas release observed across the radius of a fuel pellet[A-12.8]. The equation used to represent the observed radial gas release distribution is

---

[a] $\frac{dn}{dt}$ is eliminated and the integrating factor $e^{k' k'' t}$ is used to find C. A similar integration of Equation (A-12.4) with the solution for C substituted yields Equation (A-12.6).

$$k'' = g\left\{1.0 - \left[\exp\left(\frac{T - h}{\ell}\right) + 1\right]^{-1} + \exp\left(\frac{1.25 \times 10^{14}}{B^3}\right)\right\} \quad \text{(A-12.8)}$$

where

k'' = probability that gas will be released from grain defect traps

g,h,ℓ = constants

and T and B have been previously defined.

The term containing burnup is included to model enhanced fission gas release observed at high burnups (> 30 000 MWd/t)[A-12.9] and is an empirical fit to fission gas release data at burnups above 30 000 MWd/t.

After the fission gas reaches the grain boundaries, it can be released through pores (interconnected tunnels) open to the fuel rod free volume. While fission gas diffusion and migration of grain boundaries may assist in the accumulation of fission gases, the movement of fission gases from grain boundaries is associated with mechanical changes in the fuel[A-12.10,A-12.11]. As pointed out by Olander[A-12.12], grain boundary fission gas release occurs in one of two ways: (a) by bubble interlinkage to fissures communicating with the fuel rod free volume or (b) communication of the gas bubbles with the free volume because of stress cracking of the fuel pellet. A model for gas storage and release from grain boundaries is developed using a simplified version of the pore percolation theory[A-12.13] and a statistical distribution function similar to that used in the GRASS code[A-12.14]. This model considers only grain boundary fission gas release by bubble interlinkage to the fuel rod free volume. The statistical distribution function used in the FGASRL subcode is

$$F = \frac{\sqrt{2}}{\sqrt{\pi}\,\sigma} \int_{\rho}^{\infty} \exp\left[-(x - \rho)^2/2\sigma^2\right] dx \quad \text{(A-12.9)}$$

where

F = fractional fission gas release from grain boundaries

σ = constant

x,ρ = microstructure parameters.

The parameter ρ is a function of porosity such that as the porosity increases, ρ increases and as the grain size increases, the gas stored in the grain boundaries increases. The resulting microstructure parameter is

$$\rho = \left\{ 1 + a \quad (X^{-1} - 1) \quad g^{-3} \right\}^{-1} \qquad \text{(A-12.10)}$$

where

ρ = microstructure parameter

a = constant $(\mu m)^3$

g = grain diameter (μm)

X = fractional fuel porosity.

Evaluating Equation (A-12.9) between the limits shown gives

$$F = 1 - \text{erf}(\rho) \qquad \text{(A-12.11)}$$

Here as with the k'' function of Equation (A-12.7), a high burnup term, is added to Equation (A-12.11) to predict the enhanced gas release observed in the high burnup fuel discussed by Baroch and Rigdon[A-12.9].

For temperatures $\leq$ 2100 K

$$F = 1 - \text{erf}(\rho) + \exp(-1.25 \times 10^{14}/B^3) \qquad \text{(A-12.12)}$$

for temperatures $>$ 2100 K

$$F = 1 - \text{erf}(\rho)/(T - 2099) + \exp(-1.25 \times 10^{14}/B^3) \qquad \text{(A-12.13)}$$

where

ρ = parameter defined in Equation (A-12.10)

and the other terms have been previously defined. The last equation corresponds with Turnbull's[A-12.15] conclusion that release of krypton gas increases as the grain size of the fuel increases.

The model of fission gas stored at grain boundaries is especially relevant to reactor transient condition as has been demonstrated by the transient heating tests conducted at Argonne National Laboratory[A-12.16]. There it was found that under reactor transient conditions the fuel cracking takes place along the grain boundaries, releasing both gas trapped at the grain boundaries and gas able to diffuse to the grain boundaries during the transient. A similar effect was observed in the transient tests at the Idaho National

Engineering Laboratory in the film boiling regime[A-12.17]. To provide this "grain boundary stored gas" to transient calculations, the equations described above were included in the FGASRL gas release calculations.

12.2.2 Evaluation of Constants. To evaluate the constants in Equations (A-12.1) and (A-12.2), the subcode was correlated with water reactor fission gas release data. The data selection criteria were that the approximate centerline temperature of the irradiated fuel be documented, the operational history be documented in enough detail to be used in the FRAP-S3[A-12.18] analytical code, and the fission gas release be documented. These criteria were used because the subcode must be able to predict the gas release from such fuel rods. Using these criteria, five fuel rods for evaluating the constants of Equation (A-12.3) were chosen from four assemblies.

The AECL 2230[A-12.19] fuel rod and the AECL 1676[A-12.20] fuel rod data are especially useful in determining constants of Equation (A-12.3) because they were irradiated at a relatively constant power ($\leqslant$ 20% power variation)[A-12.21]. The rest were chosen because of their temperature or burnup. Baroch and Rigdon[A-12.9] have reported fission gas release data for Babcock & Wilcox (B&W) fuel irradiated up to 80 000 MWd/t, but a complete irradiation history is not documented. Because the Baroch and Rigdon data are for thermal reactor fuel irradiated to high burnups with corresponding enhanced gas release, their data were used to correlate the subcode for high burnups.

The fission gas release data used in evaluating the constants of the FGASRL subcode are listed in Table A-12.I. The table includes the literature source of the data used, the fuel burnup reached, and the average power of the fuel. Also listed are the FRAP-S3[A-12.18] calculated centerline temperature and the centerline temperature reported in the literature, the fractional (moles released $\div$ moles produced) gas release and the initial fuel grain size. The data in Table A-12.I are by no means all the gas release data available. Additional data which may be useful for further model development are listed in Section 12.6.

Derivation of the constants in the expression for k' [Equation (A-12.7)] is based on the assumption that movement of fission gas atoms from the fuel grains to the grain boundaries is diffusion controlled. The probability that the gas atoms will reach the grain boundaries without being trapped is assumed to be an Arrhenius function. The constant Q of Equation (A-12.7) is taken to be a number similar to the diffusional activation energy of fission gases in water reactor fuels. Activation energies for gas movement, bubble movement, etc. reported in the literature range from $\sim$ 83 720 to $\sim$ 565 000 J/mol[A-12.6, A-12.12, A-12.24]. For the calculations described in this report, Q is chosen to be 376 742.4 J/mol. Using this value and adjusting the other constants of Equation (A-12.6) to fit the experimental fuel rod gas release data, the final k' function is

$$k' = 9 \times 10^{7} \exp(-45\ 289.9/T) + 0.0005. \qquad \text{(A-12.14)}$$

TABLE A-12.I

DATA USED TO EVALUATE CONSTANTS IN FGASRL

Reference	Source	Rod	Burnup (MWd/t)	Average Density (kg/m^3)	Peak Power (kW/m)	Grain Size (μm)	Fuel Centerline Temperature (K)		Fission Gas Release (%)
							FRAP	Experimental	
Smalley	SAXTON II	B	15 896	10.3×10^3	152.0	5.0	2847	2473	36.0
Bellamy, Rich	AERE	5039	36 600	10.78×10^3	--	25.0	--	1422	3.2
Bellamy, Rich	AERE	5042	27 800	10.41×10^3	--	25.0	--	1757	1.2
Notley, MacEwan	AECL 2230	CBX	2 710	10.4×10^3	26.6	5.0	2380	2293	18.8
Notley et al	AECL 1676	DFA	344	10.7×10^3	187.3	5.0	2560	2001	4.6
Baroch, Rigdon	B&W	7	56 581	10.3×10^3	172.3	5.0	2450	2216	71.9
Baroch, Rigdon	B&W	33	35 500	10.3×10^3	204.4	5.0	2871	2060	27.4

The probability per unit time that fission gas will be released from the grain's defect traps, k'', is assumed to be a Fermi function[a]. The constants of Equation (A-12.8) are chosen such that fission gas release increases rapidly as the fuel temperature increases above 1600 K or as the fuel is irradiated above 30 000 MWd/t. The final form of k'' is

$$k'' = 0.0001 \left\{1.0-\left[\exp\left(\frac{T-1900}{40}\right)+1\right]^{-1} + \exp\left(\frac{-1.25 \times 10^{14}}{B^3}\right)\right\} . \quad \text{(A-12.15)}$$

The remainder of this section is a discussion of the behavior of Equation (A-12.6) using the constants discussed. The first term on the right side of Equation (A-12.6) is

$$\beta \left[t - \frac{(1 - k') [1 - \exp(-k\, k''\, t)]}{k'k''} \right]$$

and is the number of gas atoms created during the time step, t, that escape to the grain boundary and are not trapped within the fuel grain matrix. This can be reduced to a ratio of those gas atoms created and subsequently released to the total fission gas atoms created in time step t. This fractional release ratio is

$$F_B = 1 - \frac{(1 - k) [1 - \exp(k'k''t)]}{T\, t\, k'\, k''} . \quad \text{(A-12.16)}$$

The fraction, F_B, is plotted as a function of temperature in Figure A-12.2 for various times. Figure A-12.2 shows that for temperatures below 1600 K the gas release fraction is less than 0.001 and approaches total gas release at temperatures above 2200 K for long time steps. For time steps less than 200 h, it approaches total gas release at $\sim$ 2500 K. The second term on the right side of Equation (A-12.3), C [1 - exp(k'k''t)], is in effect the number of trapped gas moles that escape to the grain boundary during a time step t. This can be expressed as a fractional release of the number of moles trapped in the fuel grains.

$$F_C = 1 - \exp(k'k''t). \quad \text{(A-12.17)}$$

The fraction F_C (dashed lines) is also plotted in Figure A-12.2. Fission gas release from traps is similar to the release from the matrix (F_B). However, at temperatures in the range of 1700 to 2100 K, the trap release fraction is larger than the matrix release fraction.

---

[a] The Fermi function is defined as

$$f(t) = 1\Big/\left[\exp\left(\frac{T - T_o}{\Delta T} + 1\right)\right]$$

where T_o and ΔT are constants and T is the fuel temperature.

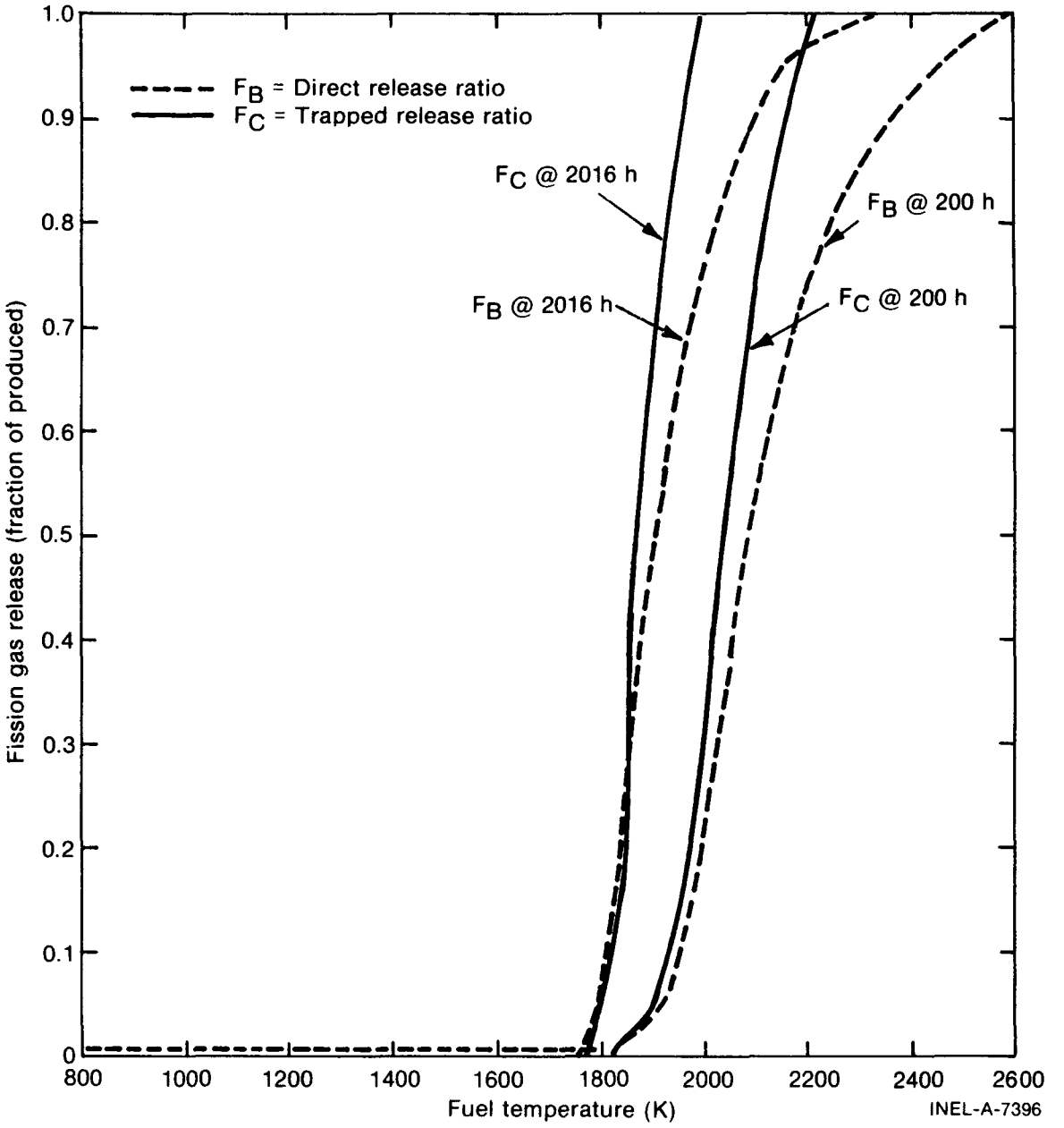

Fig. A-12.2 Temperature dependence of the terms in Equation (A-12.1).

The technique used to find constants in the expression for the calculation of the parameter ρ [Equation (A-12.10)] is simply to choose constants for the equation such that (a) ρ ranged from 0 to 1 for grain sizes between 1 and 500 μm and (b) the fractional grain boundary release depicted in Figure A-12.3 is produced.

The constant, a, of Equation (A-12.10) is 10^5 and the resulting equation to determine ρ is

$$\rho = \left\{1 + 10^5 \left(\chi^{-1} - 1\right) g^{-3}\right\}^{-1}. \qquad \text{(A-12.18)}$$

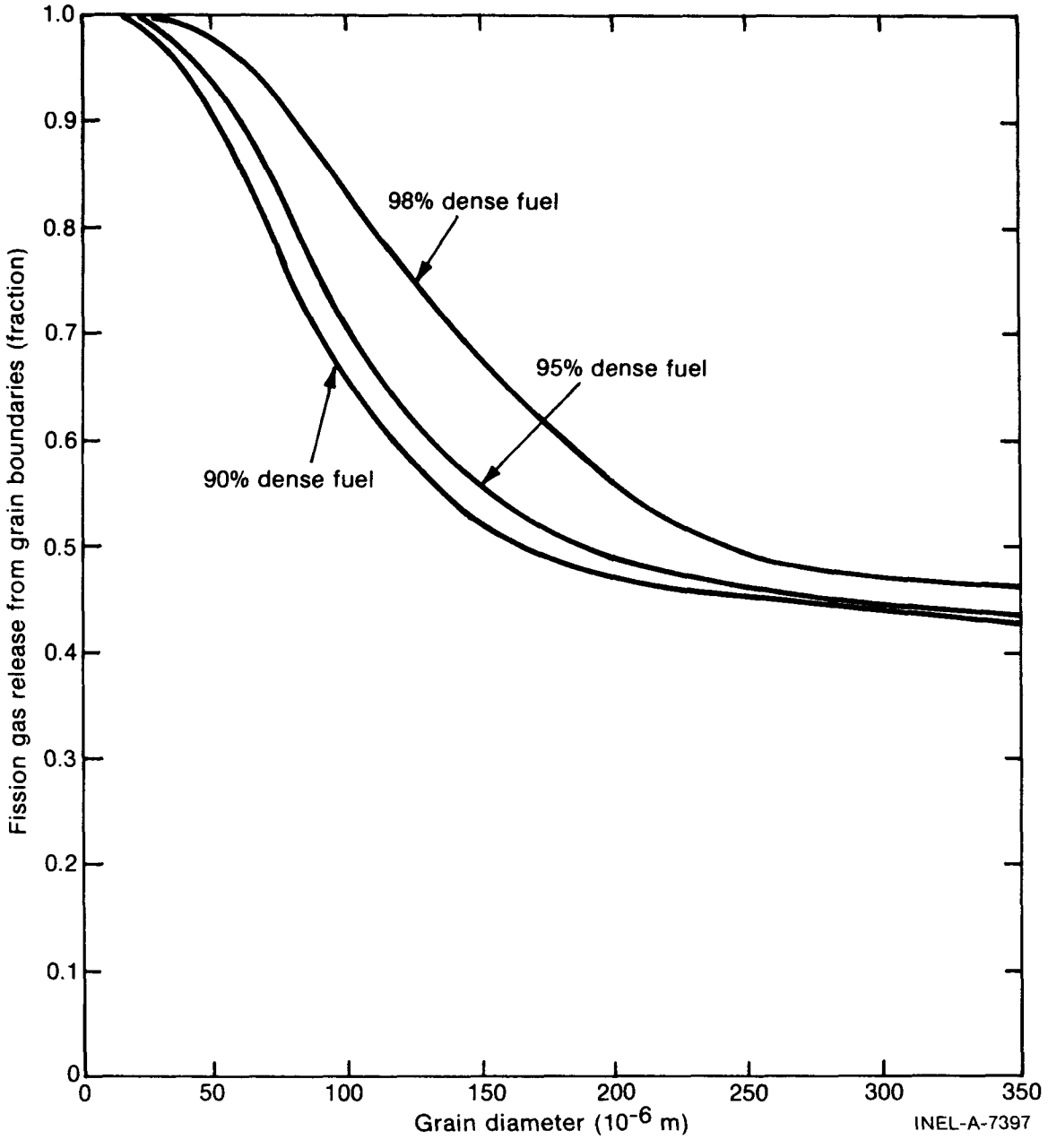

Fig. A-12.3 Fractional gas release from the grain boundaries to the fuel rod free volume.

No numerical data were available for direct correlation with these results, but (as discussed previously) the effect is important enough for it to be included in the subcode calculations.

12.3 Comparison with Data

The calculated values of the subcode developed in Section 12.2 are discussed in this section and compared with the appropriate experimental data.

Figure A-12.4 shows the correspondence of the FGASRL subcode to its data base and to data not used to develop the model. The uncertainty of the subcode predictions is the

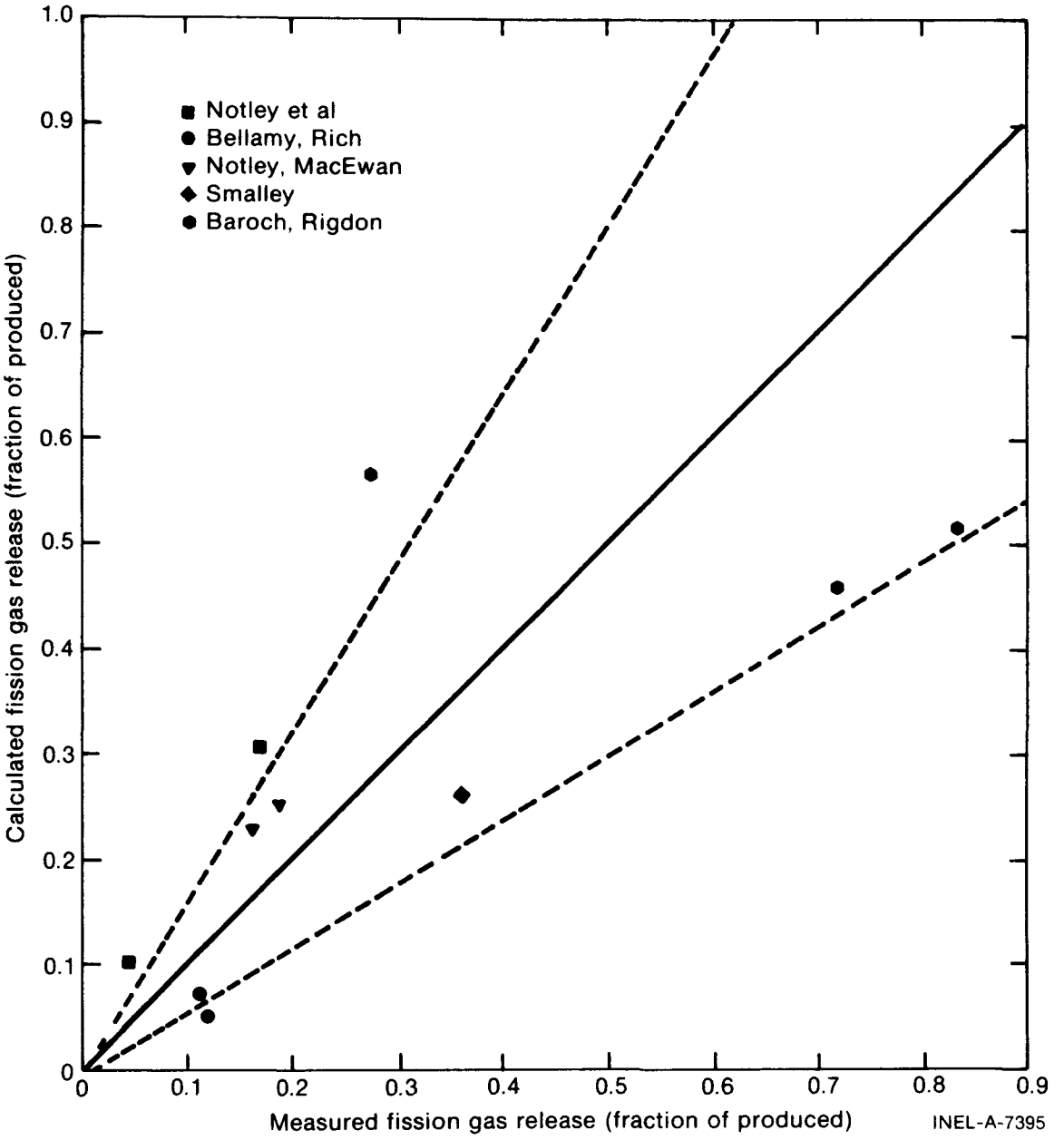

Fig. A-12.4 FGASRL fission gas release predictions compared with the release reported in related studies.

standard error of the percent difference of the FGASRL fractional fission gas release prediction divided by the experimentally determined fractional fission gas release.

$$SE = \sqrt{\sum_{i=1}^{N} \left(\frac{P_i - E_i}{E_i} \right)^2 \quad \frac{1}{N}} \qquad \text{(A-12.19)}$$

where

SE = standard error of prediction

P_i = FGASRL fractional gas release prediction (%)

E_i = experimentally determined fractional gas release (%)

N = number of data used.

Equation (A-12.19) shows that the uncertainty of the FGASRL predictions is accurate to within ±60% of the experimentally determined values. The dashed lines shown in Figure A-12.4 depict the uncertainty bands of the FGASRL predictions.

An important new feature of the revised FGASRL model is the inclusion of grain boundary storage. Sample calculations of grain boundary stored fission gas determined during a FRAP-FGASRL calculation of gas release are shown in Figure A-12.5. The lines in the figure represent the stored gas (in moles) in two specific fuel sections. The dashed line shows the gas stored in a ring at the center of the fuel column near the top of the fuel rod. Fission gas stored at this location gradually increases with increasing irradiation time and increasing grain size up to about 5000 hours. The solid line shows fission gas stored at a fuel ring halfway between the center of the fuel and the fuel edge and shows a relatively constant quantity of fission gas at the grain boundaries. The fraction of gas stored at each location shown in Figure A-12.5 is primarily a function of the gas produced during a time step and the amount that reaches the boundaries from the grain. That is, at higher irradiation powers more gas is released from the grain and grain boundary storage increases, but as power decreases this stored gas decreases as gas is released faster than it is being replaced.

The effect of the burnup term of Equation (A-12.2) and Equation (A-12.7) on the gas release predicted by the FGASRL subcode is shown in Figure A-12.6. The subcode calculations were made assuming isothermal fuel temperatures of 1500 K (solid line) and 1800 K (dashed line) and time steps of 7.2×10^6 s with 75 micron fuel grains. The solid line shows the minimum gas release calculated by the subcode at burnups above 30 000 MWd/t. The dashed line shows the added gas release calculated for fuel at temperatures above $\sim$ 1500 K. FGASRL predictions for high burnups produces releases of the same magnitude as the data reported and each experimental value reported can be directly correlated with FGASRL predictions using an accurate power and temperature history.

12.4 Fuel Fission Gas Release Subcode FGASRL Listing

A listing of the computer subcode FGASRL is presented in Table A-12.II.

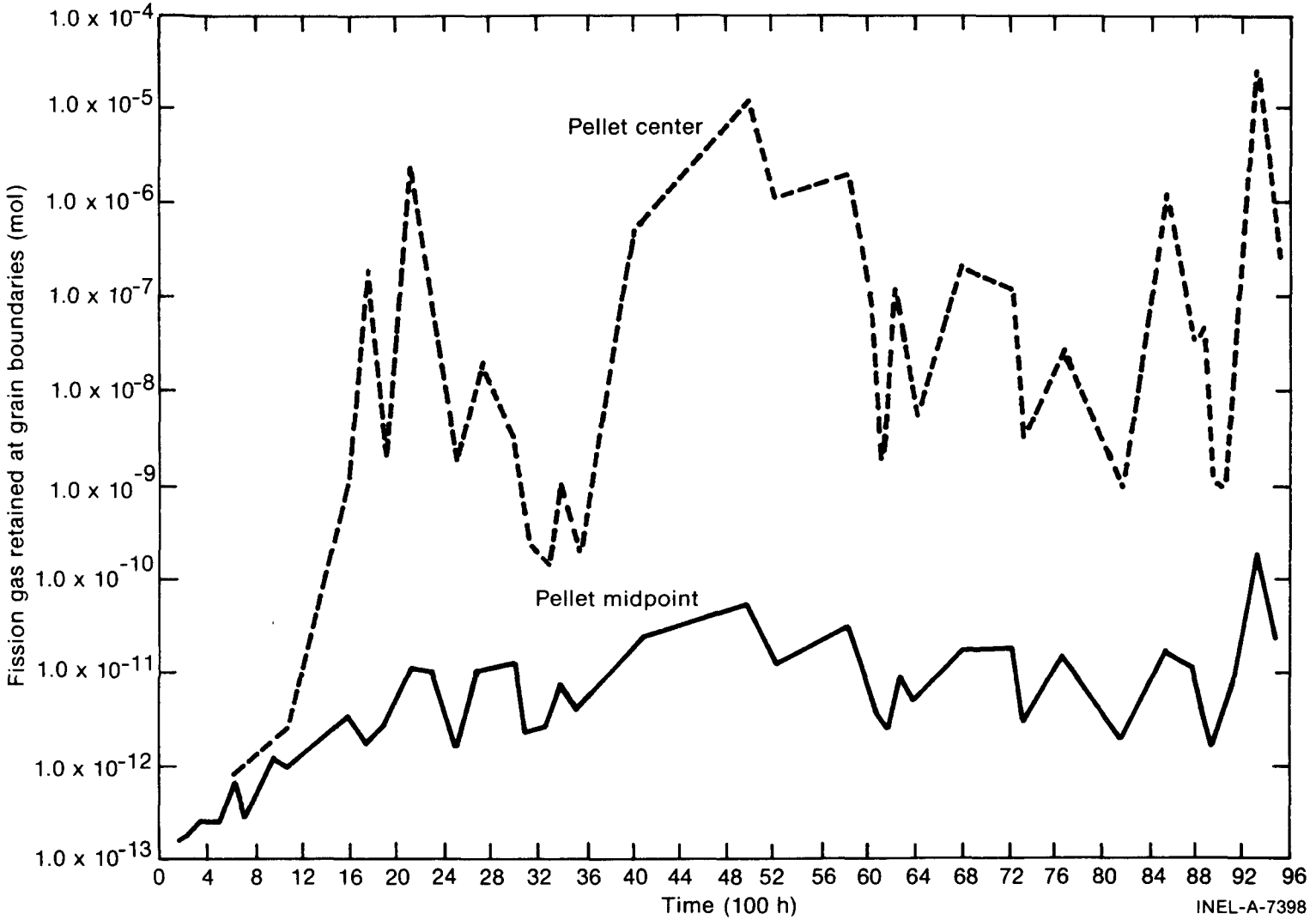

Fig. A-12.5 An example of the fission gas stored at the grain boundaries as calculated by the FGASRL subcode.

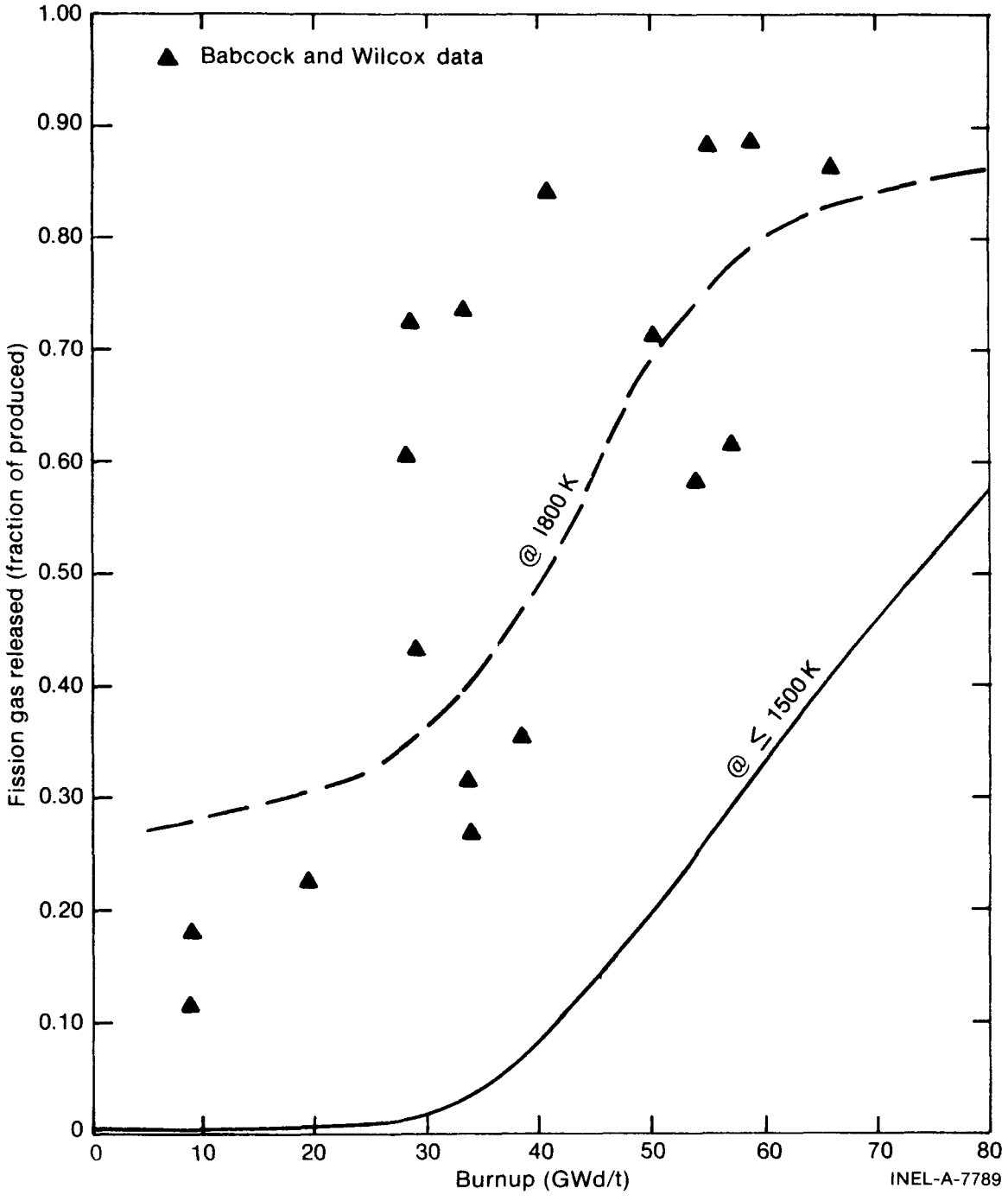

Fig. A-12.6 FGASRL gas release predictions compared with Babcock and Wilcox data.

TABLE A-12.II

LISTING OF THE FGASRL SUBCODE

```
      SUBROUTINE FGASRL(FTEMP, FDENS, BU, FGRN, COMP, FMGPR, IT,
     #                  TIME, CC2, CC1, GBBG, FMGR, GBGOUT, FMGROT)
C
C     FGASRL CALCULATES THE FISSION GAS RELEASE AS A FUNCTION
C     OF TEMPERATURE, FUEL POROSITY,TIME, GRAIN SIZE, AND BURNUP.
C
C     FTEMP   = INPUT FUEL RING AVERAGE TEMPERATURE (K)
C     FDENS   = INPUT FUEL DENSITY (KG/M**3)
C     BU      = INPUT FUEL BURNUP (MW-S/KG-U)
C     FGRN    = INPUT FUEL GRAIN SIZE (MICRONS)
C     COMP    = INPUT PLUTONIA CONTENT (WEIGHT PERCENT)
C     FMGPR   = INPUT FISSION GAS PRODUCED IN THE L FUEL RING (MOLES)
C     IT      = INPUT POWER STEP NUMBER
C     TIME    = INPUT TIME STEP LENGTH (S)
C     CC2     = INPUT CONCENTRATION OF GRAIN TRAPPED FISSION GAS
C               PER RING (MOLES/RING)
C     GBBG    = INPUT CONCENTRATION OF GRAIN BOUNDARY TRAPPED FISSION
C               GAS PER RING (MOLES/RING)
C     FMGR    = INPUT CUMULATIVE FISSION  GAS RELEASED PER FUEL
C               RING (MOLES)
C
C     CC1     = OUTPUT CONCENTRATION OF GRAIN TRAPPED FISSION GAS
C               PER RING (MOLES/RING)
C     GBGOUT  = OUTPUT CONCENTRATION OF GRAIN BOUNDARY TRAPPED FISSION
C               GAS PER RING (MOLES/RING)
C     FMGROT  = OUTPUT CUMULATIVE FISSION GAS RELEASED PER FUEL
C               RING (MOLES)
C
C     THE FGASRL CORRELATION WAS BASED ON THE FOLLOWING DATA
C           M.J.F. NOTLEY AND J.R. MACEWAN, AECL - 2230
C           M.J.F.NOTLEY, ET AL., AECL - 1676
C           W.R.SMALLEY, WCAP - 3385 - 56
C           C.E.BEYER AND C.R.HANN BNWL - 1876
C
C     AN APPROXIMATION FOR THE ERROR FUNCTION WAS USED TO EVALUATE
C     THE CONSTANTS IN THE FOLLOWING EQUATIONS
C     THE APPROXIMATION WAS TAKEN FROM
C           C.H.HASTINGS,JR., APPROXIMATIONS FOR DIGITAL COMPUTERS
C           PRINCETON UNIVERSITY PRESS 1955
C
C     THE CORRELATION USED TO CALCULATE FISSION GAS RELEASE IS THAT
C     DEVELOPED BY J. WEISMAN AND P. E. MACDONALD, ANS TRANSACTIONS,
C     VOL. 12, NUMBER 2 (NOVEMBER 1969).
C
C     FGASRL WAS CODED BY G. A. REYMANN (JULY 1976).
C     FGASRL WAS MODIFIED BY R. E. MASON (NOVEMBER 1978).
C
      ERF(X) = 1.0 - 0.348024 * 1.0/(1.0 + 0.47047 * X) +
     #         0.0958798 * (1.0/(1.0 + 0.47047 * X)) **2.0 -
     #         0.7478556 * (1.0/(1.0 + 0.47047 * X)) ** 3.0 + 0.000025
C
C                    - PROGRAM -
C
      B = BU
      T = TIME
      IF(IT .EQ. 1)   FMAA = 0.0
      IF(IT .EQ. 1)   FMGR = 0.0
      IF(IT .EQ. 1)   CC2  = 0.0
      IF(BU .LE. 0.0) B    = 1.0
C
C     CALCULATION OF THE HIGH BURNUP FACTOR
C
      BUNKEL = 1.25E14/((B / 86.4) ** 3.0)
      IF(BUNKEL .GE. 400.0) BUNKEL = 400.0
C
C     CALCULATION OF FUEL GRAIN RELEASE
C
      AK1    = 9.0E 07 * (EXP(-45289.86/FTEMP)) + 0.0005
      AK2    = 0.00005 * AK1 * (1.0 - 1.0/(EXP((FTEMP - 1900.0)/40.0)
     #         + 1.0) + EXP(- BUNKEL))
      IF(TIME .LE. 0.0) T = 1.0
      IF(AK2 * TIME .LE. 1.0E-10) AK2 = 1.0E-10/T
      F      = (1.0 - (1.0 - AK1) * ((1.0 - EXP(-AK2 * T))/
     #         (AK2 * T)))
C
      IF (F .GT. 1.0) F = 1.0
      IF (F .LE. 0.0) F = 0.0
```

TABLE A-12.II (continued)

```
C
      FMA = F * FMGPR + CC2 * (1.0 - EXP(-AK2 * T))
C
C     THE FOLLOWING CALCULATIONS PROVIDE UPPER AND LOWER BOUNDS
C     TO THE FGASRL EQUATION AND ARE NOT AN OUTPUT OF THE SUBCODE
C     UNLESS THE USER DESIRES TO MODIFY THE SUBCODE APPROPRIATELY.
C     IF THE UPPER OR LOWER BOUND IS USED IT SHOULD REPLACE FMA IN THE
C     SUBCODE.
C
C     UFGASH IS THE UPPER BOUND
      UFGASH = 1.6 * FMA
      IF (UFGASH .GE. FMGPR + CC2)  UFGASH = FMGPR + CC2
C     UFGASL IS THE LOWER BOUND
      UFGASL = 0.4 * FMA
C
      IF(GBBG .LE. 0.0) GBBG = FMA * 1.0E-06
      GBBG   = GBBG + FMA
C
C     FISSION GAS WHICH IS NOT RELEASED FROM THE GRAIN BOUNDARY IS
C     LABELED GBBG(L)
C
C     CALCULATION OF GRAIN BOUNDARY GAS RELEASE
C
      ROTH   = 11.45 * COMP/100. + (1. - COMP/100.) * 10.97
      FP     = 1.0 - 0.001 * FDENS / ROTH
      P      = 1.0/(1.0+ (1.0/FP - 1.0) * 1.0E 05/(FGRN ** 3.0))
      FBR    = (1.0 - ERF(P)) + EXP( -BUNKEL )
      IF(FTEMP .GT. 2100.) FBR = 1.0 - (1.0 - FBR)/(FTEMP - 2099.)
      IF (FBR .LE. 0.0) FBR = 0.0
      IF (FBR .GT. 1.0) FBR = 1.0
C
      FMAA   = FBR  * GBBG
      CC1    = CC2  + FMGPR - FMA
      GBGOUT = GBBG - FMAA
      FMGROT = FMGR + FMAA
C
      RETURN
      END
```

12.5 References

A-12.1. J. Weisman et al, "Fission Gas Release from UO_2 Fuel Rods with Time Varying Power Histories," *Transactions of the American Nuclear Society, 12* (1969) pp 900-901.

A-12.2. R. Soulhier, "Fission-Gas Release from UO_2 During Irradiation up to 2,000°C," *Nuclear Applications, 2* (April 1966).

A-12.3. M. R. Hayns and M. H. Wood, "Models of Fission Gas Behavior in Fast Reactor Fuels Under Steady State and Transient Conditions," *Journal of Nuclear Materials, 67* (1977) pp 155-170.

A-12.4. R. M. Carroll et al, "Fission Density, Burnup, and Temperature Effects on Fission-Gas Release From UO_2," *Nuclear Science and Engineering, 38* (1969) pp 143-155.

A-12.5. R. M. Carroll, "Fission-Gas Behavior in Fuel Materials," *Nuclear Safety, 8 No. 4* (Summer 1967) pp 345-353.

A-12.6. R. M. Carroll and O. Sisman, "In-Pile Fission-Gas Release from Single Crystal UO_2," *Nuclear Science and Engineering, 21* (1965) pp 147-158.

A-12.7. J. A. Turnbull, "The Mobility of Intragranular Bubbles in Uranium Dioxide During Irradiation," *Journal of Nuclear Materials, 62* (1976) pp 325-328.

A-12.8. D. Stahl and T. J. Partrician, *Fission-Gas Behavior During A Mild Over-Power Transient,* ANL-8069 (February 1974).

A-12.9. C. J. Baroch and M. A. Rigdon, "Irradiation Behavior of UO_2 Burnups from 10 to 80 GWd/tonne U," Paper No. 58, *Proceedings of the BNES International Conference on Nuclear Fuel Performance, October 15-19, 1973, London (CONF-731004).*

A-12.10. A. D. Whapham, "Electron Observation of the Fission-Gas Bubble Distribution in UO_2," *Nuclear Applications, 2* (1966).

A-12.11. W. Beere and G. L. Reynolds, "The Morphology and Growth Rate of Interlinked Porosity in Irradiated UO_2," *Journal of Nuclear Materials, 47* (1973) pp 51-57.

A-12.12. D. R. Olander, *Fundamental Aspects of Nuclear Reactor Fuel Elements,* U.S. Department of Commerce, Springfield, Virginia, TID-26711-P1 (1976).

A-12.13. L. R. Kelman, *Transient Fuel Response and Fission-Product Release Program – Quarterly Progress Report*, ANL-75-72 (July-September 1975).

A-12.14. R. B. Poeppel, "An Advanced Gas Release and Swelling Subroutine," *Proceedings of the ANS Conference on Fast Reactor Fuel Element Technology, New Orleans, April 13-15, 1971*, pp 311-326.

A-12.15. J. A. Turnbull, "The Effect of Grain Size on the Swelling and Gas Release Properties of UO_2 During Irradiation," *Journal of Nuclear Materials, 50* (1974) pp 380-391.

A-12.16. R. G. Sachs and J. A. Kyger, *Light-Water-Reactor Safety Research Program: Quarterly Progress Report,* ANL-77-59 (April-June 1977).

A-12.17. S. L. Seiffert, *Power-Cooling-Mismatch Test Series Test PCM-3 Postirradiation Examination*, TREE-NUREG-1187 (December 1977).

A-12.18. J. A. Dearien et al, *FRAP-S3: Analytical Models and Input Manual – FRAP-S3: A Computer Code for the Steady State Analysis of Oxide Fuel Rods – Volume 1*, TFBP-TR-164 (October 1977).

A-12.19. M. J. F. Notley and J. R. MacEwan, *The Effect of UO_2 Density of Fission Product Gas Release and Sheath Expansion*, Report AECL-2230 (1965).

A-12.20. M. J. F. Notley et al, *Zircaloy Sheathed UO_2 Fuel Elements Irradiated at Values of $\int kd\theta$ Between 40 and 83 W/cm*, AECL-1676 (December 1962).

A-12.21. C. E. Beyer and C. R. Hann, *Prediction of Fission Gas Release from UO_2 Fuel*, BNWL-1875, Battelle Northwest Laboratories (November 1974).

A-12.22. W. R. Smalley, *Saxton Core II Fuel Performance Evaluation Part I: Materials*, WCAP-3385-56, Part I (September 1971).

A-12.23. R. G. Bellamy and Rich, "Grain-Boundary, Gas Release in High Burnup Uranium Dioxide," *Journal of Nuclear Materials, 33* (1969).

A-12.24. R. M. Carroll, "Fission Product Release from UO_2," *Nuclear Safety, 4(1)* (1962).

12.6 Bibliography

The following list of reference material is pertinent to a literature review and was consulted by the FGASRL code developer.

(1) W. R. Smalley, *Evaluation of Saxton Core III Fuel Materials Performance*, WCAP-3385-57 (1974).

(2) K. Taketani and M. Ichikawa, "Fuel Irradiation Experiments by JAERI for Light Water Reactors," *Contribution to Crest Specialist Meeting, Sacley, France, October 21-24, 1973.*

(3) W. E. Bailey et al, "Effect of Temperature and Burnup on Fission-Gas Release in Mixed Oxide Fuel," *Journal of the American Ceramic Society, 49* (1970).

(4) I. Devold, *A Study of the Temperature Distribution in UO_2 Reactor Fuel Elements*, AE-318 (1968).

(5) M. F. Lyons et al, *UO_2 Fuel Rod Operation with Gross Central Melting*, GEAP-4262 (1963).

(6) R. M. Berman et al, *Irradiation Behavior of Zircaloy-Clad Fuel Rods Containing Dished End UO_2 Pellets*, WAPD-TM-629 (July 1967).

(7) J. T. Engle and H. B. Meieran, *Performance of Fuel Rods Having 97 Percent Theoretical Density UO_2 Pellets Sheathed in Zircaloy-4 and Irradiated at Low Thermal Ratings*, WAPD-TM-631 (July 1968).

(8) N. Fuhrman et al, *Evaluation of Fuel Rod Performance in Maine Yankee Core I, Task C*, EPRI-NP-218 (November 1976).

(9) *Light-Water-Reactor Safety Research Program: Quarterly Progress Report, April-June 1975*, ANL-75-58 (June 1975).

(10) Jean-Claude Janvier et al, *Irradiation of Uranium Dioxide in a Resistant Cladding Effects of Initial Diametral Gap on Overall Behavior*, CEA-R-3358 (October 1967).

(11) J. P. Stora and P. Chenebault, *Programme Cyrano-Mesure de l'integrale de conductibilite thermique d' UO_2 fritte jusqu'a 2,300°C – Evolution des gaz de fission a puissance constante*, CEA-R-3618 (1968).

(12) R. D. MacDonald and A. S. Bain, *Irradiation of Zircaloy-2 Clad UO_2 to Study Sheath Deformation*, AECL-1685 (1962).

(13) M. D. Freshly, "Mixed-Oxide Fuel Irradiations in the Plutonium Recycle Test Reactor," *Nuclear Technology, 15* (August 1972) pp 138, 141, 169, 172-173.

(14) F. H. Megerth et al, *Zircaloy-Clad UO_2 Fuel Rod Evaluation Program*, GEAP-10371 (June 1971).

(15) T. B. Burley and M. D. Freshley, "Internal Gas Pressure Behavior in Mixed-Oxide Fuel Rods During Irradiation," *Nuclear Applications and Technology, 9* (August 1970).

(16) M. J. F. Notley et al, *Measurements of the Fission Product Gas Pressures Developed in UO_2 Fuel Elements During Operation*, AECL-2662 (1966).

(17) E. De Meulemeester et al, "Review of Work Carried Out by BELGONUCLEAIRE and CEA on the Improvement and Verification of the Computer Code with the Aid of In-Pile Experimental Results," *British Nuclear Energy Society International Conference on Nuclear Fuel Performance, October 15-19, 1973.*

13. CESIUM AND IODINE RELEASE (CESIOD)

(D. L. Hagrman)

Cesium and iodine isotopes are produced in significant quantities by the fission of U-235 and Pu-239. The quantities of these isotopes released in the fuel rod pellet-cladding gap are of interest in describing possible chemical attack of cladding by fission products and fission product release in the event of cladding integrity loss.

The CESIOD subcode was programmed as a result of publications containing the assumption that all the iodine and cesium produced by fission is available to attack zircaloy cladding[A-13.1]. The subcode does not provide a realistic description of iodine release because it does not consider chemical interactions between iodine and other fission products. It is, however, some improvement over the assumption that all of the fission-produced iodine is released from a ceramic oxide fuel matrix and attacks the cladding. In view of the uncertainty caused by chemical interactions, no effort has been made to incorporate the latest values of fission yields or nonfission effects on isotope production.

13.1 Summary

Cesium and iodine releases are modeled separately for each isotope since the decay rates of the different isotopes require separate treatments. Moreover, the approximations used to model long- and short-lived isotopes are different. Long-lived isotopes accumulate in the fuel in proportion to the burnup and are released by diffusion to the gap. Short-lived isotopes achieve a steady state in which their rate of release to the fuel rod pellet-cladding gap is balanced by the decay rates of the isotopes in the fuel and in the pellet-cladding gap. The concentration of short-lived isotopes is proportional to the rate of burnup.

The input data required by the subcode are:

(1) Net fuel burnup (MWs/kg fuel)

(2) Net time at operating temperature (s)

(3) Maximum fuel temperature attained during operation prior to the constant-power (or time) step considered (K)

(4) Burnup increase during the constant-power (or time) step considered (MWs/kg fuel)

(5) Duration of the step considered (s)

(6) Fuel density (kg/m^3)

(7) Fuel temperature at the mesh point considered (K)

(8) Percent PuO_2 content of the fuel (used only to define fuel melt).

For the long-lived iodine and cesium isotopes (I-127, I-129, Cs-133, Cs-135, and Cs-137) the expression used to predict the release of the isotope to the fuel rod gap is

$$R_i = C_i B \left(\frac{4}{a} \sqrt{\frac{Dt}{\pi}} - \frac{3Dt}{2a^2} \right) \qquad \text{(A-13.1)}$$

where

R_i = the specific isotope yield (kg of the isotope/kg fuel)

C_i = the fission yield of the isotope (kg of isotope/MWs), this constant is provided by the subroutine

B = burnup (MWs/kg fuel)

D = diffusion coefficient for the isotope in fuel (m^2/s), this constant is calculated by the subroutine from the input maximum temperature

a = diffusion distance for gas release (m), this constant is estimated by the subroutine from the input fuel density

t = time since the beginning of irradiation (s).

For the short-lived iodine and cesium isotopes produced in quantity in light water reactor fuels (I-131, I-132, I-133, I-134, I-135, and Cs-138) the expression used to predict the quantity of the isotope available in the steady state condition is

$$R_i = \frac{\Delta B}{\Delta t} \frac{1}{1.732 \times 10^{10}} Y_i M_i \frac{\frac{3}{a}\sqrt{D\lambda_i}}{\left(\frac{3}{a}\sqrt{D\lambda_i} + \lambda_i\right)\lambda_i} \qquad \text{(A-13.2)}$$

where the symbols not defined in conjunction with Equation (A-13.1) are

ΔB = burnup during the step considered (MWs/kg fuel)

Δt = duration of the burnup step considered (s)

Y_i = fission yield of isotope i (atoms of i_{th} isotope/fission)

M_i = mole weight of the isotope (kg/mol)

λ_i = the decay constant of the isotope (s^{-1}).

The diffusion coefficient in Equations (A-13.1) and (A-13.2) is calculated with an exponential expression which is truncated at low temperatures:

$$D = 6.6 \times 10^{-6} \exp\left(\frac{-36\,086}{T}\right) \quad \text{for } T > 1134.054 \text{ K}$$

$$D = 10^{-19} \quad \text{for } T \leq 1134.054 \text{ K} \qquad \text{(A-13.3)}$$

where

T = the maximum fuel temperature (K) when D is used in Equation (A-13.1) or

T = the current fuel temperature when D is used in Equation (A-13.2).

The diffusion distance, a, in Equations (A-13.1) and (A-13.2) is obtained from an empirical fit to measured values of effective open surface areas per volume of fuel as determined from gas absorption experiments. The correlation is presented in Section A-13.2.1.

The basis for the model is discussed in Section A-13.2. Section A-13.3 is a review of the predictions of the model. A listing of the CESIOD subcode is provided in Section A-13.4.

13.2 Development of the Model

At fuel temperatures above 1000 K, gaseous fission products become sufficiently mobile to migrate out of the UO_2 lattice in a complex series of processes[A-13.2, A-13.3]. In the simplest useful approach to model this process the fuel is treated as a collection of spheres, Fick's law is used to describe the diffusion of fission gases from the UO_2 lattice, and the surface area per fuel volume (or, the effective radius of the spheres) is estimated from gas absorption measurements. This simple approach has been adopted to model the release of cesium and iodine to the fuel rod gap because a more sophisticated treatment of the diffusion process is not justified without including complex chemical effects. Exact models for the amounts of cesium and iodine in the rod gap would require consideration of the chemical interactions of cesium, iodine, zirconium, and oxygen as well as the details of the diffusion and gas release mechanism.

13.2.1 Derivation of the Mathematical Expressions. The equation which describes the release of stable or long-lived isotopes by diffusion is[A-13.3, A-13.4]

$$\frac{\partial \eta}{\partial t} = -D\nabla^2\eta + Y\frac{df}{dt} \qquad \text{(A-13.4)}$$

where

η = number of atoms of an isotope per unit volume of fuel (atoms/m^3)

t = time (s)

D = diffusion coefficient for the isotope (m^2/s)

Y = fission yield of the isotope (atoms of isotope/fission)

$\frac{df}{dt}$ = fission rate of the fuel [(atoms fissioned/m^3)/s], determined from the burnup rate.

Since $Y\frac{df}{dt}$ is the production rate of the isotopes, the fraction of the isotopes released from a sphere of radius "a" (a = diffusion distance for gas release) is[A-13.3]

$$R = \frac{4\pi a^2 \int_0^t \left(-D\frac{\partial \eta}{\partial r}\right)_a dt'}{\frac{4}{3}\pi a^3 Y \int_0^t \frac{df}{dt'} dt'} \qquad \text{(A-13.5)}$$

where

R = the released fraction (unitless)

$(-D\frac{\partial \eta}{\partial r})_a$ = the radial flux of isotope atoms obtained from Equation (A-13.5) (atoms/m^2).

The other symbols have been defined previously.

Equations (A-13.4) and (A-13.5) can be combined to find an expression for R. The resultant expression is[A-13.4, A-13.5]

$$R = 1 - \frac{6a^2}{90Dt} + \frac{6a^2}{\pi^4 Dt}\left[\sum_{m=1}^{\infty} \frac{1}{m^4} \exp\left(\frac{-m^2\pi^2 Dt}{a^2}\right)\right] \quad \text{(A-13.6)}$$

or, for $\frac{\pi^2 Dt}{a^2} < 1.0$

$$R \simeq \frac{4}{a}\sqrt{\frac{Dt}{\pi}} - \frac{3Dt}{2a^2} . \quad \text{(A-13.7)}$$

Multiplication of the release fraction (R) by the fission yield of an isotope (C_i) and the burnup (B) produces Equation (A-13.1) for the specific isotope yield of a long-lived isotope into the fuel rod gap. Expressions used for the diffusion coefficient (D) and the diffusion distance required for gas release (a) are discussed in Section A-13.2.2.

When the isotope is short-lived, the decay rate of the material in the UO_2 matrix and in the fuel rod gap must be considered. The rate of change of the number of isotope atoms in the fuel rod gap is the difference between the rate of isotope release from the UO_2 matrix and the rate of decay of isotope atoms in the gap.

$$\frac{dM}{dt} = \nu N - \lambda M \quad \text{(A-13.8)}$$

where

M = number of isotope atoms in the fuel rod gap

t = time (s)

ν = escape rate coefficient (s^{-1})

N = number of isotope atoms in the UO_2 matrix

λ = decay constant of the isotope (s^{-1}).

The rate of change of the number of isotope atoms inside the UO_2 matrix is the production rate less the rate of isotope release from the UO_2 matrix and the rate of decay of isotope atoms in the UO_2 matrix

$$\frac{dN}{dt} = Y \frac{df}{dt} V - \nu N - \lambda N \qquad \text{(A-13.9)}$$

where

V = volume of the UO_2 matrix (m^3)

and the other symbols have been defined in conjunction with Equations (A-13.4) and (A-13.8).

When the steady state is achieved $\frac{dM}{dt}$ and $\frac{dN}{dt}$ are both zero. Equations (A-13.8) and (A-13.9) thus imply that the steady state value of M (denoted by M_s) is

$$M_s = \frac{\nu}{\lambda} \frac{Y \frac{df}{dt} V}{\nu + \lambda} . \qquad \text{(A-13.10)}$$

If the escape rate coefficients were known experimentally, Equation (A-13.10) would be sufficient to model the number of atoms of each isotope in the gap. Since sufficient experimental data are not available, the approach used for this model is to estimate an escape rate coefficient with the collection-of-spheres idea (Section 13.2.1) used for long-lived isotopes. The diffusion equation for the steady state (constant isotope concentration in the UO_2 matrix) is

$$0 = D\nabla^2 \eta + Y \frac{df}{dt} - \lambda \eta \qquad \text{(A-13.11)}$$

where

η = number of atoms of the isotope per unit volume of fuel (atoms/m^3)

t = time (s)

D = diffusion coefficient for the isotope (m^2/s)

Y = fission yield of the isotope (atoms of isotope/fission)

$\frac{df}{dt}$ = fission rate of the fuel [(atoms fissioned/m^3)/s]

λ = decay constant of the isotope (s^{-1}).

The quantity of interest for finding the escape rate coefficient (ν) is the ratio, F, of the isotope release rate to the isotope production rate. This ratio for a sphere of radius a is

$$F = \frac{4\pi a^2 \left(-D \frac{\partial \eta}{\partial r}\right)_a}{\frac{4}{3}\pi a^3 \, Y \frac{df}{dt}} . \qquad \text{(A-13.12)}$$

Equations (A-13.11) and (A-13.12) can be combined to find an expression for F. The resultant expression is[A-13.3]

$$F = \frac{3D}{\lambda a^2}\left[\left(\frac{\lambda a^2}{D}\right)^{1/2} \coth \left(\frac{\lambda a^2}{D}\right)^{1/2} - 1\right] . \qquad \text{(A-13.13)}$$

For $\frac{\lambda a^2}{D} >> 1.0$. Equation (A-13.10) reduces to the form used in the model described here:

$$F \simeq \frac{3}{a}\sqrt{\frac{D}{\lambda}} . \qquad \text{(A-13.14)}$$

The ratio, F, of the isotope release rate to the isotope production rate may also be written in terms of the escape rate coefficient

$$F = \frac{\nu N}{Y \frac{df}{dt} V} . \qquad \text{(A-13.15)}$$

If the steady state form of Equation (A-13-9) is used to find an approximate expression for N when $\lambda >> \nu$, and if the resultant expression for N is substituted into Equation (A-13.15) one finds

$$F \approx \frac{\nu}{\lambda} . \qquad \text{(A-13.16)}$$

Finally, from Equations (A-13.14) and (A-13.16)

$$\nu \approx \frac{3}{a}\sqrt{D\lambda} \qquad \text{(A-13.17)}$$

which is the result obtained by Belle[A-13.4].

Substitution of the approximate value of ν from Equation (A-13.7) into Equation (A-13.10), conversion of the fission rate $\frac{df}{dt}$ to a burnup rate, and conversion of M to kilograms of isotope per m^3 of fuel results in Equation (A-13.2). This equation is the one used in the model for the release of the short-lived isotopes of cesium and iodine.

13.2.2 Correlations for Material Constants Used in the Model. The correlations used to obtain the diffusion coefficient for isotopes in the fuel, the diffusion radius for gas release, and the fission yields of the isotopes modeled are discussed in this section.

The correlation for the diffusion coefficient used with the model [Equation (A-13.3)] is the empirical expression recommended by Belle on page 512 of his review[A-13.4]. Recent results have not been used because improved values for the diffusion coefficient are simply not relevant until the improved techniques developed for the modeling of Xe and Kr can be adopted to provide significant improvement of the basic expressions for the release of cesium and iodine.

The correlation used for the diffusion radius is

$$a = 3\,(TD)\;10^{[20.61\;-\;TD\;(67.9\;-\;46TD)]} \qquad \text{(A-13.18)}$$

where

TD = fractional fuel density (ratio of actual density to theoretical density).

The expression is taken from the correlation for free surface area per unit volume recommended in Figure 9.18 of Belle's review[A-13.4]. Belle's figure is reproduced as Figure A-13.1 of this report. The data are estimates based on gas absorption measurements

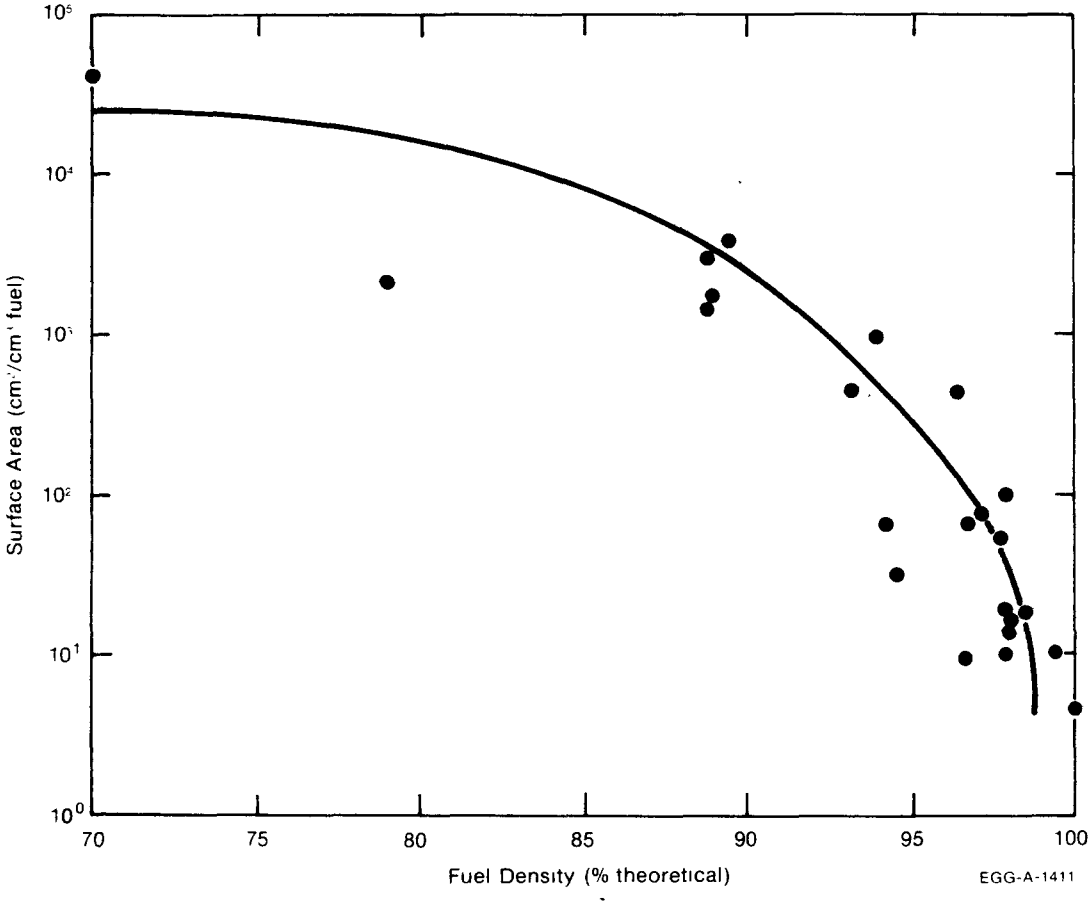

Fig. A-13.1 Surface area per unit volume recommended by Belle.

with fuels of varying theoretical densities. Although considerable scatter is exhibited by the estimates, the trend toward smaller free surface area with higher density fuel is clear.

Expressions for the fission yields of the various isotopes are based on the early work of Katcoff[A-13.6]. Since the products of fission have excess neutrons, they undergo a series of β^- decays in chains of constant mass number until a stable isotope is produced. The decay chains for mass numbers 127 and 138 and thermal fission of U-235 are reproduced in Figures A-13.2 and A-13.3. Decay chains for thermal fission of Pu-239 are similar. The

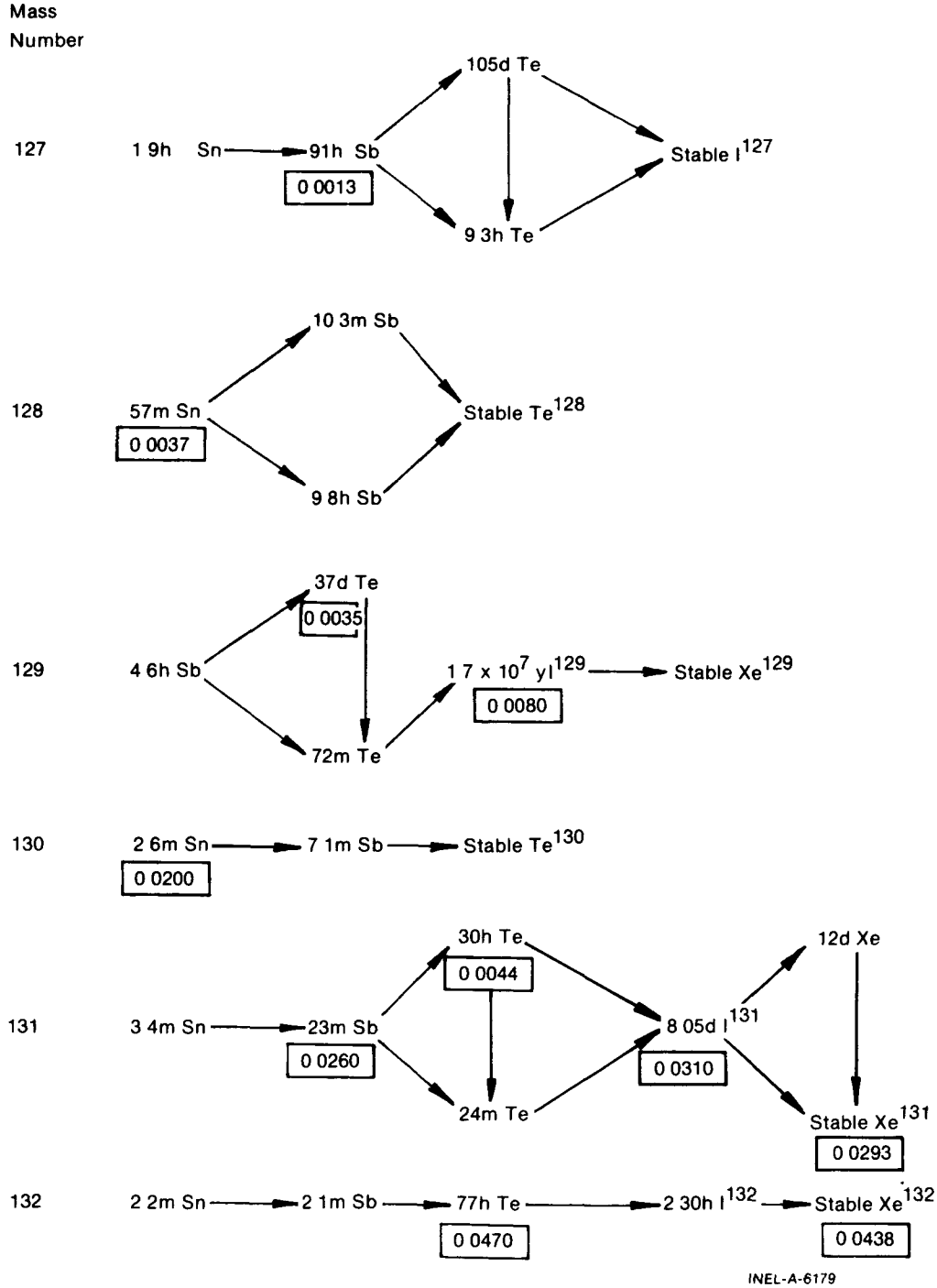

Fig. A-13.2 Fission chains for mass numbers 127 to 132 from the thermal fission of U-235.

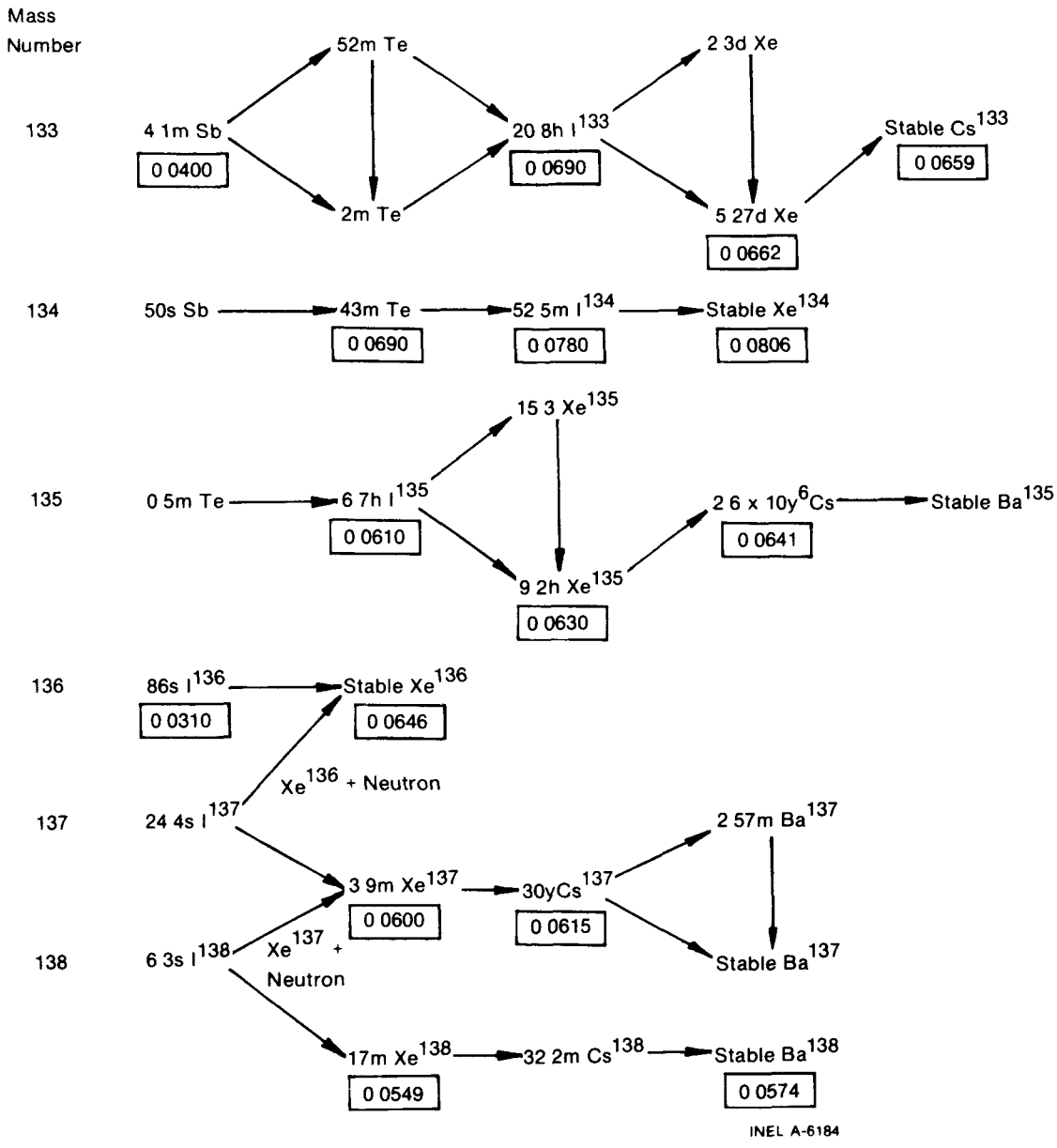

Fig. A-13.3 Fission chains for mass numbers 133 to 138 from the thermal fission of U-235.

half-life of each chain member is indicated in front of the element's chemical symbol, and the chain yields in yield per fission are indicated by the box symbol at those points in the chain where they have been measured. At points where significant neutron decay exists, such as the decay of I-137 by neutron emission to form Xe-136, the yields vary significantly along the chain.

The yields for stable and long-lived isotopes of iodine and cesium are summarized in Table A-13.I. Conversion of yields given in Figures A-13.2 and A-13.3 to yields in kilograms of isotope per megawatt seconds for use in Equation (A-13.1) is given in Equation (A-13.19)

$$C_i = \frac{Y_i \, M_i \, 10^{-2}}{N_a \, E_f} \qquad \text{(A-13.19)}$$

TABLE A-13.I

FISSION YIELDS OF STABLE AND LONG-LIVED ISOTOPES OF IODINE AND CESIUM

Isotope	Half-Life	Yield (10^{-2})	Yield (kg/MWs)
I-127	Stable	0.13	9.50×10^{-12}
I-129	1.7×10^{7} years	0.8	5.94×10^{-11}
Cs-133	Stable	6.59	5.04×10^{-10}
Cs-135	2.6×10^{6} years	6.41	4.98×10^{-10}
Cs-137	30 years	6.15	4.85×10^{-10}

where

C_i = the fission yield of isotope i (kg/MW fission energy)

Y_i = fission yield of isotope i (atoms of i_{th} isotope/fission)

M_i = mole weight of isotope i (kg/mol)

N_a = Avogadro's number (atoms/mol)

E_f = energy per fission (MWs/fission).

The fission yields for short-lived isotopes of iodine and cesium are summarized in Table A-13.II. Since the conversion from atoms released per fission to kilograms released per burnup rate is contained explicitly in Equation (A-13.2), the fission yields for short-lived isotopes are not converted to units of kg/MWs fission energy as they were in Table A-13.I.

Several short-lived isotopes of iodine and cesium are not included in Table A-13.II or in the model. They are iodine isotopes with mass numbers 130, 128, and 126 or less; cesium isotopes with mass numbers 136, 134, and 132 or less. These isotopes are not included because the relevant decay chain is terminated by a stable isotope before they are produced or because they have very short half-lives. For those with very short half-lives the large decay constants obtained from the relation will cause very small amounts of the isotope in question to be present in the steady state.

$$\lambda_i = \frac{\ln 2}{\text{half-life}} \qquad \text{(A-13.20)}$$

TABLE A-13.II

FISSION YIELDS OF SHORT-LIVED ISOTOPES
OF IODINE AND CESIUM

Isotope	Half-Life	Decay Constant (s^{-1})	Yield (unitless fraction)
I-131	8.05 days	9.97×10^{-7}	3.1×10^{-2}
I-132	2.30 hours	9.17×10^{-6}	4.3×10^{-2}
I-133	20.8 hours	8.37×10^{-5}	6.9×10^{-2}
I-134	52.5 minutes	2.22×10^{-4}	7.9×10^{-2}
I-135	6.7 hours	2.87×10^{-5}	6.1×10^{-2}
Cs-138	32.2 minutes	3.59×10^{-4}	6.6×10^{-2}

13.3 Model Calculations and Comparison with Experimental Data

Figure A-13.4 illustrates model predictions for iodine and cesium releases from 97% dense fuel as a function of fuel temperature for a burnup of 2.6×10^5 MWs/kgU at one tenth year and a burnup rate of 3×10^6 MWs/kgU per year. The mass of cesium released is approximately ten times as large as the mass of iodine released and both quantities increase rapidly as the fuel temperature increases. Two of the important components of the iodine release are shown separately. I-129 is a long-lived isotope so its contribution will increase with increasing burnup. I-131 is a short-lived isotope whose concentration in the pellet-cladding gap is a function of the burnup rate. The step increase in the release of I-129 (from 0.8×10^{-5} kg I-129/kg fuel to 1.1×10^{-5} kg I-129/kg fuel) at 3100 K is caused by the assumption that total release of long-lived isotopes occurs at fuel melt.

Figure A-13.5 illustrates the change in the predicted release of iodine when fuels of varying density are considered. Total iodine release at 1400 K for a burnup of 2.6×10^6 MWs/kgU at one year and a burnup rate of 3×10^6 MWs/kgU per year are shown for fuel densities ranging between 90 and 98% of theoretical density. Although the factor of 40 decrease in the iodine release in this density range is large, the most important variable in determining the release of iodine (and cesium) is the temperature of the fuel.

No direct measurements of the amount of cesium and iodine outside of the fuel matrix have been found. However, rod average escape rate coefficients determined from resin and loop water activities have been reported from tests of defected rods[A-13.7]. The escape rate coefficients reported and the escape rate coefficients predicted by

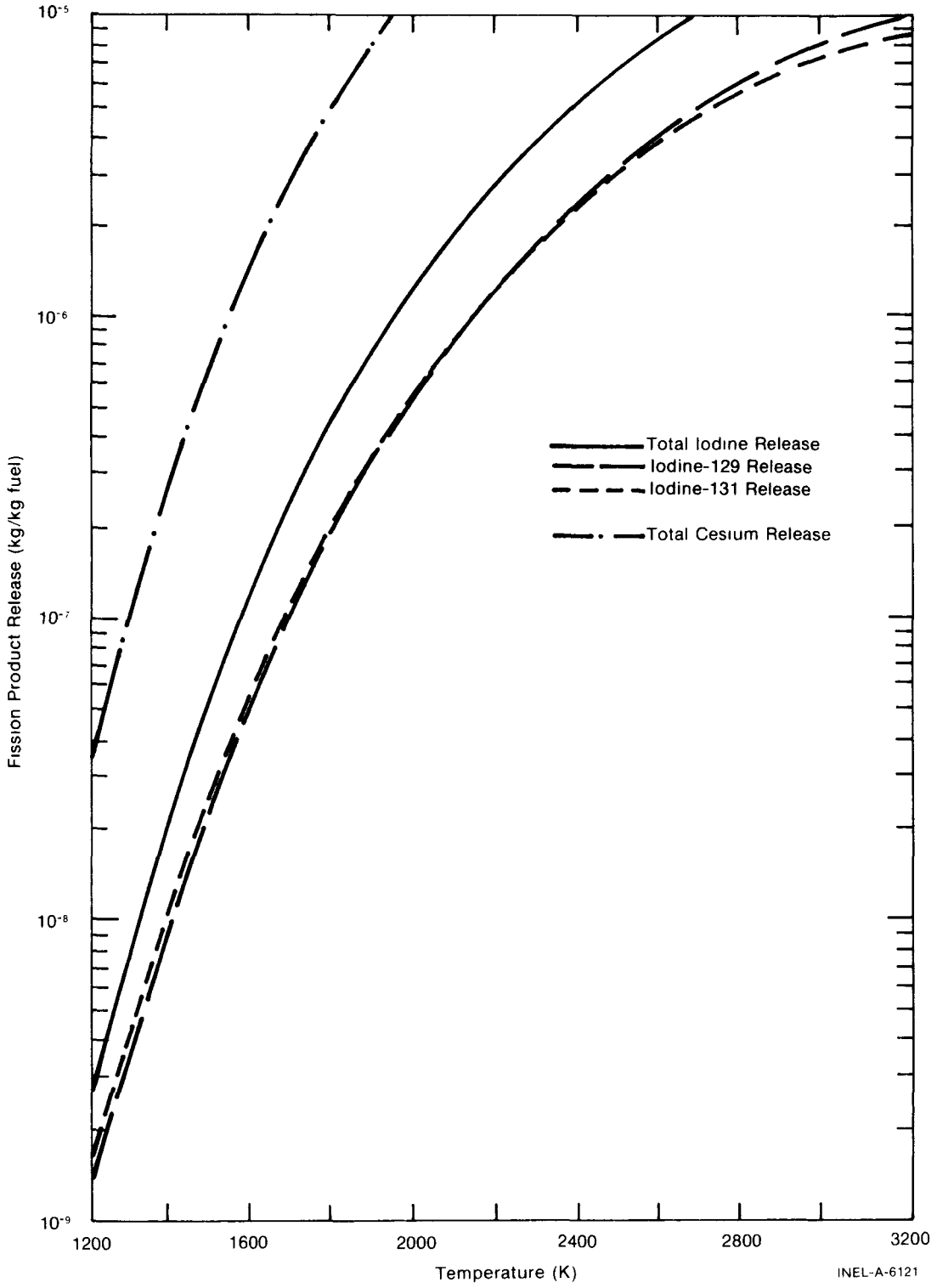

Fig. A-13.4 Model calculations for iodine and cesium releases from 97% dense fuel as a function of temperature for a burnup of 2.6 x 10^5 MWs/kgU at 0.1 year and a burnup rate of 3 x 10^6 MWs/kgU per year.

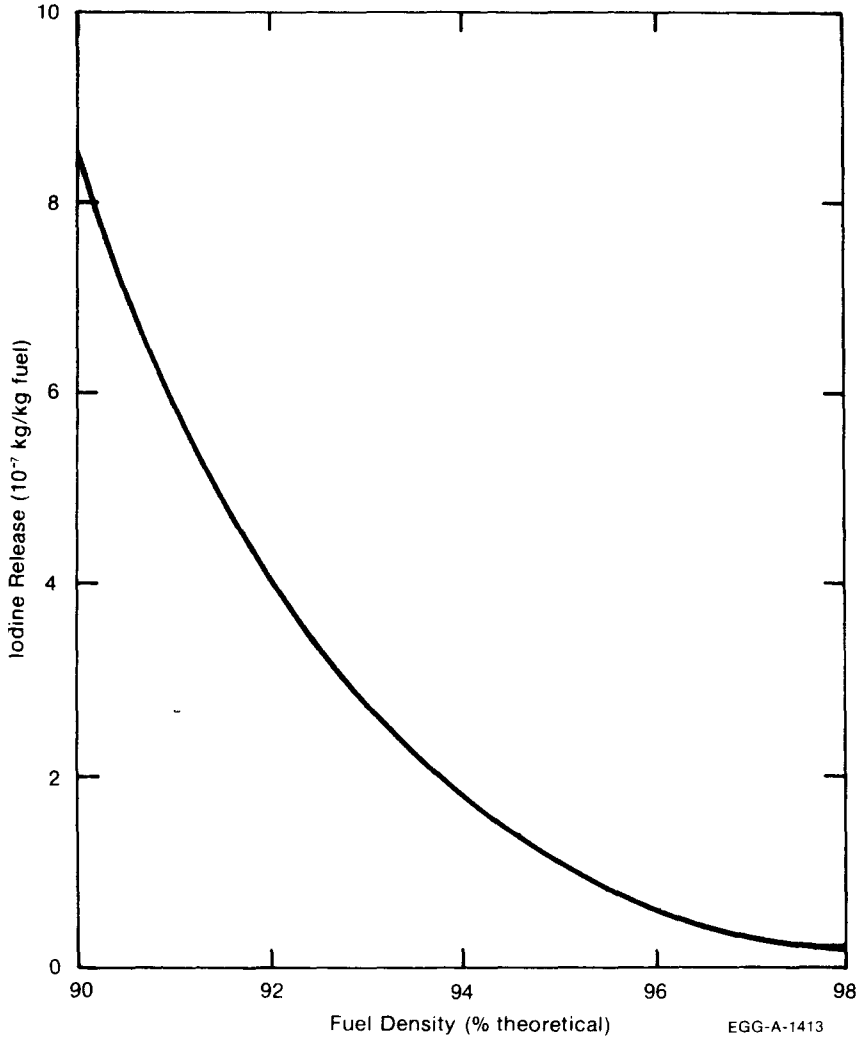

Fig. A-13.5 Iodine release from fuels of varying density with 2×10^6 MWs/kgU burnup at one year and a burnup rate of 3×10^6 MWs/kgU per year.

Equation (A-13.14) are compared in Table A-13.III. Since the temperature distribution within the fuel rods is not known, estimates of the fuel centerline temperature and the rod average diffusion constant suggested by Belle on page 521 of his review[A-13.4] have been used in Equation (A-13.13). Belle's expression is

$$\sqrt{D_t} = \frac{1}{6}\left(\sqrt{D_c} + 4\sqrt{D_m} + \sqrt{D_s}\right) \qquad \text{(A-13.21)}$$

where

D_t = the average diffusion coefficient for the rod (m^2/s)

D_s = the diffusion constant at the fuel surface temperature (m^2/s)

TABLE A-13.III

COMPARISON OF MODEL PREDICTIONS FOR ESCAPE RATE COEFFICIENTS WITH VALUES REPORTED IN WCAP-TM-159

Centerline Temperature (K)	Fuel Density	Isotope	Escape Rate Coefficient (ν) WCAP-TM-159	Escape Rate Coefficient (ν) Model
685	0.934	I-131	6.14×10^{-10}	1.62×10^{-10}
685	0.934	I-131	1.63×10^{-9}	1.62×10^{-10}
685	0.934	I-133	2.21×10^{-9}	1.48×10^{-9}
685	0.934	Cs-138	9.42×10^{-9}	4.17×10^{-10}
1535	0.934	I-131	6.08×10^{-10}	1.87×10^{-9}
1535	0.934	I-131	1.90×10^{-9}	1.87×10^{-9}
1535	0.934	I-131	1.78×10^{-9}	1.87×10^{-9}
1535	0.934	I-131	3.83×10^{-9}	1.70×10^{-8}
1535	0.934	Cs-138	2.23×10^{-7}	4.78×10^{-7}
1535	0.934	Cs-138	1.63×10^{-7}	4.78×10^{-7}
1800	0.974	I-131	2.24×10^{-9}	1.54×10^{-9}
1800	0.974	I-131	5.78×10^{-10}	1.54×10^{-9}
1800	0.974	I-131	2.93×10^{-10}	1.54×10^{-9}
1800	0.974	Cs-138	1.28×10^{-7}	3.96×10^{-7}
1800	0.974	Cs-138	6.58×10^{-8}	3.96×10^{-7}

D_m = the diffusion constant at the median fuel temperature (m^2/s)

D_c = the diffusion constant at the fuel center temperature (m^2/s).

The model underpredicts the low temperature escape rates, possibly because diffusion is not the dominant release mechanism at 685 K. At the two higher temperatures the model predictions for I-131 fall within the scatter of the data, the one value measured for I-133 is one fifth the value predicted by the model and the model predictions for Cs-138 are about 3 times the values reported.

13.4 Cesium and Iodine Release Subcode CESIOD Listing

The FORTRAN subcode CESIOD is listed in Table A-13.IV.

13.5 References

A-13.1. R. Van der Schaff, *Zirconium in Nuclear Applications,* ASTM-STP551 (August 1974), pp 479-494.

A-13.2. J. Rest, "Modeling of Fission-Gas Behavior During Steady-State and Transient Conditions," *Light-Water-Reactor Safety Research Program: Quarterly Progress Report April-June 1976,* ANL-76-87, pp 8-17.

A-13.3. D. R. Olander, *Fundamental Aspects of Nuclear Reactor Fuel Elements,* ERDA Report TID-26711-P1 (April 1976).

A-13.4. J. Belle (ed.), *Uranium Dioxide: Properties and Nuclear Applications,* TID-7546 U.S. Government Printing Office Washington, D.C. (1961).

A-13.5. A. H. Booth, *A Method of Calculating Fission-Gas Diffusion from UO_2 Fuel and Its Application to the X-2-f Loop Test,* CRDC-721 (September 1957).

A-13.6. S. Katcoff, "Fission Product Yields from Neutron-Induced Fission," *Nucleonics 18, 11,* (November 1960) pp 201-208.

A-13.7. R. Ehrenrerch, *Radiochemistry of the PWR Fuel Material Cycling Tests (WAPD-29-1 and -2) in the WAPD-29 VH-3 Loop of the Materials Testing Reactor,* WAPD-TM-159 (November 1959).

TABLE A-13.IV

LISTING OF THE CESIOD SUBCODE

```
C
C
      SUBROUTINE CESIOD(TIME  ,FTMAX ,DELBU ,DTIME ,FTEMP ,FRADEN,
     #                  CS    ,ROID)
C
      DIMENSION ROID(8),CS(5)
C
C     CESIOD CALCULATES THE AMOUNTS OF CESIUM AND IODINE ISOTOPES
C     AVAILABLE TO THE FUEL ROD GAP
C
C     ROID(1) = OUTPUT NET SPECIFIC RELEASE OF IODINE
C               (KG IODINE /KG FUEL)
C     ROID(2) = OUTPUT NET SPECIFIC RELEASE OF IODINE 127
C               (KG IODINE 127/KG FUEL) STABLE
C     ROID(3) = OUTPUT NET SPECIFIC RELEASE OF IODINE 129
C               (KG IODINE 129/KG FUEL) HALF LIFE 1.72E07 YEARS
C     ROID(4) = OUTPUT NET SPECIFIC RELEASE OF IODINE 131
C               (KG IODINE 131/KG FUEL) HALF LIFE 8.05 DAYS
C     ROID(5) = OUTPUT NET SPECIFIC RELEASE OF IODINE 132
C               (KG IODINE 132/KG FUEL) HALF LIFE 2.3 HOURS
C     ROID(6) = OUTPUT NET SPECIFIC RELEASE OF IODINE 133
C               (KG IODINE 133/KG FUEL) HALF LIFE 21 HOURS
C     ROID(7) = OUTPUT NET SPECIFIC RELEASE OF IODINE 134
C               (KG IODINE 134/KG FUEL) HALF LIFE 52 MINUTES
C     ROID(8) = OUTPUT NET SPECIFIC RELEASE OF IODINE 135
C               (KG IODINE 135/KG FUEL) HALF LIFE 6.7 HOURS
C     CS(1)   = OUTPUT NET SPECIFIC RELEASE OF CESIUM
C               (KG CESIUM/KG FUEL)
C     CS(2)   = OUTPUT NET SPECIFIC RELEASE OF CESIUM 133
C               (KG CESIUM 133/KG FUEL) STABLE
C     CS(3)   = OUTPUT NET SPECIFIC RELEASE OF CESIUM 135
C               (KG CESIUM 135/KG FUEL) HALF LIFE 2.9E06 YEARS
C     CS(4)   = OUTPUT NET SPECIFIC RELEASE OF CESIUM 137
C               (KG CESIUM 137/KG FUEL) HALF LIFE 33 YEARS
C     CS(5)   = OUTPUT NET SPECIFIC RELEASE OF CESIUM 138
C               (KG CESIUM 138/KG FUEL) HALF LIFE 32.2 MINUTES
C     FTMAX   = OUTPUT MAXIMUM TEMPERATURE ATTAINED BY THE MESHPOINT
C               DURING OPERATION TO THE END OF THE BURNUP STEP
C               CONSIDERED (K)
C
C     TIME    = INPUT TIME AT OPERATING TEMPERATURE AT END OF STEP (S)
C     FTMAX   = INPUT MAXIMUM TEMPERATURE ATTAINED BY THE MESHPOINT
C               DURING OPERATION PRIOR TO BURNUP STEP CONSIDERED
C     DELBU   = INPUT BURNUP DURING THE STEP CONSIDERED (MW-S/KG METAL)
C     DTIME   = INPUT DURATION OF THE BURNUP STEP CONSIDERED (S)
C     FTEMP   = INPUT FUEL MESHPOINT TEMPERATURE (K)
C     FRADEN  = INPUT FRACTIONAL FUEL DENSITY (RATIO OF ACTUAL
C               DENSITY TO THEORETICAL DENSITY)
C
C     THE EQUATIONS USED IN THIS SUBROUTINE ARE BASED ON DATA FROM
C     (1) J.     BELLE    URANIUM DIOXIDE, PROPERTIES AND NUCLEAR
C                         APPLICATIONS (JULY 1961)
C     (2) S.     KATCOFF  NUCLEONICS 16 (APRIL 1958) PP 78-85
C     (3) S.     KATCOFF  NUCLEONICS 18 (NOV 1960) PP 201-208
C     (4) B. F.  RIDER,   A SURVEY AND EVALUATION OF THERMAL FISSION
C                         YIELDS FOR U-235, PU-239, U-233, AND PU-241
C                         GEAP-5356 (SEPT 1967)
C
C     THIS MODEL IS FOR LWR REACTORS ONLY
C
C     CESIOD WAS CODED BY D. L. HAGRMAN JANUARY 1977
C
      COMMON  /PHYPRO   / FTMELT,FHEFUS,CTMELT,CHEFUS,CTRANB,
     #                    CTRANE,CTRANZ,FDELTA,BU    ,COMP
C
C
      DATA YUID2 / 9.50E-12/, YUID3 / 5.94E-11/,  YUID4 / 3.10E-02 /
      DATA YUID5 / 4.30E-02/, YUID6 / 6.90E-02/,  YUID7 / 7.90E-02 /
      DATA YUID8 / 6.10E-02/
      DATA YUCS2 / 5.04E-10/, YUCS3 / 4.98E-10/,  YUCS4 / 4.85E-10/
      DATA YUCS5 / 6.60E-02/
      DATA ALMDI4/ 9.97E-07/, ALMDI5/ 9.17E-06/,   ALMDI6/ 8.37E-05/
      DATA ALMDI7/ 2.22E-04/, ALMDI8/ 2.87E-05/,  ALMDC5/ 3.59E-04 /
C
C     UNITS CONVERSION
```

TABLE A-13.IV (continued)

```
C
      B = BU* 0.88
      FISR = DELBU*0.88/(1.732E10* DTIME)
C
      IF(FTEMP .GT. FTMAX) FTMAX = FTEMP
C
CC    FIND DIFFUSION RADIUS AND DIFFUSION CONSTANTS
C
      A = 3.0 * FRADEN * (10.0**(20.61 - FRADEN*(67.90-46.0*FRADEN)))
      DMAX = 6.6E-06/ EXP(3.6086E04/FTMAX)
      DNOW = 6.6E-06/ EXP(3.6086E04/FTEMP)
      IF(FTMAX .LE. 1134.054) DMAX = 1.0E-19
      IF(FTEMP .LE. 1134.054) DNOW = 1.0E-19
C
CC    FIND ESCAPE RATE COEFFICIENTS
C
      ANUI4 = 3.0 *((DNOW * ALMDI4)**0.5)/A
      ANUI5 = 3.0 *((DNOW * ALMDI5)**0.5)/A
      ANUI6 = 3.0 *((DNOW * ALMDI6)**0.5)/A
      ANUI7 = 3.0 *((DNOW * ALMDI7)**0.5)/A
      ANUI8 = 3.0 *((DNOW * ALMDI8)**0.5)/A
      ANUC5 = 3.0 *((DNOW * ALMDC5)**0.5)/A
C
CCC   FIND SPECIFIC RELEASE FOR LONG LIVED ISOTOPES
C
CCC   CHECK FOR FUEL MELT
C
      IF (FTMAX .LT. FTMELT) GO TO 20
   21 ROID(2) = YUID2 * B
      ROID(3) = YUID3 * B
      CS(2)   = YUCS2 * B
      CS(3)   = YUCS3 * B
      CS(4)   = YUCS4 * B
      GO TO 25
C
CCCC  SPECIFIC RELEASES WITHOUT MELT FOLLOW
C
CCCC  CHECK TO SEE IF RELEASE FRACTION IS GREATER THAN ONE
C
   20 F = 2.257 * ((DMAX * TIME)**0.5) / A - 1.5 * DMAX * TIME/(A**2)
      IF (F .GT. 1.0) GO TO 21
C
      ROID(2) = YUID2 * B * F
      ROID(3) = YUID3 * B * F
      CS(2)   = YUCS2 * B * F
      CS(3)   = YUCS3 * B * F
      CS(4)   = YUCS4 * B * F
C
CCC   FIND SPECIFIC RELEASES FOR SHORT LIVED ISOTOPES
C
   25 ROID(4) = FISR * 131 * YUID4 * ANUI4 /((ANUI4 + ALMDI4)* ALMDI4)
      ROID(5) = FISR * 132 * YUID5 * ANUI5 /((ANUI5 + ALMDI5)* ALMDI5)
      ROID(6) = FISR * 133 * YUID6 * ANUI6 /((ANUI6 + ALMDI6)* ALMDI6)
      ROID(7) = FISR * 134 * YUID7 * ANUI7 /((ANUI7 + ALMDI7)* ALMDI7)
      ROID(8) = FISR * 135 * YUID8 * ANUI8 /((ANUI8 + ALMDI8)* ALMDI8)
      CS(5)   = FISR * 138 * YUCS5 * ANUC5 /((ANUC5 + ALMDC5)*ALMDC5)
C
CCC   CALCULATE SUMS
C
     #ROID(1) = ROID(2) + ROID(3) + ROID(4) + ROID(5) + ROID(6)
     #         + ROID(7) + ROID(8)
      CS(1)   = CS(2) + CS(3) + CS(4) + CS(5)
      RETURN
      END
```

APPENDIX B

CLADDING MATERIAL PROPERTIES

APPENDIX B

CLADDING MATERIAL PROPERTIES

Twenty material properties of light water reactor fuel rod cladding (zircaloy -2 or -4) have been modeled for inclusion in MATPRO – Version 11. Modeling approaches range from a choice of experimental data with linear interpolation or extrapolation or both to a semiempirical expression suggested by theory.

All twenty properties are modeled as a function of the cladding temperature. In addition, such variables as flux, fluence, cold work, stress, time, and impurity content are used as arguments. Each model description characterizing a material property includes a listing of a FORTRAN subcode to enable users to independently program and utilize the correlations in the description. Some of the subcodes are interconnected, employing in part identical or very similar correlations (for example, strain versus stress, stress versus strain, and cladding ultimate strength), and some subcodes call upon others such as the physical properties subcode, PHYPRO, but all information needed to run a given subcode is contained in this handbook.

1. CLADDING SPECIFIC HEAT (CCP), AND THE EFFECT OF HYDRIDE SOLUTION ON CLADDING SPECIFIC HEAT (CHSCP)

(D. L. Hagrman)

Two function subcodes are used to describe the apparent specific heat of the zircaloys. The first, CCP, describes the true specific heat at constant pressures of the alloys and the second, CHSCP, describes the apparent addition to the specific heat because of energy used in solution of hydrides present in zircaloys. Uncertainty estimates have been determined and are returned by each function.

CCP requires only temperature as input, while CHSCP requires both temperature and the concentration of hydrogen. The hydrogen concentration may be supplied directly by the user or it may be calculated by the MATPRO function CHUPTK.

1.1 Specific Heat

For the alpha phase of the zircaloys (temperature less than 1090 K), CCP returns linear interpolations for the points listed in Table B-1.I. (Linear interpolation is computed by the subcode POLATE described in Appendix D.)

The table is based on precise data taken by Brooks and Stansbury[B-1.1] with a zircaloy-2 sample that had been vacuum annealed at 1075 K to remove hydrogen. The

TABLE B-1.I

SPECIFIC HEAT AS A FUNCTION OF TEMPERATURE - ALPHA PHASE

Temperature (K)	Specific Heat (J/kg·K)
300	281
400	302
640	331
1090	375

standard error[a] of the CCP interpolation (that is, the precision of the fit to the data) was based on the 90 points in the data base and was found to be temperature dependent. For the 57 data points between 300 and 800 K it is 1.1 J/kg·K and between 800 and 1090 K it is 2.8 J/kg·K.

For temperatures from 1090 to 1300 K (where Brooks and Stansbury do not report results) values of specific heat proposed by Deem and Eldridge[B-1.2] are adopted by MATPRO. The Deem and Eldridge values, shown in Table B-1.II, are based on their measurements of enthalpy and temperature which provide considerably less precise specific heat data than the results of Brooks and Stansbury[B-1.1].

The standard error as estimated by the Deem and Eldridge data in the region 1090 through 1310 K is 10.7 J/kg·K. Again, this standard error is a measure only of the precision of the fit since only a single data source is employed.

The specific heat as calculated by CCP is shown in Figure B-1.1. Figures B-1.2 and B-1.3 also show the CCP prediction using an expanded scale at lower temperatures and illustrating the base data from Brooks and Stansbury as well as alpha phase (300 – 1090 K) data from Deem and Eldridge that were not used in constructing CCP.

At temperatures up to 900 K, the Brooks and Stansbury data agree with the Deem and Eldridge data within 3%. Above the alpha + beta to beta transformation temperature (about 1250 K) and up to about 1320 K, a constant value of 355.7 J/kg·K was reported by Deem and Eldridge. This value agrees well with a value of 365.3 reported by Coughlin and King[B-1.3] for pure beta zirconium.

[a] The standard error is estimated for a data set by the expression: [sum of squared residuals/(number of residuals minus number of constants used to fit the data)] $^{1/2}$.

TABLE B-1.II

SPECIFIC HEAT AS A FUNCTION OF TEMPERATURE - BETA PHASE

Temperature (K)	Specific Heat (J/kg·K)
1093	502
1113	590
1133	615
1153	719
1173	816
1193	770
1213	619
1233	469
1248	356

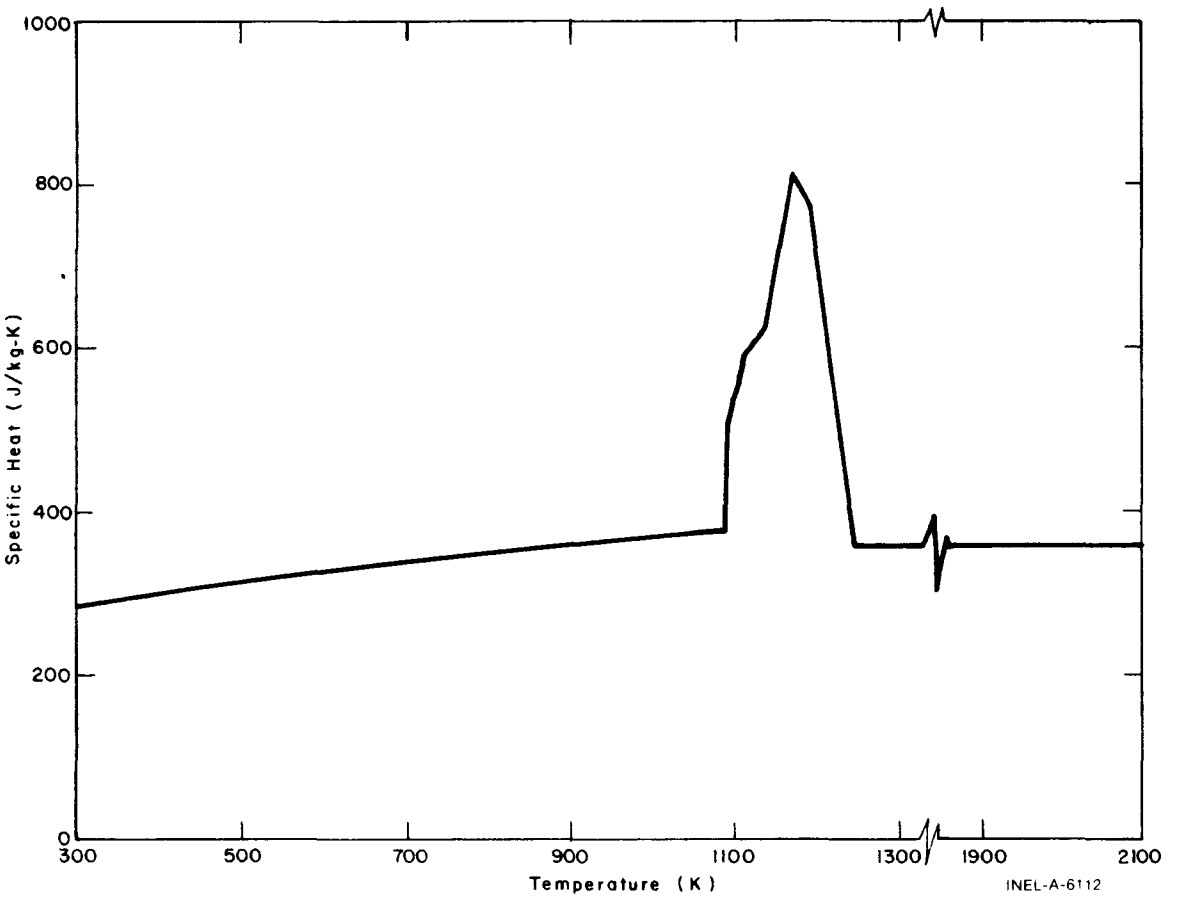

Fig. B-1.1 Specific heat of zircaloys as calculated by CCP for alloys without hydrides.

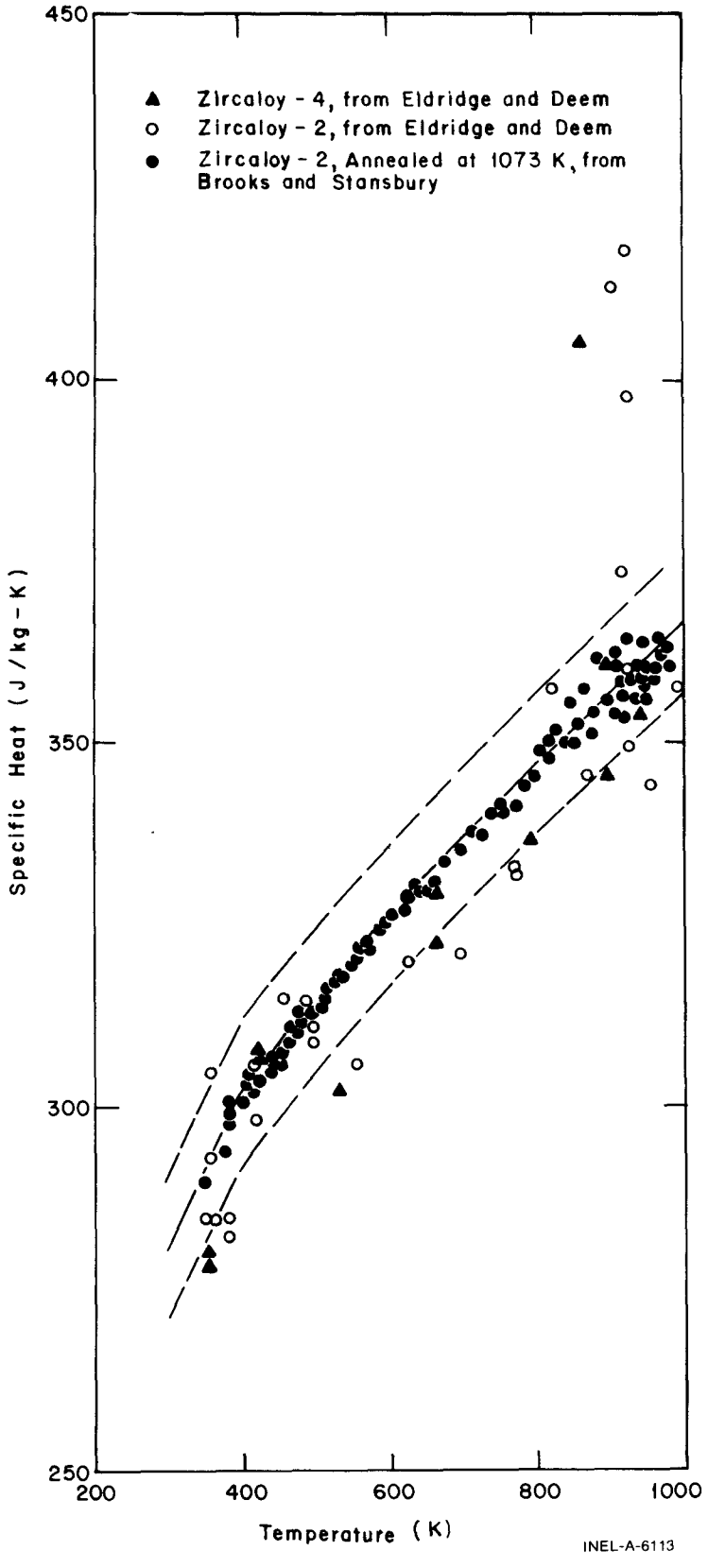

Fig. B-1.2 Available data, MATPRO expressions for specific heat, and estimated uncertainty of the MATPRO expression for temperatures from 300 to 1000 K.

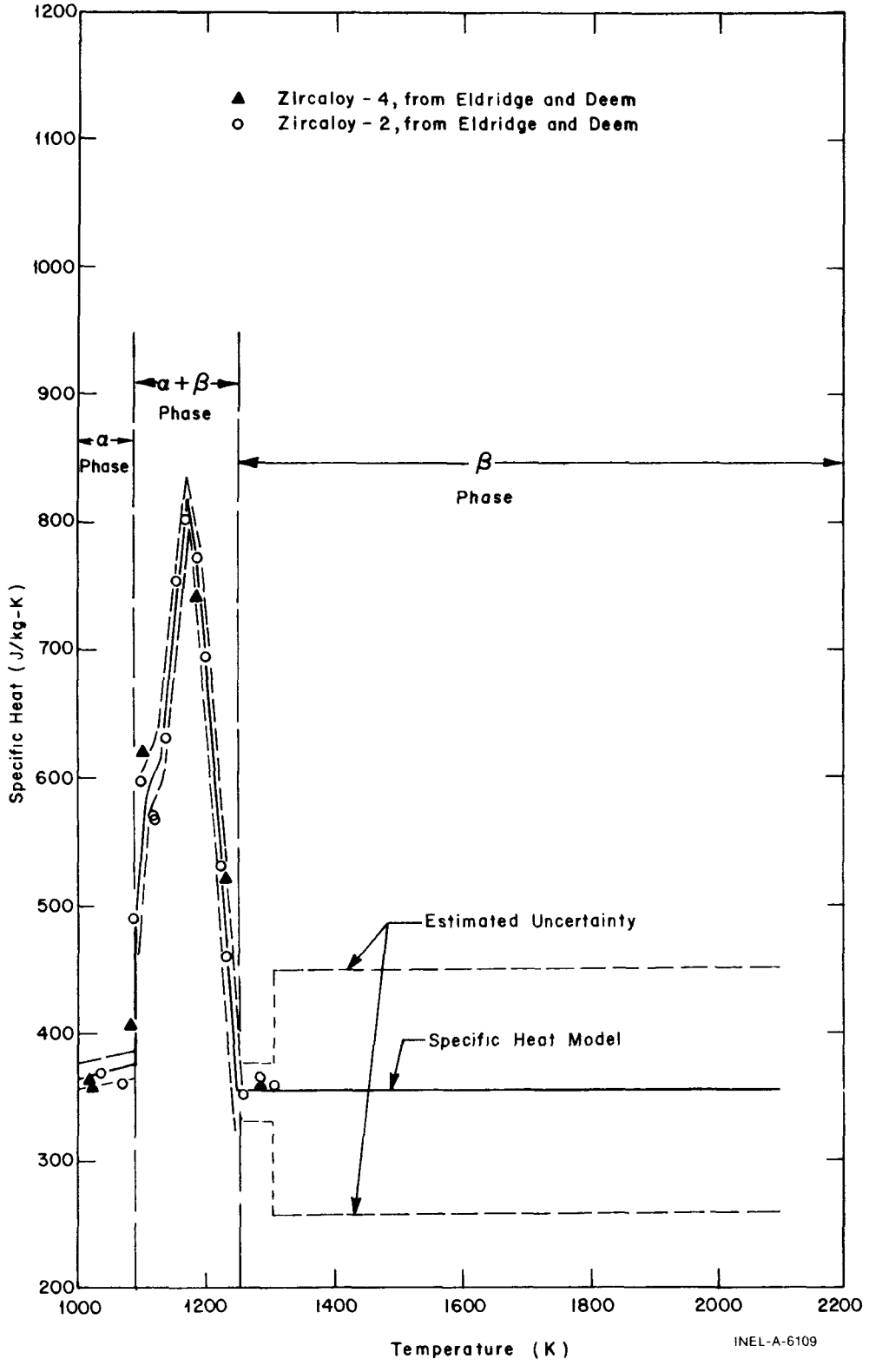

Fig. B-1.3 Available data, MATPRO expressions for specific heat, and estimated uncertainty of the MATPRO expression for temperatures from 1000 to 2100 K.

The estimated standard error of CCP for data consisting of a random sample from all zircaloy-2 and zircaloy-4 claddings is also shown in Figures B-1.2 and B-1.3. This standard error is discussed in Section B-1.3 after the discussion of the effect of hydride solution.

1.2 Effect of Hydride Solution

Values returned by the function CHSCP for the addition to the specific heat due to energy used in solution of hydrides are:

$$CHSCP = \frac{A\ B\ C}{T^2}\left[\exp\left(\frac{-B}{T}\right)\right]\left[\exp\left(\frac{T - TSOL}{0.02\ TSOL}\right) + 1\right]^{-1} \qquad \text{(B-1.1)}$$

where

CHSCP = addition to true specific heat due to hydride solution (J/kg·K)

T = cladding temperature (K)

TSOL = Minimum temperature for complete solution of the hydrogen concentration as determined with Equation (B-1.2) (K)

A = 1.332×10^5 (ppm hydrogen)

B = 4.401×10^3 (K)

C = 45.70 (J/kg·ppm hydrogen).

TSOL, the minimum temperature required for complete solution of the hydrogen in the cladding, is determined from the expression

$$TSOL = \frac{B}{\ln\left(\frac{A}{H}\right)} \qquad \text{(B-1.2)}$$

where

A and B = constants given in conjunction with Equation (B-1.1)

H = hydrogen concentration (ppm by weight).

A value of H can be determined with the function CHUPTK (Appendix B, Section 15).

Equations (B-1.1 and B-1.2) are based on data reported by Scott[B-1.4] for zirconium with and without intentional additions of hydrogen. For temperatures below 830 K, Scott (Figure 16 of Reference B-1.4) finds the logarithm of the terminal solubility of hydrogen in zirconium to be proportional to temperature. Below the temperature TSOL, when hydrides are not completely dissolved

$$\text{Energy to dissolve hydride} = \text{constant} \times \exp\left(\frac{\text{negative constant}}{\text{temperature}}\right). \quad \text{(B-1.3)}$$

It is assumed in this expression that the terminal solubility will be attained as long as undissolved hydrogen is present. The heat of solution per gram atom of hydrogen may be taken as the average of two values given by Scott (Table VII of Reference B-1.4). Equation (B-1.1) results from differentiation of this expression with respect to temperature and multiplication by the empirical factor $\left[\exp\left(\frac{T - TSOL}{0.02\ TSOL}\right) + 1\right]^{-1}$ to express the fact that the data do not show an instant termination of hydride solution with increasing temperature.

Figure B-1.4 illustrates Scott's data for two samples of zirconium iodide and a single sample of zirconium intentionally doped with approximately 300 ppm of hydrogen. The two zirconium iodide samples apparently contained some hydrogen and were fit by the MATPRO correlation [Equation (B-1.2)] assuming they contained 28 ppm hydrogen. Figure B-1.4 also shows the MATPRO correlation assuming 300 ppm hydrogen and the curve recommended by Scott for pure zirconium.

1.3 Uncertainties in Specific Heat Predictions

The systematic error (the estimated variation between values obtained with different samples) is larger than the imprecision in the base data of CCP and CHSCP.

The standard error of CCP, reflecting the systematic error for a random sample of cladding zircaloys, is estimated to be ±10 J/kg·K (±3%) in the alpha phase. This value is based on the difference between values of specific heat estimated by Deem and Eldridge from their data[B-1.2] and the more precise data from one sample of zircaloy-2 used by MATPRO. In the alpha-beta phase region and the beta region to 1300 K a roughly estimated standard error of 25 J/kg·K is assigned to CCP, based on the decreased precision of the measurements and on the lack of confirming data in this temperature range. Above 1300 K, the only basis for the assumed constant value of specific heat is the prediction of the Debye model of heat capacity for temperatures above the Debye temperature. Since no data are available, a standard error of ±100 J/kg·K is listed.

The basis for the estimate of the standard error of CHSCP over a random sample of cladding zircaloys is shown in Figure B-1.5, which compares MATPRO predictions for several concentrations of hydrogen with a curve published by Brooks and Stansbury[B-1.1] for the specific heat of zircaloy-2 tested without prior heat treatment. The unpublished data are reported to be within 1% of this curve and the MATPRO prediction is as far as 3%

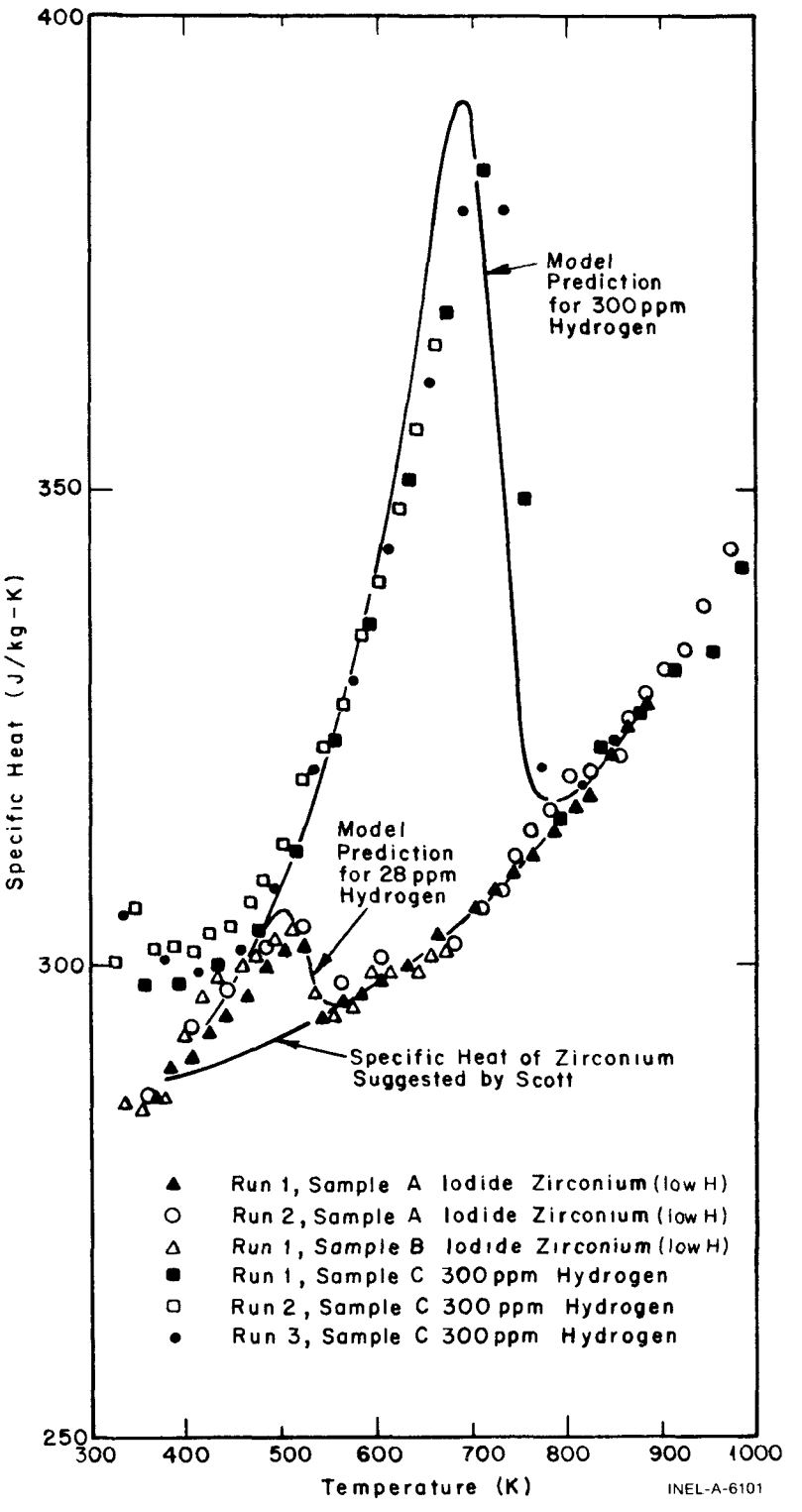

Fig. B-1.4 Data base for MATPRO prediction of the effect of hydride solution on specific heat, Scott's proposed curve for the specific heat of zirconium, and the MATPRO predictions for the effect of 28 and 300 ppm of hydrogen on the specific heat curve.

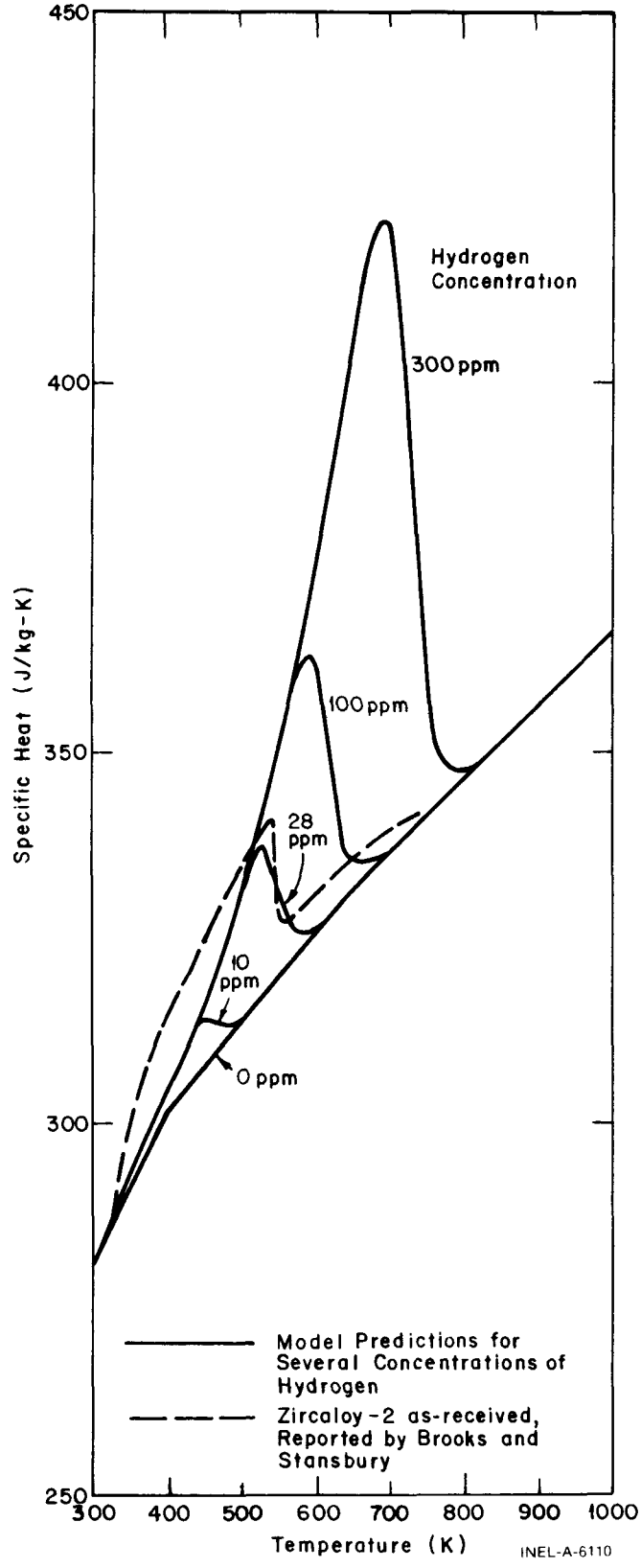

Fig. B-1.5 MATPRO predictions for apparent zircaloy specific heat for several hydrogen concentrations compared with the curve measured with as-received zircaloy-2.

(10 J/kg·K) below the reported curve. Since the prediction of CCP in this temperature range is based on precise data (±1.1 J/kg·K) taken with vacuum annealed samples of the same alloy, shown by a dashed line in Figure B-1.5, most of the discrepancy (between the dashed line and the 28 ppm H solid line) is presumed to be due to errors inherent in the application by CHSCP of the zirconium data of Scott to zircaloys. A standard error of 50% in the hydrogen-induced increment to apparent specific heat is therefore assigned to the model.

The uncertainties in CCP are summarized in Table B-1.III.

TABLE B-1.III

UNCERTAINTIES IN SPECIFIC HEAT OF ZIRCALOY

Temperature Range	Standard Error in CPP
300 < T < 1090 K	±10 J/kg·K
1090 < T < 1300 K	±25 J/kg·K
T < 1300 K	±100 J/kg·K

1.4 Cladding Specific Heat Subcode CCP, and Effect of Hydride Solution Subcode CHSCP Listings

The FORTRAN subcodes CCP and CHSCP are listed in Tables B-1.IV and B-1.V, respectively.

1.5 References

B-1.1. C. R. Brooks and E. E. Stansbury, "The Specific Heat of Zircaloy-2 from 50 to 700°C," *Journal of Nuclear Materials, 18* (1966) p 223.

B-1.2. E. A. Eldridge and H. W. Deem, *Specific Heats and Heats of Transformation of Zircaloy-2 and Low Nickel Zircaloy-2,* USAEC BM1-1803 (May 31, 1967).

B-1.3. J. P. Coughlin and E. G. King, "High-Temperature Heat Contents of Some Zirconium-Containing Substances," *Journal of the American Chemical Society, 72* (1950) p 2262.

B-1.4. J. Scott, *A Calorimetric Investigation of Zirconium, Titanium, and Zirconium Alloys from 60 to 960°C,* Ph.D. Thesis, University of Tennessee (1957).

TABLE B-1.IV

LISTING OF THE CCP SUBCODE

```
C
C
      FUNCTION CCP(CTEMP)
C
C     CCP CALCULATES THE SPECIFIC HEAT AT CONSTANT PRESSURE
C     FOR ZIRCALOYS
C
C     CCP   = OUTPUT CLADDING SPECIFIC HEAT AT CONSTANT
C             PRESSURE (J/KG-K)
C     CTEMP = INPUT CLADDING TEMPERATURE (K)
C
C     THIS CODE IS BASED ON DATA FROM
C     (1) C. R. BROOKS AND E. E. STANSBURY, "THE SPECIFIC HEAT
C     OF ZIRCALOY-2 FROM 50 TO 700 C"  JOURNAL OF NUCLEAR
C     MATERIALS 18 (1966) P 233
C     (2) E. A. ELDRIDGE AND H. W. DEEM, SPECIFIC HEATS AND HEATS
C     OF TRANSFORMATION OF ZIRCALOY-2 AND LOW NICKEL ZIRCALOY-2
C     BMI-1803 (MAY 31, 1967)
C
C     CONVERSION FROM J/(KG*K) TO CAL/(G*C) IS
C     2.390060-4 (CAL/(G*C))/(J/(KG*K))
C
C     ESTIMATED STANDARD ERROR OF THE PREDICTION OF
C     CCP FOR THE SPECIFIC HEAT OF ZIRCALOY CLADDING
C     SAMPLES -- (SUM OF SQUARED RESIDUALS/(NUMBER OF
C     RESIDUALS*DEGREES OF FREEDOM))**0.5 -- IS
C     (1)FOR TEMPERATURE LESS THAN 1090 K, 10J/KG-K)
C     (2)FOR TEMPERATURE 1090 K TO 1300 K , 25J/KG-K)
C     (3)FOR TEMPERATURE ABOVE 1300 K , 100J/KG-K)
C
C     CCP CODED BY R. L. MILLER OCTOBER 1974 AND MODIFIED BY
C     D. L. HAGRMAN MAY 1976
C
      COMMON       / LACEMDL   / MAXIDX, EMFLAG
      DIMENSION    EMFLAG(1)
C
      DIMENSION CPDATA(26)
      DATA CPDATA/   281.,  300.,   302.,  400.,   331.,640.,
     *   375.,1090.,   502.,1093.,   590.,1113.,   615.,1133.,
     *   719.,1153.,   816.,1173.,   770.,1213.,   619.,1213.,
     *   469.,1233.,   356.,1248. /
      DATA NPCP, IU / 13,1/
C
      DATA       ON        / 2HON    /,
     #           OFF       / 3HOFF   /,
     #           LOCIDX    /  4      /
      IF( EMFLAG(LOCIDX) .EQ. ON)  GO TO 10
C
      IF(CTEMP.GE.1248.0) GO TO 2
      CCP = POLATE(CPDATA,CTEMP,NPCP,IU)
      GO TO 20
    2 CCP = 356.
      GO TO 20
C
   10 CCP  = EMCCP (CTEMP)
   20 CONTINUE
      RETURN
      END
```

TABLE B-1.V

LISTING OF THE CHSCP SUBCODE

```
C
C
      FUNCTION CHSCP(PPMHYD,CTEMP,ICOR,ICM,DCO,DCI,TIME,WOXO,
     #               CHORG,PPMH2O,DP)
C
C     CHSCP CALCULATES THE APPARENT ADDITION TO SPECIFIC HEAT
C     BECAUSE OF ENERGY USED IN SOLUTION OF HYDRIDES PRESENT
C     IN ZIRCALOYS
C
C     CHSCP  = OUTPUT APPARENT ADDITION TO SPECIFIC HEAT BECAUSE
C              OF HYDRIDES PRESENT IN ZIRCALOYS (J/KG-K)
C
C     PPMHYD = INPUT CONCENTRATION OF HYDROGEN IN THE SAMPLE (PPM)
C     CTEMP  = INPUT TEMPERATURE (K)
C
C       THE FOLLOWING INPUTS ARE USED ONLY IF PPMHYD IS
C       NOT A POSITIVE NUMBER (SEE CHUPTK DESCRIPTION)
C
C     ICOR   = INPUT REACTOR CHEMISTRY INDEX
C                      .GE.2 FOR PWR
C                      .LT.2 FOR BWR
C     ICM    = INPUT CLADDING MATERIAL INDEX (2= ZIRC2, 4 = ZIRC4)
C     DCO    = INPUT CLADDING OUTSIDE DIAMETER (INCHES)
C     DCI    = INPUT CLADDING INSIDE DIAMETER (INCHES)
C     TIME   = INPUT TIME AT TEMPERATURE (S)
C     WOXO   = INPUT INITIAL OXIDE FILM WEIGHT (MG/DM**2)
C     CHORG  = INPUT INITIAL HYDROGEN CONTENT (PPM)
C     PPMH2O = INPUT FUEL WATER CONTENT (PPM)
C     DP     = INPUT FUEL PELLET DIAMETER (INCHES)
C
C     THIS CODE IS BASED ON DATA FROM
C         J. SCOTT, A CALORIMETRIC INVESTIGATION OF ZIRCONIUM,
C     TITANIUM AND ZIRCONIUM ALLOYS FROM 60 TO 960 C.  PHD THESIS
C     (UNIVERSITY OF TENNESSEE, 1957)
C
C     CHSCP CODED BY D. L. HAGRMAN MAY 1976
C
C     CONVERSION FROM J/(KG*K) TO CAL/(G*K) IS
C     2.39006D-04 (CAL/(G*C))/(J/(KG*K))
C
C     ESTIMATED STANDARD ERROR OF THE PREDICTION OF
C     CHSCP FOR THE APPARENT ADDITION TO SPECIFIC HEAT
C     BECAUSE OF ENERGY USED IN SOLUTION OF HYDRIDES PRESENT
C     IN ZIRCALOY CLADDING SAMPLES -- (SUM OF SQUARED
C     RESIDUALS/(NUMBER OF RESIDUALS*DEGREES OF FREEDOM))**0.5 --
C     IS HALF OF THE PREDICTED VALUE
C
      A = 1.332E05
      B = 4.401E03
      C = 4.570E01
      IF(PPMHYD .GT. 0.0) GO TO 20
      PPMHYD = CHUPTK(CTEMP,ICOR,ICM,DCO,DCI,TIME,WOXO,CHORG,
     #                PPMH2O,DP)
   20 T      = CTEMP
      IF(PPMHYD .LE. 0.0) PPMHYD = 1.0
      TSOL   = B/(ALOG(A/PPMHYD))
      CHSCP  = C*A*B/(T**2)* EXP(-B/T)*(1/( EXP((T-TSOL)/(TSOL/50))+1))
      RETURN
      END
```

2. CLADDING THERMAL CONDUCTIVITY (CTHCON AND ZOTCON)

(R. L. Miller)

The transfer of heat from the fuel pellet to reactor coolant depends partly on the thermal conductivity of the cladding. Accurate predictions of fuel temperatures require knowledge of both zircaloy and zirconium dioxide thermal conductivities. The former is discussed in Section B-2.1 and the latter in Section B-2.2. The FORTRAN subcodes are listed in Section B-2.3 and the references are given in Section B-2.4.

2.1 Thermal Conductivity of Zircaloy

An expression has been developed for the thermal conductivity of zircaloy-2 and -4 based on the pooled data from eight reports. This expression and the uncertainty in the correlation are presented in this section.

2.1.1 Summary. The thermal conductivity of alloys is primarily a function of temperature. Other characteristics such as residual stress levels, crystal orientation, and minor composition differences (zircaloy-2 versus zircaloy-4, for example) may have a secondary influence on thermal conductivity. Considering only temperature as the defining parameter, the thermal conductivity of zircaloy and its uncertainty are found to be:

$$k = 7.51 + 2.09 \times 10^{-2} T - 1.45 \times 10^{-5} T^2 + 7.67 \times 10^{-9} T^3 \quad \text{(B-2.1)}$$

$$\sigma_k = 1.01 \quad \text{(B-2.2)}$$

where

k = thermal conductivity of zircaloy (W/m·K)

T = temperature (K)

σ_k = standard deviation (W/m·K).

This equation predicts k very well from room temperature to the data limit of about 1800 K and may be extrapolated with some confidence to the melting point. The standard deviation of the data with respect to this correlation (σ_k) appears to be temperature independent over the data range (Figure B-2.1). Least-squares regression analysis indicates that one standard deviation for each of the constants in Equation (B-2.1) is 20 to 30% of the value of the constant.

2.1.2 Survey of Available Data. Anderson[B-2.1] reported thermal conductivity data for zircaloy-2 in the temperature range of 380 to 872 K. Chirigos et al[B-2.2] reported thermal conductivity data for zircaloy-4 between 370 and 1125 K. Feith[B-2.3] studied the thermal conductivity of zircaloy-4 between 640 and 1770 K. Lucks and Deem[B-2.4]

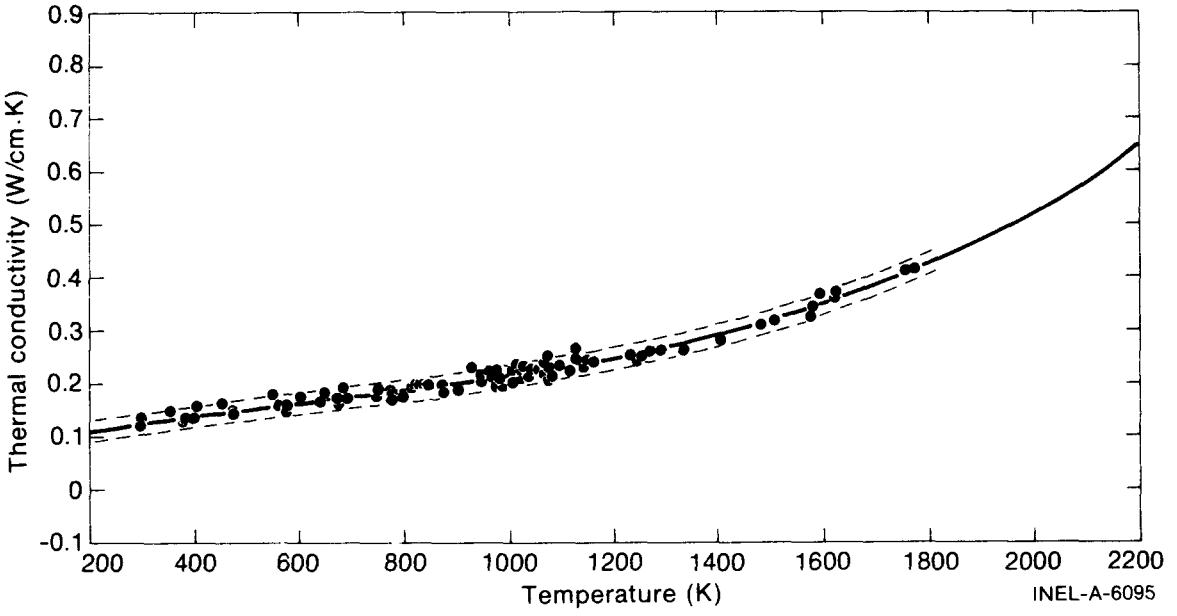

Fig. B-2.1 Thermal conductivity data, least-squares fit, and the two standard deviation limits.

measured the thermal conductivity of zircaloy-2 in the temperature range of 290 to 1075 K. Powers[B-2.5] reported three sets of thermal conductivity data for zircaloy taken from Battelle Memorial Institute (BMI) letter reports. These data cover both zircaloy-2 and -4 over temperature ranges of approximately 300 to 1000 K. Scott[B-2.6] reported the thermal conductivity of zircaloy-4 between 400 and 1060 K. Numerical values of his data were reported by Touloukian et al[B-2.7]. These data are presented in Table B-2.I.

2.1.3 Model Formulation Considering All Available Data. The data reported in Section 2.1.2 refer to zircaloy-2 and zircaloy-4 having various textures and pretest histories. The alloy chemistry and heat transfer properties of zircaloy-2 and -4 are similar enough to consider them to be a single material. The differences in thermal conductivity between the materials appears to be of the same magnitude as the statistical scatter in the data.

Texture may have an effect in the alpha phase temperature region. Zircaloy crystallizes in the hexagonal close packed configuration in the low temperature alpha phase and there may be some difference in the thermal conductivity along the prismatic and basal directions. At higher temperatures the material is body centered cubic and will not exhibit texture effects. In any case, contributions to the thermal conductivity due to texture are probably well within the scatter of the experimental data used to develop models for this property.

(1) Thermal Conductivity Model. All of the available data for thermal conductivity of zircaloy-2 and -4 were combined and analyzed using a least-squares polynomial fit of the third degree. The equation is

$$k = 7.51 + 2.09 \times 10^{-2} T - 1.45 \times 10^{-5} T^2 + 7.67 \times 10^{-9} T^3 \quad \text{(B-2.3)}$$

TABLE B-2.I

ZIRCALOY THERMAL CONDUCTIVITY DATA BASE

Temperature (K)	Experimental Thermal Conductivity (W/m·K)	Calculated Thermal Conductivity (W/m·K)	Difference Between Calculated and Experimental Thermal Conductivities	Reference	Material
380.4	13.50	13.78	-0.28	W. K. Anderson et al	Zircaloy-2
469.3	14.43	14.92	-0.49		
577.6	15.68	16.22	-0.54		
685.9	17.10	17.50	-0.40		
774.8	18.42	18.57	-0.15		
872.0	19.91	19.80	0.11		
373.2	13.60	13.69	-0.09	J. N. Chirigos et al	Zircaloy-4
473.2	14.30	14.97	-0.67		
573.2	15.20	16.17	-0.97		
673.2	16.40	17.35	-0.95		
773.2	18.00	18.55	-0.55		
873.2	20.10	19.81	0.29		
973.2	22.50	21.19	1.31		
1073.2	25.20	22.72	2.48		
1123.2	26.60	23.56	3.04		
642.2	16.30	16.98	-0.68	A. D. Feith	Zircaloy-4
678.2	16.10	17.41	-1.31		
746.2	17.60	18.22	-0.62		
780.2	18.40	18.63	-0.23		
800.2	17.70	18.88	-1.18		
819.2	19.80	19.12	0.68		
833.2	20.10	19.29	0.81		
847.2	19.60	19.47	0.13		

TABLE B-2.I (continued)

Temperature (K)	Experimental Thermal Conductivity (W/m·K)	Calculated Thermal Conductivity (W/m·K)	Difference Between Calculated and Experimental Thermal Conductivities	Reference	Material
850.2	20.00	19.51	0.49	A. D. Feith	Zircaloy-4
902.2	19.00	20.20	-1.20	(continued)	(continued)
925.2	23.10	20.51	2.59		
943.2	21.80	20.76	1.04		
946.2	20.40	20.80	-0.40		
960.2	22.10	21.00	1.10		
963.2	21.50	21.04	0.46		
969.2	21.40	21.13	0.27		
981.2	21.20	21.30	-0.10		
1005.2	22.90	21.66	1.24		
1012.2	23.60	21.76	1.84		
1019.2	21.10	21.87	-0.77		
1021.2	21.20	21.90	-0.70		
1023.2	22.60	21.93	0.67		
1025.2	23.20	21.96	1.24		
1035.2	21.80	22.12	-0.32		
1037.2	22.50	22.15	0.35		
1040.2	22.90	22.19	0.71		
1054.2	22.70	22.41	0.29		
1063.2	24.00	22.56	1.44		
1066.2	21.70	22.61	-0.91		
1079.2	21.40	22.82	-1.42		
1093.2	23.30	23.05	0.25		
1122.2	22.50	23.54	-1.04		
1128.2	24.50	23.65	0.85		

TABLE B-2.I (continued)

Temperature (K)	Experimental Thermal Conductivity (W/m·K)	Calculated Thermal Conductivity (W/m·K)	Difference Between Calculated and Experimental Thermal Conductivities	Reference	Material
1139.2	23.10	23.84	-0.74	A. D. Feith	Zircaloy-4
1152.2	24.40	24.07	0.33	(continued)	(continued)
1161.2	24.20	24.24	-0.04		
1232.2	25.30	25.60	-0.30		
1243.2	24.70	25.82	-1.12		
1253.2	25.20	26.02	-0.82		
1269.2	26.20	26.36	-0.16		
1289.2	26.50	26.79	-0.29		
1331.2	26.40	27.73	-1.33		
1401.2	27.80	29.43	-1.63		
1404.2	27.90	29.50	-1.60		
1484.2	31.10	31.67	-0.57		
1508.2	31.70	32.36	-0.66		
1576.2	32.60	34.46	-1.86		
1581.2	34.60	34.63	-0.03		
1594.2	36.80	35.05	1.75		
1624.2	36.30	36.07	0.23		
1625.2	37.30	36.10	1.20		
1755.2	41.40	41.00	0.40		
1771.2	41.80	41.66	0.14		
293.2	12.60	12.58	0.02	C. F. Lucks	Zircaloy-2
373.2	13.40	13.69	-0.29	and H. W. Deem	
473.2	14.50	14.97	-0.47		
573.2	15.60	16.17	-0.57		
673.2	17.00	17.35	-0.35		

TABLE B-2.I (continued)

Temperature (K)	Experimental Thermal Conductivity (W/m·K)	Calculated Thermal Conductivity (W/m·K)	Difference Between Calculated and Experimental Thermal Conductivities	Reference	Material
773.2	18.40	18.55	-0.15	C. F. Lucks	Zircaloy-2
873.2	19.90	19.81	0.09	and H. W. Deem	(continued)
973.2	21.50	21.19	0.31	(continued)	
1073.2	23.10	22.72	0.38		
373.2	14.11	13.69	0.42	A. E. Powers	Zircaloy-2
473.2	14.80	14.97	-0.17		
573.2	15.32	16.17	-0.85		
673.2	16.01	17.35	-1.34		
773.2	17.05	18.55	-1.50		
873.2	18.18	19.81	-1.63		
973.2	19.42	21.19	-1.77		
1073.2	20.77	22.72	-1.95		
293.2	12.55	12.58	-0.03		
373.2	13.29	13.69	-0.40		
473.2	14.37	14.97	-0.60		
573.2	15.58	16.17	-0.59		
673.2	16.88	17.35	-0.47		
773.2	18.42	18.55	-0.13		
873.2	19.91	19.81	0.10		
973.2	21.52	21.19	-0.33		
1073.2	23.02	22.72	0.30		
293.2	13.42	12.58	0.84		
373.2	13.67	13.69	-0.02		
473.2	14.16	14.97	-0.81		
573.2	15.13	16.17	-1.04		

TABLE B-2.I (continued)

Temperature (K)	Experimental Thermal Conductivity (W/m·K)	Calculated Thermal Conductivity (W/m·K)	Difference Between Calculated and Experimental Thermal Conductivities	Reference	Material
673.2	16.39	17.35	-0.96	A. E. Powers (continued)	Zircaloy-4 (continued)
773.2	18.00	18.55	-0.55		
873.2	20.17	19.81	0.36		
973.2	22.55	21.19	1.36		
403.2	15.60	14.08	1.52	D. B. Scott and Y. S. Touloukian et al	Zircaloy-4
452.1	16.30	14.70	1.60		
476.5	14.50	15.01	-0.51		
546.5	18.30	15.85	2.45		
557.6	15.80	15.99	-0.19		
602.6	17.60	16.52	1.08		
649.9	18.50	17.03	1.47		
682.1	19.20	17.45	1.75		
694.3	17.10	17.60	-0.50		
753.2	18.90	18.30	0.60		
770.3	18.90	18.51	0.39		
812.1	19.60	19.03	0.57		
826.5	20.10	19.21	0.89		
982.1	19.70	21.32	-1.62		
1000.9	20.30	21.59	-1.29		
1058.1	21.70	22.48	-0.78		

where

k = zircaloy thermal conductivity (W/m·K)

T = temperature of cladding (K).

This relation and the data are shown in Figure B-2.1.

(2) Uncertainty in Model. The standard deviation of the data with respect to Equation (B-2.3) is 1.01 W/m·K. Thirty-two of the points fall outside plus or minus one standard deviation from the curve. Four points fall outside plus or minus two standard deviations (Figure B-2.1). The standard deviations of the coefficients of Equation (B-2.3) are about 20 to 30% of the absolute value of the coefficients.

The standard deviation is small enough so that the user may have considerable confidence in the model. Jensen[B-2.8] performed a parametric analysis of several variables involved in estimation of fuel and cladding temperatures. Both steady state and transient analyses showed that variations of ±20% resulted in calculated cladding temperature variations of about 2.8 K. Fuel centerline temperatures are more sensitive to cladding thermal conductivity and showed variations of 28 K. Similar findings were reported by Korber and Unger[B-2.9].

2.2 Thermal Conductivity of Zirconium Dioxide

Kingery et al[B-2.10] reported the thermal conductivity of zirconium dioxide stabilized with calcium oxide over the temperature range 100 to 1400°C. A least-squares analysis of his data resulted in the correlation.

$$k = 1.96 - 2.41 \times 10^{-4} T + 6.43 \times 10^{-7} T^2 - 1.95 \times 10^{-10} T^3 \quad \text{(B-2.4)}$$

where

k = zirconium dioxide thermal conductivity (W/m·K)

T = temperature (K).

This correlation and its supporting data are shown in Figure B-2.2. Equation (B-2.4) is used in the ZOTCON subroutine for calculating zirconium dioxide thermal conductivity.

Maki[B-2.11] and Lapshov and Bashkatov[B-2.12] have also reported the thermal conductivity of zirconium dioxide films. Maki's data, presented in Table B-2.II cover a much smaller temperature range, show a strong temperature dependence, and generally exhibit

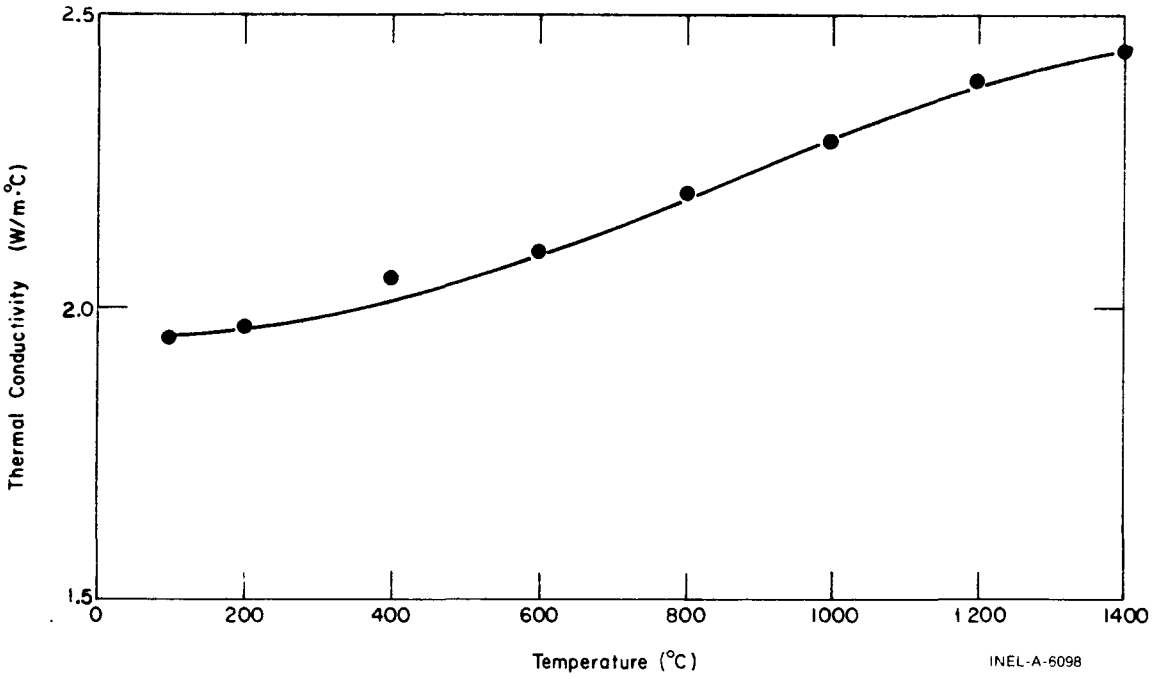

Fig. B-2.2 Thermal conductivity of zirconium dioxide as a function of temperature as calculated by the ZOTCON subcode.

larger values of thermal conductivity than the data of Kingery et al. Lapshov and Bashkatov experimented with films formed by plasma sputtering of zirconium dioxide on tungsten substrates. Their data, shown in Figure B-2.3 cover the range of 300 to 1500°C, and exhibit much greater scatter. They are substantially smaller than those of both References B-2.10 and B-2.11. The reason for the discrepancy between the data of Lapshov and Bashkatov and that of Kingery et al and Maki may be due to the fact that the sputtered or sprayed coatings are quite porous, poorly consolidated, and not very adherent to the tungsten substrate.

2.3 Cladding Thermal Conductivity Subcodes CTHCON and ZOTCON Listings

FORTRAN listings of the CTHCON and ZOTCON subcodes are given in Tables B-2.III and B-2.IV, respectively.

2.4 References

B-2.1. W. K. Anderson, C. J. Beck, A. R. Kephart, and J. S. Theilacker "Zirconium Alloys," *Reactor Structural Materials: Engineering Properties as Affected by Nuclear Reactor Service,* ASTM-STP-314, (1962) pp 62-93.

B-2.2. J. N. Chirigos et al, "Development of Zircaloy-4," *Fuel Element Fabrication,* New York: Academic Press, 1961 pp 19-55.

B-2.3. A. D. Feith, *Thermal Conductivity and Electrical Resistivity of Zircaloy-4,* GEMP-669 (October 1966).

TABLE B-2.II

THERMAL CONDUCTIVITY OF ZIRCONIUM DIOXIDE FROM MAKI[B-2.11]

Specimen	Linear Heat Rate (kW/m)	Coolant Temperature (K)	Temperature Inside Tube (K)	Apparent Thermal Conductivity (W/m·K)
2	8.08	383.5	415.9	0.76
	16.78	413.3	446.8	5.14
	29.25	473.5	502.6	6.73
	29.36	522.1	545.5	16.20
	36.19	571.1	597.5	94.10
3	8.68	383.9	425.6	0.88
	16.87	424.8	459.1	1.81
	30.67	473.0	512.8	3.26
	28.09	522.1	551.2	3.96
	39.29	593.2	608.2	6.33
4	8.65	383.4	418.7	0.70
	16.83	424.4	449.1	4.78
	28.72	473.2	501.9	6.35
	28.81	523.1	547.7	5.41
	38.33	572.7	602.8	5.45
5	7.62	383.0	417.6	1.07
	15.94	424.3	450.4	4.50
	29.29	473.8	507.0	5.76
	27.75	522.1	530.8	6.11
	35.55	573.0	604.7	6.27
6	8.10	383.2	416.2	1.20
	17.17	424.2	451.1	3.95
	27.72	473.7	504.6	4.10
	29.59	522.2	522.0	3.12
	41.43	572.8	609.7	4.00

B-2.4. C. F. Lucks and H. W. Deem, *Progress Relating to Civilian Applications During June, 1958,* R. W. Dayton and C. R. Tipton, Jr., (eds.), BMI-1273 (1958) pp 7-9.

B-2.5. A. E. Powers, *Application of the Ewing Equation for Calculating Thermal Conductivity from Electrical Conductivity,* USAEC KAPL-2146 (April 7, 1961).

B-2.6. D. B. Scott, *Physical and Mechanical Properties of Zircaloy 2 and 4,* WCAP-3269-41 (May 1965) pp 5, 9.

B-2.7. Y. S. Touloukian, R. W. Powell, C. Y. Ho, P. G. Klemens, *Thermophysical Properties of Matter, Volume 1, Thermal Conductivity,* New York: Plenum Press, 1970, pp 888-889.

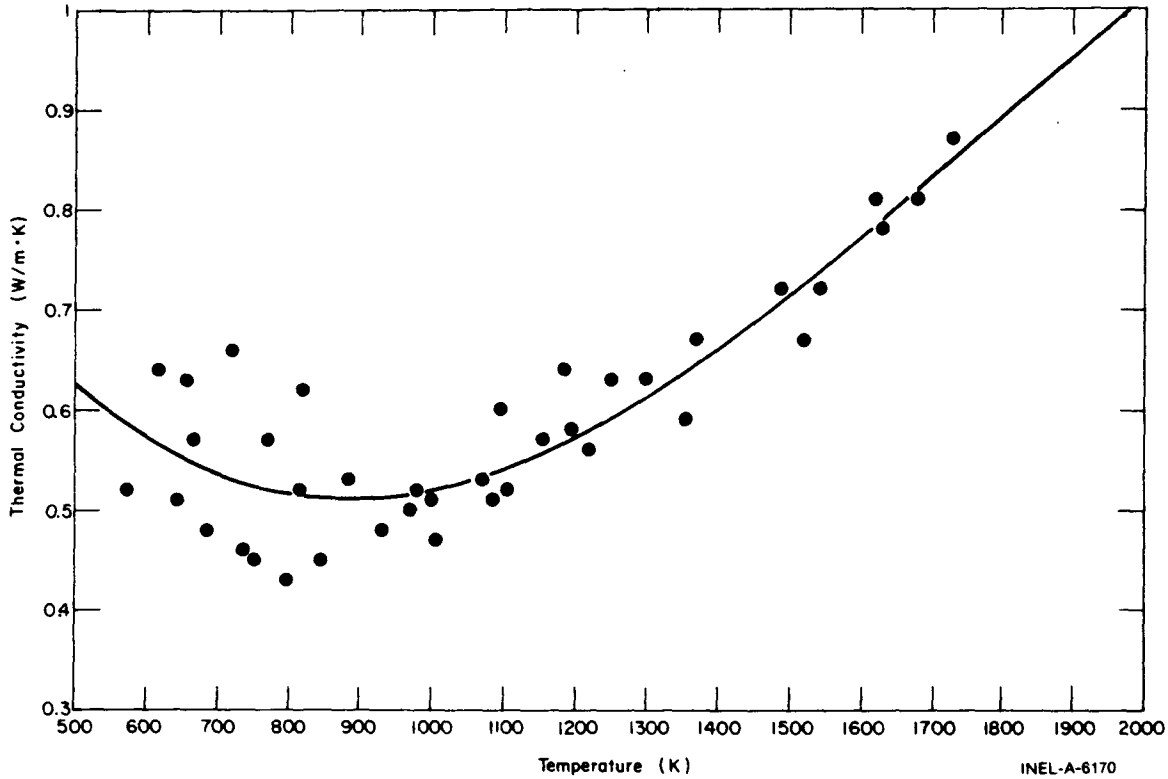

Fig. B-2.3 Temperature dependence of the thermal conductivity of zirconium dioxide according to Lapshov and Bashkatov, showing the trend line.

B-2.8. S. E. Jensen, *Parametric Studies of Fuel Pin Temperature Response,* IDO-17295 (February 1969).

B-2.9. H. Korber and H. E. Unger, "Sensitivity Study on Core Heatup and Meltdown by Variation of Heat Conductivity and Thermal Emissivity," *Transactions of the American Nuclear Society, 18* (1974) pp 234-235.

B-2.10. W. D. Kingery et al, "Thermal Conductivity: X, Data for Several Pure Oxide Materials Corrected to Zero Porosity," *Journal of the American Ceramic Society, 37* (1954) pp, 107-110.

B-2.11. H. Maki, "Heat Transfer Characteristics of Zircaloy-2 Oxide Film." *Journal of Nuclear Science and Technology, 10* (1973) pp 107-175.

B-2.12. V. N. Lapshov and A. V. Bashkatov, "Thermal Conductivity of Coatings of Zirconium Dioxide Applied by the Plasma Sputtering Method," *Heat Transfer, Soviet Research, 5* (1973) pp 19-22.

TABLE B-2.III

LISTING OF THE CTHCON SUBCODE

```
C
C
      SUBROUTINE CTHCON(CTEMP, TIME, FLUX, COLDW, CCON, CDKDT)
C
C     CTHCON CALCULATES CLADDING THERMAL CONDUCTIVITY AS A FUNCTION
C     TEMPERATURE, TIME, FLUX, AND COLD WORK
C
C     CCON   = OUTPUT THERMAL CONDUCTIVITY OF ZIRCALOY-4 (W/M-K)
C     CDKDT  = OUTPUT DERIVATIVE OF THERMAL CONDUCTIVITY WITH
C              RESPECT TO TEMPERATURE
C
C     CTEMP  = INPUT CLADDING MESHPOINT TEMPERATURE (K)
C     TIME   = INPUT TIME AT TEMPERATURE AND FLUX (S)
C     FLUX   = INPUT FAST NEUTRON FLUX ((NEUTRONS/M**2)/S)
C     COLDW  = INPUT COLD WORK (UNITLESS RATIO OF AREAS)
C
C     THE EQUATION USED IN THIS SUBCODE IS BASED ON DATA FROM
C     W.K. ANDERSON, C.J. BECK, A.R. KEPHART AND J.S. THETLACKER
C        ASTM-STP-314, 1962, PP 62 - 93
C     J.N. CHIRIGOS, C. KASS, W.S. KIRK AND G.J. SALVAGGIO
C        FUEL ELEMENT FABRICATION, ACADEMIC PRESS, 1961, PP 19 - 55
C     A.D. FEITH, GEMP-669 (OCT 1966)
C     C.F. LOCKS AND H.W. DEEM, BMI-1273 (1958) PP 7-9
C     A.E. POWERS, KAPL-2146 (1961)
C     D.B. SCOTT, WCAP-3269-41 (1965) PP 5-9
C
C     THIS VERSION OF CTHCON DOES NOT USE TIME, FLUX OR COLDWORK
C     AS PARAMETERS IN CALCULATION OF ZIRCALOY THERMAL CONDUCTIVITY
C
C     ONE STANDARD DEVIATION OF THIS FUNCTION = 1.01 W/M-K
C
C     THIS VERSION OF CTHCON WAS DEVELOPED BY R.L. MILLER, DEC 1975
C     LAST MODIFIED BY E.R. CARLSON IN JUNE 1978.
C
      COMMON   /LACMDL/  MAX1DX,EMFLAG
      DIMENSION EMFLAG(1)
      DATA       ON      / 2HON    /,
     #           OFF     / 3HOFF   /,
     #           LOCIDX  /   7     /
      IF ( EMFLAG(LOCIDX) .EQ. ON ) GO TO 10
C
      CCON =  7.511 + CTEMP * (2.088E-2 + CTEMP * (-1.450E-5 +
     #        CTEMP*7.668E-09))
      CDKDT = 2.088E-2+CTEMP*(-2.9E-5+CTEMP*2.3E-8)
      GO TO 20
C
   10 CALL EMCTN(CTEMP,TIME,FLUX,COLDW,CCON,CDKDT)
   20 CONTINUE
      RETURN
      END
```

TABLE B-2.IV

LISTING OF THE ZOTCON SUBCODE

```
C
C
      FUNCTION ZOTCON(CTEMP)
C
C     ZOTCON CALCULATES ZIRCONIUM DIOXIDE THERMAL CONDUCTIVITY AS A
C     FUNCTION OF TEMPERATURE.
C
C     ZOTCON = OUTPUT THERMAL CONDUCTIVITY OF ZRO2 (W/M-K)
C     CTEMP  = INPUT CLADDING MESHPOINT TEMPERATURE (K)
C
C     THE DATA USED TO GENERATE THIS CORRELATION WERE TAKEN FROM:
C     W.D. KINGERY, J. FRANCL, R.L. COBLE AND T. VASILOS
C     J. AMER. CERAM. SOC., 37 NO.I (1954) PP 107-110
C
C     ZOTCON WAS CODED BY R.L.MILLER IN MARCH 1974.
C     MODIFIED BY R.L. MILLER MAY 1974
C
C     USE CAUTION ABOVE 1700K
C
      T      = CTEMP
      ZOTCON = 1.9599 - T*(2.41E-4 - T*(6.43E-7 - T*1.946E-10))
      RETURN
      END
```

3. CLADDING SURFACE EMISSIVITY (ZOEMIS)

(D. L. Hagrman)

One of the important modes of heat transfer to and from cladding surfaces during an abnormal transient is radiant heat transfer. Since the energy radiated is directly proportional to the emissivity of the inner and outer cladding surfaces, surface emissivity is important in descriptions of abnormal transients.

3.1 Summary

Surface emissivities are significantly affected by surface layers on the cladding. For cladding with thin oxide coatings, the oxide surface thickness is only a few wavelengths of near infrared radiation and is partly transparent. Oxide thickness is an important parameter for these thin coatings. Thicker oxide layers are opaque so the oxide thickness is not as important as the nature of the outer oxide surface which is affected by temperature and by chemical environment. The effect of temperature has been modeled but variations in crud on the external cladding surface and chemical reaction products on the inside surface are not modeled explicitly.

The model for emissivity was constructed by considering measured emissivities reported by several investigators[B-3.1 – B-3.3]. Expressions used to predict the emissivity of zircaloy cladding surfaces are summarized below.

When the cladding surface temperature has not exceeded 1500 K, emissivities are modeled by Equations (B-3.1a) and (B-3.1b). For oxide layer thicknesses less than 3.88×10^{-6} m

$$\epsilon_1 = 0.325 + 0.1246 \times 10^6 d \qquad \text{(B-3.1a)}$$

for oxide layer thicknesses of 3.88×10^{-6} m or greater[a]

$$\epsilon_1 = 0.808642 - 50.0d \qquad \text{(B-3.1b)}$$

where

ϵ_1 = hemispherical emissivity (unitless)

d = oxide layer thickness (m).

When the maximum cladding temperature has exceeded 1500 K, emissivity is taken to be the larger of 0.325 and

$$\epsilon_2 = \epsilon_1 \exp [(1500 - T)/300] \qquad \text{(B-3.2)}$$

where

ϵ_1 = value for emissivity obtained from Equation (B-3.1)

T = maximum cladding temperature (K).

The standard error expected from the use of Equation (B-3.1) to predict emissivity in a reactor when cladding surface temperature has never exceeded 1500 K is

$$\sigma_1 = \pm 0.1. \qquad \text{(B-3.3a)}$$

When cladding temperature has exceeded 1500 K, the expected standard error is estimated by σ_2 in the expression

$$\sigma_2 = \pm 0.1 \exp [(T-1500/300]. \qquad \text{(B-3.3b)}$$

If Equations (B-3.3b) and (B-3.2) predict values of $\epsilon_2 \pm \sigma_2$ which fall inside the range of physically possible values of emissivity (0.0 - 1.0), the value σ_2 is returned as the expected standard error. If the prediction $\epsilon_2 + \sigma_2$ is greater than 1 or if $\epsilon_2 - \sigma_2$ is less than 0, the standard error of Equation (B-3.3b) is modified to limit $\epsilon_2 + \sigma_2$ at 1 and/or $\epsilon_2 - \sigma_2$ at 0.

---

[a] The use of six significant figures in Equation (B-3.1b) ensures an exact match of the values of ϵ_1 at $d = 3.88 \times 10^{-6}$ m.

The following subsection is a review of the available data on cladding emissivity. The approach used to formulate the model for emissivity is described in Section B-3.3 and Section B-3.4 discussion of the uncertainty of the model for cladding emissivity. A listing of the subroutine ZOEMIS is presented in Section B-3.5. References are contained in Section B-3.6.

3.2 Literature Review

Measurements of zircaloy-2 emissivities as a function of temperature and dissolved oxygen content were reported by Lemmon[B-3.1]. The measurements utilized the hole-in-tube method and were carried out in vacuum. Data from samples with an oxide film were reported but the nonoxidizing environment of the sample during emissivity measurements caused the emissivity to change with time. Moreover, the thicknesses of the oxide films were not reported. The Lemmon data were not used in formulating the ZOEMIS subcode because the unknown oxide thickness probably influenced the emissivity and because of complications caused by the vacuum environment.

The emissivity of zircaloy-4 was reported by Juenke and Sjodahl[B-3.2] from measurements on oxidized zircaloy in vacuum and from measurements in steam during the isothermal growth of oxide films. These authors reported a decrease in the emissivity measured in vacuum which they attributed to the formation of a metallic phase in the oxide. This metallic phase did not form in the presence of steam. The data taken in steam were used in constructing ZOEMIS because the steam environment is similar to an abnormal reactor environment.

Figure B-3.1 is a reproduction of the Juenke and Sjodahl steam data. The data suggest that emissivity decreases when oxide films become very thick (long times or high temperatures). In fact, Juenke and Sjodahl expect the total emissivity of very thick films to approach 0.3 or 0.4 which are characteristic of pure ZrO_2. However, the decrease in emissivity at temperatures greater than about 1200°C is greater than one would predict from oxide layer thickness alone. The correlation of this emissivity data with oxide layer thickness is discussed in Section B-3.3.

Juenke and Sjodahl do not include very thin oxide films but do report that the total emittance rises almost instantaneously from about 0.2 to 0.7 with the introduction of steam. Data relevant to thin films are discussed below.

The emissivity of oxide films measured in air at temperatures in the range 100 to 400°C were reported by Murphy and Havelock[B-3.3] and are reproduced in Table B-3.I. The emissivities are not strongly dependent on temperature but do increase rapidly with oxide thickness for the thin oxide layers measured. The one value of emissivity measured with an oxide thickness of 94×10^{-6} m is important because the oxide was approximately thirty times the thickness associated with the transition from "black" oxide layers to "white" oxide layers. The emissivity of this oxide, described as "white" by the authors, has a measured emissivity characteristic of surfaces which are black in the infrared region of the spectrum. Since (a) the Murphy and Havelock data were taken in an oxidizing environment

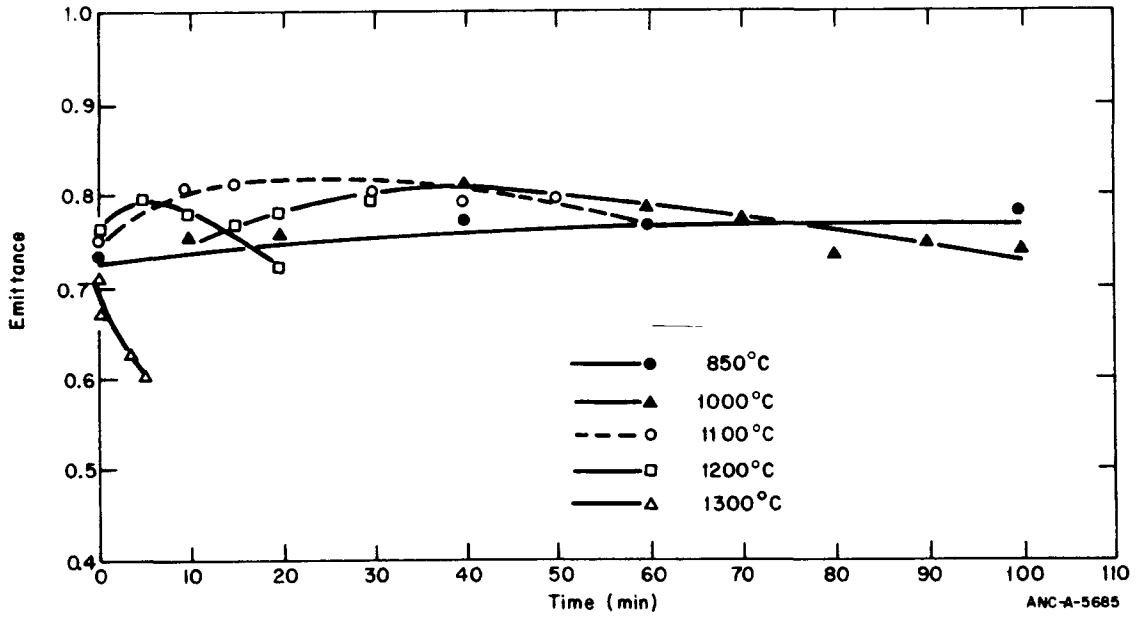

Fig. B-3.1 Total hemispherical emittance of zircaloy-4 versus time at temperature in steam.

TABLE B-3.I

EMISSIVITY OF THIN OXIDE FILMS AS REPORTED BY MURPHY AND HAVELOCK

Surface Condition	Oxide Thickness (μm)	Emissivity				
		100°C	150°C	200°C	300°C	400°C
Pickled + 2 days in air at 400°C	0.9	0.424	0.414	0.416	0.434	0.433
Pickled + 10 days in air at 400°C	1.48	0.521	0.542	0.557	0.588	--
Pickled + 55 days in 400°C steam under a pressure of 10.4 MPa	2.3	--	0.582	0.599	0.620	--
Pickled + 30 days in air at 400°C + 73 days in air at at 500°C	94	--	0.748	--	--	--

and (b) the emissivity of the 94×10^{-6} m oxide film agrees with the emissivity of films measured in steam, all of the Murphy and Havelock data were used in the formulation of ZOEMIS.

Additional data were reported by T. B. Burgoyne and A. Garlick at the OECD-CSNI meeting on the Behavior of Water Reactor Fuel Elements under Accident Conditions in Spinad, Norway, on September 13-16, 1976. Using a hot-filament calorimeter, these authors measured the emissivity of zircaloy-2 cladding surfaces coated with uniform oxide, nodular oxide, and crud. The emissivities were measured in vacuum. However, the following arguments are presented in favor of including some of these data in the data base of ZOEMIS: (a) a significant decrease in emissivity was not noticed with initial oxide thicknesses greater than 10^{-5}m until the samples were heated above approximately 800°C (the alpha-beta phase transition of zircaloy); (b) the low temperature values of emissivity measured with uniform oxides correspond closely to those measured in steam; and (c) the data taken with nodular and crud coated surfaces are representative of in-reactor surfaces not represented in other data. Data from Burgoyne and Garlick which did not show the sudden decrease in emissivity, characteristic of the change caused by a vacuum environment were used in ZOEMIS. Table B-3.II is a summary of the measurements used.

3.3 Development of the Model

Near infrared radiation has a wavelength of 1×10^{-6} m. Oxide films up to a few wavelengths thick should be partly transparent to infrared radiation and should therefore have emissivities strongly dependent on oxide thickness. The emissivity versus oxide thickness data of Murphy and Havelock[B-3.3] were fit with standard least-squares residual analysis to deduce Equation (B-3.1a).

The equation for the emissivity of oxide films thicker than 4×10^{-6} m is based on the data of Burgoyne and Garlick, Juenke and Sjodahl[B-3.2] and one measurement from Murphy and Havelock[B-3.3] as discussed in Section B-3.2. Oxide thicknesses were calculated from the time and temperatures reported by Juenke and Sjodahl using the correlation published by Cathcart[B-3.4].

$$X = [2.25 \times 10^{-6} \exp(-18\,063/T)t]^{1/2} \qquad \text{(B-3.4)}$$

where

X = the oxide layer thickness (m)

T = temperature (K)

t = time at temperature (s).

TABLE B-3.II

EMISSIVITY DATA FROM BURGOYNE AND GARLICK

Cladding Surface	Surface Layer Thickness (μm)	Measurement Temperature (K)	Emissivity (unitless)
Uniform Oxide	10	735	0.748
	10	805	0.770
	10	876	0.773
	10	885	0.773
	10	978	0.774
	10	986	0.767
	10	1072	0.791
Uniform Oxide	28	784	0.834
	28	884	0.818
	28	987	0.832
	28	1080	0.829
Nodular Oxide	130	654	0.860
	130	769	0.845
	130	775	0.857
	130	868	0.849
	130	885	0.850
	130	965	0.849
	130	975	0.837
	130	1066	0.866
	130	1149	0.841
Crud	35	677	0.918
	35	683	0.930
	35	769	0.890
	35	777	0.888
	35	870	0.899
	35	876	0.888
	35	966	0.913
	35	977	0.903

Table B-3.III lists the emissivity, time, and temperature reported by Juenke and Sjodahl together with the oxide thickness predicted using Equation (B-3.4). Values of emissivity and oxide layer thickness from Tables B-3.I, B-3.II, and B-3.III were used to establish Equation (B-3.1b).

Figure B-3.2 is a comparison of the curves generated by Equations (B-3.1a) and (B-3.1b) with the data base used to derive these equations. Predicted values of emissivity increase rapidly until the surface oxide layer thickness is 3.88×10^{-6} m then decrease very slowly with increasing surface layer thickness.

TABLE B-3.III

EMISSIVITY VERSUS OXIDE THICKNESS FROM
JUENKE AND SJODAHL'S DATA

Temperature (K)	Time (s)	Calculated Oxide Thickness (μm)	Measured Emissivity (unitless)
1125	1200	17	0.755
1125	2400	24	0.755
1125	6000	38	0.785
1275	600	31	0.750
1275	1200	43	0.773
1275	1800	53	0.795
1275	3600	75	0.790
1275	4200	81	0.775
1275	4800	86	0.738
1275	5400	92	0.755
1275	6000	96	0.740
1375	600	51	0.808
1375	900	63	0.815
1375	1200	72	0.780
1375	3000	114	0.798
1375	3600	125	0.775
1475	300	57	0.795
1475	600	80	0.780
1475	900	98	0.775
1475	1200	113	0.722
1575	210	70	0.620
1575	300	83	0.600

The values of emissivity measured by Juenke and Sjodahl at 1575 K (0.62 and 0.60) are significantly below the measured emissivities at lower temperatures. Since thicker oxide films were formed at lower temperatures, the low emissivity is not due to the thickness of the oxide film. Moreover, the low values of emissivities measured by Juenke and Sjodahl at high temperature are supported by posttest observations of cladding surfaces which have been at high temperatures[B-3.5]. Cladding surfaces which experienced film boiling and

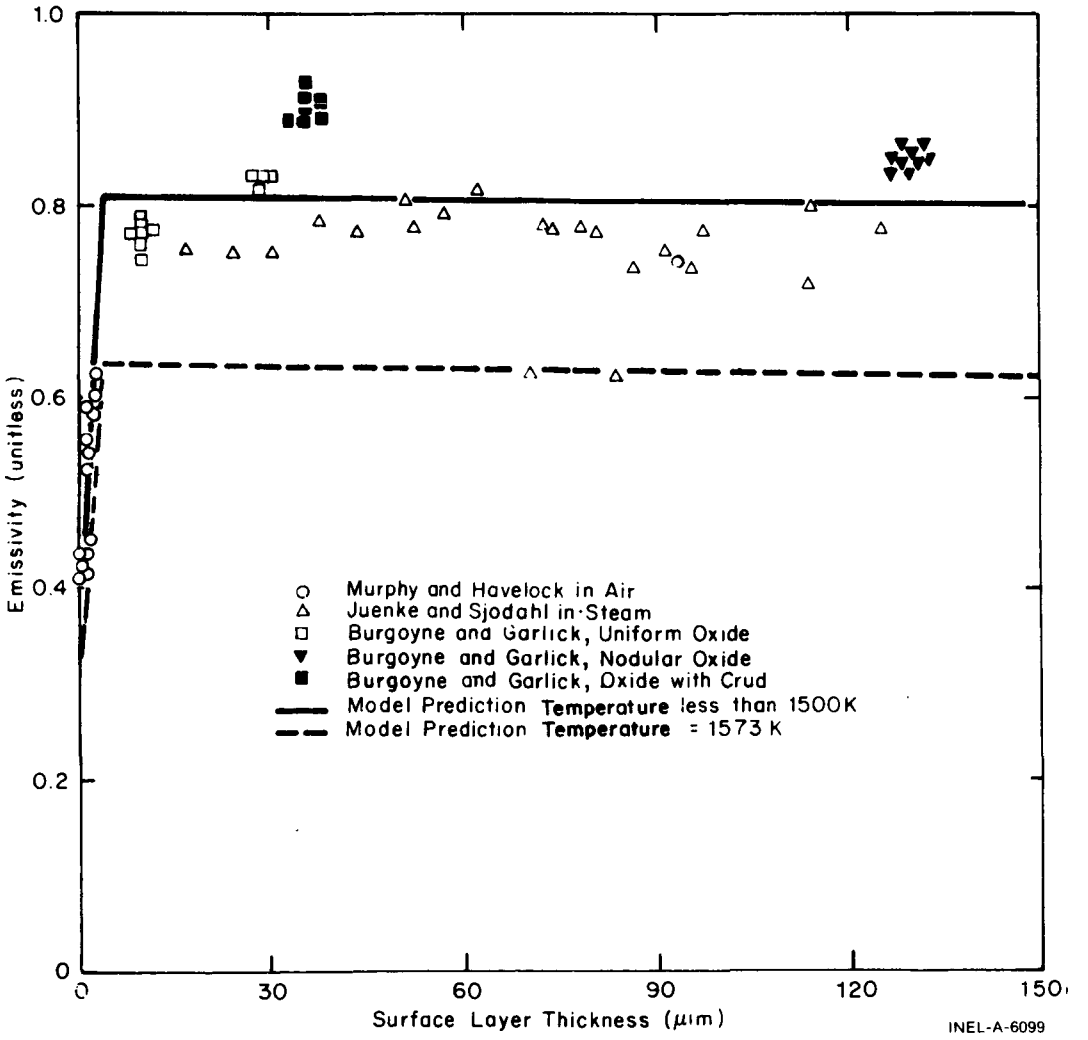

Fig. B-3.2 ZOEMIS calculations compared with the data base of the model.

therefore high temperatures, showed spalled oxide and somewhat whiter oxide surfaces in the region of the film boiling. The observations reported (Reference B-3.5) and the trend toward lower values of emissivity at higher temperatures reported by Juenke and Sjodahl at 1475 and 1575 K imply that lower cladding surface emissivities are likely at temperatures above approximately 1500 K. This trend in the limited data has been included in ZOEMIS by (a) adding a multiplicative factor to the expression for emissivity;

$$\exp[(1500 - T)/300] \tag{B-3.5}$$

where

T = the greater of 1500 K and the maximum cladding temperature

and (b) limiting the minimum emissivity to 0.325, the value predicted by the model for zero oxide thickness.

3.4 Uncertainty

The standard errors obtained with Equations (B-3.1a) and (B-3.1b) and the data base used to develop these Equations are listed in Table B-3.IV.

TABLE B-3.IV

STANDARD ERRORS OF ZOEMIS PREDICTIONS

Surface Description	Emissivity Standard Error
Oxide films < 3.88×10^{-6} m	±0.04
Pure oxide films > 3.88×10^{-6} m	±0.05
Oxide films including samples with nodular oxides and crud	±0.07

Standard errors shown in Table B-3.IV for oxide layers without the complicating features of nodular oxides or surface crud are consistent with measurement errors of ±3% estimated by Lemmon[B-3.1]. However, the model is intended to predict the emissivity of cladding surfaces with crud or UO_2 fission products as well as the oxide layer. The data from Burgoyne and Garlick (illustrated in Figure B-3.2) suggest that crud layers introduce a systematic error of approximately ±0.1. The value of ±0.1 is therefore included in ZOEMIS as the best estimate for the standard error of the model prediction for emissivity during abnormal reactor operation at temperatures below 1500 K.

The uncertainty of the prediction for emissivities above 1500 K is difficult to estimate. Equation (B-3.3b) was selected as a reasonable expression for the expected standard error of Equation (B-3.2), simply because the expression ±0.1 exp[-(1500 – maximum cladding temperature)/300] predicts a standard error approximately equal to the change in emissivity caused by the empirical multiplicative factor of Equation (B-3.5).

In Figure B-3.3, the data base and model predictions shown in Figure B-3.2 are repeated. The standard error expected with ZOEMIS for temperatures below 1500 K is shown by the cross-hatched area centered on the solid line. The cross-hatched area centered on the dashed line shows the standard error estimated for temperatures of 1573 K.

3.5 Cladding Surface Emissivity Subcode ZOEMIS Listing

A FORTRAN listing of the subcode ZOEMIS is presented in Table B-3.V.

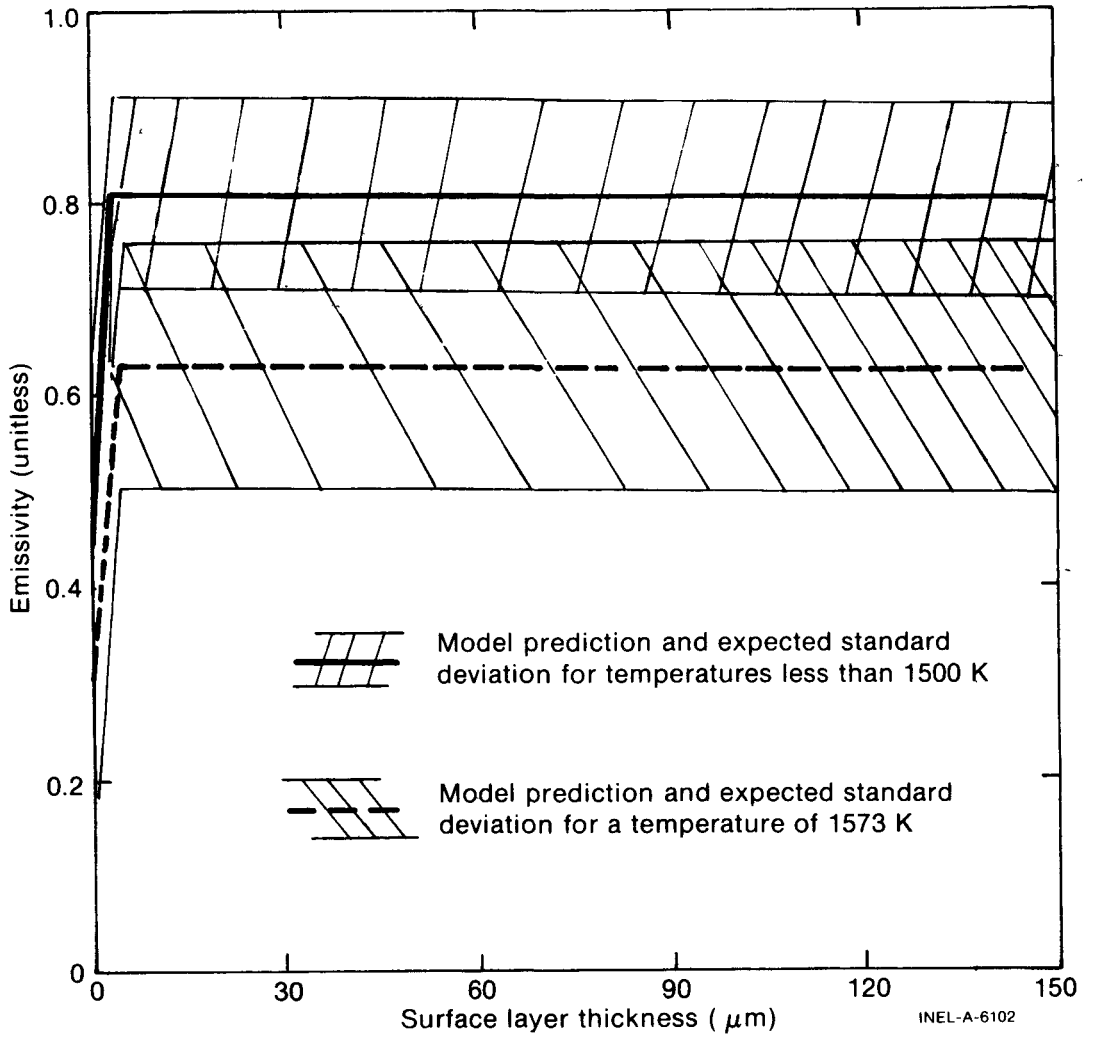

Fig. B-3.3 Expected standard errors of emissivity for temperatures below 1500 K and at 1573 K.

3.6 References

B.3-1. A. W. Lemmon, Jr., *Studies Relating to the Reaction Between Zirconium and Water at High Temperatures,* BMI-1154 (January 1957).

B-3.2. E. F. Juenke and L. H. Sjodahl, "Physical and Mechanical Properties: Emittance Measurements," *AEC Fuels and Materials Development Program,* GEMP-1008 (1968) pp 239-242.

B-3.3. E. V. Murphy and F. Havelock, "Emissivity of Zirconium Alloys in Air in the Temperature Range 100-400°C," *Journal of Nuclear Materials, 60* (1976) pp 167-176.

TABLE B-3.V

LISTING OF THE ZOEMIS SUBCODE

```
C
C
      SUBROUTINE ZOEMIS(CTMAX, ZROXID, EMISSV)
C
CC    ZOEMIS CALCULATES THE EMISSIVITY OF THE CLADDING SURFACE
CC    AS A FUNCTION OF MAXIMUM CLADDING TEMPERATURE AND
CC    OXIDE THICKNESS.  EXPECTED STANDARD ERROR OF THE
CC    CALCULATED EMISSIVITY COMPARED TO IN-REACTOR
CC    DATA IS ALSO RETURNED
CC
CC    EMISSV = OUTPUT CLADDING SURFACE EMISSIVITY (UNITLESS)
CC    PUEMIS = OUTPUT POSITIVE STANDARD ERROR EXPECTED IN EMISSV
CC             WHEN COMPARED TO IN-REACTOR DATA (NOT CURRENTLY RETURNED)
CC    UUEMIS = OUTPUT NEGATIVE STANDARD ERROR EXPECTED IN EMISSV
CC             WHEN COMPARED TO IN-REACTOR DATA (NOT CURRENTLY RETURNED)
CC
CC    CTMAX  = INPUT MAXIMUM CLADDING TEMPERATURE (K)
CC    ZROXID = INPUT OXIDE LAYER THICKNESS (M)
CC
CC    THE EQUATIONS USED IN THIS SUBROUTINE ARE BASED ON DATA FROM
CC    (1) AEC FUELS AND MATERIALS DEVELOPMENT PROGRAM PROGRESS
CC    REPORT NO. 76, USAEC REPORT GEMP - 1008 (1968). SECTION BY
CC    E. F. JUENKE AND S. J. SJODAHL, P. 239
CC    (2) T. B. BURGOYNE AND A. GARLICK, PAPER PRESENTED AT
CC    SPECIALISTS MEETING ON THE BEHAVIOUR OF WATER REACTOR
CC    FUEL ELEMENTS UNDER ACCIDENT CONDITIONS, SPATIND NORWAY
CC    (SEPTEMBER 1976)
CC    (3) E. V. MURPHY AND F. HAVELOCK, EMISSIVITY OF ZIRCONIUM
CC    ALLOYS IN AIR IN THE TEMPERATURE RANGE 100 - 400 C
CC    J. NUC. MAT., 60 (1976) PP 167-176
CC
CC    ZOEMIS CODED BY R. L. MILLER SEPT 1974
CC    MODIFIED BY D. L. HAGRMAN OCTOBER 1976
CC
C     MODEL FOR TEMPERATURES BELOW 1500K FOLLOWS
      IF(ZROXID .GE. 3.88E-06) GO TO 10
      EMISSV = 3.25E-01+1.246E05*ZROXID
      GO TO 20
   10 EMISSV = 8.08642E-01-5.00E01*ZROXID
   20 PUEMIS = 0.1
      UUEMIS = 0.1
      IF(CTMAX .LE. 1500.) GO TO 50
C
C     MODIFICATION FOR MAXIMUM TEMPERATURES ABOVE 1500 K FOLLOWS
      EMISSV = EMISSV * EXP((1.50E03-CTMAX)/3.00E02)
      IF(EMISSV .LT. 0.325) EMISSV = 0.325
      PUEMIS = PUEMIS/ EXP((1.50E03 - CTMAX)/3.00E02)
      UUEMIS = PUEMIS
C
C     STANDARD ERROR CUT OFF AT IMPOSSIBLE VALUES FOLLOWS
      IF(PUEMIS .GT. (1.00-EMISSV)) PUEMIS = 1.00 - EMISSV
      IF(UUEMIS .GT. EMISSV) UUEMIS = EMISSV
C
   50 RETURN
      END
```

B-3.4. J. V. Cathcart, *Quarterly Progress Report on the Zirconium Metal-Water Oxidation Kinetics Program Sponsored by the NRC Division of Reactor Safety Research for April – June 1976,* ORNL/NUREG-TM-41 (August 1976).

B-3.5. *Quarterly Technical Progress Report on Water Reactor Safety Programs Sponsored by the Nuclear Regulatory Commission's Division of Reactor Safety Research, October – December 1975,* ANCR-NUREG-1301 (May 1976) p 67.

4. CLADDING THERMAL EXPANSION (CTHEXP)

(G. A. Reymann)

A model is presented in this section which describes dimensional changes of zircaloy cladding caused by thermal expansion. Axial and diametral expansion are treated separately. Within the data scatter, there is no difference between zircaloy-2 and zircaloy-4, and these two materials are described by the same correlations.

4.1 Summary

The model deals with zircaloy in three different temperature ranges, corresponding to the alpha, transition, and beta phases. The alpha phase ($300 < T < 1073$ K) correlations are

$$\frac{\Delta L}{L_o} = 4.44 \times 10^{-6} T - 1.24 \times 10^{-3} \qquad \text{(B-4.1)}$$

and

$$\frac{\Delta D}{D_o} = 6.72 \times 10^{-6} T - 2.07 \times 10^{-3} \qquad \text{(B-4.2)}$$

where

$\frac{\Delta L}{L_o}$ = linear axial strain caused by thermal expansion (unitless)

L_o = axial length at a reference temperature (m)

$\frac{\Delta D}{D_o}$ = linear diametral strain caused by thermal expansion (unitless)

D_o = diameter of cladding at a reference temperature (m)

T = temperature (K).

Between 1073 and 1273 K, an interval spanning the transition region, there are very few data and only those of Scott[B-4.1] are considered. For these temperatures the expansion values are obtained by linear interpolation using Scott's data.

In the beta phase ($1273 < T <$ melting) the correlations used are

$$\frac{\Delta L}{L_o} = 9.7 \times 10^{-6} T - 1.10 \times 10^{-2} \qquad \text{(B-4.3)}$$

$$\frac{\Delta D}{D_o} = 9.7 \times 10^{-6} T - 9.45 \times 10^{-3} \qquad \text{(B-4.4)}$$

where the terms of the equations have been previously defined.

The uncertainty of the model's predictions when compared to its own data base increase with temperature in the alpha range. Therefore a percentage error is more appropriate than a single valued uncertainty. At temperatures higher than about 1073 K, where the alpha to beta phase transition begins, a quite large error is assigned because of the few data available. The uncertainty limits are

$$\pm 10\% \text{ for } 300 < T < 1073 \text{ K}$$

$$\pm 50\% \text{ for } T > 1073 \text{ K}.$$

4.2 Review of Literature

Scott, Kearns[B-4.2], and Mehan and Wiesinger[B-4.3] have published zircaloy thermal expansion data which exhibit anisotropy. Of these, only Scott has data covering the alpha to beta phase transition. Mehan and Wiesinger's data are for zircaloy-2 plate, Kearns' are for zircaloy-4 plate, and Scott's are for zircaloy-4 tubing.

A paper by Mehan and Cutler[B-5.4] contains results covering temperatures from room temperature to 1273 K. They found no anisotropic effects, and do not report all the data they obtained. In most cases, the samples were cycled into and out of the beta phase (above 1273 K) at least twice to obtain "thermal stability," and expansion data were taken only during the final run. However a single excursion into the beta phase apparently reduces anisotropic effects, even when the sample is later returned to the alpha phase[B-4.2]. Therefore, Mehan and Cutler failed to use their most significant results, those of the first runs, and their data are not used in the model.

4.3 Derivation of the CTHEXP Model

The directions which may exhibit texture differences for rolled plate and drawn tubing are shown in Figure B-4.1. Since many of the existing data are for plate specimens rather than for tubing, it is useful to consider analogous directions for plate and tubing even though it cannot be assumed that textures in analogous directions are identical. Textures and thermal expansion in the axial direction of tubing and the longitudinal direction of rolled plate are similar, as are those of the circumferential direction of tubing and the long transverse direction in rolled plate, and the radial direction of tubing and the short transverse direction of plate. These analogies make it possible to use the numerous plate data as well as tube data.

4.3.1 Low Temperature Cladding Thermal Expansion. The simple theory of the linear expansion of a solid found in most elementary physics texts, such as Sears and Zemansky[B-4.5], works well for zircaloy at low temperatures (< 1073 K). According to this theory, thermal strain is given by

$$\frac{\Delta \ell}{\ell_0} = K_1 (T - T_0) \qquad \text{(B-4.5a)}$$

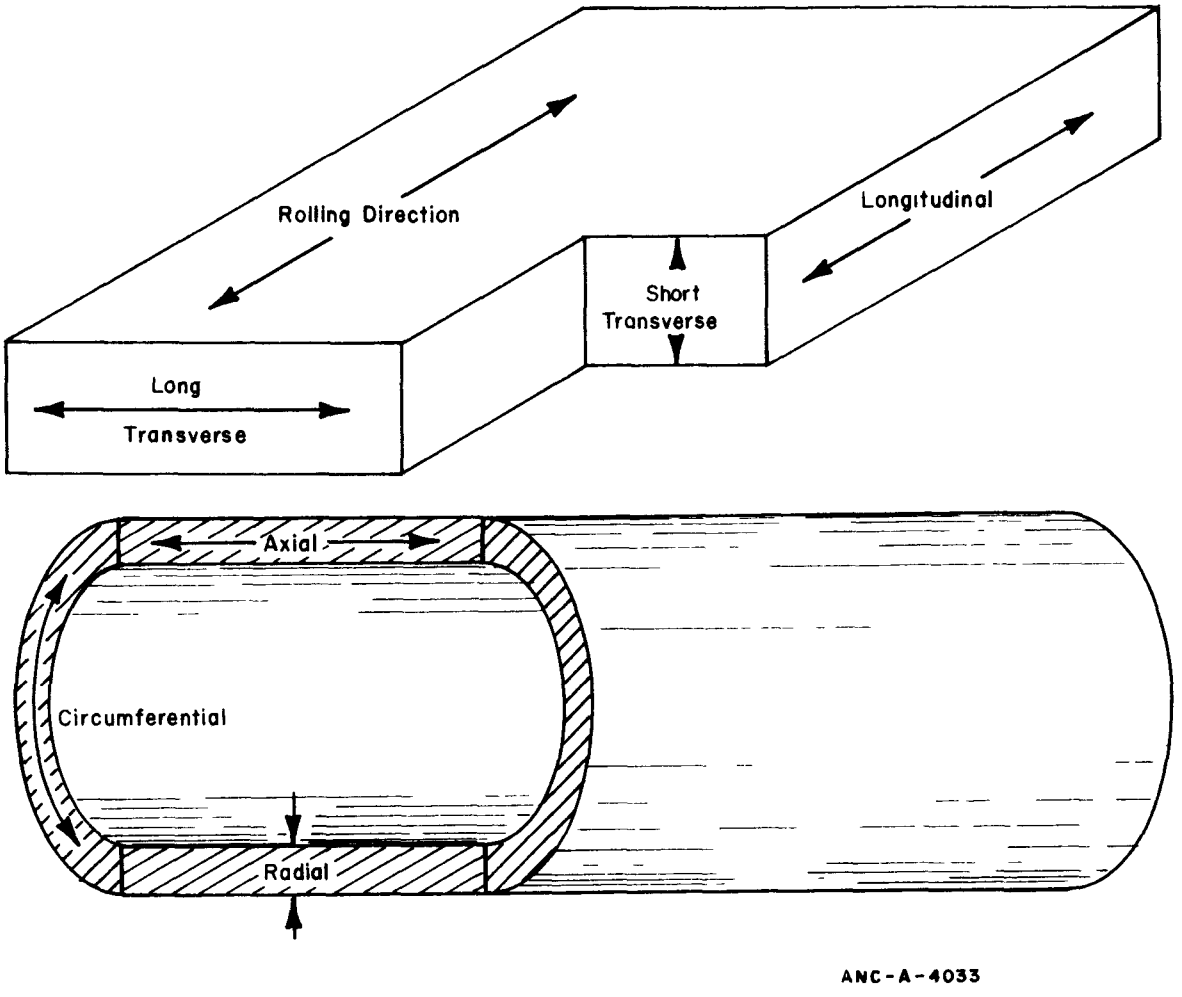

Fig. B-4.1 Nomenclature used to describe directions in rolled plate and drawn tubing.

or more generally

$$\frac{\Delta \ell}{\ell_o} = K_1 T - K_2 \qquad \text{(B-4.5b)}$$

where

ℓ = diametral or axial dimension (m)

T_o = reference temperature where $\Delta L = 0$ (K)

ℓ_o = diametral or axial dimension at the reference temperature (m)

K_1 = coefficient of linear expansion (K^{-1})

K_2 = $K_1 T_o$ (unitless).

A least-squares analysis of the data shows that when the thermal expansion strains are expressed as linear functions of temperature, the standard deviations from the data base are quite close to those found when cubic functions are used. This is good verification for expressions having the form of Equation (B-4.5b). The results are Equations (B-4.1) and (B-4.2). Since these fits were done without constraint, somewhat different reference temperatures resulted. Comparing Equations (B-4.5a) and (B-4.5b), the reference temperature is given by $T_o = K_2/K_1$. These temperatures are

T_o = 279 K for axial thermal expansion

T_o = 308 K for diametral thermal expansion.

These temperatures are of secondary importance since it is the coefficient of expansion which is most significant.

4.3.2 Cladding Thermal Expansion in the Alpha-Beta Transition Phase. Starting at about 1083 K, zircaloy undergoes a transition phase which ends at approximately 1244 K. Below 1083 K it has a hexagonal close-packed structure, called the alpha phase, and above 1244 K it normally has a body-centered cubic structure, called the beta phase. During the alpha-beta transition, there is a contraction which is partially reversed on cooling back to the alpha phase. After having been through the transition and cooled to room temperature again, the sample usually has a length different than the original. This change in length may be an increase[B-4.3] or a decrease[B-4.1] – the controlling factors are not yet defined. Because of this ambiguity only that thermal expansion which occurs during the first excursion of the as-received tubing from alpha to beta phase is modeled.

Of the sources used to formulate this model, only Scott includes this mixed phase region, and he lists only six data, all for axial expansion. It does not seem reasonable to try to find an analytical form using such limited data. Therefore, a smooth curve was drawn through Scott's data and points taken from the curve used to generate a table for this temperature range. Interpolation is accomplished through the linear interpolation subroutine POLATE (Appendix D, Section 2). Since no diametral data are available in the mixed phase region, the assumption is made that diametral thermal expansion is parallel to the curve for axial expansion, and a similar table generated for interpolation to find the diametral thermal expansion strain.

4.3.3 High Temperature Cladding Thermal Expansion. For beta phase of zircaloy, no data are available. Therefore, above 1273 K the assumption is made that the coefficient of thermal expansion was the same as that for zirconium. A constant value for this coefficient of 9.7×10^{-6} K^{-1} is reported by Lustman and Kerze[B-4.6], which also characterizes the data of Skinner and Johnston[B-4.7]. This yields

$$\frac{\Delta L}{L_o} = 9.7 \times 10^{-6} T - 1.10 \times 10^{-2} \qquad \text{(B-4.6)}$$

and

$$\frac{\Delta D}{D_o} = 9.7 \times 10^{-6} T - 9.45 \times 10^{-3} \qquad \text{(B-4.7)}$$

where the terms of the equations have been previously defined.

4.4 Uncertainty Analysis

Since the scatter of the data grows with increasing temperature, a single value for error limits does not give a representative or useful idea of the uncertainty associated with the correlations expressed by Equations (B-4.1) and (B-4.2). However the percentage deviation was more constant over the temperature range of the data with ±10% of the calculated value including nearly all of the data base.

The values returned by this model for temperatures in the transition region are about half as big as those reported by Mehan and Cutler, the only other source at these temperatures (not included in this model because of atypical heat treatment). Also, no data are available for zircaloy at higher (> 1250 K) temperatures. Therefore quite large uncertainty limits of ±50% are assumed for temperatures of more than 1073 K.

Figure B-4.2 shows the model predictions and uncertainty limits for axial thermal expansion compared with the data base, as does Figure B-4.3 for diametral expansion. The

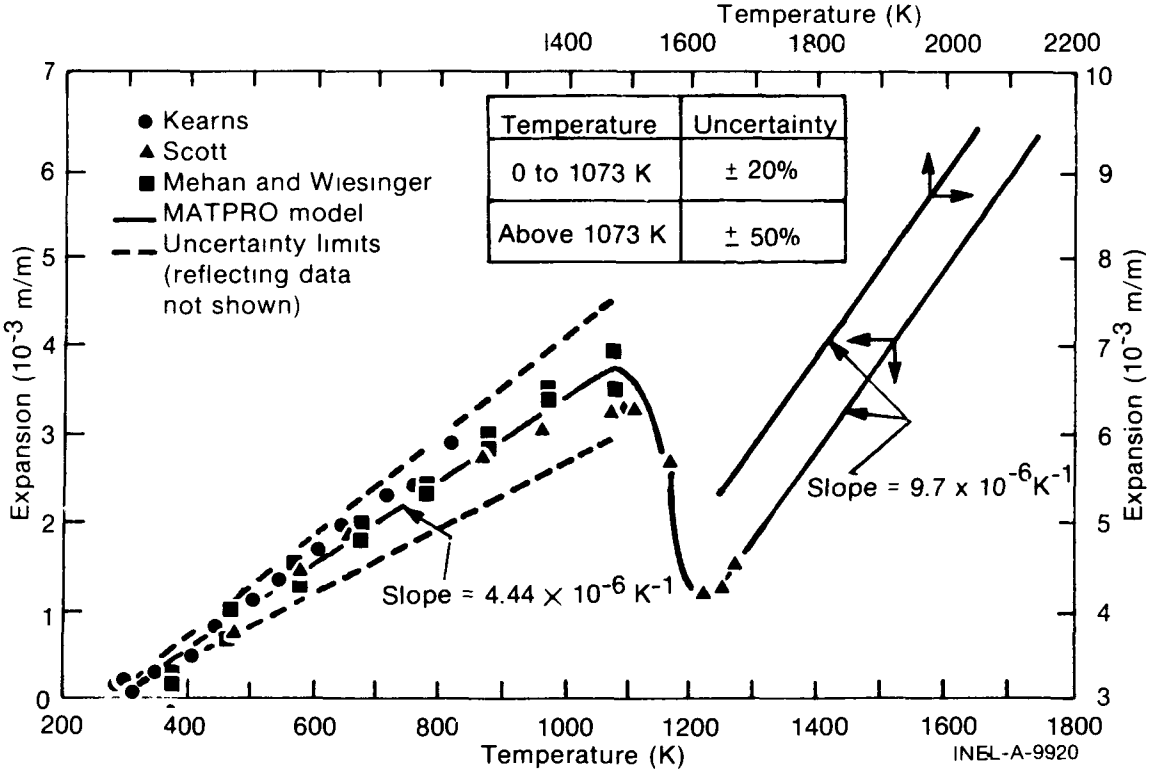

Fig. B-4.2 Axial thermal expansion of zircaloy as calculated by CTHEXP, data base, and low temperature uncertainty limits.

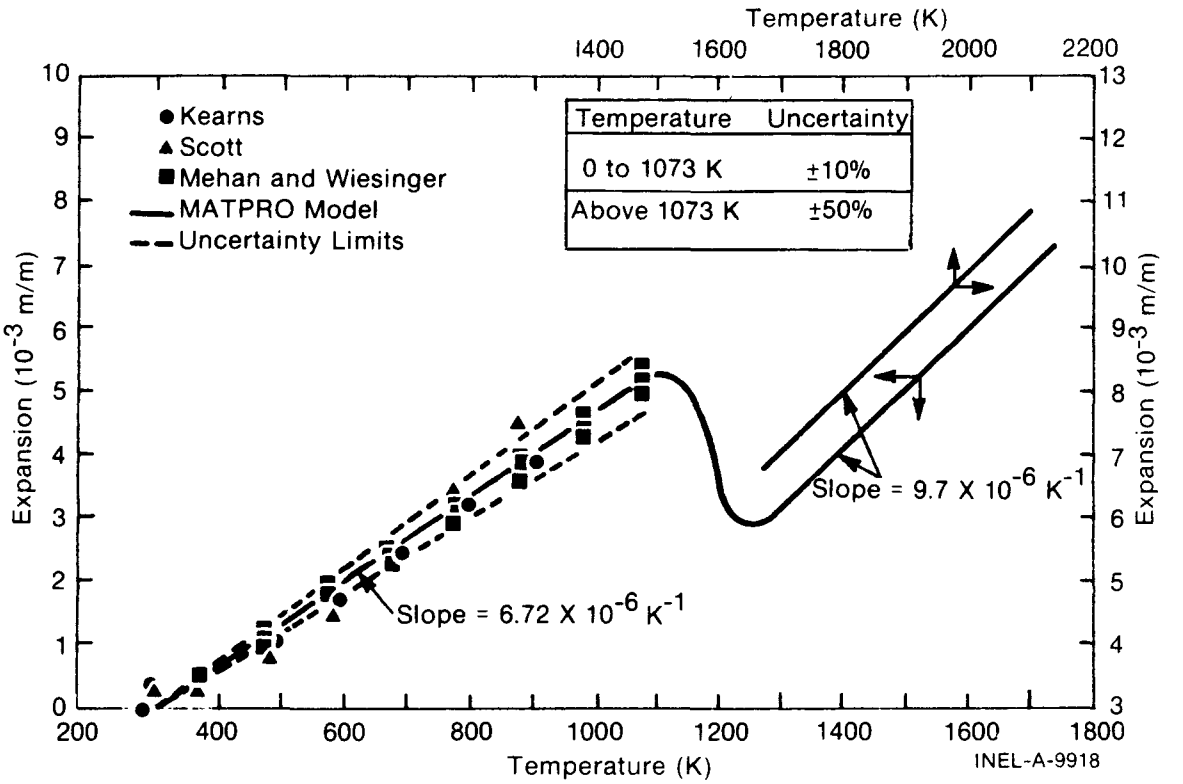

Fig. B-4.3 Diametral thermal expansion of zircaloy as calculated by CTHEXP, data base, and low temperature uncertainty limits.

uncertainty limits are only shown for temperatures in the alpha region because for other temperatures there are no data to support an error analysis and the ±50% uncertainty assigned at these higher temperatures is only a rough estimate. A comparison of the axial and diametral thermal expansion curves is shown in Figure B-4.4.

4.5 Cladding Thermal Expansion Subcode CTHEXP Listing

The FORTRAN listing of the subcode CTHEXP is given in Table B-4.I.

4.6 References

B-4.1. D. B. Scott, *Physical and Mechanical Properties of Zircaloy-2 and -4*, WCAP-3269-41 (May 1965) pp 8-12.

B-4.2. J. J. Kearns, *Thermal Expansion and Preferred Orientation in Zircaloy*, WAPD-TM-472 (1965).

B-4.3. R. L. Mehan and F. W. Wiesinger, *Mechanical Properties of Zircaloy-2*, KAPL-2110 (February 1961).

B-4.4. R. L. Mehan and G. L. Cutler, *Thermal Expansion of Zircaloy-2 Between Room Temperature and 1000°C*, KAPL-RLM-15 (1958).

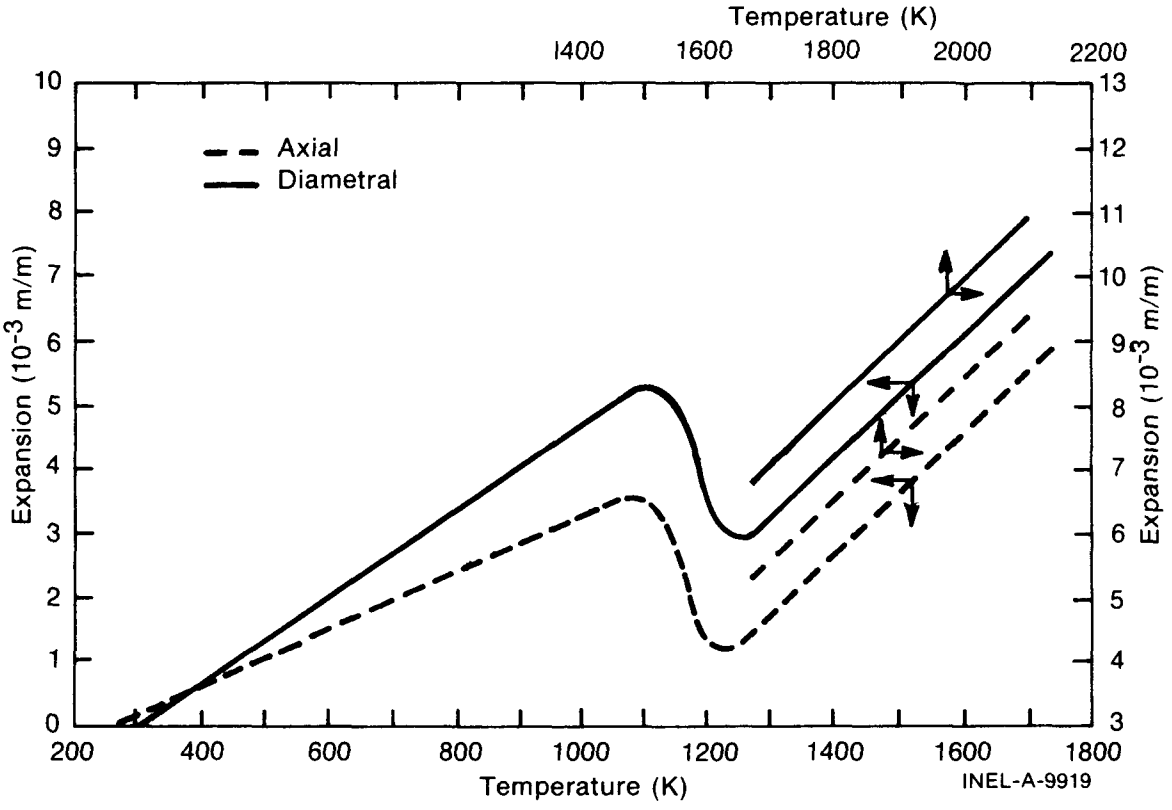

Fig. B-4.4 Comparison of axial and diametral thermal expansion.

B-4.5. F. W. Sears and M. W. Zemansky, *University Physics, 3rd Edition*, Reading, Massachusetts: Addison-Wesley Publishing Company, 1967, p 347.

B-4.6. B. Lustman and F. Kerze, Jr., *The Metallurgy of Zirconium*, New York: McGraw-Hill Book Company, Inc., 1955, p 355.

B-4.7. G. B. Skinner and U. L. Johnston, "Thermal Expansion of Zirconium Between 298 K and 1600 K," *Journal of Chemistry and Physics, 21* (August 1953) pp 1383-1384.

TABLE B-4.I

LISTING OF THE CTHEXP SUBCODE

```
C
C
      SUBROUTINE CTHEXP(CTEMP, CATHEX, CDTHEX)
C
C     CTHEXP CALCULATES AXIAL AND DIAMETRAL THERMAL EXPANSION OF
C     ZIRCALOY LWR CLADDING.
C
C     CATHEX = OUTPUT AXIAL THERMAL EXPANSION OF ZIRCALOY (M/M)
C     CDTHEX = OUTPUT DIAMETRAL THERMAL EXPANSION OF ZIRCALOY (M/M)
C
C     CTEMP  = INPUT CLADDING MESHPOINT TEMPERATURE (K)
C
C     DATA FOR THE CORRELATION FROM ROOM TEMPERATURE TO 1273K ARE
C     TAKEN FROM R.L. MEHAN AND F.W. WIESINGER, "MECHANICAL PROPERTIES
C     OF ZIRCALOY-2", USAEC REPORT RAPL-2110 (1961), D.B. SCOTT,
C     "PHYSICAL AND MECHANICAL PROPERTIES OF ZIRCALOY-2 AND -4",
C     WCAP-3269-41 (1965), AND J.J. KEARNS, "THERMAL EXPANSION
C     AND PREFERRED ORIENTATION IN ZIRCALOY", WAPD-TM-472 (1965)
C
C     ABOVE 1273K THE COEFFICIENT OF THERMAL EXPANSION USED IS THE
C     CONSTANT VALUE 9.7E-06/K RECOMMENDED BY B. LUSTMAN AND F. KERZE,
C     "THE METALLURGY OF ZIRCONIUM", MC GRAW-HILL BOOK COMPANY, NEW
C     YORK (1955) PAGE 355.
C
C     BETWEEN 1073 AND 1273K (APPROXIMATELY THE ALPHA-BETA TRANSITION
C     RANGE FOR ZIRCALOY) CTHEXP USES THE LINEAR INTERPOLATION ROUTINE
C     POLATE TO FIND THE THERMAL EXPANSION.
C
C     CTHEXP WAS ORIGINALLY CODED BY R.L. MILLER IN NOV. 1974.
C     LAST UPDATED BY G.A. REYMANN IN JUNE 1978.
C
      DIMENSION CATHXD (44)
      DIMENSION DTHEXP (44)
C
      DATA CATHXD/                                    0.0          ,     293.15    ,
     *    3.52774E-03,       1073.15  ,    3.53000E-03,     1083.15   ,
     *    3.50000E-03,       1093.15  ,    3.46000E-03,     1103.15   ,
     *    3.41000E-03,       1113.15  ,    3.33000E-03,     1123.15   ,
     *    3.21000E-03,       1133.15  ,    3.07000E-03,     1143.15   ,
     *    2.80000E-03,       1153.15  ,    2.50000E-03,     1163.15   ,
     *    2.00000E-03,       1173.15  ,    1.50000E-03,     1183.15   ,
     *    1.30000E-03,       1193.15  ,    1.16000E-03,     1203.15   ,
     *    1.13000E-03,       1213.15  ,    1.10000E-03,     1223.15   ,
     *    1.11000E-03,       1233.15  ,    1.13000E-03,     1243.15   ,
     *    1.20000E-03,       1253.15  ,    1.30000E-03,     1263.15   ,
     *    1.40000E-03,       1273.15  /
C
      DATA NPCATX, IU / 22,1 /
C
      DATA DTHEXP/                                                    4.3480E-04,  373.15,
     * 5.1395E-03, 1073.15,  5.2200E-03, 1083.15,  5.2500E-03, 1093.15,
     * 5.2800E-03, 1103.15,  5.2800E-03, 1113.15,  5.2400E-03, 1123.15,
     * 5.2200E-03, 1133.15,  5.1500E-03, 1143.15,  5.0800E-03, 1153.15,
     * 4.9000E-03, 1163.15,  4.7000E-03, 1173.15,  4.4500E-03, 1183.15,
     * 4.1000E-03, 1193.15,  3.5000E-03, 1203.15,  3.1300E-03, 1213.15,
     * 2.9700E-03, 1223.15,  2.9200E-03, 1233.15,  2.8700E-03, 1243.15,
     * 2.8600E-03, 1253.15,  2.8800E-03, 1263.15,  2.9000E-03, 1273.15/
C
      DATA NPDEXP, IU / 22,1 /
C
      IF(CTEMP.LE.1073.15) GO TO 1
      IF(CTEMP.GE.1273.15) GO TO 2
C
      CATHEX = POLATE(CATHXD,CTEMP,NPCATX,IU)
      CDTHEX = POLATE(DTHEXP,CTEMP,NPDEXP,IU)
      GO TO 20
C
    1 CATHEX = -2.506E-05 + (CTEMP-273.15)*4.441E-06
      CDTHEX = -2.3730E-04 + (CTEMP-273.15)*6.7210E-06
      GO TO 20
C
    2 CATHEX = -8.3E-03 + (CTEMP-273.15)*9.7E-06
      CDTHEX = -6.800E-03 + (CTEMP-273.15)*9.70E-06
   20 CONTINUE
      RETURN
      END
```

5. CLADDING ELASTIC MODULI (CELMOD, CSHEAR, and CELAST)

(D. L. Hagrman)

Elastic moduli are required to relate stresses to strains. The elastic moduli are defined by the generalized form of Hooke's law as elements of the fourth rank tensor which relates the second rank stress and strain tensors below the yield point. In practice, cladding is frequently assumed to be an isotropic material. In such a case only two independent elastic moduli are needed to describe the relation between elastic stress and strain. These two constants, the Young's modulus and the shear modulus, are calculated by the functions CELMOD and CSHEAR. Elements of the tensor necessary to describe anisotropic cladding are calculated by the subroutine CELAST.

5.1 Summary

Cladding elastic moduli are affected primarily by temperature and oxygen content. Fast neutron fluence, cold work and texture effects are also included in the models described herein but they are not as important as temperature and oxygen content for typical light water reactor fuel rod cladding. The models are based primarily on data published by Bunnell et al[B-5.1], Fisher and Renken[B-5.2], Armstrong and Brown[B-5.3], and Padel and Groff[B-5.4] since these data include the best description of texture for the temperature range in which they were used. Data from several other sources[B-5.5 to B-5.11] are used to evaluate the expected standard error of the CELMOD and CSHEAR codes and to estimate the effect of fast neutron fluence[B-5.12].

The expressions used in the CELMOD subcode to calculate the isotropic Young's modulus are:

(1) In the alpha phase

$$Y = (1.088 \times 10^{11} - 5.475 \times 10^{7}\ T + K_1 + K_2)/K_3 \qquad \text{(B-5.1a)}$$

(2) In the beta phase

$$Y = 9.21 \times 10^{11} - 4.05 \times 10^{7}\ T \qquad \text{(B-5.1b)}$$

(3) In the alpha + beta phase

Y = The value obtained by linear interpolation of values calculated at the alpha to alpha + beta and the alpha + beta to beta boundaries

where

Y = Young's modulus for zircaloy-2 and -4 with random texture (Pa)

T = cladding temperature (K)

K_1 = modification to account for the effect of oxidation (Pa). See Equation (B-5.2a)

K_2 = modification to account for the effect of cold work (Pa). See Equation (B-5.2b)

K_3 = modification to account for the effect of fast neutron fluence, (unitless). See Equation (B-5.2c).

The expressions used to model the effects of oxidation, cold work, and fast neutron fluence are

$$K_1 = (6.61 \times 10^{11} + 5.912 \times 10^{8}\ T)\Delta \qquad \text{(B-5.2a)}$$

$$K_2 = -2.6 \times 10^{10}\ C \qquad \text{(B-5.2b)}$$

$$K_3 = 0.88 + 0.12 \exp\ (-\Phi/10^{25}) \qquad \text{(B-5.2c)}$$

where

Δ = average oxygen concentration minus oxygen concentration of as-received cladding (kg oxygen/kg zircaloy). As-received oxygen concentrations are so small (0.0012 kg oxygen/kg zircaloy) that the exact magnitude of the as-received concentration will not affect the correlation predictions.

C = cold work (unitless ratio of areas)

ϕ = fast neutron fluence (neutron/m^2).

The standard error of the CELMOD code is 6.4×10^9 Pa.

The expressions used in the CSHEAR subcode to calculate the isotropic shear modulus are:

(1) In the alpha phase

$$G = (4.04 \times 10^{10} - 2.168 \times 10^{7}\ T + K_1 + K_2)/K_3 \qquad \text{(B-5.3a)}$$

(2) In the beta phase

$$G = 3.49 \times 10^{10} - 1.66 \times 10^{7}\ T \qquad \text{(B-5.3b)}$$

(3) In the alpha + beta phase

G = the value obtained by linear interpolation of values calculated at the alpha to alpha + beta and the alpha + beta to beta boundaries.

where

K_1 = modification to account for the effect of oxidation (Pa). See Equation (B-5.4).

and the other terms have been defined in conjunction with Equations (B-5.1a) through (B-5.1c).

The expression used to model the effect of oxidation for shear modulus is

$$K_1 = (7.07 \times 10^{11} - 2.315 \times 10^{8}\ T)\Delta \qquad \text{(B-5.4)}$$

where the terms have been previously defined.

The standard error of the CSHEAR code is 9×10^{9} Pa.

The subcode CELAST calculates elastic compliance constants for isotropic cladding. This subcode is discussed in the model development Section B-5.3 because it is the basis for the much simpler CELMOD and CSHEAR codes. The elastic moduli predicted by CELAST for typical textures are reasonably close to the moduli for isotropic cladding. Figure B-5.1 illustrates this. The solid lines represent the Young's and shear moduli for isotropic (random texture) material. The six broken lines represent reciprocal compliance constants corresponding to diagonal elements of the traditional S-matrix. Three of these quantities may be interpreted as the apparent Young's moduli for stresses in the direction indicated and the other three may be interpreted as the apparent shear moduli for shears acting normal to the direction indicated. The only modulus which departs significantly from the isotropic moduli is the Young's modulus in the radial direction. It should be noted that this modulus was based on zirconium single crystal data because appropriate zircaloy data are not available. The axial and circumferential Young's moduli are based on zircaloy-4 data and they are very similar to the isotropic Young's modulus. The increased Young's modulus in the radial direction is not expected to affect code predictions, even if zircaloy data do confirm the difference shown by the zirconium data.

Details of the elastic modulus models are presented in the following sections. Section B-5.2 is a review of available data and Section B-5.3 describes the model development.

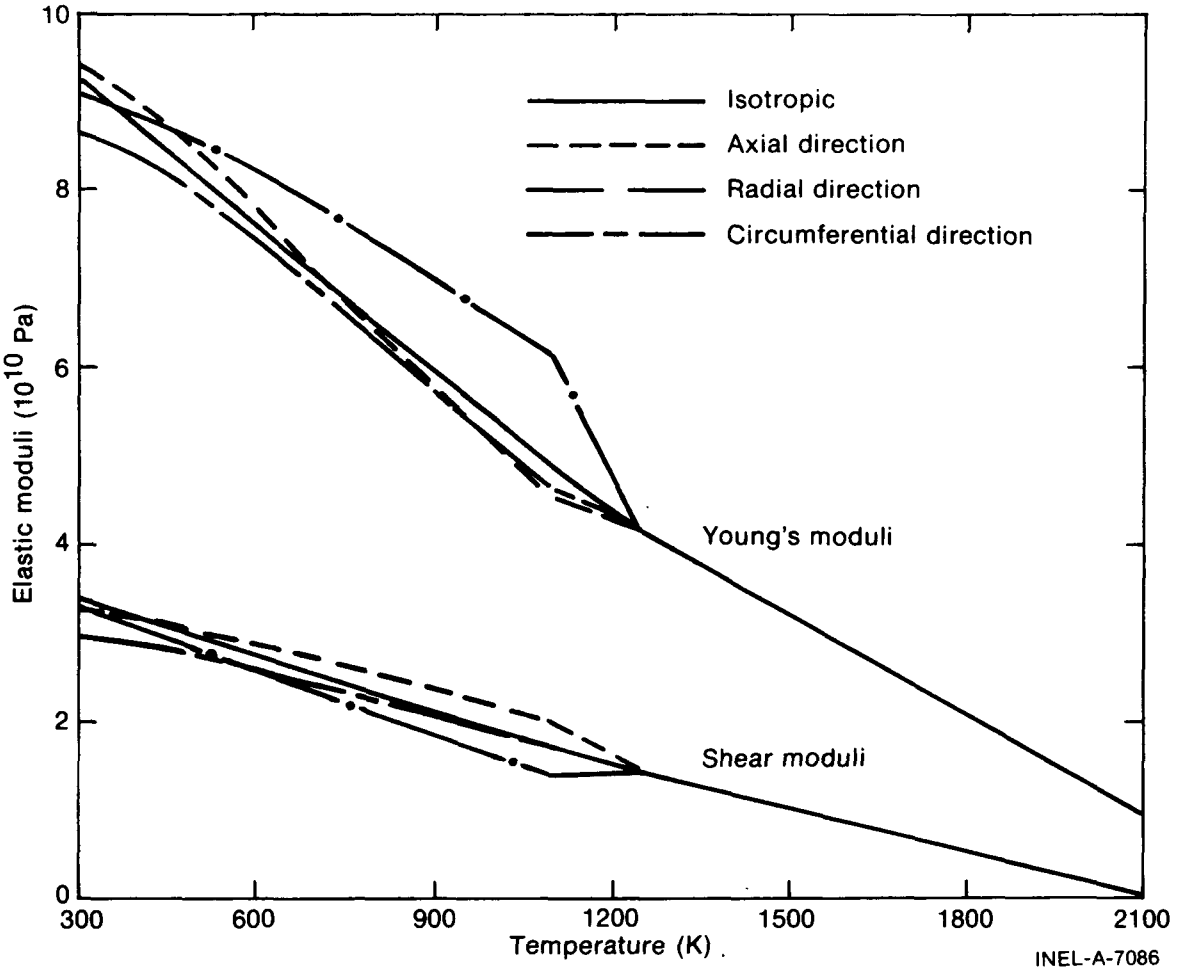

Fig. B-5.1 Elastic moduli for isotropic material compared to corresponding moduli for typical PWR cladding.

Section B-5.4 is a comparison of the model and its data base. Uncertainties are discussed in Section B-5.5. Subcode listings are presented in Section B-5.6 and Section B-5.7 contains references.

5.2 Review of Available Data

Elastic moduli measurements may be classified as either static or dynamic. The static moduli are based on measurements of stress and strain under conditions which can, in principle, be representative of in-reactor cladding. However, the accuracy of the static moduli are typically limited by the accuracy of the measurement of the strain. Dynamic measurements avoid this difficulty by vibrating a sample of known dimensions in a resonant mode and inferring the moduli from accurate measurements of resonant frequency. The advantage in accuracy of the dynamic measurements is somewhat compromised by the fact that these measurements are made with the small cyclic strains associated with resonant

modes. To date, static measurements have not achieved sufficient accuracy to show significant discrepencies with the dynamic measurements so the dynamic measurements are used as a basis for the models discussed herein.

The most complete set of applicable elastic moduli measurements available are the dynamic measurements of zirconium single crystal moduli by Fisher and Renken[B-5.2]. Measured values of the stiffness moduli[a] C_{11}, C_{33}, C_{44}, C_{13}, and C_{12} are reported at 50 K intervals from 4 K to the alpha + beta phase transition at 1135 K. The C_{11}, C_{33}, C_{44}, and C_{13} moduli vary almost linearly with temperature between 300 and 1135 K while the C_{12} modulus is reported to increase in a nonlinear fashion with temperature. Least-squares polynomial fits to Fisher and Renken's data yield the following correlations when the data at 300 K or greater are used:

$$C_{11} = 1.562 \times 10^{11} - 4.484 \times 10^{7}\ T \qquad \text{(B-5.5a)}$$

$$C_{33} = 1.746 \times 10^{11} - 3.282 \times 10^{7}\ T \qquad \text{(B-5.5b)}$$

$$C_{44} = 3.565 \times 10^{10} - 1.281 \times 10^{7}\ T \qquad \text{(B-5.5c)}$$

$$C_{12} = 6.448 \times 10^{10} + (3.1882 \times 10^{7} - 1.2318 \times 10^{4}\ T)\ T \qquad \text{(B-5.5d)}$$

$$C_{13} = 6.518 \times 10^{10} - 6.817 \times 10^{5}\ T \qquad \text{(B-5.5e)}$$

where

C_{ij} = The five independent stiffness moduli for a hexagonal crystal (Pa). (The subscripts, 1, 2, 3 refer to orthogonal coordinate axes arranged with the direction labeled 3 parallel to the <c> axis. By basal plane symmetry, the 1 and 2 axes are any orthogonal axes in the basal plane.)

T = temperature (K).

Single crystal constants have not been determined for the high temperature beta phase so measurements on polycrystalline materials of unknown texture are used. The models are

[a] The definition of elastic stiffness moduli is reviewed in subsection 5.3 in conjunction with the development of the model for the effect of texture variations.

based on dynamic measurements of the Young's modulus[a] of zirconium by Armstrong and Brown[B-5.3] and by Padel and Groff[B-5.4]. The data from these two sources are reproduced in Tables B-5.I and B-5.II. The measurements differ by less than five percent at corresponding temperatures. As discussed in Section B-5.3, compliance constants (elements of the inverse of the stiffness matrix) are obtained by assuming that the beta phase is isotropic.

TABLE B-5.I

BETA PHASE ZIRCONIUM YOUNG'S MODULUS MEASURED BY ARMSTRONG AND BROWN

Temperature (K)	Young's Modulus (10^{10} Pa)
1173	4.426
1223	4.233
1273	4.047
1323	3.861
1373	3.675
1423	3.488
1473	3.302

The alpha phase data of Fisher and Renken do not help one to address three of the effects which are under consideration in this report – the effects of zircaloy alloying elements, of oxidation, and of variations in texture. These considerations are addressed with the help of recent Young's moduli measurements in the axial and circumferential direction by L. R. Bunnell et al[B-5.1]. Bunnell's data provide important additional information because (a) they were taken with zircaloy cladding, (b) the samples contained various amounts of oxygen, and (c) an estimate of the initial texture of the material is available. Unfortunately, the texture information is only available for the as-received samples and consists of a basal pole figure published by R. H. Chapman[B-5.13].

Bunnell's data were analyzed using the model for the effect of texture developed in Section B-5.3. The axial and circumferential Young's modulus data are used to establish correlations for the effect of temperature and oxygen on two of the five independent compliance constants. The correlations for as-received and "homogenized" (annealed) cladding agree closely with the compliance constants obtained by inverting

[a] Young's modulus is defined as stress in a given direction divided by strain in the same direction.

TABLE B-5.II

BETA PHASE ZIRCONIUM YOUNG'S MODULUS MEASURED BY PADEL AND GROFF

Temperature (K)	Young's Modulus (10^{10} Pa)
1143	4.578
1156	4.544
1181	4.311
1234	4.233
1266	4.111
1281	4.122
1311	3.922
1340	3.833
1380	3.611
1395	3.544
1409	3.422
1449	3.278
1474	3.167

Equations (B-5.5a) through (B-5.5e) and lend confidence to the assumption that single crystal zirconium data is a good approximation to zircaloy data when oxygen concentrations are on the order of 0.001 weight fraction. The latter assumption is necessary because the data from zircaloy cladding are not sufficient to determine all five independent compliance constants.

Data relevant to modeling the effect of irradiation and cold work are limited both in quantity and in completeness. The Saxton Core II Fuel Performance Evaluation[B-5.12] reports elastic moduli at 630 K for irradiated cladding. The moduli were measured with a static method in the axial direction but no pole figure was provided so the effects of irradiation could not be separated from the effects of texture.

Data relevant to modeling the effect of cold work is contained (but not discussed as such) in the report by Bunnell et al[B-5.1]. The as-received material was cold-worked to about 0.75 and stress relieved for four hours at 770 K[B-5.13]. The "homogenized" material was completely annealed. Unfortunately, the effect of cold work suggested by Bunnell's dynamic measurements of Young's modulus is opposite to the trend reported by Shober et al[B-5.9] from static measurements. The dynamic measurements show a slight decrease in Young's modulus with cold work and the static measurements show a slight

increase in Young's modulus with cold work. Since neither source provides usable texture information it is impossible to tell whether the change with cold work is due to associated changes in texture, to a separate effect associated with the cold work, or to a fundamental difference in the quantity that is being measured with the different techniques. The small decrease implied by Bunnell's data was tentatively included in the models for elastic moduli because of the greater precision of the dynamic data.

Several measurements of Young's and shear moduli were not used in constructing the models for elastic moduli because texture information was not available. The data are useful, however, as an independent test of the two approximate models for isotropic cladding. Busby[B-5.5] reported the axial Young's modulus for zircaloy-4 between 300 and 645 K for five combinations of cold work and heat treatment. Busby's data are reproduced in Table B-5.III. Spasic et al[B-5.6] reported values of the static elastic modulus from room temperature to 675 K. Their data are reproduced in Table B-5.IV. The material used by Spasic et al was not characterized as to cold work or texture. It is assumed that unirradiated material in the annealed condition was used in these tests. Mehan[B-5.7] and Mehan and Wiesinger[B-5.8] reported Young's modulus data from room temperature to 1090 K. The data were taken with both static and dynamic techniques on unirradiated vacuum annealed zircaloy-2 plates. Table B-5.V is a summary of Mehan's measurements. Northwood et al[B-5.9] reported Young's modulus and shear modulus data from 293 to 773 K. The data were obtained with a resonance method and are accompanied by an excellent discussion of the effects of texture. The zircaloy-2 samples were machined from bar stock which had been annealed for one hour at 1061 K. Table B-5.VI is a summary of the zircaloy-2 data reported by Northwood et al.

5.3 Development of the Models

The equations used in the CELMOD and CSHEAR subcodes are simplified forms of the more complex expressions used in the CELAST subcode. The quantities modeled by CELAST are elastic compliance coefficients. These coefficients, and the closely related elastic stiffness coefficients, are defined by the relations[B-5.14].

$$\epsilon_i = S_{ij}\,\sigma_j \qquad \text{(B-5.6a)}$$

$$\sigma_i = C_{ij}\,\epsilon_j \qquad \text{(B-5.6b)}$$

where

ϵ_i = strain components

σ_i = stress components

S_{ij} = compliance matrix elements

C_{ij} = stiffness matrix elements.

TABLE B-5.III

YOUNG'S MODULUS MEASUREMENTS BY BUSBY

Material	Temperature (K)	Young's Modulus (10^{10} Pa)	Effective Cold Work Predicted by the Subcode CANEAL
78% Cold Work 922 K Recrystallization for 5 hours	297	9.686	0%
78% Cold Work 922 K Recrystallization for 5 hours	516	8.018	0%
78% Cold Work 922 K Recrystallization for 5 hours	644	7.515	0%
15-20% Cold Work 783 K Stress Relief for 5 hours	297	10.031	5%
15-20% Cold Work 783 K Stress Relief for 5 hours	561	8.583	5%
15-20% Cold Work 783 K Stress Relief for 5 hours	559	8.349	5%
74% Cold Work 783 K Stress Relief for 5 hours	297	9.907	25%
73% Cold Work 783 K Stress Relief for 5 hours	644	7.708	25%

Also, the usual tensor summation convention is assumed.

By inspection of Equations (B-5.6) it is clear that the compliance matrix is the reciprocal of the stiffness matrix. The author has elected to use compliance coefficients.

5.3.1 Effect of Texture Variations. Texture effects are modeled using techniques which have become fairly standard[B-5.9, B-5.15, B-5.16]. Macroscopic compliance matrix elements for polycrystalline materials are computed as the average of corresponding single crystal values, weighted by the volume fraction of grains at each orientation.

TABLE B-5.IV

YOUNG'S MODULUS MEASUREMENTS BY SPASIC ET AL

Temperature (K)	Young's Modulus (10^{10} Pa)
300	10.10
373	9.25
423	8.78
473	8.52
673	7.70
673	7.40

$$\overline{S'_{ij}} = \iiint S'_{ij}\,(\theta,\Phi)\;\rho\;(\theta,\Phi)\;dv \qquad \text{(B-5.7)}$$

where

$\overline{S'_{ij}}$ = macroscopic compliance constants (Pa^{-1})

$S'_{ij}\,(\theta,\phi)$ = single crystal compliance constants defined relative to a fixed set of coordinates. Figure B-5.2 defines the coordinates and the angles θ and ϕ.

$\rho\,(\theta,\phi)$ = volume fraction of grains with their c axes orientated at angles θ and ϕ relative to the fixed set of coordinates.

The volume fraction of grains at angles θ and ϕ can be determined from c axis pole figures.

$$\rho(\theta,\Phi) = \frac{I\,(\theta,\Phi)}{\int_0^{2\pi}\int_0^{\pi} I\,(\theta,\Phi)\,\sin\theta\,(d\theta)(d\Phi)} \qquad \text{(B-5.8)}$$

where

$I\,(\theta,\phi)$ = the diffracted X-ray intensity of the basal planes as plotted in basal pole figures.

TABLE B-5.V

YOUNG'S MODULUS MEASUREMENTS BY MEHAN

Temperature (K)	Young's Modulus (10^{10} Pa)	Method/Direction
300	9.493	Static/Not Reported
300	9.473	Static/Not Reported
300	9.459	Static/Not Reported
300	9.500	Static/Not Reported
589	7.928	Static/Not Reported
589	7.790	Static/Not Reported
297	9.804	Dynamic/Transverse
427	9.142	Dynamic/Transverse
593	8.273	Dynamic/Transverse
704	7.715	Dynamic/Transverse
298	9.921	Dynamic/Transverse
422	9.238	Dynamic/Transverse
594	8.466	Dynamic/Transverse
711	7.784	Dynamic/Transverse
811	7.246	Dynamic/Transverse
300	9.893	Dynamic/Transverse
424	9.128	Dynamic/Transverse
598	8.294	Dynamic/Transverse
703	7.715	Dynamic/Transverse
809	7.852	Dynamic/Transverse
298	9.452	Dynamic/Longitudinal
428	8.659	Dynamic/Longitudinal
591	7.535	Dynamic/Longitudinal
703	6.991	Dynamic/Longitudinal
814	6.356	Dynamic/Longitudinal
298	9.445	Dynamic/Longitudinal
430	8.597	Dynamic/Longitudinal
593	7.604	Dynamic/Longitudinal
698	6.908	Dynamic/Longitudinal
814	6.219	Dynamic/Longitudinal
303	9.445	Dynamic/Longitudinal
422	8.597	Dynamic/Longitudinal
594	7.535	Dynamic/Longitudinal
707	6.942	Dynamic/Longitudinal
822	6.253	Dynamic/Longitudinal

TABLE B-5.VI

ELASTIC MODULI MEASUREMENTS BY NORTHWOOD ET AL

Temperature (K)	Young's Modulus		Shear Modulus
	Longitudinal (10^{10} Pa)	Transverse (10^{10} Pa)	Torsional Resonant Mode (10^{10} Pa)
293	9.67	9.61	3.48
373	9.01	8.98	3.36
473	8.64	8.60	3.18
573	7.99	8.01	2.94
673	7.38	7.34	2.79
773	6.78	6.81	2.53

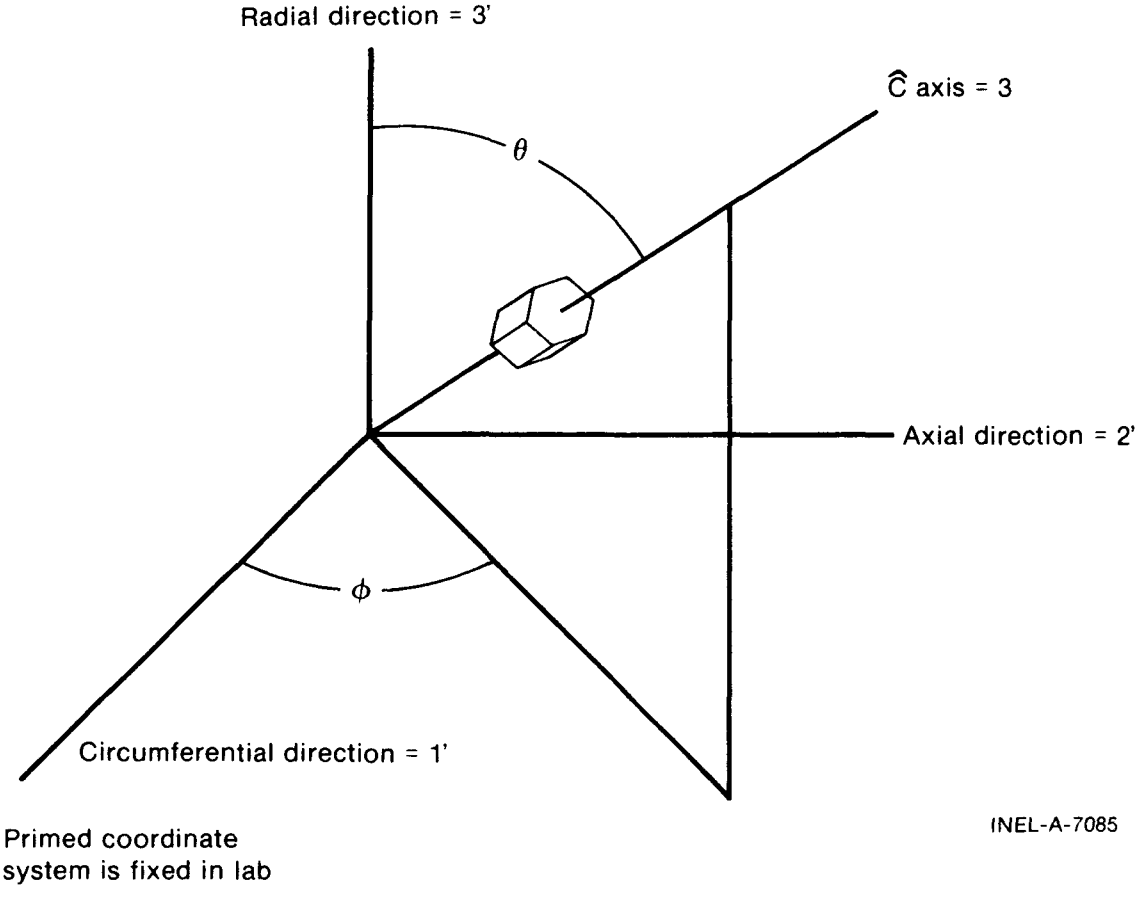

Fig. B-5.2 Reference directions selected for CELMOD/CSHEAR/CELAST analysis.

Expressions for the various single crystal compliance constants, referred to a fixed coordinate system, $S'_{ij}(\theta,\phi)$ in Equation (B-5.7), are obtained by applying standard tensor rotation techniques[B-5.17] to single crystal compliances defined relative to a set of coordinates attached to each grain, S_{ij}[a]. The traditional matrix notation is converted to a formal 4th rank tensor using the relations listed in Table B-5.VII[B-5.14]. The coordinate system is rotated with the equation

$$S'_{ijke}(\theta,\phi) = C_{ir}\, C_{js}\, C_{kt}\, C_{eu}\, S_{rstu} \qquad \text{(B-5.9)}$$

where

$S'_{ijke}(\theta,\phi)$ = single crystal compliance tensor elements measured with respect to the fixed (primed) coordinate system shown in Figure B-5.2 (Pa^{-1})

S_{ijke} = single crystal compliance tensor elements measured with respect to a coordinate system attached to each grain (Pa^{-1})

C_{ij} = elements of the rotation matrix

$$= \begin{pmatrix} \text{COS}\alpha & \text{SIN}\alpha\,\text{COS}\theta & +\text{SIN}\alpha\,\text{SIN}\theta \\ -\text{SIN}\alpha & \text{COS}\alpha\,\text{COS}\theta & +\text{COS}\alpha\,\text{SIN}\theta \\ \text{O} & -\text{SIN}\theta & \text{COS}\theta \end{pmatrix}$$

α = complement of ϕ.

The expressions which result from combining Equation (B-5.9), the relations in Table B-5.VII, and Equations (B-5.8) and (B-5.9) are available in the CELAST subcode listing. As an example, the equation relating the macroscopic elastic compliance constant $\overline{S_{33}'}$ to the single crystal compliance constants is

$$\overline{S'_{33}} = (1-2\langle\cos^2\theta\rangle + \langle\cos^4\theta\rangle)\, S_{11} + (\langle\cos^2\theta\rangle - \langle\cos^4\theta\rangle)$$
$$(2S_{13} + S_{44}) + \langle\cos^4\theta\rangle S_{33} \qquad \text{(B-5.10)}$$

---

[a] In this section, primed compliance constants are referred to a system of coordinates which are fixed. Unprimed compliance constants are referred to a system of coordinates which are determined by the orientation of each grain as shown in Figure B-5.2.

TABLE B-5.VII

RELATIONS BETWEEN FOURTH RANK TENSOR ELEMENTS
AND TRADITIONAL MATRIX ELEMENTS

Complete Compliance Tensor Elements		Traditional Matrix Elements
(S_{11ij})	=	$\begin{pmatrix} S_{11} & (1/2\ S_{16}) & (1/2\ S_{15}) \\ (1/2\ S_{16}) & S_{12} & (1/2\ S_{14}) \\ (1/2\ S_{15}) & (1/2\ S_{14}) & S_{13} \end{pmatrix}$
(S_{12ij})	= 1/2	$\begin{pmatrix} S_{61} & (1/2\ S_{66}) & (1/2\ S_{65}) \\ (1/2\ S_{66}) & S_{62} & (1/2\ S_{64}) \\ (1/2\ S_{65}) & (1/2\ S_{64}) & S_{63} \end{pmatrix}$
(S_{13ij})	= 1/2	$\begin{pmatrix} S_{51} & (1/2\ S_{56}) & (1/2\ S_{55}) \\ (1/2\ S_{56}) & S_{52} & (1/2\ S_{54}) \\ (1/2\ S_{55}) & (1/2\ S_{54}) & S_{53} \end{pmatrix}$
(S_{22ij})	=	$\begin{pmatrix} S_{21} & (1/2\ S_{26}) & (1/2\ S_{25}) \\ (1/2\ S_{26}) & S_{22} & (1/2\ S_{24}) \\ (1/2\ S_{25}) & (1/2\ S_{24}) & S_{23} \end{pmatrix}$
(S_{23ij})	= 1/2	$\begin{pmatrix} S_{41} & (1/2\ S_{46}) & (1/2\ S_{45}) \\ (1/2\ S_{46}) & S_{42} & (1/2\ S_{44}) \\ (1/2\ S_{45}) & (1/2\ S_{44}) & S_{43} \end{pmatrix}$
(S_{33ij})	=	$\begin{pmatrix} S_{31} & (1/2\ S_{36}) & (1/2\ S_{35}) \\ (1/2\ S_{36}) & S_{32} & (1/2\ S_{34}) \\ (1/2\ S_{35}) & (1/2\ S_{34}) & S_{33} \end{pmatrix}$

$S_{rsij} = S_{srij}$

where

$\overline{S_{33}'}$	=	macroscopic elastic compliance constant relating radial stress to radial strain (Figure B-5.2) (Pa^{-1})
$S_{11}, S_{13}, S_{33}, S_{44}$	=	single crystal compliance constants (Pa^{-1})
$\langle\cos^2\theta\rangle$	=	volume fraction weighted average of the squared cosine of the angle, θ (Figure B-5.2)
$\langle\cos^4\theta\rangle$	=	volume fraction weighted average of the fourth power of the angle θ.

5.3.2 Effect of Temperature. The effect of temperature on single crystal elastic compliance constants is modeled separately for the alpha and beta phases of zircaloy.

Correlations for two of the five independent elastic constants[B-5.14], S_{11} and S_{44}, are developed from Bunnell's measurements of the axial and circumferential Young's modulus of unoxidized zircaloy-4. The other three single crystal alpha phase constants, S_{33}, S_{12}, and S_{13} are modeled by finding the matrix inverse of the stiffness moduli for zirconium [Equations (B-5.5a) to (B-5.5e)]. The expressions obtained from Bunnell's data are an improvement over the alternate expressions which could be obtained from the zirconium data because Bunnell's data were taken with zircaloy-4 cladding.

In order to use the zircaloy-4 data, the pole figure provided by R. H. Chapman is input to the MATPRO subcode CTXTUR to find the orientation angle averages relating single crystal elastic compliance constants to $\overline{S_{11}'}$ and $\overline{S_{22}'}$ for this cladding. The resultant expressions are:

$$\overline{S_{11}'} = 0.65106\ S_{11} + 0.09210\ S_{33} + (0.12842)(2\ S_{13} + S_{44}) \quad \text{(B-5.11a)}$$

$$\overline{S_{22}'} = 0.88030\ S_{11} + 0.01900\ S_{33} + (0.05035)(2\ S_{13} + S_{44}) \quad \text{(B-5.11b)}$$

where

$\overline{S_{11}'}, \overline{S_{22}'}$	=	macroscopic elastic compliance constants (Pa^{-1})
$S_{11}, S_{13}, S_{33}, S_{44}$	=	single crystal compliance constants (Pa^{-1}).

Inspection of the defining relation for the elastic compliance constants [Equation (B-5.5a)] and the reference direction conventions used in this report (Figure B-5.2) shows that $\overline{S_{11}}$ is the reciprocal of Young's modulus measured in the circumferential direction of the cladding and $\overline{S_{22}}$ is the reciprocal of Young's modulus measured in the axial direction of the cladding. Thus Equations (B-5.11a) and (B-5.11b) can be used with Bunnell's measurements of the circumferential and axial Young's modulus of this cladding and the inverse matrix values of S_{33} and S_{13} to find least-squares correlations for S_{11} and S_{44} as a function of temperature.

The correlations found from a least-squares fit to Bunnell's data are:

$$S_{11} = 0.1028 \times 10^{-10} + T\,(-0.5417 \times 10^{-14} + T\,0.1476 \times 10^{-16}) \quad \text{(B-5.12a)}$$

$$S_{44} = 0.3904 \times 10^{-10} + T\,(-0.8118 \times 10^{-14} + T\,0.2115 \times 10^{-16}) \quad \text{(B-5.12b)}$$

where the terms of the equations have been previously defined.

Equation (B-5.12a) predicts values of S_{11} which vary from zero to 10% below the value of S_{11} predicted by the zirconium data of Fisher and Renken[B-5.16]. Equation (B-5.12b) predicts values of S_{44} which are about 20% above the value of S_{44} predicted by the zirconium data of Fisher and Renken[B-5.16].

In the beta phase[a], only two independent single crystal compliance constants are employed. The independent constants are S_{11} and S_{44}. By classical symmetry arguments, $S_{33} = S_{11}$, $S_{23} = S_{13} = S_{12}$. A correlation for one of the constants is obtained from a least-squares fit to the beta phase zirconium Young's modulus data of Armstrong and Brown[B-5.3] and Padel and Groff[B-5.4]. The expression is

$$S_{11}^{-1} = Y = 9.21 \times 10^{10} - 4.05 \times 10^{7} \quad \text{(B-5.13)}$$

where

S_{11} = elastic compliance constant for beta phase zircaloy (Pa^{-1})

Y = Young's modulus for beta phase zircaloy (Pa)

T = cladding temperature (K).

---

[a] The beta phase is body centered cubic and has therefore been assumed isotropic.

Since no measurements of the shear modulus in beta phase zirconium are available, the second constant, S_{44}, is estimated by extrapolation of an approximate expression for the shear modulus of isotropic alpha phase zirconium to the higher temperatures of the beta phase.

The phase boundaries of the alpha, alpha + beta, and beta phases are determined with correlations based on data from Figure III.33 of Reference B-5.18. Compliance constants in the alpha + beta phase region are obtained by interpolating between these constants at the boundaries of this region.

5.3.3 Effect of Oxygen. The only data available to model the effect of oxygen on the single crystal compliance constants are Bunnell's measurements of axial and circumferential Young's moduli as a function of oxygen concentration[B-5.1]. The effect of oxygen on the alpha phase compliance constants is modeled in much the same way that Bunnell's data were used to correlate changes in the single crystal compliance constants S_{11} and S_{44} with temperature. The three step procedure is outlined as follows:

(1) Equation (B-5.11b) is used with measured values of the axial Young's modulus ($\overline{1/S'_{22}}$), approximate (zirconium) values of S_{33}, S_{13}, and S_{44} in the small terms containing these factors and the measured values of oxygen concentration to find a least-squares fit correlation between S_{11} and the oxygen concentration.

(2) Equation (B-5.11a) is used with measured values of the circumferential Young's modulus ($\overline{1/S'_{11}}$), the expression for S_{11} obtained in step (1), approximate (zirconium) values of S_{33} and S_{13} and the measured values of oxygen concentration to find a least-squares fit correlation for S_{44} as a function of oxygen concentration. The correlations obtained are

$$\frac{1}{S_{11}} = \frac{1}{(S_{11})_o} + (6.61 \times 10^{11} + 5.912 \times 10^{8}\ T)\Delta \qquad \text{(B-5.14a)}$$

$$\frac{1}{S_{44}} = \frac{1}{(S_{44})_o} + (7.07 \times 10^{11} + 2.315 \times 10^{8}\ T)\Delta \qquad \text{(B-5.14b)}$$

where

S_{11}, S_{44} = elastic compliance constants for oxidized zircaloy (Pa^{-1})

$(S_{11})_o$, $(S_{44})_o$ = elastic compliance constants for as-received zircaloy (Pa^{-1})

T = cladding temperature (K)

Δ = average oxygen concentration minus oxygen concentration of as-received cladding (kg oxygen/kg zircaloy).

(3) Equation (B-5.14a) is assumed to apply to S_{13}, S_{33}, and S_{12}.

The effect of oxygen in the beta phase has been neglected because no relevant data are available and because an exact knowledge of elastic moduli at the high temperatures of the beta phase is not likely to be important to code applications.

5.3.4 Effect of Cold Work. Bunnell's measurements of the Young's modulus of cold-worked stress relieved cladding were compared to his Young's modulus measurements of "homogenized" (annealed) cladding to estimate cold work effects. Measured values of the axial Young's modulus for the stress relieved material are related to S_{11} with Equation (B-5.11b). The differences between $(S_{11})^{-1}$ in the cold-worked material and (S_{11}) computed for annealed material [Equation (B-5.12a)] are assumed to be proportional to the cold work (assumed = 0.5). The correlation resulting from an average of the six low temperature data on as-received cladding is

$$\frac{1}{S_{11}} = \frac{1}{(S_{11})_o} - 2.6 \times 10^{10}\ C \qquad \text{(B-5.15)}$$

where

S_{11} = elastic compliance constant for cold-worked zircaloy (Pa^{-1})

$(S_{11})_o$ = elastic compliance constant for annealed zircaloy (Pa^{-1})

C = cold work (unitless ratio of areas).

No modification of S_{44} was implied by Bunnell's measurements of the Young's modulus in the circumferential direction.

5.3.5 Effect of Irradiation. Data from the Saxton Core II Fuel Performance Evaluation[B-5.12] are used to estimate fast neutron fluence effects on elastic compliance constants. Since no pole figures for this material were found, measured values of the axial Young's modulus for the irradiated material are related to S_{11}, S_{33}, S_{13}, and S_{44} with Equation (B-5.14b). The four compliance constants are assumed to decrease by a single factor due to the fluence and the factor is determined by comparing the measured values of Young's modulus to the values predicted for unirradiated material. The factor which results from the comparison is:

$$\frac{S_{ij}}{(S_{ij})_o} = 0.88 \qquad \text{(B-5.16a)}$$

where

S_{ij} = each of the compliance constants for the irradiated cladding (Pa^{-1})

$(S_{ij})o$ = each of the compliance constants predicted for unirradiated cladding (Pa^{-1}).

Measured values of fast neutron fluences received by the Saxton rods varied from 2.2 to 3.4 10^{25} neutrons/m^2 and no correlation with the fluence was found. The fluence dependence is therefore modeled by replacing Equation (B-5.16a) with an assumed fluence dependent expression

$$H = 0.88 + 0.12 \exp(-\Phi/10^{25}) \qquad \text{(B-5.16b)}$$

where

H = ratio of compliance constants for irradiated material to compliance constants for unirradiated material

ϕ = fast neutron fluence (neutrons/m^2).

5.3.6 Derivation of the CELMOD and CSHEAR Codes from the CELAST Code. It has been mentioned in Section B-5.3.2 that the compliance tensor contains only two independent constants for isotropic (random distribution of C axes) cladding. Moreover, the definition of the compliance tensor implies that the constants may be interpreted as the reciprocals of Young's modulus and the shear modulus

$$\overline{(S'_{ij})}_{isotropic} = \begin{pmatrix} Y^{-1} & a & a & 0 & 0 & 0 \\ a & Y^{-1} & a & 0 & 0 & 0 \\ a & a & Y^{-1} & 0 & 0 & 0 \\ 0 & 0 & 0 & G^{-1} & 0 & 0 \\ 0 & 0 & 0 & 0 & G^{-1} & 0 \\ 0 & 0 & 0 & 0 & 0 & G^{-1} \end{pmatrix} \qquad \text{(B-5.17)}$$

where

$\overline{(S'_{ij})}_{isotropic}$	=	compliance matrix for isotropic cladding (Pa^{-1})
Y	=	Young's modulus for isotropic cladding (Pa)
G	=	shear modulus for isotropic cladding (Pa)
a	=	$\frac{1}{Y} - \frac{1}{2G}$ (Pa^{-1}).

Expressions for the isotropic Young's moduling and shear modulus in the alpha phase are obtained by computing S_{11} and S_{44} for the isotropic case with the CELAST code. Isotropic values of the several averages required by the code are computed by taking $I(\theta, \phi) = 1$ in Equation (B-5.8). The resultant values of the isotropic Young's and shear moduli decreased nearly linearly with temperature for temperatures above 450 K. The isotropic alpha phase Young's and shear moduli are therefore modeled with simple linear correlations obtained by fitting straight lines to their values at 623 and 1023 K. The resultant correlations are:

$$Y = 1.088\ 10" - 5.475\ 10^{7}\ T \qquad \text{(B-5.18a)}$$

$$G = 4.04\ 10^{10} - 2.168\ 10^{7}\ T \qquad \text{(B-5.18b)}$$

where the terms have been defined in Equation (B-5.17).

Equation (B-5.18b) is extrapolated to the high temperatures of beta phase zircaloy because no high temperature shear modulus data are available. The expression used in CELMOD for the Young's modulus of isotropic cladding is identical to the expression used in the CELAST code [Equation (B-5.13)].

Expressions for the change in Young's and shear moduli with increased oxygen, cold work and fast neutron fluence are taken directly from the CELAST code. Expressions for the changes in the reciprocal of S_{11} are applied to Young's modulus and changes in the reciprocal of S_{44} are applied to the shear modulus.

5.4 Comparison of Models and Data Base

Figures B-5.3 and B-5.4 compare predictions obtained with the CELAST code to the measurements of axial and circumferential Young's moduli by Bunnell. Predicted moduli increase with increasing oxygen and decrease with increasing temperature. Both predicted and measured axial Young's moduli for homogenized (annealed) cladding at room temperature are larger than the corresponding circumferential Young's moduli but the

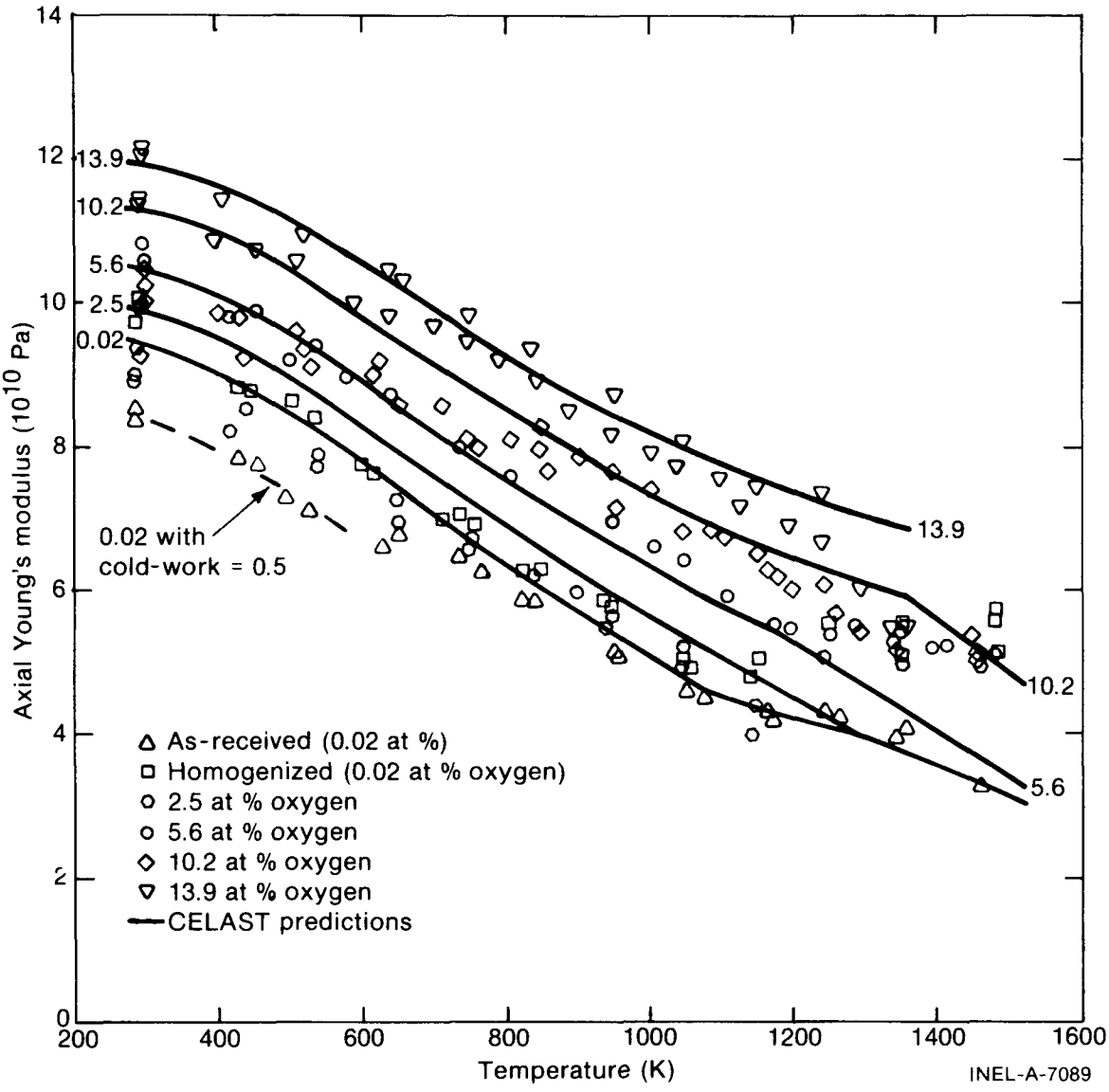

Fig. B-5.3 Measured values of axial Young's modulus compared to values predicted by the CELAST subcode for several oxygen concentrations and temperatures in the range 300 to 1500 K.

difference disappears at temperatures above 800 K. Even at room temperature, the difference is only slightly larger than the standard error of the model predictions. However, the low value of the circumferential Young's modulus is consistent with a minimum in predicted Young's modulus versus c-axis direction reported by Northwood[B-5.9].

Figure B-5.5 is a comparison of the Young's modulus predicted using the CELAST code with the beta phase zirconium data of Armstrong and Brown[B-5.3] and Padel and Groff[B-5.4]. The data show very little scatter, but are based on measurements of the Young's modulus of zirconium. The CELAST code has introduced a slight discontinuity in slope at 1240 K, the alpha + beta to beta phase boundary. For higher concentrations of oxygen, this discontinuity would appear at higher temperatures. The discontinuity is significant only in interpreting the physical meaning of the code predictions.

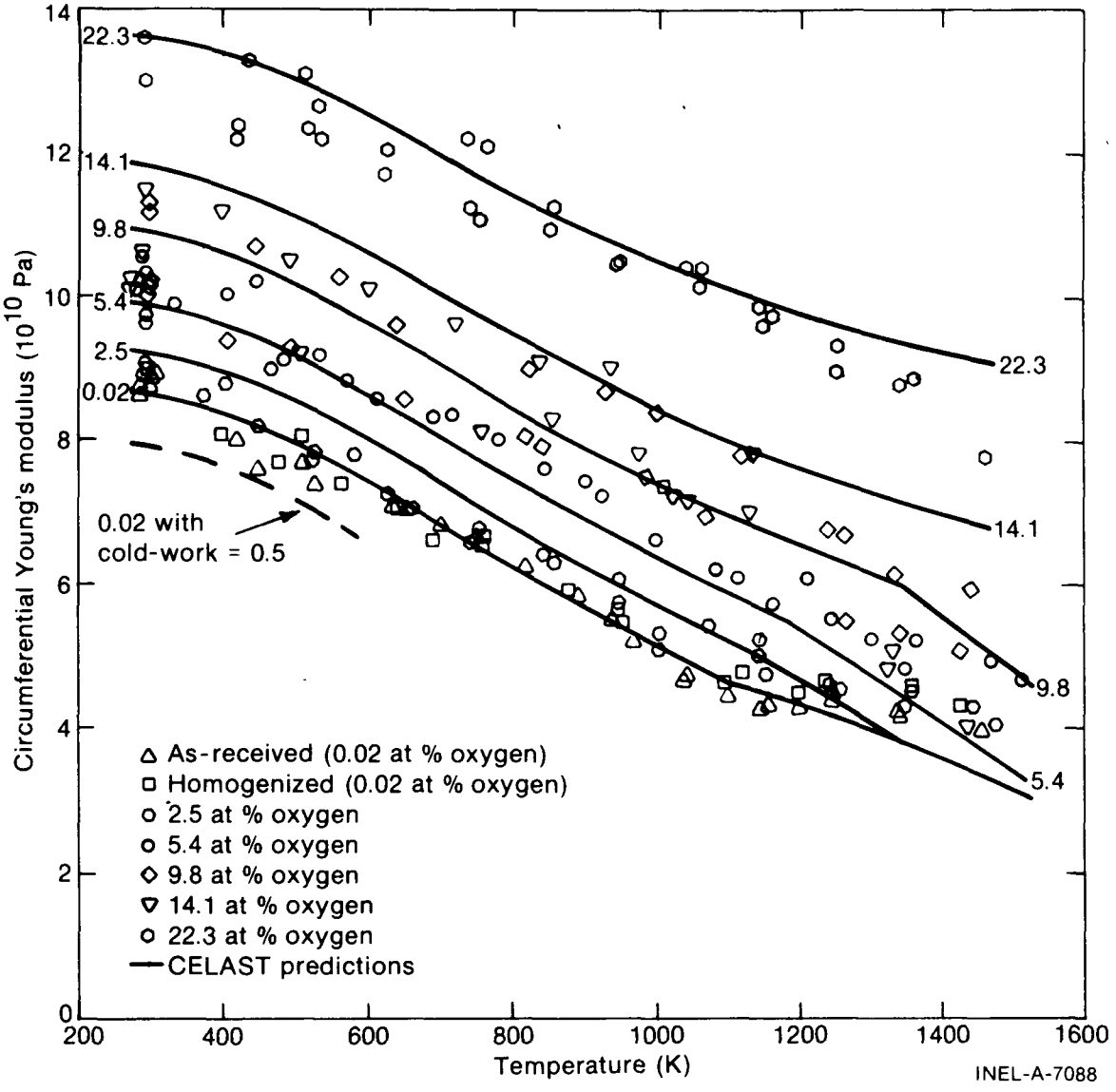

Fig. B-5.4 Measured values of circumferential Young's modulus compared to values predicted by the CELAST subcode for several oxygen concentrations and temperatures in the range of 300 to 1500 K.

5.5 Expected Standard Error of the CELMOD and CSHEAR Codes

An estimate of the uncertainty of the CELMOD code is obtained by computing the standard error[a] of the code with the data of Tables B-5.III to B-5.VI. For this calculation, the small effects of cold work are ignored. The standard error is 6.4×10^9 Pa. Since (a) the data used to estimate standard error are not used in the data base of the model (b) the effects of texture, cold work, oxygen, and irradiation are not large compared to temperature effects, and (c) the residuals do not vary in any regular fashion with temperature, this

[a] The standard error is estimated with a data set by the expression: [sum of squared residuals/(number of residuals – number of constants used to fit the data)] $^{1/2}$.

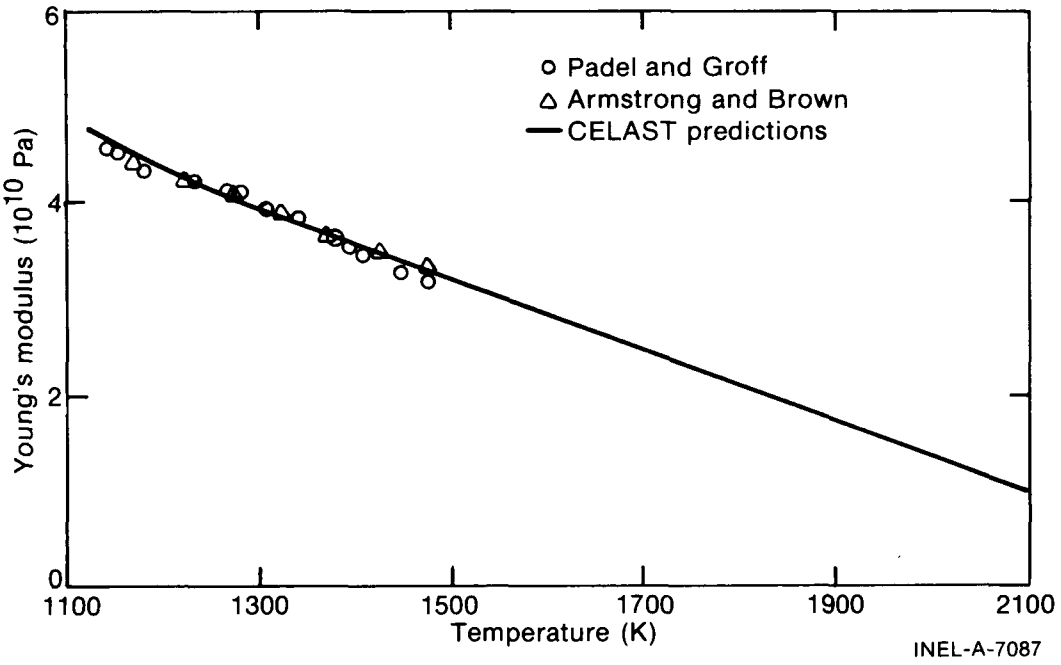

Fig. B-5.5 Comparison of the Young's modulus predicted with the CELAST code to the beta phase zirconium data of Padel and Groff, and Armstrong and Brown.

number is assumed to be a reasonable estimate of the expected standard error of the CELMOD code for in-reactor problems. At normal light water reactor temperatures, this standard error is 10% of the predicted value.

The uncertainty of the CSHEAR code is estimated by computing the standard error of the code with a large block of data (214 measurements) reported by Bunnell[B-5.1]. The data are not used in the development of the codes described here because the author has not yet been able to interpret the effect of texture on the "torsional wave" used by Bunnell to measure shear modulus. The standard error, assuming the cladding was isotropic, is 9×10^9 Pa. At normal LWR temperatures, the standard error of the isotropic shear is 30% of the predicted value.

5.6 Cladding Elastic Moduli Subcodes CELMOD, CSHEAR, and CELAST Listings

Tables B-5.VIII to B-5.X present listings of the subcodes CELMOD, CSHEAR, and CELAST. The expected standard errors are computed within the functions CELMOD and CSHEAR but are not returned. In a future simultaneous revision of these subcodes and the FRAP codes which use them, all uncertainties will be stored in a separate common block.

5.7 References

B-5.1. L. R. Bunnell et al, *High Temperature Properties of Zircaloy-Oxygen Alloys*, EPRI NP-524 (March 1977).

TABLE B-5.VIII

LISTING OF THE CELMOD SUBCODE

```
C
C
      FUNCTION CELMOD(CTEMP, FNCK, CWKF, DELOXY)
C
C     CELMOD CALCULATES CLADDING YOUNG'S MODULUS AS A FUNCTION
C     OF TEMPERATURE, FAST NEUTRON FLUENCE, COLD WORK, AND AVERAGE
C     OXYGEN CONCENTRATION.  GRAIN ORIENTATION IS ASSUMED RANDOM.
C     THE EXPECTED STANDARD ERROR IS COMPUTED BUT NOT RETURNED
C     (UCELMD)
C
C     CELMOD = OUTPUT YOUNG'S MODULUS FOR ZIRCALOY 2 AND 4
C              WITH RANDOM TEXTURE (PA)
C     UCELMD = OUTPUT STANDARD ERROR EXPECTED IN CELMOD (PA)
C              (NOT CURRENTLY RETURNED)
C
C     CTEMP  = INPUT CLADDING TEMPERATURE (K)
C     FNCK   = INPUT EFFECTIVE FAST FLUENCE (NEUTRONS/(M**2))
C     CWKF   = INPUT EFFECTIVE COLD WORK (UNITLESS RATIO OF AREAS)
C     DELOXY = INPUT AVERAGE OXYGEN CONCENTRATION EXCLUDING
C              OXIDE LAYER - AVERAGE OXYGEN CONCENTRATION OF
C              AS-RECEIVED CLADDING  (KG OXYGEN/KG ZIRCALOY)
C
C     THE YOUNG'S MODULUS CALCULATED BY THIS FUNCTION IS BASED ON
C     DATA FROM THE FOLLOWING REFERENCES
C     (1) L. R. BUNNELL, G. B. MELLINGER  AND J. L. BATES, HIGH
C     TEMPERATURE PROPERTIES OF ZIRCALOY - OXYGEN ALLOYS, EPRI
C     REPORT NP - 524 (1977)
C     (2) E. S. FISHER AND C. J. RENKEN, PHYSICAL REVIEW 135 2A
C     (20 JULY 1964) PP A482 - 494.
C     (3) P. E. ARMSTRONG AND H. L. BROWN, TRANSACTIONS OF THE
C     METALLURGICAL SOCIETY OF AIME 230 (AUGUST 1964)
C     PP 962 - 966
C     (4) A. PADEL AND A. GROFF, JOURNAL OF NUCLEAR MATERIALS 59
C     (1976) PP 325 - 326.
C     (5) W. R. SMALLEY, SAXTON CORE II FUEL PERFORMANCE EVALUATION.
C     PART I: MATERIALS, WCAP-3385-56 (SEPTEMBER 1971)
C
C     THE EXPECTED STANDARD ERROR WAS DERIVED USING ADDITIONAL
C     DATA FROM THE FOLLOWING REFERENCES
C     (1)C. C. BUSBY AND C.R. WOODS (EDS.) "PROPERTIES OF ZIRCALOY-4
C     TUBING", USAEC REPORT WAPD-TM-585 (DECEMBER 1966) P 65
C     (2) Z. SPASIC, M. PAVLOVIC AND G. SIMIS, CONFERENCE ON
C     THE USE OF ZIRCONIUM ALLOYS IN NUCLEAR REACTORS, MARIANSKE
C     LANZE, CZECH. CONF-681086 (1968) PP 277 - 284
C     (3) R. L. MEHAN, MODULUS OF ELASTICITY OF ZIRCALOY-2 BETWEEN
C     ROOM TEMPERATURE AND 1000 F, KAPL-M-RLM-16 (JULY 1958)
C     (4) D. O. NORTHWOOD, I. M LONDON, AND L. E. BAHEN, JOURNAL
C     OF NUCLEAR MATERIALS 55 (1975) PP 299-310
C     (5) F. R. SHOBER, J. A. VAN ECHO, L. L. MARSH JR. AND
C     J. R. KEELER, THE MECHANICAL PROPERTIES OF ZIRCONIUM  AND
C     ZIRCALOY-2, BMI-1168 (1957)
C
C     CELMOD WAS CODED BY R. L. MILLER IN MARCH 1974.
C     UPDATED AND CORRECTED BY B. W. BURNHAM IN OCTOBER 1975
C     MODIFIED BY B. W. BURNHAM OCTOBER 1977
C     MODIFIED BY D. L. HAGRMAN DECEMBER 1977
C
      COMMON       /LACEMDL   /MAXIDX, EMFLAG
      DIMENSION    EMFLAG(1)
C
      DATA         ON         / 2HON  /,
     #             OFF        / 3HOFF /,
     #             LOCIDX     /   5   /
      IF (EMFLAG(LOCIDX) .EQ. ON)  GO TO 100
C
C     BEST ESTIMATE MODEL YOUNG'S MODULUS
      C1 = (1.16E+11+CTEMP*1.037E+08) * 5.7015
      C2 = 1.0
      IF(FNCK .GT. 1.0E+22) C2 = 0.88*(1.0 - EXP(-FNCK/1.0E+25))
     #                           + EXP(-FNCK/1.0E+25)
      C3 = -2.6E+10
      CELMOD = (1.086E+11-5.475E+07*CTEMP + C1*DELOXY + C3*CWKF )/C2
      IF(CTEMP .LT. 1090. ) GO TO 101
```

TABLE B-5.VIII (continued)

```
C
C       CALCULATE A TO A + B AND A + B TO B BOUNDARIES
        WFOX = DELOXY + 0.0012
        TAAB = 1094. + WFOX * (-1.289E+03 + WFOX * 7.914E+05)
        IF ( WFOX .LT. 0.025) GO TO 15
        TAAB = 1556.4 + 3.8281E+04*(WFOX - 0.025)
   15   TABB = 392.46*((100*DELOXY + 0.1242807)**2 + 3.1417)
        IF (DELOXY .LT. 4.7308937E-03) GO TO 25
        TABB = (100*DELOXY + 0.12) * 491.157 + 1081.7413
   25   CONTINUE
C
        IF (CTEMP .LT. TAAB) GO TO 101
        IF (CTEMP .GT. TABB) GO TO 35
        AMODL  = (1.088E+11-5.475E+07*TAAB + C1*DELOXY + C3*CWKF )/C2
        AMODR  = 9.21E+10 - TABB *4.05E+07
        CELMOD = AMODL + (CTEMP - TAAB ) * (AMODR - AMODL )/(TABB - TAAB)
        GO TO 101
   35   CELMOD = 9.21E+10 - CTEMP*4.05E+07
        GO TO 101
C
C       EM MODEL YOUNG'S MODULUS
  100   CELMOD = EMCLEM (CTEMP)
  101   CONTINUE
        IF(CELMOD .LT. 1.0 ) CELMOD = 1.0
        UCELMD = 6.4E+09
C
        RETURN
        END
```


B-5.2. E. S. Fisher and C. J. Renken, "Single-Crystal Elastic Moduli and the hcp → bcc Transformation in Ti, Zr, and Hf," *Physical Review, 135 2A* (July 20, 1964) pp A482-494.

B-5.3. P. E. Armstrong and H. L. Brown, "Dynamic Young's Modulus Measurements above 1000°C on Some Pure Polycrystalline Metals and Commercial Graphites," *Transactions of the Metallurgical Society of AIME 230* (August 1964) pp 962-966.

B-5.4. A. Padel and A. Groff, "Variation du Module de Young du Zirconium β en Fonction de la Temperature," *Journal of Nuclear Materials 59* (1976) pp 325-326.

B-5.5. C. C. Busby, *Properties of Zircaloy-4 Tubing,* WAPD-TM-585 (December 1966) p 65.

B-5.6. Z. Spasic et al, *Conference on the Use of Zirconium Alloys in Nuclear Reactors,* Marlanske Lanze, Czechoslovakia, USAEC CONF-681086 (1968) pp 277-284.

B-5.7. R. L. Mehan, *Modulus of Elasticity of Zircaloy-2 Between Room Temperature and 1000°F,* KAPL-M-RLM-16 (July 1958).

B-5.8. R. L. Mehan and F. W. Wiesinger, *Mechanical Properties of Zircaloy-2,* KAPL-2110 (February 1961) pp 11-12.

B-5.9. D. O. Northwood et al, "Elastic Constants of Zirconium Alloys," *Journal of Nuclear Materials, 55* (1975) pp 299-310.

TABLE B-5.IX

LISTING OF THE CSHEAR SUBCODE

```
C
CC
      FUNCTION CSHEAR(CTEMP, FNCK, CWKF, DELOXY)
C
C     CSHEAR CALCULATES THE SHEAR MODULUS OF ZIRCALOY-2 AND -4
C     AS A FUNCTION OF TEMPERATURE, FAST NEUTRON FLUENCE,
C     COLD WORK, AND AVERAGE OXYGEN CONCENTRATION.  GRAIN
C     ORIENTATION IS ASSUMED RANDOM.
C     THE EXPECTED STANDARD ERROR IS COMPUTED BUT NOT RETURNED
C     (UCSHER)
C
C     CSHEAR = OUTPUT SHEAR MODULUS FOR ZIRCALOY-2 AND -4
C              WITH RANDOM TEXTURE (PA)
C     UCSHER = OUTPUT STANDARD ERROR EXPECTED IN CSHEAR (PA)
C              (NOT CURRENTLY RETURNED)
C
C     CTEMP  = INPUT CLADDING TEMPERATURE (K)
C     FNCK   = INPUT EFFECTIVE FAST FLUENCE (NEUTRONS/(M**2))
C     CWKF   = INPUT EFFECTIVE COLD WORK (UNITLESS RATIO OF AREAS)
C     DELOXY = INPUT AVERAGE OXYGEN CONCENTRATION EXCLUDING
C              OXIDE LAYER - AVERAGE OXYGEN CONCENTRATION OF
C              AS-RECEIVED CLADDING  (KG OXYGEN/KG ZIRCALOY)
C
C     THE SHEAR MODULUS CALCULATED BY THIS FUNCTION IS BASED ON
C     DATA FROM THE FOLLOWING REFERENCES
C     (1) L. R. BUNNELL, G. B. MELLINGER  AND J. L. BATES, HIGH
C     TEMPERATURE PROPERTIES OF ZIRCALOY - OXYGEN ALLOYS, EPRI
C     REPORT NP - 524 (1977)
C     (2) E. S. FISHER AND C. J. RENKEN, PHYSICAL REVIEW 135 2A
C     (20 JULY 1964) PP A482 - 494.
C     (3) P. E. ARMSTRONG AND H. L. BROWN, TRANSACTIONS OF THE
C     METALLURGICAL SOCIETY OF AIME 230 (AUGUST 1964)
C     PP 962 - 966
C     (4) A. PADEL AND A. GROFF, JOURNAL OF NUCLEAR MATERIALS 59
C     (1976) PP 325 - 326.
C     (5) W. R. SMALLEY, SAXTON CORE II FUEL PERFORMANCE EVALUATION.
C     PART I: MATERIALS, WCAP-3385-56 (SEPTEMBER 1971)
C
C     CSHEAR WAS CODED BY R. L. MILLER, JUNE 1974
C     MODIFIED BY D. L. HAGRMAN DECEMBER 1977
C
      C1 = 7.67E+11 - CTEMP*2.315E+08
      C2 = 1.0
      IF(FNCK .GT. 1.0E+22) C2 = 0.88*(1.0 - EXP(-FNCK/1.0E+25))
     #                           + EXP(-FNCK/1.0E+25)
      C3 = -2.6E+10
      CSHEAR = (4.04E+10-2.168E+07*CTEMP + C1*DELOXY + C3*CWKF)/C2
      IF(CTEMP .LT. 1090. ) GO TO 101
C
C     CALCULATE A TO A + B AND A + B TO B BOUNDARIES
      WFOX = DELOXY + 0.0012
      TAAB = 1094. + WFOX * (-1.289E+03 + WFOX * 7.914E+05)
      IF ( WFOX .LT. 0.025) GO TO 15
      TAAB = 1556.4 + 3.8281E+04*(WFOX - 0.025)
   15 TABB = 392.46*((100*DELOXY + 0.1242807)**2 + 3.1417)
      IF (DELOXY .LT. 4.7308937E-03) GO TO 25
      TABB = (100*DELOXY + 0.12) * 491.157 + 1081.7413
   25 CONTINUE
C
      IF (CTEMP .LT. TAAB) GO TO 101
      IF (CTEMP .GT. TABB) GO TO 35
      AMODL  = (4.04E+10-2.168E+07*TAAB  + C1*DELOXY + C3*CWKF)/C2
      AMODR  = 3.49E+10 - TABB *1.66E+07
      CSHEAR = AMODL + (CTEMP - TAAB ) * (AMODR - AMODL )/(TABB - TAAB)
      GO TO 101
   35 CSHEAR = 3.49E+10 - CTEMP*1.66E+07
  101 CONTINUE
      IF(CSHEAR .LT. 1.0 ) CSHEAR = 1.0
      UCSHER = 9.0E+09
C
      RETURN
      END
```

TABLE B-5.X

LISTING OF THE CELAST SUBCODE

```
C
C
      SUBROUTINE CELAST(COSTH2,COSTH4,COSFI2,COSFI4,CT2CF2,CT2CF4,
     #                  CT4CF2,CT4CF4,CTEMP,FNCK,CWKF,DELOXY,CRS)
C
      DIMENSION CC(12),CS(12),CRS(9)
C
C     CELAST CALCULATES ELASTIC COMPLIANCE CONSTANTS OF ZIRCALOY
C     FROM ORIENTATION PARAMETERS
C
C     IN THE FOLLOWING, THETA IS THE ANGLE BETWEEN THE RADIAL
C     OR NORMAL DIRECTION OF THE SAMPLE AND THE BASAL POLE
C     DIRECTION. PHI IS THE ANGLE BETWEEN THE PROJECTION OF THE
C     BASAL POLE DIRECTION ONTO THE PLANE CONTAINING THE AXIAL
C     AND CIRCUMFERENTIAL DIRECTIONS AND THE CIRCUMFERENTIAL
C     DIRECTION. ALPHA IS THE COMPLEMENT OF PHI.
C
C     CRS(I) = OUTPUT ELASTIC COMPLIANCE CONSTANTS (1/PA). S MATRIX
C              ELEMENTS ARE
C
C               ( CRS(1)  CRS(7)  CRS(9)    0       0       0    )
C               ( CRS(7)  CRS(2)  CRS(8)    0       0       0    )
C               ( CRS(9)  CRS(8)  CRS(3)    0       0       0    )
C               (   0       0       0     CRS(4)    0       0    )
C               (   0       0       0       0     CRS(5)    0    )
C               (   0       0       0       0       0     CRS(6) )
C
C              WHERE DIRECTION 1 IS CIRCUMFERENTIAL OR TRANSVERSE
C                              2 IS AXIAL OR LONGITUDINAL
C                              3 IS RADIAL OR NORMAL
C
C     COSTH2 = INPUT VOLUME FRACTION WEIGHTED AVERAGE OF THE SQUARED
C              COSINE OF THETA (UNITLESS)
C     COSTH4 = INPUT VOLUME FRACTION WEIGHTED AVERAGE OF THE
C              FOURTH POWER OF THE COSINE OF THETA (UNITLESS)
C     COSFI2 = INPUT VOLUME FRACTION WEIGHTED AVERAGE OF THE SQUARED
C              COSINE OF ALPHA (UNITLESS RATIO)
C     COSFI4 = INPUT VOLUME FRACTION WEIGHTED AVERAGE OF THE
C              FOURTH POWER OF THE COSINE OF ALPHA (UNITLESS)
C     CT2CF2 = INPUT VOLUME FRACTION WEIGHTED AVERAGE OF THE PRODUCT
C              OF THE SQUARED COSINE OF THETA AND THE SQUARED COSINE
C              OF ALPHA (UNITLESS)
C     CT2CF4 = INPUT VOLUME FRACTION WEIGHTED AVERAGE OF THE PRODUCT
C              OF THE SQUARED COSINE OF THETA AND THE FOURTH POWER OF
C              THE COSINE OF ALPHA (UNITLESS)
C     CT4CF2 = INPUT VOLUME FRACTION WEIGHTED AVERAGE OF THE PRODUCT
C              OF THE FOURTH POWER OF THE COSINE OF THETA AND THE
C              SQUARED COSINE OF ALPHA (UNITLESS)
C     CT4CF4 = INPUT VOLUME FRACTION WEIGHTED AVERAGE OF THE PRODUCT
C              OF THE FOURTH POWER OF THE COSINE OF THETA AND THE
C              FOURTH POWER OF THE COSINE OF ALPHA (UNITLESS)
C     CTEMP  = INPUT CLADDING TEMPERATURE (K)
C     FNCK   = INPUT EFFECTIVE FAST FLUENCE (NEUTRONS/(M**2))
C     CWKF   = INPUT EFFECTIVE COLD WORK (UNITLESS RATIO OF AREAS)
C     DELOXY = INPUT AVERAGE OXYGEN CONCENTRATION EXCLUDING
C              OXIDE LAYER - AVERAGE OXYGEN CONCENTRATION OF
C              AS RECEIVED CLADDING  (KG OXYGEN/KG ZIRCALOY)
C
C     THE ELASTIC COMPLIANCE CONSTANTS ARE BASED ON DATA FROM
C     (1) L. R. BUNNELL, G. B. MELLINGER  AND J. L. BATES, HIGH
C     TEMPERATURE PROPERTIES OF ZIRCALOY - OXYGEN ALLOYS, EPRI
C     REPORT NP - 524 (1977)
C     (2) E. S. FISHER AND C. J. RENKEN, PHYSICAL REVIEW 135 2A
C     (20 JULY 1964) PP A482 - 494.
C     (3) P. E. ARMSTRONG AND H. L. BROWN, TRANSACTIONS OF THE
C     METALLURGICAL SOCIETY OF AIME 230 (AUGUST 1964)
C     PP 962 - 966
C     (4) A. PADEL AND A. GROFF, JOURNAL OF NUCLEAR MATERIALS 59
C     (1976) PP 325 - 326.
```

TABLE B-5.X (continued)

```
C     (5) W. R. SMALLEY, SAXTON CORE II FUEL PERFORMANCE EVALUATION.
C     PART I: MATERIALS, WCAP-3385-56 (SEPTEMBER 1971)
C
C     CELAST WAS CODED BY D. L. HAGRMAN IN DECEMBER 1977
C
      CC(1) = 1.562E+11- 4.484E+07*CTEMP
      CC(2) = 1.746E+11- 3.282E+07*CTEMP
      CC(3) = 3.565E+10- 1.281E+07*CTEMP
      CC(5) = 6.448E+10+ CTEMP*(3.1882E+07- CTEMP*1.2318E+04)
      CC(6) = 6.518E+10- 6.817E+05*CTEMP
      IF( CC(1) .LT. (0.999*CC(5))) CC(5) = 0.999*CC(1)
      CC(4) = (CC(1) - CC(5))/2.
      FACTOR= (CC(1) - CC(5))*((CC(1) + CC(5))*CC(2) - 2*((CC(6)**2)))
      CS(1) = 0.102841E-10 + CTEMP * (-0.541683E-14 + CTEMP *
     #        0.147552E-16)
      CS(2) = (CC(1) + CC(5))*(CC(1) - CC(5))/FACTOR
      CS(3) = 0.390354E-10+CTEMP * (-0.81186E-14+ CTEMP *
     #        0.211523E-16)
      CS(4) = 1.0/CC(4)
      CS(5) = ((CC(6))**2-(CC(5)*CC(2)))/FACTOR
      CS(6) = (CC(5) - CC(1))*CC(6)/FACTOR
      B     = (1.16E+11+ CTEMP*1.037E+08) * 5.7015
      BS    = (1.24E+11- CTEMP*0.406E+08) * 5.7015
      C2    = 1.0
      IF(FNCK .GT. 1.0E+22) C2 = 0.88*(1.0 - EXP(-FNCK/1.0E+25))
     #                         + EXP(-FNCK/1.0E+25)
      C3    = -2.6E+10
      CS(1) = C2/(1.0/CS(1) + B  * DELOXY + C3 * CWKF )
      CS(2) = C2/(1.0/CS(2) + B  * DELOXY + C3 * CWKF )
      CS(3) = C2/(1.0/CS(3) + BS * DELOXY )
      CS(5) = C2/(1.0/CS(5) + B  * DELOXY + C3 * CWKF )
      CS(6) = C2/(1.0/CS(6) + B  * DELOXY + C3 * CWKF )
      IF( CS(1) .LT. (0.999*CS(5))) CS(5) = 0.999*CS(1)
      CS(4) = 2*(CS(1) - CS(5))
      CRS(1)   = (COSFI4-2*CT2CF4+CT4CF4+2*CT2CF2-2*CT4CF2+COSTH4)*CS(1)
     # + (1.0 -2*COSFI2 + COSFI4 -2*COSTH2 +4*CT2CF2-2*CT2CF4
     # + COSTH4 - 2*CT4CF2 + CT4CF4) * CS(2) + (-COSFI4 + 2*CT2CF4
     # - CT4CF4 + COSFI2 - 3*CT2CF2 +2*CT4CF2 + COSTH2 - COSTH4 )
     # * ( 2* CS(6) + CS(3) )
      CRS(2)   = (COSFI4-2*CT2CF4+CT4CF4-2*COSFI2+2*CT2CF2+1.0)*CS(1)
     # + (COSFI4 - 2*CT2CF4 + CT4CF4 )*CS(2) + (COSFI2 - COSFI4
     # + 2*CT2CF4 - CT2CF2 - CT4CF4) * (2*CS(6) + CS(3))
      CRS(3)   = (1.0 - 2*COSTH2 + COSTH4) * CS(1)
     # +(COSTH2 - COSTH4)* (2*CS(6) + CS(3)) + COSTH4 * CS(2)
      CRS(4)   = ( 2 * (1.0 - COSTH2 - COSFI2) + 6 *  CT2CF2
     # -4 * CT4CF2 ) *CS(1) + 4 * ( CT2CF2 - CT4CF2 ) * CS(2)
     # + ( COSTH2 + COSFI2 - 5 * CT2CF2 + 4 * CT4CF2 ) * CS(3)
     # + 2 * (-1.0 + COSTH2 + COSFI2 - CT2CF2 ) * CS(5)
     # + 8 * (-CT2CF2 + CT4CF2 ) * CS(6)
      CRS(5)   = (COSTH2 - COSTH4 + 0.5*COSFI2 - 1.5*CT2CF2 + CT4CF2) *
     # CS(1) + (COSTH2 - COSTH4 - CT2CF2 + CT4CF2 ) * CS(2) +
     # (1.0 - 4*COSTH2 + 4*COSTH4 - COSFI2 + 5*CT2CF2 - 4*CT4CF2)*0.25*
     # CS(3) - 0.5*(COSFI2 - CT2CF2)*CS(5) - 2*(COSTH2 - COSTH4 -CT2CF2
     # +CT4CF2 )*CS(6)
      CRS(5) = 4.0 * CRS(5)
      CRS(6)   = (0.5*COSTH2 + COSFI2 - COSFI4 - 2*CT2CF2 + 2*CT2CF4 +
     # CT4CF2 - CT4CF4) * CS(1) + (COSFI2 - COSFI4 - 2*CT2CF2 +2*CT2CF4+
     # CT4CF2 - CT4CF4) * CS(2) + (1.0 - 4*COSFI2 + 4*COSFI4 - COSTH2 +
     # 8*CT2CF2 - 8*CT2CF4 - 4*CT4CF2 + 4*CT4CF4 ) * 0.25*CS(3) -
     # 0.5*COSTH2 * CS(5) -2.0 * (COSFI2 - COSFI4 - 2*CT2CF2 +
     # 2 * CT2CF4 + CT4CF2 - CT4CF4 ) * CS(6)
      CRS(6) = 4.0 * CRS(6)
      CRS(7)   = (COSFI2 - COSFI4 - 2*CT2CF2 + 2*CT2CF4 + CT4CF2
     # - CT4CF4) * CS(1) + (COSFI2 - COSFI4 -2*CT2CF2 + 2*CT2CF4
     # + CT4CF2 - CT4CF4) * ( CS(2) - CS(3) ) + COSTH2 * CS(5)
     # + ( 1.0 - COSTH2 - 2*COSFI2 + 2*COSFI4 + 4*CT2CF2 - 4*CT2CF4
     # - 2*CT4CF2 + 2*CT4CF4) * CS(6)
      CRS(8)   = (CT2CF2 - CT4CF2) * ( CS(1) + CS(2) - CS(3) ) +
     # (1.0 - COSTH2 - COSFI2+ CT2CF2) * CS(5) + ( COSTH2 + COSFI2
     # - 3*CT2CF2 + 2*CT4CF2 ) * CS(6)
      CRS(9)   = (COSTH2 - COSTH4 - CT2CF2 + CT4CF2) * ( CS(1) +
     # CS(2) - CS(3) ) + (COSFI2 - CT2CF2) * CS(5) + (1.0 - 2*COSTH2
     # +2*COSTH4 - COSFI2 + 3*CT2CF2 - 2*CT4CF2) * CS(6)
      IF(CTEMP .LT. 1090. ) GO TO 101
```

TABLE B-5.X (continued)

```
C
C     CALCULATE A TO A + B AND A + B TO B BOUNDARIES
      WFOX = DELOXY + 0.0012
      TAAB = 1094. + WFOX * (-1.289E+03 + WFOX * 7.914E+05)
      IF ( WFOX .LT. 0.025) GO TO 15
      TAAB = 1556.4 + 3.8281E+04*(WFOX - 0.025)
   15 TABB = 392.46*((100*DELOXY + 0.1242807)**2 + 3.1417)
      IF (DELOXY .LT. 4.7308937E-03) GO TO 25
      TABB = (100*DELOXY + 0.12) * 491.157 + 1081.7413
   25 CONTINUE
C
      IF (CTEMP .LT. TAAB) GO TO 101
      IF (CTEMP .GT. TABB) GO TO 35
      CC(7) = 1.562E+11- 4.434E+07*TAAB
      CC(8) = 1.746E+11- 3.282E+07*TAAB
      CC(9) = 3.565E+10- 1.281E+07*TAAB
      CC(11)= 6.448E+10+ TAAB *(3.1882E+07- TAAB *1.2318E+04)
      CC(12)= 6.518E+10- 6.817E+05*TAAB
      IF( CC(7) .LT. (0.999*CC(11))) CC(11) = 0.999*CC(7)
      FXCTOR = (CC(7) -CC(11))*((CC(7) +CC(11))*CC(8) -2*((CC(12)**2)))
      CS(7) = 0.1026416-10 + TAAB  * (-0.541683E-14 + TAAB  *
     # 0.147552E-16 )
      CS(8) = (CC(7) +CC(11))*(CC(7) -CC(11))/FXCTOR
      CS(9) = 0.390354E-10+TAAB  * (-0.81186E-14+ TAAB  *
     # 0.211523E-16)
      CS(11)=((CC(12))**2-(CC(11)*CC(8)))/FXCTOR
      CS(12)=(CC(11) -CC(7))*CC(12)/FXCTOR
      BT=(1.16E+11+ TAAB *1.037E+08) * 5.7015
      BST=(1.24E+11- TAAB *0.406E+08) * 5.7015
      CS(7) = C2/(1.0/CS(7) + BT * DELOXY + C3 * CWKF )
      CS(8) = C2/(1.0/CS(8) + BT * DELOXY + C3 * CWKF )
      CS(9) = C2/(1.0/CS(9) + BST* DELOXY )
      CS(11)= C2/(1.0/CS(11)+ BT * DELOXY + C3 * CWKF )
      CS(12)= C2/(1.0/CS(12)+ BT * DELOXY + C3 * CWKF )
      IF( CS(7) .LT. (0.999*CS(11))) CS(11) = 0.999*CS(7)
      CS(10)= 2*(CS(7) - CS(11))
      CLS1      = (COSFI4-2*CT2CF4+CT4CF4+2*CT2CF2-2*CT4CF2+COSTH4)*CS(7)
     # + (1.0 -2*COSFI2 + COSFI4 -2*COSTH2 +4*CT2CF2-2*CT2CF4
     # + COSTH4 - 2*CT4CF2 + CT4CF4) * CS(8) +  (-COSFI4 + 2*CT2CF4
     # - CT4CF4 + COSFI2 - 3*CT2CF2 +2*CT4CF2 + COSTH2 - COSTH4 )
     # * ( 2* CS(12)+ CS(9) )
      CLS2      = (COSFI4-2*CT2CF4+CT4CF4-2*COSFI2+2*CT2CF2+1.0)*CS(7)
     # + (COSFI4 - 2*CT2CF4 + CT4CF4 )*CS(8) + (COSFI2 - COSFI4
     # + 2*CT2CF4 - CT2CF2 - CT4CF4) * (2*CS(12)+ CS(9))
      CLS3      = (1.0 - 2*COSTH2 + COSTH4) * CS(7)
     # +(COSTH2 - COSTH4)* (2*CS(12)+ CS(9)) + COSTH4 * CS(8)
      CLS4      =  ( 2 * (1.0 - COSTH2 - COSFI2) + 6 *  CT2CF2
     # -4 * CT4CF2 ) *CS(7) + 4 * ( CT2CF2 - CT4CF2 ) * CS(8)
     # + ( COSTH2 + COSFI2 - 5 * CT2CF2 + 4 * CT4CF2 ) * CS(9)
     # + 2 * (-1.0 + COSTH2 + COSFI2 - CT2CF2 ) * CS(11)
     # + 8 * (-CT2CF2 + CT4CF2 ) * CS(12)
      CLS5      = (COSTH2 - COSTH4 + 0.5*COSFI2 - 1.5*CT2CF2 + CT4CF2) *
     # CS(7) +  (COSTH2 - COSTH4 - CT2CF2 + CT4CF2 ) * CS(8)  +
     # (1.0 - 4*COSTH2 + 4*COSTH4 - COSFI2 + 5*CT2CF2 - 4*CT4CF2)*0.25*
     # CS(9) - 0.5*(COSFI2 - CT2CF2)*CS(11)- 2*(COSTH2 - COSTH4 -CT2CF2
     # +CT4CF2 )*CS(12)
      CLS5 = CLS5 * 4.0
      CLS6      = (0.5*COSTH2 + COSFI2 - COSFI4 - 2*CT2CF2 + 2*CT2CF4 +
     # CT4CF2 - CT4CF4) * CS(7) + (COSFI2 - COSFI4 - 2*CT2CF2 +2*CT2CF4+
     # CT4CF2 - CT4CF4) * CS(8) + (1.0 - 4*COSFI2 + 4*COSFI4 - COSTH2 +
     # 8*CT2CF2 - 8*CT2CF4 - 4*CT4CF2 + 4*CT4CF4 ) * 0.25*CS(9) -
     # 0.5*COSTH2 * CS(11)-2.0 * (COSFI2 - COSFI4 - 2*CT2CF2 +
     # 2 * CT2CF4 + CT4CF2 - CT4CF4 ) * CS(12)
      CLS6 = CLS6 * 4.0
      CLS7      = (COSFI2 - COSFI4 - 2*CT2CF2 + 2*CT2CF4 + CT4CF2
     # - CT4CF4) * CS(7) + (COSFI2 - COSFI4 -2*CT2CF2 + 2*CT2CF4
     # + CT4CF2 - CT4CF4) * ( CS(8) - CS(9) ) + COSTH2 * CS(11)
     # + ( 1.0 - COSTH2 - 2*COSFI2 + 2*COSFI4 + 4*CT2CF2 - 4*CT2CF4
     # - 2*CT4CF2 + 2*CT4CF4) * CS(12)
      CLS8      = (CT2CF2 - CT4CF2) * ( CS(7) + CS(8) - CS(9) ) +
     # (1.0 - COSTH2 - COSFI2+ CT2CF2) * CS(11)+ ( COSTH2 + COSFI2
     # - 3*CT2CF2 + 2*CT4CF2 ) * CS(12)
      CLS9      = (COSTH2 - COSTH4 - CT2CF2 + CT4CF2) * ( CS(7) +
     # CS(8) - CS(9) ) + (COSFI2 - CT2CF2) * CS(11)+ (1.0 - 2*COSTH2
     # +2*COSTH4 - COSFI2 + 3*CT2CF2 - 2*CT4CF2) * CS(12)
      CTS1    = 9.21E+10 - TABB * 4.05E+07
      CTS2 = CTS1
```

TABLE B-5.X (continued)

```
      CTS3 = CTS1
      CTS4 = 3.49E+10 - TABB * 1.66E+07
      CTS5 = CTS4
      CTS6 = CTS4
      CTS7 = (2*CTS4*CTS1)/(2*CTS4 - CTS1)
      CTS8 = CTS7
      CTS9 = CTS7
      CRS(1) = 1.0/((1.0/CLS1) + (CTEMP - TAAB) * (CTS1 - (1.0/CLS1))/
     #         (TABB - TAAB))
      CRS(2) = 1.0/((1.0/CLS2) + (CTEMP - TAAB) * (CTS2 - (1.0/CLS2))/
     #         (TABB - TAAB))
      CRS(3) = 1.0/((1.0/CLS3) + (CTEMP - TAAB) * (CTS3 - (1.0/CLS3))/
     #         (TABB - TAAB))
      CRS(4) = 1.0/((1.0/CLS4) + (CTEMP - TAAB) * (CTS4 - (1.0/CLS4))/
     #         (TABB - TAAB))
      CRS(5) = 1.0/((1.0/CLS5) + (CTEMP - TAAB) * (CTS5 - (1.0/CLS5))/
     #         (TABB - TAAB))
      CRS(6) = 1.0/((1.0/CLS6) + (CTEMP - TAAB) * (CTS6 - (1.0/CLS6))/
     #         (TABB - TAAB))
      CRS(7) = 1.0/((1.0/CLS7) + (CTEMP - TAAB) * (CTS7 - (1.0/CLS7))/
     #         (TABB - TAAB))
      CRS(8) = 1.0/((1.0/CLS8) + (CTEMP - TAAB) * (CTS8 - (1.0/CLS8))/
     #         (TABB - TAAB))
      CRS(9) = 1.0/((1.0/CLS9) + (CTEMP - TAAB) * (CTS9 - (1.0/CLS9))/
     #         (TABB - TAAB))
      GO TO 101
C
   35 CRS(1) = 1.0/(9.21E+10 - CTEMP*4.05E+07)
      CRS(2) = CRS(1)
      CRS(3) = CRS(1)
      CRS(4) = 1.0/(3.49E+10 - CTEMP*1.66E+07)
      CRS(5) = CRS(4)
      CRS(6) = CRS(4)
      CRS(7) = CRS(1) - 0.5*CRS(4)
      CRS(8) = CRS(7)
      CRS(9) = CRS(7)
  101 CONTINUE
C
      RETURN

      END
```


B-5.10. F. B. Shober et al, *The Mechanical Properties of Zirconium and Zircaloy-2,* BMI-1168 (1957).

B-5.11. C. L. Whitmarsh, *Review of Zircaloy-2 and Zircaloy-4 Properties Relevant to N. S. Savannah Reactor Design,* ORNL-3281 (1962).

B-5.12. W. R. Smalley, *Saxton Core II Fuel Performance Evaluation Part I: Materials,* WCAP-3385-56 (September 1971).

B-5.13. R. H. Chapman, *Characterization of Zircaloy-4 Tubing Procured for Fuel Cladding Research Programs,* ORNL/NUREG/TM-29 (July 1976).

B-5.14. G. E. Dieter, *Mechanical Metallurgy,* McGraw-Hill Book Company, New York (1976).

B-5.15. J. J. Kearns, *Thermal Expansion and Preferred Orientation in Zircaloy,* WAPD-TM-472 (November 1965).

B-5.16. H. S. Rosenbaum and J. E. Lewis, "Use of Pole Figure Data to Compute Elasticity Coefficient of Zirconium Sheet," *Journal of Nuclear Materials, 67* (1977) pp 273-282.

B-5.17. R. B. Leighton, *Principles of Modern Physics,* McGraw-Hill Book Company, Inc., New York (1959).

B-5.18. H. M Chung et al, "Mechanical Properties of Zircaloy Containing Oxygen," *In Light-Water-Reactor Safety Research Program: Quarterly Progress Report January – March 1976,* ANL-76-49.

6. CLADDING AXIAL GROWTH (CAGROW)

(D. L. Hagrman)

A model for calculating the fractional change in length of zircaloy tubes due to irradiation-induced growth is presented in this section. Effects of fast neutron fluence, tubing texture, cladding temperature, and cold work are included and apply equally well to zircaloy-2 and zircaloy-4. The change in length of commercial fuel rods due to irradiation growth is small, however, it can be a significant fraction of the clearance between the rod and the top and bottom assembly nozzles. Contact with the nozzles can cause rods to bow and possibly fail at points where rods contact each other.

6.1 Summary

The following equation has been developed to model the irradiation growth of zircaloy tubes at temperatures between 40 and 360°C (the normal range of cladding temperatures in LWRs).

$$\frac{\Delta L}{L} = A \left[\exp\left(240.8/T\right)\right] (\phi t)^{1/2} \left(1 - 3 f_z\right) (1 + 2.0\ CW) \quad \text{(B-6.1)}$$

where

$\frac{\Delta L}{L}$ = fractional change in length due to growth

A = $1.407 \times 10^{-16} \left(\text{neutrons/m}^3\right)^{-1/2}$

T = cladding temperature (K)

ϕ = fast neutron flux (neutrons/m^2·s) (E > 1.0 MeV)

t = time (s)

f_z = texture factor[a] for the tubing axis

CW = cold work (fraction of cross-sectional area reduction).

Axial growth for temperatures below 40°C is approximated by using T = 40°C in Equation (B-6.1) and growth above 360°C is approximated by using T = 360°C.

A comparison of values calculated by the CAGROW subroutine for fully annealed material with experimental results is presented in Figure B-6.1. Comparison with the data shown from cold-worked tubes was not possible because the exact amount of cold work was not reported.

6.2 Background and Approach

The irradiation growth of zircaloy cladding appears to be quite sensitive to texture. Therefore, the effects of texture were considered first and the data were normalized to a standard texture ($f_z = 0.05$) before considering other effects on axial growth. The model was developed further by modeling the effects of fluence and irradiation temperature on the growth of annealed specimens. Finally the effects of texture, fluence, and temperature were removed from the cold-worked specimen data using the model based on annealed specimens (the data were normalized to a texture of 0.05, a fluence of $2 \times 10^{25} n/m^2$, and a temperature of 300°C) and the effect of cold work modeled. It should be noted, however, that the effect of cold work may not be treated completely since the limited data base did not allow treatment of interactions between cold work and fluence, temperature, and texture.

In CAGROW it is assumed that fast neutron flux and temperature both affect the growth rate by varying the concentration of interstitials which are free to migrate and cause growth. Since theoretical considerations imply a complex relation between the temperature, fast neutron flux, time, and the rate of growth, an empirical approach was used to approximate these effects. An empirical approach was also used to model the effect of cold work on zircaloy tube growth. The limited data were fit using an independent factor of the form (1 + constant x cold work) – the least complex form consistent with the preliminary data reported to date. The main conclusion is that cold work increases the rate of growth at low fluence. At higher fluences, the growth rate of annealed tubing may decrease rapidly. Cold worked tubing continues to grow at higher fluences at nearly the rate established during early irradiation.

---

[a] f_z is the effective fraction of cells aligned with their <0001> axis parallel to the tubing axis as determined by X-ray diffraction analysis. A value of $f_z = 0.05$ is typical[B-6.1].

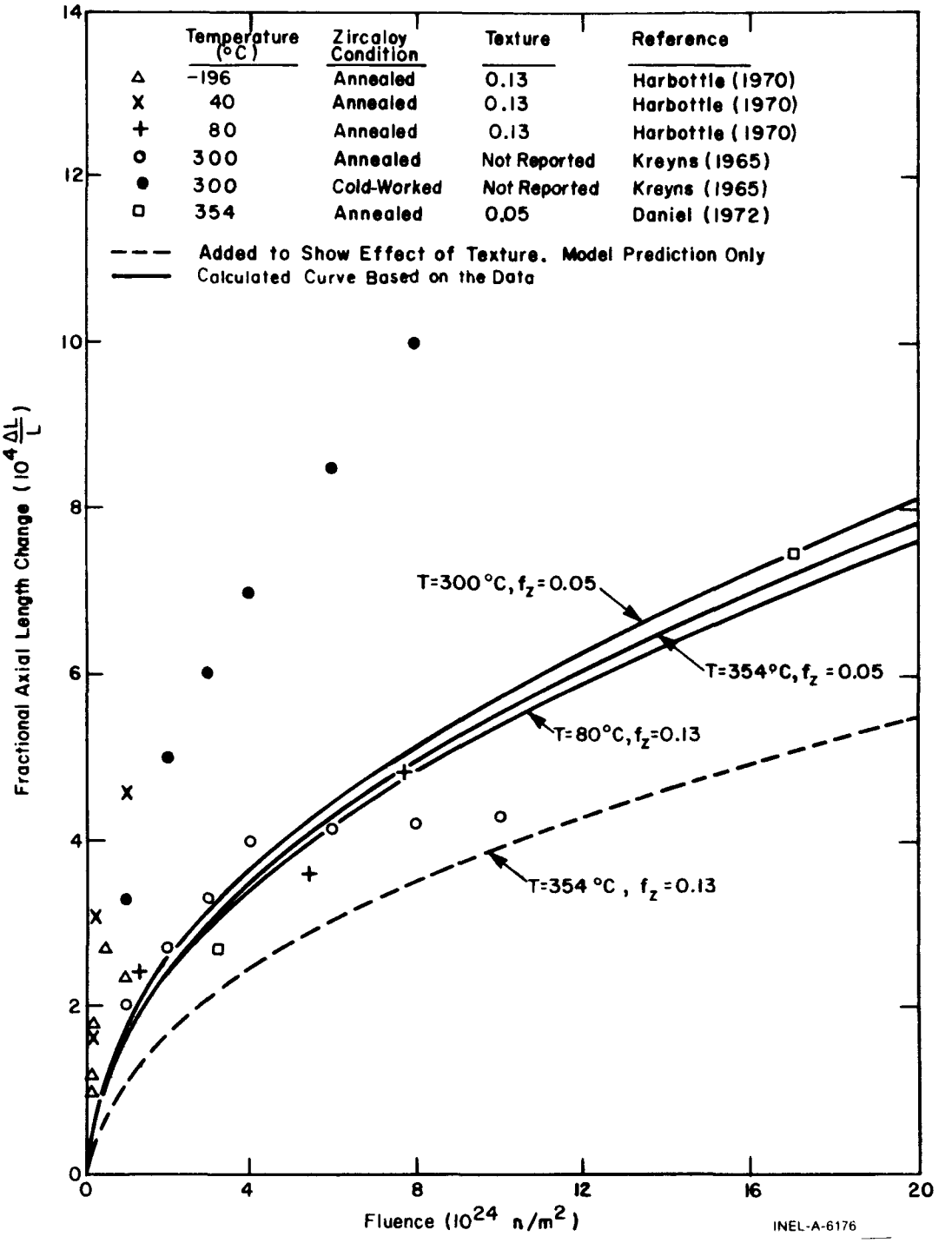

Fig. B-6.1 Model predictions and measured values of zircaloy tube axial growth as a function of fast neutron fluence, irradiation temperature, cold work, and texture coefficient f_z.

6.3 Review of Experimental Data

Samples of zirconium, zircaloy-2, and zircaloy-4 irradiated in a fast neutron flux (E>1 MeV) to fluences of 10^{25} n/m^2 show typical axial growth on the order of 0.1% of length or less. Since the effects of fuel-cladding mechanical interactions and pressure differentials across the cladding compete with the smaller effects of irradiation growth, the relatively plentiful data[B-6.2, B-6.3, B-6.4] are not directly useful in determining the change in cladding length due to irradiation growth. Data on thimble tubes or other structural elements relatively free of confounding effects would be useful, but none have been published. Table B-6.I summarizes the data used for development of the model.

Early data on irradiation induced axial growth of zircaloy-4 tubing at 300°C were obtained by Kreyns[B-6.5]. His experiments indicated that growth of cold-worked tubing is proportional to the square root of the fast neutron fluence up to its maximum fluence (10^{25} n/m^2). Growth of annealed tubing appeared to saturate at a fluence of 4×10^{24} n/m^2 and a fractional length change of 4×10^{-4}. However, subsequent data taken by other investigators have indicated that saturation is not determined by fluence or net growth.

Harbottle[B-6.6] reported the difference in growth strains of transverse and longitudinal strips cut from zircaloy-2 pressure tubes. The strips were annealed and then irradiated at -196, 40, and 80°C. The basal pole texture was found to be 13% in the direction of the tube axis and 36% in the circumferential direction, both before and after the cutting and annealing process. Harbottle's differential growth strains were converted to absolute values of axial growth strains by using the equation

$$\frac{1 - 3 f_z}{1 - 3 f_\phi} = \frac{\text{growth strain in axial direction}}{\text{growth strain in circumferential direction}} \qquad \text{(B-6.2)}$$

where

f_z and f_θ = the texture factors in the axial and circumferential directions, respectively.

A somewhat different approach was taken by Daniel[B-6.1, B-6.7] in a series of experiments which measured both diameter and length changes of fuel rods. The effects of fuel-cladding interactions and pressure differentials across the cladding on measured changes in rod length could be separated from the effect of cladding growth since no fuel-cladding mechanical interaction was present in one experiment series. The separation was achieved by noting that the expected ratio of length to diameter changes is very different for fuel-cladding interactions, creep due to pressure differentials across the rod, and irradiation-induced growth. In particular, the fractional change in diameter due to growth was predicted to be very small for typical cladding diameters and textures. Therefore, a plot of the measured change in length as a function of the measured change in diameter at a single fluence could be used to determine the change in length due to growth by simply

TABLE B-6.I

MEASUREMENTS OF GROWTH IN ZIRCALOY TUBING

Source	$\Delta L/L$ (10^{-4})	Differential[a] $\Delta L/L$(10^{-4})	Fast Fluence (10^{22} n/m^2)	Material	Fast Flux (10^{17} n/m^2·s)	Irradiation Temperature (°C)
Kreyns, reference [B-6.5]	2		100	Annealed zircaloy-4	(?)	300
	2.7		200			
	3.3		300			
	4.0		400			
	4.15		600			
	4.2		800			
	4.3		1000			
	3.3		100	Cold-worked zircaloy-4	(?)	300
	5		200			
	6		300			
	7		400			
	8.5		600			
	10		800			
Daniel, reference [B-6.1, 6.7]	2.7		310	Annealed zircaloy-4	12.5	354
	7.5		1700			
Harbottle, reference [B-6.6]		1.2 ± 0.2	4.9	Annealed zircaloy-2	3	-196
		1.5 ± 0.3	9.7			
		2.3 ± 0.3	19			
		3.5 ± 0.5	50			
		3.0 ± 0.1	98			
		2.1 ± 0.2	8.2	Annealed zircaloy-2	3	40
		4.0 ± 0.2	29			
		5.6 ± 0.4	100			
		3.1 ± 0.4	130	Annealed zircaloy-2	12	80
		4.7 ± 0.4	540			
		6.3 ± 1.0	770			

[a] Only the difference between longitudinal and transverse changes in length was reported.

extrapolating to zero change in diameter with data which did not contain fuel-cladding mechanical interactions. Daniel determined the fractional change in length at two values of fluence. His results[a] are particularly significant because they provide a measure of growth of annealed cladding at high fluence and do not show the saturation which Kreyns[B-6.5] observed.

6.4 The Effect of Texture on Axial and Circumferential Growth

Single crystal texture effects are related to polycrystalline growth. Growth is pictured simply as a reduction of the c-axis dimension of individual grains and an increase of the basal plane dimensions of the grains. The analysis is carried out with the help of an abstract picture of grains made up of schematic immobile unit cells which decrease their c-axis length by a fraction n and increase their a_1, a_2, and a_3 axis lengths by a fraction m. Although the picture of changing unit cell size does not represent atomic behavior within the grain, the growth of the grain is reproduced by the abstract picture.

Figure B-6.2 illustrates the change in the axis lengths of the schematic unit cells. Growth of the three axes in the basal plane is assumed to be equal because of the symmetry of the lattice. The relation between the decrease of the c-axis dimension and the increase of the a-axes dimensions is dependent on the details of the atomic model used to describe growth. For models which imply that the volume of the grain (and schematic unit cell) remains constant, $(1 + m) = (1 - n)^{-1/2}$. This value for $1 + m$ will be assumed at the last stage

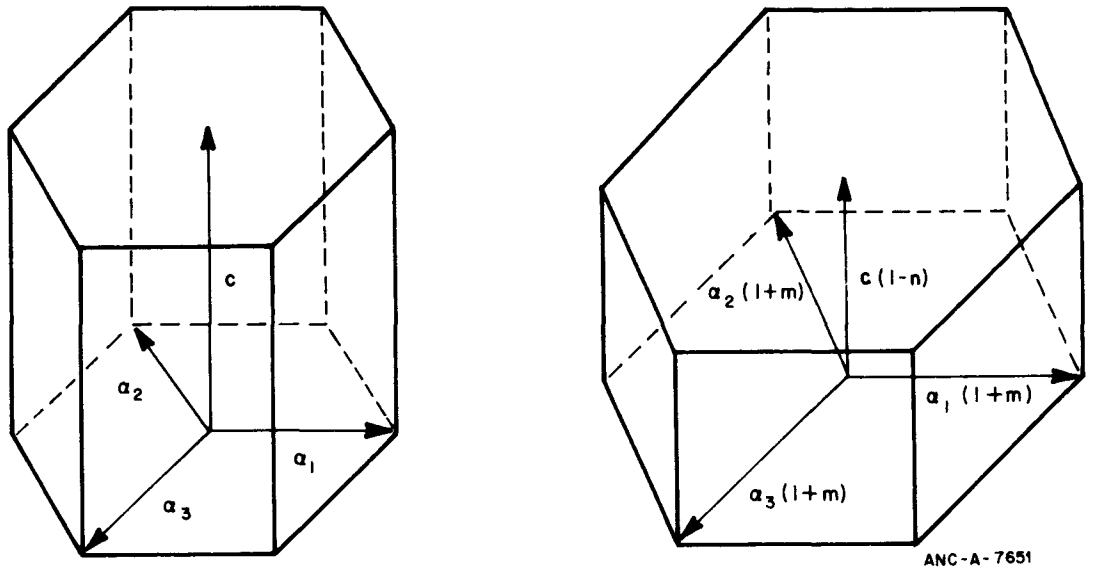

Fig. B-6.2 The growth of schematic unit cells in a grain.

[a] A growth component of strain equal to 7.5×10^{-4} at a fluence of 17×10^{24} n/m^2 and a growth strain of 2.7×10^{-4} at a fluence 3.1×10^{24} n/m^2 were indicated by Daniel[B-6.1, B-6.7].

of the derivation of the effect of texture. It should be noted that the assumption is not made on the basis of a detailed atomic model. The constant-volume assumption is made on the basis of experimental evidence[B-6.8, B-6.9] and this evidence has been somewhat contradictory.

6.4.1 Use of the X-Ray Diffraction Orientations Parameter to Relate Single-Crystal Models to Polycrystalline Results. The effective fraction of grains aligned with their c-axes parallel to a reference direction (axial, circumferential, or radial direction of the tube) is usually taken to be an orientation parameter[B-6.10] determined from X-ray diffraction studies. This parameter is formally defined as the average of the squared cosine of the azimuthal angle between the c-axis of individual grains and the reference direction, weighted by the volume fraction V_i occupied by cells at a given azimuthal angle θ_i. That is,

$$F = \frac{\sum_i V_i \cos^2 \theta_i}{\sum_j V_j} . \qquad \text{(B-6.3)}$$

It is shown in Reference B-6.10 that polycrystalline bulk properties in a reference direction can be expressed as

$$P_{ref} = f P_{\parallel} + (1 - f) P_{\perp} \qquad \text{(B-6.4)}$$

if the property has the following characteristics (a)

$$P_{\eta} = P_{\parallel} \cos^2 \eta + P_{\perp} \sin^2 \eta$$

where

P_{η} = the single crystal property in a direction at an angle η to the axis

$P_{\parallel}$ = the single crystal property along the c-axis

$P_{\perp}$ = the single crystal property perpendicular to the c-axis

and (b) the property in a reference direction of the polycrystalline sample is the volume-weighted summation of this property in its individual crystals.

A property of the schematic unit cells which satisfies condition (a) is the square of the distance between two points imbedded in the schematic unit cell. That is, if $\frac{-x}{2}, \frac{-y}{2}, \frac{-z}{2}$ and $\frac{x}{2}, \frac{y}{2}, \frac{z}{2}$ are coordinates of two points in the cell relative to an origin at the middle of the cell, the squared distance between the points is

$$\ell^2 = Z^2 + X^2 + Y^2 \tag{B-6.5a}$$

or

$$\ell^2 = \ell_o^2 (1 - n)^2 \cos^2\theta + \ell_o^2 (1 + m)^2 \sin^2\theta \tag{B-6.5b}$$

where

ℓ_o	=	the distance between the points
n and m	=	parameters which describe cell change
θ	=	the angle between the c-axis and the line between the points.

It is assumed here that condition (b) of the previous paragraph is also satisfied.

Equations (B-6.4) and (B-6.5) can be used to express the fractional change in the distance between two points of polycrystalline sample. $P_{\parallel}$ and $P_{\perp}$ of Equation (B-6.4) are identified as $\ell_o^2 (1 - m)^2$ and $\ell^2 (1 + m)^2$ in Equation (B-6.5) so that ℓ^2 (the square of the distance between points of polycrystalline sample) is

$$\ell^2 = f (1 - n)^2 \ell_o^2 + (1 - f) (1 + m)^2 \ell_o^2. \tag{B-6.6}$$

The fractional change in length along the reference direction of a polycrystalline sample will then be

$$\frac{\Delta\ell}{\ell_o} = \frac{\ell - \ell_o}{\ell_o} = \sqrt{f (1 - n)^2 + (1 - f) (1 + m)^2} - 1. \tag{B-6.7}$$

The parameters n and m represent the average fractional growth along the c- and a-axes of single crystals. Since growth in zirconium alloys is typically less than 1%, n and m are small numbers and a Taylor series expansion of the radical about n = m = 0 is possible. The expansion yields

$$\frac{\Delta\ell}{\ell_o} \simeq 1 + m - (n + m) f + \text{terms of order } n^2, m^2, \text{ and } nm. \tag{B-6.8}$$

If (1 + m) is taken equal to $(1 - n)^{-1/2}$ in order to impose the restriction of a constant volume on the grain, the Taylor series expansion yields

$$\frac{\Delta \ell}{\ell_o} \simeq \frac{n}{2}(1 - 3f) + \text{terms of order } n^2. \qquad \text{(B-6.9)}$$

The assumption of constant volume is made here in lieu of a successful atomic level model for kinetics of growth.

6.4.2 Application of the Result of Section B-6.4.1 to Measurements of Growth in Different Directions. Equations (B-6.8) and (B-6.9) have been derived without reference to any particular direction. Thus for the axial component of growth, $\frac{\Delta \ell}{\ell}$ is measured along the tubing axis and f is the axial orientation parameter, f_z. If a change in tubing circumference (or diameter of the tube since the diameter is π-1 times the circumference) is being considered, $\frac{\Delta \ell}{\ell}$ is the fractional change in the tubing diameter or circumference, and f is f_θ, the tangential orientation parameter.

6.5 Analysis of Irradiation-Induced Growth Factors Other than Texture

The fast neutron flux (in addition to fluence) and the residual stress in the tubing may affect growth (References B-6.6 and B-6.11) but no attempt has been made to include these effects due to lack of data. Also, no significant difference in the growth rates of zirconium, zircaloy-2, and zircaloy-4 has been reported, so no distinction between their growth rates has been incorporated into the model. As mentioned in Section B-6.2, the first step in developing the model was to account for differences in growth due to differences in texture. The factor (1 + 3f) of Equation (B-6.9) was used to adjust growth measured with arbitrary textures to values expected for f = 0.05. The results are illustrated in Figure B-6.3.

6.5.1 The Effect of Fast Neutron Fluence on Irradiation Growth. Many investigators have treated the effect of fast fluence by fitting in the empirical expression

$$\text{growth strain} \propto (\text{fluence})^q \qquad \text{(B-6.10)}$$

to the data[B-6.6, B-6.8] with resultant values of q in the range 0.3 - 0.8. Although good agreement can be obtained by allowing q to vary for each set of data, the results of such empirical fits are somewhat misleading. Hesketh[B-6.12] has derived a dependence on the square root of fluence [q = 0.5 in Equation (B-6.10)] and data from individual irradiations have not demonstrated a clear departure (other than saturation effects) from this rule. This point is illustrated in Figure B-6.4 by showing a plot of axial growth as a function of the square root of the fluence.

Departures from q = 0.5 would be indicated by curvature of the data in Figure B-6.4. Except for apparent saturation effects on annealed tubes at 300°C, these departures are much less pronounced than differences due to different temperatures, fluences, and cold

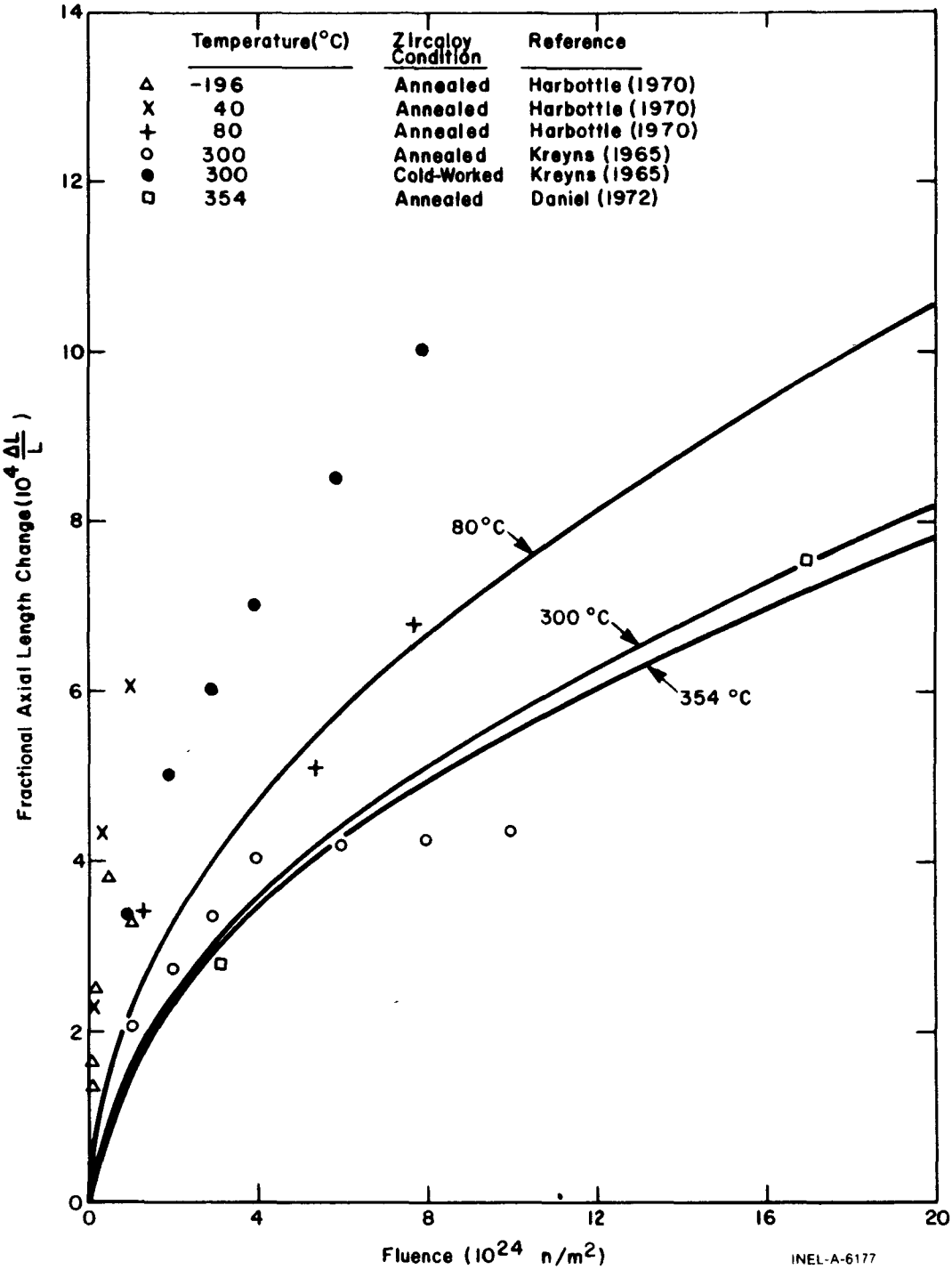

Fig. B-6.3 Model predictions and measured values of the growth of zircaloy tubes adjusted to a common texture coefficient of $f_z = 0.05$.

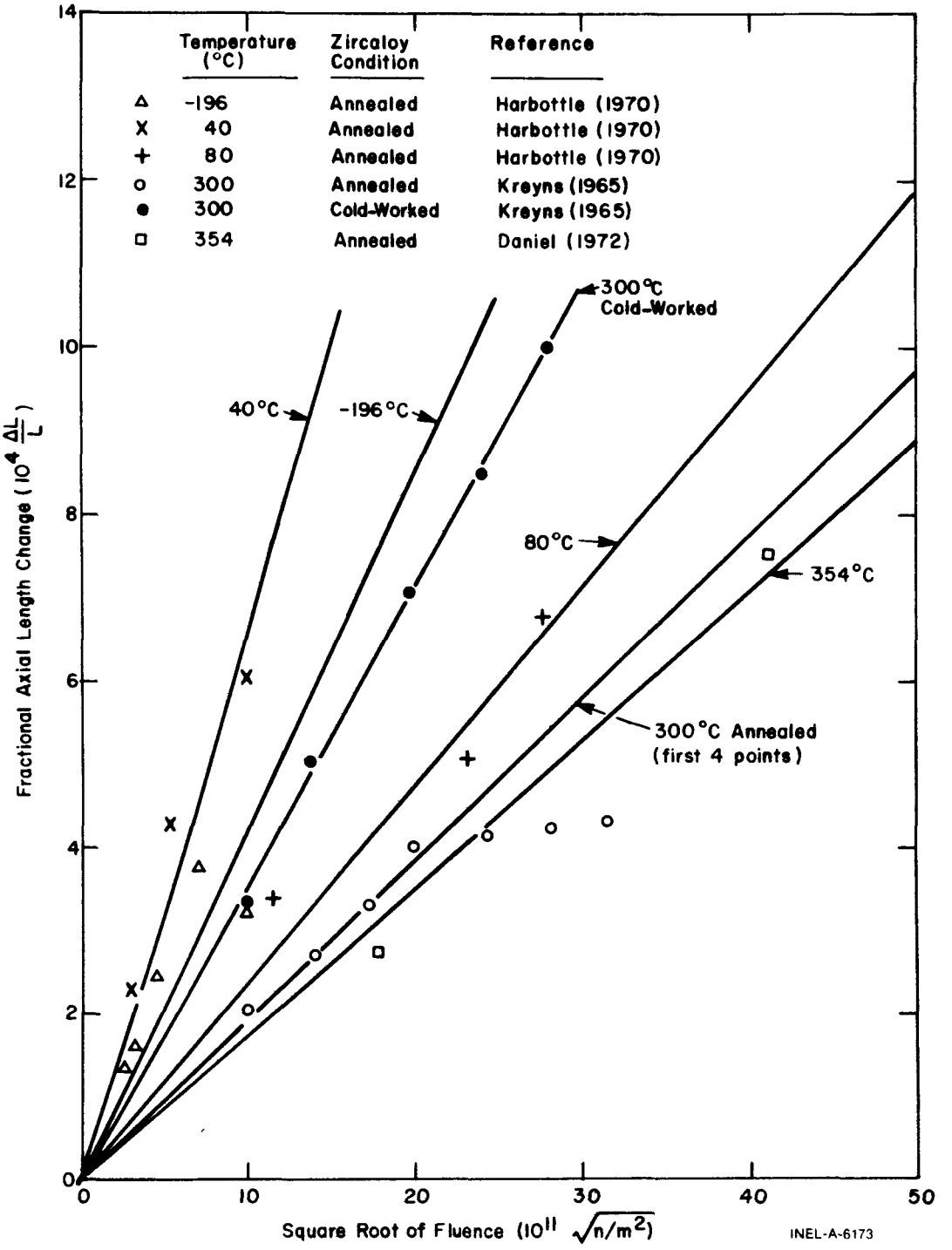

Fig. B-6.4 Zircaloy growth versus square root of fast neutron fluence for data adjusted to a common tube texture coefficient of $f_z = 0.05$ with linear least-squares fits superimposed.

work. Moreover, there is a physical basis for expecting temperature and flux to modify the effect of a given fluence. Therefore, the exponent in Equation (B-6.10) is fixed in the model at 0.5.

6.5.2 The Effect of Temperature on Irradiation-Induced Growth. It has been suggested by Harbottle that growth is proportional to the instantaneous concentration of interstitials. This implies that growth should be directly proportional to the rate of interstitial production (which is proportional to neutron flux ϕ) and inversely proportional to the rate of interstitial removal. Since interstitial removal is proportional to exp (-interstitial migration energy/RT), the following expression for growth should apply.

$$\frac{\Delta L}{L} \propto \phi \exp\ (E_M/RT) \qquad \text{(B-6.11)}$$

where

E_M = interstitial migration energy

R = gas constant.

When Equation (B-6.11) is compared to data, E_M varies with temperature as expected, but any simple variation of E_M with temperature is not consistent with all experiments. A constant value for E_M has been used in the model due to these inconsistencies and because it has been suggested that the dependence of E_M on temperature will be too complex[B-6.13] to evaluate with existing data. E_M will actually change in poorly defined steps as the modes of interstitial migration change with increasing temperature. However, Figures B-6.1, B-6.3, and B-6.4 indicate that there is a relatively small temperature dependence in the normal operating temperature range for light water reactors. Use of a small and constant value for E_M is therefore justified. A comparison of Equation (B-6.11) with the data shown in Figure B-6.4, then, results in the following correlation:

$$\frac{\Delta L}{L} \propto \exp\ (240.8/T)\ . \qquad \text{(B-6.12)}$$

The fast flux factor of Equation (B-6.11) has been incorporated in the constant A of the full expression for growth, Equation (B-6.1).

The detailed data comparisons made while deriving Equation (B-6.12) provide justification for the functional dependence shown. When Harbottle's[B-6.6] data for growth under fast fluxes differing by a factor of two (at 40 and 80°C - See Table B-6.I) are compared, they are consistent with a value of E_m = 0.3 eV. This value of E_m is reasonable for atomic migration in that temperature range. When other data are examined, values of E_m = 0.075 eV result at -196°C and of E_m = 0.517 eV at 354°C. This range of values is also reasonable[B-6.14], lending confidence to the functional dependence given by Equations (B-6.11) and (B-6.12).

6.5.3 The Effect of Cold Work on Irradiation Growth. The observed effects of cold work have not been successfully explained in detail in the literature. For this model, general conclusions have been drawn from the available measurements and an empirical expression formed. The data taken by Kreyns on cold-worked zircaloy-4 tubes at 300°C agree very well with a square root of fluence dependence as shown in Figure B-6.5. To compare these

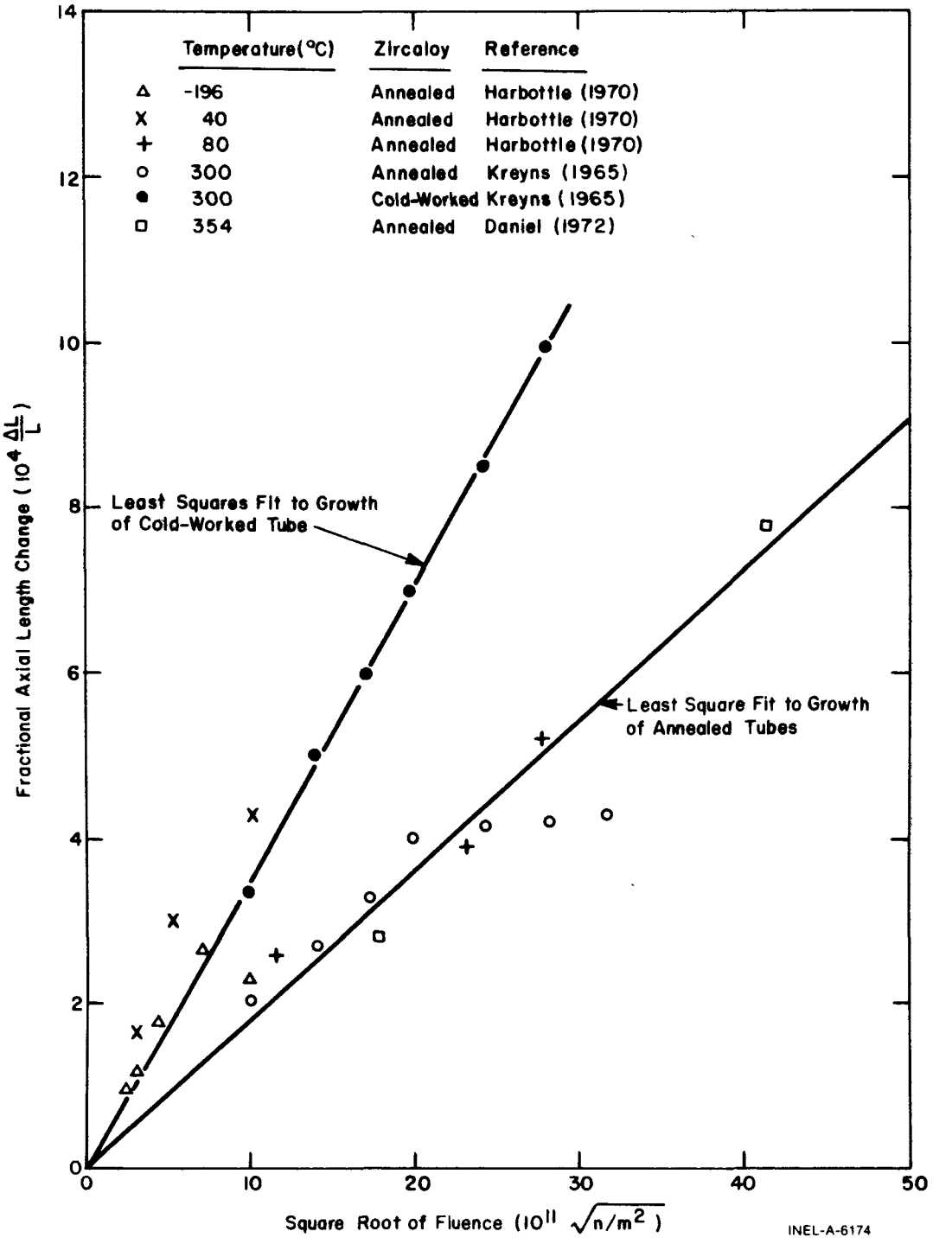

Fig. B-6.5 Zircaloy growth versus square root of fast neutron fluence for data adjusted to a common tube texture coefficient of $f_z = 0.05$ and to a common temperature of 300°C, with linear least-squares fits superimposed.

results with those for annealed tubes, the annealed data shown in Figure B-6.4 were normalized to 300°C using Equation (B-6.12). Figure B-6.5 then indicates that the net effect of cold work is to increase the growth rate in the unsaturated range of fluence. Neither the dependence on the square root of the fluence nor the intercept at zero fluence are changed by cold work.

The only available data on the effect of varying the amount of cold work are reported in Figure 19 of Reference B-6.8 which indicates the following approximate irradiation growth fractions in the longitudinal direction of zircaloy-4 plate specimens at 300°C (Table B-6.II). The data are reasonably consistent with a linear relationship between growth and

TABLE B-6.II

ZIRCALOY GROWTH DATA AS A FUNCTION OF COLD WORK AND FLUENCE

Fast Fluence (10^{24} n/m^2)	Cold Work		
	0%	20%	78%
14	7.4×10^{-4}	7.8×10^{-4}	17.4×10^{-4}
20	8.2×10^{-4}	11.7×10^{-4}	24.4×10^{-4}
30	9.2×10^{-4}	17.3×10^{-4}	36.3×10^{-4}

cold work and have been incorporated into the model by assuming a factor of the form (1 + D x cold work). Values of D determined from the data at three different fluences are listed in Table B-6.III where

$$D = \frac{1}{\text{cold work}} \left[\frac{\text{Growth with cold work}}{\text{Growth without cold work}} - 1 \right]. \qquad \text{(B-6.13)}$$

The value D = 2.0, given by the data at the lower fluences, is used in the model since the measured growth with 0% cold work (Table B-6.II) show gross saturation effects similar to the effects apparent in the high fluence data of Kreyns. The model thus sacrifices a description of these gross saturation effects in order to fit the cold work data and the majority of the annealed tubing data.

6.6 Evaluation of the Model and Its Uncertainty

The normalization of all the annealed data to identical conditions (texture coefficient $f_z = 0.05$, temperature at 300°C) as shown in Figure B-6.5, provides a test of the model. The model predicts irradiation-induced growth reasonably well except for data taken at fluences less than 10^{24} neutrons/m^2 and except for greater than normal saturation effects

TABLE B-6.III

DETERMINATION OF COLD WORK COEFFICIENT

Fast Fluence (10^{24} n/m^2)	D
14	1.7
20	2.0
30	3.8

seen in some annealed samples. Figure B-6.1 leads to the same conclusion and also indicates the relative effects of the temperature, texture, and fluence variables as predicted by the model. [The factor A used in Equation (B-6.1) for these curves was derived from a linear least-squares fit to the data of Figure B-6.5.]

Further refinement of the model to explain the relatively high growth measured at low fluence and to explain the gross saturation effects observed on some samples, has not been attempted. In the low fluence case there are competing processes that may explain the high values sometimes found, and there is no way to distinguish between them without additional data. These effects are:

(1) Stress relief causing additional length changes (Reference B-6.11)

(2) Variation in fast flux causing different growth rates (Reference B-6.6)

(3) Variation in interstitial migration energy with temperature causing error in the temperature model (as discussed in Section B-6.5.2).

Similar problems exist with attempts to model the gross saturation effects observed in some experiments by Kreyns using tubing and by Fidleris[B-6.8] using plate samples. There are sufficient data to indicate clearly that these saturation effects in growth are not simply a function of the fluence or the growth strain. However, few data are available to appraise correlations between saturation and other parameters.

An estimate of the uncertainty can be obtained by comparing predictions of the model with data not used in formulating the model. For example, the plate specimen data listed in Table B-6.II for 0% cold work (and 300°C) were not used to formulate the predicted growth of annealed tubes. When these data are compared with the model predictions for annealed growth at 300°C, a discrepancy of approximately 10% is found.

This 10% discrepancy is consistent with the scatter of the data at fluences above 10^{24} n/m^2 in Figure B-6.5 and thus is a reasonable estimate of the model's uncertainty in the temperature range from 40 to 360°C.

The uncertainty for temperatures outside of this range and for fluences less than 10^{24} n/m^2 may be substantially greater than 10%. In the low fluence range, inspection of Figure B-6.5 suggests uncertainties on the order of 100%. Such large discrepancies may be due to stress relief effects[B-6.11]. For temperatures much outside the range 40 to 360°C increased error will be caused by the presence of different modes of interstitial or vacancy migration causing different rates of zircaloy growth.

6.7 Cladding Axial Growth Subcode CAGROW Listing

A listing of the FORTRAN subcode CAGROW is presented in Table B-6.IV.

6.8 References

B-6.1. R. C. Daniel, "In-Pile Dimensional Changes of Zircaloy-4 Tubing Having Low Hoop Stresses (Light Water Breeder Reactor Development Program)," *Nuclear Technology, 14* (May 1972) pp 171-186.

B-6.2. W. R. Smalley, *Evaluation of Saxton Core III Fuel Materials Performance* WCAP-3385-57 (1974).

B-6.3. J. B. Melehan, *Yankee Core Evaluation Program Quarterly Progress Report for the Period Ending September 30, 1969,* WCAP-3017-6091 (December 1969).

B-6.4. E. T. Laats and P. E. MacDonald, *Halden Project Fuel Behavior Test Program – Experimental Data Report for Test Assemblies IFA-226 and IFA-239,* NRC-OECD (March 1975).

B-6.5. P. H. Kreyns, quoted by E. Duncombe et al, *Comparisons with Experiment of Calculated Changes and Failure Analysis of Irradiated Bulk Oxide Fuel Test Rods Using the CYGRO-1 Computer Program,* WAPD-TM-583 (September 1966).

B-6.6. J. E. Harbottle, "The Temperature and Neutron Dose Dependence of Irradiation Growth in Zircaloy-2," *Irradiation Effect on Structural Alloys for Nuclear Reactor Applications,* ASTM-STP-485 (1970) pp 287-299.

B-6.7. R. Daniel, *In-Pile Dimensional Changes of Zircaloy-4 Tubing Having Low Hoop Stresses (LWBR Development Program),* WAPD-TM-973 (July 1971).

B-6.8. V. Fidleris, "Summary of Experimental Results on In-Reactor Creep and Irradiation Growth of Zirconium Alloys," *Atomic Energy Review, 13* (1975) p 51.

TABLE B-6.IV

LISTING OF THE CAGROW SUBCODE

```
C
C
      FUNCTION CAGROW(CTEMP,CFLUX,TIME,CATEXF,COLDW)
C
C     CAGROW CALCULATES AXIAL CLADDING GROWTH STRAIN AS A FUNCTION OF
C     TEMPERATURE (CTEMP), FAST NEUTRON FLUX (CFLUX), TIME,
C     AXIAL TEXTURE FACTOR (CATEXF), AND COLD WORK (COLDW).
C
C     CTEMP  = INPUT CLADDING TEMPERATURE (K)
C     CFLUX  = INPUT FAST NEUTRON FLUX ((NEUTRONS/M**2)/SEC)
C     TIME   = INPUT TIME AT TEMPERATURE (SECONDS)
C     CATEXF = INPUT TEXTURE FACTOR FOR THE AXIAL DIRECTION (NO UNITS)
C     COLDW  = INPUT COLD WORK (METERS**2/METER**2)
C     CAGROW = OUTPUT AXIAL CLADDING GROWTH STRAIN (METERS/METER)
C
C     THE EQUATION USED IN THIS SUBROUTINE WAS BASED ON DATA FROM
C     (1) P.H. KREYNS QUOTED BY E. DUNCOMBE, J.E. MAYER AND W.A. COFFMAN
C     COMPARISONS WITH EXPERIMENT OF CALCULATED CHANGES AND FAILURE
C     ANALYSIS OF IRRADIATED BULK OXIDE FUEL TEST RODS USING THE
C     CYGRO-1 COMPUTER PROGRAM, WESTINGHOUSE REPORT WAPD-TM-583, 1966
C     (2) J.E. HARBOTTLE  "THE TEMPERATURE AND NEUTRON DOSE DEPENDENCE
C     OF IRRADIATION GROWTH IN ZIRCALOY-2" IN ASTM-STP-484 (1970)
C     (3) R.C. DARIEL, "IN-PILE DIMENSIONAL CHANGES OF ZIRCALOY-4 TUBING
C     HAVING LOW HOOP STRESSES (LWBR DEVELOPMENT PROGRAM)", NUCLEAR
C     TECH. 14 (1972)
C     (4) R.B. ADAMSON  FROM FIDLERIS, AECL-4766
C
C     CAGROW CODED BY D.L. HAGRMAN, AUGUST 1975
C
      T = CTEMP
      IF(T .GT. 633.0) T = 633.0
      IF(T .LT. 313.0) T = 313.0
C
      CAGROW = 1.407E-16 * EXP(2.408E+2/T) * SQRT(CFLUX * TIME) *
     #         (1.0 - 3.0 * CATEXF) * (1.0 + 0.02 * COLDW)
      RETURN
      END
```


B-6.9. S. N. Buckley, "Discussion at Institute of Metals Spring Meeting," *Journal of the Institute of Metals, 97* (1969) p 61.

B-6.10. J. J. Kearns, *Thermal Expansion and Preferred Orientation in Zircaloy,* WAPD-TM-472 (November 1965).

B-6.11. V. Fidleris, "The Effect of Cold-Work and Stress-Relieving on the Irradiation Growth Behavior of Zirconium Alloys," *Journal of Nuclear Materials, 46* (1973) pp 356-360.

B-6.12. R. V. Hesketh, "Non-linear Growth in Zircaloy-4," *Journal of Nuclear Materials, 30* (1969) pp 217-222.

B-6.13. S. H. Bush, *Irradiation Effects in Cladding and Structural Materials,* New York: Rowman and Littlefield (1965) p 143.

B-6.14. A. Seeger and H. Mehren, "Analysis of Self-Diffusion and Equilibrium Measurements," *Vacancies and Interstitials Metals,* A. Seeger (ed.), New York: American Elsevien Publishing Co., Inc., 1970, p 892.

7. CLADDING CREEP (CCRPR)

(D. L. Hagrman)

Cladding creep during steady state operation is important in modeling the size and shape of the fuel-cladding gap and thus in evaluating gap heat transfer. A correlation is presented in this section to describe the creep of zircaloy cladding under compression in light water reactors. The correlation is based primarily on end-of-life examinations of PWR (pressurized water reactor) cladding and on out-of-pile measurements of cladding shape changes with time.

7.1 Summary

The CCRPR subroutine calculates the circumferential component of cladding creep strain as a function of cladding temperature, circumferential cladding stress, fast neutron flux and time. The correlation used to describe cladding creepdown when there is no fast neutron flux is

$$\dot{\epsilon}_p = (5 \times 10^{-23})\, \sigma^2 \left[(3.47 \times 10^{-19})\, \frac{\sigma^3}{|\sigma|} \exp(-U/T) - \epsilon_p\right] \exp(-U/T) \quad \text{(B-7.1)}$$

where

$\dot{\epsilon}_p$ = circumferential component of strain rate in zero flux (s^{-1})

ϵ_p = circumferential strain in zero flux (unitless ratio)

σ = circumferential component of stress (Pa)

T = temperature (K)

U = apparent activation energy divided by the gas constant (K)
$= (2.1427 \times 10^2) + T[(-5.324 \times 10^{-1}) + T(1.17889 \times 10^{-4}) + T(3.3486 \times 10^{-7})]$.

In fast neutron fluxes, the strain rate given by Equation (B-7.1) is increased. The equation used to describe the increase in the strain rate due to the fast neutron flux is

$$\dot{\epsilon}_i = \frac{2.2 \times 10^{-7}}{T^7} (\phi^{0.65})\, \sigma \exp\left(\frac{-5000}{T}\right) \quad \text{(B-7.2)}$$

where

$\dot{\epsilon}_i$ = increase in the circumferential component of strain rate due to fast neutron flux (s^{-1})

ϕ = fast neutron flux [neutrons/($m^2 \cdot s$)], E > 1 MeV.

The expression used for total in-reactor creep is the sum of the separately integrated forms of Equations (B-7.1) and (B-7.2). The integrated equation for creep strain during a time interval with constant stress, temperature, and fast neutron flux is

$$\epsilon_{final} = \epsilon_{initial} + \left[(3.47 \times 10^{-19}) \frac{\sigma^3}{|\sigma|} \exp(-U/T) - \epsilon_{p\ initial}\right] \left[1 - \exp\left[-5 \times 10^{-23}\ \sigma^2 \exp(-U/T)\ \Delta t\right]\right] + \frac{2.2 \times 10^{-7}}{T^7} (\phi^{0.65})\ \sigma \exp\left(\frac{-5000}{T}\right) \Delta t. \quad \text{(B-7.3)}$$

where

ϵ_{final} = circumferential component of strain at the end of a time step (unitless ratio)

$\epsilon_{initial}$ = circumferential component of strain at the start of a time step (unitless ratio)

$\epsilon_{p\ initial}$ = primary (zero flux) part of the circumferential component of strain at the start of a time step (unitless ratio). The primary part of the strain at the end of a time step, $\epsilon_{p\ final}$, is calculated and returned by the subroutine CCRPR so that it may be stored for use as $\epsilon_{p\ initial}$ in any subsequent time step

Δt = time step size (s)

and the other terms of the equation have been previously defined.

Based on the limited in-reactor data available, a standard error of one half of the strain predicted by Equation (B-7.3) is anticipated.

The following sections discuss available data, development of the model and uncertainty of the model. Section 7.5 contains a listing of the subcode CCRPR.

7.2 Survey of the Available Data

This section is a review of the theoretical results and data presently available for use in modeling a code for cladding creepdown. However, data are not available which accurately measure deformation as a function of time under typical LWR steady state conditions. Therefore, a number of references which only address the problem of modeling creep of zirconium-base alloys are listed in a bibliography (Section 7.7).

7.2.1 Effect of Stress. Dollins and Nichols[B-7.1] have discussed physical models which attempt to explain the in-pile creep of cladding. For the temperature range 523 to 623 K, they believe the controlling mechanism for in-pile creep at stresses below 69 to 103 MPa is the preferred alignment of irradiation-induced dislocation loops during nucleation. At higher stresses, the effective stress at dislocations is thought to be sufficiently large to allow dislocation glide between the neutron produced depleted zones. The creep rate would then be controlled by dislocation climb out of these zones. At still higher stresses, above 415 MPa, Dollins and Nichols expect the dislocations to cut through the depleted zones without climb. Although some of Dollins' ideas have been challenged recently[B-7.2], their predicted linear stress dependence of strain rate at low stress is supported by several authors[B-7.3 – B-7.6] and their idea that the strain rate at high stress is proportional to approximately the one hundredth power of stress is consistent with the MATPRO subcodes CSIGMA and CSTRES[B-7.7]. Unfortunately, Dollins and Nichols predict a complex relation between strain rate and stress for intermediate stresses. The dependence of strain rate on stress is expected to vary from the tenth power of stress to the first power and then to the fourth power as stress increases. Also, in this region many of the data cited are from Zr-2.5Nb, an alloy which may exhibit different properties than zircaloy-2 or zircaloy-4.

A similar, but less theoretically based stress dependence is proposed by Fidleris in his review[B-7.6]. He reported that the creep rate varies linearly with stress at temperatures around 570 K and stresses less than one third the yield stress. With increasing stress, the strain rate is reported to be proportional to higher powers of stress, reaching a power of 100 at stresses of 600 MPa. Like Dollins and Nichols, Fidleris relies primarily on Zr-2.5Nb data in the intermediate stress region.

7.2.2 Effects of Temperature and Fast Neutron Flux. Fidleris discusses several important parameters not treated by Dollins and Nichols. The in-reactor creep rate is found to depend on material, flux, temperature, and direction of testing as well as stress. The fast neutron flux seems to cause a completely different kind of creep. At temperatures below half the melting temperature (2100 K) and stresses lower than the yield stress, the in-reactor creep reaches a constant rate while the out-of-reactor creep rate becomes negligibly small with time. The steady state creep rate is stated to be independent of test history or strain, at least for fast neutron fluences below 3×10^{24} neutrons/m^2 ($E > 1$MeV).

Because of the very different behavior of in-reactor and out-of-reactor creep under tensile stress, recent models[B-7.8] have treated the in-reactor creep as the sum of the

out-of-reactor creep and an additional irradiation-induced creep. The assumption will be adopted in Section B-7.3 of this report because it is the most convenient of several equally arbitrary assumptions.

Below 450 K, Fidleris reports that the out-of-reactor tensile creep strain can be described by

$$\varepsilon = A\ (\log\ t) + B \qquad \text{(B-7.4a)}$$

where

ϵ = strain

t = time

A, B = constants.

Below 450 K, temperature is reported to have very little effect and, for stresses below the yield stress, the strain is less than 0.001. In the range 450 to 800 K, Fidleris reports that the out-of-reactor tensile creep strain is often

$$\varepsilon = A\ (t^m) + B \qquad \text{(B-7.4b)}$$

where ϵ, t, A and B were defined in conjunction with Equation (B-7.3) and m is a constant between zero and one. Mechanical recovery of some of the strain is possible and dynamic strain aging frequently causes anomalously low creep strains and rates.

In the range 450 to 800 K, the apparent activation energy[a] for out-of-reactor creep of annealed zirconium is reported to decrease from large values at either extreme of the temperature range to a minimum of about 159 J/mol at 620 K. A third degree polynomial in temperature was developed from the curve presented by Fidleris (Figure 3 of Reference B-7.6). The resultant expression is

$$Q = (3.5625 \times 10^3) + T\ [-8.8519 + T(1.9601 \times 10^{-3}) + T\ (5.5675 \times 10^{-6})] \qquad \text{(B-7.5)}$$

[a] The apparent activation energy is proportional to the slope of the $\log \dot{\epsilon}$ versus $\frac{1}{T}$ curve at constant stress and fast neutron flux.

where

T = temperature (K)

Q = apparent activation energy (J/mol).

The activation energy for in-reactor creep is reported by Fidleris to be about 4.18×10^4 J/mol at 570 K. At higher temperatures, he reports that the in-reactor activation energy appears to increase. This would mean that the irradiation-induced component of creep is decreasing with increasing temperature. For all temperatures, Fidleris suggests that the in-reactor creep is approximately proportional to the fast neutron flux.

Other investigators treat the effects of fast neutron flux and temperature on irradiation-induced creep in different ways. Although most authors agree that the in-reactor addition to cladding creep rate is proportional to ϕ^a, where ϕ is the fast flux, there is disagreement about the magnitude of the exponent a. Duffin and Nichols[B-7.9], Piercy[B-7.10], and Ross-Ross and Hunt[B-7.5] also suggest that the creep rate is directly proportional to the fast flux. Wood[B-7.11, B-7.12] uses $\dot{\epsilon} \propto \phi^{0.85}$, Kohn[B-7.13] uses $\phi^{0.65}$, and Gilbert[B-7.14] uses $\phi^{0.5}$. The most logical approach seems to be that of Kohn who models the flux enhancement in the form $AT^{-7}\ \phi^{0.65} \exp(-B/T)$ where A and B are constants. This functional form has the virtue of cutting off the flux term at high temperatures as well as automatically accounting for the fact that the higher the flux level is, the higher the temperature must be to negate the effect of flux.

7.2.3 Effect of Material. At 573 K, the zircaloy-2 creep rate is reported by Fidleris[B-7.6] to increase continuously with grain size. However, within the limited range of grain sizes formed in recrystallized zircaloy-2 (6 to 20 μm) very little variation in creep rate with grain size is reported.

Kohn[B-7.13] has reported that the biaxial creep rate of Zr-2.5Nb fuel cladding is about 10 times higher than that of pressure-tube material under similar conditions. He states that texture differences between the materials and the overaged precipitate structure in the as-manufactured fuel cladding can explain the difference in creep rates. The importance of texture is disputed by Stehle et al[B-7.15] who reported that the mechanical anisotropy (especially in long time creep) is surprisingly low compared to the short time anisotropy at room temperature. An effort to include an explicit model for recovery effects would be premature at this time. A similar conclusion seems appropriate in the case of the related effects of texture and grain size. There is simply not enough well characterized information available to support an explicit model at this time.

7.2.4 Application of Tensile Data to Creep Under Compressive Stress. In spite of the great body of literature which deals with creep in zirconium-based alloys, (a) most of the experimental results discussed are from uniaxial specimens tested under tension in the longitudinal direction and (b) none of the many theoretical models proposed to explain in-reactor creep effects has yet gained universal acceptance. Picklesimer[B-7.16] and Stehle et al[B-7.15] pointed out that compressive properties can differ from tensile

properties and that an adequate treatment of stress-strain behavior will allow the stress-strain properties of zircaloy to vary with the sign of the stress. The creepdown of tubes under external pressure is less than expected from the theory based on tensile or internal pressure creep results[B-7.15].

Because the basic creep mechanism is not well understood and there are differences between tensile and compressive creep, the uniaxial and even the limited biaxial tensile data may actually be misleading when applied to compressive creep without a thorough understanding of the basic mechanism. The extensive tensile data are therefore used only when insufficient compressive data are available. Details which might be modeled empirically with tensile creep data have been omitted because such detail may not be correct for creepdown.

7.2.5 Biaxial Compressive Creep. The biaxial compressive data now available include out-of-reactor measurements of strain versus time at two stresses and one temperature as well as postirradiation measurements of average cladding diameter. These data will be discussed in somewhat more detail than the tensile data since they are the main foundation of the model being developed.

The out-of-reactor data are from Hobson's recent measurements of cladding radial displacement as a function of time[B-7.17 – B-7.19]. As Hobson pointed out[B-7.19], the exact shape of the cladding surface cannot be determined with point-by-point data from a few radial probes. He also pointed out that the exact stress state at any point in the sample is related to the geometry of the sample. In spite of these complications, the data can be analyzed to obtain an expression for the average circumferential strain as discussed in the next section of this report.

Measured postirradiation strains of three sets of PWR cladding are available. Average rod diameters at varying axial locations and burnups were reported as part of the Saxton Plutonium Project[B-7.20, B-7.21]. The circumferential strain implied by the reduced diameter was about 3×10^{-3}. However, cladding ridging was reported on several of the rods used in the averaging process. The Saxton data were not used to construct the creepdown model because of the probability that the ridging is an indication of a relatively large effect of pellet-cladding interaction on the cladding creepdown. However, they were used to help estimate upper bounds on the uncertainty of the model.

A. A. Bauer et al[B-7.22 – B-7.26] reported larger strains using spent fuel rods from (a) the Carolina Power and Light, H. B. Robinson 2 Power Plant[B-7.22] and (b) the Oconee-I reactor[B-7.23]. The Robinson rods were operated for 799 equivalent full power days at an average fast neutron flux of 6.3×10^{17} neutrons/(m^2·s), $E > 1$ MeV to a fluence of 4.4×10^{25} neutrons/m^2($E > 1$ MeV)[B-7.24]. The Oconee rods were removed from that plant as part of a fuel surveillance program conducted by Babcock and Wilcox[B-7.23]. The peak fast neutron fluence of the Oconee rods is 2.3×10^{25} neutrons/m^2($E > 1$ MeV)[B-7.26].

Bauer et al reported the average diameter of the Robinson rods over the central fuel region is about 1.06 cm, compared with a nominal preirradiation diameter of 1.07 cm[B-7.25]. The implied circumferential strain of the rods is about -9.5 x 10^{-3}. The Oconee rods had an average diameter over the central fuel region of about 1.08 cm, compared to a nominal preirradiation diameter of 1.09 cm[B-7.26]. The implied circumferential strain of the Oconee rods is about -7 x 10^{-3}. Although no ridging is reported by Bauer et al, there is no conclusive reason to suppose that pellet-cladding interaction was absent in the Oconee/Robinson rods. The significant ovality of the cladding[B-7.25, B-7.26] and the increase in ovality reported from other data[B-7.27, B-7.28] suggest a significant interaction in most PWR cladding (it is this point which makes the planned in-reactor strain versus time data of Hobson[B-7.19] so important). The postirradiation strains reported by Bauer are employed as discussed in the next section because they are the most representative data yet available to describe in-reactor creepdown of cladding.

7.3 Development of the Model

It was concluded in the last section that the most relevant data for modeling cladding creepdown under steady state LWR reactor conditions are the out-of-reactor data of Hobson and the postirradiation diameter measurements of Bauer et al. In the development of the CCRPR subcode, Hobson's data are used to obtain an expression for primary creep which is assumed to apply to in-reactor deformation where no relevant data are yet available. The two sets of data from Bauer are used to estimate the flux induced steady state creep rate in-reactor for typical PWR conditions. Finally, the trends reported from scattered tensile creep data are used to estimate the effects of changes in temperature, stress, and fast neutron flux to values not typical of LWR reactor conditions.

7.3.1 Out-of-Reactor Creepdown. The data reported by Hobson are radial displacements of the cladding surface at various azimuthal angles and axial positions (6.35 mm apart). Twenty probes were used to measure the displacement and they were arranged in a double helix pattern over a 50.8 mm length of cladding as shown by probe number in Table B-7.I. This table and the one which follows are arranged so that they may be visualized as a surface split along the cylinder's axis and "rolled out" in the plane of the page.

Measured radial displacements as a function of time from each probe for three long time tests have been reported by Hobson[B-7.19]. The tests were conducted at a temperature of 644 K and for times up to approximately 1000 hours. Two differential pressures were used – 15.86 MPa in two of the tests and 14.48 MPa in the third test.

An effort to model the displacement of the entire surface of the cladding has been initiated by Hobson[B-7.19]. The analysis described here is not as general. It is intended to determine only the average circumferential component of creep strain.

The first step in this analysis is to estimate the shape of the cladding surface represented by the various probe measurements. This is done by inspecting plots of the radial displacement measured by the probes for each test. Table B-7.II and Figure B-7.1 are

TABLE B-7.I

SURFACE COORDINATES OF PROBES WHICH MEASURE RADIAL DISPLACEMENT[a]

Axial Position (mm)	Azimuthal Angle (degrees)							
	0	45	90	135	180	225	270	315
0.00	1	--	--	--	--	13	--	--
6.35	--	4	--	--	--	16	--	--
12.70	--	--	7	--	--	--	19	--
19.05	--	--	--	10	--	--	--	22
25.40	2	--	8	--	14	--	20	--
31.75	--	5	--	--	--	17	--	--
38.10	--	--	9	--	--	--	21	--
44.45	--	--	--	11	--	--	--	23
50.80	3	--	--	--	15	--	--	--

[a] Probe numbers are inserted in the table to facilitate comparison to Reference B-7.19.

an example of the way this is done. The table was constructed from Hobson's data for Test 269-4 (14.48 MPa pressure) at 200 hours and the figure is a polar plot of the radial displacement as a function of the azimuthal angle of the probe. The plot exaggerates the radial displacement by a factor of ten compared to the scale of the circle which represents zero displacement. From an inspection of the figure it can be seen that the radial displacements at 200 hours in Test 260-4 are consistent with the assumption that the cladding surface was an ellipse with major axis between 0^{o} and 45^{o} and the center of the ellipse displaced slightly toward the $180^{o} - 270^{o}$ quadrant. There is some variation with axial position, as shown by the "scatter" in the displacements with common azimuthal angles and different axial positions.

The elliptical shape and gradual axial variation are also consistent with general descriptions of cladding surfaces after creepdown given by Stehle et al[B-7.29] and by Bauer et al[B-7.25]. Based on several plots like Figure B-7.1 and the general descriptions just mentioned, the author has concluded (a) an ellipse is a reasonable approximation for the cladding surface at any given height prior to extensive fuel-cladding interaction and (b) the major and minor axis (length and/or orientation) vary slowly with axial position.

TABLE B-7.II

RADIAL DISPLACEMENTS AT 200 HOURS IN TEST 269-4[a] (10^{-3} mm)

Axial Position (mm)	Azimuthal Angle (degrees)							
	0	45	90	135	180	225	270	315
0.00	4	--	--	--	12	--	--	--
6.35	--	6	--	--	--	12	--	--
12.70	--	--	-48	--	--	--	12	--
19.05	--	--	--	-19	--	--	--	-29
25.40	31	--	-63	--	40	--	-58	--
31.75	--	3	--	--	--	31	--	--
38.10	--	--	-77	--	--	--	-60	--
44.45	--	--	--	-36	--	--	--	-38
50.80	31	--	--	--	32	--	--	--

[a] 14.48 MPa pressure differential and 0.127 mm pellet-cladding gap B-7.19 .

The second part of the analysis of Hobson's data is to convert the radial displacements at one axial position to an estimate of circumferential strain, assuming that the surface is an ellipse. This is accomplished as outlined in the six steps below.

(1) The circumference of the elliptical surface is related to the major and minor semi-axis lengths with the approximate expression

$$c \simeq 2\pi \sqrt{\frac{a^2 + b^2}{2}} \qquad \text{(B-7.6)}$$

where

c = circumference

a, b = semi-axis lengths.

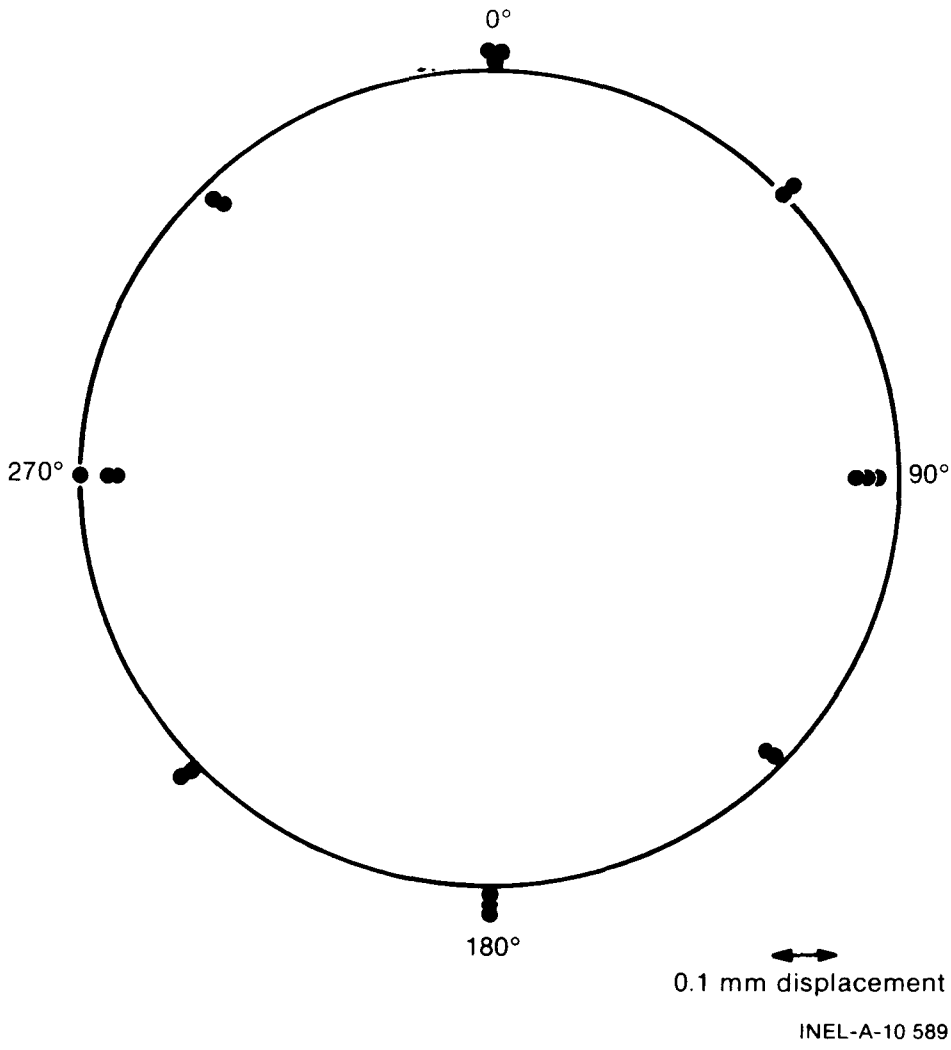

Fig. B-7.1 Radial displacement of cladding surface at 200 hours in Test 269-4.

Equation (B-7.6) is exact when a = b.

(2) The average[a] circumferential strain is defined as

$$\varepsilon_\theta = \oint_{\text{circumference}} \frac{dl}{l} \simeq \frac{c_{final} - c_{initial}}{c_{initial}} \qquad \text{(B-7.7)}$$

[a] Local strains will vary across the thickness and around the circumference of the cladding. For this preliminary analysis, these variations were neglected.

where

ϵ_θ = average circumferential strain

$c_{initial}$ = initial circumference

c_{final} = final circumference.

(3) Equations (B-7.6) and (B-7.7) are combined to obtain the expression

$$\epsilon_\theta \simeq \sqrt{\frac{a^2_{final} + b^2_{final}}{a^2_{initial} + b^2_{initial}}} - 1 \qquad \text{(B-7.8)}$$

(4) $a_{initial}$ and $b_{initial}$ are assumed equal to r_o and a_{final} and b_{final} are the initial values plus Δa and Δb.

(5) A Taylor series expansion to order $\frac{\Delta a}{r_o}$ and $\frac{\Delta b}{r_o}$ is used with Equation (B-7.8) and step (4) to find

$$\epsilon_\theta \simeq \frac{1}{2}\left(\frac{\Delta a + \Delta b}{r_o}\right) \qquad \text{(B-7.9)}$$

where

r_o = initial radius of the outside (circular) surface of the cladding (m)

$\Delta a, \Delta b$ = change of the major and minor semi-axis lengths (m).

(6) Measurements of the radial displacements at one axial position (25.4 mm) and azimuthal angles of 0^o, 90^o, 180^o, and 270^o are available from Hobson's data. If these four measurements happen to occur along the major and minor axis of the ellipse, Equation (B-7.9) is sufficient to convert the data to an expression for the average circumferential component of the strain. When the radial displacements at 25.4 mm are not measured along the major and minor axis of the ellipse, the derivation is more complex, but the result (to order $\frac{\Delta a}{r_o}$ and $\frac{\Delta b}{r_o}$ in the Taylor series expansion) is an equation of the same form as Equation (B-7.9) with Δa and Δb replaced by the average radial

displacements along any two axes at right angles to each other and at any angle to the major and minor axis of the ellipse. That is

$$\varepsilon_\theta \simeq \frac{1}{2}\left(\frac{\Delta a' + \Delta b'}{r_o}\right) \qquad \text{(B-7.10)}$$

where

$\Delta a', \Delta b'$ = change of the cladding radius measured along any mutually perpendicular axes at one axial position (m).

The third part of the analysis of Hobson's data is to describe the circumferential strains obtained from the data and Equation (B-7.10). Figure B-7.2 displays the calculated average circumferential strain from the two tests at 15.86 MPa differential pressure. During the first 600 hours, the strains are remarkably consistent. During the last 400 hours of the tests, the strain in Test 269-27 was noticeably larger than that of Test 269-8. Test 269-27 had a large simulated axial gap centered about the axial position of the four probes used to determine the strain. Test 269-8 had only a small axial gap. The differences in strains at long times is probably due to the effect of the different contact times with the simulated fuel.

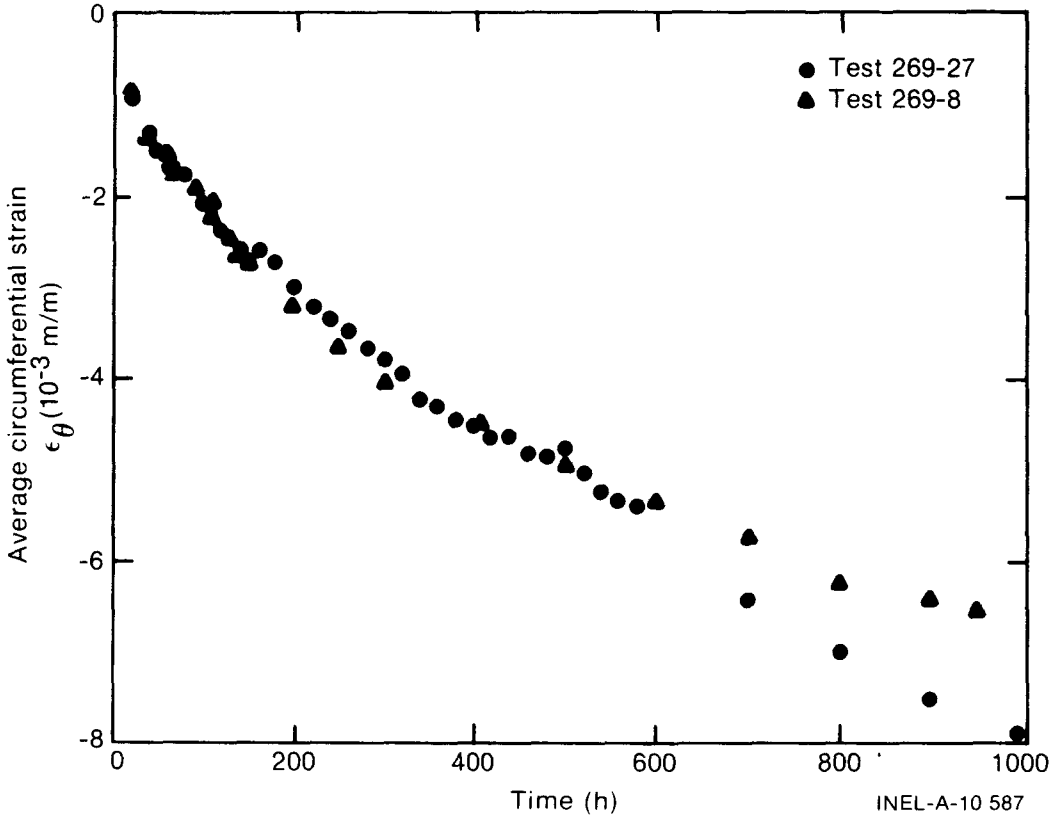

Fig. B-7.2 Average circumferential strain as a function of time at 15.86 MPa differential pressure.

Figure B-7.3 illustrates the strain versus time results obtained from the 14.48 MPa test. The strain at any time is significantly smaller than the strains obtained with the 15.86 MPa tests.

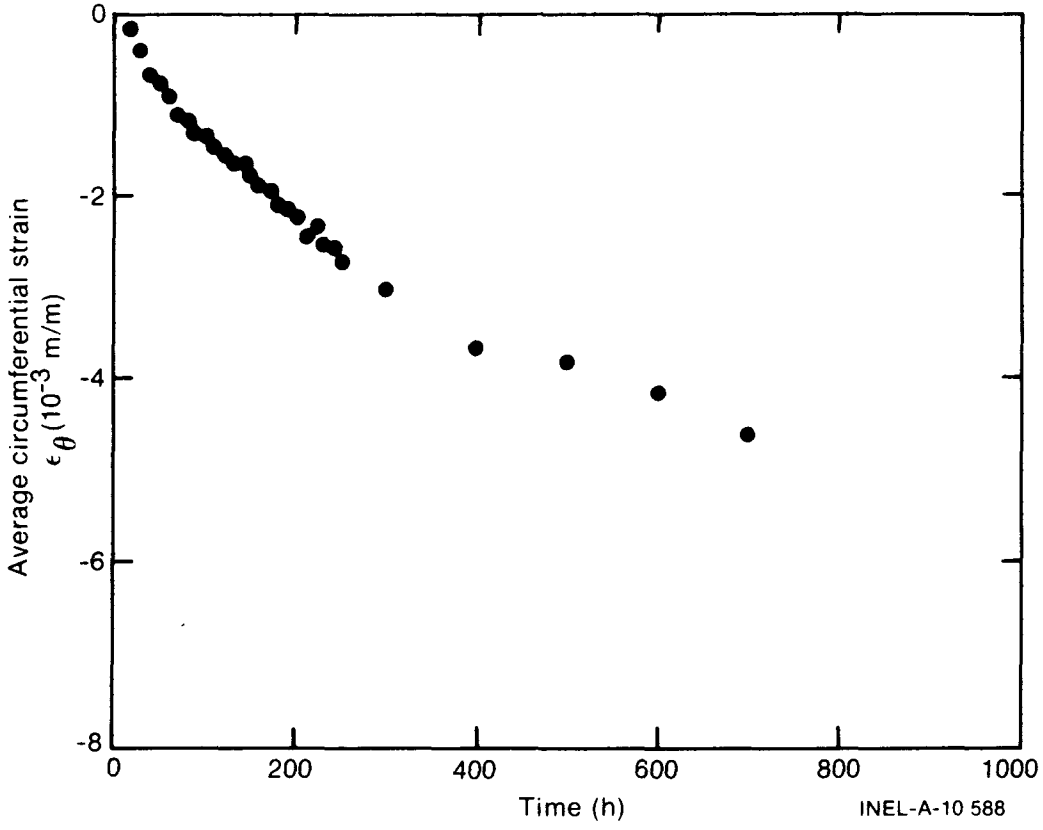

Fig. B-7.3 Average circumferential strain as a function of time at 14.48 MPa differential pressure.

In an effort to describe the strain versus time results shown in Figures B-7.2 and B-7.3, the constants in Equations (B-7.4a) and (B-7.4b) were fit to selected strain-time pairs. Each equation was then tested by extrapolating to longer or shorter times and comparing the predicted strains to strain-time pairs not used in determining the constants A and B. Neither equation passed this test. Equation (B-7.4a) consistently had too much curvature[a] and Equation (B-7.4b) consistently had too little curvature.

The equation finally adopted is

$$\epsilon_\theta = A\,[1 - \exp(-Bt)] \qquad \text{(B-7.11)}$$

---

[a] $\left(\frac{d^2\epsilon_\theta}{dt^2}\right)$ too large.

where

ϵ_θ = average circumferential strain (m/m)

t = time (s)

A, B = constants[a].

(1) For the 14.85 MPa test,
$A = -5.32 \times 10^{-3}$
$B = 7.64 \times 10^{-7}$/s.

(2) For the 15.86 MPa test,
$A = -6.32 \times 10^{-3}$
$B = 9.17 \times 10^{-7}$/s.

The constants A and B are determined with a complex two-step process:

(1) A value of B was guessed and one strain-time pair (ϵ_o, t_o) was selected as a reference. Other strain-time pairs (ϵ_j, t_j) were then used to find an improved guess for B according to the relation

$$B_j = \ln\left(1 - \frac{\epsilon_j \left[1 - \exp\left(-B_{guessed}\, t_o\right)\right]}{\epsilon_o}\right) \qquad \text{(B-7.12)}$$

(2) Once a single value of B which worked for several strain-time pairs was determined, a least-squares fit was carried out to determine A.

The two sets of values for A and B were used to estimate the effect of changes in stress. A and B were assumed to be dependent on stress to some power, n, and the value of n was calculated from the expressions

$$n_A = \frac{\ln\left(\frac{A \text{ at } 15.85 \text{ MPa}}{A \text{ at } 14.48 \text{ MPa}}\right)}{\ln\left(\frac{15.86}{14.48}\right)} = 1.89 \qquad \text{(B-7.13a)}$$

$$n_B = \frac{\ln\left(\frac{B \text{ at } 15.86 \text{ MPa}}{B \text{ at } 14.48 \text{ MPa}}\right)}{\ln\left(\frac{15.86}{14.48}\right)} = 2.01. \qquad \text{(B-7.13b)}$$

[a] The so-called constants are actually functions of stress and temperature.

In view of the limited number of tests, both values of n were assumed to be 2. This result implies a strain rate proportional to the fourth power of stress[a], a conclusion which agrees with one of the intermediate stress regions suggested by Dollins and Nichols and mentioned in Section B-7.2.

Since all of Hobson's data were taken at 644 K, no expression for the effect of temperature can be derived from these data. The activation energy proposed by Fidleris for tensile creep (Equation B-7.5) has thus been adopted. The expression proposed by Fidleris was for strain rate, a quantity proportional to A times B. Thus the square root of the traditional Arrhenius factor has been used for both A and B.

The resultant expressions for A and B of Equation (B-7.11) in terms of their values at 644 K and stress of 124.5 MPa (pressure differential = 14.48 MPa) are

$$A = (-5.32 \times 10^{-3}) \frac{\sigma^2}{(1.245 \times 10^8)^2} \left[\frac{\exp(-U/2T)}{\exp(-U/1288)}\right] \qquad \text{(B-7.14a)}$$

$$B = (7.64 \times 10^{-7}) \frac{\sigma^2}{(1.245 \times 10^8)^2} \left[\frac{\exp(-U/2T)}{\exp(-U/1288)}\right] \qquad \text{(B-7.14b)}$$

where

σ = circumferential stress (Pa)

T = temperature (K)

U = apparent activation energy given by Equation (B-7.5)/the gas constant.

The final step required to obtain the equation used for out-of-reactor creep [Equation (B-7.1) of Section B-7.1] from Equations (B-7.11), (B-7.14a), and (B-7.14b) is the elimination of time as an independent variable. The mathematical operations are trivial: Equation (B-7.11) is differentiated with respect to time and the resultant equation is used with Equation (B-7.11) to express the strain rate as a function of strain.

The physical implication of eliminating the explicit time dependence from Equation (B-7.11) is not as trivial as the mathematics. Equation (B-7.1) implies that strain rate is a function of strain, not time. Equations (B-7.1) and (B-7.11) are equivalent physically only if the effect of prior strain on strain rate is not in turn affected by time at temperature. A more proper treatment would include an explicit expression for the recovery of the effects of prior strain, similar to the model for the high temperature, short time transient recovery

[a] The time derivative of Equation (B-7.11) is proportional to A times B.

of cold work effects. In view of the extremely limited supply of applicable data, it has been concluded that the effort to include an explicit model for recovery effects would be premature.

7.3.2 In-Reactor Creepdown. It was mentioned in Section B-7.2 that the in-reactor creep rate becomes constant after long times. The difference between the creep strains from the two sets of rods studied by Bauer et al (see Section B-7.2.5) should therefore represent a constant creep rate.

$$\dot{\varepsilon}_{\text{steady state}} = \frac{\varepsilon_2 - \varepsilon_1}{t_2 - t_1} \qquad \text{(B-7.15)}$$

where

ϵ_2 = strain of the Robinson rods

ϵ_1 = strain of the Oconee rods

t_2 = equivalent full power time for the Robinson rods

t_1 = equivalent full power time for the Oconee rods.

Values for ϵ_2, ϵ_1, and t_2 are given in Section B-7.2.5 and an estimate of the equivalent full power time for the Oconee rods was obtained by multiplying the equivalent full power time of the Robinson rods by the ratio of the fast neutron fluences for the two sets of rods

$$t_1 = 799 \text{ days } \frac{2.3 \times 10^{25} \text{ fast neutrons/m}^2}{4.4 \times 10^{25} \text{ fast neutrons/m}^2} = 418 \text{ days} \qquad \text{(B-7.16)}$$

The steady state creep rate obtained from Equations (B-7.15) and (B-7.16) and the values of ϵ_2, ϵ_1, and t_2 given in Section B-7.2.5 is -7.6×10^{-11}/s.

It was concluded in Sections B-7.2.1 and B-7.2.2 that the best representation of the in-reactor creep rate is an equation of the form

$$\dot{\varepsilon}_{\text{steady state}} = (C/T^7)\ \phi^{0.65}\ \exp\ (-D/T)\ \sigma^p \qquad \text{(B-7.17)}$$

where

σ = circumferential stress (Pa)

C, D, p = constants.

Since the value of $\dot{\epsilon}_{steady\ state}$ just obtained will serve to evaluate only one of the three constants, some source other than the published creepdown data had to be used to estimate two of the constants C, D, and p.

An estimate for the value of p is obtained by applying the theoretical results of Dollins and Nichols (see Section B-7.2). These results are used by noting that in-reactor differential pressures typically begin at about 11 MPa and decrease due to the buildup of fission products[B-7.19, B-7.20]. Since the initial pressure differential corresponds to a hoop stress of about 105 MPa, the fuel rods should be operating in the region where the preferred alignment of irradiation-induced dislocation loops is important. In this region Dollins and Nichols expect the creep rate to be proportional to the first power of stress.

The constant D is taken from the activation energy of 4.18×10^4 J/mol ($D = 4.18 \times 10^4$ J/mol times the gas constant) suggested by Fidleris (see Section B-7.2).

After estimates for the constants p and D are obtained, a value for C is obtained by using (a) the estimated values of p and D, (b) the steady state creep rate of -7.6×10^{-11}/s from Equations (B-7.15) and (B-7.16), (c) typical in-reactor values of temperature (620 K) and stress (104 MPa), and (d) the reported fast neutron flux in the Robinson reactor (6.3×10^{17} fast neutrons/m^2) in Equation (B-7.17). The resultant equation is Equation (B-7.2) of the summary.

At this time, there are no published measurements of cladding circumferential strain as a function of time with nonzero flux and compressive stress. There is therefore no experimental basis for an expression for short time (non-steady state) in-reactor creep strains. The most convenient of several equally arbitrary assumptions which could be made to provide the required expression, namely that the total in-reactor creep is the sum of the separately integrated out-of-reactor and steady state in-reactor creep rates, was therefore used. The resultant expression is Equation (B-7.3) of the summary.

7.4 Uncertainty of the Model

The lack of an extensive data base makes the assignment of uncertainty limits very tentative. For the Robinson rods, the model predicts a net creep strain of -9.1×10^{-3} versus a measured strain of about -9.5×10^{-3}. Similarly, the model predicted and measured strains of the Oconee rods are -6.8×10^{-3} and -7×10^{-3}. However, the irradiation contribution to the creep rate is determined with data from the Robinson and Oconee rods so the "errors" of 0.04 and 0.03 are probably unrealistically small[a].

---

[a] The primary component of the strain was *not* determined with the Robinson/Oconee rods. The assumption that in-reactor creep strain is the sum of the out-of-reactor strain and an independent, irradiation induced steady state component is indirectly supported by these small errors.

A more realistic estimate of the model's uncertainty is probably obtained by comparing model predictions to the "intermediate burnup" group of rods from the Saxton reactor[B-7.20]. The minimum average rod diameter for these rods, 0.9947 cm, corresponds to a strain of about -3 x 10^{-3}. The strain predicted by the creepdown model developed in Section B-7.3 ($\sigma \sim 10^8$ Pa, T = 640 K, $\phi = 10^{18}$ neutrons > 1.0 MeV/m^2 and time = 9360 h) is -6.9 x 10^{-3}. Although there is good reason to suspect that most of the difference between the model prediction and the Saxton data is due to pellet-cladding interaction, there are no other independent in-reactor creepdown data to assess the uncertainty of the model. For that reason, an expected error of + 50% is suggested until the model can be tested with applicable data.

7.5 Cladding Creep Subcode (CCRPR) Listing

A listing of the FORTRAN subcode CCRPR is given in Table B-7.III. The expected standard error is computed within the subcode, but is not returned. In a future simultaneous revision of the subcode and the codes which use it, the uncertainty will be stored in a common block.

7.6 References

B-7.1. C. C. Dollins and F. A. Nichols, "Mechanisms of Irradiation Creep in Zirconium-Base Alloys," *Zirconium in Nuclear Applications,* ASTM-STP-551, (1974) pp 229-248.

B-7.2. D. O. Northwood, "Comments on 'In-Pile Dimensional Changes in Neutron Irradiated Zirconium Base Alloys'," *Journal of Nuclear Materials, 64* (1977) pp 316-319.

B-7.3. P. A. Ross-Ross and V. Fidleris, "Design Basis for Creep of Zirconium Alloy Components in a Fast Neutron Flux," *International Conference on Creep and Fatigue in Elevated Temperature Applications, Philadelphia and Sheffield,* United Kingdom (1973) pp 216.1-216.7.

B-7.4. P. H. Kreyns and M. W. Burkart, "Radiation-Enhanced Relaxation in Zircaloy-4 and Zr/2.5 wt% Nb/0.5 wt% Cu Alloys," *Journal of Nuclear Materials, 26* (1968) pp 87-104.

B-7.5. P. A. Ross-Ross and Hunt, "The In-Reactor Creep of Cold-Worked Zircaloy-2 and Zirconium-2.5 wt% Niobium Pressure Tubes," *Journal of Nuclear Materials, 26* (1968) pp 2-17.

B-7.6. V. Fidleris, "Summary of Experimental Results on In-Reactor Creep and Irradiation Growth of Zirconium Alloys," *Atomic Energy Review, 13* (1975) pp 51-80.

TABLE B-7.III

LISTING OF THE CCRPR SUBCODE

```
C
C
      SUBROUTINE CCRPR(CTEMP,CHSTRS,CFLUX,DELT,STRNPH,STRNIH,
     #                 STRANH,RSTRNH)
C
CCCCC CCRPR CALCULATES THE PRIMARY AND IRRADIATION-CAUSED
CCCCC CIRCUMFERENTIAL COMPONENTS OF CLADDING CREEP STRAIN
CCCCC AS A FUNCTION OF CLADDING TEMPERATURE,THE CIRCUMFERENTIAL
CCCCC COMPONENT OF CLADDING STRESS, FAST NEUTRON FLUX,
CCCCC TIME STEP SIZE, AND THE PRIMARY CIRCUMFERENTIAL
CCCCC COMPONENT OF CLADDING STRAIN AT THE START OF A TIME
CCCCC STEP.  THE STRAIN RATE AT THE START OF THE TIME STEP
CCCCC IS ALSO CALCULATED.
CCCCC
CCCCC STRANH = OUTPUT TOTAL CIRCUMFERENTIAL COMPONENT OF CLADDING
CCCCC            CREEP STRAIN AT THE END OF A TIME STEP
CCCCC            (UNITLESS RATIO)
CCCCC STRNPH = OUTPUT PRIMARY PART OF CIRCUMFERENTIAL COMPONENT OF
CCCCC            CLADDING CREEP STRAIN AT THE END OF A TIME STEP
CCCCC            (UNITLESS RATIO)
CCCCC STRNIH = OUTPUT IRRADIATION-CAUSED PART OF CURCUMFERENTIAL
CCCCC            COMPONENT OF CLADDING CREEP STRAIN AT THE END
CCCCC            OF A TIME STEP (UNITLESS RATIO)
CCCCC RSTRNH = OUTPUT CIRCUMFERENTIAL COMPONENT OF CLADDING
CCCCC            CREEP STRAIN RATE AT THE INPUT PRIMARY
CCCCC            CIRCUMFERENTIAL CREEP STRAIN (S**(-1))
CCCCC UTRANH = OUTPUT EXPECTED STANDARD ERROR OF STRANH
CCCCC            (NOT CURRENTLY RETURNED)
CCCCC
CCCCC CTEMP  = INPUT CLADDING TEMPERATURE (K)
CCCCC CHSTRS = INPUT CIRCUMFERENTIAL COMPONENT OF CLADDING
CCCCC            STRESS (PA)
CCCCC CFLUX  = INPUT FAST NEUTRON FLUX (NEUTRONS/((M**2)*S))
CCCCC DELT   = INPUT TIME STEP SIZE (S)
CCCCC STRNPH = INPUT PRIMARY PART OF CIRCUMFERENTIAL
CCCCC            COMPONENT OF CLADDING CREEP STRAIN AT THE
CCCCC            START OF A TIME STEP (UNITLESS RATIO)
CCCCC STRANH = INPUT CIRCUMFERENTIAL COMPONENT OF CLADDING
CCCCC            CREEP STRAIN AT THE START OF A TIME STEP
CCCCC            (UNITLESS RATIO)
CCCCC
CCCCC THE EQUATIONS USED IN THIS SUBROUTINE ARE BASED ON DATA FROM
CCCCC (1) D. O. HOBSON, CREEPDOWN OF ZIRCALOY FUEL CLADDING
CCCCC     INITIAL TESTS, ORNL/NUREG/TM-181 (APRIL 1978)
CCCCC (2) A. A. BAUER, L. M. LOWRY AND J. S. PERRIN, PROGRESS ON
CCCCC     EVALUATING STRENGTH AND DUCTILITY OF IRRADIATED ZIRCALOY
CCCCC     DURING JULY THROUGH SEPTEMBER 1975, BMI-1938 (SEPTEMBER
CCCCC     1975)
CCCCC (3) A. A. BAUER, L. M. LOWRY AND J. S. PERRIN, EVALUATING
CCCCC     STRENGTH AND DUCTILITY OF IRRADIATED ZIRCALOY, QUARTERLY
CCCCC     PROGRESS REPORT JANUARY THROUGH MARCH 1977, BMI-NUREG-1971
CCCCC     (APRIL 1977)
CCCCC
CCCCC CCRPR WAS CODED BY C. E. DIXON JUNE 1975
CCCCC MODIFIED BY G. A. REYMANN NOV 1976
CCCCC MODIFIED BY D. L. HAGRMAN JUNE 1978
C
      T = CTEMP
      IF(CTEMP .LT. 500.) T = 500.
      IF(CTEMP .GT. 700.) T = 700.
      AQ = 2.1427E+02 + T*(-5.324E-01 + T*(1.17889E-04 + T*3.3486E-07))
      A = (3.47E-19)*(EXP(-AQ/CTEMP)) *  (CHSTRS**3.)/ABS(CHSTRS)
      B = (5.00E-23)*(EXP(-AQ/CTEMP)) * (CHSTRS**2.)
      C = (2.20E-07)*(EXP(-5000./CTEMP))*CHSTRS/(CTEMP**7.)
      RSTNPH = B * (A - STRNPH)
      RSTNIH = 0.0
      IF(CFLUX .GT. 1.0E+00) RSTNIH = C * (CFLUX**0.65)
      STRNIH = RSTNIH * DELT + STRANH - STRNPH
      STRNPH = (A - STRNPH)*(1. - EXP(-B * DELT)) + STRNPH
      STRANH = STRNPH + STRNIH
      RSTRNH = RSTNPH + RSTNIH
C
      RETURN
      END
```

B-7.7. G. A. Reymann (ed.), *MATPRO – Version 10, A Handbook of Materials Properties for Use in the Analysis of Light Water Reactor Fuel Rod Behavior,* TREE-NUREG-1180 (February 1978).

B-7.8. O. D. Sherby and A. K. Miller, *Development of the Materials Code, MATMOD (Constitutive Equations for Zircaloy),* NP-567 (December 1977).

B-7.9. W. J. Duffin and F. A. Nichols, "The Effect of Irradiation on Diffusion-Controlled Creep Processes," *Journal of Nuclear Materials, 45* (1972/1973) pp 302-316.

B-7.10. G. R. Piercy, "Mechanisms for the In-Reactor Creep of Zirconium Alloys," *Journal of Nuclear Materials, 26* (1968) pp 18-50.

B-7.11. D. S. Wood, "Dose Dependence of Irradiation Creep of Zircaloy-2," *Properties of Reactor Structural Alloys After Neutron or Particle Irradiation,* ASTM-STP-570, (1975) pp 207-217.

B-7.12. D. S. Wood and B. Watkins, "A Creep Limit Approach to the Design of Zircaloy-2 Reactor Pressure Tubes at 275°C," *Journal of Nuclear Materials, 41* (1971) pp 327-340.

B-7.13. E. Kohn, "In-Reactor Creep of Zr-2.5Nb Fuel Cladding," *Zirconium in the Nuclear Industry,* ASTM-STP-633 (1977) pp 402-417.

B-7.14. E. R. Gilbert, "In-Reactor Creep of Reactor Materials," *Reactor Technology, 14* (Fall 1971) pp 258-285.

B-7.15. H. Stehle et al, "Mechanical Properties, Anisotropy and Microstructure of Zircaloy Canning Tubes," *Zirconium in the Nuclear Industry,* ASTM-STP-663, American Society for Testing and Materials (December 1977) pp 486-507.

B-7.16. M. L. Picklesimer, "Deformation, Creep, and Fracture in Alpha-Zirconium Alloys," *Electrochemical Technology, 4* (1966) pp 289-300.

B-7.17. D. O. Hobson and C. V. Dodd, *Interim Report on the Creepdown of Zircaloy Fuel Cladding,* ORNL/NUREG/TM-103 (May 1977).

B-7.18. D. O. Hobson, *Quarterly Progress Report on the Creepdown and Collapse of Zircaloy Fuel Cladding for July 1976 – March 1977,* ORNL/NUREG/TM-125 (July 1977).

B-7.19. D. O. Hobson, *Creepdown of Zircaloy Fuel Cladding – Initial Tests,* ORNL/NUREG/TM-181 (April 1978).

B-7.20. W. R. Smalley, *Saxton Core II Fuel Performance Evaluation Part I: Materials,* WCAP-3385-56 (September 1971).

B-7-21. W. R. Smalley, *Evaluation of Saxton Core III Fuel Materials Performance,* WCAP-3385-57 (July 1974).

B-7.22. A. A. Bauer et al, *Progress on Evaluating Strength and Ductility of Irradiated Zircaloy During April through June 1975,* BMI-1935 (June 1975).

B-7.23. A. A. Bauer et al, *Evaluating Strength and Ductility of Irradiated Zircaloy, Quarterly Progress Report October through December 1976,* BMI-NUREG-1967 (January 1977).

B-7.24. A. A. Bauer et al, *Evaluating Strength and Ductility of Irradiated Zircaloy, Quarterly Progress Report for October through December 1975,* BMI-1942 (December 1975).

B-7.25. A. A. Bauer et al, *Progress on Evaluating Strength and Ductility of Irradiated Zircaloy During July through September 1975,* BMI-1938 (September 1975).

B-7.26. A. A. Bauer et al, *Evaluating Strength and Ductility of Irradiated Zircaloy, Quarterly Progress Report January through March 1977,* BMI-NUREG-1971 (April 1977).

B-7.27. D. G. Franklin and H. D. Fisher, "Requirements for In-Reactor Zircaloy Creep Measurements for Application in the Design of PWR Fuel," *Journal of Nuclear Materials, 65* (1977) pp 192-199.

B-7.28. D. G. Franklin and W. A. Franz, "Numerical Model for the Anisotropic Creep of Zircaloy," *Zirconium in the Nuclear Industry,* ASTM-STP-633 (1977) pp 365-384.

B-7.29. H. Stehle et al, "Uranium Dioxide Properties for LWR Fuel Rods," *Nuclear Engineering and Design, 33* (1975) pp 230-260.

7.7 Bibliography

The following list of reference material is pertinent to a literature review and was consulted by the CCRPR code developer.

(1) G. Dressler et al, "Determination of Complete Plane Stress Yield of Zircaloy Tubing," *Zirconium in Nuclear Applications* ASTM-STP-551 (1974) pp 72-103.

(2) V. Fidleris, "Uniaxial In-Reactor Creep of Zirconium Alloys," *Journal of Nuclear Materials, 26* (1968) pp 51-76.

(3) P. J. Pankaskie, *Irradiation Effects on the Mechanical Properties of Zirconium and Dilute Zirconium Alloys – A Review,* BN-SA-618 (July 1976, updated November 1976).

(4) C. E. Coleman, "Tertiary Creep in Cold-Worked Zircaloy-2," *Journal of Nuclear Materials, 42* (1971) pp 180-190.

(5) C. C. Busby and L. S. White, *Some High Temperature Mechanical Properties of Internally Pressurized Zircaloy-4 Tubing,* WAPD-TM-1243 (February 1976).

(6) M. Gartner and H. Stehle, *In-Pile Creep Behavior of Zircaloy-4 Cladding Tubes at 400°C,* Siemens Aktiengesellschaft Reaktortechnik (September 1972).

(7) M. Bernstein, "Diffusion Creep in Zirconium and Certain Zirconium Alloys," *Transactions of the Metallurgical Society of AIME, 329* (1969) pp 1518-1522.

(8) F. A. Nichols, "On the Mechanisms of Irradiation Creep in Zirconium-Base Alloys," *Journal of Nuclear Materials, 37* (1970) pp 59-70.

(9) V. Fidleris, "Uniaxial In-Reactor Creep of Zirconium Alloys," *Journal of Nuclear Materials, 26* (1967) pp 51-76.

(10) F. L. Yagee and A. Purohit, "Biaxial Creep Characteristics of GCFR Cladding at 650° and 32.4-ksi Hoop Stress," *Transactions of the American Nuclear Society, 22* (November 1975) p 182.

(11) E. F. Ibrahim and C. E. Coleman, "Effect of Stress Sensitivity on Stress-Rupture Ductility of Zircaloy-2 and Zr-2.5 wt% Nb," *Canadian Metallurgical Quarterly, 12,* 3 (1973) pp 285-287.

(12) V. Fidleris, "The Effect of Texture and Strain Aging on Creep of Zircaloy-2," *Applications Related Phenomena for Zirconium and Its Alloys,* ASTM-STP-458 (1969) pp 1-17.

(13) F. J. Azzarto et al, "Unirradiated, In-Pile and Post-Irradiation Low Strain Rate Tensile Properties of Zircaloy-4," *Journal of Nuclear Materials, 30* (1969) pp 208-218.

(14) W. R. Smalley, *Saxton Plutonium Program: Semi Annual Progress Report for the Period Ending June 30, 1969,* WCAP-3385-20 (October 1969).

(15) T. E. Caye and W. R. Smalley, *Saxton Plutonium-Project, Quarterly Progress Report for the Period Ending December 31, 1970,* WCAP-3385-26 (March 1970).

(16) E. F. Ibrahim, "In-Reactor Tubular Creep of Zircaloy-2 at 260°C and 300°C," *Journal of Nuclear Materials, 46* (1973) pp 196-182.

(17) H. Conrad, "Experimental Evaluation of Creep and Stress-Rupture," *Mechanical Behavior of Materials at Elevated Temperatures,* New York: McGraw-Hill Book Company, Inc., (1961) p 149.

(18) F. A. Nichols, "Theory of the Creep of Zircaloy During Neutron Irradiation," *Journal of Nuclear Materials, 30* (1969) pp 249-270.

(19) V. Fidleris and C. D. Williams, "Influence of Neutron Irradiation of Zircaloy-2 at 300°C," *Journal of Electrochemical Technology, 4* (May – June 1966) pp 258-267.

(20) E. F. Ibrahim, "In-Reactor Creep of Zirconium – 2.5 Nb Tubes at 570 K," *Zirconium in Nuclear Applications,* ASTM-STP-551 (1974) pp 249-262.

(21) C. E. Ells and V. Fidleris, "Effect of Neutron Irradiation on Tensile Properties of the Zirconium – 2.5 Weight Percent Niobium Alloy," *Journal of Electrochemical Technology, 4* (May – June 1966) pp 268-274.

(22) E. R. Gilbert, "In-Reactor Creep of Zr-2.5 wt% Nb," *Journal of Nuclear Materials, 26* (1968) pp 105-111.

(23) W. J. Langford and L. E. J. Mooder, "Metallurgical Properties of Irradiated Cold-Worked of Zr-2.5 wt% Nb Pressure Tubes," *Journal of Nuclear Materials, 30* (1969) pp 292-302.

(24) E. F. Ibrahim, "In-Reactor Creep of Zirconium-Alloy Tubes and Its Correlation with Uniaxial Data," *Applications-Related Phenomena for Zircaloy and Its Alloys,* ASTM-STP-458 (1969) pp 18-36.

(25) T. M. Frenkel and M. Weisz, "Effect of the Annealing Temperature on the Creep Strength of Cold-Worked Zircaloy-4 Cladding," *Zirconium in Nuclear Applications,* ASTM-STP-551 (1974) pp 140-144.

(26) K. Källström et al, "Creep Strength of Zircaloy Tubing at 400°C as Dependent on Metallurgical Structure and Texture," *Zirconium in Nuclear Applications,* ASTM-STP-551 (1974) pp 160-168.

(27) C. R. Woods (ed.), *Properties of Zircaloy-4 Tubing,* WAPD-TM-585 (December 1966).

8. CLADDING STRESS VERSUS STRAIN (CSTRES, CSIGMA, CANEAL)

(D. L. Hagrman and G. A. Reymann)

This section is a description of materials properties subcodes for relating stress to strain. The subroutine CSTRES calculates cladding true and engineering stress as a function of true strain, strain rate, temperature, cold work, fast neutron fluence, and average oxygen concentration in the cladding. A second subcode, CSIGMA, is provided to return only the power law expression for true stress. The third subcode, CANEAL, is provided to describe annealing of cold work and irradiation effects. Preliminary estimates of coefficients of anisotropy, defined to treat the uniaxial stress-strain law of CSTRES and CSIGMA as an effective stress-strain relation, are also returned.

8.1 Summary

This section is intended as an introduction to the common features of all the plastic deformation subcodes in MATPRO as well as the particular features of CSTRES and CSIGMA. All input strain or stress values are assumed by MATPRO mechanical property routines to be true strain[a] or true stress[b]. With the exception of the function CSIGMA, MATPRO output is both true and engineering stress or strain. In CSTRES, true stress is converted to engineering stress by using the constant volume approximation for uniaxial loading.

$$\text{engineering stress}^{[c]} = \frac{\text{true stress}}{1 + \text{engineering strain}} = \frac{\text{true stress}}{\exp(\text{true strain})} \tag{B-8.1}$$

Two different equations are used in MATPRO to relate true stress to true strain. In the elastic region, Hooke's law is used:

$$\sigma = E\,\varepsilon \tag{B-8.2}$$

where

σ = true stress

ϵ = the true strain

E = the modulus of elasticity (calculated by CELMOD as a function of temperature).

In the plastic region the relation

$$\sigma = K\,\varepsilon^{n}\left[\frac{\dot{\varepsilon}}{10^{-3}/s}\right]^{m} \tag{B-8.3}$$

---

[a] True strain equals the change in length divided by length at the instant of change integrated from the original to the final length.

[b] True stress equals force per unit cross-sectional area determined at the instant of measurement of the force.

[c] Engineering stress equals force per unit cross-sectional area with area determined at zero strain.

where

σ = the true stress

K = the strength coefficient

n = the strain hardening exponent

$\dot{\epsilon}$ = the true strain rate[a]

m = the strain rate sensitivity constant.

The transition from the elastic to the plastic region is defined to be the nonzero intersection of the curves predicted by Equations (B-8.2) and (B-8.3).

Effects of cladding temperature, cold work, irradiation, in-reactor annealing, and oxidation on mechanical properties are expressed as changes in the strength coefficient, K; the strain hardening exponent, n; and the strain rate sensitivity constant, m; of Equation (B-8.3). For fully annealed material, the temperature and strain rate dependent values of n, K, and m are as follows.

Values of n:

for $T < 850$ kelvins

$$n = -1.86 \times 10^{-2} + T[7.110 \times 10^{-4} - T\,(7.721 \times 10^{-7})]. \quad \text{(B-8.4a)}$$

for $T \geqslant 850$ kelvins

$$n = 0.027908. \quad \text{(B-8.4b)}$$

Values of K:

for $T \leqslant 730$ kelvins

$$K = 1.0884 \times 10^{9} - T[1.0571 \times 10^{6}] \quad \text{(B-8.5a)}$$

for $730 < T < 900$ kelvins

$$K = A_1 + T[A_2 + T(A_3 + T\,A_4)] \quad \text{(B-8.5b)}$$

---

[a] For an input value of $\dot{\epsilon}$ less than 10^{-5}/s, the input value $\dot{\epsilon}$ is replaced by 10^{-5}/s.

where[a]

$A_1 = -8.152540534 \times 10^9$

$A_2 = 3.368940331 \times 10^7$

$A_3 = -4.317334084 \times 10^4$

$A_4 = 1.769348499 \times 10^1$

for $T \geqslant 900$ kelvins

$$K = \exp\left(8.755 + \frac{8663}{T}\right) \qquad \text{(B-8.5c)}$$

Values of m (for all ϵ):

for $T \leqslant 730$ kelvins

$$m = 0.02 \qquad \text{(B-8.6a)}$$

for $730 < T < 900$ kelvins

$$m = A_5 + T[A_6 + T(A_7 + TA_8)] \qquad \text{(B-8.6b)}$$

where

$A_5 = 2.063172161 \times 10^1$

$A_6 = -7.704552983 \times 10^{-2}$

$A_7 = 9.504843067 \times 10^{-5}$

$A_8 = -3.860960716 \times 10^{-8}$

for $900 \leqslant T \leqslant 1090$ kelvins

$$m = -6.47 \times 10^{-2} + T(2.203 \times 10^{-4}) \qquad \text{(B-8.6c)}$$

---

[a] The constants A_1 to A_8 have been determined to ten significant figures in order to avoid discontinuities at 730 and 900 K.

for $1090 < T \leq 1172.5$ kelvins

$$m = -6.47 \times 10^{-2} + T(2.203 \times 10^{-4}) + \begin{cases} 0 \text{ if } \dot{\varepsilon} \geq 6.34 \times 10^{-3}/s \text{ or} \\ (6.78 \times 10^{-2}) \ln (6.34 \times 10^{-3}/\dot{\varepsilon}) \left[(T - 1090)/82.5\right] \\ \text{if } \dot{\varepsilon} < 6.34 \times 10^{-3}/s \end{cases} \quad \text{(B-8.6d)}$$

for $1172.5 < T \leq 1255$ kelvins

$$m = -6.47 \times 10^{-2} + 2.203 \times 10^{-4}\, T + \begin{cases} 0 \text{ if } \dot{\varepsilon} \geq 6.34 \times 10^{-3}/\text{sec, or} \\ 6.78 \times 10^{-2} \ln (6.34 \times 10^{-3}/\varepsilon)\left[(1255 - T)/82.5\right] \\ \text{if } \dot{\varepsilon} < 6.34 \times 10^{-3}/\text{sec} \end{cases} \quad \text{(B-8.6e)}$$

for $T \geq 1255$ kelvins

$$m = -6.47 \times 10^{-2} + 2.203 \times 10^{-4}\, T \quad \text{(B-8.6f)}$$

where

T = temperature (kelvins)

$\dot{\epsilon}$ = true strain rate (s^{-1}).

The coefficients of anisotropy [defined to use the uniaxial stress-strain law, Equation (B-8.3), as an effective stress-strain relation for anisotropic material] are

$$A1 = \frac{R}{R+1} \quad \text{(B-8.7a)}$$

$$A2 = -\frac{R-5.4}{4.4\,(R+1)} \quad \text{(B-8.7b)}$$

$$A3 = \frac{1}{R+1} \quad \text{(B-8.7c)}$$

where

R = the ratio of circumferential to radial strain during a uniaxial tensile test.

Expressions for the yield stress and effective strain in terms of these constants are reviewed in Section B-8.3. If input values of R are not available the following estimates are provided:

for $T > 1203.233$ kelvins

$$R = 1 \tag{B-8.8a}$$

for $T < 1203.233$ kelvins and $\epsilon < 0.15$

$$R = 2.65 + T\left[1.36 \times 10^{-3} - T(2.27 \times 10^{-6})\right] \tag{B-8.8b}$$

for $T < 1203.233$ kelvins and $0.15 < \epsilon < 0.30$

$$R = 1 - \frac{0.3}{0.0225}\left[1 - R_o\right]\varepsilon_{eff} + \frac{1}{0.0225}\left[1-R_o\right](\dot{\varepsilon}_{eff})^2 \tag{B-8.8c}$$

for effective strains greater than 0.30

$$R = 1 \tag{B-8.8d}$$

where

ϵ_{eff} = effective strain

R_o = the value of R given by Equation (B-8.8b).

The change in the strain hardening exponent due to irradiation and cold working of cladding is described by multiplying the value of n given in Equations (B-8.4a) and (B-8.4b) by

$$RIC = \left[0.847 \exp(-39.2\ CWN) + 0.153 + CWN\left(-9.16 \times 10^{-2} + 0.229\ CWN\right)\right] \exp\left[\frac{-(\phi)^{1/3}}{3.73 \times 10^{7} + (2 \times 10^{8}\ CWN)}\right] \tag{B-8.9}$$

where

RIC = strain hardening exponent for irradiated and cold-worked material divided by the expression in Equations (B-8.4a) and (B-8.4b)

CWN = effective cold work for strain hardening exponent (unitless ratio of areas)

ϕ = effective fast neutron fluence (neutrons > 1.0 MeV/m^2).

The change in the strength coefficient due to irradiation and cold working of the cladding is modeled with the expression

$$DK = (0.546\ COLDW)\ K + (5.54 \times 10^{-18})\Phi \qquad \text{(B-8.10)}$$

where

DK = strength coefficient for irradiated and cold-worked material minus the expression in Equation (B-8.5) (Pa)

CWK = effective cold work for strength coefficient (unitless ratio of areas)

and the other terms have been previously defined.

The strain rate sensitivity exponent does not change as a function of irradiation or cold work.

Preliminary correlations for the changes in the strain hardening exponent, strength coefficient and strain rate sensitivity exponent due to oxidation of the cladding are, respectively,

$$RNO = 1 + \left[1250 - \frac{1250}{\exp\left[\frac{T-1380}{20}\right] + 1}\right] Y \qquad \text{(B-8.11)}$$

$$RKO = 1 + \left[1120 - \frac{990}{\exp\left[\frac{T-1300}{61}\right] + 1}\right] Y \qquad \text{(B-8.12)}$$

and

$$RMO = \exp(-69Y) \qquad \text{(B-8.13)}$$

where

RNO = strain hardening exponent for oxidized cladding divided by strain hardening exponent for zircaloy cladding with as-received oxygen concentration

RKO = strength coefficient for oxidized cladding divided by strength coefficient for zircaloy cladding with as-received oxygen concentration

RMO = strain rate sensitivity exponent for oxidized cladding divided by strain rate sensitivity exponent for zircaloy with as-received oxygen concentration

T = temperature (kelvins)

Y = average oxygen concentration increase (kg oxygen/kg zircaloy).

The development of the expressions for m, K, and n as functions of temperature is discussed in the following section. Section B-8.3 is a description of the development of coefficients describing cladding anisotropy. Sections B-8.4 and B-8.5 present the models for irradiation and cold work effects and for annealing of these effects. The effect of absorbed oxygen on cladding plastic deformation is discussed in Section B-8.6. A few examples of the output of CSTRES are presented in Section B-8.7; however, comparisons of model predictions and experimental data are made in the description of the CSTRAN subcode, which predicts cladding strain as a function of applied stress.

8.2 Temperature Dependence of m, K, and n

The strain rate sensitivity constant, m, of zircaloy-2 and zircaloy-4 is evaluated with data obtained from References B-8.1 through B-8.5. Most of the values of m plotted in Figure B-8.1, at temperatures higher than 900 kelvins, were given in Reference B-8.2 as a function of engineering strain for strain rate changes centered around 10^{-3}/s. No significant dependence on strain was indicated, so m is modeled without strain dependence. Outside the alpha + beta transition phase region (taken as 1090 to 1255 kelvins) significant dependence of m on strain rate again was not observed. Within the alpha + beta transition region and at strain rates below 6.34×10^{-3}, m was a strong function of the strain rate.

In the MATPRO plastic deformation models, values of m from data taken at temperatures below 730 kelvins are approximated with a constant, m = 0.02 while data for temperatures above 900 kelvins and outside the alpha + beta transition phase region are modeled as a linear function of temperature. The value of m in the region from 730 to 900 kelvins is modeled by a third degree polynomial in temperature with the constants determined so that the values and slopes of the polynomial match the values and slopes of the other expressions for m at the boundaries of the 730 to 900 kelvins region. The values of m predicted by Equations (B-8.6a) to (B-8.6f) are illustrated in Figure B-8.1 along with the data. The two points at 561 kelvins are particularly interesting because they are estimates based on high strain rate (4/s) tests with irradiated material. They do not appear to be significantly different from the values of m obtained at lower strain rates with unirradiated material. A distinction between data from zircaloy-2 and zircaloy-4 became evident at the two higher test temperatures. The lower group of points at 1573 and 1673 kelvins are from zircaloy-2.

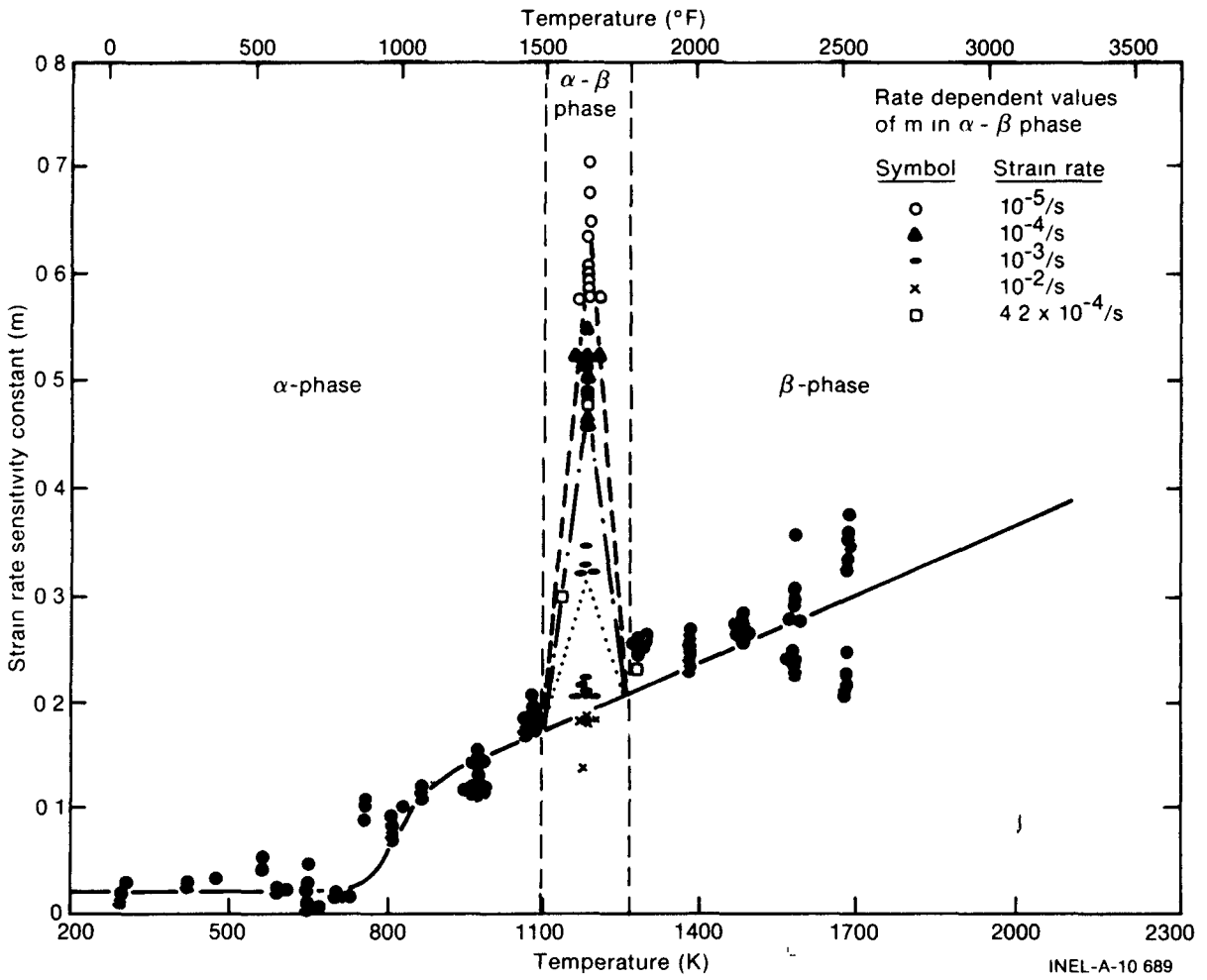

Fig. B-8.1 Strain rate sensitivity constant and data base used by MATPRO mechanical properties routines.

Most of the values of m in the alpha + beta transition phase region were also obtained from data presented in Reference B-8.2. The strain rate dependent values measured at 1173 kelvins were assumed to reflect an additive increase in m due to the mixed phases. When the increase is plotted against the logarithm of the strain rate, the effect of varying strain rates on m can be closely approximated by

$$\Delta m = 0.1253 + 0.1562 \log_{10} \left(\frac{10^{-3}/s}{\text{STRAIN RATE}} \right) \qquad \text{(B-8.14)}$$

which was obtained by a least-squares fit to the data. The fit is illustrated in Figure B-8.2. For strain rates outside the range 10^{-5} to 6.34×10^{-3}/s the change in m is taken to be equal to its value at the nearest point of this range.

In the present model, it is assumed that m increases linearly from its value at the edges of the alpha + beta transition phase region to a maximum at 1173 K in the center of the region as shown in Figure B-8.1. Further data on m as a function of temperature and strain rate in the α-β transition region will be required if this approximation is to be refined.

Values of K and n as a function of temperature from room temperature to 775 kelvins are based on data from tensile tests on zircaloy-4 tubes[B-8.1 – B-8.6]. The effects of varying amounts of cold work and stress relief in the tubing tested were removed prior to determining the temperature dependence of K by using models described in Section B-8.4. Similarly the effects of different strain rates were removed with the model discussed in previous paragraphs of this section. The data for K, modified to represent annealed tubing, are shown in Figure B-8.3 along with the least-squares fit line used to describe the behavior of the data below 730 kelvins.

Strain rate effects and annealing effects were removed from K as follows: (a) K′, as given in Reference B-8.1 for use in the expression $\sigma = K' \epsilon^n$, was redefined to be equal to

$$K' = K \left(\frac{\dot{\epsilon}}{10^{-3}/s} \right)^m \qquad \text{(B-8.15)}$$

(b) the fractional change in K expected from varying amounts of cold work and annealing was removed to give values for the K of annealed tubing consistent with the model adopted by MATPRO for the effects of cold work and annealing.

Values of K above 755 kelvins were calculated from ultimate tensile strength (presumed = maximum *engineering* strength) of Reference B-8.7 and Reference B-8.2. In order to estimate K, it is assumed in Equation (B-8.3) that $\epsilon = \frac{n}{1+m}$ when engineering stress is maximum. Thus Equation (B-8.3) at maximum engineering stress can be rewritten using Equation (B-8.1) to give:

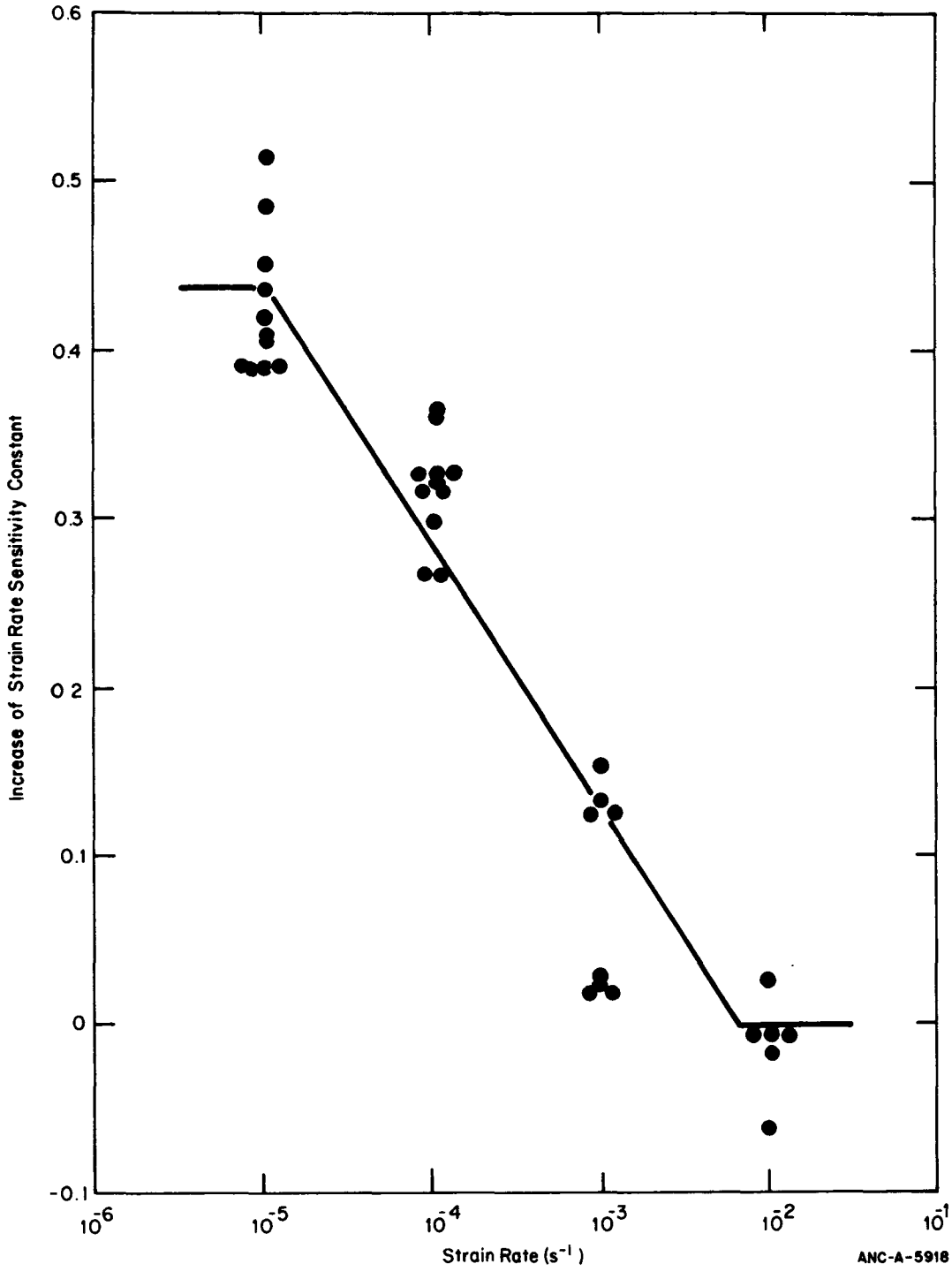

Fig. B-8.2 Increase in the strain rate sensitivity constant at 1173 K as a function of strain rate.

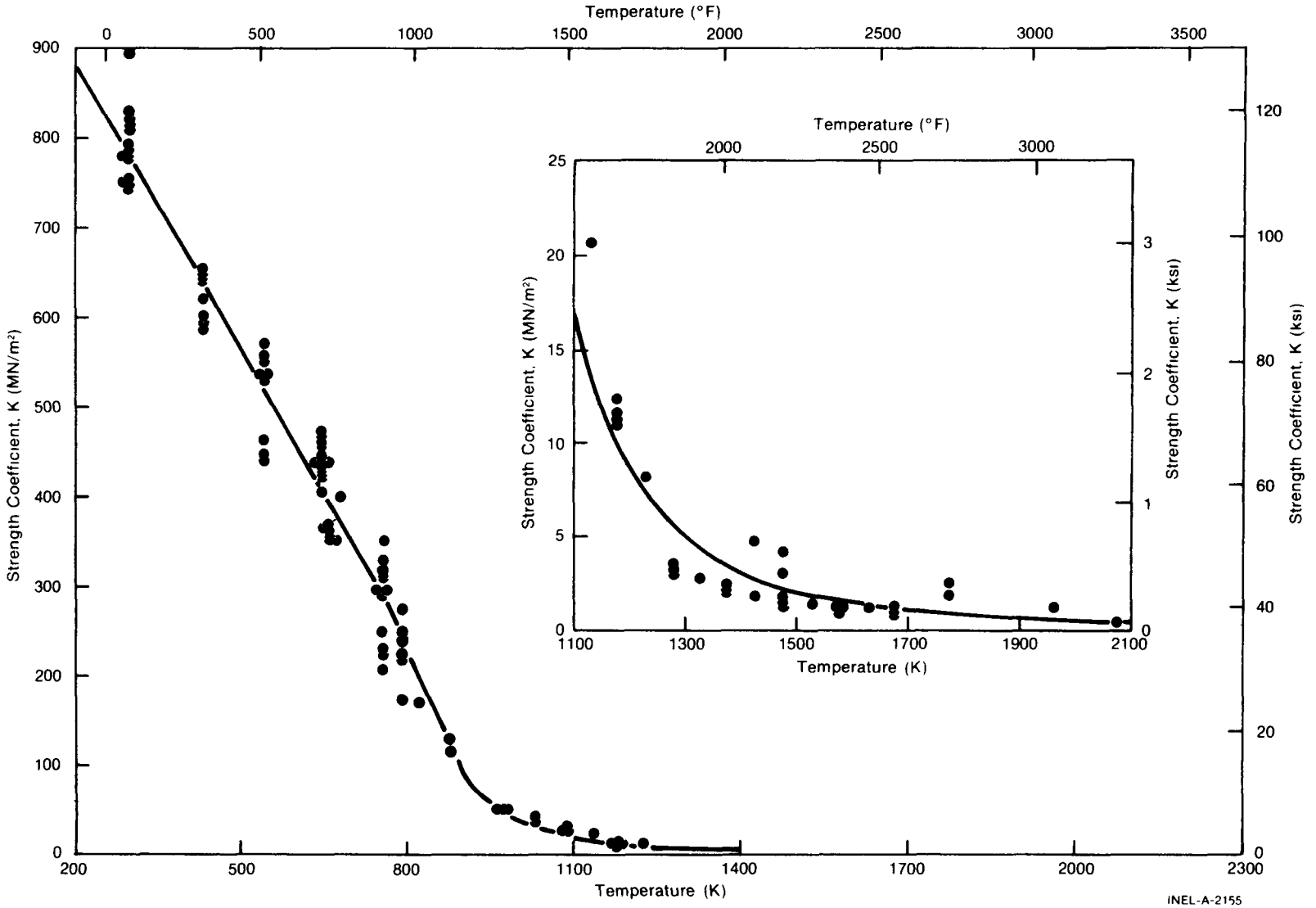

Fig. B-8.3 Data for strength coefficient (K), modified to represent annealed tubing with the analytical expressions used in MATPRO to represent K as a function of temperature.

$$K = \frac{\sigma_{ultimate}}{\left(\frac{n}{1+m}\right)^n \left(\frac{\dot{\varepsilon}}{10^{-3}/s}\right)^m} = \frac{S_{max}\ \exp\left(\frac{n}{1+m}\right)}{\left(\frac{n}{1+m}\right)^n \left(\frac{\dot{\varepsilon}}{10^{-3}/s}\right)^m} \qquad \text{(B-8.16)}$$

where

S_{max} = the maximum of the engineering stress defined in Equation (B-8.1)

$\sigma_{ultimate}$ = the ultimate tensile strength (UTS)

and the other terms are defined in conjunction with Equation (B-8.3).

The temperature dependence of the data above 900 kelvins is described with an exponential function [Equation (B-8.5c)] and the data between 730 and 900 kelvins by a third degree polynomial in temperature [Equation (B-8.5b)]. The constants of this polynomial are determined so that it matches the values and slopes of the other expression for K at the boundaries of the 730 to 900 kelvins region.

These results should be regarded as incomplete since it is known[B-8.2, B-8.9] that the high temperature stress-strain curves should be divided into two or three different stages with each stage described by different values of n and K.

The expression for n as a function of temperature used in MATPRO is based on a least-squares fit to data reported by Reference B-8.1. Effects of cold work and an incomplete anneal on the values of n are approximated simply by multiplying the expression used to fit the data taken with 70% cold-worked and stress-relieved material by 1.38 to approximate values of n obtained with fully annealed zircaloy. Figure B-8.4 shows the base data and the expressions used for both the stress-relieved value of n (left side scale) and annealed values of n (right side scale).

Above 755 kelvins, n would be expected to decrease to zero near the alpha + beta transition phase. However, recent results[B-8.10] have indicated that the behavior may be more complex. In the current mechanical properties model, the quadratic expression which is fit to data from 300 to 755 kelvins is continued to 850 kelvins where the value of n is 0.028 for annealed zircaloy. Above this temperature, n is assumed to be constant and equal to 0.028. The present version of MATPRO does not set n = 0 because several of the routines which use MATPRO become unstable for very small values of n.

8.3 Coefficients Describing Anisotropy

The coefficients describing anisotropy, A1, A2, and A3, are based on data reported by Busby[B-8.11, B-8.12] and on an analysis by Merkle[B-8.13]. The coefficients A1 to A3 are defined to make the effective stress-strain curve coincide with the tubing axial uniaxial stress-strain curve modeled by MATPRO correlations.

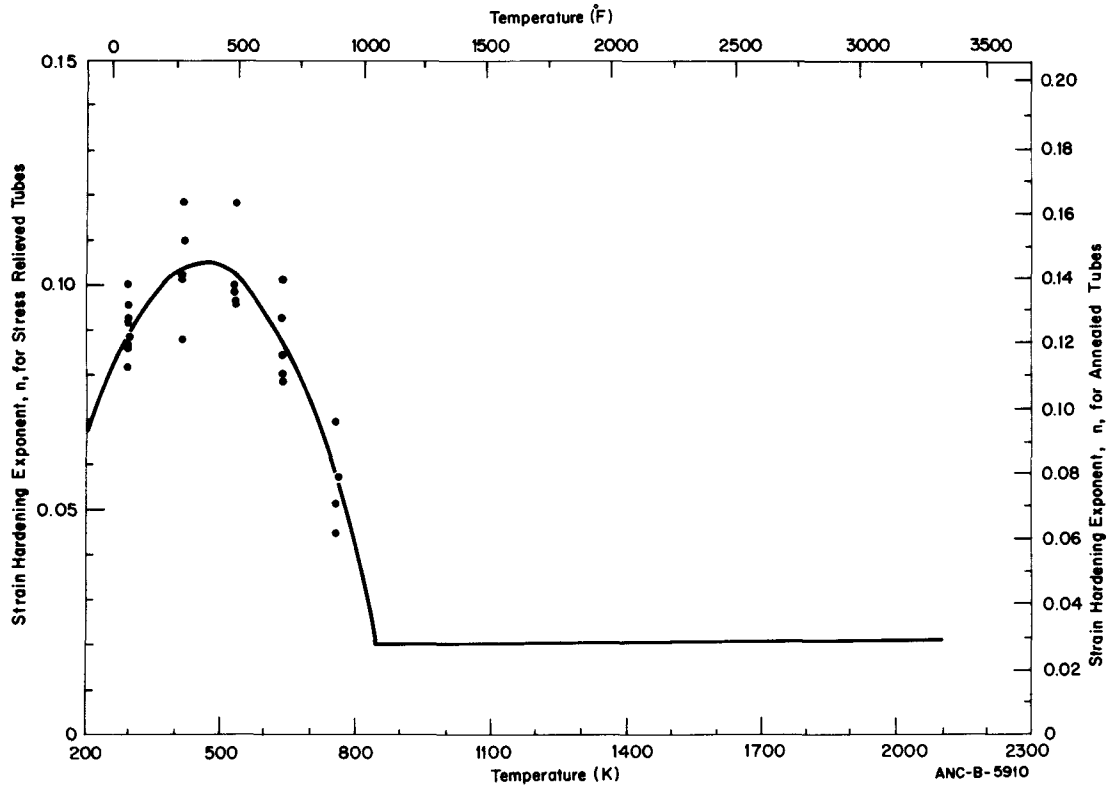

Fig. B-8.4 Base data and the expression used to represent the strain hardening exponent for annealed tubes.

In Merkle's analysis, the yield function is given by

$$f = \left[A1\left(\sigma_1-\sigma_2\right)^2 + A2\left(\sigma_2-\sigma_3\right)^2 + A3\left(\sigma_3-\sigma_1\right)^2\right]^{1/2} \qquad \text{(B-8.17)}$$

where

f	=	yield function (Pa)
A1, A2, A3	=	coefficients of anisotropy
$\sigma_1, \sigma_2, \sigma_3$	=	principal axis stress components (Pa).

For constant principal stress component ratios and constant principal plastic strain increment ratios during loading, Merkle finds an effective plastic strain given by

$$\varepsilon_{eff} = \frac{1}{A1\ A2 + A2\ A3 + A3\ A1}\left[A1\left(A2\ \varepsilon_1 - A3\varepsilon_2\right)^2 + A2\left(A3\varepsilon_2 - A1\varepsilon_3\right)^2 + A3\left(A1\varepsilon_3 - A2\varepsilon_1\right)^2\right]^{1/2} \qquad \text{(B-8.18)}$$

where

ϵ_{eff} = effective plastic strain

$\epsilon_1, \epsilon_2, \epsilon_3$ = principal axis strain components.

Strain components are given by

$$\epsilon_1 = \frac{1}{B}\left[\sigma_1 (A1 + A3) - \sigma_2 A1 - \sigma_3 A3\right] \quad \text{(B-8.19a)}$$

$$\epsilon_2 = \frac{1}{B}\left[-\sigma_1 A1 + \sigma_2 (A2 + A1) - \sigma_3 A2\right] \quad \text{(B-8.19b)}$$

$$\epsilon_3 = \frac{1}{B}\left[-\sigma_1 A3 - \sigma_2 A2 + \sigma_3 (A3 + A2)\right] \quad \text{(B-8.19c)}$$

where

B = the plastic modulus of the effective stress-strain curve.

Three conditions are required to evaluate the constants A1, A2, and A3. One is imposed to make the effective stress-strain curve coincide with the MATPRO curve for uniaxial stress-strain in the axial direction (that is, to make $f = \sigma_1$ and $\epsilon_{eff} = \epsilon_1$, for $\sigma_2 = \sigma_3 = 0$). This condition is

$$A1 + A3 = 1. \quad \text{(B-8.20)}$$

A second condition can be obtained from measurements of the ratio of contractile strains in an axial tension test. For this test [corresponding to $\sigma_2 = \sigma_3 = 0$ in Equations (B-8.19a to B-8.19c)] the ratio of contractile strains for constant strain ratios during loading is

$$R = \frac{d\epsilon_2}{d\epsilon_3} = \frac{\epsilon_2}{\epsilon_3} = \frac{A1}{A3} \quad \text{(B-8.21)}$$

where

R = the measured contractile strain ratio $\left(\frac{d\epsilon_2}{d\epsilon_3}\right)$.

The third condition required to evaluate the anisotropy constants can be obtained from measurements of the ratio of contractile strains in a circumferential uniaxial test on tubing. For this test [$\sigma_1 = \sigma_3 = 0$ in Equations (B-8-19a to B-8.19c)] the ratio of contractile strains for constant strain ratios during loading is

$$P = \frac{d\epsilon_1}{d\epsilon_3} = \frac{\epsilon_1}{\epsilon_3} = \frac{A1}{A2} \qquad \text{(B-8.22)}$$

The second equality of Equations (B-8.21) and (B-8.22) assumes the strain ratios are constant. The assumption that ratios remain constant during loading is not justified for strains above about 0.20 and may not be justified below 0.05. Considerable experimental and theoretical development will be required to remove this deficiency from the model by accounting for texture changes during an arbitrary loading history.

Solution of Equations (B-8.20), (B-8.21), and (B-8.22) for A1, A2, and A3 in terms of measured values of R and P gives

$$A1 = \frac{R}{R+1} \qquad \text{(B-8.23a)}$$

$$A2 = \frac{R}{P(R+1)} \qquad \text{(B-8.23b)}$$

$$A3 = \frac{1}{R+1} \qquad \text{(B-8.23c)}$$

Values of ϵ_2 and ϵ_3 for tubing axial tensile tests are reported by Busby[B-8.11] who found that (a) the ratio R changes with increasing strain (although it was approximately constant for strains in the range 0.05 to 0.2) and (b) values of R observed at strains as high as the point of instability were generally consistent with crystallographic texture; that is, smaller contractile strains were observed in the direction which had the larger percentage of basal poles. Values of R reported by Busby in tubing uniaxial tests ranged from 0.85 to 2.5. Later measurements by Busby using a different lot of tubing[B-8.12] yielded values of R = 1.9 to 2.8 and recent measurements of Miyamoto et al[B-8.14] gave R = 3.13.

The ratio P has been estimated by Busby[B-8.12] from uniaxial tests transverse to the rolling direction of plate material to be approximately 1.7 R for typical commerical tubing. The recent measurement by Miyamoto et al of R = 3.13 and P = 5.78 is consistent with this estimate.

The measurements discussed above were made at 294, 590, and 644 kelvins, respectively. However, a description of material properties for accident analysis must account for material behavior at higher temperatures. The data base used to estimate the value of R at high temperature comes from a series of tensile tests conducted by Busby on one lot of tubing[B-8.12]. In these tests, Busby found a tendency for R to decrease with increasing temperatures up to 922 kelvins. Busby's measured values of R for this lot and the predictions of the expression used in MATPRO to describe the change in R are shown in Figure B-8.5. The predicted R decreases to 1.0 at a temperature of 1203.233 kelvins which is near the end of alpha + beta phase transition. Since the beta phase has a cubic crystal structure, it would be expected to be nearly isotropic (R = 1). For this reason, R is taken to be 1.0 at temperatures above 1203.233 kelvins. The line in Figure B-8.4 represents Equations (B-8.8a) and (B-8.8b).

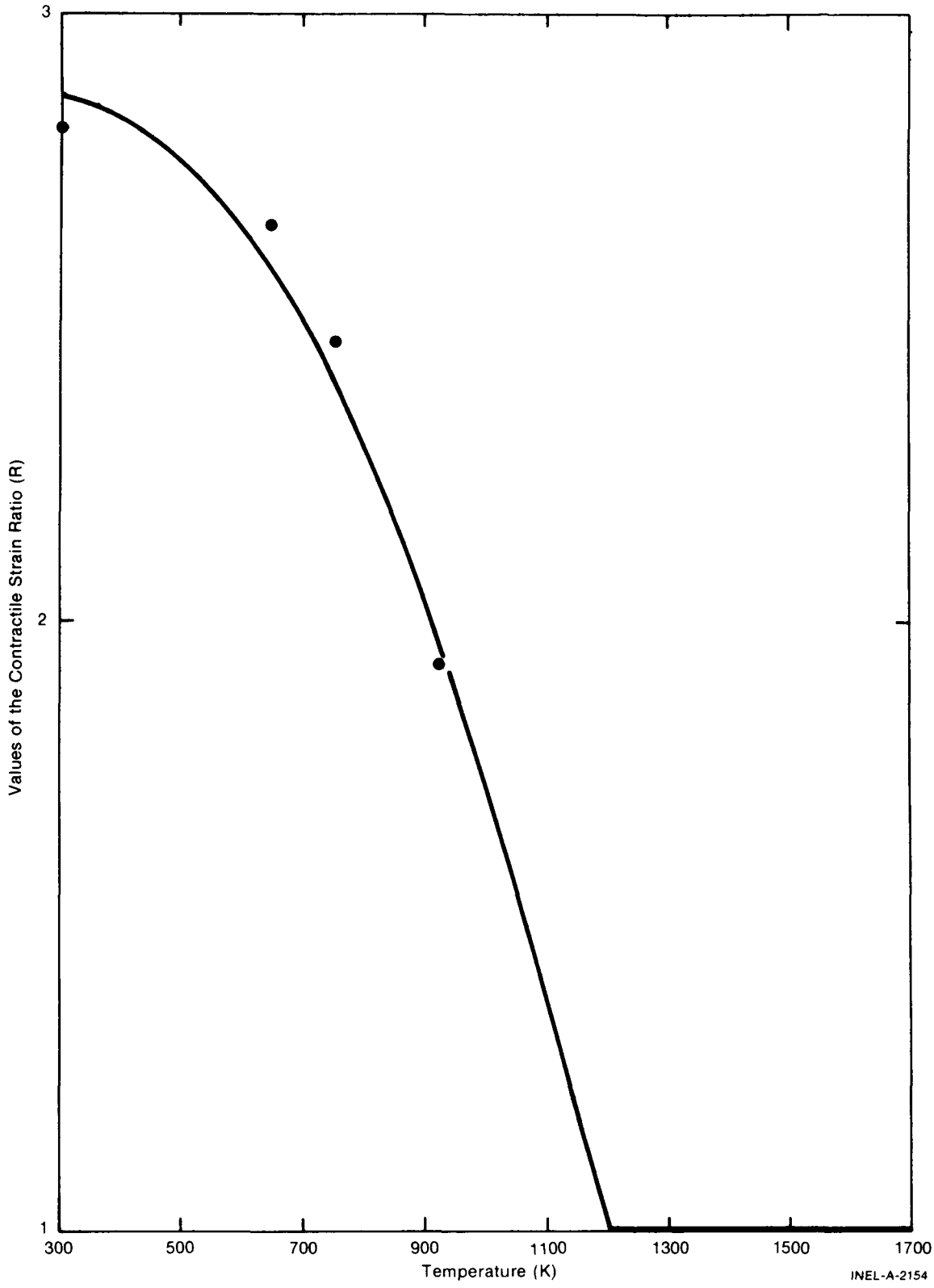

Fig. B-8.5 The contractile strain ratio determined by Busby for a single lot of tubing and the values predicted by MATPRO.

Although Busby recommends use of the estimate $P = 1.7R$[B-8.12] for tubing which has been fabricated in a relatively normal manner and heat treated in the alpha phase temperature range, values of the parameter P are not reported for temperatures above 644 kelvins. In order to provide preliminary estimates of the change of the value P with temperature, the assumptions outlined below are employed.

(1) Busby's parameter, $Q = \frac{d\epsilon_1}{d\epsilon_2}$, measured during a uniaxial test in the radial direction, was introduced.

(2) Since Q and P, like R, should be consistent with the crystallographic texture, P and Q should approach 1.0 as the cladding becomes isotropic. The ratio of the difference P - 1.0 and Q - 1.0 is assumed to be constant.

$$\frac{P-1}{Q-1} = \text{a constant} = C. \tag{B-8.24}$$

(3) The relation $\frac{RQ}{P} = 1$ derived by Busby, was used with Equation (B-8.24) to deduce the expression

$$Q = \frac{P}{R} = \frac{1 - C}{R - C} . \tag{B-8.25}$$

(4) Finally, Busby's recommended low temperature values, R = 2.8 and $\frac{P}{R} = 1.7$, were used with Equation (B-8.25) to find C = 5.4.

The expressions for A1, A2, and A3 which result from substituting Equation (B-8.25) with C = 5.4 into Equations (B-8.23) are Equations (B-8.7a) to (B-8.7c). As mentioned previously, R is a complex function of strain for large strains. The existing data do not allow even a preliminary model of this change for biaxial stress states. The constants A1, A2, and A3 are therefore assumed to approach their values of isotropic material (A1 = A2 = A3 = 0.5) for large strains. The isotropic assumption was tested against the assumption that the constants A1, A2, and A3 remain unchanged at large strains by comparing closed tube burst strength predictions with Busby's reported values. The isotropic assumption produced predictions which were consistently closer to the measured values. The expression used to return the low strain values of R and thus the constants A1, A2, and A3 to their isotropic values as effective strain increases from 0.15 to 0.30 is Equation (B-8.8c).

8.4 Effects of Irradiation, Cold Work, and Annealing

Extensive testing to determine the effects of irradiation and cold work on zircaloy mechanical properties at room temperatures has been carried out by Bement[B-8.8]. Unfortunately, published tests at high temperatures[B-8.15 – B-8.17] do not yet include a similar series of tests on a single lot of material. Thus variation in mechanical properties due

to uncharacterized differences in the materials such as different textures[B-8.18] or different grain sizes[B-8.17, B-8.1] have caused considerable scatter among the high temperature data. Therefore, this model is based primarily on data from Reference B-8.8, using ratios to describe the complex effects of irradiation and cold work.

8.4.1 Effect of Cold Work on the Strength Coefficient. Strength coefficients from Reference B-8.8 are plotted in Figure B-8.6. Although texture effects are evident in annealed material and irradiation does tend to increase the strength coefficient slightly, the dominant correlation is a linear increase in the strength coefficient with cold work. A linear least-squares fit yields the room temperature correlation

$$K' = 624.4 + 341\ CWK = 624.4\ (1+ 0.546\ CWK) \qquad \text{(B-8.26)}$$

where

CWK = the cold work for strength coefficient

K ' = strength coefficient at room temperature (MN/m^2).

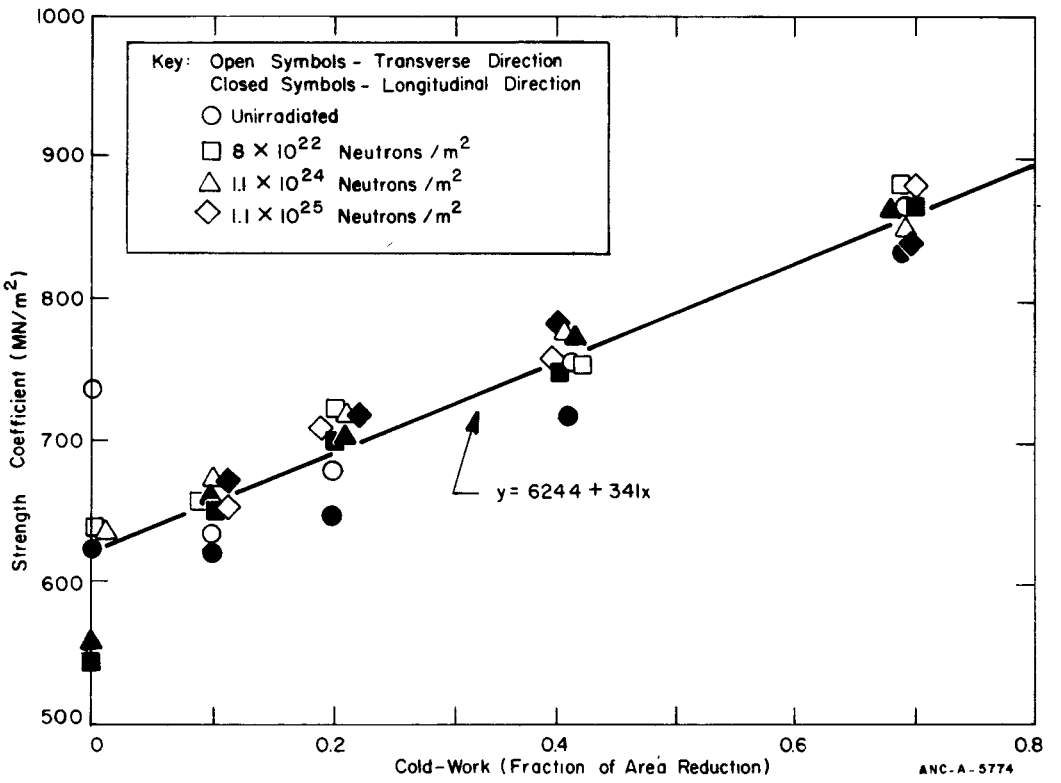

Fig. B-8.6 Data and least-squares fit to strength coefficients as a function of cold work and irradiation at room temperature.

To estimate the effect of temperature on this correlation, values of the strength coefficient determined from the limited data from References B-8.15 and B-8.16 at temperatures of 553 and 573 kelvins were also fit to a straight line with the resultant correlation:

$$K' = 373 + 238\ CWK = 373\ (1 + 0.64\ CWK). \tag{B-8.27}$$

Comparison of the two results shows that they are consistent with a temperature dependent expression of the form:

$$K' = K'\ (T)\ \ [1 + \text{constant}\ CWK] \tag{B-8.28}$$

where

$K'(T)$ = the temperature dependent function describing the behavior of the strength coefficient of annealed zircaloy [Equations (B-8.5a) to (B-8.5c)].

The form of Equation (B-8.28) has therefore been assumed. The constant coefficient of the cold work term is taken to be 0.546 as determined at room temperature because the room temperature data exhibit much less scatter than the high temperature data which were taken from several different sources.

8.4.2 Effect of Cold Work on the Strain Hardening Exponent. Figure B-8.7 illustrates the effect of cold work and irradiation on the strain hardening exponent, n, as determined at room temperature in Reference B-8.8. The strain hardening exponent of unirradiated material shown in Figure B-8.7 can be described by the empirical relation

$$n = 0.11\ \exp(-39.2\ CWN) + 0.03(CWN)^2 - 0.12(CWN) + 0.021. \tag{B-8.29}$$

where

CWN = effective cold work for strain hardening exponent.

This expression is essentially a decreasing exponential function for small values of cold work and a slowly increasing parabola for large values of cold work.

At higher temperatures, trends exhibited by the limited and scattered values of n (which have been obtained at 553 kelvins[B-8.15] and 573 kelvins[B-8.16]) are consistent with the assumption that the fractional changes in n with cold work are similar to the fractional changes in n at room temperature. The following functional relationship is assumed in the present model

$$n(\text{temperature, cold work}) = n(T)\ \frac{n(\text{cold work})}{n(\text{at 0 cold work})}. \tag{B-8.30}$$

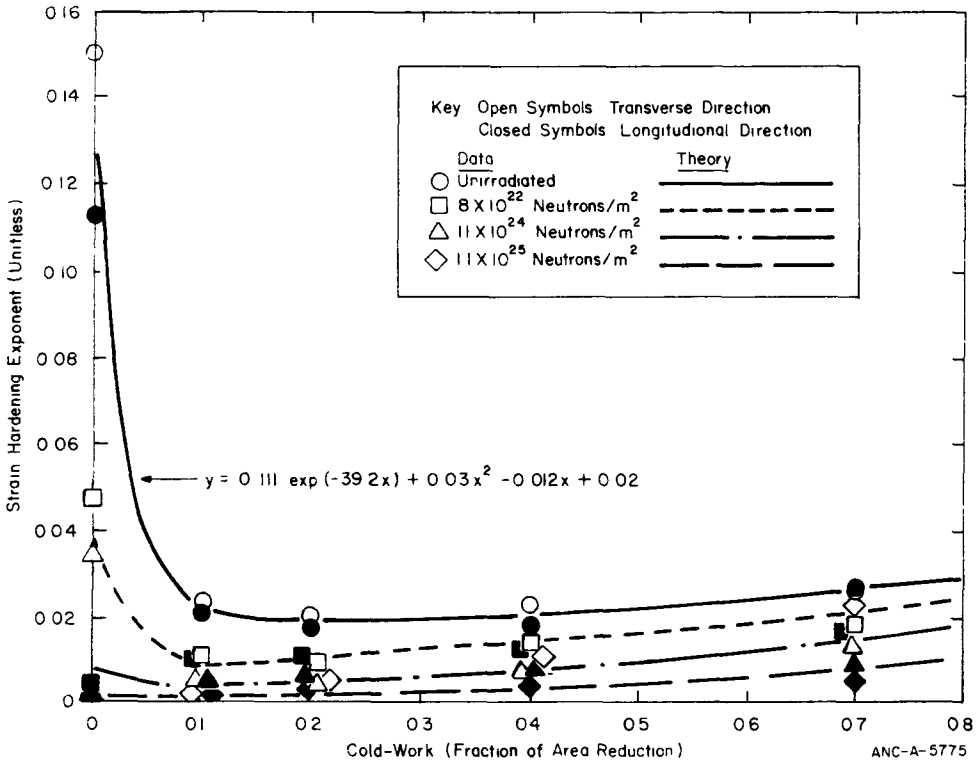

Fig. B-8.7 Data and analytical functions for strain hardening coefficient as a function of cold work and irradiation at room temperature.

When the expression for n as a function of cold work, given by Equation (B-8.29), is substituted into Equation (B-8.30) the following expression is obtained:

$$n = n(T)\,\frac{0.11\,\exp\,[-39.2(CWN)] + 0.03(CWN)^2 - 0.012(CWN) + 0.021}{0.132} \qquad \text{(B-8.31)}$$

where

$n\,(T) =$ given by Equation (B-8.4a).

8.4.3 Effect of Irradiation on K. The data from Reference B-8.8 plotted in Figure B-8.6 show little effect of irradiation on the strength coefficient. However, the irradiation of these samples was conducted at 333 kelvins and it is probable that irradiation at reactor operating temperature produces different results[B-8.19].

The most applicable data for modeling the effect of irradiation on cladding are the measurements of ultimate strength and uniform elongation reported by Bauer et al[B-8.20, B-8.21]. Their measurements were taken with cladding irradiated in the Carolina Power and Light H. B. Robinson Reactor to fast neutron fluences of 4×10^{25} fast neutrons/m^2. Testing was performed at 644 kelvins. Unfortunately, they were unable to test unirradiated samples from the lot of tubing they used, so use of their data must rely on nominal preirradiated ultimate strengths[B-8.21].

Since Bauer's data are most representative of in-reactor irradiation damage they are used instead of the data from Reference B-8.8 to find an expression for the effect of irradiation on K. Strength coefficients for irradiated cladding at 644 kelvins were determined with Equation (B-8.16) and tensile test results given in Table I of Reference B-8.20 (samples P8-20, P8-34, and P8-46). Equations (B-8.5a) and (B-8.28) were then used to estimate the strength coefficient for annealed cladding and the cold work contribution to the strength coefficient (for typical cold work of 0.5) at 644 kelvins. The difference between the strength coefficient of the irradiated material and the predicted strength coefficient of cold-worked material is presumed to be due to irradiation effects. Furthermore, the effect of irradiation is assumed to be proportional to the fast neutron fluence. The second term of Equation (B-8.10) resulted from these assumptions.

At present the best evidence in support of a linear dependence of K on fast neutron fluence is the fact that the small effect of irradiation on the samples of Reference B-8.8 are not inconsistent with the predictions of Equation (B-8.10) for the relatively low fluences reported in that reference.

8.4.4 Effect of Irradiation on n. The effect of irradiation on the strain hardening exponent, n, is complex. Figure B-8.7 shows that the fractional change in n due to irradiation at 333 kelvins is large in annealed material and somewhat less in material that has been heavily cold-worked. Furthermore, the effect of irradiation is highly nonlinear. Increasing amounts of irradiation produce continually decreasing changes in n.

These features are described empirically in the irradiation model by expressing the ratio of the value of n after irradiation to the value of n before irradiation as an exponential multiplier with a moderating cold work dependent term in the argument of the exponent. The strain hardening exponent of irradiated material is then:

$$n = n(\text{unirradiated})\ \exp[-(\text{fluence})^{1/3}/(A + B\ CWN)] \qquad \text{(B-8.32)}$$

where

$$A = 3.73 \times 10^{7}\ (\text{neutrons/m}^2)^{1/3}$$

$$B = 2.0 \times 10^{8}\ (\text{neutrons/m}^2)^{1/3}$$

and n(unirradiated) is defined in Equation B-8.31.

8.5 Thermal Annealing of Cold Work and Irradiation Damage

The thermal annealing of cold work and irradiation damage are modeled with rate equations which keep track of effective cold work and fast neutron fluence for use in Equations (B-8.9) and (B-8.10). These rate equations are contained in the subcode CANEAL.

The expression used to find the ratio of effective cold work for the strength coefficient at the end of a time step divided by effective cold work at the beginning of an isothermal time step is

$$FK = \exp\left[-1.504\left(1 + 2.2 \times 10^{-25}\,\phi_{KO}\right)(t)\exp\left(\frac{-2.33 \times 10^{18}}{T^6}\right)\right] \quad \text{(B-8.33)}$$

where

FK = effective cold work for strength coefficient at the end of a time step divided by effective cold work at the beginning of a time step

ϕ_{KO} = effective fast neutron fluence for strength coefficient at the start of the time step (neutrons/m^2)

t = time step size (s)

T = cladding temperature (kelvins).

The effective fast neutron fluence for calculating the strength coefficient after an isothermal time step is computed with the expression

$$\frac{10^{20}}{\phi_K} = 2.49 \times 10^{-6}\,(t)\exp\left(\frac{-5.35 \times 10^{23}}{T^8}\right) + \frac{10^{20}}{\phi_{KO}} \quad \text{(B-8.34)}$$

where

ϕ_K = effective fast neutron fluence for strength coefficient at the end of a time step (neutrons/m^2).

The expression to find the ratio of effective cold work for the strain hardening exponent at the end of a time step divided by effective cold work for strain hardening exponent at the beginning of an isothermal time step is

$$FN = \exp\left[-12.032\left(1 + 2.2 \times 10^{-25}\,\phi_{NO}\right)(t)\exp\left(\frac{-2.33 \times 10^{18}}{T^6}\right)\right] \quad \text{(B-8.35)}$$

where

FN = effective cold work for strain hardening exponent at the end of a time step divided by effective cold work for strain hardening exponent at the beginning of a time step

ϕ_{NO} = effective fast neutron fluence for the strain hardening exponent at the start of the time step (neutrons/m^2).

The effective fast neutron fluence for calculating the strain hardening exponent after an isothermal time step is computed with the expression

$$\frac{10^{20}}{\phi_N} = 2.49 \times 10^{-3} (t) \exp\left(\frac{-5.35 \times 10^{23}}{T^8}\right) + \frac{10^{20}}{\phi_{NO}} \qquad \text{(B-8.36)}$$

where

ϕ_N = effective fast neutron fluence for strain hardening exponent at the end of a time step (neutrons/m^2).

If the time step is not isothermal, Equations (B-8.33) to (B-8.36) must be modified to include the effect of varying temperature. The modification used in MATPRO-11 is

$$\exp\left(\frac{-Q}{T^m}\right) \longrightarrow \left[\exp\left(\frac{-Q}{TO^m}\right)\right]^{\frac{\left[\exp\left(Q\left(\frac{dT}{dt}\right) t \left(\frac{m}{TO^{m+1}}\right)\right)-1\right]}{Q\left(\frac{dT}{dt}\right) t \left(\frac{m}{TO^{m+1}}\right)}} \qquad \text{(B-8.37)}$$

where

Q, m = the constants which appear in the isothermal expression

TO = temperature at the start of the time step (kelvins)

$\frac{dT}{dt}$ = average rate of change of temperature expected during the time step (kelvins/s).

Expression (B-8.37) is exact for a constant rate of temperature change and is only an approximation for nonlinear temperature changes. Alternate expressions have been developed by Markworth[B-8.22].

8.5.2 Available Data. Howe and Thomas reported postirradiation annealing studies on annealed, 13.1 percent cold-worked and tempered 25.5 percent cold-worked zircaloy-2 irradiated at 493 and 553 kelvins with integrated fast neutron fluxes of 3.6×10^{23} neutrons/m^2 and $2.7\ 10^{24}$/m^2[B-8.23]. Specimens were given one hour anneals in vacuum at various temperatures. The nominal room temperature ultimate stresses measured with these samples are listed in Table B-8.I.

TABLE B-8.I

ROOM TEMPERATURE ULTIMATE STRENGTHS OF CLADDING
ANNEALED FOR ONE HOUR FROM HOWE AND THOMAS

Cold Work (%)	Neutron Fluence (n/m^2)	Annealing Temperature (kelvins)	Ultimate Strength (MPa)
0	3.6×10^{23}	555	634
0	3.6×10^{23}	625	588
0	3.6×10^{23}	675	513
0	3.6×10^{23}	725	513
0	3.6×10^{23}	775	500
0	3.6×10^{23}	875	500
0	3.6×10^{23}	975	499
25.5	0	555	619
25.5	0	675	614
25.5	0	775	603
25.5	0	875	530
25.5	0	975	512
25.5	2.7×10^{24}	555	728
25.5	2.7×10^{24}	625	712
25.5	2.7×10^{24}	675	675
25.5	2.7×10^{24}	725	626
25.5	2.7×10^{24}	775	579
25.5	2.7×10^{24}	875	504
25.5	2.7×10^{24}	975	486

The data from irradiated annealed zircaloy-2 shows that irradiation-induced hardening in this material is completely annealed out by one hour at temperatures above 775 kelvins and that most of the recovery occurs in the temperature range 575 to 675 kelvins. From their recovery data with 25.5% cold-worked zircaloy-2, Howe and Thomas concluded that:

(1) The recovery occurring in the temperature range 550 to 725 kelvins is the annealing out of irradiation damage rather than cold work.

(2) The irradiation damage in cold-worked material is completely annealed out by one hour at approximately 725 kelvins.

(3) The recovery from 725 to 973 kelvins for irradiated material is fairly similar to that for unirradiated material. However, there is an indication that the irradiated material recovers slightly faster.

Since the one hour anneals of Howe and Thomas represent times which are long compared to LOCA (loss-of-coolant-accident) blowdown and refill times, the data are used only for general guidance and verification of the models developed from shorter annealing times reported by Bauer et al. In particular, the data support the ideas that (a) irradiation damage anneals before cold work and (b) irradiation damage affects the rate of annealing of cold work but may be treated as a perturbation of the cold work annealing.

Bauer et al have reported yield strengths, ultimate strength, uniform elongations (engineering strain at maximum load), and total elongations from annealing studies of both cold-worked and irradiated cold-worked zircaloy cladding material[B-8.6, B-8.20]. The unirradiated cold-worked cladding was from a standard lot of tubing which has been characterized by R. H. Chapman[B-8.24]. The irradiated cladding was obtained from spent fuel rods irradiated in the Carolina Power and Light H. B. Robinson Plant to a fast neutron fluence of approximately $4.4 \times 10^{25}/m^2$.

Ultimate strengths and uniform elongations obtained at 644 kelvins and a strain rate of 0.025/min with the unirradiated cladding are listed in Table B-8.II. With a heating rate of 5.6 kelvins/s most of the recovery of both strength and uniform elongation occurs between temperatures of 894 and 978 kelvins. However, the recovery has barely started at 978 kelvins when the heating rate is 27.8 kelvins/s. Since the annealing times at temperature are short, the maximum temperature required to anneal these samples is considerably higher than the temperatures reported by Howe and Thomas.

Tables B-8.III and B-8.IV are a summary of Bauer et al's measurements of ultimate strengths and uniform elongations of annealed irradiated tubing. The measurements were performed at 644 kelvins and a strain rate of 0.025/min. The results in Table B-8.III were obtained with transient anneals similar to those used with the unirradiated tubing. Table B-8.IV summarizes results from isothermal anneals similar to the anneals carried out by Howe and Thomas.

TABLE B-8.II

644 K TEST RESULTS FOR UNIRRADIATED TRANSIENT ANNEALED CLADDING[B-8.6]

Specimen Number[a]	Heating Rate (kelvins/s)	Maximum Temperature (kelvins)	Ultimate Strength (MPa)	Uniform Elongation (percent)
as-received	--	644	434.5	4.1
0781-8	5.6	811	434	4.1
0781-7	5.6	866	432	4.1
0781-6	5.6	894	409	4.8
0781-5	5.6	978	252	24.3
0781-4	27.8	811	434	3.6
0781-3	27.8	866	438	3.3
0781-2	27.8	894	432	3.6
0781-1	27.8	978	422	4.6

[a] The number 0781 is the rod number.

The annealing behavior of the irradiated cladding is different than the behavior of the unirradiated material. Ultimate strengths obtained with irradiated material which had little or no annealing are substantually higher than the ultimate strengths of the unirradiated material. However, transient anneals which begin to affect the strength of cold-worked material (5.6 kelvins/s to 866 and 894 kelvins or 27.8 kelvins/s to 978 kelvins) leave the irradiated material with strengths which are below the strengths of the unirradiated material after corresponding anneals. It is possible that these differences are due to the fact that the tubing does not come from the same lot but a similar trend has been shown by the studies of Howe and Thomas on material from one lot. It has thus been concluded that irradiation for long times at reactor operating temperatures causes a significant increase in the strength of zircaloy cladding and enhances the annealing of the strength increase due to cold work.

Comparison of uniform elongation measurements with the unirradiated and irradiated cladding (Tables B-8.5.II and B-8.5.III) shows that the effect of irradiation on this parameter is different than its effect on ultimate strength. The uniform elongation of the unannealed irradiated material is less than the uniform elongation of the unannealed unirradiated material but there is no obvious increase in the rate of recovery from cold work effects because of the irradiation. Therefore, models which describe annealing by keeping

TABLE B-8.III

644 K TEST RESULTS FOR IRRADIATED TRANSIENT ANNEALED CLADDING[B-8.20]

Specimen Number[a]	Heating Rate (kelvins/s)	Maximum Temperature (kelvins)	Ultimate Strength (MPa)	Uniform Elongation (percent)
PB-20	--	644	622.8	4.1
PB-34	--	644	650.3	4.0
PB-46	--	644	660.9	2.8
H10-20	--	644	694.0	3.8
P4-50-55	0.6	700	674	2.1
P4-55-60	0.6	755	633	2.7
P4-89-1/2-94-1/2	0.6	811	574.5	2.3
P4-94-1/2-99-1/2	0.6	894	286.1	9.57
Pr-89-1/2-104-1/2	0.6	978	268.9	9.21
P4-111-116	5.6	700	653	2.0
P4-45-50	5.6	755	676	2.4
P4-35-3/4-46-3/4	5.6	811	595.2	2.35
Pr-70-3/4-75-3/4	5.6	866	349.3	2.94
Pr-75-3/4-80-3/4	5.6	894	313.7	4.77
Pr-80-1/2-89-1/2	5.6	978	287.3	10.56
014-106-1/2-111-1/2	13.9	755	717	2.4
A8-120-3/4-125-3/4	13.9	811	652.7	2.27
P4-16-1/2-21-1/2	13.9	866	577.9	2.50
P4-21-1/2-26-1/2	13.9	894	456.2	2.16
P4-26-1/2-31-1/2	13.9	978	304.5	5.74
P4-65-70	27.8	755	671	2.1
A1-29-1/2-34-1/2	27.8	811	721.6	2.70
A8-105-3/4-110-3/4	27.8	866	671.0	2.70
A8-110-3/4-115-3/4	27.8	894	597.5	2.06
A8-115-3/4-120-3/4	27.8	978	348.2	3.49
P4-116-21	27.8	1033	329	4.7
014-111-1/2-116-1/2	27.8	1144	338	8.6
014-37-42	27.8	1255	340	10.5

[a] The letter and number, letter, or number before the first hyphen identify the rod number; that is, Rod P8, Rod Pr-9, Rod 014, etc.)

TABLE B-8.IV

644 K TEST RESULTS FOR IRRADIATED, ISOTHERMALLY ANNEALED CLADDING[B-8.20]

Specimen Number[a]	Temperature (kelvins/s)	Time at Temperature (minute)	Ultimate Strength (MPa)	Uniform Elongation (percent)
P8-20	644	--	622.8	4.1
P8-34	644	--	650.3	4.0
P8-46	644	--	660.9	2.8
H10-20	644	--	694.0	3.8
H10-5	700	60	615.9	3.35
H10-41	755	10	590.6	2.85
H10-17	755	60	556.2	3.06
P4-60-65	811	1	560	2.9
A1-24-1/2-29-1/2	811	10	363.1	3.2
H10-18	811	30	371.1	5.10
A1-105-3/4-110-3/4	866	1	332.1	4.52
A1-99-104	866	5	311.4	8.03
H10-3	866	30	321.7	10.1
A1-110-3/4-115-3/4	894	1	308.9	7.90
H10-4	894	30	319.4	13.93
A1-116-1/2-121-1/2	978	1	305.6	7.67
H10-16	978	30	311.4	11.80

[a] The letter and number before the first hyphen identifies the rod number; that is, Rod P8, Rod H10, and Rod A1.

track of effective cold work and effective fluence should be set up to use different values of these parameters for predicting strength and elongation.

The isothermal annealing effects reproduced in Table B-8.IV are similar to those of Table B-8.III in that recovery of ultimate strength precedes recovery of uniform elongation. However, several additional features of the annealing of cold-worked and irradiated zircaloy cladding become apparent from the isothermal data.

(1) The four tests at 644 kelvins show that approximately 10% sample-to-sample scatter should be expected in the measured values of strength. In particular, Rod H10 shows consistently high strength. Variation of the order of a percent seems to be

present in the uniform elongation data. Models for annealing will therefore have to emphasize general trends and avoid exact fits to individual measurements.

(2) Irradiation effects on the strength of zircaloy cladding do not seem to saturate at the low fluences used by Howe and Thomas. The two sixty minute anneals show strengths at 644 kelvins similar to the room temperature strengths measured after similar anneals by Howe and Thomas. If the tensile test data had been taken at similar temperatures, the cladding measured by Bauer would show considerably greater strength.

(3) Time at temperature during annealing is less important for the irradiated material than for the unirradiated material. The model developed in Section 8.5.3 for annealing of the effect of cold work on strength predicts that the log of the departure of strength parameters from their annealed values for two isothermal anneals which differ only in the time at temperature should be proportional to the reciprocal ratio of the annealing times. The major component of the increase of the strengths in Table B-8.5.IV is much less dependent on time at temperature than this relation would imply[a].

The net impression left by the data of Tables B-8.I to B-8.IV is that at least two different processes are important in the annealing of cold-worked and irradiated cladding and that the annealing of the irradiation caused component follows a rate equation which is different than the rate equation for the cold work component. Data which could be used to model these separate processes (for example, annealing studies with one lot of material irradiated to several different fluences) are not yet available. Therefore the model developed in the next section is a strictly empirical attempt to reproduce the data we do have with a reasonably concise set of correlations.

8.5.3 Model Development. The approach used to develop the annealing models presented here is to develop a model for the annealing of cold-worked cladding and modify it to fit data from cold-worked and irradiated material. The model for recovery kinetics in

[a] For example, the ten and sixty minute anneals at 775 kelvins have ultimate strengths which are 279.2 and 244.8 MPa above the fully annealed ultimate strength of sample H10-16. An equation with the form of Equation B-8.2 would imply that the ratio of the logs of the two strengths should be 1/6 or 0.17. The ratio is 0.98.

cold-worked cladding is based on the suggestion by Byrne[B-8.25] that recovery[a] data frequently conform to the assumption that the rate of recovery of a property from its cold-worked value is proportional to the instantaneous value of the property. If the property is the strength coefficient[b] the rate equation for recovery is

$$\frac{dK}{dt} = - f_T [K-K_A] \tag{B-8.38}$$

where

K = strength coefficient of cold-worked cladding (MPa)

K_A = strength coefficient of annealed cladding (MPa)

t = time (s)

f_T = a temperature dependent factor.

Since isothermal annealing data with unirradiated cold-worked tubing are not available, the effect of temperature on the factor f_T in Equation (B-8.38) had to be determined from the limited transient annealing data of Table B-8.II. The method used to do this is outlined as follows:

(1) The change of the factor f_T in Equation (B-8.38) is assumed to be represented by the expression

$$f_T = B \exp\left(\frac{-Q}{T^m}\right) \tag{B-8.39}$$

where

B, Q, m = positive constants

T = temperature (kelvins).

(2) Equation (B-8.38) is integrated over a very short (approximately isothermal) time interval to produce a differential expression for the change in strength coefficient.

$$\frac{K_{final} - K_A}{K_{initial} - K_A} = \exp\left(-B \left[t_{final} - t_{initial}\right] \exp\left(\frac{-Q}{T^m}\right)\right) \tag{B-8.40}$$

---

[a] A separate model for recrystallization kinetics was developed but not used because only limited recrystallization data are available.

[b] Since the change in the strength coefficient is modeled as a linear function of cold work, one can use cold work instead of the strength coefficient in this equation.

(3) The long interval beginning at a temperature T_i and ending at a temperature T_f is divided into η. Small intervals and the temperature during any small interval is assumed constant. The net change in K is the product of η terms like Equation (B-8.40) for each interval

$$\frac{K_{final} - K_A}{K_{initial} - K_A} = \prod_{j=1}^{\eta} \exp\left(-B\left[\frac{t_{final} - t_{initial}}{\eta}\right] \exp\left(\frac{-Q}{T_j^m}\right)\right) \quad \text{(B-8.41a)}$$

$$\frac{K_{final} - K_A}{K_{initial} - K_A} = \exp\left(-B\left[\frac{t_{final} - t_{initial}}{\eta}\right] \sum_{j=1}^{\eta} \exp\left(\frac{-Q}{T_j^m}\right)\right) \quad \text{(B-8.41b)}$$

where

T_j = the temperature during the jth interval.

(4) When the temperature change is a linear function of time, T_j in Equation (B-8.41) can be obtained by interpolation between the initial and final temperatures. The linear interpolation[a], a Taylor series expansion, and a power series summation yield:

$$\sum_{j=1}^{\eta} \exp\left(\frac{-Q}{T_j^m}\right) = \sum_{j=1}^{\eta} \exp\left(\frac{-Q}{\left[T_f - \left(\frac{T_f - T_i}{2\eta}\right) - (\eta - j)\left(\frac{T_f - T_i}{\eta}\right)\right]^m}\right) \quad \text{(B-8.42a)}$$

$$= \sum_{j=1}^{\eta} \exp\left(\frac{-Q}{\left[T_f - \left(\frac{T_f - T_i}{2\eta}\right)\right]^m}\left[1 + \frac{m(\eta - j)\frac{T_f - T_i}{\eta}}{T_f - \left(\frac{T_f - T_i}{2\eta}\right)} + \cdots\right]\right) \quad \text{(B-8.42b)}$$

---

[a] The interpolation may start with the final temperature as is done here:

$$T_j = T_f - \left[\frac{T_f - T_i}{2\eta}\right] - [\eta - j]\left[\frac{T_f - T_i}{\eta}\right]$$

or it may start with the initial temperature so that

$$T_j = T_i + \left[\frac{T_f - T_i}{2\eta}\right] + j\left[\frac{T_f - T_i}{\eta}\right]$$

The second form was used for coding the annealing model because it yields a result in terms of the initial temperature.

$$= \left[\exp\left(\frac{-Q}{\left[T_f - \left(\frac{T_f-T_i}{2\eta}\right)\right]^m}\right)\right] \left[\frac{1 - \exp\left(\frac{-m(T_f-T_i)\ Q}{\left[T_f - \left(\frac{T_f-T_i}{2\eta}\right)\right]^{m+1}}\right)}{1 - \exp\left(\frac{-m(T_f-T_i)\ Q}{\eta\left[T_f - \left(\frac{T_f-T_i}{2\eta}\right)\right]^{m+1}}\right)}\right] \quad \text{(B-8.42c)}$$

(5) Equation (B-8.42c) is substituted into Equation (B-8.41b) and the limit as the number of short intervals approaches infinity ($\eta \rightarrow \infty$) is determined. The resultant expression is

$$\frac{K_f-K_A}{K_i-K_A} = \exp\left(-B\left[\exp\left[-Q/\left(T_f\right)^m\right]\right]\left[\frac{1-\exp\left[-Q\left(T_f-T_i\right)^m/\left(T_f\right)^{m+1}\right]}{\frac{Q\left[T_f-T_i\right]^m}{T_f{}^{m+1}}}\right](t_f-t_i)\right) \quad \text{(B-8.43)}$$

(6) Ultimate strengths and uniform elongations from Table B-8.II are used to determine the strength coefficient[a] after the various anneals described in this table.

(7) The strength coefficients of step (6) are used to determine Q, B, and m. For the current MATPRO version, the values of K_f after the anneals to 866 and 978 kelvins at 5.6 kelvins/s were used with the value of K_i from the as-received material and Equation (B-8.43) to determine B and Q with assumed trial values of K_A between 364 and 442 MPa and assumed trial integral values of m between 1 and 9. Finally, the values of Q, B, K_i, K_A, and m for each trial were used in Equation (B-8.43) to predict K_f for the six anneals which were not already considered. The predictions were compared with the data. The trial values of K_A and m which most successfully predicted both the post-anneal data and the as-received strength coefficient (using the stress relief annealing schedule provided in Reference B-8.24) were K_A = 406 MPa and m = 6. The value m = 6 and the values of Q and B which produced the successful predictions ($Q = 2.33 \times 10^{18}$ and B = 1.504) are therefore adopted for the model.

---

[a] The procedure used to determine a strength coefficient from ultimate strength and uniform elongation data is discussed in conjunction with Equation (B-8.16).

A similar procedure as just described in the previous 7 steps could be used to develop a model for the effect of cold work annealing on the strain hardening exponent. However, the complex form of the expression relating cold work and the strain hardening exponent would complicate the solution considerably. For the time being, the rate of annealing of effective cold work for the strain hardening exponent is assumed to be proportional to the rate of annealing of the effective cold work for the strength coefficient. The best fit is obtained with a value of B eight times as large as the B used for the strength coefficient.

The rest of this section describes the development of models for the annealing of cold-worked and irradiated cladding. It was concluded in Section B-8.5.2 that the principal features of the annealing data with irradiated cladding are

(1) The increased rate of recovery from cold work effects when material has been irradiated

(2) The apparent difference between the annealing kinetics of cold work damage and the annealing kinetics of the irradiation caused increase in strength.

Based on these conclusions, the first step in producing the model for the effect of annealing on the strength coefficient of irradiated cladding is to modify the model for cold work annealing to include the irradiation-caused enhancement of the recovery of the strength coefficient from cold work effects. The modification of the cold work annealing model is based on the information in Table B-8.V[a]. The first two columns identify the annealing tests and column three lists the strength coefficients calculated from the ultimate strengths and uniform elongations of Bauer's isothermal annealing tests (Table B-8.IV). The column titled residual strength coefficient is the strength coefficient minus the sum of the strength coefficient for annealed cladding and the contribution of cold work calculated with the unmodified model for cold work annealing. The column titled CW/CW_o is the initial cold work divided into the post-anneal cold work predicted by the unmodified cold work annealing model. Comparison of the residual strengths and the column titled CW/CW_o shows that the residual strength coefficient is negative whenever the cold work is predicted to be partly annealed (CW/CW_o in the range 0.4 to 0.8). The most reasonable interpretation of this feature is to assume that the irradiation enhances the rate of annealing of the cold work. The change required to model this effect is to replace the constant B in Equation (B-8.43) by a function which increases with increasing fluence. The expression adopted for the strength coefficient annealing model is

$$B = 1.504\ [1 + 2.2\times10^{-25}\Phi] \qquad \text{(B-8.44)}$$

[a] A similar table was constructed from Bauer's transient annealing data. The transient data gave no new information.

TABLE B-8.V

STRENGTH AND RESIDUAL STRENGTH COEFFICIENTS
AFTER ISOTHERMAL ANNEALS

Temperature (kelvins)	Time at Temperature (minute)	Strength Coefficient (MPa)	Residual Strength Coefficient (MPa)	CW/CW_o
644	as-received	750.7	191.7	1
644	as-received	781.5	222.5	1
644	as-received	763.4	204.4	1
644	as-received	828.9	205.9	1
700	60	724.8	101.8	1
755	10	683.5	61.0	0.997
755	60	648.2	28.3	0.982
811	1	649.7	94.5	0.975
811	10	425.2	-100.1	0.780
811	30	460.8	-72.6	0.475
866	1	387.9	-125.1	0.700
866	5	417.2	-14.3	0.167
866	30	451.6	-0.9	0.000
894	1	411.3	-54.7	0.392
894	30	483.2	30.7	0.000
978	1	406.0	0	0.002
978	30	452.5	0	0.000

where

B = the rate constant in Equation (B-8.43)

ϕ = fast neutron fluence (neutrons/m^2).

Table B-8.VI lists the information of Table B-8.V using the revised rate constant of Equation (B-8.44). The residual strength coefficients are close to zero for temperatures above 866 kelvins and for the two long isothermal anneals at 811 kelvins.

The second step in producing a model for the effect of annealing on the strength coefficient of irradiated cladding is the derivation of expressions to describe the annealing of the residual strength coefficient. The expressions for the annealing of the residual strength coefficient are based on the values of this parameter presented in Table B-8.VI and on residual strengths obtained with the transient test data of Table B-8.III.

TABLE B-8.VI

STRENGTH AND RESIDUAL STRENGTH COEFFICIENTS
WITH MODIFIED COLD WORK ANNEALING MODEL

Temperature (kelvins)	Time at Temperature (minute)	Strength Coefficient (MPa)	Residual Strength Coefficient (MPa)	CW/CW_o
644	as-received	750.7	191.7	1
644	as-received	781.5	222.5	1
644	as-received	763.4	204.4	1
644	as-received	828.9	205.9	1
700	60	724.8	101.8	1
755	10	683.5	65.8	0.969
755	60	648.2	54.7	0.827
811	1	649.7	239.9	0.025
811	10	425.2	19.2	0.000
811	30	460.8	8.3	0.000
866	1	387.9	-18.1	0.000
866	5	417.2	+11.2	0.000
866	30	451.6	-0.9	0.000
894	1	411.3	+ 5.3	0.000
894	30	483.2	+30.7	0.000
978	1	406.0	0	0.000
978	30	452.5	0	0.000

Tables B-8.VII and B-8.VIII are a summary of the strength coefficients and residual strength coefficients obtained with the transient test data. Table B-8.VII groups the tests with equal maximum temperature together and Table B-8.VIII groups tests with equal heating rates together. Several trends used to develop the model for the annealing of the residual strength coefficient are apparent from an inspection of Tables B-8.VII and B-8.VIII.

Inspection of the data in Table B-8.VII shows that the residual strength coefficient does not anneal significantly in any of the tests with a maximum temperature of 755 kelvins. All of the tests with maximum temperature of 978 kelvins show essentially complete annealing. The tests with maximum temperatures of 811 kelvins show varying amounts of annealing but the effect of different heating rates (or, said another way,

TABLE B-8.VII

STRENGTH AND RESIDUAL STRENGTH COEFFICIENTS
AFTER TRANSIENT ANNEALS

Heating Rate (kelvins/s)	Maximum Temperature (kelvins)	Strength Coefficient (MPa)	Residual Strength Coefficient (MPa)	CW/CW_o
as-received	644	750.7	191.7	1
as-received	644	781.5	222.5	1
as-received	644	763.4	204.4	1
as-received	644	828.9	205.9	1
0.6	700	758.5	199.5	1
5.6	700	732.4	173.4	1
0.6	755	728.5	169.7	0.999
5.6	755	769.4	210.4	1.0
13.9	755	816.5	257.5	1.0
27.8	755	755.4	196.4	1.0
0.6	811	651.8	111.0	0.881
5.6	811	676.5	119.5	0.987
13.9	811	739.7	181.5	0.995
27.8	811	830.7	272.1	0.997
5.6	866	405.5	-115.0	0.749
13.9	866	660.5	118.2	0.891
27.8	866	772.4	220.0	0.944
0.6	894	397.0	-9.0	0.000
5.6	894	385.8	-79.7	0.389
13.9	894	514.9	4.0	0.685
27.8	894	681.8	149.2	0.828
0.6	978	370.1	-35.9	0.000
5.6	978	407.1	+1.1	0.000
13.9	978	384.9	-22.4	0.009
27.8	978	411.6	-8.7	0.932
27.8	1033	403.6	-2.4	0.001
27.8	1144	458.7	+52.7	0.000
27.8	1255	481.1	+75.1	0.000

TABLE B-8.VIII

STRENGTH AND RESIDUAL STRENGTH COEFFICIENTS
AFTER TRANSIENT ANNEALS

Heating Rate (kelvins/s)	Maximum Temperature (kelvins)	Residual Strength Coefficient (MPa)
as-received	644	191.7
as-received	644	222.5
as-received	644	204.4
as-received	644	205.4
0.6	700	199.5
0.6	755	169.7
0.6	811	111.0
0.6	894	-9.0
0.6	978	-35.9
5.6	700	173.4
5.6	755	210.4
5.6	811	119.5
5.6	866	-115.0
5.6	894	-79.7
5.6	978	
13.9	755	257.5
13.9	811	181.5
13.9	866	118.2
13.9	894	4.0
13.9	978	-22.4
27.8	755	196.4
27.8	811	272.1
27.8	866	222.0
27.8	894	149.2
27.8	978	-8.7
27.8	1033	-2.4
27.8	1144	+52.7
27.8	1255	+75.1

different times at temperature) on the residual strength coefficient is much less than one would expect from an expression like Equation (B-8.43). If an equation of the form of Equation (B-8.43) were used to model the annealing of the residual strength coefficient, the ratio of the logs of the measured residual strength coefficients after two anneals to the same maximum temperature would be predicted to be proportional to the heating rates. The four residual strengths measured after anneals with a maximum temperature of 811 kelvins (where annealing changes are greater than the scatter of the data) show significantly less dependence on heating rate. This observation is supported by the isothermal annealing data

of Table B-8.VI which also show relatively little dependence on the time at a given temperature.

When the transient data are grouped with equal heating rates together (Table B-8.VIII) a very strong dependence of residual strength on maximum temperature is apparent. For all of the heating rates, the annealing of the residual strength occurs over a range of maximum temperatures only about 75 kelvins wide. Moreover, the center of this 75 kelvins band is increased by only about 100 kelvins when the heating rate is increased by a factor of 50.

The approach used to model the annealing of the residual strength coefficient is to assume that this component is not subject to the rate equation used for the annealing of cold work effects. The assumption is logical not only because of the information in Tables B-8.VI and B-8.VIII but also because the probable cause of the residual strength coefficient is radiation damage – vacancies, interstitials, and dislocation loops, rather than cold work effects.

To describe the annealing of the residual strength coefficient, an empirical rate equation which is a generalized form of Equations (B-8.38) and (B-8.39) was written[a].

$$\frac{dy}{dt} = -B \exp\left(\frac{-Q}{T^m}\right) y^p \qquad \text{(B-8.45)}$$

where

y	=	irradiation contribution to the strength coefficient (MPa)
T	=	temperature (kelvins)
t	=	time (s)
B, Q, m,p	=	positive constants to be evaluated by comparison to the residual strength coefficient data of Tables B-8.VI to B-8.VIII.

The procedure used with the rate equation for the annealing of cold work effects [Steps (2) to (5) after Equation (B-8.39)] was repeated with Equation (B-8.45) to produce a differential expression for the change in y during a time interval with a linear change in temperature. The differential expression is

[a] Since the change in the strength coefficient due to irradiation is modeled as a linear function of fast neutron fluence [Equation (B-8.10)] one could use the fast neutron fluence in place of the variable y in this equation. The net effect would be a change of the constant B.

$$\frac{1}{(y_f)^{p-1}} = [p-1]\, B \left[\exp\left(\frac{-Q}{(T_f)^m}\right)\right] \left[\frac{1 - \exp\left(\frac{-Q\,[T_f-T_i]^m}{(T_f)^{m+1}}\right)}{\frac{Q\,[T_f-T_i]^m}{(T_f)^{m+1}}}\right] [t_f-t_i] + \frac{1}{(y_i)^{p-1}} \qquad \text{(B-8.46)}$$

Where terms with subscripts i refer to initial values and terms with subscripts f refer to final values of the terms in Equation (B-8.45).

The authors were unable to find a completely analytical method to obtain a best fit of Equation (B-8.45) to the data. However several observations aided in finding values of B, Q, m, and p which provide a fit which is within the scatter of the data.

(1) The factor

$$\frac{1 - \exp\left(\frac{-Q[T_f-T_i]^m}{(T_f)^{m+1}}\right)}{\frac{Q[T_f-T_i]^m}{(T_f)^{m+1}}}$$

can be viewed as a correction for the fact that the temperature did not remain at T_f throughout the anneal. It is not relevant to the fundamental annealing properties of the cladding.

(2) Increasing m increases the sensitivity of the change in y to the temperature because the factor exp $[-Q/(T_f)^m]$ is more sensitive to temperature when m is larger.

(3) Increasing p decreases the sensitivity of the change in y to the time span t_f-t_i. This is most easily seen by noting that for large y_i, y_f is proportional to

$$[t_f-t_i]^{\frac{1}{p-1}}$$

For large values of p, the $\frac{1}{p-1}$th root of t_f-t_i is relatively insensitive to t_f-t_i.

The residual strength data of Tables B-8.VI and B-8.VIII were fit by trying integral values of m and p, and using pairs of residual strengths from Table B-8.VIII in conjunction with the average value of the as-received residual strength (206 MPa) and Equation (B-8.46) to solve for trial values of Q and B. Predictions of Equation (B-8.46) with each trial set of m, p, Q, and B were then compared to all the residual strengths of Tables B-8.VI and B-8.VII. The best fit to the residual strength data was obtained with $m = 8$, $p = 2$, $Q = 5.35 \times 10^{23}$, and $B = 4.50 \times 10^{-3}$[a].

Two trivial steps are required to convert Equation (B-8.46) to the form actually used in MATPRO subcodes.

(1) The equation is transformed to an equivalent expression in terms of the initial temperature and heating rate. This transformation allows all the required input information to be parameters at the beginning of a time step. The transformation is carried out by using an alternate linear interpolation for temperature as noted in conjunction with Equation (B-8.42a).

(2) The equation is modified to express the change in residual strength in terms of an effective fluence for use in Equation (B-8.10).

The expression for the rate of annealing of the effective fast neutron fluence for strain hardening [Equation (B-8.36)] is obtained by assuming that the rate of annealing of the effective fast neutron fluence for the strain hardening exponent is proportional to the rate of annealing of the effective fluence for the strength coefficient. The model development is complicated by the fact that the cladding used to construct the model experienced three periods at high temperature in addition to the actual annealing test.

(1) The stress relief anneal

(2) The two-year in-reactor life of the rod

(3) The normal thermal transients during postirradiation handling of the rods[B-8.26].

The effective fast neutron fluence for the strain hardening exponent at the start of the actual annealing test can be estimated from Bauer's as-received data (Tables B-8.III or B-8.IV), Equation (B-8.4) and Equation (B-8.9). A maximum effective fluence of 8.4×10^{22} neutrons/m^2 (for zero effective cold work) is found. Since the measured fast neutron fluence was 4.3×10^{25} neutrons/m^2, considerable annealing of the radiation damage component which determines the strain hardening exponent must be assumed either in-reactor or during postirradiation handling of the rods.

---

[a] The 13.9 K/s anneals to 811 and 866 K were used to find these values of Q and B.

The constants used in Equation (B-8.36) are obtained by (a) assuming as-received effective fast neutron fluences in the range 1 x 10^{21} to 8 x 10^{22} neutrons/m^2, (b) determining a constant of proportionality between the annealing rates of effective fast neutron fluences for strength and strain hardening which yields a prediction consistent with the annealing data, (c) checking the first two steps by applying the annealing model to the in-reactor history to see if the assumed as-received effective fast neutron fluence and annealing rate are consistent. Self consistent results are obtained with an as-received effective fast neutron fluence for strain hardening of 2 x 10^{22} neutrons/m^2 and a constant of proportionality of 1000.

8.5.4 Comparison of Annealing Models to Data. Tables B-8.IX through B-8.XI are comparisons of the predicted strength coefficients and strain hardening coefficients to the

TABLE B-8.IX

COMPARISON OF MODEL PREDICTIONS OF K AND n
WITH DATA BASE FOR UNIRRADIATED CLADDING

Heating Rate (kelvin/s)	Maximum Temperature (kelvins)	Strength Coefficient (MPa)		Strain Hardening Exponent	
		From Data	Predicted	From Data	Predicted
as-received	644	524	524	0.040	0.040
5.6	811	524	524	0.040	0.040
5.6	866	520	521	0.040	0.047
5.6	894	503	515	0.047	0.062
5.6	978	444	457	0.218	0.119
27.8	811	515	524	0.035	0.040
27.8	866	514	524	0.033	0.041
27.8	894	513	522	0.035	0.044
27.8	978	516	505	0.045	0.087

data base used to construct the annealing models. The limited data for unirradiated cladding appear in Table B-8.IX. The cladding used in these tests had been 70% cold-worked then stress-relieved according to schedules published by R. H. Chapman[B-8.24]. Equations (B-8.33) and (B-8.35) predict an effective cold work of 50% for the strength coefficient and 4% for the strain hardening exponent after the stress relief anneal. Both strength coefficient and ductility are well predicted by the model.

Tables B-8.X and B-8.XI compare model predictions for strength coefficients and strain hardening exponents with corresponding values derived from Bauer's measurements with cold-worked and irradiated cladding. No annealing schedule has been published for this material but published nominal preirradiation values[B-8.21] are consistent with the assumption that the annealing schedule was similar to the unirradiated cladding. Therefore the effective cold works of 50% and 4% were also used to describe the irradiated cladding.

TABLE B-8.X

COMPARISON OF MODEL PREDICTIONS OF K AND n WITH DATA BASE FOR TRANSIENT ANNEALS OF IRRADIATED CLADDING

Heating Rate (kelvins/s)	Maximum Temperature (kelvins)	Strength Coefficient (MPa)		Strain Hardening Exponent	
		From Data	Predicted	From Data	Predicted
as-received	644	750.7	765.1	0.040	0.024
as-received	644	781.5	765.1	0.039	0.024
as-received	644	763.4	765.1	0.028	0.024
as-received	644	828.9	765.1	0.037	0.024
0.6	700	758.5	764.6	0.021	0.024
0.6	755	728.5	721.3	0.027	0.024
0.6	811	651.8	574.1	0.023	0.029
0.6	894	397.0	442.7	0.091	0.092
0.6	978	370.1	409.9	0.088	0.100
5.6	700	732.4	765.1	0.020	0.024
5.6	755	769.4	759.9	0.024	0.024
5.6	811	676.5	706.2	0.023	0.025
5.6	866	405.5	598.7	0.029	0.030
5.6	894	385.8	547.0	0.047	0.041
5.6	978	407.1	441.0	0.100	0.083
13.9	755	816.5	762.9	0.024	0.024
13.9	811	739.7	736.9	0.022	0.024
13.9	866	680.5	660.5	0.025	0.026
13.9	894	514.9	611.6	0.021	0.031
13.9	978	384.9	482.9	0.056	0.071
27.8	755	755.4	764.0	0.021	0.024
27.8	811	830.7	750.2	0.027	0.024
27.8	866	772.4	700.6	0.027	0.025
27.8	894	681.8	662.1	0.026	0.027
27.8	978	411.6	532.3	0.034	0.054
27.8	1033	403.6	476.4	0.046	0.074
27.8	1144	458.7	439.7	0.083	0.081
27.8	1255	481.1	428.7	0.100	0.084

8.6 Effects of Oxygen Concentration on Plastic Deformation

The general effect of oxygen concentration on the mechanical properties of zircaloy is to increase the strength and decrease the ductility of the zircaloy. This section describes the correlations used to modify specific parts of the general stress-strain correlation [Equation (B-8.3)].

TABLE B-8.XI

COMPARISON OF MODEL PREDICTIONS OF K AND n WITH DATA BASE FOR ISOTHERMAL ANNEALS OF IRRADIATED CLADDING

Temperature (kelvins)	Time (minutes)	Strength Coefficient (MPa)		Strain Hardening Exponent	
		From Data	Predicted	From Data	Predicted
644	as-received	750.7	765.1	0.040	0.024
644	as-received	781.5	765.1	0.039	0.024
644	as-received	763.4	765.1	0.028	0.024
644	as-received	828.9	765.1	0.037	0.024
700	60	724.8	700.8	0.033	0.024
755	10	683.5	567.7	0.028	0.028
755	60	648.2	512.7	0.030	0.036
811	1	649.7	547.9	0.029	0.032
811	10	425.2	421.9	0.031	0.080
811	30	460.8	409.5	0.050	0.100
866	1	387.9	428.5	0.044	0.080
866	5	417.2	411.3	0.077	0.097
866	30	451.6	408.0	0.096	0.106
894	1	411.3	420.4	0.076	0.088
894	30	483.2	407.8	0.130	0.108
978	1	406.0	414.2	0.074	0.093
978	30	452.5	407.6	0.112	0.110

8.6.1 Effects of Oxygen Concentration on the Strength Coefficient. There are no data which may be used directly to find the influence of oxygen on the strength coefficient. However, data do exist which may be manipulated to yield this information. Because different types of data are available for high and low temperatures, different analytical techniques were used for these temperature ranges and the analyses are presented separately.

(1) Low Temperature Strength Coefficient Data. In the range 300 to 650 kelvins, which includes typical light-water-reactor operating temperatures, the effect of oxygen concentration may be obtained from measurements of the change in the ultimate tensile strength (UTS) of zircaloy as a function of oxygen content. The true strain at maximum engineering stress, that is, the engineering stress at the onset of plastic instability in a tensile test on sheet specimens at constant strain rate, is given by Equation (B-8.16) which is rewritten here for convenience:

$$K = \frac{S_{max} \exp\left(\frac{n}{1+m}\right)}{\left(\frac{n}{1+m}\right)^{n} \left(\frac{\dot{\epsilon}}{10^{-3}/s}\right)^{m}} \qquad \text{(B-8.47)}$$

where

S_{max} = the ultimate tensile strength in a tensile test (Pa).

When $\dot{\epsilon}$ was specified in the data, it was 10^{-3}/s. Since 10^{-3}/s is a typical value for $\dot{\epsilon}$ in tensile tests, this value was assumed when not specified. In this case Equation (B-8.47) reduces to

$$K = S_{max}\left[\frac{\exp\left(\frac{n}{m+1}\right)}{\left(\frac{n}{m+1}\right)^{n}}\right]. \qquad \text{(B-8.48)}$$

A paper by Rubenstein[B-8.27] gives values for the UTS as a function of oxygen concentration for temperatures ranging from about 300 to 650 kelvins. For this range, MATPRO estimates an m of 0.02 for as-received zircaloy. Therefore m has very little effect on the value of K calculated with Equation (B-8.48) and can be neglected. The value for n predicted by MATPRO varies from 0.119 to 0.144 in this temperature range, causing the term $\exp(n)/n^n$ of Equation (B-8.47) (with m = 0) to vary from 1.45 to 1.53. If this term is replaced by 1.49 for all temperatures, the maximum error introduced is smaller than 3%, which is substantially less than the scatter in the data. Therefore, the strength coefficient in this temperature range has been calculated by simply multiplying the UTS by 1.49. Strength coefficients calculated in this way using data taken from Rubenstein are presented in Table B-8.XII. The lowest concentration for each temperature (9×10^{-3} weight fraction) was assumed to be the concentration of the as-fabricated zircaloy. With this information, the ratio K/K_0, where K_0 is the strength coefficient of as-received zircaloy, may be calculated, and these data are also shown in the table.

(2) High Temperature Strength Coefficient Data. All of the information used to model the effects of oxygen concentration on the high temperature plastic deformation of zircaloy was taken from a report by Chung, Garde, and Kassner[B-8.28] of the Argonne National Laboratory. Rather than reporting the stress associated with a given strain, however, the Argonne group made a computer fit of their data to a flow curve equation known as the Ludwik Equation[B-8.29],

$$\sigma = K \epsilon^{n} + \sigma_0 \qquad \text{(B-8.49)}$$

and reported only the parameters K, n, and σ_0 for many different strain intervals and oxygen concentrations. The additional variable σ_0 will cause the stress σ resulting from Equation (B-8.49) for a given ϵ to differ from that of Equation (B-8.3) for the same K and n.

TABLE B-8.XII

STRENGTH COEFFICIENT CALCULATED WITH DATA OF L. S. RUBENSTEIN

Temperature (kelvins)	Oxygen Content (weight fraction)	Ultimate Tensile Strength (MPa)	Calculated K (MPa)	K/K_o
297	0.0009	524	781	1.00
297	0.0018	616	918	1.18
297	0.0034	785	1170	1.50
297	0.0063	949	1414	1.81
422	0.0009	354	527	1.00
422	0.0034	544	811	1.54
422	0.0063	680	1013	1.92
533	0.0009	266	396	1.00
533	0.0018	298	444	1.12
533	0.0034	361	538	1.36
533	0.0063	462	688	1.74
644	0.0009	227	338	1.00
644	0.0018	241	359	1.06
644	0.0034	283	422	1.25
644	0.0063	373	556	1.64

The Argonne curves generally start at strains of 0.0004 and their data are fit accurately to the Ludwik equation by dividing the flow curve into two or three strain intervals with different values of K, n, and σ_o for each interval. There are scattered examples in the Argonne results indicating that this approach may be inappropriate for small strains. In several of these cases σ_o is less than zero. Since σ_o can be interpreted as the yeild stress[B-8.29] a negative value indicates a physical inconsistency. To avoid these problems, the Argonne correlations were used only for strains greater than an arbitrarily chosen minimum of 0.002.

To get a base for a model, "data" were generated using Equation (B-8.49) and fit to Equation (B-8.3), (the "Holloman" Equation). The strain interval (from 0.002 to the maximum reported strain) was divided into 20 equally spaced intervals for each temperature-oxygen content combination. The Ludwik equations were then used to find a stress associated with each strain, and the resulting stress-strain pairs were fit by the method of least-squares to the Holloman Equation. Only those tests where $\dot{\epsilon} = 10^{-3}/s$ were used. This included 82 equations describing 60 different samples. The fluctuations in the resulting strength coefficient and the strain hardening exponent were much smaller for the Holloman Equation than they were for the Ludwik Equation.

For these derived data the ratio (K/K_o) was calculated as was done with the low temperature data. As with the Rubenstein data, (K/K_o) increases with oxygen concentration for all temperatures.

(3) Correlation for the Effect of Oxygen Concentration on the Strength Coefficient. Because little is known about the physical mechanism causing the strength coefficient of zircaloy to change with oxygen concentration, a model based on theory is not possible at this time. An empirical fit to the data is therefore the approach chosen. In addition to fitting the data, the correlation should satisfy the obvious condition that $(K/K_o) = 1$ when $C = C_o$. A quite simple correlation which does this is

$$\frac{K}{K_o} = a_0 + a_1 (C-C_o) \qquad \text{(B-8.50)}$$

where

C = oxygen concentration (weight fraction)

C_o = oxygen concentration of as-received zircaloy (weight fraction)

a_0 = 1.0

a_1 = a function of temperature to be determined (weight fraction)$^{-1}$.

An equation of the form of Equation (B-8.50) for each temperature can be generated by a least-squares fitting technique using the data. However, this technique does not always give $a_0 = 1.0$. For most cases a_0 is close to 1.0, but there are exceptions. Thus a least-squares fitting technique with the constraint that $a_0 = 1$ was used. With this constraint, values for a_1 were calculated for each temperature. These results are presented in Table B-8.XIII.

The ratio (K/K_o) derived from Equation (B-8.50) with $a_0 = 1$ and a_1 taken from Table B-8.XIII is plotted as a function of oxygen concentration for all temperatures used in Figure B-8.8. The data are shown on the same figure. The six lowest temperatures are represented by a single line with $a_1 = 130$ because they are too close together to be distinguishable.

The general characteristics of the temperature dependence of a_1 are that it is relatively constant until about 1200 kelvins, rises rapidly between 1200 and 1400 kelvins, and then begins to level off. The leveling off is based on only the data point at the highest temperature. However there are too few data to justify a sophisticated correlation. A single function can be found which fits the data with acceptable accuracy over the entire temperature range, thus having the advantages of automatically avoiding discontinuities and fitting compactly into a computer routine. For $300 < T < 1673$ kelvins, the function is

TABLE B-8.XIII

RATE OF CHANGE OF K/K_o WITH OXYGEN CONTENT

Temperature (kelvins)	a_1
297	160
422	178
533	137
644	115
1123	89
1173	95
1223	343
1273	541
1323	676
1373	891
1673	1116

$$a_1 = 1120 - \frac{990}{\exp\left[\frac{T-1301.5}{61}\right] + 1} \cdot \qquad \text{(B-8.51)}$$

Equation (B-8.51) is plotted as function of temperature in Figure B-8.9 where it is compared with the data from Table B-8.XIII.

A comparison of the values of (K/K_o) predicted by Equations (B-8.50) and (B-8.51) with the data shows the average percentage error is 12%. All the points except those at 1123 and 1173 kelvins have percentage errors of this size or less. At these two temperatures the average percentage error is 45%. These uncertainties can serve only as a rough guide in assessing the accuracy of the model since they were calculated by comparing the correlation to its own data base.

8.6.2 Effect of Oxygen Concentration on the Strain Hardening Exponent. The methods of development and the form of the equations used to correlate oxygen content with changes in the strain hardening exponent, n, are identical to those used for the analogous changes in the strength coefficient.

(1) High Temperature Strain Hardening Exponent Data. The only data available are those from Chung et al which were all taken at high temperature.

(2) Correlation for the Effect of Oxygen Concentration on the Strain Hardening Exponent. The ratio (n/n_o) is modeled using the equation

$$\frac{n}{n_o} = 1 + a_2 (C-C_o) \qquad \text{(B-8.52)}$$

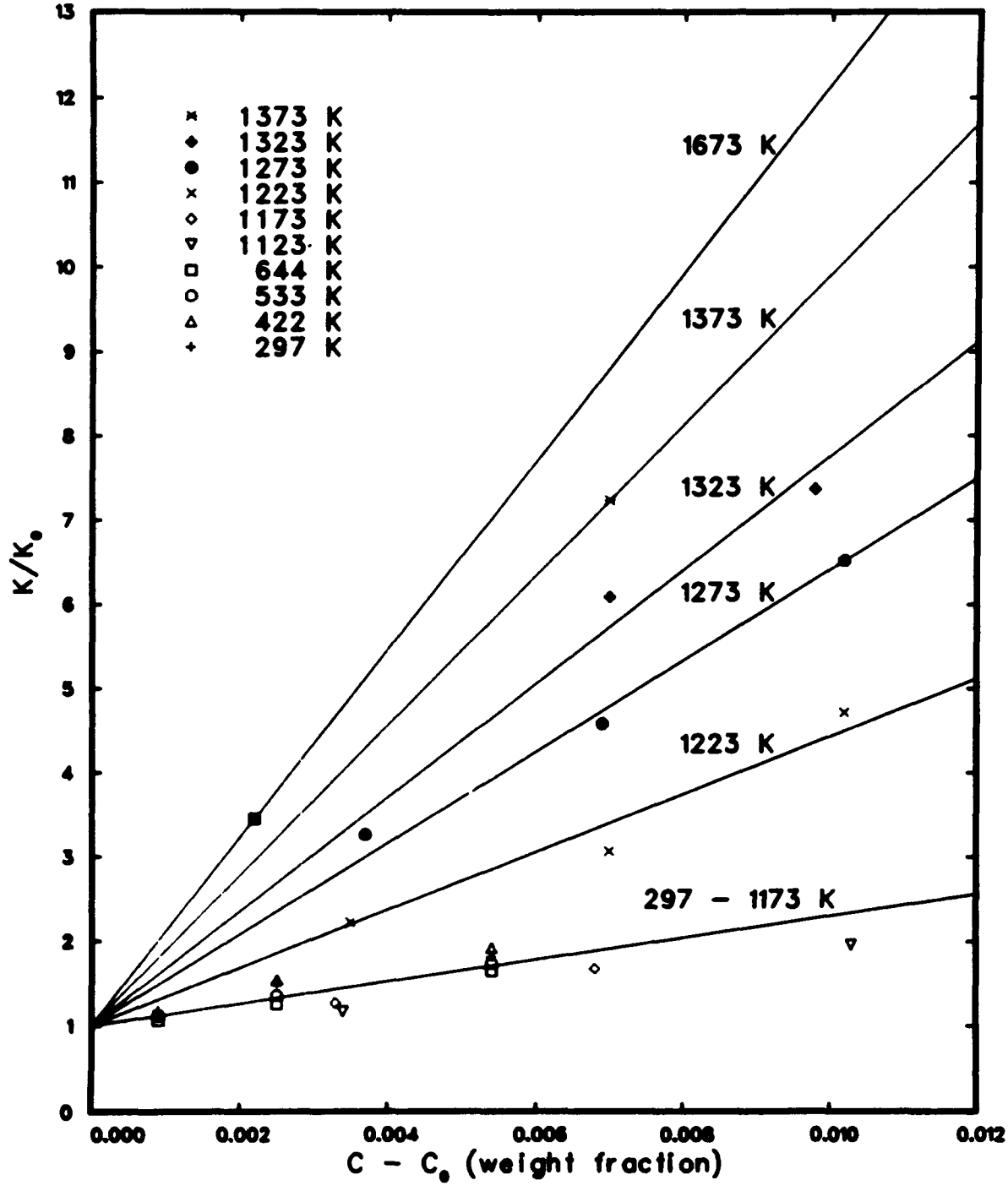

Fig. B-8.8 Calculated ratios of the strength coefficients of zircaloy containing oxygen (K) and the strength coefficients of as-fabricated zircaloy (K_o) as a function of oxygen concentration for several temperatures.

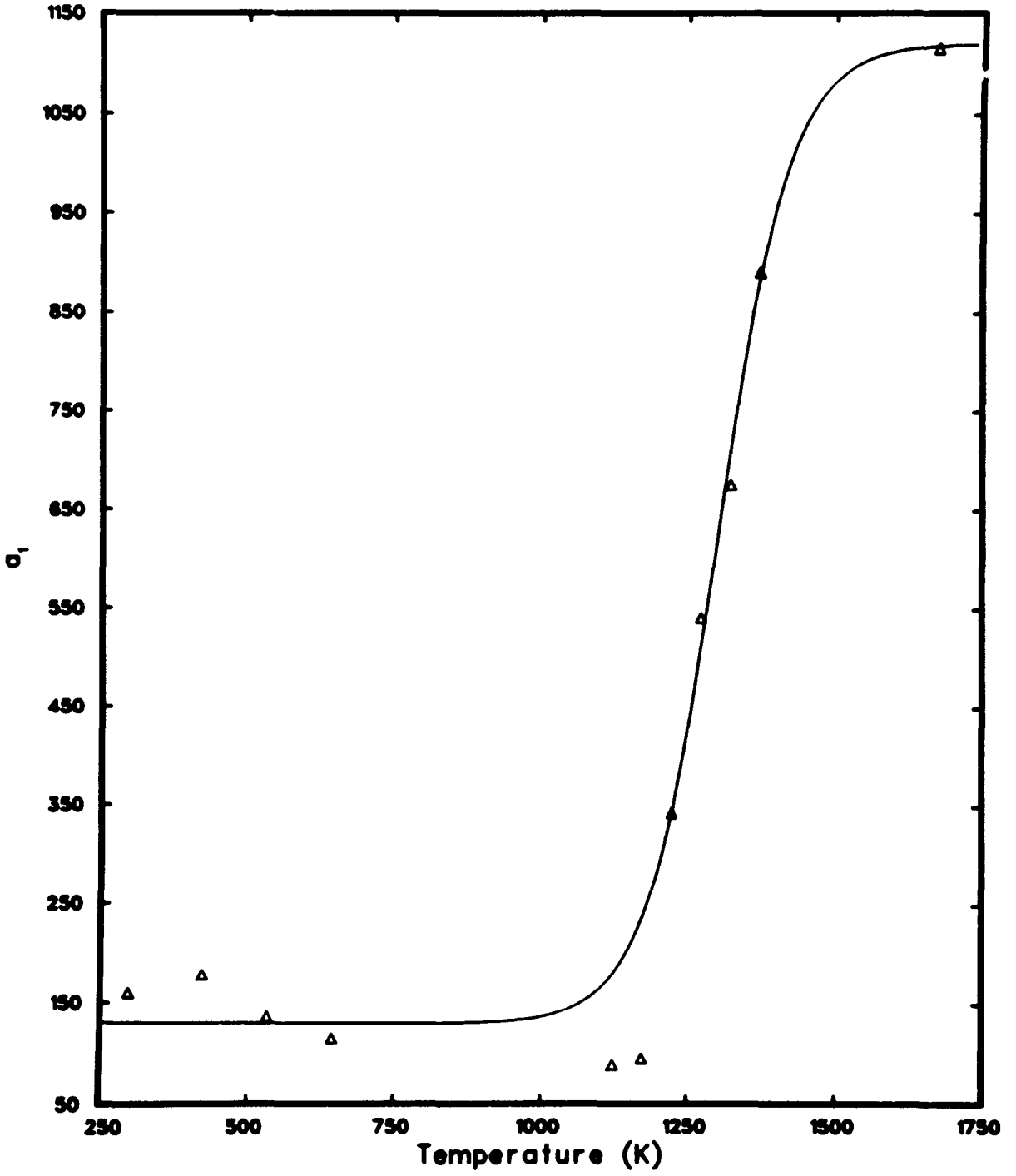

Fig. B-8.9 Calculated curve and data showing the rate of change of the zircaloy strength coefficient with oxygen content as a function of temperature.

where

a_2 = a function of temperature to be determined.

A fit of Equation (B-8.52) to the data gives the values for a_2 listed in Table B-8.XIV.

TABLE B-8.XIV

RATE OF CHANGE OF n/n_o WITH OXYGEN CONTENT

Temperature (kelvins)	a_2
1123	-19.0
1173	4.9
1223	-12.7
1273	-11.1
1323	340.0
1373	244.3
1673	1245.0

The lines given by Equation (B-8.52) using the values of a_2 listed in Table B-8.XIV are plotted in Figure B-8.10 with their data bases.

The data presented in Table B-8.XIV and Figure B-8.10 show considerable scatter. It is possible that this is a reflection of actual physical processes. Systematic oscillations in such things as the total strain at failure and the strain at maximum engineering stress have been repeatedly documented in the Argonne Quarterly Reports[B-8.28, B-8.30 – B-8.32], and these oscillations may be due in part to variations in the strain hardening exponent. More data are needed to accurately quantify these variations. Therefore only the general features that the coefficient a_2 in Equation (B-8.52) is very small below about 1300 kelvins, rises rapidly between 1300 and 1400 kelvins and then levels off above 1500 kelvins are treated in this model. The function used is

$$a_2 = 1250 - \frac{1250}{\exp(T-1380/20) + 1} \qquad \text{(B-8.53)}$$

for $1123 < T < 1673$ kelvins.

Equation (B-8.53) is plotted in Figure B-8.11 where it is compared with the data from Table B-8.XIV.

At temperatures below 1100 kelvins, a_2 calculated with Equation (B-8.53) is negligibly small, so that $(n/n_o) = 1$. This means that the strain hardening exponent is unchanged by the presence of oxygen. Therefore the lower limit of the model may be extended down to operating temperatures without affecting the stress-strain laws now in MATPRO.

The uncertainty in the predictions of Equations (B-8.52) and (B-8.53) when compared with the data base is quite large. The one standard deviation limits are ±42%. There are two data which are in error by more than 100%, but since the data indicate that the strain hardening exponent changes by a factor of five or more in some cases, the model is certainly better than entirely neglecting oxygen effects.

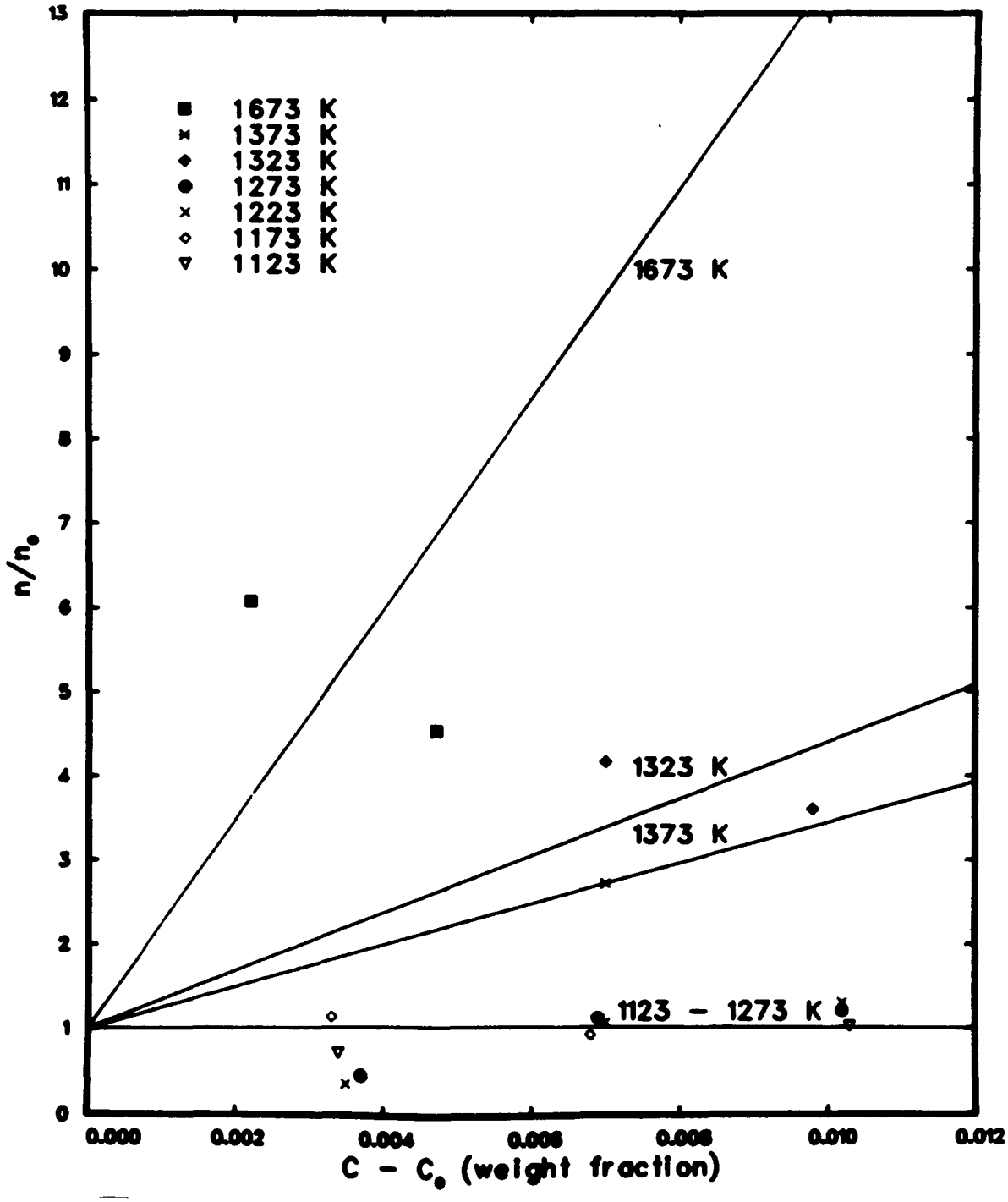

Fig. B-8.10 Calculated ratios of the strain hardening exponents of zircaloy containing oxygen (n) and the strain hardening exponents of as-fabricated zircaloy (n_0) as a function of oxygen concentration for several temperatures.

8.6.3 Effect of Oxygen Concentration on the Strain Rate Sensitivity Exponent. As with the strength coefficient and the strain hardening exponent, the data used for determining the effect of oxygen concentration on the strain rate sensitivity exponent (m) of Equation (B-8.3) are taken from Chung et al. In this case however the data may be used directly, since they are consistent with the Holloman Equation [Equation (B-8.3)], as will be shown in the next subsection.

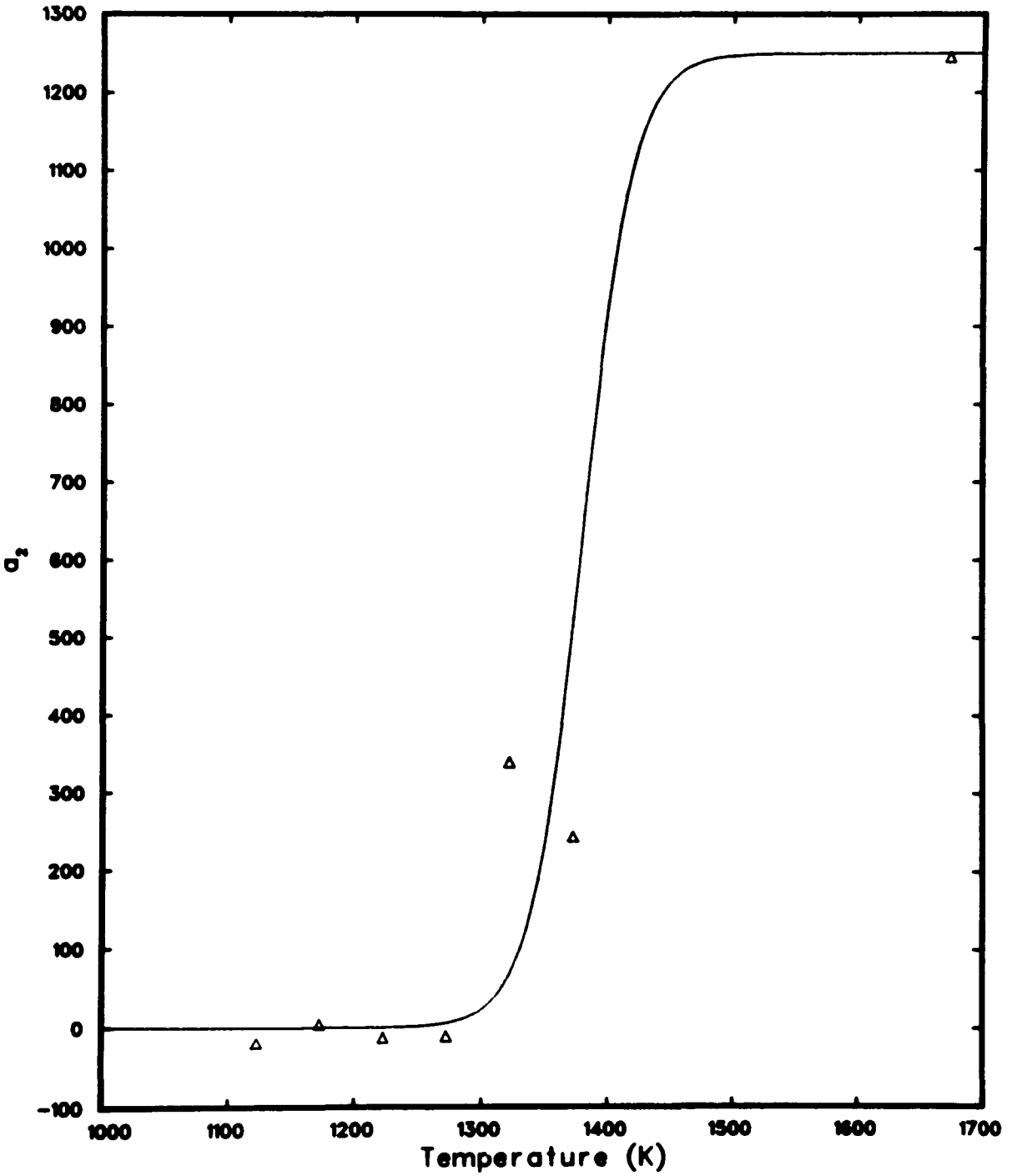

Fig. B-8.11 Calculated curve and data showing the rate of change of the zircaloy strain hardening exponent as function of temperature.

(1) Experimental Technique. Chung et al[B-8.9] measured m by quickly changing the strain rate during a stress-strain test, causing a change in the stress, σ. If the change occurs rapidly, the strain itself does not change significantly during the transient, and m may be found from the equation

$$(\sigma_1/\sigma_2) = (\dot{\varepsilon}_1/\dot{\varepsilon}_2)^m \qquad \text{(B-8.54a)}$$

or

$$m = \frac{\ln (\sigma_1/\sigma_2)}{\ln (\dot{\varepsilon}_1/\dot{\varepsilon}_2)} \qquad \text{(B-8.54b)}$$

where

σ_1 = stress immediately before the transient (Pa)

σ_2 = stress immediately after the transient (Pa)

$\dot{\epsilon}_1$ = strain rate before the transient (s^{-1})

$\dot{\epsilon}_2$ = strain rate after the transient (s^{-1}).

Taking the logarithm of both sides of Equation (B-8.3) for two cases with different stresses and strain rates, but the same strain,

$$\ln (\sigma_1) = \ln (K) + n [\ln (\varepsilon)] + m [\ln (\dot{\varepsilon}_1)] - m[\ln (10^{-3})] \qquad \text{(B-8.55a)}$$

$$\ln (\sigma_2) = \ln (K) + n [\ln (\varepsilon)] + m[\ln (\dot{\varepsilon}_2)] - m[\ln (10^{-3})]. \qquad \text{(B-8.55b)}$$

Subtracting Equation (B-8.55b) from Equation (B-8.55a) yields Equation (B-8.54b), so the strain rate sensitivity exponents measured by Chung et al may be used directly in Equation (B-8.3).

(2) High Temperature Strain Rate Sensitivity Exponent Data. The data were taken from two Argonne Quarterly Reports[B-8.28, B-8.30] and as with the strain hardening exponent, cover the temperature range from 1123 to 1673 kelvins. These data are shown in Figure B-8.12, where m is plotted as a function of oxygen concentration for seven temperatures. The changes in m with temperature reflect the changes predicted by MATPRO. The 1173 kelvins curve is anomalous because at this temperature the as-received zircaloy is in the alpha + beta transition phase region[a]. It is evident that m decreases with increasing C in all cases, and each curve resembles an exponential decay, although the scatter in the data precludes quantification of the temperature dependence.

Only the ratio (m/m_o) as a function of concentration was modeled as shown in Figure B-8.13. The equation used was

$$\frac{m}{m_o} = \exp [-69 (C-C_o)] \qquad \text{(B-8.56)}$$

[a] This explanation will not suffice to explain the low values of m at 1473 kelvins, where the material remains in the beta region over the entire range of oxygen concentrations reported, as may be seen in the phase diagram, Figure B-8.14, taken from Chung et al[B-8.28].

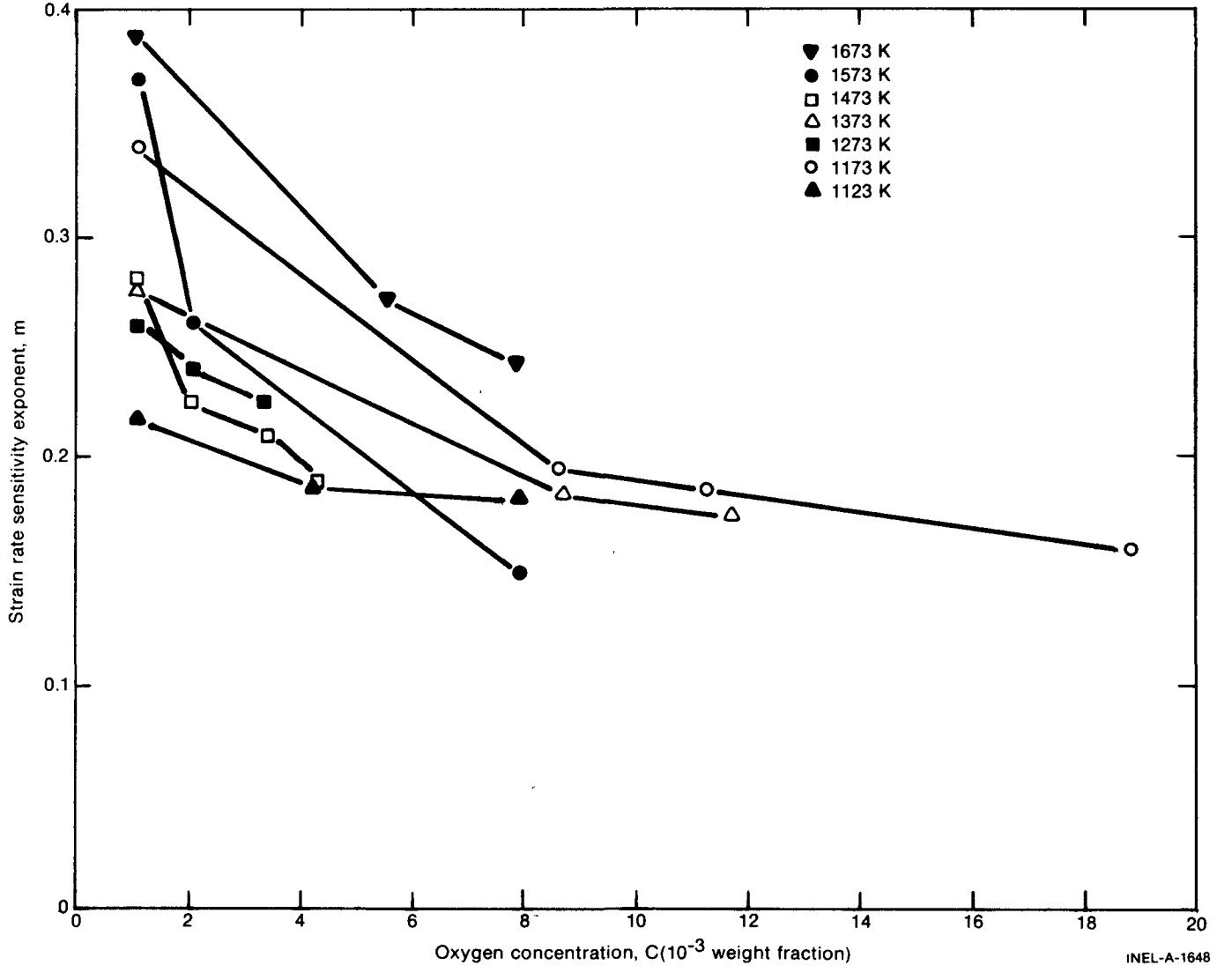

Fig. B-8.12 Strain rate sensitivity exponent (m) data as a function of oxygen concentration from Chung et al.

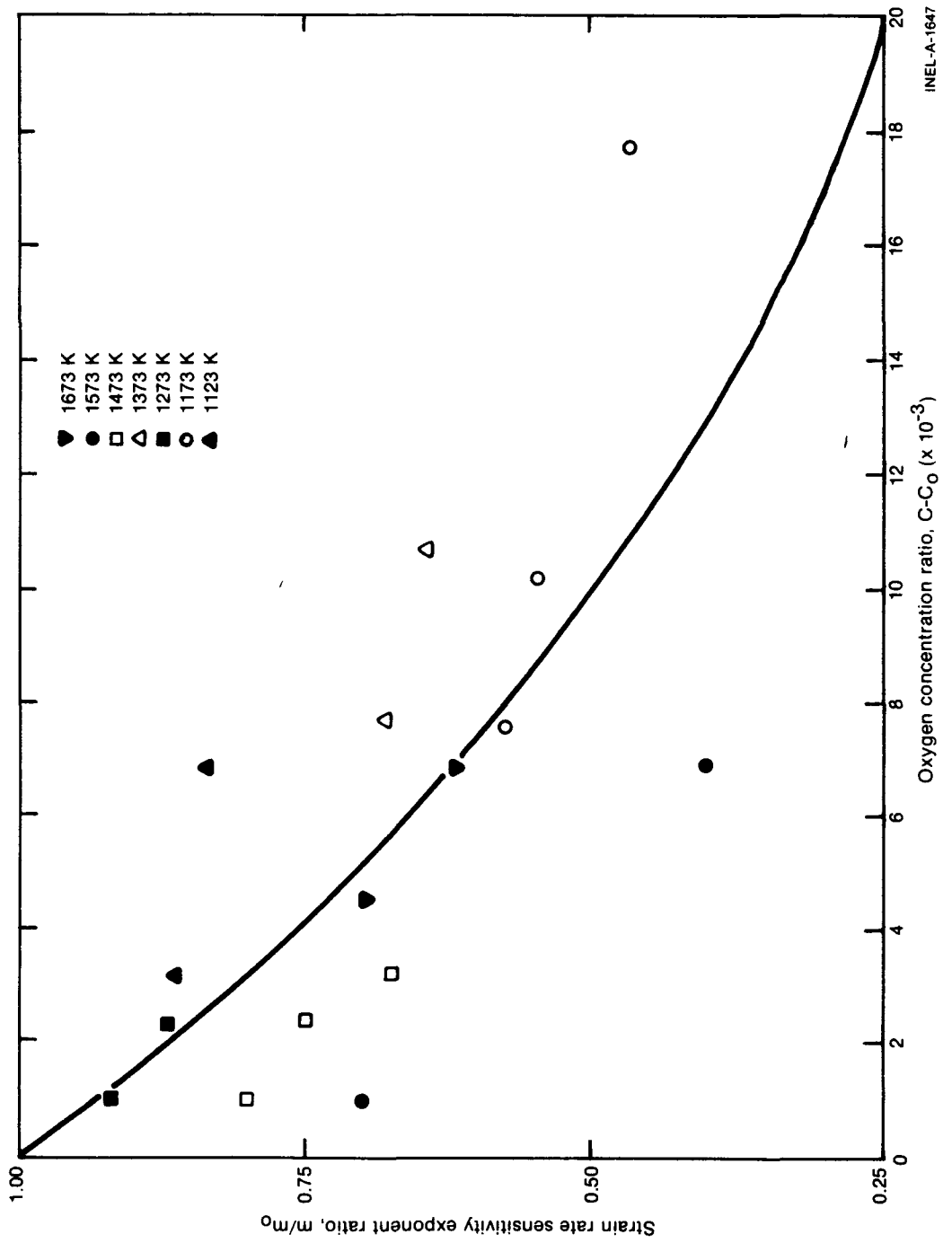

Fig. B-8.13 The ratio m/m_o as a function of oxygen concentration showing Chung et al data and the line used to fit to these data.

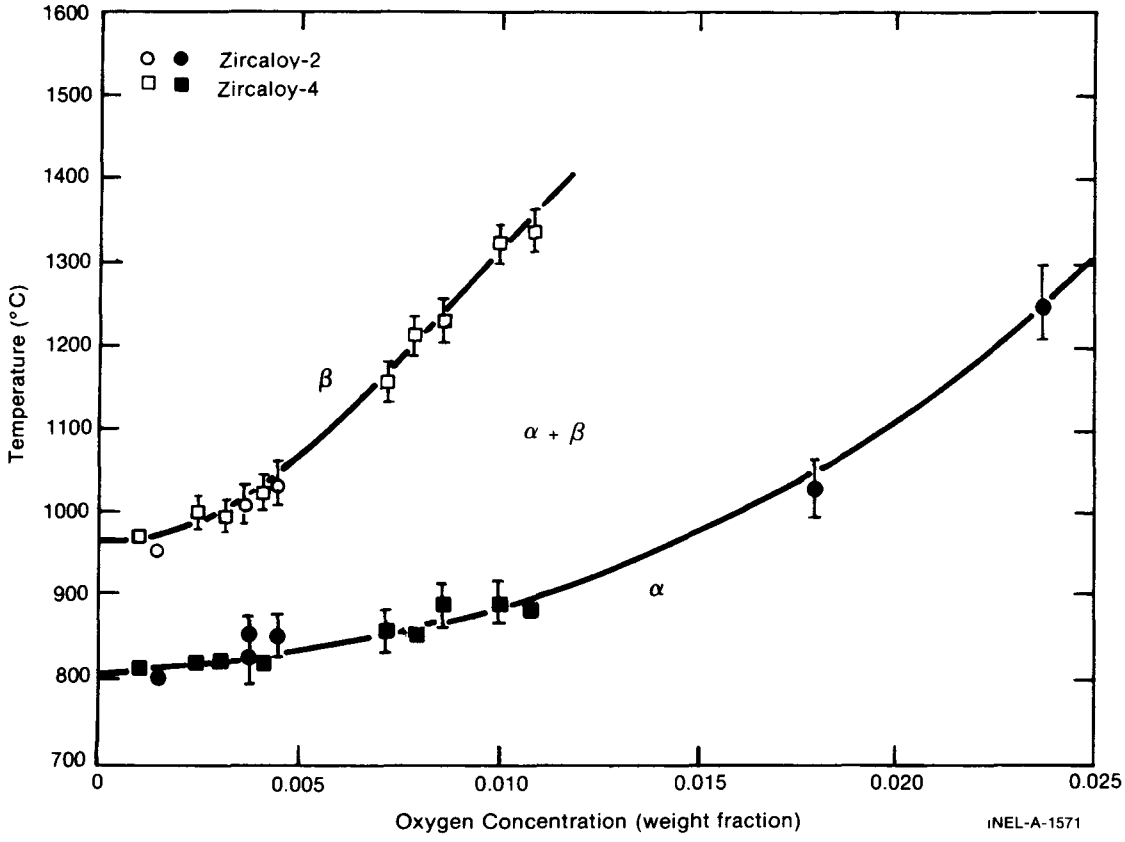

Fig. B-8.14 Zircaloy-oxygen phase diagram, taken from Chung et al.

where

m_o = strain rate sensitivity constant for as-received material.

The number 69 in the argument of the exponent in Equation (B-8.56) was obtained by a least-squares fit of the data to the equation.

The quality of the fit of Equation (B-8.56), using Chung's values for m_o can be seen in Figure B-8.13. Although a quantitative statement cannot be made at this time, the scatter may be partly the result of phase transitions which can occur even isothermally with changes in oxygen content (Figure B-8.14). For example, at 1123 kelvins, m_o is measured using material which is midway through the alpha + beta transition phase; while the material at the highest oxygen concentration point at 1123 kelvins is oxygen-stabilized, alpha phase, zircaloy. That this point is quite far from the calculated curve may be a reflection of the failure to consider the effects of the phase transition.

To include the 68% of the data which should fall within one standard deviation from the calculated line, the coefficient 69 of Equation (B-8.56) must be given quite large uncertainty limits: ±40. The data lying below the calculated line in Figure B-8.13, especially those for which $(C\text{-}C_o) = 10^{-3}$, contribute much to the uncertainty because they require particularly large values to make the curve drop abruptly enough from its starting point to pass through them.

8.6.4 Flow Curves Showing the Effect of Oxygen Concentration. Three figures are presented in this section to show how oxygen concentration affects the plastic deformation portion of the stress-strain curves predicted by MATPRO. Equations (B-8.50) to (B-8.53) and Equation (B-8.56) were used in conjunction with the MATPRO subroutines to generate these plots. All plots show two curves, one for as-fabricated zircaloy ($C-C_o = 0$) and one for zircaloy containing a total of about five times the as-fabricated oxygen level ($C-C_o = 0.005$ weight fraction). Unless otherwise specified, the as-fabricated oxygen content, C_o, was assumed to be 0.0012 weight fraction.

Figure B-8.15 shows the flow curves at 600 kelvins, a temperature typical of PWR normal operation. The strain rate was taken as 10^{-3}/s, so that the strain rate dependence on oxygen content was not a factor. At this temperature Equations (B-8.52) and (B-8.53) predict a completely negligible change in n, the strain hardening exponent. The entire difference between the curves thus results from the change in K, which, for these conditions increases by a factor of 1.65.

Figure B-8.16 shows flow curves for conditions the same as those of Figure B-8.15 except that the temperature is 1400 kelvins, which is characteristic of temperatures postulated for reactor accidents such as a loss-of-coolant accident or a power-cooling-mismatch. At this temperature, K increases by a factor of 5.8 and n by a factor of 5.6. Since the curve with $C-C_o = 0$ is nearly flat except at very small strains, the increasing slope of the curve for $C-C_o \neq 0$ is largely due to the change in n caused by the extra oxygen.

Figure B-8.17 shows the stress required to cause a strain of 0.1 at various strain rates. This figure is included to illustrate the effect of oxygen concentration on the strain rate exponent. Nearly all of the difference between the oxidized and unoxidized cladding is caused by the change in the strength coefficient. Careful examination of the curves will show a slightly increasing separation between them as the strain rate increases. The separation of the curves increases by only 2.5% as the strain rate changes from 10^{-4} to 10^{-2}. However, under these conditions, if m were unchanged by oxygen concentration, but K still affected, the increase would be 9.3%. In general the effect of oxygen concentration on m is to increase $\frac{d\sigma}{d\dot{\epsilon}}$ for $\dot{\epsilon} < 10^{-3}$/s and to decrease $\frac{d\sigma}{d\dot{\epsilon}}$ for $\dot{\epsilon} > 10^{-3}$/s. For the strain rate range of Figure B-8.17, approximately nine-tenths of the strain rates are greater than 10^{-3}/s, therefore the net effect is a slope smaller than would be found if m were not a function of oxygen concentration. These observations must still be regarded as tentative since Equation (B-8.20) was derived from data taken at strain rates close to 10^{-3}/s and these data exhibited large scatter.

8.7 Cladding Stress Subcodes CSTRES, CSIGMA, and CANEAL Listings

Tables B-8.XV to B-8.XVII are listings of the CSTRES, CSIGMA, and CANEAL subcodes, respectively. The subroutine CKMN presented in Table B-8.XVIII is called by CSTRES and CSIGMA to obtain values for the strength coefficient, strain rate sensitivity exponent, and strain hardening exponent.

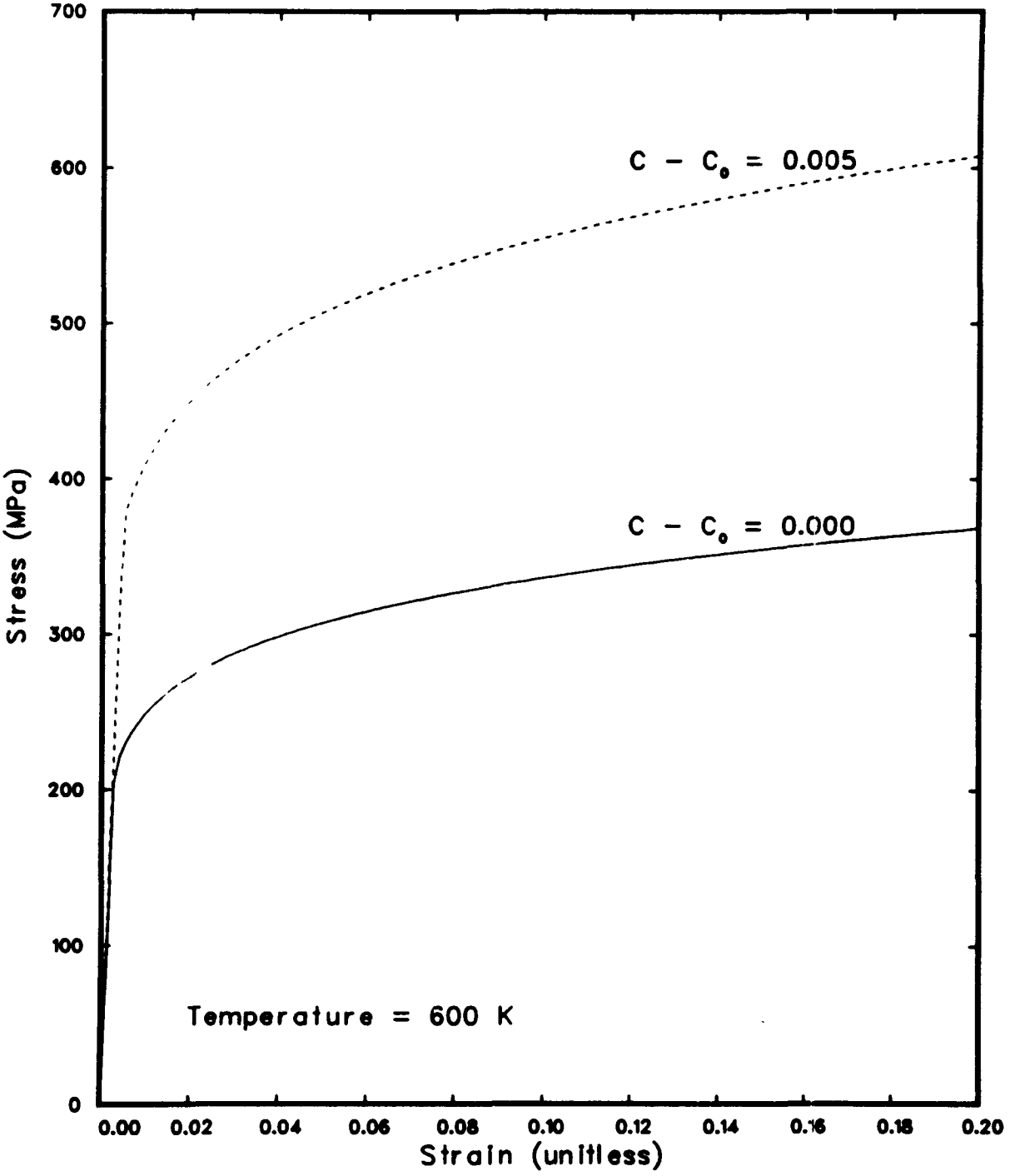

Fig. B-8.15 Stress as a function of strain at a strain rate of 10^{-3}/s for two oxygen concentrations at 600 K.

8.8 References

B-8.1. C. C. Busby, "Longitudinal Uniaxial Tensile and Compressive Properties," *Properties of Zircaloy-4 Tubing*, WAPD-TM-585 (December 1966).

B-8.2. H. M. Chung, A. M. Garde, T. F. Kassner, *Light-Water-Reactor Safety Research Program: Quarterly Progress Report, April-June 1975*, ANL-75-58 (June 13, 1975).

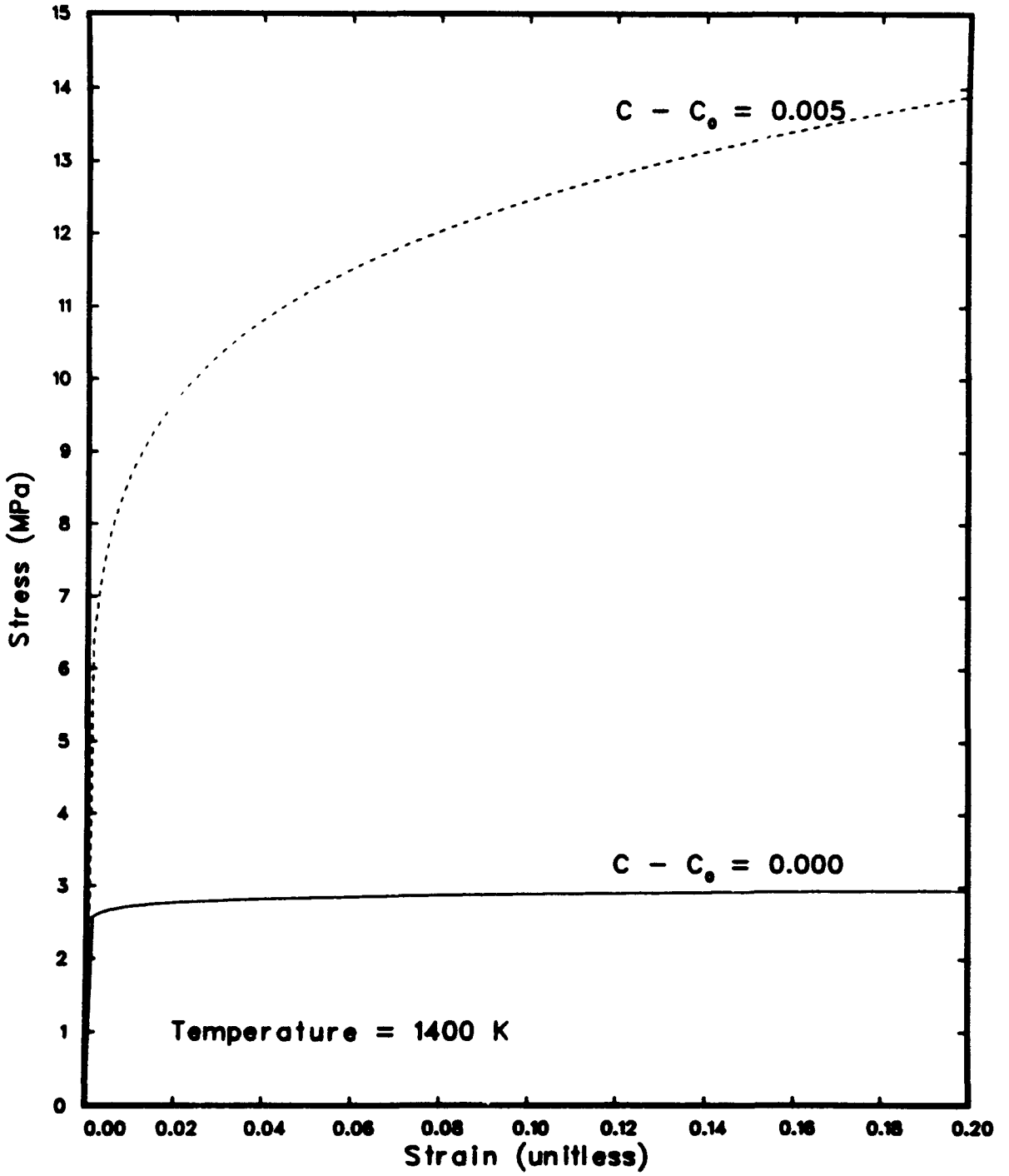

Fig. B-8.16 Stress as a function of strain at a strain rate of 10^{-3}/s for two oxygen concentrations at 1400 K.

B-8.3. R. L. Mehan and F. W. Wiesinger, *Mechanical Properties of Zircaloy-2,* KAPL-2110 (February 1, 1961).

B-8.4. D. Lee and W. A. Backofen, "Superplasticity in Some Titanium and Zirconium Alloys," *Transactions of the Metallurgical Society of AIME, 239* (July 1967) pp 1034-1040.

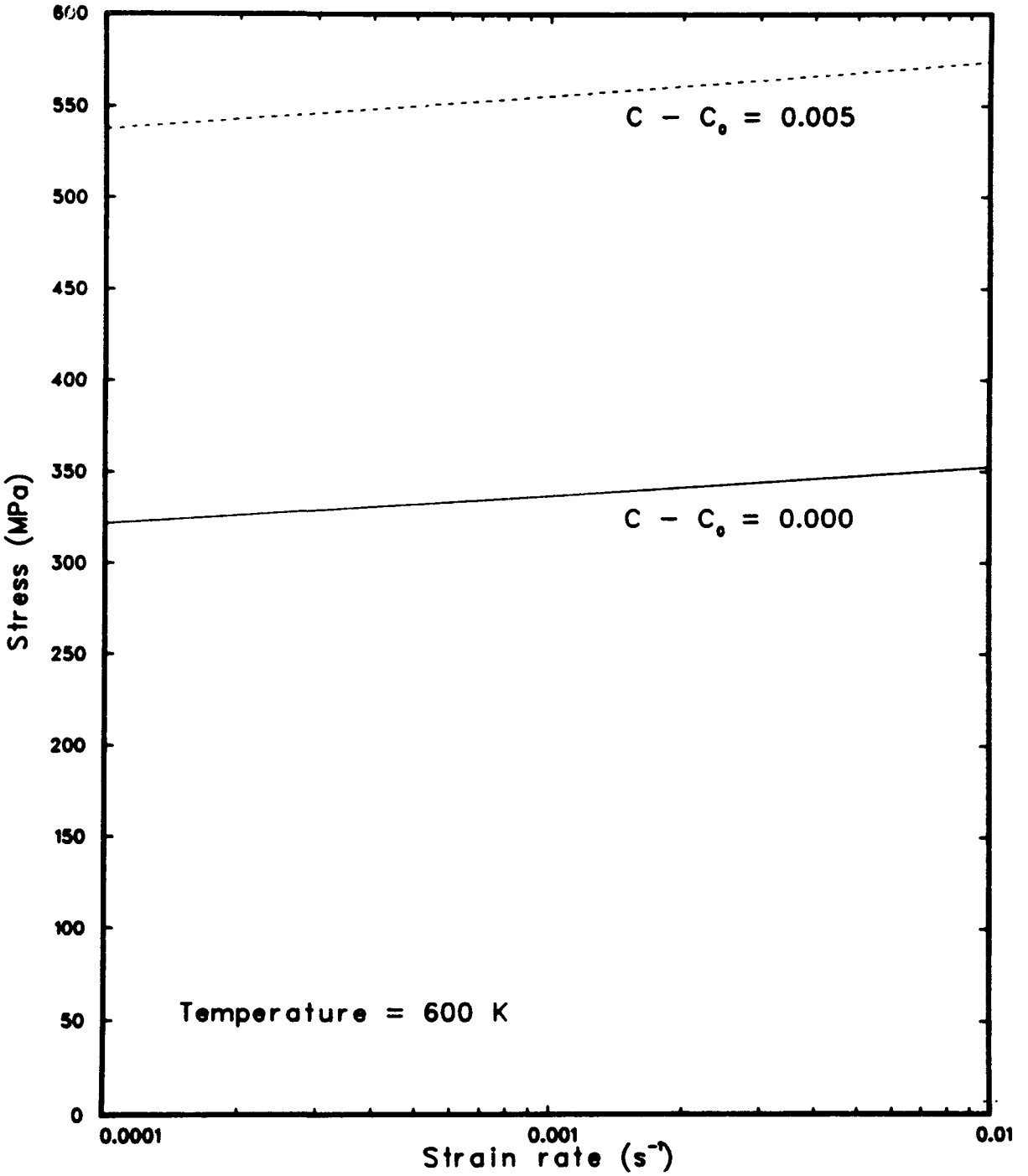

Fig. B-8.17 Stress as a function of strain rate at a strain of 0.1 for two oxygen concentrations at 600 K.

B-8.5. P. J. Crescimanno, *High Strain Rate Tensile Tests of Zircaloy at 550°F (LWBR Development Program)*, WAPD-TM-1263 (February 1976).

B-8.6. A. A. Bauer, L. M. Lowry, J. S. Perrin, *Evaluating Strength and Ductility of Irradiated Zircaloy: Quarterly Progress Report, July-September 1976*, BMI-NUREG-1961 (October 1976).

TABLE B-8.XV

LISTING OF THE CSTRES SUBCODE

```
C
C
      SUBROUTINE CSTRES(CTEMP,DELOXY,ANRIN,FNCK,FNCN,CWKF,CWNF,
     #                  RSTRAN,STRANT,STREST,STRESE,A1,A2,A3)
C
C     CSTRES CALCULATES CLADDING STRESS AS A FUNCTION OF
C          TRUE CLADDING STRAIN, TRUE CLADDING STRAIN RATE,
C          CLADDING TEMPERATURE, AVERAGE OXYGEN CONCENTRATION
C          IN CLADDING, FAST NEUTRON FLUENCE, AND COLD WORK
C
C     A1,A2, AND A3 = OUTPUT COEFFICIENTS OF ANISOTROPY (UNITLESS)
C     STREST = OUTPUT CLADDING TRUE STRESS (PA)
C     STRESE = OUTPUT CLADDING ENGINEERING STRESS (PA)
C
C     STRANT = INPUT TRUE STRAIN (UNITLESS )
C     RSTRAN = INPUT TRUE STRAIN RATE (S**(-1))
C     CTEMP  = INPUT CLADDING MESHPOINT TEMPERATURE (K)
C     DELOXY = INPUT AVERAGE OXYGEN CONCENTRATION EXCLUDING
C              OXIDE LAYER - AVERAGE OXYGEN CONCENTRATION OF
C              AS RECEIVED CLADDING  (KG OXYGEN/KG ZIRCALOY)
C     ANRIN  = INPUT CONTRACTILE STRAIN RATIO DURING UNIAXIAL TENSILE
C              TEST, CIRCUMFERENTIAL STRAIN/RADIAL STRAIN,
C              IF UNKNOWN, INPUT ZERO OR NEGATIVE NUMBER (M/M)
C     FNCK   = INPUT EFFECTIVE FAST FLUENCE FOR STRENGTH
C              COEFFICIENT (NEUTRONS/(M**2))
C     FNCN   = INPUT EFFECTIVE FAST FLUENCE FOR STRAIN HARDENING
C              EXPONENT (NEUTRONS/(M**2))
C     CWKF   = INPUT EFFECTIVE COLD WORK FOR STRENGTH
C              COEFFICIENT (UNITLESS RATIO OF AREAS)
C     CWNF   = INPUT EFFECTIVE COLD WORK FOR STRAIN HARDENING
C              EXPONENT (UNITLESS RATIO OF AREAS)
C
C     THE SUBCODES USED IN THIS SUBROUTINE ARE CKMN AND CELMOD.
C
C     CONVERSION FROM PA  TO  PSI  IS 1.4505E-04 (PSI/PA)
C
C     CSTRES WAS ADAPTED FROM CSTRAN (A SUBROUTINE BY R.L. MILLER AND
C     R.R. HOBBINS) BY G.A. BERNA IN APRIL 1975
C     MODIFIED BY D.L. HAGRMAN JUNE 1978.
C
      CALL CKMN(CTEMP,DELOXY,FNCK,FNCN,CWKF,CWNF,RSTRAN,AK,AN,AM)
      T = CTEMP
C     ANISOTROPY CONSTANTS
      IF(T .GT. 1203.233) GO TO 605
      IF(STRANT .GT. 0.3) GO TO 605
      RR = 2.65 +T*(1.36E-03 - T*2.27E-06)
      IF(STRANT .LT. 0.15) GO TO 610
      RR = 1. + (STRANT*(1. - RR)/2.25E-02)*(STRANT - 3.0E-01)
      GO TO 610
  605 RR =   1.0
  610 IF(ANRIN .GT. 0.) RR = ANRIN
      A1 =   RR/(RR + 1.0)
      A2 = -(RR - 5.4)/(4.4 * (RR+1.0))
      A3 =   1.0/(RR + 1.0)
C
      ELMOD  = CELMOD(CTEMP, FNCK, CWKF, DELOXY)
C
      CSTRS1 = ELMOD * STRANT
      ARG    = AK * ((RSTRAN/1.0E-3)**AM)
      CSTRS2 = ARG * (STRANT**AN)
      STREST = AMIN1(CSTRS1,CSTRS2)
      STRESE = STREST/ EXP(STRANT)
C
      RETURN
      END
```

TABLE B-8.XVI

LISTING OF THE CSIGMA SUBCODE

```
C
C
      SUBROUTINE CSIGMA(CTEMP,DELOXY,ANRIN,FNCK,FNCN,CWKF,CWNF,
     #                  RSTRAN,STRANT,STREST,A1,A2,A3)
C
CCC   CSIGMA CALCULATES POWER LAW TRUE STRESS AS A FUNCTION OF
CCC        TRUE CLADDING STRAIN, TRUE CLADDING STRAIN RATE,
CCC        CLADDING TEMPERATURE, AVERAGE OXYGEN CONCENTRATION
CCC        IN CLADDING, FAST NEUTRON FLUENCE, AND COLD WORK
CCC
CCC   A1,A2, AND A3 = OUTPUT COEFFICIENTS OF ANISOTROPY (UNITLESS)
CCC   STREST = OUTPUT POWER LAW TRUE STRESS (PA)
CCC
CCC   STRANT = INPUT TRUE STRAIN (UNITLESS )
CCC   RSTRAN = INPUT TRUE STRAIN RATE (S**(-1))
C     CTEMP  = INPUT CLADDING MESHPOINT TEMPERATURE (K)
C     DELOXY = INPUT AVERAGE OXYGEN CONCENTRATION EXCLUDING
C              OXIDE LAYER - AVERAGE OXYGEN CONCENTRATION OF
C              AS RECEIVED CLADDING  (KG OXYGEN/KG ZIRCALOY)
C     ANRIN  = INPUT CONTRACTILE STRAIN RATIO DURING UNIAXIAL TENSILE
C              TEST. CIRCUMFERENTIAL STRAIN/RADIAL STRAIN.
C              IF UNKNOWN, INPUT ZERO OR NEGATIVE NUMBER (M/M)
C     FNCK   = INPUT EFFECTIVE FAST FLUENCE FOR STRENGTH
C              COEFFICIENT (NEUTRONS/(M**2))
C     FNCN   = INPUT EFFECTIVE FAST FLUENCE FOR STRAIN HARDENING
C              EXPONENT (NEUTRONS/(M**2))
C     CWKF   = INPUT EFFECTIVE COLD WORK FOR STRENGTH
C              COEFFICIENT (UNITLESS RATIO OF AREAS)
C     CWNF   = INPUT EFFECTIVE COLD WORK FOR STRAIN HARDENING
C              EXPONENT (UNITLESS RATIO OF AREAS)
CCC
CCC   CONVERSION FROM PA  TO  PSI  IS 1.4505E-04 (PSI/PA)
CCC
CCC   CSIGMA WAS CODED BY M. BOHN AND MODIFIED BY D. L. HAGRMAN
CCC   IN FEBRUARY 1977
CCC   MODIFIED BY D. L. HAGRMAN OCTOBER 1977
C
      CALL CKMN(CTEMP,DELOXY,FNCK,FNCN,CWKF,CWNF,RSTRAN,AK,AN,AM)
      T  = CTEMP
C     ANISOTROPY CONSTANTS
      IF(T .GT. 1203.233) GO TO 605
      IF(STRANT .GT. 0.3) GO TO 605
      RR = 2.65 +T*(1.36E-03 - T*2.27E-06)
      IF(STRANT .LT. 0.15) GO TO 610
      RR = 1. + (STRANT*(1. - RR)/2.25E-02)*(STRANT - 3.0E-01)
      GO TO 610
  605 RR  =  1.0
  610 IF(ANRIN .GT. 0.) RR = ANRIN
      A1  =  RR/(RR + 1.0)
      A2  = -(RR - 5.4)/(4.4 * (RR+1.0))
      A3  =  1.0/(RR + 1.0)
C
      STREST  = AK * (STRANT**AN) * ((RSTRAN/1.0E-3)**AM)
      RETURN
      END
```


B-8.7. H. C. Brassfield et al, *Recommended Property and Reaction Kinetics Data for Use in Evaluating a Light-Water Cooled Reactor Loss-of-Coolant Incident Involving Zircaloy-4 or 304-SS-Clad UO_2*, GEMP-482 (April 1968).

B-8.8. A. L. Bement, Jr., *Effects of Cold-Work and Neutron Irradiation on the Tensile Properties of Zircaloy-2*, HW-74955 (April 1963).

B-8.9. H. M. Chung, A. M. Garde, T. F. Kassner, *Light-Water-Reactor Safety Research Program: Quarterly Progress Report, January-March 1975*, ANL-75-28 (June 12, 1975).

TABLE B-8.XVII

LISTING OF THE CANEAL SUBCODE

```
C
C
      SUBROUTINE CANEAL(CFLUX,DELH,CTEMP,RTEMP,FNCK,FNCN,CWKF,CWNF)
C
C     CANEAL CALCULATES THE CHANGE IN EFFECTIVE FLUENCE AND
C     EFFECTIVE COLD WORK DURING A TIME STEP
C
C     FNCK  = OUTPUT EFFECTIVE FAST FLUENCE FOR STRENGTH COEFFICIENT
C             AT TIME STEP FINISH (NEUTRONS/(M**2))
C     FNCN  = OUTPUT EFFECTIVE FAST FLUENCE FOR STRAIN HARDENING
C             EXPONENT AT TIME STEP FINISH (NEUTRONS/(M**2))
C     CWKF  = OUTPUT EFFECTIVE COLD WORK FOR STRENGTH COEFFICIENT
C             AT TIME STEP FINISH (UNITLESS RATIO OF AREAS)
C     CWNF  = OUTPUT EFFECTIVE COLD WORK FOR STRAIN HARDENING
C             EXPONENT AT TIME STEP FINISH (UNITLESS RATIO OF AREAS)
C
C     CFLUX = INPUT FAST NEUTRON FLUX ((NEUTRONS/M**2)/S)
C     DELH  = INPUT TIME STEP SIZE (S)
C     CTEMP = INPUT CLADDING TEMPERATURE AT START OF TIME STEP (K)
C     RTEMP = INPUT AVERAGE RATE OF CHANGE OF TEMPERATURE (K/S)
C     FNCK  = INPUT EFFECTIVE FAST FLUENCE FOR STRENGTH COEFFICIENT
C             AT TIME STEP START (NEUTRONS/(M**2))
C     FNCN  = INPUT EFFECTIVE FAST FLUENCE FOR STRAIN HARDENING
C             EXPONENT AT TIME STEP START (NEUTRONS/(M**2))
C     CWKF  = INPUT EFFECTIVE COLD WORK FOR STRENGTH COEFFICIENT
C             AT TIME STEP START (UNITLESS RATIO OF AREAS)
C     CWNF  = INPUT EFFECTIVE COLD WORK FOR STRAIN HARDENING
C             EXPONENT AT TIME STEP START (UNITLESS RATIO OF AREAS)
C
C     THE EQUATIONS USED IN THIS SUBROUTINE ARE BASED ON DATA FROM
C     (1)  A. A. BAUER, L. M. LOWRY, AND J. S. PERRIN, EVALUATING
C     STRENGTH AND DUCTILITY OF IRRADIATED ZIRCALOY. QUARTERLY
C     PROGRESS REPORT FOR APRIL THROUGH JUNE 1976,
C     BMI-NUREG-1956 (JULY 1976)
C     (2)  A. A. BAUER, L. M. LOWRY, AND J. S. PERRIN, EVALUATING
C     STRENGTH AND DUCTILITY OF IRRADIATED ZIRCALOY. QUARTERLY
C     PROGRESS REPORT FOR JULY THROUGH SEPTEMBER, 1976, BMI-NUREG-1961
C     (OCTOBER 1976)
C     (3)  A. A. BAUER, L. M. LOWRY, AND J. S. PERRIN, EVALUATING
C     STRENGTH AND DUCTILITY OF IRRADIATED ZIRCALOY. QUARTERLY
C     PROGRESS REPORT FOR OCTOBER THROUGH DECEMBER 1976,
C     BMI-NUREG-1967 (JANUARY 1977)
C
C     CODED BY D. L. HAGRMAN OCTOBER 1977
C     MODIFIED BY G. A. REYMANN AND M. A. MORGAN MARCH 1978
C     MODIFIED BY D. L. HAGRMAN JUNE 1978
C
      T = CTEMP
C
C     UPDATE FLUENCE
      FNCK = FNCK + CFLUX * DELH
      FNCN = FNCN + CFLUX * DELH
C
C     ANNEALING MODEL
      IF(T .LE. 5.0E+02) GO TO 12
      IF(CWKF .LE. 1.0E-20) GO TO 10
      QK = 2.33E+18
      BK = (1.504E+00) * (1.0E+00 + (2.2E-25) * FNCK)
      DISOK = QK * RTEMP * DELH * (T**(-7)) * 6.0
      IF(ABS(DISOK) .LT. 1.0E-04) FNISOK = 1.0
      IF(ABS(DISOK) .GE. 1.50E+02) GO TO 2
      IF(ABS(DISOK) .GE. 1.0E-04) FNISOK = (EXP(DISOK) - 1.0)/DISOK
      CWKF = EXP(-BK * DELH * EXP(-QK * (T**(-6))) * FNISOK) * CWKF
   10 IF(CWNF .LE. 1.0E-20) GO TO 11
C
      QN = 2.33E+18
      BN = (1.504E+00) * (1.0E+00 + (2.2E-25) * FNCN) * 8.0
      DISON = QN * RTEMP * DELH * (T**(-7)) * 6.0
      IF(ABS(DISON) .LT. 1.0E-04) FNISON = 1.0
      IF(ABS(DISON) .GE. 1.0E-04) FNISON = (EXP(DISON) - 1.0)/DISON
      IF(ABS(DISON) .GE. 1.50E+02) GO TO 2
      CWNF = EXP(-BN * DELH * EXP(-QN * (T**(-6))) * FNISON) * CWNF
   11 IF(FNCK .LE. 1.0E+14) GO TO 1
```

TABLE B-8.XVII (continued)

```
C
      BKI = 2.49E-06
      QKI = 5.35E+23
      DISOKI = QKI* RTEMP * DELH * (T**(-09)) *08.0
      IF(ABS(DISOKI) .LT. 1.0E-04) FNISKI = 1.0
      IF(ABS(DISOKI) .GE. 1.50E+02) GO TO 2
      IF(ABS(DISOKI) .GE. 1.0E-04) FNISKI = (EXP(DISOKI) - 1.0)/DISOKI
      FNCK   = FNCK/1.0E+20
      FNCK   = (BKI * DELH * (EXP(-QKI * (T**(-08)))) * FNISKI
     #          + (FNCK)**(-1))**(-(1.0/1.0))
      FNCK   = FNCK * 1.0E+20
C
    1 IF(FNCN  .LE. 1.0E+14) GO TO 12
      BNI    = BKI * 1000.
      QNI    = QKI
      FNISNI = FNISKI
      FNCN   = FNCN/1.0E+20
      FNCN   = (BNI * DELH * (EXP(-QNI * (T**(-08)))) * FNISNI
     #          + (FNCN)**(-1))**(-(1.0/1.0))
      FNCN   = FNCN * 1.0E+20
      GO TO 12
    2 WRITE 901
  901 FORMAT(51H  TIME STEP TOO LARGE FOR CLADDING ANNEALING MODEL )
C
   12 CONTINUE
      RETURN
      END
```


B-8.10. H. M. Chung, A. M. Garde, T. F. Kassner, *Light-Water-Reactor Safety Research Program: Quarterly Progress Report, July-September 1975,* ANL-75-72.

B-8.11. C. C. Busby and G. J. Salvaggio, "Biaxial Properties," *Properties of Zircaloy-4 Tubing,* WAPD-TM-585 (December 1966).

B-8.12. C. C. Busby and K. B. Marsh, *High Temperature Deformation and Burst Characteristics of Recrystallized Zircaloy-4 Tubing,* WAPD-TM-900 (January 1970).

B-8.13. J. G. Merkle, *An Engineering Approach to Multiaxial Plasticity,* ORNL-4138 (July 1967).

B-8.14. Y. Miyamoto, Y. Komatsu, N. Nagai, "Mechanical Behavior of Zircaloy-2 Tubing Under Biaxial Stresses," *Journal of Nuclear Materials, 61* (1976) pp 53-65.

B-8.15. A. Cowan and W. J. Langford, "Effect of Hydrogen and Neutron Irradiation on the Failure of Flawed Zircaloy-2 Pressure Tubes," *Journal of Nuclear Materials, 30* (1969) pp 271-281.

B-8.16. L. M. Howe and W. R. Thomas, "The Effects of Neutron Irradiation on the Tensile Properties of Zircaloy-2," *Journal of Nuclear Materials, 2* (1960) pp 248-260.

B-8.17. G. J. Salvaggio, "Effects of Irradiation on Mechanical Properties," *Properties of Zircaloy-4 Tubing,* WAPD-TM-585 (December 1966).

TABLE B-8.XVIII

LISTING OF THE CKMN SUBCODE

```
C
C
      SUBROUTINE CKMN(CTEMP,DELOXY,FNCK,FNCN,CWKF,CWNF,RSTRAN,AK,AN,AM)
C
CC    CKMN CALCULATES PARAMETERS FOR THE CLADDING EQUATION OF STATE
CC    AS A FUNCTION OF TEMPERATURE, AVERAGE OXYGEN CONCENTRATION,
CC    FAST NEUTRON FLUENCE, AND COLD WORK
CC
CC    AK      = OUTPUT STRENGTH COEFFICIENT (PA)
CC    AN      = OUTPUT STRAIN HARDENING EXPONENT (UNITLESS)
CC    AM      = OUTPUT STRAIN RATE SENSITIVITY EXPONENT (UNITLESS)
CC
CC    CTEMP   = INPUT CLADDING MESHPOINT TEMPERATURE (K)
CC    DELOXY  = INPUT AVERAGE OXYGEN CONCENTRATION EXCLUDING
CC              OXIDE LAYER - AVERAGE OXYGEN CONCENTRATION OF
CC              AS RECEIVED CLADDING (KG OXYGEN/KG ZIRCALOY)
CC    FNCK    = INPUT EFFECTIVE FAST FLUENCE FOR STRENGTH
CC              COEFFICIENT (NEUTRONS/(M**2))
CC    FNCN    = INPUT EFFECTIVE FAST FLUENCE FOR STRAIN HARDENING
CC              EXPONENT (NEUTRONS/(M**2))
CC    CWKF    = INPUT EFFECTIVE COLD WORK FOR STRENGTH
CC              COEFFICIENT (UNITLESS RATIO OF AREAS)
CC    CWNF    = INPUT EFFECTIVE COLD WORK FOR STRAIN HARDENING
CC              EXPONENT (UNITLESS RATIO OF AREAS)
CC    RSTRAN  = INPUT ESTIMATED TRUE STRAIN RATE (S**(-1))
CC
CC    THE EQUATIONS USED IN THIS SUBROUTINE ARE BASED ON DATA FROM
CC    (1) C.R. WOODS, PROPERTIES OF ZIRCALOY-4 TUBING, WAPD-TM-585
CC    (1966)
CC    (2)ULTIMATE STRENGTH DATA OF H.C. BRASSFIELD,ET AL.
CC    GEMP-482(1968)
CC    (3)A.L. BEMENT, JR., EFFECTS OF COLD WORK AND NEUTRON
CC    IRRADIATION ON THE TENSILE PROPERTIES OF ZIRCALOY-2,
CC    HW-74955
CC    (4) A. COWAN AND W.J. LANGFORD J.NUCLEAR MATER.
CC    30 (1969) PP 271-281
CC    (5) L.M. HOWE AND W.R. THOMAS, J. NUC. MAT.
CC    1 (1960) P 248
CC    (6) A. M. GARDE LIGHT-WATER-REACTOR SAFETY RESEARCH
CC    PROGRAM QUARTERLY PROGRESS REPORT APRIL - JUNE 1975
CC    ANL-75-58
CC    (7) A. M. GARDE LIGHT-WATER-REACTOR SAFETY RESEARCH
CC    PROGRAM QUARTERLY PROGRESS REPORT JULY - SEPTEMBER 1975
CC    ANL-75-72
CC    (8) R.L. MEHAN AND F.W. WIESINGER, MECHANICAL PROPERTIES
CC    OF ZIRCALOY-2, KAPL-2110
CC    (9) D. LEE AND W.A. BACKOFEN TRANS.AIME 239  (1967) PP 1034-1040
CC    (10) C.C. BUSBY AND K.B. MARSH, HIGH TEMPERATURE DEFORMATION
CC    AND BURST CHARACTERISTICS OF RECRYSTALLIZED ZIRCALOY-4 TUBING,
CC    WAPD-TM-900 (JANUARY 1970)
CC
CC    CODED BY D. L. HAGRMAN AUGUST 1977
CC    MODIFIED BY D. L. HAGRMAN OCTOBER 1977
C
      T = CTEMP
C
C     LIMIT STRAIN RATE TO A MINIMUM OF 1.0E-05
      IF(RSTRAN .LT. 1.0E-05) RSTRAN = 1.0E-05
C
C     FIND STRAIN RATE EXPONENT, AM,  EXCEPT IN ALPHA - BETA REGION
      IF(T .GT. 730.0) GO TO 6
      AM = 2.00E-2
      GO TO 9
    6 IF(T .GE. 900.0) GO TO 8
      A  =  20.63172161
      B  = - 0.07704552983
      C  =   9.504843067E-05
      D  =  -3.860960716E-08
      AM = A + T*(B+ T*(C+ D*T))
      GO TO 9
    8 AM = -6.47E-2+T*2.203E-4
    9 AM = AM *  EXP(-69.*DELOXY)
C
C     FIND STRAIN HARDENING EXPONENT, AN
      AN = (-1.86E-02 + T*(7.11E-04 - T*7.721E-07)) *
```

TABLE B-8.XVIII (continued)

```
     #      (8.47E-01 * EXP(-3.92E+01*CWNF)  + 1.53E-01 +
     #      CWNF  * (-9.16E-02 + CWNF *2.29E-01)) *
     #      EXP(-((FNCN)**0.33)/(3.73E+07 + 2.0E+08*CWNF))
      IF(T .GE. 850.) AN = 0.027908 *
     #      (8.47E-01 * EXP(-3.92E+01*CWNF)  + 1.53E-01 +
     #      CWNF  * (-9.16E-02 + CWNF *2.29E-01)) *
     #      EXP(-((FNCN)**0.33)/(3.73E+07 + 2.0E+08*CWNF))
      AN = AN*(1. +(1250. - (1250./(EXP((T-1380.)/20.) +1.)))
     #      *DELOXY)
C
C     FIND STRENGTH COEFFICIENT, AK
      E   = -8.152540534E09
      F   =  3.368940331E07
      G   = -4.317334084E04
      H   =  1.769348499E01
      IF(T .GT. 730.0) GO TO 14
      AK = (1.0884E09 - 1.0571E06 * T) * (1.0 + 5.46E-01 * CWKF)
      GO TO 16
   14 IF(T .GE. 900.) GO TO 15
      AK = (E + T*(F + T*(G + T*H))) * (1.0 + 5.46E-01*CWKF)
      GO TO 16
   15 AK =  EXP(8.755E00 +(8.663E03/T)) * (1.0 + 5.46E-01* CWKF)
   16 CONTINUE
      AK = AK*(1. + (1120.-(990./(EXP((T-1301.5)/61.) + 1.)))
     #      *DELOXY)
      AKIRR = (5.54E-18) * FNCK
      AK = AK + AKIRR
C
C     MODIFY STRAIN RATE EXPONENT, AM, IN ALPHA - BETA REGION
      IF(RSTRAN .GE. 6.34E-3) GO TO 100
      IF(T .LE. 1090.) GO TO 100
      IF(T .GE. 1255.) GO TO 100
      IF(T .GT. 1172.5) GO TO 24
      AM = AM +(6.78E-2*ALOG(6.34E-3/RSTRAN)*((T-1090.)/82.5))*
     #      EXP(-69. * DELOXY)
      GO TO 100
   24 AM = AM +(6.78E-2*ALOG(6.34E-3/RSTRAN)*((1255.-T)/82.5))*
     #      EXP(-69. * DELOXY)
  100 CONTINUE
      RETURN
      END
```


B-8.18. G. F. Fieger and D. Lee, "Strength and Ductility of Neutron Irradiated and Textured Zircaloy-2," *Zirconium in Nuclear Applications,* ASTM-STP-551 (1973) pp 355-369.

B-8.19. D. R. Olander, *Fundamental Aspects of Nuclear Reactor Fuel Elements,* TID-26711-P1.

B-8.20. A. A. Bauer, L. M. Lowry, J. S. Perrin, *Evaluating Strength and Ductility of Irradiated Zircaloy: Quarterly Progress Report, April-June 1976,* BMI-NUREG-1956 (July 1976).

B-8.21. A. A. Bauer, L. M. Lowry, J. S. Perrin, *Evaluating Strength and Ductility of Irradiated Zircaloy: Quarterly Progress Report, October-December 1976,* BMI-NUREG-1967 (January 1977).

B-8.22. A. A. Bauer et al, *Evaluating Strength and Ductility of Irradiated Zircaloy: Quarterly Progress Report, October-December 1977,* BMI-NUREG-1992 and NUREG/CR-0026 (January 1978).

B-8.23. L. M. Howe and W. R. Thomas, "The Effect of Neutron Irradiation on the Tensile Properties of Zircaloy-2," *Journal of Nuclear Materials, 2* (1960) pp 248-260.

B-8.24. R. H. Chapman, *Characterization of Zircaloy-4 Tubing Procured for Research Programs,* ORNL/NUREG/TM-29 (July 1976).

B-8.25. J. G. Byrne, *Recovery, Recrystallization, and Grain Growth,* New York: The Macmillan Company (1965).

B-8.26. A. A. Bauer, L. M. Lowry, J. S. Perrin, *Progress on Evaluating Strength and Ductility of Irradiated Zircaloy During July Through September 1975,* BMI-1938 (September 1975).

B-8.27. L. S. Rubenstein et al, "Effect of Oxygen on the Properties of Zircaloy-2," *Transactions of the American Society for Metals, 54* (1961) pp 20-30.

B-8.28. H. M. Chung, A. M. Garde, T. F. Kassner, *Light-Water-Reactor Safety Research Program: Quarterly Progress Report, January-March 1976,* ANL-76-49.

B-8.29. G. E. Dieter, *Mechanical Metallurgy,* Second Edition, New York: McGraw-Hill Book Company, Inc. (1976).

B-8.30. H. M. Chung, A. M. Garde, T. F. Kassner, *Light-Water-Reactor Safety Research Program: Quarterly Progress Report, October-December 1975,* ANL-76-15.

B-8.31. H. M. Chung, A. M. Garde, T. F. Kassner, *Light-Water-Reactor Safety Research Program: Quarterly Progress Report, July-September 1976,* ANL-76-121.

B-8.32. H. M. Chung, A. M. Garde, T. F. Kassner, *Light-Water-Reactor Safety Research Program: Quarterly Progress Report, January-March 1977,* ANL-77-34.

9. CLADDING STRAIN VERSUS STRESS (CSTRAN AND CSTRNI)

(D. L. Hagrman)

The subroutines CSTRAN and CSTRNI calculate cladding true strain and engineering strain as functions of true stress, temperature, cold work, fast neutron fluence, and average oxygen concentration in the cladding. The two codes employ different means for inverting

the basic equation[a] for stress as a function of strain and strain rate to find an expression for strain. CSTRAN uses strain rate and stress to calculate a strain. The user must be certain that the input strain rate is consistent with the predicted strain. CSTRNI uses the initial strain and the time step size to find the strain at the end of the time step.

Since the basic equation of state necessary to describe cladding plastic deformation is discussed in conjunction with the subcodes CSTRES and CSIGMA, it will not be discussed here. This section consists of a model description (Subsection B-9.1), examples (Subsection B-9.2), subcode listings (Subsection B-9.3), and references (Subsection B-9.4).

9.1 Model Description

The CSTRAN and CSTRNI codes use Hooke's law in the elastic region

$$\epsilon = \frac{\sigma}{E} \tag{B-9.1}$$

where

ϵ = true strain (m/m)

σ = true stress (Pa)

E = Young's modulus[b] (Pa)

In the plastic region, the equation of state developed for the CSIGMA and CSTRES subcodes is used to relate stress and strain.

$$\sigma = K\epsilon^n \left[\frac{\dot{\epsilon}}{10^3/s}\right]^m \tag{B-9.2}$$

where

K = strength coefficient (Pa)

m = strain rate sensitivity constant (unitless)

n = strain hardening exponent (unitless)

$\dot{\epsilon}$ = true strain rate (s^{-1}).

---

[a] Equation (B-8.3) of the CSTRES code description.

[b] The subcode CELMOD provides a value for Young's modulus.

The transition from the elastic to the plastic region is defined to be the nonzero intersection of the curves resulting from Equations (B-9.1) and (B-9.2).

The strain returned by the CSTRAN subcode in the plastic region is obtained from the equation

$$\varepsilon = \left[\frac{\sigma}{K \left[\frac{\dot{\varepsilon}}{10^3/s} \right]^m} \right]^{1/n} . \qquad \text{(B-9.3)}$$

Input values of $\dot{\epsilon}$ are limited to be greater than or equal to 10^{-5}/s in the CSTRAN subcode.

The subcode CSTRNI does not require user-input strain rates. The expression used to find strain in this subcode is obtained by integrating an alternate form of Equation (B-9.2).

$$\varepsilon^n \left[\frac{d\varepsilon}{dt} \right]^m = (10^{-3})^m \frac{\sigma}{K} \qquad \text{(B-9.4)}$$

where

$\frac{d\epsilon}{dt}$ = $\dot{\epsilon}$, the true strain rate (s^{-1}).

The integrated equation requires input values of strain at the beginning of a time step of duration Δt.

$$\varepsilon_f = \left[\left(\frac{n}{m} + 1\right) 10^{-3} \left(\frac{\sigma}{K}\right)^{1/m} \Delta t + \varepsilon_i^{\left(\frac{n}{m} + 1\right)} \right]^{\frac{m}{n+m}} \qquad \text{(B-9.5)}$$

where

ϵ_f = true strain at the end of a time interval (m/m)

ϵ_i = true strain at the beginning of a time interval (m/m)

Δt = duration of the time interval (s).

Equation (B-9.5) assumes that the stress, σ, is constant during the time step. A Taylor series expansion of a time dependent stress shows that Equation (B-9.5) is approximately valid as long as the change in stress during the time interval is small compared to the stress at the start of the interval.

If temperature is between 1090 and 1255 kelvins, the parameter m in Equation (B-9.5) is a function of strain rate and an iteration is necessary. The approximate strain rate obtained from the expression:

$$\dot{\varepsilon} = (\varepsilon_f - \varepsilon_i) / \Delta t \qquad \text{(B-9.6)}$$

is used to find an improved value for m and Equation (B-9.5) is used to find a revised value for ϵ_f with the improved value of m. The iteration is repeated ten times.

Although the equations used to find plastic strain in CSTRAN and CSTRNI appear to be quite different, it can easily be shown that the expression in CSTRNI is equivalent to the expression in CSTRAN with a strain rate equal to the expression in Equation (B-9.6).

A Taylor series expansion at Equation (B-9.5) for small Δt shows

$$\varepsilon_f \cong \varepsilon_i \left[1 + \frac{10^{-3} \left(\frac{\sigma}{K}\right)^{\frac{1}{m}} \Delta t}{(\varepsilon_i)^{\frac{n+m}{m}}} \right] \qquad \text{(B-9.7)}$$

Equation (B-9.7) can be rearranged to show

$$\left(\frac{\varepsilon_f - \varepsilon_i}{\Delta t \; 10^{-3}} \right)^m = \frac{1}{(\varepsilon_i)^n} \quad \frac{\sigma}{K}$$

which is Equation (B-9.3) with Equation (B-9.6) used for $\dot{\epsilon}$ and ϵ_i used for ϵ.

9.2 Examples of Subcode Calculations

Table B-9.I is an example of a simple program written to calculate the deformation of a symmetric, closed cylinder using the CSTRNI code. The program (a) reads the necessary initial parameters; (b) calls CSTRNI to determine the effective strain at the end of an input time step; (c) calculates circumferential, radial, and axial strains using Equations (B-8.18) and (B-8.19) of the previous section; (d) calculates the true stress at the end of the time step; and (e) repeats the process for the next time steps.

Figure B-9.1 illustrates calculated circumferential, axial, and radial engineering strains for symmetric burst of a closed end tube with the following input parameters:

Pressure = 5.2 MPa

Temperature = 1023 kelvins

Initial tubing OD = 1.092×10^{-5} m

Initial tubing wall thickness = 6.34×10^{-7} m

TABLE B-9.I

LISTING OF SYMMETRIC CYLINDER DEFORMATION PROGRAM

```
      PROGRAM CHECK (INPUT,OUTPUT)
C
C     CODED BY D. L. HAGRMAN AND M. P. BOHN MARCH 1978
C     REVISED TO CONSIDER APPROXIMATE RADIAL STRESS - DLH APRIL 1978
C
C     READ INITIAL STATE
   10 READ 900,IT
  900 FORMAT(I10)
      IF(IT .GT. 0) GO TO 1000
      READ 901,CFLUX,FNCK,FNCN,CWKF,CWNF,DELOXY,RTEMP,AMRIN
  901 FORMAT(8E10.2)
      READ 902,PI,PO,RIO,ROO,CTEMP,DELH,MODE
      RI = RIO
      RO = ROO
  902 FORMAT(6E10.2,I10)
C     DO NOT ENTER EXACT ZEROS FOR COMPONENTS OF STRAIN.
C     STRANO EXPRESSION CAN'T HANDLE SQUARE ROOT OF ZERO
      READ 903,STRANR,STRANC,STRANA,A1,A2,A3
  903 FORMAT(6E10.2)
      PRINT 904,AMRIN
  904 FORMAT(//10H AMRIN =  ,E14.4)
      STRANO = ((A1*(A2*STRANA - A3*STRANC)**2.0 + A2*(A3*STRANC
     # - A1*STRANR)**2.0 + A3*(A1*STRANR - A2*STRANA)**2.0)**0.5) /
     # (A1*A2 + A2*A3 + A3*A1)
      PRINT 905,STRANR,STRANC,STRANA,STRANO
  905 FORMAT(65H INITIAL RADIAL, CIRCUMFERENTIAL, AXIAL AND EFFECTIVE ST
     #RAINS ARE,4E16.5)
      K = 1
      DTIME = 0.0
      STRANT = STRAMO
C
   20 STRESH = (PI*RI - PO*RO)/(RO - RI)
      STRESA = (PI*RI*RI - PO*RO*RO)/(RO*RO - RI*RI)
      STRESR = -(PI*RI + PO*RO)/(RI + RO)
      STREST = (A1*(STRESA-STRESH)**2.0 + A2*(STRESH-STRESR)**2.0
     #  + A3*(STRESR - STRESA)**2.0)**0.5
      PRINT 906,CFLUX,FNCK,FNCN,CWKF,CWNF,DELOXY,CTEMP,DELH,K
  906 FORMAT(/1X,8E15.4,I10)
      PRINT 907,STRESH,STRESA,STRESR,STREST
  907 FORMAT(14H HOOP STRESS =,E12.4,15H AXIAL STRESS =,E12.4,16H RADIAL
     # STRESS =,E12.4,19H EFFECTIVE STRESS =,E12.4)
C
      CALL CSTRNI(DELH,CTEMP,DELOXY,AMRIN,FNCK,FNCN,CWKF,CWNF,
     # STREST,STRANT,STRANE,A1,A2,A3)
      IF(STRANT .LT. STRANO) STRANT = STRANO
C
      DEP = STRANT - STRANO
      STRANC = DEP * (A1*(STRESH - STRESA) + A2*(STRESH - STRESR))/
     #     STREST + STRANC
      STRANR = DEP * (A2*(STRESR - STRESH) + A3*(STRESR - STRESA))/
     #     STREST + STRANR
      STRANA = DEP * (A3*(STRESA - STRESR) + A1*(STRESA - STRESH))/
     #     STREST + STRANA
      TRANEC = EXP(STRANC) - 1.0
      TRANER = EXP(STRANR) - 1.0
      TRANEA = EXP(STRANA) - 1.0
      DTIME = DTIME + DELH
      PRINT 908,TRANEC,TRANER,TRANEA,DTIME
  908 FORMAT(25H CIRCUMFERENTIAL STRAIN =,E15.4,16H RADIAL STRAIN =,E15.
     #4,15H AXIAL STRAIN =,E15.4,12H TIME(SEC) =,E15.2)
C
C     START UPDATE FOR NEXT STEP -- DEFINE INITIAL STRAIN,RADII.
C     SAVE TEMPERATURE AND TIME STEP SIZE FOR ANNEALING MODEL
      K = K + 1
      STRANO = STRANT
C
C     UPDATE INSIDE AND OUTSIDE RADII CONSISTENT WITH CONSERVATION
C     OF VOLUME
      RO = 0.5*(ROO + RIO)* EXP(STRANC) + 0.5*(ROO - RIO)* EXP(STRANR)
      RI = 0.5*(ROO + RIO)* EXP(STRANC) - 0.5*(ROO - RIO)* EXP(STRANR)
C     SPECIAL PRINT - OUT
      TRANRD = (RO - ROO)/ROO
      PRINT 999, TRANRD
  999 FORMAT(28H RADIUS ENGINEERING STRAIN =,E15.4)
```

TABLE B-9.I (continued)

```
C
C
      CTEMPO = CTEMP
      DELHO = DELH
      IF(STRAN0 .GT. 1.25) K = 151
C
C     SELECT UPDATE MODE
C          MODE = 0   READ NEW PI,PO,CTEMP,DELH AND KIT.
C                     KIT GREATER THAN ZERO OR STRAIN GREATER
C                     THAN 1.25 OR MORE THAN 150 STEPS STOPS THE PROCESS
C          MODE = 1   PI = CORRELATION. DELH REDUCED FOR LARGE STRAINS
C                     MORE THAN 150 STEPS OR STRAIN GREATER THAN 1.25
C                     STOPS THE PROCESS
C          MODE = 2   ISOTHERMAL PRESSURE RAMPED AT THE RATE
C                     READ IN FOR PRATE
C
      IF(MODE) 1000,101,110
  101 READ 909,PI,PO,CTEMP,DELH,KIT
  909 FORMAT(4E10.2,I10)
      PRINT 910,PI,PO,CTEMP,DELH
  910 FORMAT(/27H UPDATED PI,PO,CTEMP,DELH =,4E15.5)
      IF(KIT .GT. 0 ) GO TO 102
      IF(STRAN0 .GT. 1.25) GO TO 101
      GO TO 110
  102 K = 151
  110 IF(MODE - 1) 890,111,120
  111 PI = 5.2E+06
      IF(TRANEC .GT. 1.0E-02) DELH = 1.00E+00
      IF(TRANEC .GT. 1.00E-01) DELH = 5.00E-01
      IF(TRANEC .GT. 1.00E+00) DELH = 1.00E-02
      STRSHE = (PI*RI0-PO*ROO)/(ROO-RI)
      PRINT 911,STRSHE
  911 FORMAT(/34H UPDATED ENGINEERING HOOP STRESS =,E16.5)
  120 IF(MODE - 2) 890,121,130
  121 IF(K .GT. 2) GO TO 122
      READ 912,PRATE
  912 FORMAT(E10.2)
  122 PI = PI + DELH * PRATE
      IF(TRANEC .GT. 1.0E-02) DELH = 1.00E+00
      IF(TRANEC .GT. 1.0E-01) DELH = 2.50E-01
      IF(TRANEC .GT. 3.0E-01) DELH = 1.00E-02
      STRSHE = (PI*RI0-PO*ROO)/(ROO-RI)
      PRINT 911,STRSHE
  130 CONTINUE
C
C
  890 RTEMP = (CTEMP - CTEMPO)/(DELHO + 0.5*DELH)
C     ANNEALING MODEL TAKES AVERAGE TEMPERATURE AS INITIAL TEMPERATURE
C     AND TRIES TO ESTIMEATE THE TEMPERATURE AT THE END OF THE PREVIOUS
C     TIME STEP WITH AVERAGE TEMPERATURE * RTEMP.  THIS EXPRESSION
C     FOR RTEMP APPROXIMATES THE TRUE TEMPERATURE CHANGE FAIRLY WELL
C     AS LONG AS THE TIME STEPS ARE SMALL
      CALL CANEAL(CFLUX,DELHO,CTEMPO,RTEMP,FNCK,FNCN,CWKF,CWNF)
      IF(K .GT. 150) GO TO 10
      IF(K .LE. 150) GO TO 20
 1000 STOP
      END
```

Cold work = 0

Fluence = 0.

The circumferential strain increases slowly at first, then begins to increase rapidly as the decreasing wall thickness and increasing radius of the cylinder cause the true stress to increase. The axial strain is negative because of the anisotropy of the cladding. In the more realistic asymmetric case, circumferential variations in temperature cause local strains to vary around the circumference of the tube. Varying axial strains will cause the tube to bend and enhance circumferential variations in temperature when there is a source or sink of heat inside the tube.

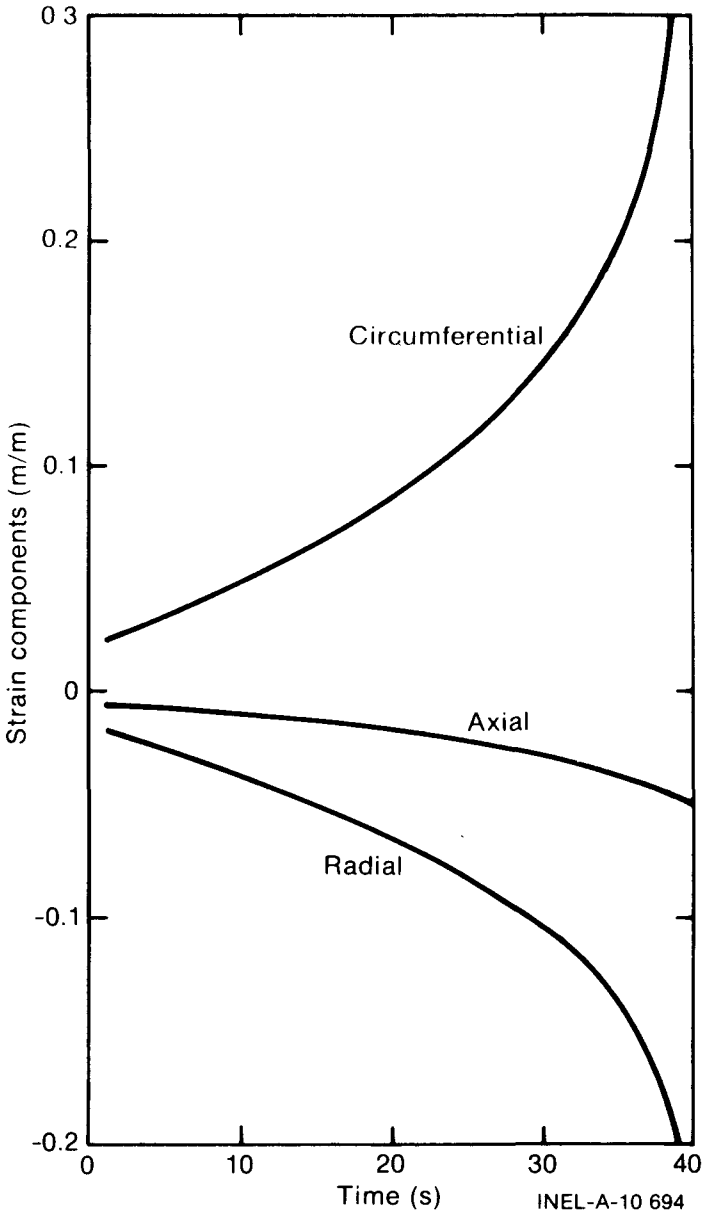

Fig. B-9.1 Calculated circumferential, axial, and radial engineering strains as a function of time for a closed end tube burst test at 1023 kelvins with a constant internal pressure of 5.2 MPa.

Figure B-9.2 is a comparison between predicted circumferential strain for the symmetric problem just described and measured diametral strains during the initial part of a stress rupture test by H. M. Chung[B-9.1] on cladding with the dimensions, pressure, and temperature given in the last paragraph. The strain is slightly overpredicted when the typical coefficients of anisotropy developed in Section B-8[a] are employed and significantly overpredicted when the cladding is assumed to be isotropic. The strain is slightly underpredicted when a temperature 5 kelvins lower than the 1023 kelvins temperature reported by Chung is assumed. Another curve (shown on Figure B-9.2) illustrates predicted strains for a tube with twice the as-received oxygen concentration. The tube is assumed to have been homogenized so that the oxygen is evenly distributed.

[a] Section B-8 of this handbook.

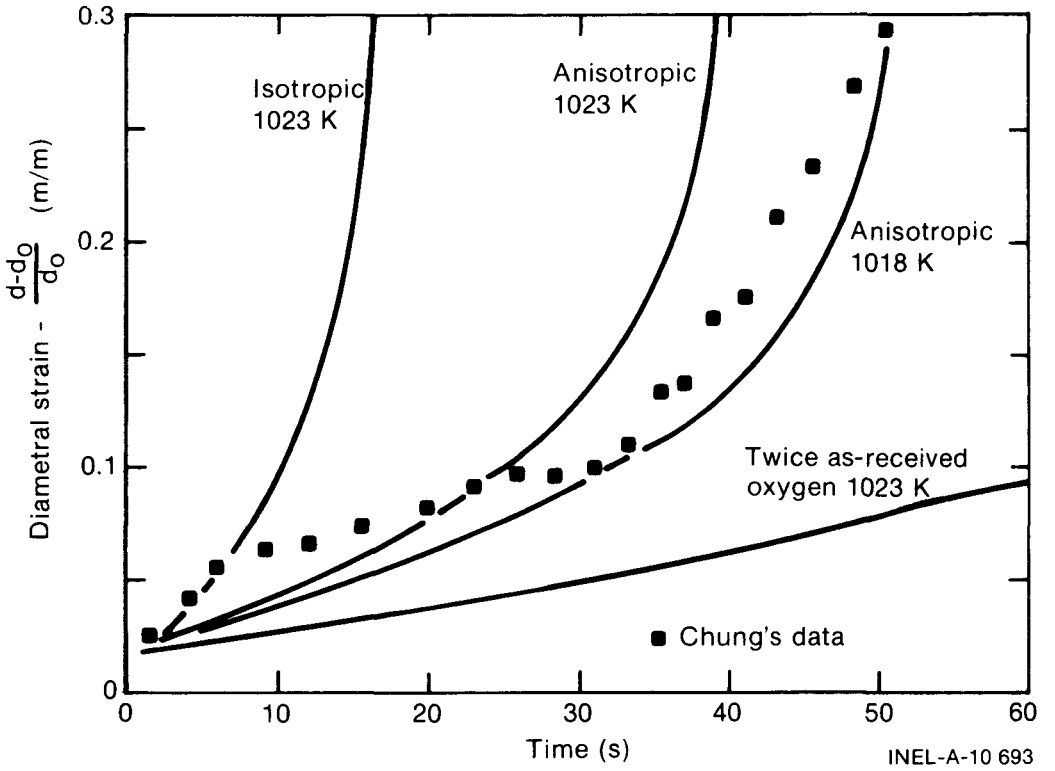

Fig. B-9.2 Diametral strain as a function of time for anisotropic cladding at 1023 and 1018 kelvins and for isotropic and oxidized cladding at 1023 kelvins compared to measured diametral strain in Chung's 5.2 MPa test.

Chung's test was selected as a particularly good test of the equation of state because (a) strain was measured as a function of time, (b) the cladding was heated by an electric current so that most of the complicating effects of local variations in temperature were absent, and (c) the stress rupture test is particularly sensitive to small errors in the equation of state because temperature is held constant for a long period of time.

Transient temperature tests reported by Hardy[B-9.2] offer an opportunity to test the equation of state at temperatures in the range 900 to 1400 kelvins. Figure B-9.3 is a comparison of predicted circumferential strain versus the maximum diametral expansions measured by Hardy for a heating rate of 25 kelvins per second and internal pressures at 5.5, 1.4, and 0.3 MPa. The 5.5 MPa tests are accurately predicted and the strains of the 0.3 MPa tests are usually underpredicted.

It is interesting to note that the root mean square difference between the reported temperature and the temperature at which the equation of state reproduces the measured strain of Hardy's data is ±35 kelvins for the 5.5 and 1.4 MPa tests and ±60 kelvins for the 0.3 MPa curve. Uncertainties of ±25 kelvins in both the basic data of the equation of state and Hardy's measured temperature would be sufficient to explain the discrepancy observed in the two low temperature curves while errors of ±40 kelvins would be required to explain the deviation of the high temperature curve. Similar deviations have been found at temperatures of 900 to 1400 kelvins in comparison of predicted behavior and burst data of

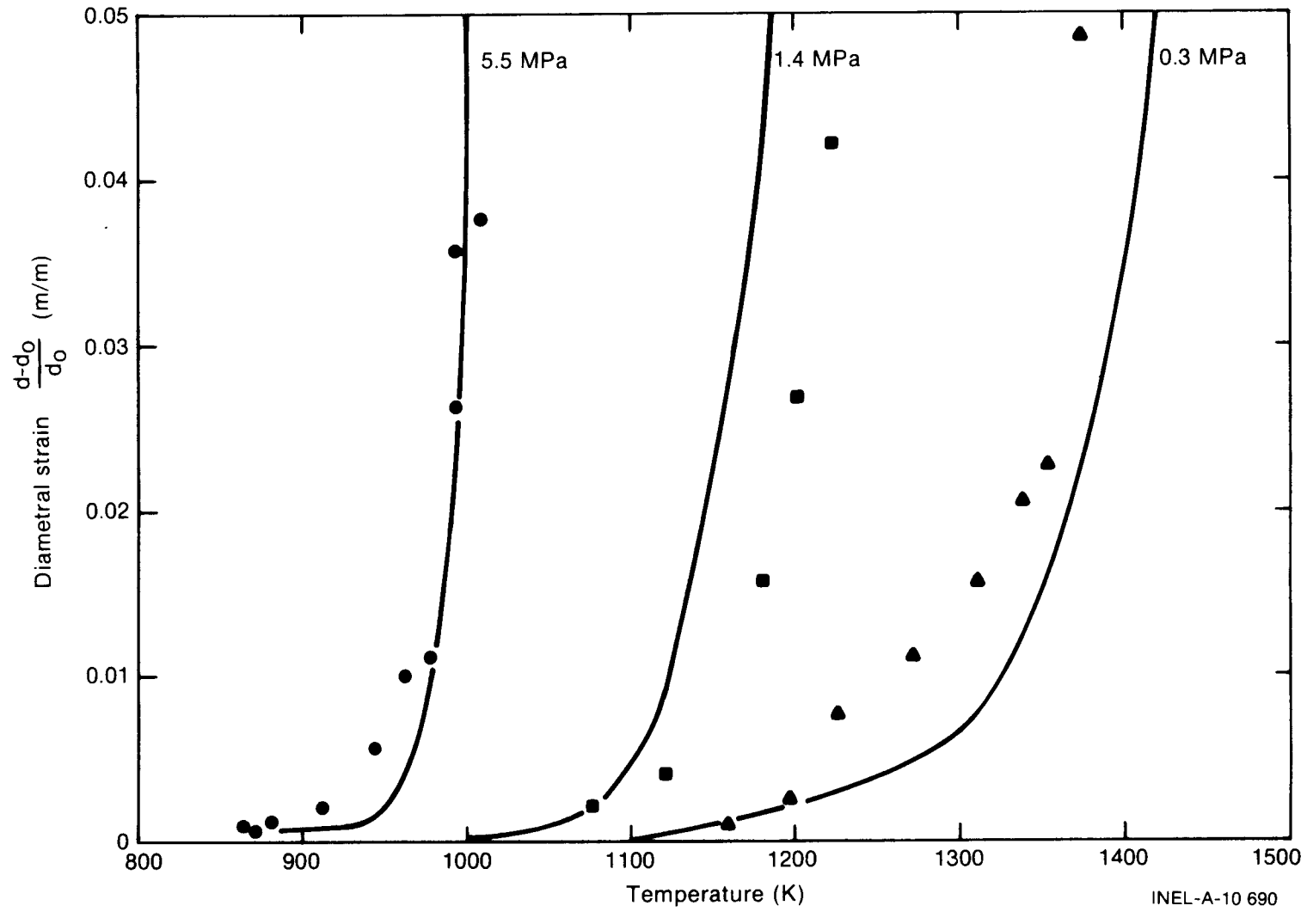

Fig. B-9.3 Comparison of predicted circumferential strain versus the maximum diametral expansion measured by Hardy for a heating rate of 25 kelvins/s and internal pressures of 5.5, 1.4, and 0.3 MPa.

Hobson and Rittenhouse[B-9.3] and in comparisons to isothermal burst tests of Busby and Marsh[B-9.4]. Moreover, comparison to the high temperature (1300 to 1700 kelvins) burst data of Hobson and Rittenhouse shows an increasing trend to overpredict the strength of tubes at temperatures above 1300 kelvins.

9.3 Cladding Strain Versus Stress Subcodes CSTRAN and CSTRNI Listings

Listings of the FORTRAN subcodes CSTRAN and CSTRNI are given in Tables B-9.II and B-9.III, respectively.

9.4 References

B-9.1. H. M. Chung, A. M. Garde, T. F. Kassner, *Light-Water-Reactor Safety Research Program: Quarterly Progress Report for July-September 1976,* ANL-76-121.

B-9.2. D. G. Hardy, "High Temperature Expansion and Rupture Behavior of Zircaloy Tubing," *Topical Meeting on Water-Reactor Safety, Salt Lake City, Utah, March 26-28, 1973,* CONF. 730304 (March 1974).

B-9.3. D. O. Hobson and P. L. Rittenhouse, *Deformation and Rupture Behavior of Light-Water Reactor Fuel Cladding,* ORNL-4727 (October 1971).

B-9.4. C. C. Busby and K. B. Marsh, *High Temperature Deformation and Burst Characteristics of Recrystallized Zircaloy-4 Tubing,* WAPD-TM-900 (January 1970).

TABLE B-9.II

LISTING OF THE CSTRAN SUBCODE

```
C
C
      SUBROUTINE CSTRAN(CTEMP,DELOXY,ANRIN,FNCK,FNCN,CWKF,CWNF,
     #                  RSTRAN,STREST,STRANT,STRANE,A1,A2,A3)
C
CCCCC CSTRAN CALCULATES CLADDING STRAIN AS A FUNCTION OF
CCCCC TRUE CLADDING STRESS, TRUE CLADDING STRAIN RATE,
CCCCC CLADDING TEMPERATURE, AVERAGE OXYGEN CONCENTRATION
CCCCC IN CLADDING, FAST NEUTRON FLUENCE, AND COLD WORK.
CCCCC NO INTERNAL ITERATIONS ARE CONTAINED IN CSTRAN.  IT IS
CCCCC ASSUMED THAT THE USER WILL ITERATE THE INPUT VALUE
CCCCC OF RSTRAN.  SEE SUBCODE CSTRNI FOR ITERATED VERSION.
CCCCC
CCCCC A1,A2, AND A3 = OUTPUT COEFFICIENTS OF ANISOTROPY (UNITLESS)
CCCCC STRANT = OUTPUT TRUE STRAIN (M/M)
CCCCC STRANE = OUTPUT ENGINEERING STRAIN (M/M)
CCCCC
CCCCC CONVERSION FROM PA  TO  PSI  IS 1.4505E-04 (PSI/PA)
CCCCC
CCCCC STREST = INPUT TRUE STRESS (PA)
CCCCC STRANT = INPUT TRUE STRAIN AT START OF TIME STEP (M/M)
CCCCC RSTRAN = INPUT TRUE STRAIN RATE (S**(-1))
CCCCC CTEMP  = INPUT CLADDING RESPOINT TEMPERATURE (K)
CCCCC DELOXY = INPUT AVERAGE OXYGEN CONCENTRATION EXCLUDING
CCCCC          OXIDE LAYER - AVERAGE OXYGEN CONCENTRATION OF
CCCCC          AS RECEIVED CLADDING  (KG OXYGEN/KG ZIRCALOY)
CCCCC ANRIN  = INPUT CONTRACTILE STRAIN RATIO DURING UNIAXIAL TENSILE
CCCCC          TEST (CIRCUMFERENTIAL STRAIN/RADIAL STRAIN).
CCCCC          IF UNKNOWN, INPUT ZERO OR NEGATIVE NUMBER (M/M)
CCCCC FNCK   = INPUT EFFECTIVE FAST FLUENCE FOR STRENGTH
CCCCC          COEFFICIENT (NEUTRONS/(M**2))
CCCCC FNCN   = INPUT EFFECTIVE FAST FLUENCE FOR STRAIN HARDENING
CCCCC          EXPONENT (NEUTRONS/(M**2))
CCCCC CWKF   = INPUT EFFECTIVE COLD WORK FOR STRENGTH
CCCCC          COEFFICIENT (UNITLESS RATIO OF AREAS)
CCCCC CWNF   = INPUT EFFECTIVE COLD WORK FOR STRAIN HARDENING
CCCCC          EXPONENT (UNITLESS RATIO OF AREAS)
CCCCC
CCCCC THE SUBCODES USED IN THIS SUBROUTINE ARE CKMN AND CELMOD.
CCCCC
CCCCC CSTRAN WAS CODED BY R. L. MILLER AND R. R. HOBBINS
CCCCC IN MARCH 1974
CCCCC MODIFIED BY D. L. HAGRMAN JUNE 1978.
C
      CALL CKMN(CTEMP,DELOXY,FNCK,FNCN,CWKF,CWNF,RSTRAN,AK,AN,AM)
      T = CTEMP
C     ANISOTROPY CONSTANTS
      IF(ANRIN .GT. (1.0 - 1.0E-10) .AND. ANRIN .LT. (1.0 + 1.0E-10))
     #   GO TO 605
      IF(T .GT. 1203.233) GO TO 605
      IF(STRANT .GT. 0.3) GO TO 605
      RR = 2.65 +T*(1.36E-03 - T*2.27E-06)
      IF(STRANT .LT. 0.15) GO TO 610
      RR = 1. + (STRANT*(1. - RR)/2.25E-02)*(STRANT - 3.0E-01)
      GO TO 610
  605 RR = 1.0
  610 IF(ANRIN .GT. 0.) RR = ANRIN
      A1 =   RR/(RR + 1.0)
      A2 = -(RR - 5.4)/(4.4 * (RR+1.0))
      A3 =   1.0/(RR + 1.0)
C
      ELMOD = CELMOD(CTEMP, FNCK, CWKF,DELOXY)
C
C     CALCULATION OF STRAIN FOLLOWS
      STRAN1 = STREST/ELMOD
      STRAN2 = (STREST/(AK* ((RSTRAN/1.0E-03)**AM)))**(1.0/AN)
      IF(STRAN2 .GT. STRAN1) STRANT = STRAN2
      IF(STRAN2 .LE. STRAN1) STRANT = STRAN1
      STRANE = EXP(STRANT) - 1.0
C
      RETURN
      END
```

TABLE B-9.III

LISTING OF THE CSTRNI SUBCODE

```
      SUBROUTINE CSTRNI(DELH,CTEMP,DELOXY,ANRIN,FNCK,FNCN,CWKF,CWNF,
     #                  STREST,STRANT,STRANE,RSTRAN,A1,A2,A3)
C
C     CSTRNI CALCULATES CLADDING STRAIN AS A FUNCTION OF
C     TRUE CLADDING STRESS, INITIAL TRUE CLADDING STRAIN,
C     TIME STEP SIZE, CLADDING TEMPERATURE, AVERAGE OXYGEN
C     CONCENTRATION IN CLADDING, FAST NEUTRON FLUENCE,
C     AND COLD WORK.
C
C     A1,A2, AND A3 = OUTPUT COEFFICIENTS OF ANISOTROPY (UNITLESS)
C     STRANT = OUTPUT TRUE STRAIN (M/M)
C     STRANE = OUTPUT ENGINEERING STRAIN (M/M)
C     RSTRAN = OUTPUT TRUE STRAIN RATE (S**(-1))
C
C     STREST = INPUT TRUE STRESS (PA)
C     STRANT = INPUT ESTIMATED TRUE STRAIN
C              AT START OF TIME STEP (M/M)
C     DELH   = INPUT TIME STEP SIZE (S)
C     CTEMP  = INPUT CLADDING MESHPOINT TEMPERATURE (K)
C     DELOXY = INPUT AVERAGE OXYGEN CONCENTRATION EXCLUDING
C              OXIDE LAYER - AVERAGE OXYGEN CONCENTRATION OF
C              AS RECEIVED CLADDING  (KG OXYGEN/KG ZIRCALOY)
C     ANRIN  = INPUT CONTRACTILE STRAIN RATIO DURING UNIAXIAL TENSILE
C              TEST. CIRCUMFERENTIAL STRAIN/RADIAL STRAIN.
C              IF UNKNOWN, INPUT ZERO OR NEGATIVE NUMBER (M/M)
C     FNCK   = INPUT EFFECTIVE FAST FLUENCE FOR STRENGTH
C              COEFFICIENT (NEUTRONS/(M**2))
C     FNCN   = INPUT EFFECTIVE FAST FLUENCE FOR STRAIN HARDENING
C              EXPONENT (NEUTRONS/(M**2))
C     CWKF   = INPUT EFFECTIVE COLD WORK FOR STRENGTH
C              COEFFICIENT (UNITLESS RATIO OF AREAS)
C     CWNF   = INPUT EFFECTIVE COLD WORK FOR STRAIN HARDENING
C              EXPONENT (UNITLESS RATIO OF AREAS)
C
C     THE SUBCODES USED IN THIS SUBROUTINE ARE CKMN AND CELMOD.
C
C     CONVERSION FROM PA  TO  PSI  IS 1.4505E-04 (PSI/PA)
C
C     CSTRNI WAS CODED BY D. L. HAGRMAN OCTOBER 1977
C     MODIFIED BY D. L. HAGRMAN JUNE 1978.
C
      RSTRAN = 1.0E-03
      CALL CKMN(CTEMP,DELOXY,FNCK,FNCN,CWKF,CWNF,RSTRAN,AK,AN,AM)
      T = CTEMP
C     ANISOTROPY CONSTANTS
      IF(T .GT. 1203.233) GO TO 605
      IF(STRANT .GT. 0.3) GO TO 605
      RR = 2.65 +T*(1.36E-03 - T*2.27E-06)
      IF(STRANT .LT. 0.15) GO TO 610
      RR = 1. + (STRANT*(1. - RR)/2.25E-02)*(STRANT - 3.0E-01)
      GO TO 610
C
  605 RR = 1.0
  610 IF(ANRIN .GT. 0.) RR = ANRIN
      A1 = RR/(RR + 1.0)
      A2 =-(RR - 5.4)/(4.4 * (RR+1.0))
      A3 = 1.0/(RR + 1.0)
C
      ELMOD  = CELMOD(CTEMP, FNCK, CWKF,DELOXY)
C
C     CALCULATION OF STRAIN FOLLOWS
      STRAN1 = STREST/ELMOD
C
      IF(STRANT .LT. 1.0E-15) STRANT = 1.0E-15
      STRAN4 = STRANT
      II = 0
  104 STRANT = ((AN/AM+1.0)*(1.0E-03)*((STREST/AK)**(1/AM))*DELH
     #          + (STRAN4)**(AN/AM + 1.0))**(AM/(AN+AM))
      RSTRAN = (STRANT - STRAN4)/DELH
C     CORRECT AM FOR REVISED RSTRAN IF NECESSARY
      IF(T .LT. 1090.) GO TO 200
      IF(T .GT. 1255.) GO TO 200
      IF(RSTRAN .GT. 6.34E-03) GO TO 200
      II = II + 1
      AM = -6.4E-02 + T*2.203E-04
      IF(T .GT. 1172.5) GO TO 124
```

TABLE B-9.III (continued)

```
      AM = AM + 6.78E-02*ALOG(6.34E-03/RSTRAN)*((T-1090.)/82.5)
      GO TO 125
  124 AM = AM + 6.78E-02*ALOG(6.34E-03/RSTRAN)*((1255.-T)/82.5)
  125 AM = AM +  EXP(-69. * DELOXY)
      IF(II .LT. 10) GO TO 104
C
  200 STRAN2 = STRANT
      IF(STRAN2 .GT. STRAN1) STRANT = STRAN2
      IF(STRAN2 .LE. STRAN1) STRANT = STRAN1
      IF(STRANT .GT. 225.)   STRANT = 225.
      STRANE =  EXP(STRANT) - 1.0
C
      RETURN
      END
```

10. CLADDING TEXTURE FACTORS (CTXTUR)

(D. L. Hagrman)

Texture factors are required to model all structure-sensitive materials properties. The subroutine CTXTUR calculates the numbers needed to describe material texture for those materials properties subcodes which specifically consider texture variations[a].

10.1 Description of the Model

The input information for the subcode CTXTUR is obtained from a basal pole figure. The pole figure is a stereographic plot of the relative number of basal poles found at specified orientations. Figure B-10.1 is a schematic illustration showing the relation between the basal pole intensity (concentration found from X-ray diffraction) at one orientation and the intensity on a typical pole figure. The intensity, I, at an angle θ to the radial direction and ϕ to the circumferential direction of a cladding sample is projected from its orientation on a sphere of arbitrary diameter to the radius r and angle ϕ in the circumferential-axial plane and recorded on the plot as a number, I.

The radius r on the pole figure is related to the angle θ by

$$\frac{r}{r_o} = \tan\left(\frac{\theta}{2}\right) \qquad \text{(B-10.1)}$$

where

r_o = radius of the sphere shown in Figure B-10.1 and of the pole figure plot.

The input information required by CTXTUR is a nine by nine array of basal pole intensities from a pole figure. If θ and ϕ are the angles defined in Figure B-10.1, element

[a] In the MATPRO 11 package only CELAST (B.5) and CAGROW (B.6) require this information.

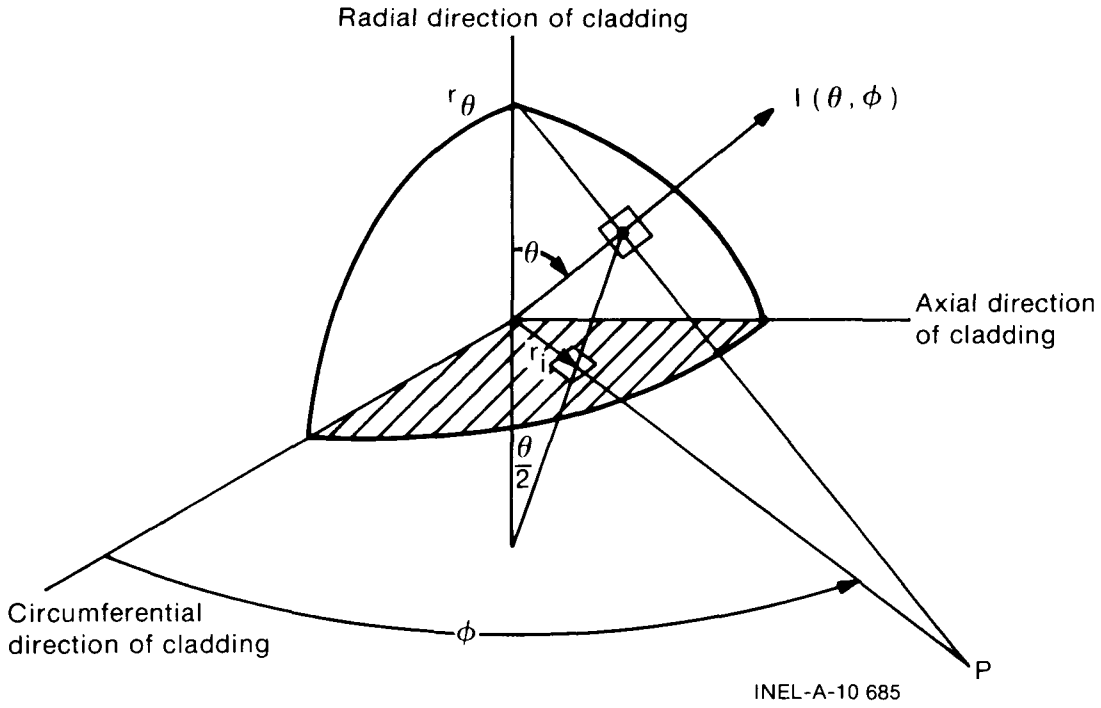

Fig. B-10.1 Schematic illustration showing the relation between basal pole intensity at one orientation (θ,ϕ) and the plotted value of the intensity at (r, ϕ) on a pole figure.

(1,1) of the input array is the average intensity for θ from 0 to 10 degrees and ϕ from 0 to 10 degrees. Element (1,2) is the average intensity for θ from 0 to 10 degrees and ϕ from 10 to 20 degrees, and so on.

A typical input grid is presented in Figure B-10.2. Input element (1,1) would be the average basal pole intensity in the area labeled (1,1) and so on. For the present version of this routine the pole figure is assumed to represent material with mirror plane symmetry about the planes containing two of the three axes so only one quadrant of the pole figure is used.

Eight volume fraction weighted averages of various cosines are returned by the CTXTUR subcode. In each case, the volume weighted average is defined by the integral

$$\langle g \rangle = \int_0^{2\pi} \int_0^{\pi} g(\theta,\phi)\ \rho(\theta,\phi)\ \sin\theta\ d\theta\ d\phi \qquad \text{(B-10.2)}$$

where

g = any function of the angles θ and ϕ which have been previously defined

$\langle g \rangle$ = volume fraction weighted average of g

$\rho(\theta,\phi)$ = volume fraction of grains with their c axes orientated in the region $\sin\theta\ d\phi\ d\theta$ about ϕ and θ.

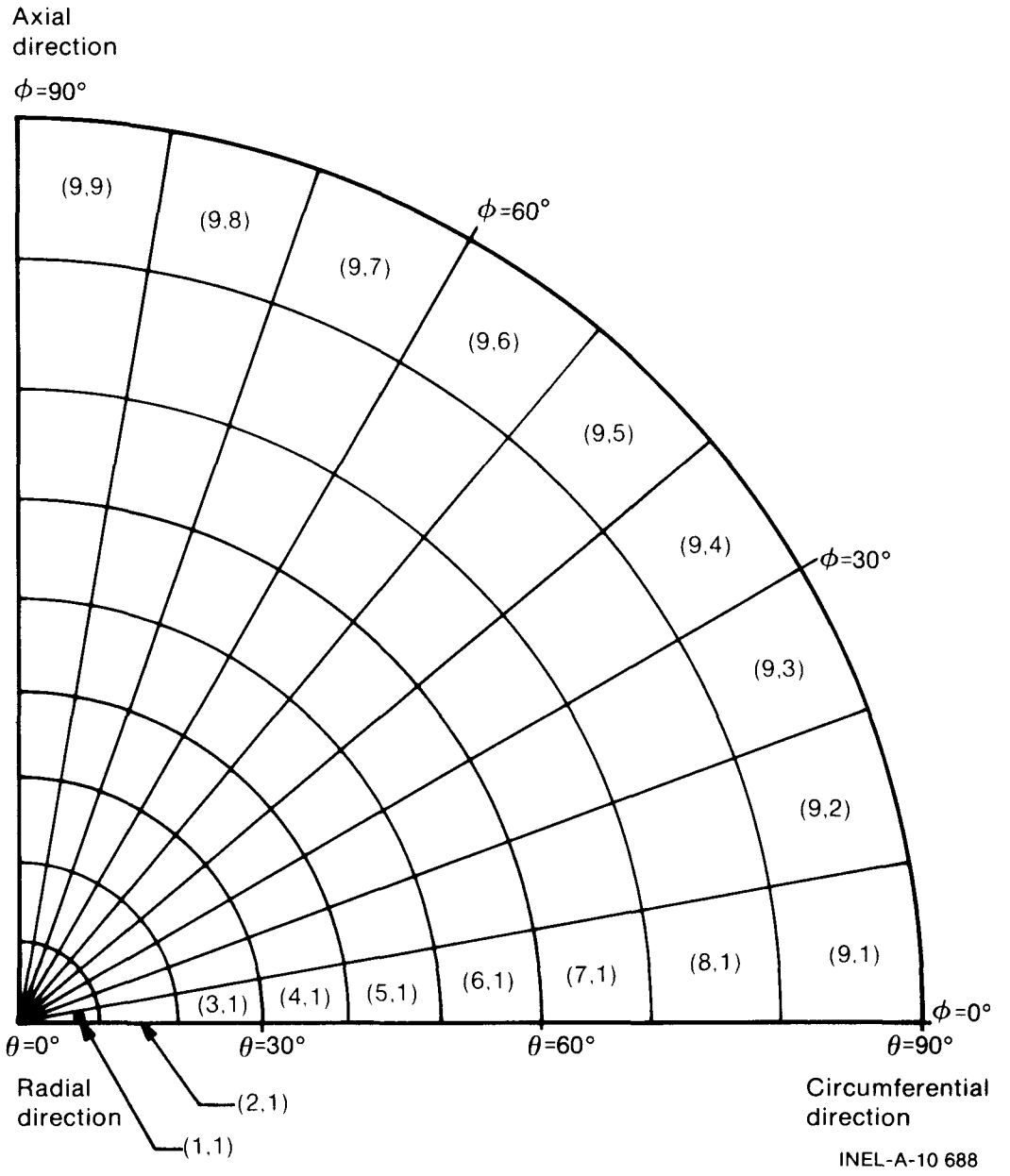

Fig. B-10.2 Input grid for CTXTUR subcode.

The function ρ is determined by normalizing the input average intensity values to $\frac{1}{4\pi}$ for randomly distributed basal poles. The exact normalization equation is

$$\rho(\theta,\phi) = \frac{I(\theta,\phi)}{\int_0^{2\pi}\int_0^{\pi} I(\theta,\phi)\,\sin\theta\,d\theta\,d\phi} \qquad \text{(B-10.3)}$$

where

$I(\theta, \phi)$ = the diffracted X-ray intensity of the basal planes at (θ,ϕ) as plotted in basal pole figures.

Equation B-10.3 is approximated with a sum of the average X-ray intensities which are required input information.

$$\rho_{r,s} \quad \frac{\text{Input Element } (r,s)}{\sum_{i=1}^{9}\sum_{j=1}^{9} \text{Input Element } (i,j)\ \sin\theta_i \left[\frac{\pi}{18}\ \text{radians}\right]^2} \qquad \text{(B-10.4)}$$

where

$\rho_{r,s}$ = average fraction of grains with their c axis oriented in the (i,j)th grid element

$\sin\theta_i$ = sine of the angle θ at the center of the (i,j)th grid element.

Once the weighting factors $\rho_{r,s}$ have been obtained from the pole figure, the averages defined in Equation (B-10.2) are approximated with the sum

$$\langle g \rangle = \sum_{r=1}^{9}\sum_{s=1}^{9} g_{r,s}\ \rho_{r,s}\ \sin\theta_{r,s}\ \left[\frac{\pi}{18}\ \text{radians}\right]^2 \qquad \text{(B-10.5)}$$

where

$g_{r,s}$ = the value of g at the center of the (r,s) element.

The eight volume fraction weighted averages returned by the CTXTUR subcode are $\langle\cos^2\theta\rangle$, $\langle\cos^4\theta\rangle$, $\langle\cos^2\alpha\rangle$, $\langle\cos^4\alpha\rangle$, $\langle\cos^2\theta\cos^2\alpha\rangle$, $\langle\cos^2\theta\cos^4\alpha\rangle$, $\langle\cos^4\theta\cos^2\alpha\rangle$, and $\langle\cos^4\theta\cos^4\alpha\rangle$[a], where α is the complement of ϕ.

Several other frequently used texture factors can be obtained from the eight averages which are returned. For example, the cosine of the angle between the direction defined by θ and ϕ in Figure B-10.3 and the circumferential direction of the cladding is

$$\cos\Psi = \sin\theta\sin\alpha \qquad \text{(B-10.6)}$$

The circumferential texture factor defined by Kearns[B-10.1] is thus

$$f_\theta = \langle\cos^2\Psi\rangle = \langle 1\rangle - \langle\cos^2\theta\rangle - \langle\cos^2\alpha\rangle + \langle\cos^2\theta\cos^2\alpha\rangle \qquad \text{(B-10.7)}$$

where

f_θ = circumferential texture factor.

---

[a] For the mirror plane symmetry assumed in this routine, some of these outputs are redundant. For instance, $\langle\cos^2\theta\cos^2\alpha\rangle = \langle\cos^2\alpha\rangle\langle\cos^2\theta\rangle$. The extra outputs are included in case the routine needs to be generalized in the future to consider material without mirror plane symmetry.

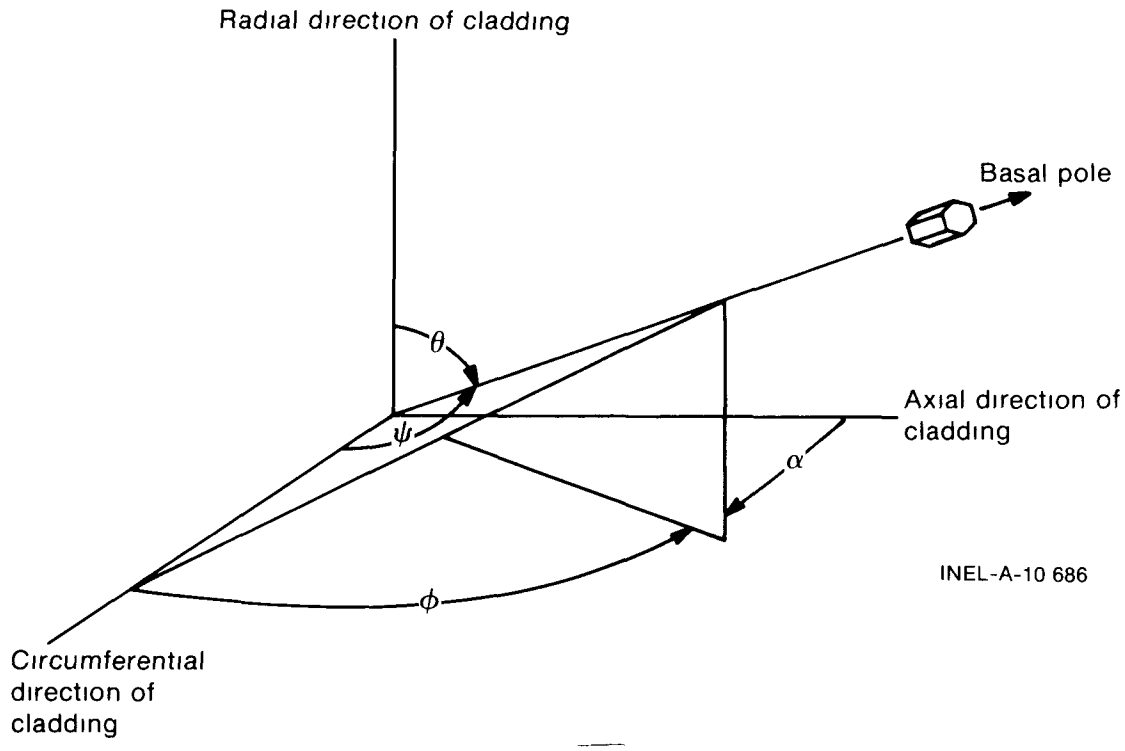

Fig. B-10.3 Relation between angles used in the definition of Kearn's texture factor (f_ϕ) and angles averaged by CTXTUR subcode.

Similarly the axial texture factor of Kearns is

$$f_z = \langle \cos^2\alpha \rangle - \langle \cos^2\theta \cos^2\alpha \rangle \qquad \text{(B-10.8)}$$

where

f_z = axial texture factor.

10.2 Cladding Texture Factors Subcode CTXTUR Listing

The subcode CTXTUR is listed in Table B-10.I.

10.3 Reference

B-10.1. J. J. Kearns, *Thermal Expansion and Preferred Orientation in Zircaloy*, WAPD-TM-472 (November 1965).

TABLE B-10.I

LISTING OF THE CTXTUR SUBCODE

```
      SUBROUTINE CTXTUR(TENSTY,COSTH2,COSTH4,COSFI2,COSFI4,
     #                  CT2CF2,CT2CF4,CT4CF2,CT4CF4)
C
      DIMENSION TENSTY(9,9),COS2TH(9,9),COS4TH(9,9),COS2FI(9,9),
     #COS4FI(9,9),C2TC2F(9,9),C2TC4F(9,9),C4TC4F(9,9),AN(9),C2(9),C4(9),
     #C4TC2F(9,9),B2(9),B4(9),CA(9)
C
C     CTXTUR CALCULATES ORIENTATION PARAMETERS FROM BASAL POLE
C     FIGURE INTENSITY GRIDS
C
C     IN THE FOLLOWING, THETA IS THE ANGLE BETWEEN THE RADIAL
C     OR NORMAL DIRECTION OF THE SAMPLE AND THE BASAL POLE
C     DIRECTION. PHI IS THE ANGLE BETWEEN THE PROJECTION OF THE
C     BASAL POLE DIRECTION ONTO THE PLANE CONTAINING THE AXIAL
C     AND CIRCUMFERENTIAL DIRECTIONS AND THE CIRCUMFERENTIAL
C     DIRECTION. ALPHA IS THE COMPLEMENT OF PHI.
C
C     COSTH2 = OUTPUT VOLUME FRACTION WEIGHTED AVERAGE OF THE SQUARED
C              COSINE OF THETA (UNITLESS)
C     COSTH4 = OUTPUT VOLUME FRACTION WEIGHTED AVERAGE OF THE
C              FOURTH POWER OF THE COSINE OF THETA (UNITLESS)
C     COSFI2 = OUTPUT VOLUME FRACTION WEIGHTED AVERAGE OF THE SQUARED
C              COSINE OF ALPHA (UNITLESS RATIO)
C     COSFI4 = OUTPUT VOLUME FRACTION WEIGHTED AVERAGE OF THE
C              FOURTH POWER OF THE COSINE OF ALPHA (UNITLESS)
C     CT2CF2 = OUTPUT VOLUME FRACTION WEIGHTED AVERAGE OF THE PRODUCT
C              OF THE SQUARED COSINE OF THETA AND THE SQUARED COSINE
C              OF ALPHA (UNITLESS)
C     CT2CF4 = OUTPUT VOLUME FRACTION WEIGHTED AVERAGE OF THE PRODUCT
C              OF THE SQUARED COSINE OF THETA AND THE FOURTH POWER OF
C              THE COSINE OF ALPHA (UNITLESS)
C     CT4CF2 = OUTPUT VOLUME FRACTION WEIGHTED AVERAGE OF THE PRODUCT
C              OF THE FOURTH POWER OF THE COSINE OF THETA AND THE
C              SQUARED COSINE OF ALPHA (UNITLESS)
C     CT4CF4 = OUTPUT VOLUME FRACTION WEIGHTED AVERAGE OF THE PRODUCT
C              OF THE FOURTH POWER OF THE COSINE OF THETA AND THE
C              FOURTH POWER OF THE COSINE OF ALPHA (UNITLESS)
C
C     TENSTY = INPUT DIMENSIONED ARRAY OF BASAL POLE INTENSITIES
C              FROM A POLE FIGURE. ELEMENT TENSTY(1,1) IS THE AVERAGE
C              INTENSITY FOR THETA FROM 0 TO 10 DEGREES AND PHI
C              FROM 0 TO 10 DEGREES. ELEMENT TENSTY(1,2) IS THE
C              AVERAGE INTENSITY FOR THETA FROM 0 TO 10 DEGREES
C              AND PHI FROM 10 TO 20 DEGREES. ETC. FOR THE
C              ENTIRE POLE FIGURE. (ARBITRARY UNITS)
C
C     THE CALCULATION OF ORIENTATION PARAMETERS IS BASED ON
C     AN APPROACH SUGGESTED BY THE FOLLOWING REFERENCES
C     (1) J. J. KEARNS, THERMAL EXPANSION AND PREFERRED ORIENTATION
C         IN ZIRCALOY, WAPD-TM-472 (NOV. 1965)
C     (2) H. S. ROSENBAUM AND J. E. LEWIS, USE OF POLE FIGURE DATA
C         TO COMPUTE ELASTICITY COEFFICIENTS OF ZIRCONIUM SHEET,
C         JOURNAL OF NUCLEAR MATERIALS 67 (1977) PP 273-282
C
C     CTXTUR WAS CODED BY D. L. HAGRMAN IN DECEMBER 1977
C
C     FIND ANGLES AT GRID CENTERS
      DO 20 J=1,9
      AN(J) = (2*J - 1) * 8.726646E-02
      CA(J) = 1.570796 - AN(J)
C
      B2(J) = (COS(CA(J)))**2
      B4(J) = (B2(J))**2
      C2(J) = (COS(AN(J)))**2
   20 C4(J) = (C2(J))**2
C
C     FIND NORMALIZATION CONSTANT
      TNSTYN = 0.0
      DO 10 J=1,9
      DO 10 I=1,9
   10 TNSTYN = TNSTYN + TENSTY(I,J) * SIN(AN(I))
C
```

TABLE B-10.I (continued)

```
C       FIND RHO * SINE(THETA)
        DO 15 J=1,9
        DO 15 I=1,9
   15 TENSTY(I,J) = TENSTY(I,J)*SIN(AN(I))/TNSTYN
C
C       FIND RHO * SINE(THETA) * ARGUMENT
        DO 25 J=1,9
        DO 25 I=1,9
        COS2TH(I,J) = TENSTY(I,J)*C2(I)
        COS4TH(I,J) = TENSTY(I,J)*C4(I)
        COS2FI(I,J) = TENSTY(I,J)*B2(J)
        COS4FI(I,J) = TENSTY(I,J)*B4(J)
        C2TC2F(I,J) = TENSTY(I,J)*C2(I)*B2(J)
        C2TC4F(I,J) = TENSTY(I,J)*C2(I)*B4(J)
        C4TC2F(I,J) = TENSTY(I,J)*C4(I)*B2(J)
   25 C4TC4F(I,J) = TENSTY(I,J)*C4(I)*B4(J)
C
C       FIND VOLUME WEIGHTED AVERAGES
        COSTH2 = 0.0
        COSTH4 = 0.0
        COSFI2 = 0.0
        COSFI4 = 0.0
        CT2CF2 = 0.0
        CT2CF4 = 0.0
        CT4CF2 = 0.0
        CT4CF4 = 0.0
        DO 30 J=1,9
        DO 30 I=1,9
        COSTH2 = COSTH2 + COS2TH(I,J)
        COSTH4 = COSTH4 + COS4TH(I,J)
        COSFI2 = COSFI2 + COS2FI(I,J)
        COSFI4 = COSFI4 + COS4FI(I,J)
        CT2CF2 = CT2CF2 + C2TC2F(I,J)
        CT2CF4 = CT2CF4 + C2TC4F(I,J)
        CT4CF2 = CT4CF2 + C4TC2F(I,J)
   30 CT4CF4 = CT4CF4 + C4TC4F(I,J)
C
        RETURN
        END
```

11. CLADDING MECHANICAL LIMITS (CMLIMT), CLADDING STRAIN AT RUPTURE (CSRUPT), CLADDING WALL THINNING (CTHIN) AND CLADDING LOCAL STRAINS AT RUPTURE (CLOCRP)

(D. L. Hagrman)

Four subcodes are provided to calculate various zircaloy cladding mechanical limits. The first, CMLIMT, calculates true and engineering values of strain at yield, strain at maximum load, yield strength and ultimate strength in a uniaxial test as well as circumferential elongation at burst, circumferential elongation at instability and hoop stress at burst for a closed tube burst test. The second subcode, CSRUPT, repeats the correlation for total circumferential strain at rupture and adds expressions for the uncertainty of the correlation. The third, CTHIN calculates the ratio (average cladding wall thickness/minimum wall thickness) at rupture. The fourth, CLOCRP, predicts local strains at failure of zircaloy cladding in the temperature range 1050 to 1370 K.

CMLIMT is designed for general use with fuel rod analysis programs while CSRUPT is designed specifically for use with subcodes which describe fuel rod integrity limits using a

statistical approach. CTHIN is a preliminary subcode for relating engineering stress at failure (a commonly used criterion) to true hoop stress at failure. CLOCRP is a preliminary code intended for use with models which predict local strains instead of circumferentially averaged strains.

11.1 Summary

The required input information for CMLIMT is the average temperature at an axial node, an estimate of temperature variation within the axial node, cold work, fast neutron fluence ($E > 1$ MeV), average oxygen concentration, and strain rate. The equations used by CMLIMT for true strain at yield, true strain at maximum load, yield strength and ultimate strength in a uniaxial stress test are, respectively,

$$\text{True Strain at Yield} = \left[\frac{K}{E}\left(\frac{\dot{\epsilon}}{10^{-3}}\right)^{m}\right]^{\frac{1}{1-n}}. \tag{B-11.1}$$

$$\text{True Strain at Maximum Load} = \frac{n}{1+m} \tag{B-11.2}$$

$$\text{True Yield Strength} = \frac{K}{E^{n}}\left(\frac{\dot{\epsilon}}{10^{-3}}\right)^{m\,\frac{1}{1-n}} \tag{B-11.3}$$

$$\text{True Ultimate Strength} = K\left(\frac{\dot{\epsilon}}{10^{-3}}\right)^{m}\left(\frac{n}{1+m}\right)^{n} \tag{B-11.4}$$

where

K = strength coefficient (Pa)

n = strain hardening exponent (unitless)

$\dot{\epsilon}$ = true strain rate (s^{-1})

m = strain rate sensitivity constant (unitless)

E = Young's modulus (Pa).

K, n, and m are calculated with the subcode CKMN discussed in the description of CSTRES (Section B-8, this appendix), E is obtained by calling the function CELMOD (Section B-5, this appendix), and ϵ is required input information. The strain rate, ϵ should be determined from values of strain closely spaced in time. Rates averaged over long periods of time may not provide a good description of the instantaneous state of the material.

The following four correlations predict circumferential elongation of cladding at rupture.

for temperatures less than 1090 kelvins,

$$STRRPE = (0.198 + 4.16 \times 10^{-4}T + 2.06 \times 10^{-7}T^2)R\ D \quad \text{(B-11.5a)}$$

for temperatures between 1090 and 1170 kelvins

$$STRRPE = (9.06231055 - 7.491855 \times 10^{-3}T)\ D \quad \text{(B-11.5b)}$$

for temperatures between 1170 and 1600 kelvins

$$STRRPE = (-1.436 + 2.045 \times 10^{-3}T - 4.82 \times 10^{-7}T^2)\ D \quad \text{(B-11.5c)}$$

for temperatures greater than 1600 kelvins

$$STRRPE = 0.60208\ D \quad \text{(B-11.5d)}$$

where

STRRPE	=	circumferential elongation at rupture (rupture circumference minus initial circumference divided by initial circumference)
T	=	average temperature at rupture (kelvins)
R	=	factor which accounts for the effects of irradiation and cold work on the circumferential elongation of zircaloy cladding at rupture
D	=	factor which accounts for the effects of temperature variation on the circumferential elongation of zircaloy at rupture.

R = 1 for annealed material and decreases with irradiation or cold work. D = 1 when the temperature variation in the node is zero and decreases with increasing temperature variation. The factors R and D are described in Section B-11.3.

The circumferential elongation at instability returned by CMLIMT is one-fourth the circumferential elongation at burst of annealed cladding with no temperature variation when temperature is less than or equal to 1090 kelvins. For temperatures above 1255 kelvins the instability strain is one-half the burst strain. For temperatures between 1090 and 1255 kelvins the instability strain is determined by interpolation

for temperatures less than 1090 kelvins

$$\text{Instability Strain} = \frac{0.25\ STRRPE}{RD}\ . \quad \text{(B-11.6a)}$$

for temperatures between 1090 and 1255 kelvins

$$\text{Instability Strain} = \left(1 + \frac{T-1090}{165}\right)\left(\frac{0.25\ \text{STRRPE}}{RD}\right) . \qquad \text{(B-11.6b)}$$

for temperatures greater than 1255 kelvins

$$\text{Instability Strain} = \frac{0.50\ \text{STRRPE}}{RD} . \qquad \text{(B-11.6c)}$$

The terms of the Equations (B-11.6a) to (B-11.6c) have been previously defined.

The correlation for hoop stress at burst in a closed tube burst test used in CMLIMT is a preliminary expression which was derived without consideration of cold work, irradiation, oxidation, strain, or temperature variation effects.

$$S = 10^{\left[8.42 + T\left[2.78 \times 10^{-3} + T(-4.87 \times 10^{-6} + T\ 1.49 \times 10^{-9})\right]\right]} \qquad \text{(B-11.7)}$$

where

S = engineering hoop stress at burst (Pa)

T = temperature at rupture (kelvins).

Both engineering and true stress and strain are returned by CMLIMT. To obtain engineering strains or stresses from true strain[a] or true stress[b] in Equations (B-11.1) to (B-11.4) the true values are converted to engineering stress[c] or engineering strain[d] using the relations

$$\text{engineering stress} = \frac{\text{true stress}}{\exp(\text{true strain})} \qquad \text{(B-11.8)}$$

$$\text{engineering strain} = \exp(\text{true strain}) - 1. \qquad \text{(B-11.9a)}$$

The inverse of Equation (B-11.9a),

$$\text{true strain} = \ln(\text{engineering strain} + 1) \qquad \text{(B-11.9b)}$$

---

[a] True strain = the change in length divided by the length at the instant of change and integrated from initial to final length $\int_{Lo}^{L} \frac{d\ell}{\ell}$.

[b] True stress = the force per unit cross-sectional area with the area determined at the instant of measurement of the force.

[c] Engineering stress = the force per unit cross-sectional area with the area determined when the strain was zero.

[d] Engineering strain = the change in length divided by the original length.

is used with the engineering strains from Equations (B-11.5) and (B-11.6) to obtain true strains. No expression for true stress at burst is available in MATPRO 11. Instead an effective true hoop stress at failure for symmetric deformation is calculated with Equations (B-11.5) and (B-11.7)

$$\sigma_{symm} = S\ (1 + STRRPE)^2. \qquad \text{(B-11.10)}$$

The expressions used in the CSRUPT subcode for expected standard error[a] of the prediction for circumferential elongation are as follows:

for temperatures less than 800 kelvins

$$\sigma = \text{the smaller of } 0.08 \text{ or the predicted value} \qquad \text{(B-11.11a)}$$

for temperatures between 800 and 1090 kelvins

$$\sigma = (0.36/290)\ (T-800) + 0.08 \qquad \text{(B-11.11b)}$$

for temperatures between 1090 and 1170 kelvins

$$\sigma = -4.125 \times 10^{-3}\ (T-1090) + 0.44 \qquad \text{(B-11.11c)}$$

for temperatures above 1170 kelvins

$$\sigma = 0.11 \qquad \text{(B-11.11d)}$$

where

σ = expected standard error (Pa)

T = temperature at rupture (kelvins).

The standard errors given by Equations (B-11.11) were determined with the assumption that temperature variations were zero.

The expression used in the CTHIN subcode to calculate the ratio (average wall thickness/minimum wall thickness) at rupture is

$$RT = \left[\frac{1.0 + STRRPE/D}{1.0 + STRRPE}\right]^2 \qquad \text{(B-11.12)}$$

[a] The standard error (σ) of a model is estimated with a set of data by the expression: (sum of squared residuals/number of residuals minus the number of constants used to fit the data)$^{1/2}$.

where

RT = average wall thickness/minimum wall thickness

and the other terms were defined in conjunction with Equations (B-11.5a) through (B-11.5d).

Cladding local temperature is the only required input information for the local strain subcode (CLOCRP). For temperatures in kelvins, true local radial (wall thickness) and true local circumferential strains at rupture are given by the correlations

$$\text{Circumferential strain} = -0.415 + (0.001368 \times \text{temperature}) \quad \text{(B-11.13)}$$

$$\text{Radial strain} = -0.0107 - (0.001305 \times \text{temperature}). \quad \text{(B-11.14)}$$

Corresponding engineering strains are calculated with Expression (B-11.9a). The CLOCRP subcode is preliminary since it is based only on seven cross sections of tubes burst between 1090 and 1320 kelvins. However, surprisingly consistent results are obtained with these few tests. Local circumferential and local radial (wall thickness) strains at rupture are found to be closely approximated with linear functions of temperature. This implies that the pronounced minimum in average circumferential expansion during the alpha-beta phase transition is a localization of circumferential strain rather than a reduction of the local strain required for rupture.

The following section describes the derivation of Equations (B-11.1) to (B-11.4). The correlations for circumferential rupture elongation and circumferential instability elongation, Equations (B-11.5) and (B-11.6), are discussed in Section B-11.3. The uncertainty of the expression for circumferential elongation at rupture is discussed in Section B-11.4. Equations (B-11.7) and (B-11.10) for hoop stress at burst and Equation (B-11.12) for average wall thickness divided by minimum wall thickness are derived in Section B-11.5. The preliminary correlations for local strain at failure, Equations (B-11.13) and (B-11.14), are discussed in Section B-11.6. Section B-11.7 contains examples of the output of the CMLIMT and CSRUPT codes. Subcode listings are provided in Section B-11.8 and references are contained in Section B-11.9.

11.2 Derivation of Expressions for Yield and Maximum Load Points in a Uniaxial Stress Test

The yield point is taken to be the nonzero intersection of the stress-strain curves given by Hooke's law for the elastic region

$$\sigma = E\,\varepsilon. \quad \text{(B-11.15)}$$

and by the modified power law used in CSTRES and CSTRAN for the plastic region

$$\sigma = K \epsilon^{n} \left(\frac{\dot{\epsilon}}{10^{-3}}\right)^{m} \qquad \text{(B-11.16)}$$

where

σ = true stress (Pa)

ϵ = true strain (unitless)

$\dot{\epsilon}$ = true strain rate (s^{-1})

E = Young's modulus (Pa)

K = strength coefficient (Pa)

n = strain hardening exponent (unitless)

m = strain rate sensitivity constant (unitless).

Solution of these simultaneous equations gives the yield strain and yield strength described by Equations (B-11.1) and (B-11.3), respectively.

The point of maximum load in a uniaxial stress test at constant engineering strain rate is found by converting the true stress and true strain rate in Equation (B-11.16) to their engineering equivalents

$$\sigma = S \exp(\epsilon) \qquad \text{(B-11.17)}$$

$$\dot{\epsilon} = \dot{e}/\exp(\epsilon) \qquad \text{(B-11.18)}$$

where

S = engineering stress (Pa)

$\dot{e}$ = engineering strain rate (s^{-1}).

The derivative of S with respect to ϵ is zero at the true strain given by Equation (B-11.2) and the true stress at this strain is given by Equation (B-11.4).

11.3 Expressions for Circumferential Rupture Elongation and Circumferential Instability Elongation

The expression for circumferential rupture elongation is derived by modeling isothermal burst elongation for annealed cladding first and adding factors to consider the

effects of irradiation, cold work, and temperature variation. Equation (B-115a) with R = 1 for annealed tubing and D = 1 for nearly uniform temperature at temperatures below 1090 kelvins is obtained from a least-squares fit to data when taken from tests in inert atmospheres[B-11.1 – B-11.4]. Data from References B-11.1 and B-11.4 are from isothermal tests on annealed tubes while the other two sources describe transient tests on cold-worked and stress-relieved tubes at temperatures sufficiently high to anneal the cold work effects.

Equations (B-11.5b), (B-11.5c), and (B-11.5d), for uniform temperatures above 1090 kelvins are based on tests in steam environments[B-11.5 – B-11.8]. Equation (B-11.5c) with D = 1 is a least-squares fit to the data in steam reported in References B-11.5 to B-11.8. Equation (B-11.5b) is constructed by inspection of the limited data in the region from 1090 to 1170 kelvins (the first half of the alpha + beta transition region of zircaloy). The circumferential elongation to failure is simply set equal to a constant in Equation (B-11.5d) because of the lack of data.

Analytical expressions for the circumferential elongation at rupture of cold-worked or irradiated cladding are obtained by multiplying the elongation of annealed cladding by the factor R used in Equation (B-11.5a). R is defined by

$$R = PQ \tag{B-11.19}$$

where

P = all effects of cold work

Q = all effects of irradiation.

When annealing has not occurred, the values of P and Q are

$$P_o = \left[\frac{\exp\ (-21 \times COLDW) + 0.33}{1.33}\right] \tag{B-11.20}$$

and

$$Q_o = \left[\frac{1 + 2\ \exp\ (-FNCE/10^{23})}{3}\right] \tag{B-11.21}$$

where

COLDW = cold work (fraction of cross-sectional area reduction)

FNCE = fast neutron fluence (neutrons/m^2)

P_o = effects of cold work without annealing

Q_o = effects of irradiation without annealing.

Equations (B-11.20) and (B-11.21) are based on data of Reference B-11.9 from tensile tests using flat plates because measurements of circumferential elongation to rupture as a function of irradiation and cold work in a single lot of tubing are not available. The axial elongation to failure in tensile tests is known to differ from circumferential deformation to rupture[B-11.10]. However, the ratio of circumferential strains of highly irradiated and annealed tubing is similar to the ratio of axial strains measured during tensile tests or irradiated and annealed material.

Figure B-11.1 compares the ratios obtained using the values of elongation at failure reported in Reference B-11.9 and the model based on these data [Equations (B-11.20) and (B-11.21)]. Cold work to an area reduction of 0.1 causes a drastic change in ductility but further cold work has little effect. Irradiation effects have become saturated by the time the fast neutron fluence is 10^{24} neutrons/m^2. Since typical end-of-life values of fast fluence are 4×10^{25} neutrons/m^2, most of the change in strain to rupture of the cladding occurs at beginning-of-life.

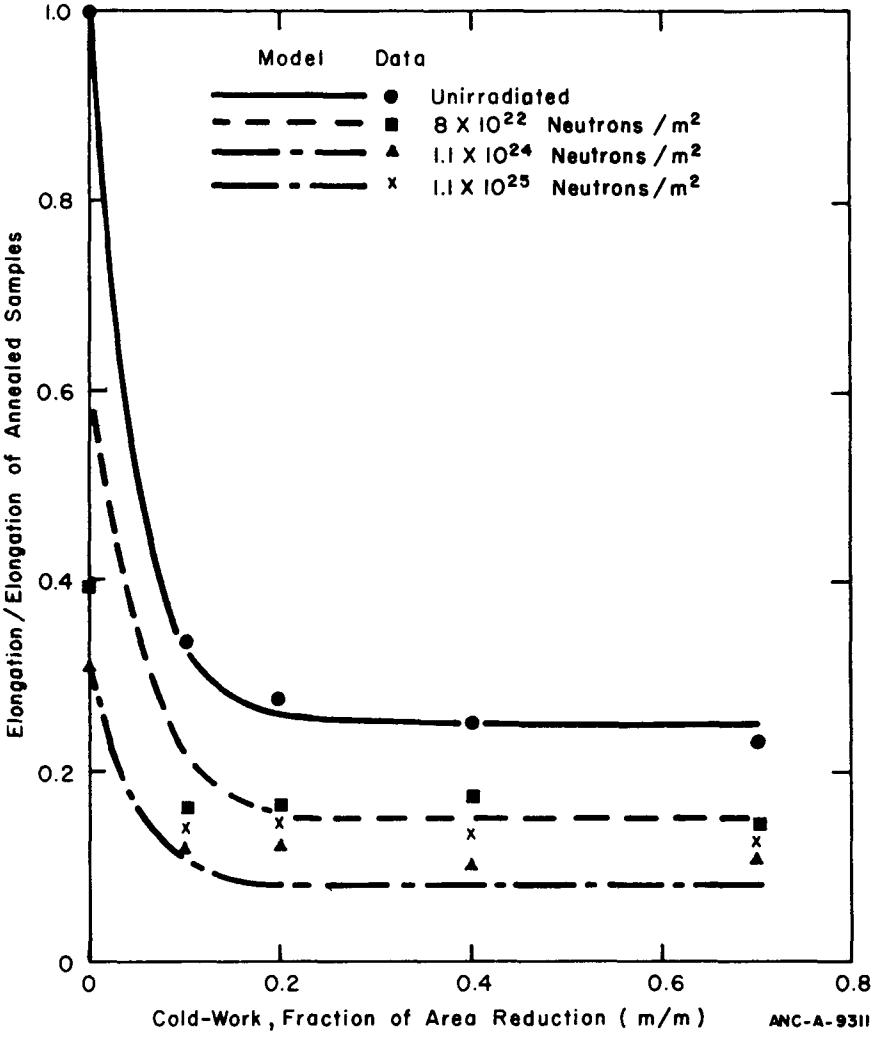

Fig. B-11.1 Ratios of elongation at failure for samples with varying amounts of cold work and fast neutron fluence to elongation at failure of an annealed sample.

Specific models for the effect of annealing of cold work and irradiation damage on circumferential elongation at rupture have not been constructed. These effects are approximated in the current version of MATPRO by replacing the cold work and fast neutron variables in Equations (B-11.20) and (B-11.21) by the effective cold work and fast neutron fluence for the strain hardening exponent[a].

An approximate expression for the effect of temperature variation on circumferential elongation at rupture was obtained by fitting recent data taken at temperatures near 1050 kelvins[B-11.11]. These data and MATPRO's prediction are shown in Figure B-11.2. Circumferential elongation decreases from 0.8 with only a few degrees temperature variation to 0.25 with 100 kelvins variation. The least-squares expression obtained by fitting an exponential function to the data is

$$\bar{e}_\theta = \exp\ (-0.0111\ \Delta T - 0.359) \qquad \text{(B-11.22)}$$

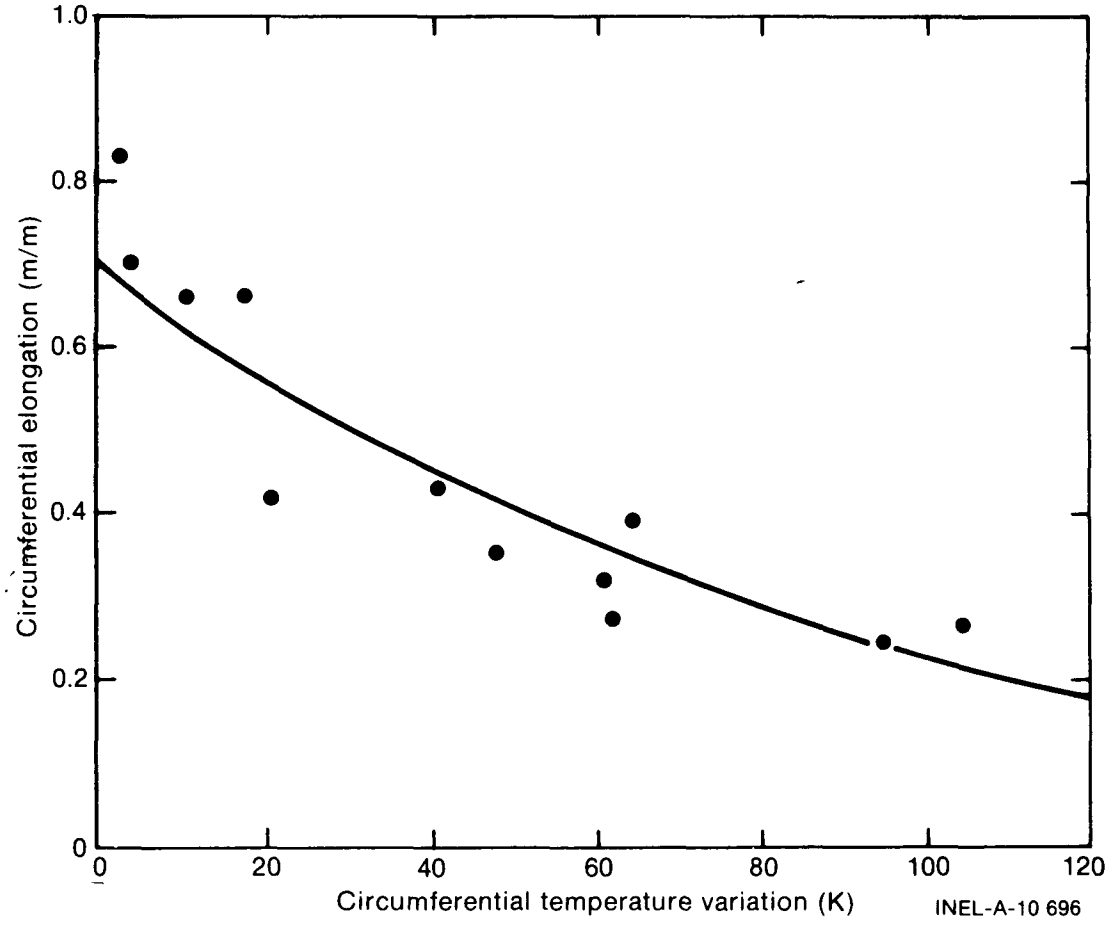

Fig. B-11.2 Base data and MATPRO correlation for effect of circumferential temperature variation on circumferential elongation.

[a] Effective cold work and fast neutron fluence for the strain hardening exponent are returned by the CANEAL subcode of Section B-8.

where

$\bar{e}_\theta$ = circumferential elongation (m/m)

ΔT = temperature variation (kelvins).

Since no other data are available, the reduction in circumferential elongation is assumed to be a function of the circumferential temperature gradient, independent of the average temperature. The resultant expression for the reduction in circumferential elongation due to temperature variation is

$$D = \exp(-0.0111\ \Delta T) \qquad \text{(B-11.23)}$$

where

D = ratio of circumferential elongation at rupture with a temperature variation to the isothermal elongation

ΔT = temperature variation (kelvins).

The correlation for circumferential elongation at instability, Equation (B-11.6), is based on data reported in Figures III-20 and III-22 of Reference B-11.12. The data and the MATPRO correlation are reproduced in Figure B-11.3. Since the two figures of Reference B-11.12 refer to different heating rates and different applied constraints, no effort is made to produce a detailed correlation at this time. The data conform roughly to one-fourth the circumferential elongation at rupture in the alpha phase region (temperature less than 1090 kelvins) and one-half the circumferential elongation at rupture in the beta phase region (temperature above 1255 kelvins) so these values are used.

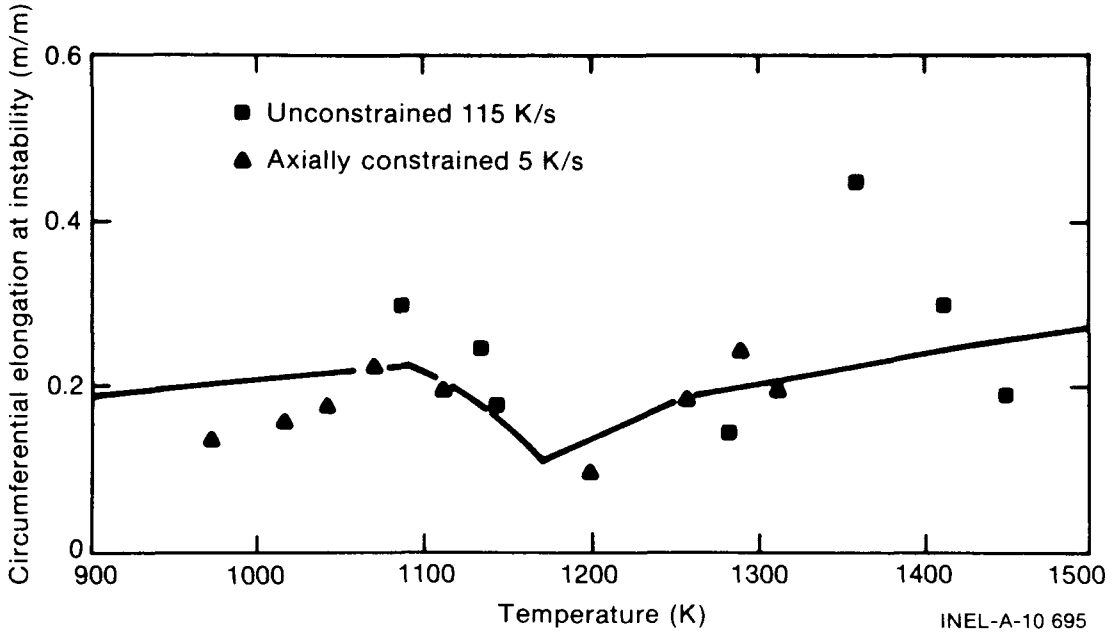

Fig. B-11.3 Measured circumferential elongation at instability compared to the MATPRO correlation.

11.4 Uncertainty of the Expression for Circumferential Elongation at Rupture

Equations (B-11.11a) through (B-11.11d) are based on the standard error of Equations (B-11.5a) through (B-11.5d) with $R = 1$ and $D = 1$. The error is evaluated with the model's own data base. These results are listed in Table B-11.I.

TABLE B-11.I

STANDARD ERROR OF PREDICTED STRAINS AT RUPTURE

Temperature Range (kelvins)	Standard Error (m/m)
290 to 800	0.082
800 to 1090	0.258
1170 to 1600	0.108

Equations (B-11.11a) and (B-11.11d) state results listed in Table B-11.I. Equation (B-11.11b) was obtained by noting that the scatter of measured values of strain at rupture increases as the beginning of the alpha + beta transition is approached. The average value for the region from 800 to 1090 kelvins, 0.26, is assumed to apply to the middle of the temperature range 800 to 1090 kelvins, and the uncertainty is assumed to increase linearly up to 1090 kelvins. In the region from 1090 to 1170 kelvins Equation (B-11.11c) is derived by assuming the uncertainty decreases from its value at 1090 kelvins to the value found for data taken above 1170 kelvins.

11.5 Expressions for Circumferential Stress at Burst

Equation (B-11.7) was derived using data from several burst tests[B-11.1, B-11.3, B-11.5, B-11.13 – B-11.17]. However, better data are now available and will be included in a revised burst stress correlation. Many of the new data include cross sections of burst tubes. It should thus be possible to estimate true stress at failure and eliminate much of the scatter in the older data which include only engineering stress at failure.

The interim approach to estimating true stress at failure uses Equation (B-11.23) for the reduction in circumferential elongation due to temperature variation. Three cross sections, corresponding to three different models, are considered. They are shown in Figure B-11.4. Figure B-11.4a represents the actual asymmetric cladding with local thinning at the hot spot and relatively little deformation at the coolest temperature. Figure B-11.4b represents an idealized symmetric deformation modeled by analytical codes which do not consider asymmetric deformation. The circumference of Figures B-11.4a and B-11.4b are equal. Figure B-11.4c represents a symmetrically deformed cladding with true stress equal to the maximum hoop stress of the actual asymmetric cladding.

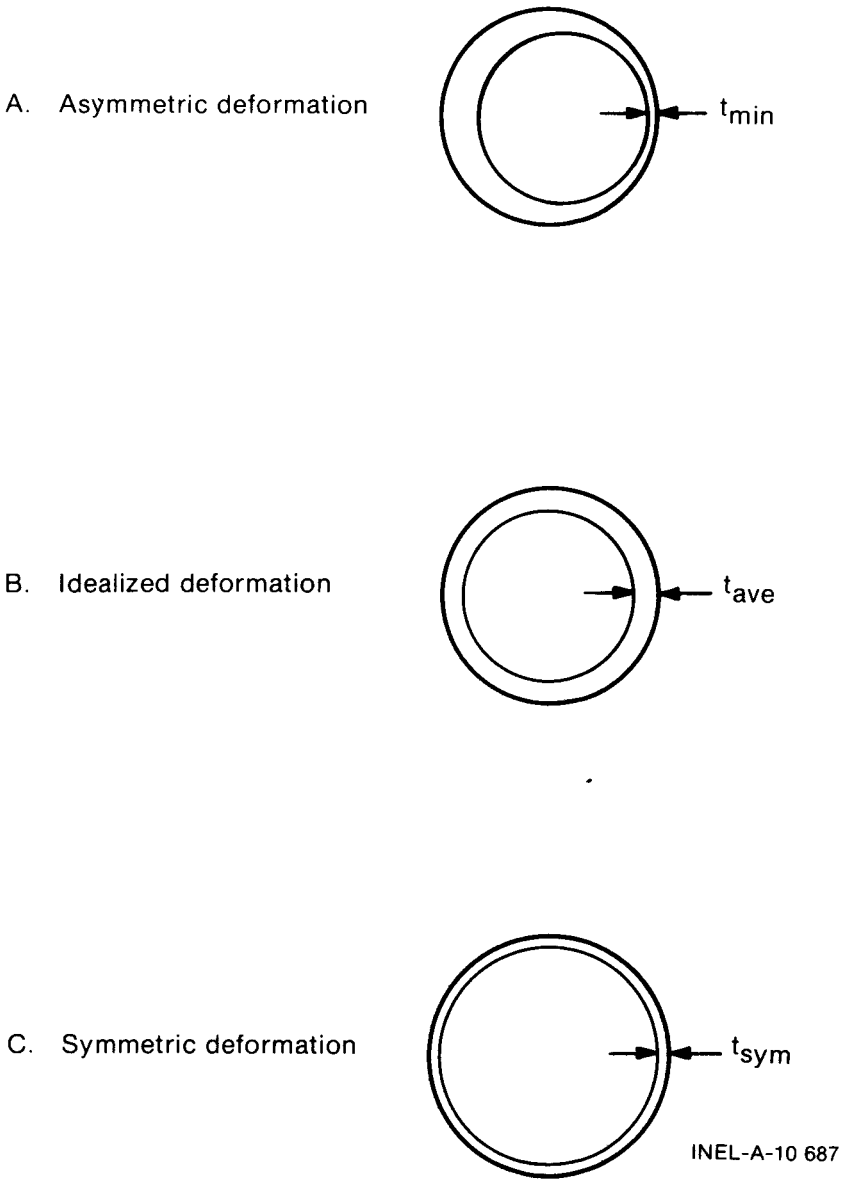

Fig. B-11.4 Schematic cross sections of cladding at burst.

An analytical model which assumes symmetry can not return both the correct circumference and the correct maximum stress of asymmetric deformation. However, it may be able to return the correct circumference and consider an effective stress which is equal to the maximum stress of the asymmetric deformation for predicting overstress failure. The remainder of this subsection is a derivation of expressions for the effective stress.

The maximum local true circumferential stress of the asymmetric deformation is approximately

$$\sigma_\theta = \frac{\Delta P \, r_a}{t_{min}} \qquad \text{(B-11.24)}$$

where

σ_θ = maximum circumferential stress calculated with asymmetric deformation (Pa)

ΔP = pressure differential (Pa)

r_a = radius of the cladding (m)

t_{min} = minimum cladding wall thickness (m).

The circumferential stress which will be used to predict the idealized deformation is approximately

$$\bar{\sigma}_\theta = \frac{\Delta P \; r_a}{t_{ave}} \tag{B-11.25}$$

where

$\bar{\sigma}_\theta$ = circumferential stress calculated with idealized deformation (Pa)

t_{ave} = wall thickness of the cladding predicted with idealized deformation (m).

From Equations (B-11.24) and (B-11.25), the circumferential stress at failure calculated with idealized deformation is related to the maximum local true stress by the equation

$$\bar{\sigma}_\theta = \sigma_\theta \frac{t_{min}}{t_{ave}} \tag{B-11.26}$$

The ratio $\frac{t_{min}}{t_{ave}}$ in Equation (B-11.26) is related to the reduction in circumferential elongation at failure. Since the maximum true local stress of asymmetric deformation and the circumferential stress of symmetric deformation are both equal to the burst stress,

$$\frac{\Delta P \; r_a}{t_{min}} = \frac{\Delta P \; r_{sym}}{t_{sym}} \tag{B-11.27}$$

where

r_{sym} = cross-sectional radius of symmetrically deformed cladding (m)

t_{sym} = wall thickness of symmetrically deformed cladding (m)

and the other terms were defined previously.

The incompressibility relations with the simplifying assumption that axial strain is less than radial or circumferential strain imply that the areas of the idealized and symmetrically deformed cladding are equal. This in turn implies

$$r_a\ t_{ave} = r_{sym}\ t_{sym}. \tag{B-11.28}$$

Equations (B-11.27) and (B-11.28) can be combined to show

$$\frac{t_{min}}{t_{ave}} = \left[\frac{r_a}{r_{sym}}\right]^2. \tag{B-11.29}$$

The radii r_a and r_c are related to the circumferential elongation of A and C, (Figure B-11.4)

$$r_a = r_o\ (1.0 + \text{elongation of A}) \tag{B-11.30a}$$

$$r_{sym} = r_o\ (1.0 + \text{elongation of C}) \tag{B-11.30b}$$

where

r_o = initial radius of the cladding.

From Equations (B-11.29) and (B-11.30)

$$\frac{t_{min}}{t_{ave}} = \left[\frac{1.0 + \text{elongation of asymmetrically deformed tube}}{1.0 + \text{elongation of symmetrically deformed tube}}\right]^2. \tag{B-11.31}$$

Equation (B-11.12), the correlation used in the CTHIN subcode, is the reciprocal of Equation (B-11.31). The correlation for effective hoop stress at failure with an idealized symmetric deformation, Equation (B-11.10), is obtained from Equation (B-11.25), Equation (B-11.30a), and the incompressibility relations.

11.6 Expressions for Local Strain at Failure

The expression for effective stress at failure discussed in Section B-11.5 is the most physical and therefore the preferred MATPRO criterion for predicting cladding failure. However, the strain at failure is also required information which may not be predicted with sufficient accuracy or efficiency by using a knowledge of stress versus time in conjunction with the relations for plastic deformation discussed in Sections B.8 and B.9 this appendix. The preliminary correlations for local strain at failure discussed in this section are therefore developed to supplement the expressions just derived for failure stress.

Photographs of cross sections taken perpendicular to the axis of several zircaloy tubes burst at Argonne National Laboratory[B-11.12, B-11.18, B-11.19] are used to determine strain components at cladding rupture. Expansion of the tubes is assumed to consist of two

parts. The first part, uniform expansion, is assumed to be symmetric in the plane of the tubing cross section[a] and the second part, ballooning, is assumed to consist of equal axial and circumferential strains localized on the side of the tube which burst. Neither of these assumptions has been verified, but neither is necessary to determine radial strains. The assumptions will affect only the relative values of circumferential and axial strains.

To find local uniform strains, the center of curvature of the side of the tube away from the burst is located by drawing chords on the side of the cross section opposite the burst and constructing perpendiculars to the chords, as illustrated in Figure B-11.5. The uniform circumferential strain is calculated by comparing the circumference of the circle

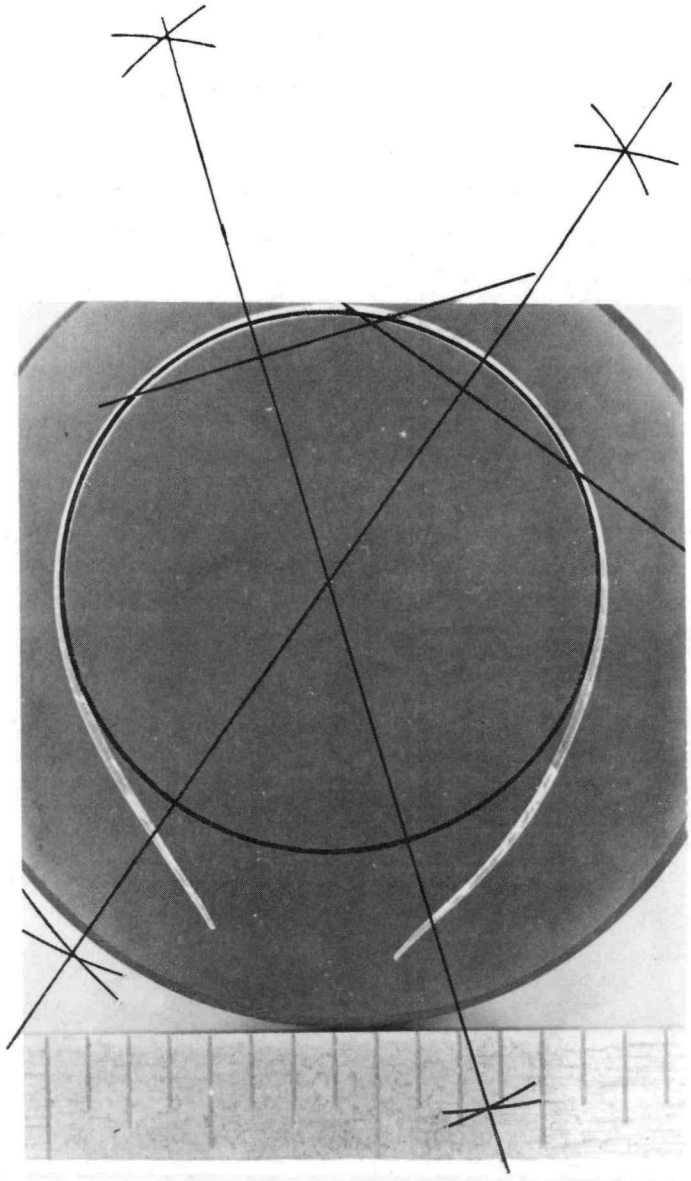

Fig. B-11.5 Cross section, perpendicular to the axis, of a zircaloy tube showing location of the center of curvature of the side opposite the burst region.

[a] The assumption of symmetric deformation during the first part of these tests may be reasonable because circumferential variation in temperature should be minimized by the use of self-resistance heating.

constructed at the center of curvature to the circumference of the original tubing[B-11.18]. Local strain is assumed to be equal to the average circumferential strain. Local radial strain during uniform deformation is computed from measurements of cladding wall thickness in the circular part of the cladding cross section and published values[B-11.18] of the initial wall thickness. Local axial uniform strain is calculated using the incompressibility relation[a]

$$\exp(\varepsilon_\theta)\exp(\varepsilon_z)\exp(\varepsilon_r) = 1 \qquad \text{(B-11.32)}$$

where

$\epsilon_\theta, \epsilon_z, \epsilon_r$ = the circumferential, axial, and radial components of local true strain.

Strain during the ballooning part of the deformation are calculated by measuring the wall thickness adjacent to the burst[b]. The radial strain during the ballooning part is given by

$$\varepsilon_r' = \ln \frac{W_{burst}}{W_{uniform}} \qquad \text{(B-11.33)}$$

where

$\epsilon_{r'}$ = true local radial strain during the ballooning deformation

W_{burst} = wall thickness adjacent to the burst

$W_{uniform}$ = wall thickness after uniform deformation.

Since circumferential and axial strains are assumed to be equal during the ballooning part of the burst, the incompressibility relation can be used in conjunction with Equation (B-11.33) to find the axial and circumferential strains during ballooning. The incompressibility equation with equal axial and radial strains is

$$\varepsilon_\theta' = \frac{\varepsilon_r'}{2} \qquad \text{(B-11.34)}$$

---

[a] In terms of engineering strains, the relation is $(1 + e_\theta)(1 + e_z)(1 + e_r) = 1$ where e_θ, e_z, and e_r are the circumferential, axial, and radial components of local engineering strain.

[b] Most burst edges displayed a fracture-like line approximately 45 degrees from the radial direction. The wall thickness was measured adjacent to this line or, if the line could not be distinguished, 0.25mm from the burst tear.

where

ϵ_θ' = the true circumferential strain during ballooning

ϵ_r' = the true local radial strain during ballooning.

True strains are additive so the net local components of strain at rupture are sums of the uniform and ballooning parts of each component. These sums, the burst temperatures, and the heating rates for seven bursts are shown in Table B-11.II. Although there is considerable scatter in the uniform and ballooning parts of the strain, there is an apparent correlation of both the net circumferential and net radial strains at rupture with temperature.

TABLE B-11.II

COMPONENTS OF LOCAL TRUE STRAIN FOR SEVEN BURSTS

Burst Temperature (kelvins)	Heating Rate (kelvins/s)		True Strains		
			Circumferential	Radial	Axial
1089	5	Uniform	0.71	-0.49	-0.23
		Balloon	0.41	-0.82	0.41
		Total	1.12	-1.31	0.18
1129	115	Uniform	0.45	-0.19	-0.26
		Balloon	0.55	-1.11	0.55
		Total	1.00	-1.30	0.29
1138	115	Uniform	0.67	-0.46	-0.21
		Balloon	0.64	-1.28	0.64
		Total	1.31	-1.74	0.43
1164	115	Uniform	0.30	-0.09	-0.21
		Balloon	0.77	-1.54	0.77
		Total	1.07	-1.63	0.56
1278	130	Uniform	0.67	-0.33	-0.34
		Balloon	0.70	-1.40	0.70
		Total	1.37	-1.73	0.36
1348	115	Uniform	0.72	-0.43	-0.29
		Balloon	0.60	-1.20	0.60
		Total	1.32	-1.63	0.31
1369	115	Uniform	0.85	-0.45	-0.40
		Balloon	0.70	-1.40	0.70
		Total	1.55	-1.85	0.30

Figure B-11.6 illustrates the correlation of the components of true local strain at rupture with burst temperature. The axial strain components are included in the figure for reference despite the fact that this component has not been included in CLOCRP. The local circumferential strains at rupture increase linearly with temperature, and the local radial strains decrease (become more negative) with temperature. The predictions of Equations (B-11.13) and (B-11.14) used in CLOCRP to represent true local circumferential and radial strains are also illustrated. These equations are linear least-squares fit to the seven values of the circumferential and axial strains illustrated. The one test done at a heating rate of 5 K/s does not deviate from the trend of the other tests which represent heating rates of approximately 115 kelvins/s.

11.7 Examples of CMLIMT and CSRUPT Output

The predicted circumferential elongation at rupture for annealed zircaloy tubing and the data base used to derive the model are shown in Figure B-11.7. Dashed lines denote limits defined by the standard error of the prediction as estimated from its data base. Fractional elongation at failure increases with increasing temperatures until the alpha + beta transition begins and then decreases with temperature to a minimum of about 0.3 at 1200 kelvins. At temperatures above 1200 kelvins, the temperature gradients and steam environment cause strain to become localized and limit the elongation ratio to less than 0.75.

The standard error of the prediction for annealed tubes remains constant to about 800 kelvins, increases rapidly to a maximum of ±0.44 at 1090 kelvins, and decreases to ±0.11 for temperatures above 1170 kelvins. It is expected that the correlation and the standard error determined with this data base will apply to LWR abnormal or accident situations since (a) all of the data above 1090 kelvins were taken in a steam environment, (b) most of the tubing tested contained internal mandrels to restrict axial deformation, and (c) the data from in-reactor tests are similar to the rest of the data base.

Irradiation and cold work strongly influence the circumferential elongation at rupture at temperatures less than 850 kelvins. Figure B-11.8 compares the model predictions for annealed cladding with prediction for cladding cold worked to 0.1 area reduction and then irradiated to a fast fluence of 10^{24} neutrons/m^2 or more. Test results obtained with irradiated cladding and the standard error predicted by the model are included in the figure. The large increase in elongation at 620 to 700 kelvins reflects annealing of irradiation damage and cold work, respectively.

Figure B-11.9 shows the predicted circumferential elongation for temperature variations of 0, 10, 50, and 100 kelvins at temperatures up to 1090 kelvins and variations of 0.0 kelvins above 1255 kelvins. Temperature variations are presumed to be zero in the beta phase (temperatures above 1255 kelvins) because the minimal anisotropy of this phase will not cause the cladding to bow into internal sources of heat during deformation.

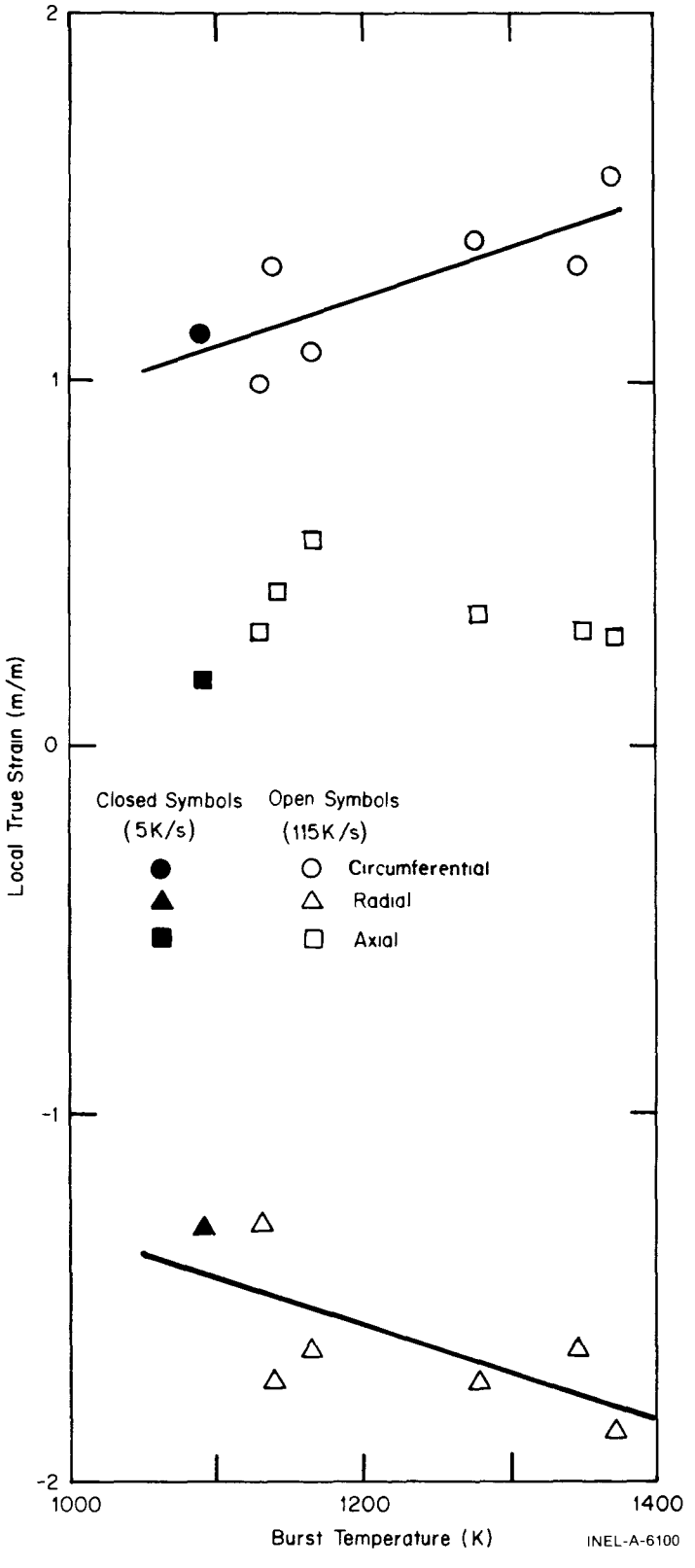

Fig. B-11.6 Graphic correlation of the components of true local strain at rupture with temperature.

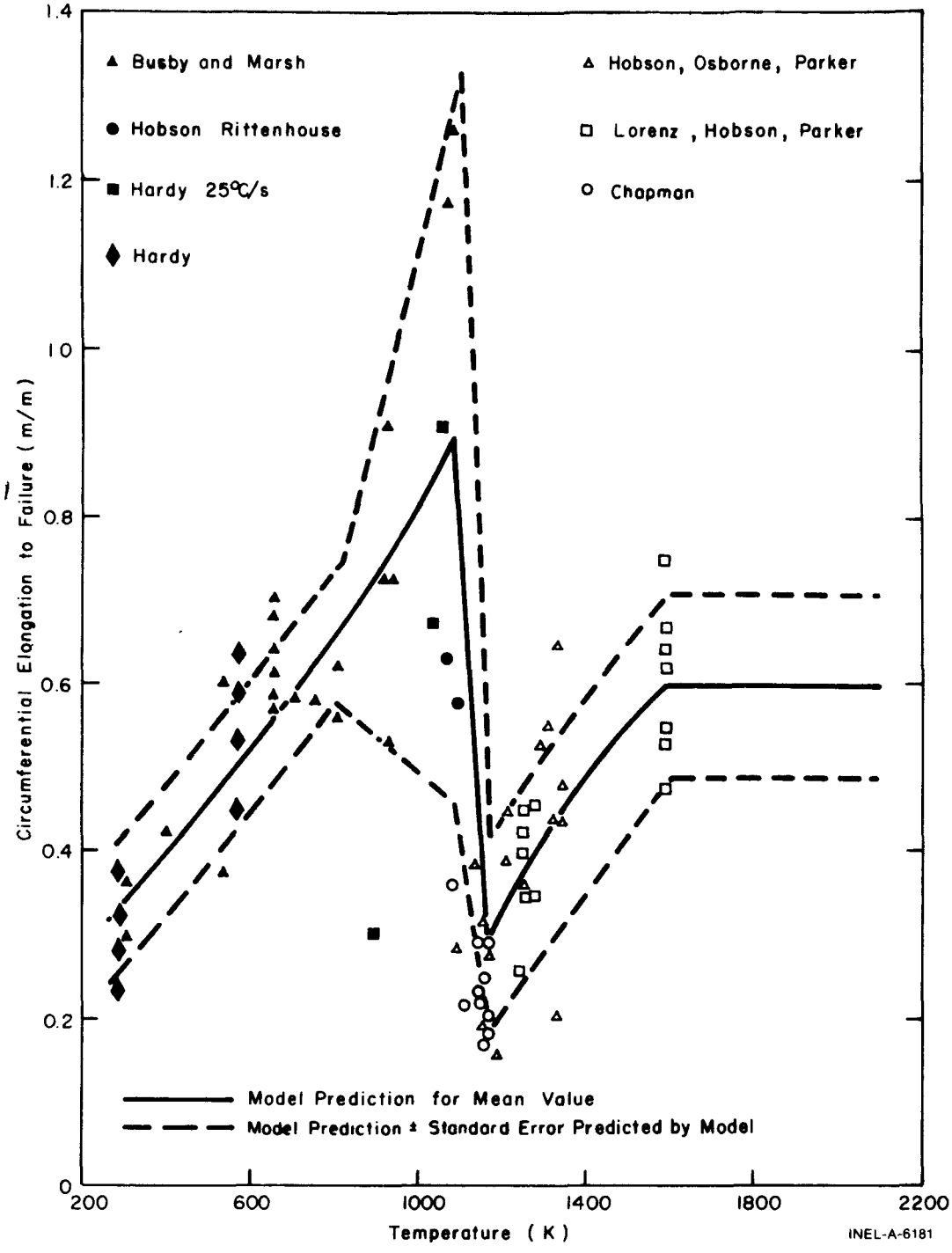

Fig. B-11.7 Predicted circumferential elongation at rupture, measured values, and standard error of new in-reactor data predicted as a function of temperature by the CSRUPT model for annealed tubing.

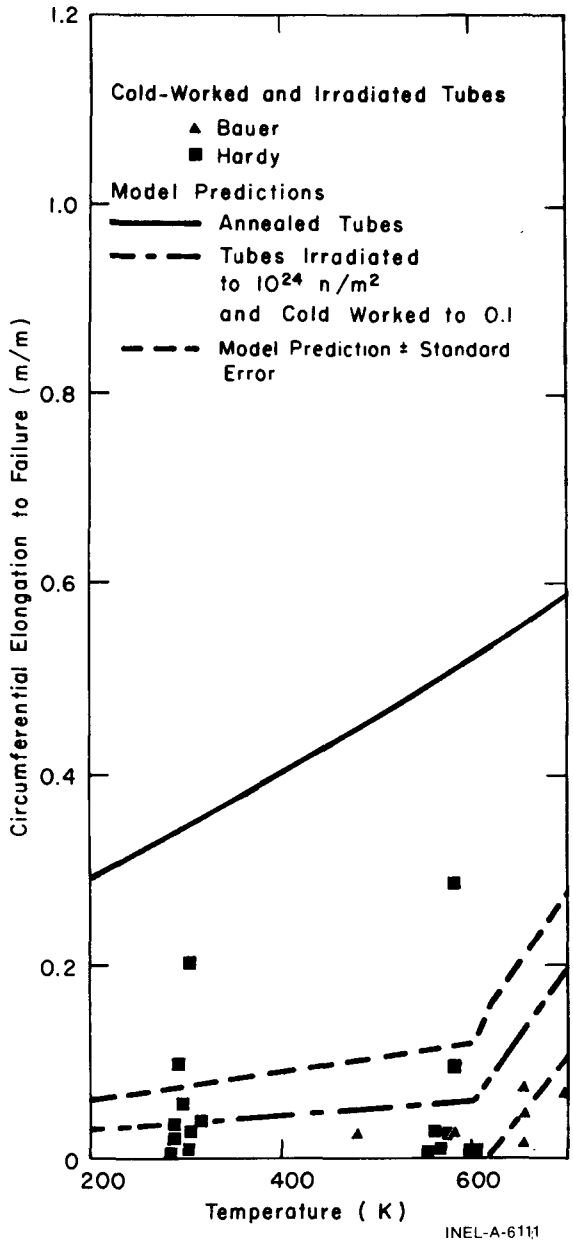

Fig. B-11.8 Predicted circumferential elongation at rupture of annealed cladding compared to predictions and measurements for cold-worked and irradiated cladding.

11.8 Cladding Mechanical Limits CMLIMT, Cladding Strain at Rupture CSRUPT, Cladding Wall Thinning CTHIN, and Cladding Local Strains at Ruputre CLOCRP Subcode Listings

A listing of the FORTRAN subcode CMLIMT used for calculating strain at yield, strain at maximum load, yield strength, ultimate strength, circumferential elongation at burst, circumferential elongation at instability and hoop stress at burst is given in Table B-11.III. The listing of the subcode CSRUPT which returns strain to rupture and the standard error expected with the correlation is presented in Table B-11.IV. Table B-11.V is a

listing of the CTHIN subcode used to find the ratio (average cladding wall thickness/ minimum wall thickness) at rupture and Table B-11.VI is a listing of the CLOCRP subcode for calculating local strain at failure.

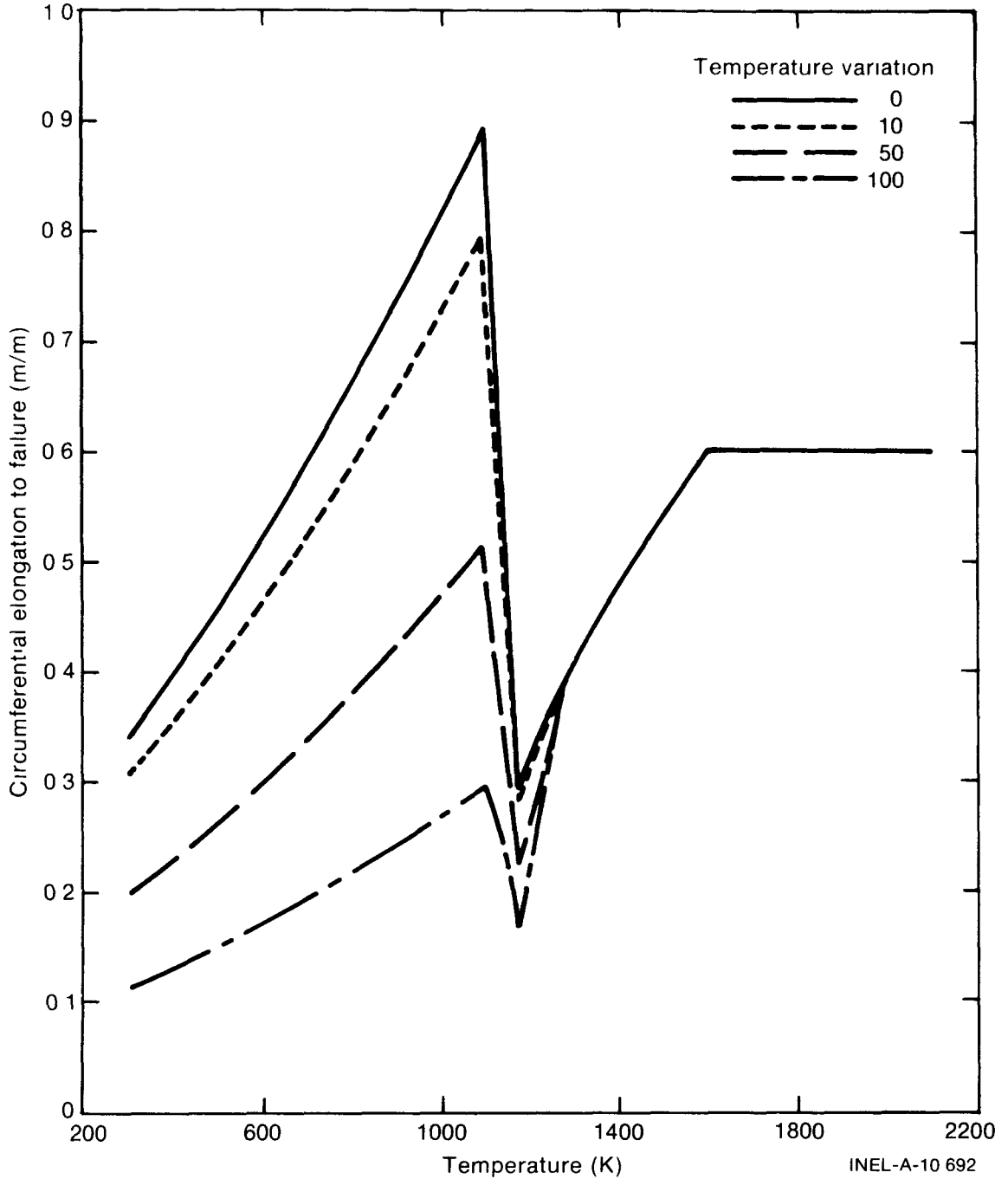

Fig. B-11.9 Predicted circumferential elongation to failure as a function of temperature variation and temperature.

TABLE B-11.III

LISTING OF THE CMLIMT SUBCODE

```
C
      SUBROUTINE CMLIMT(CTEMP,DELOXY,FNCK,FNCN,CWKF,CWNF,RSTRAN,
     #  DELTMP,STRNYT,STRNYE,STRNUT,STRNUE,STRNIT,STRNIE,STRRPE,
     #  STRRPT,CYLDST,CYLDSE,CULTST,CULTSE,CBRSST,CBRSTE)
C
C     CMLIMT CALCULATES CLADDING STESSS AND STRAIN AT THE TRANSITION
C     BETWEEN ELASTIC AND PLASTIC REGIONS, AND AT MAXIMUM LOAD AS A
C     FUNCTION OF TEMPERATURE, FAST NEUTRON FLUENCE, COLD WORK, AVERAGE
C     OXYGEN CONCENTRATION IN CLADDING AND STRAIN RATE.
C     CIRCUMFERENTIAL STRAINS AT INSTABILITY AND RUPTURE ARE
C     ALSO CALCULATED.
C
C     STRNYT = OUTPUT TRUE STRAIN AT YIELD (M/M)
C     STRNYE = OUTPUT ENGINEERING STRAIN AT YIELD (M/M)
C     STRNUT = OUTPUT TRUE STRAIN AT MAXIMUM LOAD (M/M)
C     STRNUE = OUTPUT ENGINEERING STRAIN AT MAXIMUM LOAD (M/M)
C     STRRPT = OUTPUT TRUE STRAIN AT RUPTURE (M/M)
C     STRRPE = OUTPUT ENGINEERING STRAIN AT RUPTURE (M/M)
C     STRNIE = OUTPUT ENGINEERING CIRCUMFERENTIAL INSTABILITY
C              STRAIN (M/M)
C     STRNIT = OUTPUT TRUE CIRCUMFERENTIAL INSTABILITY STRAIN (M/M)
C     CYLDST = OUTPUT TRUE YIELD STRENGTH (PA)
C     CYLDSE = OUTPUT ENGINEERING YIELD STRENGTH (PA)
C     CULTST = OUTPUT TRUE ULTIMATE STRENGTH (PA)
C     CULTSE = OUTPUT ENGINEERING ULTIMATE STRENGTH (PA)
C     CBRSST = OUTPUT EFFECTIVE TRUE HOOP STRESS AT BURST
C              FOR SYMMETRIC CLADDING APPROXIMATION WITH
C              CIRCUMFERENCE EQUAL TO THE ACTUAL CLADDING
C              CIRCUMFERENCE (PA)
C     CBRSTE = OUTPUT ENGINEERING HOOP STRESS AT BURST (PA)
C
C     CTEMP  = INPUT AVERAGE CLADDING TEMPERATURE (K)
C     DELOXY = INPUT AVERAGE OXYGEN CONCENTRATION EXCLUDING
C              OXIDE LAYER - AVERAGE OXYGEN CONCENTRATION OF
C              AS RECEIVED CLADDING  (KG OXYGEN/KG ZIRCALOY)
C     FNCK   = INPUT EFFECTIVE FAST FLUENCE FOR STRENGTH
C              COEFFICIENT (NEUTRONS/(M**2))
C     FNCN   = INPUT EFFECTIVE FAST FLUENCE FOR STRAIN HARDENING
C              EXPONENT (NEUTRONS/(M**2))
C     CWKF   = INPUT EFFECTIVE COLD WORK FOR STRENGTH
C              COEFFICIENT (UNITLESS RATIO OF AREAS)
C     CWNF   = INPUT EFFECTIVE COLD WORK FOR STRAIN HARDENING
C              EXPONENT (UNITLESS RATIO OF AREAS)
C     RSTRAN = INPUT TRUE STRAIN RATE (S**(-1))
C     DELTMP = INPUT CIRCUMFERENTIAL TEMPERATURE VARIATION
C              --HOTTEST LESS COLDEST TEMPERATURES (K)
C     ESTIMATED VALUES OF DELTMP ARE
C          (A) FOR CLADDING WITH EXTERNAL THERMOCOUPLES AND IN FILM
C              BOILING  DELTMP = 150K
C          (B) FOR CLADDING WITH INTERNAL HEATING IN STEAM AND
C              WITHOUT EXTERNAL THERMOCOUPLES
C                   DELTMP = 0 IF TEMPERATURE IS ABOVE 1255K
C                          = 50 * (1255 - TEMPERATURE) / 165 IF
C                            TEMPERATURE IS BETWEEN 1090 AND 1255K
C                          = 50 IF TEMPERATURE IS BELOW 1090K
C          (C) FOR CLADDING IN A FURNACE
C                   DELTMP = 0
C          (D) FOR SELF - RESISTANCE HEATED CLADDING WITH COOL FILLER
C                   DELTMP = (HEATING RATE)/1000K/S) * VALUES OF (B)
C
C     THE EQUATIONS USED IN THIS SUBROUTINE ARE BASED ON DATA FROM
C     (1) D.G. HARDY,  HIGH TEMPERATURE EXPANSION AND RUPTURE
C     BEHAVIOR OF ZIRCALOY TUBING  IN TOPICAL MEETING ON
C     WATER REACTOR SAFETY CONF-7303 (1973)
C     (2)D.O. HOBSON AND P.L. RITTENHOUSE,  DEFORMATION AND RUPTURE
C     BEHAVIOR OF LIGHT WATER REACTOR FUEL CLADDING  ORNL-4727 (1971)
C     (3) D. O. HOBSON, H. F. OSBORNE, AND G. W. PARKER,  COMPARISON
C     OF RUPTURE DATA FROM IRRADIATED FUEL RODS AND UNIRRADIATED
C     CLADDING, NUCL. TECH. 17 (AUGUST 1971) P 479
C     (4) R. A. LORENZ, D. O. HOBSON AND G. W. PARKER,  FUEL ROD
C     FAILURE UNDER LOSS OF COOLANT CONDITIONS IN TREAT,  NUCL.
C     TECH. 17 (AUGUST 1971) P 502
C     (5) R. H. CHAPMAN, MULTIROD BURST TEST PROGRAM QUARTERLY
C     REPORT FOR JULY - SEPTEMBER, 1975, ORNL-TM-5154 (DECEMBER 1975)
```

TABLE B-11.III (continued)

```
C     (6) R. H. CHAPMAN, MULTIROD BURST TEST PROGRAM QUARTERLY
C     REPORT FOR OCTOBER - DECEMBER, 1975,  ORNL/NUREG/TM-10 (MAY 1976)
C     (7) A. A. BAUER, L. M. LOWRY, AND J. S. PERRIN, EVALUATING
C     STRENGTH AND DUCTILITY OF IRRADIATED ZIRCALOY. QUARTERLY
C     PROGRESS REPORT FOR JANUARY THROUGH MARCH, 1976, BMI-NUREG-1948
C     (MARCH 1976)
C     (8) H. M. CHUNG LIGHT-WATER-REACTOR SAFETY RESEARCH
C     PROGRAM QUARTERLY PROGRESS REPORT JANUARY - MARCH 1976,
C     ANL-76-49
C
C     CODED BY D. L. HAGRMAN JANUARY 1976
C     MODIFIED BY D.L. HAGRMAN JUNE 1978.
C
      CALL CKMN(CTEMP,DELOXY,FNCK,FNCN,CWKF,CWNF,RSTRAN,AK,AN,AM)
C
      ELMOD = CELMOD(CTEMP, FNCK, CWKF, DELOXY)
C
      T = CTEMP
      AG = AK * ((RSTRAN/1.0E-3)**AM)
C
C     CALCULATE STRAIN AT YIELD
      STRNYT = ((AG/ELMOD)**(1.0/(1.0 - AN)))
      STRNYE =  EXP(STRNYT) - 1.0
C
C     CALCULATE STRAIN AT MAXIMUM LOAD
      STRNUT = AN/(1. + AM)
      STRNUE =  EXP(AN) - 1.0
C
C     CALCULATE  STRAIN AT RUPTURE FOR SYMMETRIC CASE
      P = 1.0
      Q = 1.0
      IF (T.GT.1090.) GO TO 201
      STRRPE = 1.98E-1+T*(4.16E-04+T*2.06E-07)
      P =  (EXP(-2.1E01*CWNF) + 3.3E-01)/1.33
      IF(FNCN .LT. 1.0E21) GO TO 121
      Q = (1.00 + 2.00 *  EXP(-FNCN/1.0CE23))/3.00
      GO TO 141
  121 CONTINUE
  141 STRRPE = STRRPE * P * Q
      GO TO 501
  201 IF (T.GT.1170.) GO TO 301
      STRRPE = 9.06231055E00-T*7.491855E-03
      GO TO 501
  301 IF (T.GT.1600.) GO TO 401
      STRRPE = -1.436E00+T*(2.045E-03-T*4.82E-07)
      GO TO 501
  401 STRRPE = 6.0208E-1
  501 CONTINUE
C
C     CALCULATE CIRCUMFERENTIAL INSTABILITY STRAIN
      STRNIE = (STRRPE * 0.25)/(P*Q)
      IF(T .LE. 1090.) GO TO 605
      STRNIE = (STRRPE * 0.25*(1. + (T-1090.)/165.))/(P*Q)
      IF(T .GE. 1255.) GO TO 605
      STRNIE = (STRRPE * 0.50)/(P*Q)
  605 STRNIT = ALOG(1.0 + STRNUE)
C
C     CALCULATE EFFECTIVE TRUE HOOP STRESS AT BURST
      TAVMIN = ((1.0 + STRRPE)/(1.0 + STRRPE* EXP(-1.11E-02*DELTMP)))
     #                **2.0
      FT = (CTEMP - 273.15) * 1.8 + 32.
      CBRSTE =(10**(5.00E+00+FT*(3.27E-04-FT*(1.14E-06-FT*2.56E-10))))/
     #        1.4505E-04
      CBRSST = CBRSTE * (( 1.0 + STRRPE)**(2.0)) / TAVMIN
C
C     MODIFY STRAIN AT RUPTURE FOR TEMPERATURE GRADIENT EFFECTS
      STRRPE = STRRPE *  EXP(-1.11E-02*DELTMP)
      STRRPT = ALOG( 1.0 + STRRPE)
      STRRPT = ALOG( 1.0 + STRRPE)
C
C     CALCULATE YIELD STRENGTH
      CYLDST = (AG/(ELMOD**AN))**(1.0/(1.0-AN))
      CYLDSE = CYLDST/EXP(STRNYT)
```

TABLE B-11.III (continued)

```
C
C     CALCULATE ULTIMATE STRENGTH
      CULTST = AG * (STRNUT**AN)
      CULTSE = CULTST/EXP(STRNUT)
C
      RETURN
      END
```

11.9 References

B-11.1. C. C. Busby and K. B. Marsh, *High Temperature Deformation and Burst Characteristics of Recrystallized Zircaloy-4 Tubing,* WAPD-TM-900 (January 1970).

B-11.2. D. G. Hardy, "High Temperature Expansion and Rupture Behavior of Zircaloy Tubing," *Topical Meeting on Water Reactor Safety, Salt Lake City, American Nuclear Society, March 26-28, 1973,* CONF-730304.

B-11.3. D. O. Hobson and P. L. Rittenhouse, *Deformation and Rupture of Light-Water Reactor Fuel Cladding,* ORNL-4727 (October 1971).

B-11.4. D. G. Hardy, "The Effect of Neutron Irradiation on the Mechanical Properties of Zirconium Alloy Fuel Cladding in Uniaxial and Biaxial Tests," *Irradiation Effects on Structural Alloys For Nuclear Reactor Application,* ASTM-STP-484, American Society for Testing and Materials (1970) pp 215-258.

B-11.5. D. O. Hobson, M. F. Osborne, G. W. Parker, "Comparison of Rupture Data From Irradiated Fuel Rods and Unirradiated Cladding," *Nuclear Technology, 17* (August 1971) p 479.

B-11.6. R. A. Lorenz, D. O. Hobson, G. W. Parker, "Fuel Rod Failure Under Loss-of-Coolant Conditions in TREAT," *Nuclear Technology, 17* (August 1971) p 502.

B-11.7. R. H. Chapman, *Multirod Burst Test Program: Quarterly Progress Report, July-September 1975,* ORNL-TM-5150 (December 1975).

B-11.8. R. H. Chapman, *Multirod Burst Test Program: Quarterly Progress Report, October-December 1975,* ORNL/NUREG/TM-10 (May 1976).

B-11.9. A. L. Bement, Jr., *Effects of Cold-Work and Neutron Irradiation on the Tensile Properties of Zircaloy-2,* HW-74955 (April 1963).

B-11.10. A. A. Bauer, L. M. Lowry, J. S. Perrin, *Evaluating Strength and Ductility of Irradiated Zircaloy: Quarterly Progress Report, January-March 1976,* BM1-NUREG-1948 (March 1976).

TABLE B-11.IV

LISTING OF THE CSRUPT SUBCODE

```
C
      SUBROUTINE CSRUPT(CTEMP, FNCN, CWNF,DELTMP,STRRPE,USTRPE,
     #                  STRRPT,USTRTP,USTRTN)
C
C     CSRUPT CALCULATES THE FRACTIONAL INCREASE IN CLADDING
C     CIRCUMFERENCE AT FAILURE IN A STEAM INVIRONMENT AS A
C     FUNCTION OF TEMPERATURE, FAST NEUTRON FLUENCE, AND
C     COLD WORK.  THE EXPECTED STANDARD ERROR IS ALSO RETURNED.
C
C     STRRPE = OUTPUT AVERAGE CIRCUMFERENTIAL ENGINEERING STRAIN
C              AT RUPTURE (M/M)
C     USTRPE = OUTPUT EXPECTED STANDARD ERROR IN STRRPE (M/M)
C     STRRPT = OUTPUT TRUE STRAIN AT RUPTURE (M/M)
C     USTRTP = OUTPUT POSITIVE STANDARD ERROR OF STRRPT WHICH
C              CORRESPONDS TO USTRPE (M/M)
C     USTRTN = OUTPUT NEGATIVE STANDARD ERROR OF STRRPT WHICH
C              CORRESPONDS TO USTRPE (M/M)
C     NOTE  A NON SYMMETRIC DISTRIBUTION IS OBTAINED IN TERMS OF TRUE
C           STRESS BECAUSE THE TRANSFORMATION FROM ENGINEERING STRESS
C           TO TRUE STRESS IS NON LINEAR
C
C     CTEMP  = INPUT AVERAGE CLADDING TEMPERATURE (K)
C     FNCN   = INPUT EFFECTIVE FAST FLUENCE FOR STRAIN HARDENING
C              EXPONENT (NEUTRONS/(M**2))
C     CWNF   = INPUT EFFECTIVE COLD WORK FOR STRAIN HARDENING
C              EXPONENT (UNITLESS RATIO OF AREAS)
C     DELTMP = INPUT CIRCUMFERENTIAL TEMPERATURE VARIATION
C              --HOTTEST LESS COLDEST TEMPERATURES (K)
C     ESTIMATED VALUES OF DELTMP ARE
C          (A) FOR CLADDING WITH EXTERNAL THERMOCOUPLES AND IN FILM
C              BOILING  DELTMP = 150K
C          (B) FOR CLADDING WITH INTERNAL HEATING IN STEAM AND
C              WITHOUT EXTERNAL THERMOCOUPLES
C                  DELTMP = 0 IF TEMPERATURE IS ABOVE 1255K
C                         = 50 * (1255 - TEMPERATURE) / 165 IF
C                           TEMPERATURE IS BETWEEN 1090 AND 1255K
C                         = 50 IF TEMPERATURE IS BELOW 1090K
C          (C) FOR CLADDING IN A FURNACE
C              DELTMP = 0
C          (D) FOR SELF - RESISTANCE HEATED CLADDING WITH COOL FILLER
C                  DELTMP = (HEATING RATE)/(1000K/S) * VALUES FROM (B)
C
C     THE EQUATIONS USED IN THIS SUBROUTINE ARE BASED ON DATA FROM
C     (1)C.C. BUSBY AND K.B. MARSH, HIGH TEMPERATURE DEFORMATION
C     BURST CHARACTERISTICS OF RECRYSTALLIZED ZIRCALOY-4 TUBING
C     WAPD-TM-900 (1970)
C     (2) D.G. HARDY,  HIGH TEMPERATURE EXPANSION AND RUPTURE
C     BEHAVIOR OF ZIRCALOY TUBING,  IN TOPICAL MEETING ON
C     WATER REACTOR SAFETY CONF-7303 (1973)
C     (3)D.O. HOBSON AND P.L. RITTENHOUSE,  DEFORMATION AND RUPTURE
C     BEHAVIOR OF LIGHT WATER REACTOR FUEL CLADDING ORNL-4727 (1971)
C     (4) D. O. HOBSON, M. F. OSBORNE, AND G. W. PARKER,  COMPARISON
C     OF RUPTURE DATA FROM IRRADIATED FUEL RODS AND UNIRRADIATED
C     CLADDING,  NUCL. TECH. 17 (AUGUST 1971) P 479
C     (5) R. A. LORENZ, D. O. HOBSON AND G. W. PARKER,  FUEL ROD
C     FAILURE UNDER LOSS OF COOLANT CONDITIONS IN TREAT,  NUCL.
C     TECH. 17 (AUGUST 1971) P 502
C     (6) R. H. CHAPMAN, MULTIROD BURST TEST PROGRAM QUARTERLY
C     REPORT FOR JULY - SEPTEMBER, 1975, ORNL-TM-5154 (DECEMBER 1975)
C     (7) R. H. CHAPMAN, MULTIROD BURST TEST PROGRAM QUARTERLY
C     REPORT FOR OCTOBER - DECEMBER, 1975,  ORNL/NUREG/TM-10 (MAY 1976)
C     (8) A. A. BAUER, L. M. LOWRY, AND J. S. PERRIN, EVALUATING
C     STRENGTH AND DUCTILITY OF IRRADIATED ZIRCALOY, QUARTERLY
C     PROGRESS REPORT FOR JANUARY THROUGH MARCH, 1976, BMI-NUREG-1948
C     (MARCH 1976)
C     (9)  A. L. BEMENT, JR., EFFECTS OF COLD WORK AND NEUTRON
C     IRRADIATION ON THE TENSILE PROPERTIES OF ZIRCALOY-2,
C     USAEC REPORT HW-74955
C
C     CODED BY D. L. HAGRMAN JULY 1976
C     MODIFIED BY D.L. HAGRMAN JUNE 1978.
```

TABLE B-11.IV (continued)

```
      T = CTEMP
C     CALCULATE  STRAIN AT RUPTURE FOR SYMMETRIC CASE
      P = 1.0
      Q = 1.0
      IF (T.GT.1090.) GO TO 201
      STRRPE = 1.58E-1+T*(4.16E-04+T*2.06E-07)
      P = (EXP(-2.1E01*CWNF) + 3.3E-01)/1.33
      IF(FNCN .GE. 1.0E21) Q = (1.0 + 2.0 * EXP(-FNCN/1.0E23))/3.0
      STRRPE = STRRPE * P * Q
      GO TO 501
  201 IF (T.GT.1170.) GO TO 301
      STRRPE = 9.0231055E00-T*7.491855E-03
      GO TO 501
  301 IF (T.GT.1600.) GO TO 401
      STRRPE = -1.436E00+T*(2.045E-03-T*4.82E-07)
      GO TO 501
  401 STRRPE = 6.0208E-1
  501 CONTINUE
C
C     MODIFY STRAIN AT RUPTURE FOR TEMPERATURE GRADIENT EFFECTS
      STRRPE = STRRPE * EXP(-1.11E-02*DELTMP)
C
      USTRPE = 8.0E-02
      IF( T .LT. 800.) GO TO 601
      USTRPE = (3.6E-01/2.90E+02) * ( T - 8.00E+02) + 8.00E-02
      IF( T . LT. 1090.) GO TO 601
      USTRPE = -4.125E-03* ( T - 1.09E+03) + 4.4E-01
      IF( T .LT. 1170.) GO TO 601
      USTRPE = 1.1E-01
  601 IF(USTRPE .GT. (0.9*STRRPE)) USTRPE = 0.9*STRRPE
C
C     CONVERSION TO TRUE STRAINS FOLLOWS
      STRRPT = ALOG( 1.0 + STRRPE)
      USTRTP = ALOG ( 1.0 + STRRPE + USTRPE ) - STRRPT
      USTRTN = STRRPT - ALOG ( 1.0 + STRRPE - USTRPE )
C
      RETURN
      END
```


B-11.11. K. Wiehr et al, *Jahreskolloquim 1977 des Projekts Nukleare Sicherheit.*

B-11.12. H. M. Chung, A. M. Garde, T. F. Kassner, *Light-Water-Reactor Safety Research Program: Quarterly Progress Report, January-March 1976,* ANL-76-49 (June 1976).

B-11.13. M. F. Osborne and G. W. Parker, *The Effects of Irradiation on the Failure of Zircaloy-Clad Fuel Rods,* ORNL-3626 (January 1972).

B-11.14. D. G. Hardy, "The Effect of Neutron Irradiation on the Mechanical Properties of Zirconium Alloy Fuel Cladding in Uniaxial and Biaxial Tests," *Symposium on Irradiation Effects on Structural Alloys for Nuclear Reactor Application, Niagara Falls, Canada, June 29-July 1, 1970,* ASTM-STP-484 (1971) pp 215-216.

B-11.15. W. J. Langford, "Metallurgical Properties of Cold-Worked Zircaloy-2 Pressure Tubes Irradiated Under CANDU-PHW Power Reactor Conditions," *Symposium on Irradiation Effects on Structural Alloys for Nuclear Reactor Application, Niagara Falls, Canada, June 29-July 1, 1970,* ASTM-STP-484 (1971) pp 259-286.

TABLE B-11.V

LISTING OF THE CTHIN SUBCODE

```
C
      FUNCTION CTHIN(DELTMP,CTEMP)
C
C     CTHIN CALCULATES AVERAGE CLADDING WALL THICKNESS/MINIMUM
C     WALL THICKNESS AS A FUNCTION OF CIRCUMFERENTIAL TEMPERATURE
C     DIFFERENCE AND CLADDING TEMPERATURE
C
C     CTHIN  = OUTPUT AVERAGE WALL THICKNESS/MINIMUM WALL
C              THICKNESS (UNITLESS RATIO)
C
C     DELTMP = INPUT CIRCUMFERENTIAL TEMPERATURE VARIATION
C              --HOTTEST LESS COLDEST TEMPERATURES (K)
C
C     THE EQUATIONS USED IN THIS FUNCTION ARE BASED ON DATA FROM
C     (1) K. WIEHR, F. ERBACHER, V. HARTEN, W. JUST, H. J. NEITZEL,
C     P. SCHAFFNER AND H. SCHMIDT, JAHRESKOLLOQUIUM 1977 DES
C     PROJEKTS NUKLEARE SICHERHEIT
C
C     CODED BY D. L. HAGRMAN MARCH 1978
C
C     THIS FUNCTION IS BASED ON A PRELIMINARY CORRELATION OBTAINED
C     FROM DATA AT 1050K ONLY.
C
C     ESTIMATED VALUES OF DELTMP ARE
C          (A) FOR CLADDING WITH EXTERNAL THERMOCOUPLES AND IN FILM
C              BOILING  DELTMP = 150K
C          (B) FOR CLADDING WITH INTERNAL HEATING IN STEAM AND
C              WITHOUT EXTERNAL THERMOCOUPLES
C                   DELTMP = 0 IF TEMPERATURE IS ABOVE 1255K
C                          = 50 * (1255 - TEMPERATURE) / 165 IF
C                            TEMPERATURE IS BETWEEN 1090 AND 1255K
C                          = 50 IF TEMPERATURE IS BELOW 1090K
C          (C) FOR CLADDING IN A FURNACE
C              DELTMP = 0
C          (D) FOR SELF - RESISTANCE HEATED CLADDING WITH COOL FILLER
C              DELTMP = (HEATING RATE)/(1000K/S) * VALUES FROM (B)
C
      T = CTEMP
      IF (T.GT.1090.) GO TO 201
      STRRPE = 1.98E-1+T*(4.16E-04+T*2.06E-07)
  201 IF (T.GT.1170.) GO TO 301
      STRRPE = 9.0631055E00-T*7.491855E-03
      GO TO 501
  301 IF (T.GT.1600.) GO TO 401
      STRRPE = -1.436 + T * (2.045E-03-T*4.82E-07)
      GO TO 501
  401 STRRPE = 6.0208E-1
C
  501 CONTINUE
      CTHIN  = ((1.0 + STRRPE)/(1.0 + STRRPE* EXP(-1.11E-02*DELTMP)))
     #         **2.0
      RETURN
C
      END
```

B-11.16. W. R. Smalley, *Saxton Core II Fuel Performance Evaluation, Part I: Materials,* WCAP-3385-56 (September 1971) pp 4-84, 4-65.

B-11.17. D. G. Hardy, "Burst Testing of Zircaloy Cladding from Irradiated Pickering-Type Fuel Bundles," *Symposium on the Effects of Radiation on Substructure and Mechanical Properties of Metals and Alloys, Los Angeles, June 25-30, 1972,* ASTM-STP-529 (1973) pp 415-435.

TABLE B-11.VI

LISTING OF THE CLOCRP SUBCODE

```
      SUBROUTINE CLOCRP(CTEMP,CRTSTN,CCTSTN,CRESTN,CCESTN)
C
C     CLCCRP CALCULATES THE LOCAL TRUE AND ENGINEERING STRAINS
C     TO RUPTURE FOR ZIRCALOY CLADDING BALLOONING
C
C     CRTSTN = OUTPUT CLADDING TRUE RADIAL STRAIN (M/M)
C     CCTSTN = OUTPUT CLADDING TRUE CIRCUMFERENTIAL STRAIN (M/M)
C     CRESTN = OUTPUT CLADDING ENGINEERING RADIAL STRAIN (M/M)
C     CCESTN = OUTPUT CLADDING ENGINEERING CIRCUMFERENTIAL
C              STRAIN (M/M)
C
C     CTEMP  = INPUT CLADDING TEMPERATURE (K)
C
C     THE EQUATIONS USED IN THIS SUBROUTINE ARE BASED ON DATA FROM
C         H. M.CHUNG PRIVATE COMMUNICATION (1976)
C
C     CODED BY D. L. HAGRMAN SEPTEMBER 1976
C
C     CAUTION SHOULD BE EXERCISED IN USING THIS CORRELATION
C     FOR TEMPERATURES NOT IN THE RANGE 1090 - 1369 K
C
      T  = CTEMP
      AR = -1.0687E-02
      BR = -1.3054E-03
      AC = -4.1498E-01
      BC =  1.3676E-03
C
      CRTSTN = AR + BR*T
      CCTSTN = AC + BC*T
C
      CRESTN =  EXP(CRTSTN) - 1.0
      CCESTN =  EXP(CCTSTN) - 1.0
      RETURN
      END
```

B-11.18. H. M. Chung, A. M. Garde, T. F. Kassner, *Light-Water-Reactor Safety Research Program: Quarterly Progress Report, July-September 1975*, ANL-75-72.

B-11.19. H. M. Chung et al, *Light-Water-Reactor Safety Research Program: Quarterly Progress Report, October-December 1975*, ANL-76-15.

12. CLADDING CYCLIC FATIGUE (CFATIG)

(D. L. Hagrman)

The subcode CFATIG provides preliminary estimates of material constants in a format compatible with the use of fracture mechanics to model the effect of cyclic fatigue as described in the following equations.

12.1 Summary

High cycle (nominally elastic strain) fatigue uses material constants in an equation of the following form

for $\Delta K \geq 9.5 \times 10^6$ N/m$^{1.5}$,

$$\frac{d\ell}{dN} = B\ (\Delta K)^m \qquad \text{(B-12.1a)}$$

and for $\Delta K < 9.5 \times 10^6$ N/m$^{1.5}$,

$$\frac{d\ell}{dN} = 0 \qquad \text{(B-12.1b)}$$

where

$\frac{d\ell}{dN}$ = the change in crack length per cycle (m/cycle)

ΔK = the stress intensity range (MN/m$^{1.5}$)

B, m = material parameters returned by the CFATIG code.

The exponent m is

$$m = 15 - 12 \exp\ (-\phi/10^{24}) \qquad \text{(B-12.2)}$$

where

ϕ = the fast neutron fluence (neutrons/m^2).

The parameter B in Equation (B-12.1a) is computed from the following expressions

for fast neutron fluences less than 10^{25} neutrons/m^2,

$$B = 2 \times 10^{-11}\ \left[15.531432^{12}\ [\exp\ (-\Phi/10^{24})-1]\right] \qquad \text{(B-12.3a)}$$

for fast neutron fluences of 10^{25} neutrons/m^2 or more,

$$B = 1.0165786 \times 10^{-25}. \qquad \text{(B-12.3b)}$$

Low cycle (plastic strain) fatigue uses material constants intended for use in the equation proposed by Tomkins[B-12.1].

$$\frac{d\ell}{dN} = K(\Delta\varepsilon)^{1/\alpha}\ \ell \qquad \text{(B-12.4)}$$

where

$\Delta\epsilon$ = plastic strain amplitude (unitless)

ℓ = crack length (m)

α,K = material parameters.

The value returned by CFATIG for the dimensionless material parameter K is 10.7 and the value for α is 0.6.

12.2 Basis for High Cycle Fatigue Material Constants

Constants for the description of high cycle crack propagation are based on data taken by Rao[B-12.2] and preliminary measurements by Walker and Kass[B-12.3]. S-N (stress versus number of cycles to failure) data reported by O'Donnell and Langer[B-12.4] are not incorporated into the model because the effect of varying initial crack sizes is not known.

Rao's measurements of crack growth rates as a function of stress intensity (from Figure 4 of Reference B-12.2) are reproduced in Table B-12.I. The parameter m in Equation (B-12.1a) is equal to the slope of a plot of log $(\frac{d\ell}{dN})$ against log ΔK. The value of m obtained from a least-squares fit to a plot of the data of Table B-12.I is 3.3.

The preliminary data of Walker and Kass (Figure 9 of Reference B-12.2) were analyzed with the same approach used for the data of Rao. The straight line used by Walker and Kass to summarize data from unirradiated samples is equivalent to a value of m = 2.8 in Equation (B-12.1a).

Walker and Kass also reported crack growth rates from eleven samples which received fast neutron fluences from 5 to 19 x 10^{24} neutrons/m^2. A linear least-squares fit to a [log (stress intensity) versus log (crack growth rate)] plot of these measurements suggests that a value of m = 15.7 in Equation (B-12.1a) would yield the best description of irradiated zircaloy.

The exponential form of Equation (B-12.2) is an estimate relating the values of m = 3 for unirradiated zircaloy and m = 15 for zircaloy irradiated to a fast neutron fluence of 10^{25} neutrons/m^2. A decreasing exponential is typical of the change of material constants with fluence.

Values of the parameter B for unirradiated zircaloy were determined by substituting measurements of crack growth rate and stress intensity range into Equation (B-12.1a) with m = 3. Values of B determined from the two sets of data shown in Table B-12.I were averaged to obtain 12.7 and 6 x 10^{-30} for stress intensities in $N/m^{1.5}$. Two additional estimates for B were obtained by repeating the "solution" of Equation (B-12.3) with Rao's

TABLE B-12.I

CRACK GROWTH RATE VERSUS STRESS INTENSITY RANGE FROM RAO

Stress Intensity Range ($MN/m^{1.5}$)	Crack Growth Rate (10^{-8} m/cycle)
20.5	4.0
25.5	11.3
31.6	22.1
37.4	37.8
45.3	69.2
54.9	134.5
20.5	9.4
25.5	22.4
31.6	42.5
37.4	71.4
45.3	116.7
54.9	203.8

measurements of crack growth rates at constant stress intensity (Figure 9 of Reference B-12.2). Analysis of data from these two samples yielded $B = 19.3 \times 10^{-30}$ and $B = 16 \times 10^{-30}$. A fifth estimate for B in unirradiated zircaloy was obtained using the Walker and Kass summary of their data with unirradiated material. Their straight line fit corresponds to a value of $B = 48 \times 10^{-30}$.

The only data used to find B for irradiated zircaloy are the eleven measurements of crack growth rate and stress intensity factor range by Walker and Kass discussed earlier in this section. The average value of B from these data and Equation (B-12.1) with m = 15 was $B = 10^{-25}$.

The expression used to model B [Equation (B-12.3)] is a fit to the average of the five estimates for B at zero fast neutron fluence and the one value of B at fluences on the order of 10^{25} neutrons/m^2. The functional dependence of B on fast neutron fluence is an estimate based on the data at zero and 10^{25} neutrons/m^2. The value of B for fluences between 10^{24} and 10^{25} neutrons/m^2 has been determined to cause the predicted value of crack growth rate to remain constant at stress intensity factors of 15.531432 $MN/m^{1.5}$.

The value $\Delta K_{min} = 9.5\ MN/m^{1.5}$ in Equation (B-12.1) is based on a test by Rao at this stress intensity range. No change in crack length was observed in this test.

12.3 Basis for Low Cycle Fatigue Material Constants

The values returned for the material parameters in Equation (B-12.4) are based on the data and analysis of Pettersson[B-12.5]. Pettersson has shown that Equation (B-12.4) can be integrated and expressed in the form of the Coffin-Manson relationship.

$$\Delta E = C\ N_f^{-\alpha} \tag{B-12.5}$$

where

ΔE = plastic strain range

N_f = number of cycles to failure

C, α = material parameters.

The constant α is the same material parameter as the constant α in Equation (B-12.4). Pettersson shows that the constant C is related to the material constant K of Equation (B-12.4) by the following expressions

for uniaxial straining,

$$C^{1/\alpha} = \frac{\ln (\ell_f/\ell_o)}{K} \simeq \frac{4.83}{K} \tag{B-12.6}$$

for bend tests

$$C^{1/\alpha} = \frac{1}{K} \int_{\ell_o/t}^{\ell_f/t} \frac{dX}{X(1-X)^{1/\alpha}} \simeq \frac{6.26}{K} \tag{B-12.7}$$

where

ℓ_o = the initial crack length (m)

ℓ_f = the final crack length (m)

t = the specimen thickness (m).

The constants α and log C which Pettersson reports from fits to his data are listed in Table B-12.II along with the constant K obtained from Equation (B-12.7).

TABLE B-12.II

LOW CYCLE FATIGUE MATERIAL PARAMETERS

Fast Fluence (neutrons/m^2)	Material Parameter, α (unitless)	log C (unitless)	Material Parameter, K (unitless)
0	0.60	1.87	10.3
1.3×10^{24}	0.64	1.96	11.7
2.6×10^{24}	0.56	1.75	10.1
Average	0.6	--	10.7

12.4 Cladding Cyclic Fatigue Subcode CFATIG Listing

A listing of the FORTRAN subcode CFATIG is provided in Table B-12.III.

12.5 References

B-12.1. B. Tomkins, "Fatigue Crack Propagation – An Analysis," *Philosophical, 18* (1968) p 1041.

B-12.2. V. S. Rao, *High Cycle Fatigue Crack Growth of Two Zirconium Alloys,* AE-486 (March 1974).

B-12.3. T. J. Walker and J. N. Kass, "Variation of Zircaloy Fracture Toughness in Irradiation," *Zirconium in Nuclear Applications,* ASTM-STP-551 (1974) pp 328-354.

B-12.4. W. J. O'Donnell and B. F. Langer, "Fatigue Design Basis for Zircaloy Components," *Nuclear Science and Engineering, 20,* 1 (1964).

B-12.5. K. Pettersson, "Low Cycle Fatigue Properties of Zircaloy Cladding," *Journal of Nuclear Materials, 56* (1975) pp 91-102.

TABLE B-12.III

LISTING OF THE CFATIG SUBCODE

```
      SUBROUTINE CFATIG(CTEMP    ,FFNCE    ,HICOEF   ,HIEXP    ,THRSH,
     #                  ALOCOF   ,ALOEXP)
C
C     CFATIG CALCULATES COEFFICIENTS AND EXPONENTS FOR HIGH
C     AND LOW CYCLE FATIGUE FAILURE EXPRESSIONS OF THE FOLLOWING
C     FORMS
C
C     FOR HIGH CYCLE FAILURE IN ZIRCALOY
C           DL/DN = HICOEF*(STRESS INTENSITY CHANGE)**HIEXP
C     FOR LOW CYCLE FAILURE IN ZIRCALOY
C           DL/DN = ALOCOF*L*(PLASTIC STRAIN RANGE)**ALOEXP
C     WHERE DL/DN IS THE CHANGE IN CRACK LENGTH PER CYCLE (M/CYCLE)
C           AND L IS THE CRACK LENGTH (M)
C
C     HICOEF = OUTPUT HIGH CYCLE EXPRESSION COEFFICIENT((M/CYCLE)/
C              (1.0E06 NEUTRONS/METER**1.5)**HIEXP)
C     HIEXP  = OUTPUT HIGH CYCLE EXPRESSION EXPONENT (UNITLESS)
C     THRSH  = OUTPUT MINIMUM STRESS INTENSITY FOR CRACK (MPA)
C     ALOCOF = OUTPUT LOW CYCLE EXPRESSION COEFFICIENT ((M/CYCLE)/M)
C     ALOEXP = OUTPUT LOW CYCLE EXPRESSION EXPONENT (UNITLESS)
C
C     CTEMP  = INPUT CLADDING MESHPOINT TEMPERATURE (K)
C     FFNCE  = INPUT FAST NEUTRON FLUENCE (NEUTRONS/M**2)
C
C     THE EQUATIONS USED IN THIS SUBROUTINE ARE BASED ON DATA FROM
C     (1) V. S. RAO, HIGH CYCLE FATIGUE CRACK GROWTH OF TWO ZIRCONIUM
C     ALLOYS, AE-466  (MARCH 1974)
C     (2) T. J. WALKER AND J. N. KASS, VARIATION OF ZIRCALOY FRACTURE
C     TOUGHNESS IN IRRADIATION, ASTM-STP-551, (1970) PP 328-354
C     (3) K. PETTERSSON, "LOW CYCLE FATIGUE PROPERTIES OF ZIRCALOY
C     CLADDING", J. NUCLEAR MATERIALS 56 (1975) PP 91-102.
C     INPUT CTEMP IS NOT USED IN THIS VERSION OF CFATIG
C
C     CODED BY D. L. HAGRMAN FEBRUARY 1977
C     UPDATED BY D.L. HAGRMAN SEPT 1977
C
C
C     CALCULATE HIGH CYCLE CONSTANTS
C
      HICOEF = 1.0165786E-25
      IF(FFNCE .GT. 1.0E25) GO TO 5
      HICOEF = 2.0E-11*(15.531432**(12.C*( EXP(-FFNCE/1.0E24)-1)))
    5 HIEXP  = 15.0 - 12.0* EXP(-FFNCE/1.0E24)
      THRSH  = 9.5
C
C     CALCULATE LLW CYCLE CONSTANTS
C
      ALOCOF = 10.7
      ALOEXP = 1.67
      RETURN
      END
```

13. CLADDING COLLAPSE PRESSURE (CCLAPS)

(D. L. Hagrman)

The subcode CCLAPS is new; produced to aid in the prediction of cladding collapse into axial gaps between fuel pellets. It is based on a correlation developed by D. O. Hobson[B-13.1] which predicts collapse pressure for temperatures between 590 and 700 K. This preliminary version of the subcode does not apply to the description of high temperature (900 K) collapse or "waisting" of cladding into pellet-to-pellet gaps which has been observed during power-cooling-mismatch (PCM) accident tests[B-13.2].

The required input parameters for the function CCLAPS are cladding temperature (K), the largest pellet-to-pellet gap in the node considered (meters), and the room temperature midwall diamond-pyramid hardness number (DPH) of the cladding. An additional input argument, pellet-to-cladding gap size (meters) is not used by this preliminary version of the model but is included in the argument list to allow for future improvement of the model when more data become available. The function returns the pressure at which collapse is predicted by Hobson's correlation.

When measured values of hardness for the particular lot of tubing under consideration are not available, it is suggested that the user input Hobson's measured values. These were reported[B-13.3] as follows: for 80% cold-worked and 775 K stress-relieved material, hardness equals 238 DPH and for fully recrystallized material hardness equals 180 DPH.

The expression for collapse pressure derived by Hobson[B-13.1] is

$$P = 6895 \left[15\,660 + \frac{G}{2.17 \times 10^{-4}\, G - 4.57 \times 10^{-7}} - 183\, H + 0.729\, H^2 - 7.40 \times 10^{-4}\, H^3 - 3.762\, T \right] \quad \text{(B-13.1)}$$

where

P = collapse pressure (Pa)

G = pellet-to-pellet gap (m)

H = room temperature midwall hardness (DPH)

T = test temperature (K).

Hobson's correlation is based on out-of-pile tests with unirradiated cladding and pellet-to-cladding gaps of 0.20 mm (0.008 in.). Some tests were conducted with other pellet-to-cladding gaps sizes[B-13.3] but were not included in the data base of the correlation.

13.1 Cladding Collapse Pressure Subcode CCLAPS Listing

Table B-13.I is a listing of the function CCLAPS.

13.2 References

B-13.1. D. O. Hobson, *Quarterly Progress Report on the Creepdown and Collapse of Zircaloy Fuel Cladding Program Sponsored by the NRC Division of Reactor Safety Research for April-June 1976*, ORNL/NUREG/TM-52 (October 1976).

TABLE B-13.I

LISTING OF THE CCLAPS SUBCODE

```
C
C
      FUNCTION CCLAPS(PTPGAP,PTCGAP,CMDPH,CTEMP)
C
CCCCCC PTCGAP = INPUT PELLET TO CLADDING GAP (METERS)
CCCCCC PTPGAP = INPUT LARGEST PELLET TO PELLET GAP IN NODE (METERS)
CCCCCC CMDPH  = INPUT ROOM TEMPERATURE MIDWALL DIAMOND PYRAMID
CCCCCC          HARDNESS NUMBER (KG/MILLIMETER**2)
CCCCCC CTEMP  = INPUT CLADDING MESHPOINT TEMPERATURE (K)
CCCCCC
CCCCCC CCLAPS = OUTPUT COLLAPSE PRESSURE (PA)
CCCCCC
CCCCCC THE EQUATIONS USED IN THIS FUNCTION ARE BASED ON DATA FROM
CCCCCC (1) D. O. HOBSON, QUARTERLY PROGRESS REPORT ON THE CREEPDOWN
CCCCCC AND COLLAPSE OF ZIRCALOY FUEL CLADDING PROGRAM SPONSORED
CCCCCC BY THE NRC DIVISION OF REACTOR SAFETY RESEARCH FOR JANUARY -
CCCCCC MARCH 1976, ORNL/NUREG/TM-51
CCCCCC (2) D. L. HOBSON, QUARTERLY PROGRESS REPORT ON THE CREEPDOWN
CCCCCC AND COLLAPSE OF ZIRCALOY FUEL CLADDING PROGRAM SPONSORED
CCCCCC BY THE NRC DIVISION OF REACTOR SAFETY RESEARCH FOR APRIL -
CCCCCC JUNE 1976, ORNL/NUREG/TM-52
CCCCCC
CCCCCC CCLAPS CODED BY D. L. HAGRMAN JUNE 1977
CCCCC
      PPSI = 1566C. + PTPGAP/(2.17E-04*PTPGAP - 4.57E-07) + CMDPH *
     #       (-183. + CMDPH*(0.729 - CMDPH*7.4E-04)) - 3.762*CTEMP
C
      CCLAPS = 6895.0 * PPSI
C
      RETURN
      END
```

B-13.2. J. B. Ferguson (ed), *Quarterly Technical Progress Report on Water Reactor Safety Programs Sponsored by the Nuclear Regulatory Commissions Division of Reactor Safety Research October-December 1976*, TREE-NUREG-1070 (April 1977) p 37.

B-13.3. D. O. Hobson, *Quarterly Progress Report on the Creepdown and Collapse of Zircaloy Fuel Cladding Program Sponsored by the NRC Division of Reactor Safety Research for January-March 1976*, ORNL/NUREG/TM-51 (October 1976).

14. CLADDING OXIDATION (CORROS AND COBILD)

(D. L. Hagrman and G. A. Reymann)

The oxidation of zircaloy cladding is an important subject because zircaloy containing oxygen is more brittle than oxygen-free zircaloy and, therefore, has less ability to deform plastically under stress. Moreover, the oxidation reaction is exothermic and at high temperatures, such as might occur during a loss-of-coolant accident, the reaction may proceed rapidly enough so its heat can significantly influence the cladding temperature.

The correlations developed are used in safety analysis to determine the extent of the oxidation, to assess the strength of the cladding, and to predict the cladding temperature.

14.1 Summary

Low temperature oxidation is summarized in Section B-14.1.1 and high temperature oxidation is summarized in Section B-14.1.2.

14.1.1 Low Temperature Oxidation (CORROS). The subroutine CORROS returns an expression for the thickness of the oxide layer on zircaloy cladding during typical reactor operation at temperatures of 523 to 673 K. Required input values are temperature at the outer surface of the oxide, initial oxide film thickness, length of time at the given temperature, type of reactor (BWR or PWR), heat flux across the oxide layer, and zircaloy oxide thermal conductivity.

Cladding oxidation during normal LWR operation occurs in two stages, depending on the oxide thickness and to some extent on the temperature of the oxide. For thin oxides the rate of oxidation is controlled by the entire oxide layer. When the oxide layer becomes thicker, a change of the outer portion occurs and further oxidation is controlled by the intact inner layer. The transition between stages is described in terms of thickness of the oxide layer at transition.

$$X_{TRAN} = 7.749 \times 10^{-6} \exp\left(\frac{-790}{T}\right) \qquad \text{(B-14.1)}$$

where

X_{TRAN} = thickness of the oxide layer at transition point (m) (typically 1.9×10^{-6} m thick)

T = temperature of the oxide-metal interface (K).

Values of the thickness of the oxide layer on the outside of the cladding are given by Equations (B-14.2a), (B-14.2b), and (B-14.2c) for pretransition and posttransition oxide films.

For pretransition oxide films:

$$X_{PRE} = [4.976 \times 10^{-9} A(t) \exp\left(\frac{-15\,660}{T}\right) + X_o{}^3]^{1/3} \qquad \text{(B-14.2a)}$$

for posttransition oxide films when X_o, the initial oxide thickness, is less than X_{TRAN}:

$$X_{POST} = 82.88 A [t - t_{TRAN}] \exp\left(\frac{-14\,080}{T}\right) + X_{TRAN} \qquad \text{(B-14.2b)}$$

and when X_o is greater than the transition thickness:

$$X_{POST} = 82.88 A [t] \exp\left(\frac{-14\,080}{T}\right) + X_o \qquad \text{(B-14.2c)}$$

where

X_{TRAN} = thickness of the oxide layer at the transition point (Equation B-14.1).

X_{PRE} = thickness of the oxide layer when a pretransition oxide film exists (m).

X_{POST} = thickness of the oxide layer when the oxide film is in the posttransition state (m).

X_o = initial thickness of the cladding oxide layer expressed in meters. This term can be approximated as $X_o = 0$ for etched cladding, but it becomes important if extensive prefilming has occurred or if oxidation is carried out in several steps which take place at different temperatures or in different coolant chemistries.

t = time at temperature (days).

A = a parameter describing enhancement of the cladding oxidation rate in a reactor environment. Typical reactor chemistries and flux levels result in a value of A = 1.5 for a PWR and 9 for a BWR. However, the factor is apparently a function of temperature, as discussed in Section B-14.2.3. A value for A is determined in the subcode by user specification of BWR or PWR chemistry with an input parameter ICOR.

T = temperature of the oxide-metal interface calculated by the code from the input value of the temperature at the outer oxide surface, the heat flux across the oxide and the thermal conductivity of the oxide layer (K).

t_{TRAN} = time of transition between states (pre- and posttransition). This time is calculated in the code from the inverse of Equation B-14.2a.

14.1.2 High Temperature Oxidation (COBILD). For the high temperature range (1273 to 1773 K) neither the flux level nor the coolant chemistry has an important influence on the extent of oxidation. At these reactor operating temperatures the "coolant" has become steam, and oxidation proceeds much more rapidly than at normal operating temperatures. The oxidation process is more complex than it is at low temperature. Oxygen

diffuses through the oxide layer into the underlying zircaloy causing this material to become embrittled. Complete embrittlement criteria therefore require oxygen concentration profiles throughout the cladding. The COBILD subcode provides this information for future MATPRO embrittlement models. It was adapted from another code, BUILD5, written by R. Pawel[B-14.1] of Oak Ridge National Laboratory. Calculations of the oxygen weight fractions and the linear power generation due to the metal-water reaction are the only important parts of COBILD not in BUILD5.

Because the COBILD model is more complicated than many others in this document, only a qualitative description is given in this introductory section and details are presented in Section B-14.3. Unlike BUILD5 which can run independently, COBILD is designed for use in a complete fuel rod program such as FRAP-T2[B-14.2]. This type of program works in time steps. At the end of each step, COBILD is called and passed quantities from the main program, including the duration of the time step, temperature at the beginning and end of the step, original unoxidized cladding dimensions, thicknesses of the various layers and their oxygen concentrations, and total oxygen uptake at the beginning of the step. After updating several of these to conform to conditions at the end of the time step, it returns values for each of them.

The layer thicknesses and total oxygen uptake are calculated by numerical integration using parabolic oxidation kinetics equations published by J. V. Cathcart of ORNL[B-14.3]. When these calculations are completed, oxygen concentrations are calculated with classical diffusion theory, again by numerical integration. Finally, oxygen weight fractions in the various layers and the linear heating rate are calculated.

The code was written for temperatures above the beginning of the alpha + beta phase transition in zircaloy (1083 K). It therefore returns information pertaining to the three separate layers which would be present at these temperatures: the oxide, oxygen-stabilized alpha, and beta layers.

14.2 Low Temperature Oxidation Model (CORROS)

In this section a model is developed which describes the oxidation of zircaloy cladding at normal reactor operating temperatures (523 to 673 K).

14.2.1 Physical Picture Used in the Model. Investigators generally agree[B-14.4, B-14.5] that oxidation of zirconium alloys by water in the temperature range from 573 to 673 K proceeds by the migration of oxygen vacancies from the oxide-metal interface through the oxide layer to the oxide-coolant surface (and the accompanying migration of oxygen in the opposite direction). The vacancies at the metal-oxide surface are generated by the large chemical affinity of zirconium for oxygen. Although the rate of oxidation is controlled in part by vacancy migration, the process of oxygen transfer from coolant to metal is not complete until the vacancy is annihilated by an oxygen ion at the oxide-coolant surface. Thus, the suggestion that in-pile oxidation rates are affected by the supply of oxygen ions or atoms at the surface is consistent with oxygen rate control by

vacancy diffusion. In other words, the net flux of oxygen atoms into the metal is equal to the product of the vacancy flux times the probability that a vacancy will be annihilated by an oxygen atom, and that probability is affected by the supply of oxygen ions at the outer surface of the oxide whenever a competing mode for vacancy annihilation exists.

Detailed mechanisms for the posttransition time dependence of oxide growth have not been established in the literature[B-14.6, B-14.7]. Proposed mechanisms are discussed in conjunction with the models developed in Sections B-14.2.2 and B-14.2.3.

14.2.2 Out-of-Pile Basis for the Oxidation Model. An out-of-pile model is considered in this section because well characterized data[B-14.4] on oxidation as a function of time and temperature have been published only for out-of-pile corrosion. Principal features of the oxidation models are:

(1) The pretransition oxidation rate is time dependent and inversely proportional to the square of the (uniform) oxide thickness.

(2) The posttransition oxidation rate of a macroscopic surface is constant and proportional to the average of the local rates determined by an intact inner oxide layer. Figure B-14.1 presents a schematic picture of the posttransition model of the oxide film.

Oxidation of materials which form a protective oxide layer is frequently found to conform to the assumption that the rate determining process is the diffusion of oxygen atoms across the oxide. In these metals, the flux of atoms arriving at the metal and thus the rate of oxidation are determined by the concentration gradient across the oxide and are inversely proportional to the oxide thickness[B-14.8].

$$\frac{dy}{dt'} = \frac{k}{y} \qquad \text{(B-14.3)}$$

where

y = oxide thickness

t′ = time

k = a constant.

Integration of this equation from $y = 0$ at $t' = 0$ to $y = X$ at $t' = t$ yields a "parabolic" time dependence, $X = (2k\,t)^{1/2}$ which is frequently observed experimentally.

A slight generalization in the derivation of "parabolic" oxidation produces a result consistent with the measured time dependence of zircaloy corrosion. As discussed, vacancy migration is one factor in the rate controlling mechanism. If the vacancies have a limited lifetime, the flux of vacancies arriving at the oxide-coolant surface will be proportional to

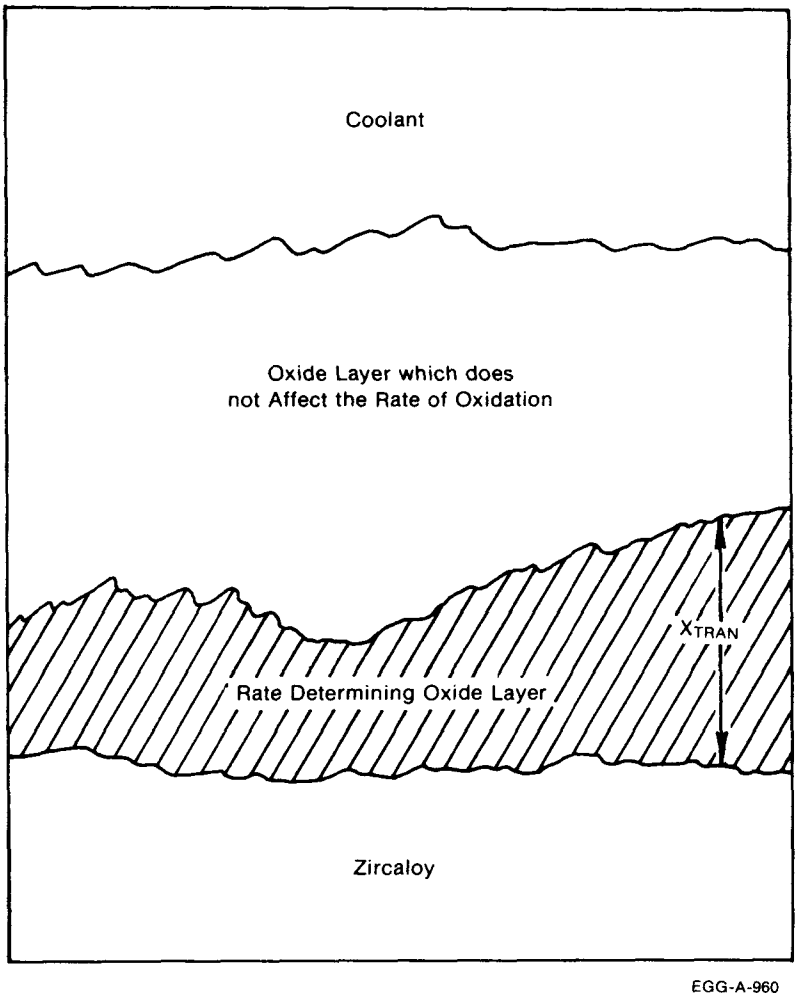

Fig. B-14.1 Schematic of posttransition oxide showing an intact rate determining layer of varying thickness, with another oxide layer which does not affect the oxidation rate.

the inverse of the time, $t_{diffusion}$, required for a vacancy to diffuse to the oxide-coolant surface. Since this time is proportional to the square of the average diffusion distance ($t_{diffusion} \propto y^2$) the net flux vacancy arriving at the oxide-coolant surface and thus the rate of oxidation should be proportional to the inverse of the square of the oxide thickness which the vacancies must cross.

From the physical arguments of the last paragraph, the vacancy lifetime-limited rate of oxide growth should be $\frac{dy}{dt'} = \frac{c}{y^2}$ where c is not a function of time or oxide thickness. Integration of the rate equation from $y = X_o$ at $t' = 0$ to $y = X$ at $t' = t$, gives $X = (3ct + X_o^3)^{1/3}$.

The $t^{1/3}$ dependence of the oxide layer was obtained directly from the assumption that the oxide growth is proportional to the inverse squared oxide thickness without specific reference to the vacancy migration picture. If the concept of a temperature dependent vacancy concentration at the metal-oxide surface is introduced, the constant c can be replaced with a temperature dependent form $c = R \exp(-T_o/T)$ where R and T_o are

constants and T is the temperature of the oxide-metal interface. The rate of oxidation in the pretransition stage is then

$$\frac{dy}{dt'} = \frac{R \exp(-T_o/T)}{y^2} \qquad \text{(B-14.4a)}$$

where

y = the oxide layer thickness at time t'.

Integration of Equation (B-14.4a) from $y = X_o$ at $t' = 0$ to $y = X$ at $t' = t$ gives

$$X = [3Rt \exp(-T_o/T) + X_o^3]^{1/3}. \qquad \text{(B-14.4b)}$$

Posttransition oxidation is viewed in this section as a series of pretransition modes. An inner oxide layer with thickness that varies as a function of surface position is presumed to control the rate of oxidation until this inner layer grows to the transition thickness. At this time the inner layer changes to an outer layer which does not affect the oxidation rate, and growth of a new inner layer begins. The representation is adopted because it successfully relates pretransition and posttransition oxidation rates (out-of-pile).

If the representation with an inner oxide film of varying thickness is correct, the rate controlling inner part of the oxide layer should join the outer layer at a thickness approximately equal to the transition thickness but at a time determined by local conditions. After several cycles the growth rates of the inner oxide layer at different locations on the surface of a macroscopic oxide film will be out of phase and the rate of growth of the entire surface film at any time (which is what is observed in most experiments) will be the time average rate of growth at any one place on the surface.

$$\left(\frac{dy}{dt}\right)_{\substack{\text{average}\\ \text{over}\\ \text{surface}}} = \frac{X_{TRAN}}{t_{TRAN_o}} = \frac{3 R \exp(-T_o/T)}{X_{TRAN}^2} \qquad \text{(B-14.5)}$$

where

X_{TRAN} = the thickness of the oxide layer at transition (m)

t_{TRAN_o} = the time necessary for an oxide film to grow from almost zero thickness to the transition thickness, according to Equation (B-14.4b), (s)

T = temperature

T_o = temperature constant (K)

R = constant (m^3/day).

Empirical relations based on out-of-pile data are published in Reference B-14.5. These relations are as follows:

$$\text{pretransition oxidation} = (27.1 \pm 0.8)\ 10^3\ t^{1/3} \exp\left(\frac{-5220}{T}\right) \qquad \text{(B-14.6)}$$

$$\text{posttransition oxidation} = (23.0 \pm 0.7) 10^8\ t \exp\left(\frac{-14\ 400}{T}\right) \qquad \text{(B-14.7)}$$

$$\text{weight gain at transition} = (123 \pm 4) \exp\left(\frac{-790}{T}\right) \qquad \text{(B-14.8)}$$

where

oxidation = weight gain (mg/dm^2)

T = temperature (K)

t = time (days).

Since the posttransition oxidation is viewed as being a series of pretransition modes which are separated by local loss of the inside oxide film, one would expect to obtain the pre- and posttransition oxidation rates with a single set of constants. In fact, the empirical constants determined by Van der Linde[B-14.5] for the pre- and posttransition oxidation rates [Equation (B-14.6) and (B-14.7)] can be reproduced with a single set of parameters, $T_o = 14\ 080$ K, $R = 1.659 \times 10^{-9} \frac{m^3}{day}$, and $X_{TRAN} = 7.749 \times 10^{-6}$ m exp (-790/T). Oxidation rates obtained using these constants and Equations (B-14.4) and (B-14.5) are within the ±4% error reported by Van der Linde for oxidation rates obtained using Equations (B-14.6) and (B-14.7).

14.2.3 Generalization to an In-Pile Model. Prediction of in-pile corrosion is complicated because the important variables of local temperature and reactor chemistry are not always reported; thermal gradients exist across the oxide film (causing the oxide outer surface temperature to differ from the oxide-metal interface temperature), and data on the time dependence of corrosion are limited. If in-pile corrosion enhancement is due to irradiation damage of the oxide layer as has been suggested[B-14.9, B-14.10], a new mechanism must be added to the present model. However, if the observed enhancements result from an increased supply of oxygen atoms or oxygen ions as suggested by other workers[B-14.11], a simple change of the rate constant in the out-of-pile equation will describe the increased oxidation observed in reactors. Changes in oxidation due to in-pile chemical effects are incorporated into the present model with an enchancement factor, A, which describes a multiplicative in-pile enhancement of the out-of-pile oxidation rate due to an increased supply of oxygen ions.

Rate equations for in-pile oxidation are thus:

for pretransition regime

$$\left(\frac{dX}{dt}\right)_{pre} = \frac{AR \exp(-T_o/T)}{X^2} \qquad \text{(B-14.9)}$$

for posttransition regime

$$\left(\frac{dX}{dt}\right)_{post} = \frac{3\ AR \exp(-T_o/T)}{X_{TRAN}^2} \qquad \text{(B-14.10)}$$

where the terms of the equations have been previously defined.

The integrated forms of these equations are:

$$X_{PRE} = \left[3\ AR\ t \exp(-T_o/T) + X_o^3\right]^{1/3} \qquad \text{(B-14.11)}$$

and

$$X_{POST} = \frac{3\ AR\ (t-t_{TRAN}) \exp(-T_o/T)}{X_{TRAN}^2} + X_{TRAN} \qquad \text{(B-14.12a)}$$

if X_o is less than X_{TRAN}, or if X_o is greater than X_{TRAN}:

$$X_{POST} = \frac{3\ AR\ t \exp(-T_o/T)}{X_{TRAN}^2} + X_o. \qquad \text{(B-14.12b)}$$

An interesting result (and a good test of the theory if time dependent in-reactor data become available) is the fact that the rate enhancement factor A does not result in a linear change in the oxide thickness for pretransition films. That is, although the oxidation rate is enhanced by factor A, the pretransition oxide film thickness at a given time is merely $A^{1/3}$ as thick as it would have been without the in-pile enhancement. Since the posttransition oxidation is linear in time, both the rate and change in oxide thickness at a particular time are enhanced by factor A.

The metal-oxide temperature is computed from the temperature at the outer oxide surface, the heat flux across the oxide surface, and the thermal conductivity of the oxide layer by Equation (B-14.13)

$$T = T_c + Q\ (X/KO2) \qquad \text{(B-14.13)}$$

where

T = temperature of the oxide-metal interface (K)

T_c = temperature of the outer surface of the oxide (K)

Q = heat flux across the oxide layer (W/m^2)

X = oxide layer thickness (m)

KO2 = thermal conductivity of the oxide layer (W/m·K).

Since the term Q(X/KO2) normally is a small correction to the temperature of the outer oxide surface, the correction to the temperature is approximated with an iteration. For the first step X is approximated as the initial oxide thickness. The oxide thickness is then computed with Equation (B-14.11) or Equation (B-14.12) and the resultant value is inserted for X in Equation (B-14.13).

An adequate data base for a careful prediction of oxidation enhancements in reactor environments is not available in spite of several past studies which have concentrated on the effects of dissolved oxygen[B-14.12, B-14.13], fast neutron flux[B-14.13], fast neutron fluence[B-14.14], and γ-irradiation[B-14.11]. As an interim measure, this model correlates the oxidation enhancement with only two of the more important variables: temperature and reactor environment.

(1) BWR Environments. Several authors[B-14.10, B-14.11, B-14.15] report that oxidation enhancement increases rapidly with decreasing temperatures in BWR environments. Values of the enhancement factor A, proposed in References B-14.10 and B-14.15 are plotted in Figure B-14.2 along with an average value of A = 9 found necessary to obtain a reasonable fit of the model developed here to the oxidation data presented in Reference B-14.16 and B-14.17 (pH 7 water with 30 ppm oxygen content in the steam). It is recommended that the straight line sketched between these points be used to estimate the enhancement in a typical BWR environment, and an analytical expression corresponding to this straight line has been programmed into CORROS using the expression

$$A = 4.840 \times 10^{5} \exp\left(-1.945 \times 10^{-2} T_c\right) \qquad \text{(B-14.14)}$$

for $500 < T < 673$ K.

where

A = the enhancement factor

T_c = the temperature at the outer oxide surface (K).

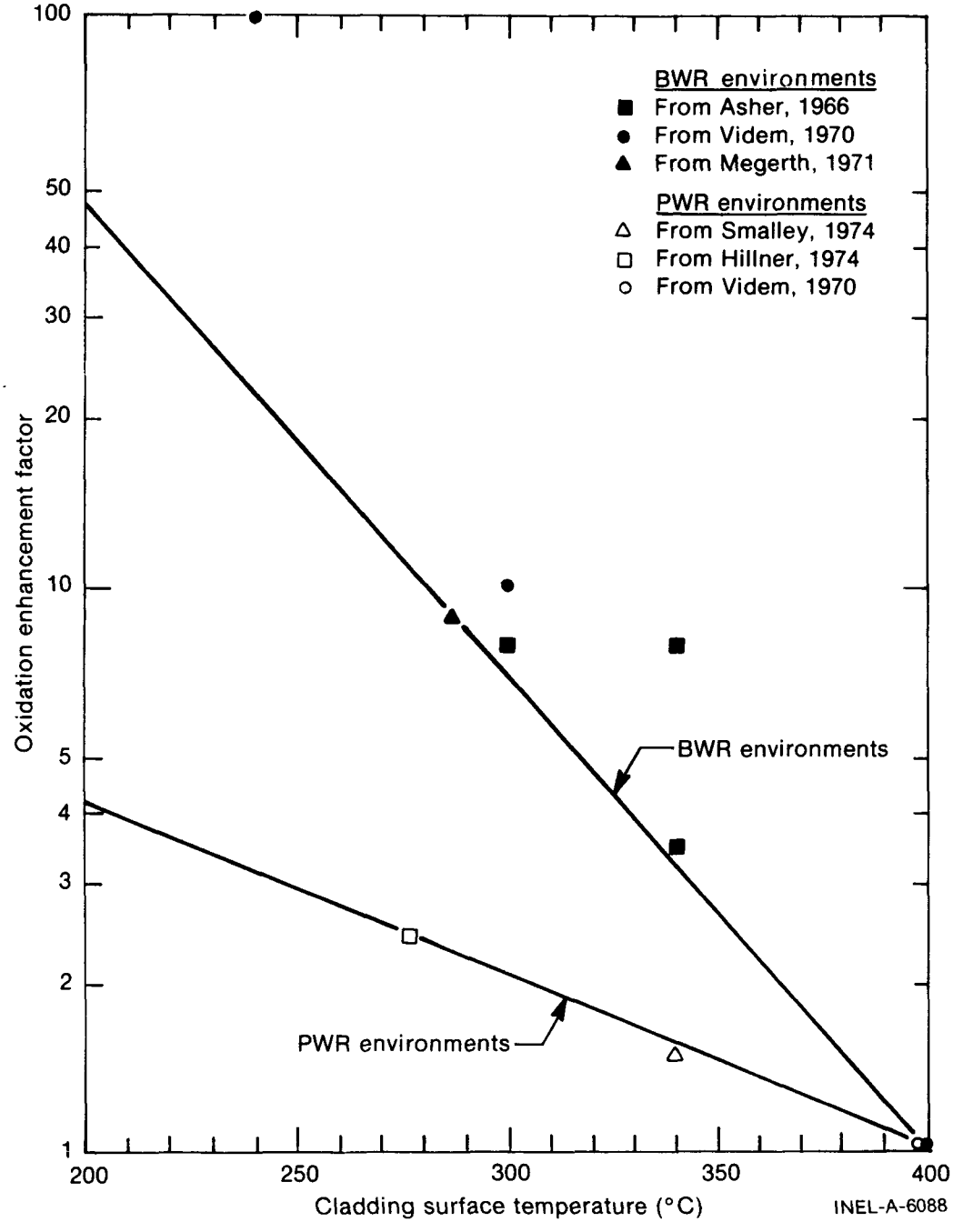

Fig. B-14.2 Estimates of enhancements over out-of-pile oxidation rates when cladding is irradiated in typical BWR and PWR environments.

(2) PWR Environments. "Enhancement factors" have been reported to be about 2.4[B-14.18] for zircaloy-2 rods in the Shippingport PWR. A fit of Equation (B-14.2b) to values of oxide thickness reported in Reference B-14.17 agreed with this value and a similar fit of the equation to values reported from Saxton PWR rods[B-14.19, B-14.20], resulted in a value of A = 1.5. These values are also plotted in Figure B-14.2. The relatively small value of A in PWR environments (which do not contain dissolved oxygen in the bulk coolant) is consistent with the picture of enhanced oxygen atom and ion supply rates due to ionization of dissolved oxygen. As in the case of BWR environments, the straight line sketched between these points is used by CORROS to estimate the enhancement in a typical PWR environment.

The equation for $500 < T < 673$ K is

$$A = 1.203 \times 10^{2} \exp\left(-7.118 \times 10^{-3} T_c\right) \qquad \text{(B-14.15)}$$

where

A = the enhancement factor

T_c = the temperature at the oxide-coolant surface (K).

14.2.4 Comparison with In-Pile Data. The average value predictions of the model developed in this section are compared with the values reported for individual samples in Figures B-14.3 through B-14.5. There is considerable scatter in the data from individual rods, with maximum measured values of oxide thickness as large as twice the average values. In some cases, such as the Shippingport data of Figure B-14.3, variations are generally consistent with the idea that temperature variations are responsible. In other cases, such as the Saxton data of Figure B-14.4, variations are not explained solely by temperature variation and the cause is probably related to local variations in coolant quality or chemistry caused by nucleate boiling or to contaminants. Similarly, variations in the coolant along the BWR rods could contribute to the large scatter in the BWR data of Figure B-14.5. Note that the duration of the pretransition period varies considerably in Figures B-14.3, B-14.4, and B-14.5. Figures B-14.3 and B-14.4 refer to PWRs with relatively low oxidation rate enhancements. However, the temperature is higher in the case of Figure B-14.4, producing a shorter pretransition period due to more rapid oxidation. Figure B-14.5 refers to a BWR, having low temperatures but large oxidation enhancement factors (9 in this case). This enhancement overwhelms the temperature effect and results in an even shorter pretransition period so that the relatively rapid posttransition oxidation is predicted to start early in the BWR.

14.3 High Temperature Oxidation Model (COBILD)

Because of the integrations described in Section B-14.1.2, COBILD is capable of handling calculations for which the temperature is changing with time. Further details of these calculations are described in this section.

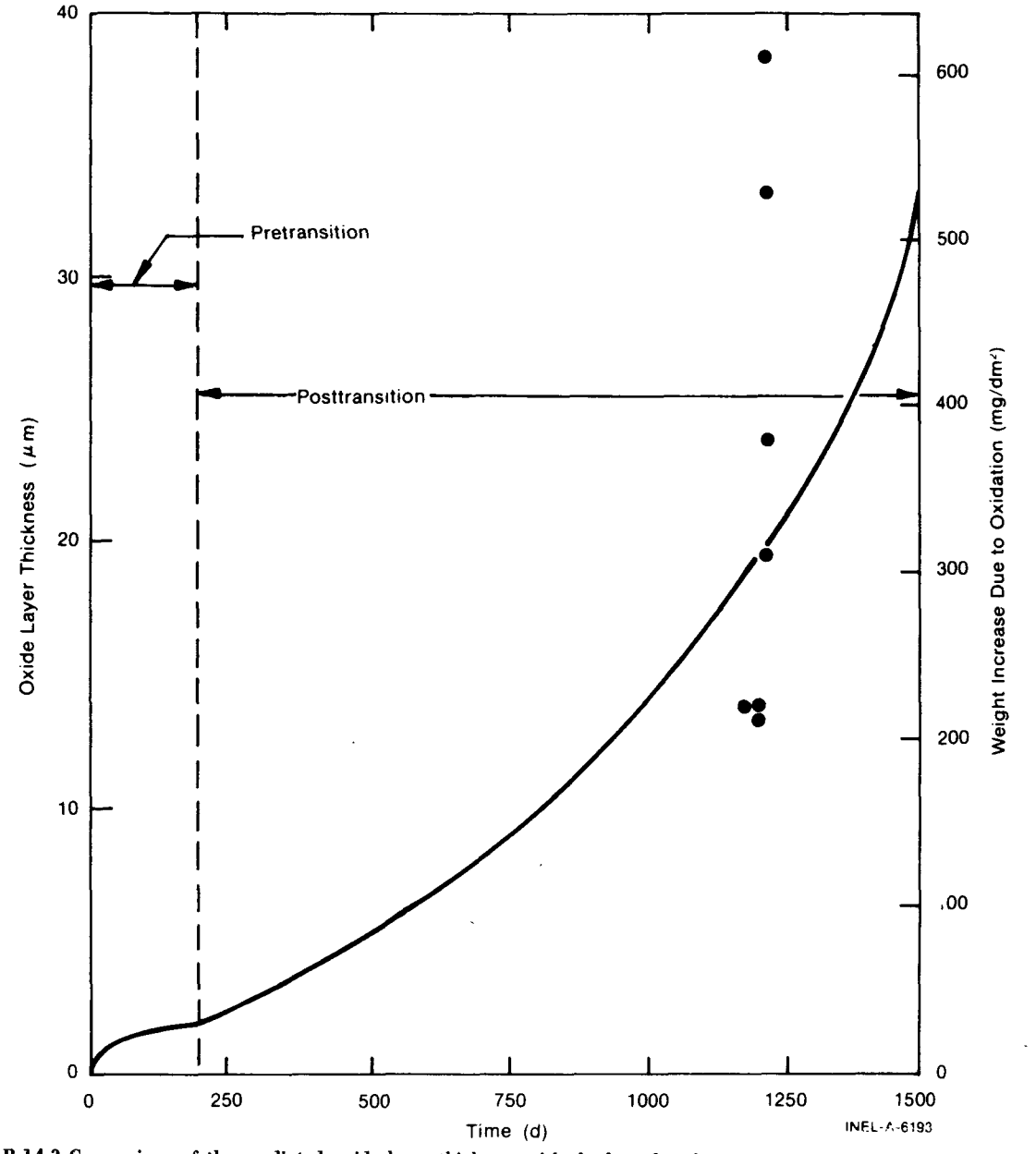

Fig. B-14.3 Comparison of the predicted oxide layer thickness with the base data from average values of six Shippingport zircaloy-2 rods in a PWR environment at 277°C.

14.3.1 Layer Thicknesses and Total Weight Gain. The oxide and oxygen-stabilized alpha layer thicknesses, as well as the total oxygen uptake are all calculated using isothermal parabolic rate equations published by J. V. Cathcart[B-14.3] of ORNL. According to these kinetics, the time rate of change of a kinetic parameter is inversely proportional to the instantaneous magnitude of the parameter, and the constant of proportionality is itself an Arrhenius function of temperature

$$\frac{dG}{dt} = \frac{1}{G} A \exp(-B/T) \qquad \text{(B-14.16)}$$

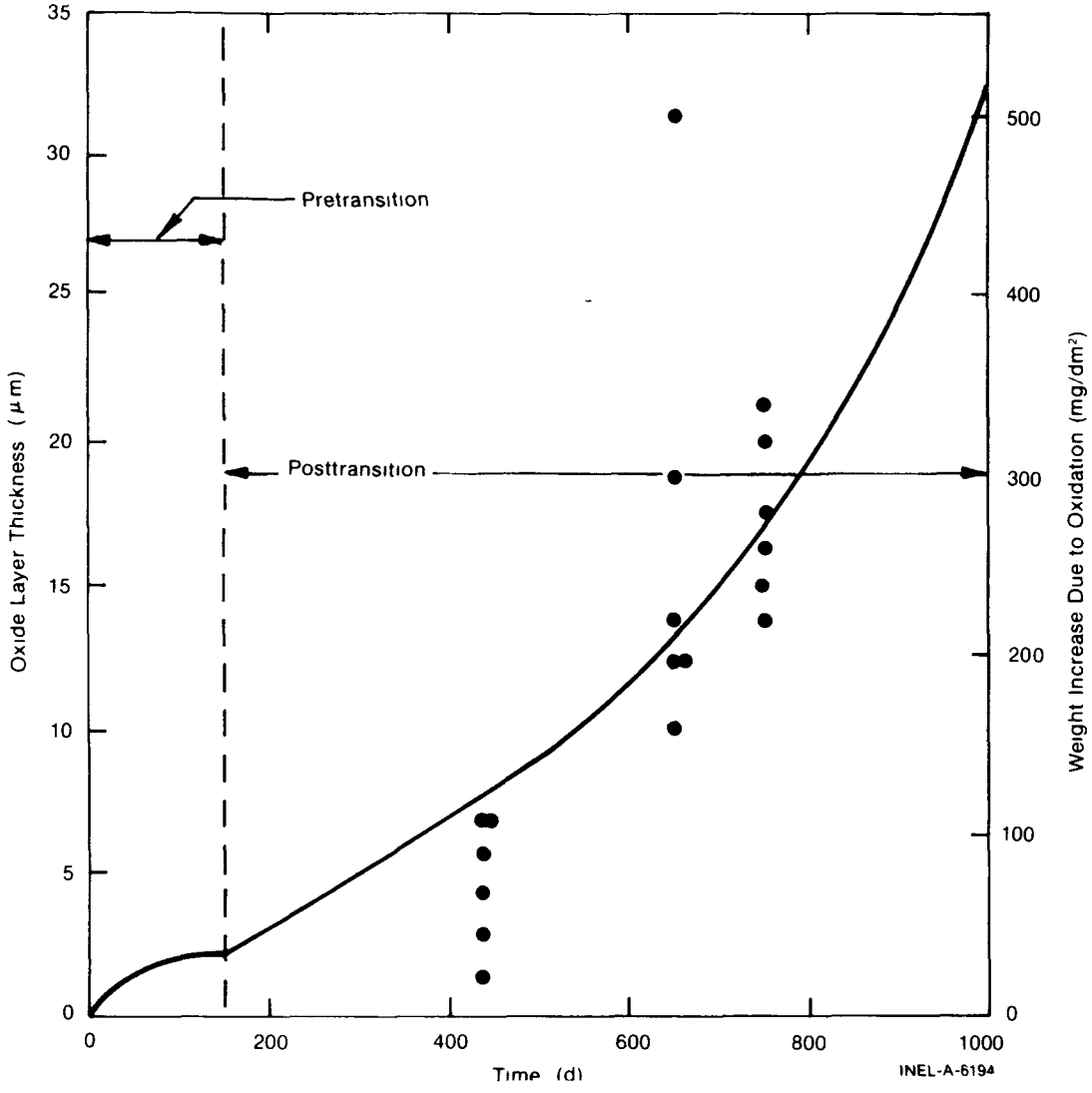

Fig. B-14.4 Comparison of the predicted oxide layer thickness with the base data from Saxton zircaloy-4 rods in a PWR at 340°C.

where

G = the kinetic parameter (that is, weight gain)

t = time (s)

A,B = constants

T = temperature (K).

Equation (B-14.16) may be rearranged and integrated to obtain

$$G_2 = [G_1^2 + 2\ A \exp\ (-B/T)\ DT]^{1/2} \qquad \text{(B-14.17)}$$

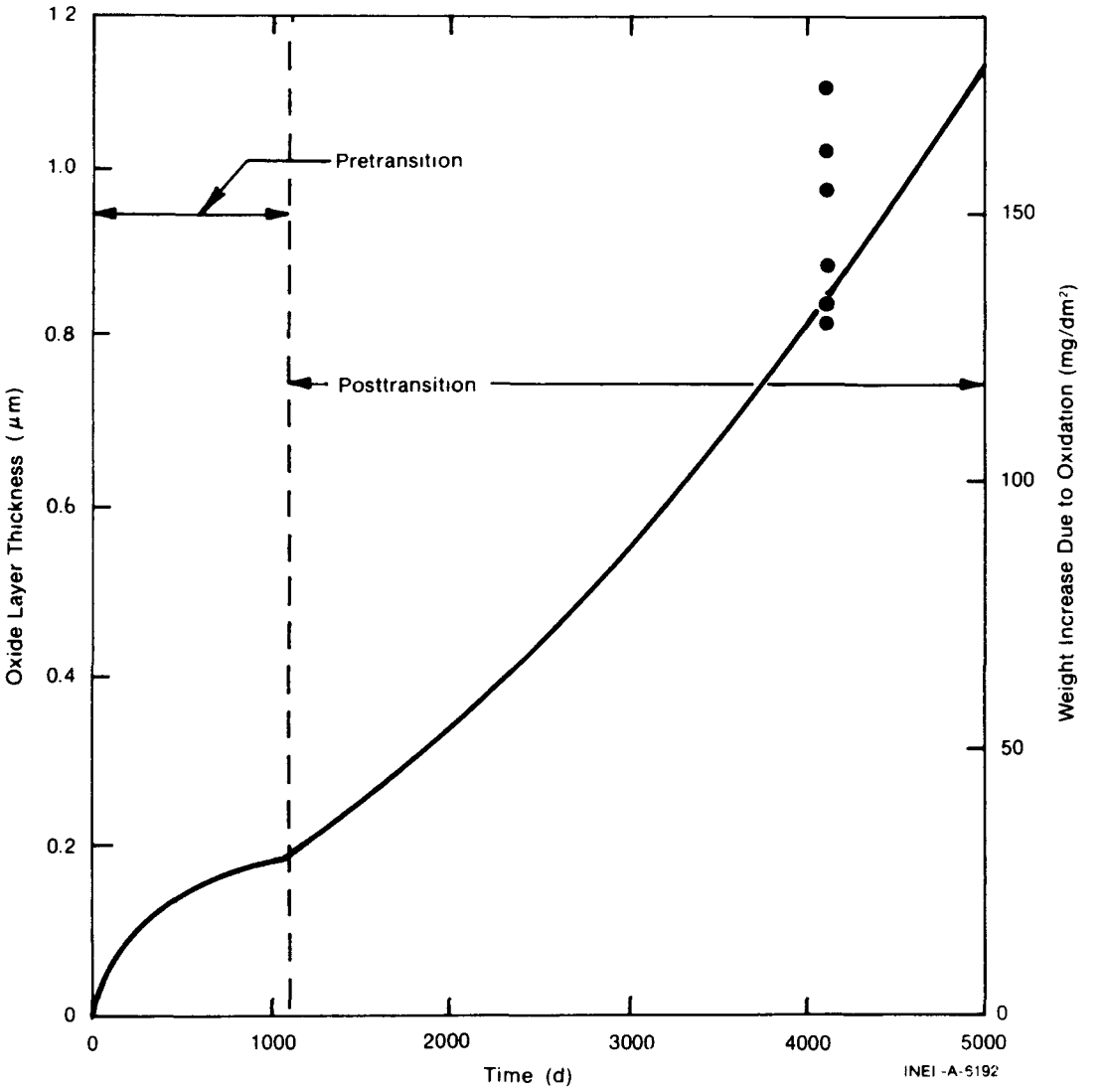

Fig. B-14.5 Comparison of the predicted oxide layer thickness with the data base from zircaloy-2 rods irradiated in the Vallecitos and Dresden BWR's at 286°C.

where

G_2 = value of the parameter at the end of the time step

G_1 = value of the parameter at the beginning of the time step

DT = COBILD time step (taken as 0.2 x main program's time step).

The use of parabolic kinetics to describe the total oxygen uptake and the ZrO_2 and oxygen-stabilized alpha layer thicknesses has been extensively documented by experimenters in several countries. In this country, there has been a series of reports from ORNL[B-14.3, B-14.21 – B-14.24] and from Worcester Polytechnic Institute[B-14.25, B-14.26]. There have been similar reports by Urbanic in Canada[B-14.27], by Leistikow in

Germany[B-14.28, B-14.29] and Kawasaki in Japan[B-14.30]. The correlations from J. V. Cathcart of ORNL were chosen for these three quantities because they were found to give the best fit to the pooled data. Pertinent information for each of the three variables using the Cathcart correlations is given in Table B-14.I.

TABLE B-14.I

PARAMETERS FOR PARABOLIC KINETICS EQUATIONS

Parameter	Units	A	B
Oxide Thickness	meter	1.126×10^{-6} m^2/s	1.806×10^{4} K
Alpha Thickness	meter	7.615×10^{-5} m^2/s	2.423×10^{4} K
Weight Gain	kg/m^2	1.680×10^{1} $(kg/m^2)^2$	2.007×10^{4} K

The correlation given here for the weight gain differs slightly from that of Reference B-14.3 to account for a "stoichiometry gradient," that is, the oxide layer changes from approximately stoichiometric at the coolant side to slightly hypostoichiometric at the oxide-to-alpha interface.

Integration to find a value of each of these three quantities is done by an iterative process where the temperature is assumed to change linearly from start to finish of the time step. The COBILD time step is found by dividing the main program's step by five. Five iterations through equations of the form of Equation (B-14.17) are then carried out with the temperature updated to the average temperature during the iteration. A comparison with data of the ZrO_2 thicknesses calculated with Cathcart's equation is shown in Figure B-14.6. A similarly good fit is obtained when the alpha thickness and weight gain correlations are compared with the data. The data were all taken under isothermal conditions.

To calculate oxygen weight fractions, it is necessary to find the thickness of the wall which is neither ZrO_2 nor oxygen-stabilized alpha. This is calculated with the equation

$$BX = TX - AX - \frac{2}{3} OX \qquad \text{(B-14.18)}$$

where

BX = total beta thickness (m)

TX = the original thickness of the cladding wall before any oxidation occurred (m)

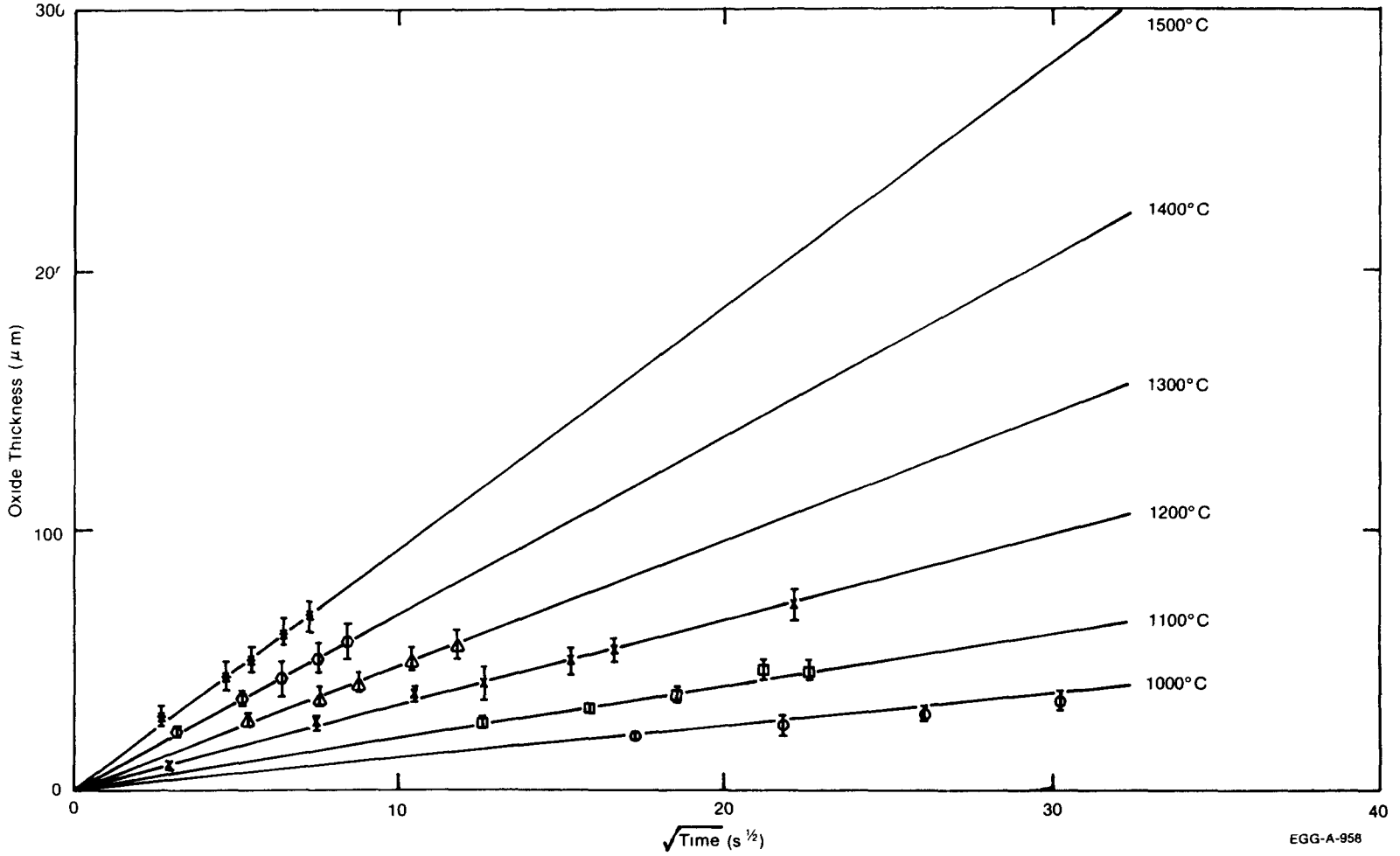

Fig. B-14.6 Comparison of calculated and measured ZrO_2 thicknesses as a function of time.

AX = total alpha thickness (m)

OX = total oxide thickness (m).

The oxide thickness in Equation (B-14.18) must be multiplied by two-thirds because of the 50% volume expansion which occurs when zircaloy oxidizes to form ZrO_2. In this one dimensional model, all the expansion is assumed to take place in the radial direction. Swelling of the lattice due to the presence of oxygen at interstitial sites is neglected.

The temperature range, for which the correlations summarized in Equation (B-14.17) and Table B-14.I are valid, is clearly important. Cathcart gives 1273 to 1773 K[B-14.3]. The range for the low temperature oxidation routine CORROS used in MATPRO has an upper limit of 673 K. The region between 673 to 1273 K has until now been ignored in MATPRO, under the assumption that no reactor would operate in this condition for a significant time. While this assumption is probably valid, the situation is not entirely comfortable, and recent results allow at least a tentative connection between the low and high temperature oxidation models. A paper by Schanz and Leistikow[B-14.28] states that parabolic kinetics are not bad, down to 1173 K. Other results from Leistikow[B-14.29] show that to about 1073 K, a weight gain proportional to the cube root of the time is appropriate. This is the type of correlation used in CORROS, and the agreement between CORROS and Leistikow's data is good up to about 1073 K. Cathcart's correlation also agrees with these data to within 10% when the temperature is greater than 1073 K. Since 1083 K is the beginning of the alpha + beta transition phase, it is a natural place to start using COBILD. It is therefore recommended that the upper limit of CORROS be extended from 673 to 1083 K, and that COBILD be used whenever the temperature is greater than 1083 K.

14.3.2 Oxygen Profile in the Beta Zircaloy. After the layer thicknesses are determined, the remaining beta thickness is divided by 8.0 to find the internodal spacing in the beta. Oxygen concentrations are calculated at each of these equally spaced radial nodes using finite difference techniques to solve a one-dimensional moving boundary problem in a wall of finite thickness. The two basic assumptions are that the concentration at the alpha to beta interface (the first node) is always the saturation concentration for beta zircaloy[B-14.31] and that diffusion of oxygen into the beta region does not begin until the temperature is greater than that at the end of the alpha + beta transition (1243 K). It is also assumed that the initial oxygen concentration throughout the as-fabricated metal is 0.0012 weight fraction. The oxygen concentration of the nine beta nodes is calculated by an iterative process of five steps, each of a duration equal to one-fifth of the main program's time step. During these iterations, the positions of the nodes do not move. The diffusion constant is found with an Arrhenius equation, published by R. A. Perkins[B-14.32] using a temperature which is the average of those at the beginning and end of the time step. Thus the oxygen redistribution encompasses a time equal to that of the layer thickness growth.

The basic equation for calculating oxygen redistribution is similar to that used in SIMTRAN[B-14.33].

$$\Delta C_n = \frac{D_{ox}}{X^2} (C_{n-1} + C_{n+1} - 2C_n)DT \qquad \text{(B-14.19)}$$

where

ΔC_n = change in oxygen concentration at the n^{th} node (kg/m^2)

D_{ox} = diffusion coefficient in beta zircaloy (m^2/s)

C_n = oxygen concentration at the n^{th} node (Kg/m^2)

X = internodal spacing (m).

Because of the growth of the external layers, the values passed to the subcode for concentrations in the beta layer are no longer proper initial conditions to update these concentrations. To compensate for the decrease in beta thickness, a least-squares parabola is calculated for every three successive input concentration data, starting with the node at the alpha-to-beta interface. A good approximation to the correct initial concentration at the new position of each node may then be found by interpolation on the parabola.

A stability criterion was added to the code to give an error message if conditions are such that diffusion is occurring too rapidly. A quantity named "MOD" (for modulus) is calculated,

$$MOD = \frac{X^2}{D_{ox}DT}. \qquad \text{(B-14.20)}$$

According to classical finite difference techniques, when MOD becomes less than 2.0, oxygen diffusion is occurring too rapidly and the method becomes unstable. Therefore, whenever MOD is less than 2.0, COBILD prints an error message and terminates. In several sample problems run to check COBILD, this happened only in the most extreme cases; for example, when the temperature was close to the cladding melting point.

If COBILD does not terminate due to an excess diffusion rate, then at the end of the oxygen redistribution calculation the total oxygen in the beta is calculated using the concentrations at the nine nodes and integrating by Simpson's rule.

14.3.3 Oxygen Weight Fraction in the Beta Zircaloy. As described in the preceding subsection, the total oxygen in the beta region is calculated. This quantity, called BWT, has units of kg/m^2 and is the total mass of oxygen in the full beta thickness for each square meter at the alpha-to-beta interface. To find the ratio of this mass to the mass of beta zircaloy, it is divided by the product of the density of zircaloy and the beta thickness. This divisor is the mass of zircaloy per square meter of alpha-to-beta interface. The weight

fraction of oxygen in as-fabricated zircaloy (0.0012) is subtracted from this, since BWT includes all the oxygen in the beta region. The result is

$$BWTFRO = \frac{BWT}{6490BX} - 0.0012 \qquad \text{(B-14.21)}$$

where

BWTFRO	=	oxygen weight fraction in beta in excess of the as-fabricated content (dimensionless)
BWT	=	total oxygen in beta (kg/m^2)
6490	=	density of zircaloy (kg/m^3)
BX	=	thickness of beta layer (meters)
0.0012	=	oxygen weight fraction of as-fabricated zircaloy.

14.3.4 Oxygen Weight Fraction in the Alpha Zircaloy. The calculation of this quantity, specified as AWTFRO, is similar to that used for BWTFRO. Basically the procedure is to find the total oxygen weight in the alpha region by subtracting the oxygen uptake in the beta and oxide regions from the total uptake and dividing by the mass of zircaloy in the alpha layer. AWTFRO is given by

$$AWTFRO = \frac{[W1 - (BWT-0.0012 \cdot 6490 \cdot BX) - (5820 \cdot 0.26 \cdot OX)]}{6490 \cdot AX} \qquad \text{(B-14.22)}$$

where

AWTFRO	=	oxygen weight fraction in alpha layer in excess of the as-fabricated content (dimensionless)
W1	=	total oxygen uptake (kg/m^2)
5820	=	density of ZrO_2 (kg/m^3)
0.26	=	oxygen weight fraction in ZrO_2 (dimensionless)
OX	=	thickness of the oxide layer (m)
AX	=	thickness of the alpha layer (m).

Since most of the oxygen goes into oxide, the first and last terms are of comparable size, and both much bigger than the middle term. So a small number is calculated by taking the difference between two much bigger numbers. In addition, the calculations of W1, BX, and OX are all independent of one another. Therefore, AWTFRO, as calculated with Equation (B-14.22), may be negative. In several problems run to check the code, negative alpha weight fractions occurred only in a few cases during the first time steps and their absolute values were small. The problem is avoided in the code which sets AWTFRO = 0.0 if the calculated value is negative.

14.3.5 Linear Power Generation Due to the Metal-Water Reaction. The zirconium metal-water reaction is exothermic. Knowing the mass of zirconium converted to ZrO_2 during a timestep and the heat of reaction, the heating rate resulting from this reaction may be found. However, such a calculation will underpredict because it neglects the heat of solution of the dissolved oxygen in the material beneath the oxide layer. To get a more realistic heating rate, an "effective" oxide thickness is computed for use in the heating rate calculation. This effective thickness, found by assuming that all the oxygen uptake goes into forming ZrO_2, is

$$XO = \frac{W1}{5820.0 \cdot 0.26} \qquad \text{(B-14.23)}$$

where

XO = effective oxide thickness (m)

W1 = total oxygen uptake (kg/m^2)

5820 = density of ZrO_2 (kg/m^3)

0.26 = weight fraction of oxygen in ZrO_2.

The radius of the part of the rod which has not yet been oxidized is equal to the original radius minus two-thirds of the oxide thickness. The two-thirds factor is necessary due to the 50% expansion which occurs when zirconium is converted to ZrO_2. The volume of zirconium converted in a time step is

$$\Delta V = L\pi (R_o - 2/3\ XO_i)^2 - L\pi (R_o - 2/3\ XO_f)^2 \qquad \text{(B-14.24)}$$

where

L = length of the fuel rod (m)

R_o = original rod radius (m)

XO_i = effective oxide thickness at the beginning of the time step (m)

XO_f = effective oxide thickness at the end of the time step (m).

Expanding Equation (B-14.24) and rearranging gives

$$\Delta V = \frac{4L\pi}{3}\left[R_o - \frac{XO_f + XO_i}{3}\right](XO_f - XO_i). \qquad \text{(B-14.25)}$$

Except in extreme cases where very extensive oxidation has occurred, R_o will be much greater than $(XO_f + XO_i)/3$ and this latter term may be neglected in Equation (B-14.25). In addition, neglecting this smaller term leads to a more conservative result; that is, the calculation yields a greater volume of converted zircaloy. With this approximation, Equation (B-14.25) becomes

$$\Delta V = \frac{4L\pi}{3} R_o (XO_f - XO_i). \qquad \text{(B-14.26)}$$

To obtain the heat generation rate per unit length due to the conversion of zirconium to ZrO_2, Equation (B-14.26) is multiplied by the density of zirconium and by the exothermal heat of reaction per kilogram from the conversion, then divided by both the length of the rod and the duration of the time step. The result is

$$P = \frac{[6490(6.45 \times 10^6)\ 2.10\ DROD\ (XO_f - XO_i)]}{DT} \qquad \text{(B-14.27)}$$

where

P = rate of heat generation per meter (W/m)

6.45×10^6 = heat of reaction per kg of Zr (J/kg)

DROD = original rod diameter (m)

DT = duration of time step (s).

A plot of P versus temperature for a fuel rod with initial radius $R_o = 6.25 \times 10^{-3}$m is shown in Figure B-14.7 for various initial oxide thicknesses and a time step of one second.

Equation (B-14.27) may underpredict the oxidation heating rate because it uses the heat released in the reaction

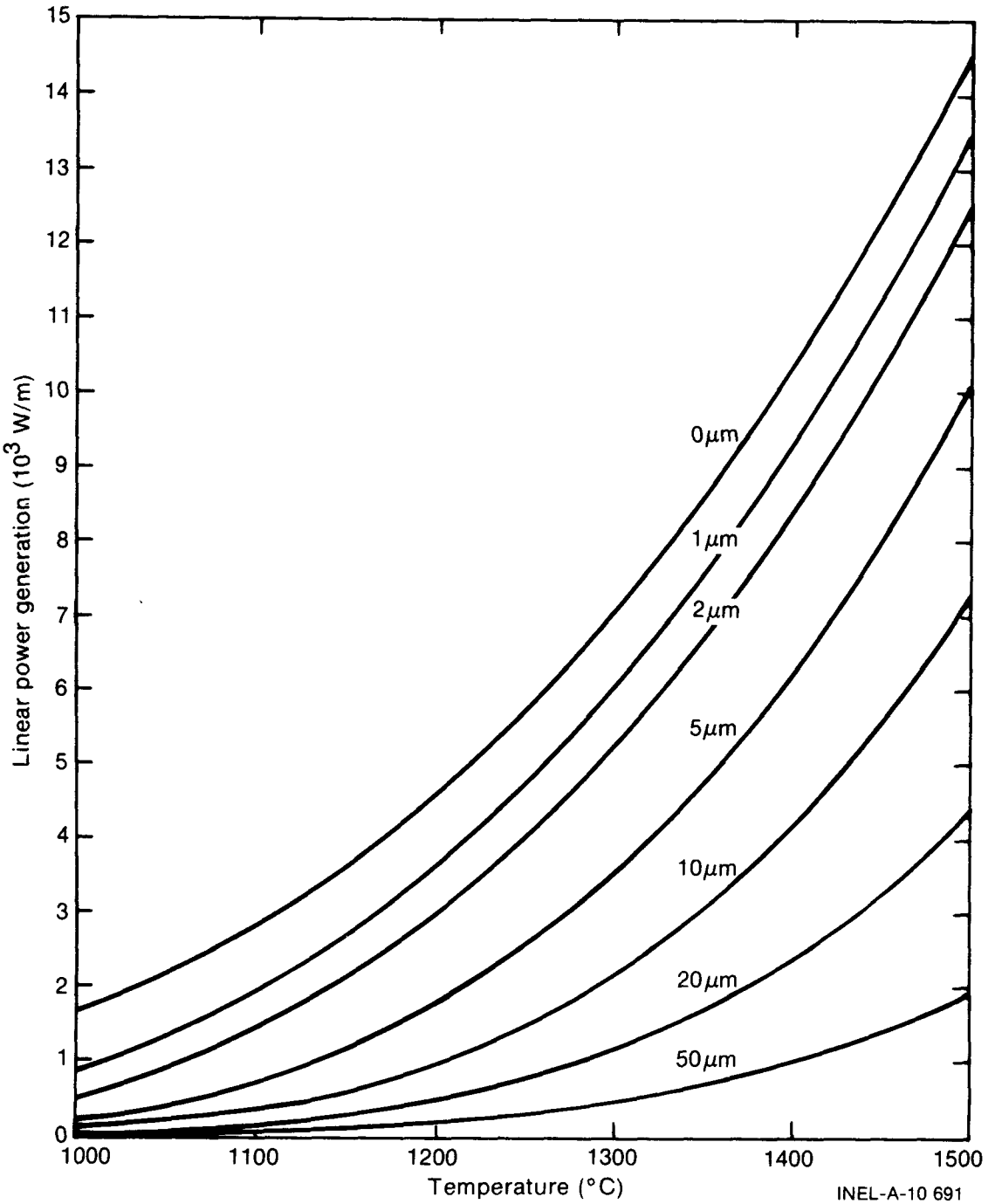

Fig. B-14.7 Linear power generation for a rod of initial diameter 1.25×10^{-2} m as a function of temperature for various initial oxide thicknesses.

$$2\ H_2O + Zr \rightarrow 2H_2 + ZrO_2 + Q \qquad \text{(B-14.28)}$$

with $Q = 6.5 \times 10^6$ joules per kilogram of zircaloy reacted[B-14.34]. Q is smaller by nearly a factor of two than Q_1, the heat released in the following reaction.

$$Zr + O_2 \rightarrow ZrO_2 + Q_1 \qquad \text{(B-14.29)}$$

where

Q_1 = 1.204×10^7 joules per kilogram of zircaloy reacted[B-14.33].

The difference arises because Equation (B-14.28) includes heat required for the endothermic dissociation of water reaction.

$$H_2O + O_2 \rightarrow H_2 + O. \qquad \text{(B-14.30)}$$

The dissociation described by Equation (B-14.30) must take place either at the oxide-to-coolant interface or within the coolant itself. The oxygen thus liberated then diffuses through the oxide layer and combines with the zircaloy at the metal-to-oxide interface according to Equation (B-14.29). It is clearly Q_1 and not Q which causes the cladding to heat. However, Q_2 must ultimately come from the rod as well, cooling it. In a closed system Equation (B-14.28) then would be adequate. A problem can arise because the system is not strictly closed. As an example, dissociation may occur near one rod, cooling it, and oxidation within an adjacent rod, heating it. The assumption made here is that these processes average out and Equation (B-14.28) is satisfactory.

14.3.6 Uncertainty of the COBILD Model. Cathcart has analyzed the uncertainty in his measurements thoroughly[B-14.23]. In an earlier report[B-14.35] he reported joint 90% confidence levels for the rate constants [A exp (-B/T)] of Equation (B-14.16). The word "joint" is used to indicate the uncertainty of the rate constant as a whole rather than uncertainties in the parameters A and B separately. His conclusions are presented in Table B-14.II. These uncertainties are recommended for use with COBILD because Cathcart's correlations are used.

The numbers given in Table B-14.II are for isothermal oxidation only. There are no comparable statistics available for time dependent problems, largely because of the difficulty in obtaining reliable temperature measurements under transient conditions. In fact, the BUILD5 code has been used "in reverse" to obtain temperature estimates from oxide and alpha thicknesses measured in postirradiation examinations[B-14.36]. In such cases the temperatures computed have been found to be in good agreement with temperature estimates from the cladding microstructure.

TABLE B-14.II

90% JOINT CONFIDENCE INTERVALS FOR THE PARABOLIC RATE CONSTANTS FOR OXIDE LAYER GROWTH, ALPHA LAYER GROWTH, AND TOTAL OXYGEN UPTAKE

	Percent Deviation from Expected Value at Quantity		
	1050°C	1250°C	1500°C
Oxide Layer	+4.9 -4.7	+2.5 -2.4	+4.3 -4.1
Alpha Layer	+12.1 -10.8	+6.1 -5.8	-10.1 -9.2
Oxygen Uptake	+3.4 -3.3	+1.7 -1.7	+3.0 -2.9

14.4 Cladding Oxidation Subcodes CORROS and COBILD Listings

The FORTRAN subcodes CORROS and COBILD are presented in Tables B-14.III and B-14.IV, respectively.

14.5 References

B-14.1. R. E. Pawel, "Diffusion in a Finite System with a Moving Boundary," *Journal of Nuclear Materials, 49* (1973/74) pp 281-290.

B-14.2. J. A. Dearien et al, *FRAP-T2: A Computer Code for Transient Analysis of Oxide Fuel Rods – Volume 1 – Analytical Models and Input Manual,* TREE-NUREG-1040 (March 1977).

B-14.3. J. V. Cathcart, *Quarterly Progress Report on the Zirconium Metal-Water Oxidation Kinetics Program Sponsored by the NRC Division of Reactor Safety Research for April – June 1976,* ORNL/NUREG/TM-41 (August 1976).

B-14.4. E. Hillner, *Hydrogen Absorption in Zircaloy During Aqueous Corrosion, Effect of Environment,* WAPD-TM-411 (November 1964).

B-14.5. A. Van der Linde, *Calculation of the Safe Life Time Expectancy of Zirconium Alloy Canning in the Fuel-Elements of the Nero Reactor,* RCN-41 (July 1965).

B-14.6. B. Cox, "Comments on the Paper 'The Influence of Oxide Stress on the Breakaway Oxidation of Zircaloy-2' By D. H. Bradhurst and P. M. Heuer," *Journal of Nuclear Materials, 41* (1970) p 96.

TABLE B-14.III

LISTING OF THE CORROS SUBCODE

```
C
C     SUBROUTINE  CORROS(TCOI    ,QCI     ,ZRO2AI  ,ZRO2BI  ,ZOXKI
     #                  ,ICOR    ,DELHI)
C
C     CORROS CALCULATES THE THICKNESS OF THE OXIDE LAYER ON
C     THE OUTSIDE OF ZIRCALOY CLADDING
C
C     ZRO2BI = OUTPUT NEW OXIDE THICKNESS (M)
C
C     TCOI   = INPUT ZRO2-COOLANT INTERFACE TEMPERATURE (K)
C     QCI    = INPUT AXIAL INCREMENT HEAT FLUX (W/M**2)
C     ZRO2AI = INPUT OXIDE THICKNESS AT END OF PREVIOUS TIME STEP (M)
C     ZOXKI  = INPUT ZIRCONIUM OXIDE THERMAL CONDUCTIVITY (W/M-K)
C     ICOR   = INPUT REACTOR CHEMISTRY INDEX
C                    .GE.2 FOR PWR
C                    .LT.2 FOR BWR
C     DELHI  = INPUT TIME STEP (S)
C
C     THE EQUATIONS USED IN THIS SUBROUTINE ARE BASED ON DATA FROM
C     (1) A. VAN DER LINDE, CALCULATION OF THE SAFE LIFETIME EXPECTANCY
C     OF ZIRCONIUM ALLOY CANNING IN THE FUEL ELEMENTS OF THE NERO
C     REACTOR, RCN-41 (1965)
C     (2) F. H. MEGERTH, C. P. RUIZ, U. E. WOLFF, ZIRCALOY-CLAD UO2
C     FUEL ROD EVALUATION PROGRAM FINAL REPORT, GEAP-10371 (1971)
C     (3) W. R. SMALLEY, SAXTON CORE II FUEL PERFORMANCE EVALUATION
C     PART I MATERIALS, WCAP-3385-56 (1971)
C     (4) W. R. SMALLEY, EVALUATION OF SAXTON CORE III FUEL
C     MATERIALS PERFORMANCE, WCAP-3385-57 (1974)
C     (5) E. HILLNER, CORROSION AND HYDRIDING PERFORMANCE OF ZIRCALOY
C     TUBING AFTER EXTENDED EXPOSURE IN THE SHIPPINGPORT PWR,
C     SYMPOSIUM ON ZIRCONIUM IN NUCLEAR APPLICATIONS, ASTM STP 551
C     (1974)
C
C     THIS MODEL SHOULD NOT BE USED OUTSIDE THE TEMPERATURE RANGE
C     523.15 - 673.15K (250-400 C)
C
C     CONVERSION FROM (MG/DM**2) OXIDE WEIGHT GAIN TO:
C     (1)OXIDE THICKNESS IN DM IS 6.3E-7 DM/(MG/DM**2)
C     (2)OXIDE THICKNESS IN MILS IS 2.5E-3 MILS/(MG/DM**2)
C     (3)OXIDE THICKNESS IN MICROMETERS IS .063 MICROMETER/(MG/DM**2)
C
C     CORROS WAS CODED BY D.L. HAGRMAN IN JANUARY 1977.
C
      OXIDE1 = 0.0
      OXIDE2 = 0.0
C
      IF(TCOI .LE. 366.5) GO TO 40
      IF(ZRO2AI .LE. 0.0) ZRO2AI = 1.0 E-10
      TCOIC = TCOI + QCI * ZRO2AI/ZOXKI
      WTRAN = 7.7490E-06*  EXP(-7.90E02/TCOIC)
      IF(TCOI .GT. 673.) GO TO 13
      IF(ICOR.GE.2) GO TO 10
C
C     BWR ENVIRONMENT
      A = 4.840E05 *  EXP(-1.945E-02 * TCOI)
      IF(TCOI.LE.500.) A = 28.92887
      GO TO 15
C
C     PWR ENVIRONMENT
   10 A = 1.203E02 *  EXP(-7.118E-03 * TCOI)
      IF(TCOI.LE.500.) A = 3.424614
      GO TO 15
C
   13 A = 1.0
C
   15 IF(ZRO2AI .GT. WTRAN) GO TO 30
C
      OXIDE1 = ZRO2AI
      DO 20 I = 1, 2
   20 OXIDE1= (4.976E-09*A*EXP(-1.566E04/(TCOI + QCI*OXIDE1/ZOXKI)) *
     #       (DELHI/8.64E4) + ZRO2AI **3.) **0.333
      IF(OXIDE1 .LT. WTRAN) GO TO 45
```

TABLE B-14.III (continued)

```
      OXIDE2 = ZRO2AI
      DO 25 I = 1, 2
   25 OXIDE2 = 8.288E01*A*EXP(-1.408E04/(TCOI + QCI*OXIDE2/ZOXKI)) *
     #        DELHI/8.64E04 + ((ZRO2AI**3)/(WTRAN**2))
      GO TO 50
C
   30 OXIDE2 = ZRO2AI
      DO 35 I = 1, 2
   35 OXIDE2 = 8.288E01 * A * EXP(-1.408E04/(TCOI + QCI * OXIDE2/ZOXKI))
     #        * DELHI/8.64E04 + ZRO2AI
      GO TO 50
   40 ZRC2BI = ZRO2AI
      GO TO 55
   45 ZRC2BI = OXIDE1
      GO TO 55
   50 ZRO2BI = OXIDE2
   55 CONTINUE
      RETURN
      END
```


B-14.7. D. H. Bradhurst and P. M. Heuer, "Reply to Comments by B. Cox on 'The Influence of Oxide Stress on the Breakaway Oxidation of Zircaloy-2,' " *Journal of Nuclear Materials, 41* (1971) p 101.

B-14.8. W. Jost, *Diffusion in Solids, Liquids, Gases,* New York: Academic Press Inc., 1972, p 341.

B-14.9. D. H. Bradhurst, P. J. Shirvington, P. M. Heuer, "The Effects of Radiation and Oxygen on the Aqueous Oxidation of Zirconium and its Alloys at 290°C," *Journal of Nuclear Materials, 46* (1973) p 53.

B-14.10. R. C. Asher et al, "Effects of Radiation on the Oxidation and Hydrogen Absorption of Zirconium Alloys in Steam," *Electrochemical Technology, 4* (1966) p 231.

B-14.11. L. Lunde and K. Videm, "Effects of Surface Treatment on the Irradiation Enhancement of Corrosion of Zircaloy-2 in HBWR," *Zirconium in Nuclear Applications,* ASTM-STP-551 (1974) pp 514-526.

B-14.12. A. B. Johnson, Jr., "Effects of Nuclear Radiation on the Corrosion, Hydriding, and Oxide Properties of Six Zirconium Alloys," *Applications-Related Phenomena for Zirconium and Its Alloys, ASTM-STP-458* (1969) pp 301-324.

B-14.13. W. A. Burns, *Effects of Fast Neutron Irradiation, Fabrication History, and Water Oxygen on the Environmental Behavior of Zirconium Alloys,* BNWL-88 (1965).

B-14.14. A. B. Johnson, Jr., and J. E. Irvin, *Radiation-Enhanced Oxidation of Zircaloy-2 in pH-10 LiOH and pH-10 NH_4OH,* BNWL-463 (1967).

TABLE B-14.IV

LISTING OF THE COBILD SUBCODE

```
C
      SUBROUTINE COBILD(T1,T2,DT,AM5,Y8,Y9,AA1,AB1,AC1,AD1,AE1,AF1,AG1,
     #                  AH1,AI1,BWTFRO,AWTFRO,NINB,W1,P,DROD)
C
C     THIS PROGRAM IS FOR **ONE-SIDE** OXIDATION.
C
C     THIS PROGRAM WAS ADAPTED FROM THE PROGRAM "BUILD5" WRITTEN BY
C     R. PAWEL AT OAK RIDGE NATIONAL LABORATORY (ORNL).
C
C     IT USES DATA AND ANALYSES FROM J.V. CATHCART OF ORNL TO GIVE
C     THE OXIDE AND OXYGEN-STABILIZED ALPHA ARRHENIUS RATE EQUATIONS
C     TO COMPUTE XI AND REMAINING BETA THICKNESSES FOR A TRANSIENT.
C
C     OXYGEN PROFILES ARE COMPUTED ON THE BASIS OF A
C     FINITE DIFFERENCE METHOD ASSUMING THE TRANSIENT TO BE COMPOSED
C     OF A SERIES OF ISOTHERMAL SEGMENTS.
C
      DIMENSION AA(6),AB(6),AC(6),AD(6),AE(6),AF(6),AG(6),AH(6),AI(6)
C
C     T1      = TEMP AT BEGINNING OF TIME STEP (K)
C     T2      = TEMP AT END OF TIME STEP (K)
C     DT      = DURATION OF TIME STEP (SEC)
C     AM5     = ORIGINAL  SPECIMEN WALL THICKNESS (M)
C     Y8      = OXIDE THICKNESS AT BEGINNING OF TIME STEP (M)
C     Y9      = OXYGEN STABILIZED ALPHA THICKNESS AT BEGINNING OF TIME
C               STEP (M)
C     AA1-AI1 = OXYGEN CONCENTRATIONS IN PRIOR BETA AT EQUIDISTANT NODES
C               AA1 IS THE CONCENTRATION AT THE BETA - ALPHA+BETA
C               INTERFACE AND AI1 IS THE CONCENTRATION AT THE INNER
C               SURFACE OF THE CLADDING (WEIGHT FRACTION OF OXYGEN)
C     BWTFRO  = AVERAGE OXYGEN CONCENTRATION IN BETA (WT. FRACTION)
C     AWTFRO  = AVERAGE OXYGEN CONCENTRATION IN ALPHA (WT. FRACTION)
C     NINB    = NUMBER OF NODES IN BETA
C     W1      = TOTAL OXYGEN UPTAKE (KG/M**2)
C     P       = POWER GENERATED BY ZR-H2O REACTION IN TIME STEP (W/M)
C     DROD    = DIAMETER OF AS-RECEIVED ROD (M).
C
C     COBILD WAS CODED BY G.A. REYMANN IN JULY 1977.
C     LAST UPDATED BY G.A. REYMANN IN JUNE 1978.
C
      AM5    = 100.*AM5
      Y8     = 100.*Y8
      Y9     = 100.*Y9
      AA(1)  = 100.*AA1
      AB(1)  = 100.*AB1
      AC(1)  = 100.*AC1
      AD(1)  = 100.*AD1
      AE(1)  = 100.*AE1
      AF(1)  = 100.*AF1
      AG(1)  = 100.*AG1
      AH(1)  = 100.*AH1
      AI(1)  = 100.*AI1
      Y80    = W1/(0.26*5820.0)
      W1     = W1/10.
C
      AM2 = 1.0E10
C     AM2 = ARTIFICIALLY LARGE MODULUS.
C
      AL2 = AM5 - (2.0*Y8/3.0+Y9)
C     AL2 = BETA THICKNESS AT START OF EACH TIME STEP.
C
      AZ3 = DT/5.0
C     AZ3 IS THE TIME INCREMENT FOR THE XI INTEGRATION.
C
      AR  = (T2-T1)/DT
C
      Y5  = AZ3
  550 AZ8 = T1 + AR*Y5 - AZ3*AR/2
C     AZ8 = AV. TEMP DURING INCREMENT
C
      Y6 = 2.0*(1.12569E-02)*EXP(-3.58908E04/(1.987*AZ8))
      Y7 = 2.00*0.761490*EXP(-4.81418E04/(1.987*AZ8))
C
      Y8 =  SQRT(Y8**2 + Y6*AZ3)
C     Y8 = OXIDE LAYER THICKNESS AFTER INCREMENT.
```

TABLE B-14.IV (continued)

```
C
      Y9 = SQRT(Y9**2 + Y7*AZ3)
C     Y9 = ALPHA LAYER THICKNESS AFTER INCREMENT
      IF(Y9 .LT. 1.0E-09) Y9 = 1.0E-09
C
      W2 = 2.0*0.16800*EXP(-39870.0/(1.987*AZ8))
C
      W1 = SQRT(W1**2 + W2*AZ3)
C     W1 = TOTAL OXY. CONC. AFTER INCREMENT
      W11 = Y8*(5.82)*0.26
C     W11 IS THE MINIMUM OXYGEN IN (GM/CM**2) NECESSARY TO FORM THE
C         OXIDE LAYER.
      IF((W1-W11).LE. 0.0) W1 = W11
C
      Y5 = Y5 + AZ3
      IF(Y5 .LE. DT) GO TO 550
C
      AZ8 = (T1+T2)/2.0
C     AZ8 = THE TEMPERATURE DURING THE INTERVAL, (K).
C
      AS1 = 0.12
C     AS1 = C(S), THE SATURATION CONCENTRATION, (WT. %)
C
      IF(AZ8 .LT. 1239.0)  GO TO 2106
      AS1 = -0.0042807 +  SQRT((AZ8/392.46)- 3.1417)
      IF(AZ8 .LT. 1373.) GO TO 2106
      AS1 = (AZ8 - 1081.7)/491.157
 2106 CONTINUE
C
      AL5 =  (SQRT(9.E00/8.))*(2.480E-02)*EXP(-2.620E04/(1.987*AZ8))
C     AL5 = D(OX IN BETA), (CM**2/SEC), DICK PERKINS '76 DATA
C
      AL8 = AM5 - (2.0*Y8/3.0+Y9)
C     AL8 = BETA THICKNESS AT END OF EACH TIME STEP.
      AL4 = AL2 - AL8
C     AL4 = DELTA BETA DURING STEP
C
      AL7 = AL2/8.0
      IF(AL4 .GT. AL7) GO TO 2770
C
      AM3 = AL4/(2.0*AL2)
      AM4 = (AL4**2)/(2.0*(AL2**2))
      AL6 = AL8/8.0
C     AL6 = H(X), THE DISTANCE INCREMENT FOR FD NETWORK.
C
      AM1 = (AL6**2)/(AL5*AZ3)
      IF(AM1 .LT. 2.0) GO TO 2785
      IF(AM2 .LT. AM1) GO TO 2256
      AM2 = AM1
C     STORES SMALLEST MODULUS FOR STABILITY CRITERION CHECK.
C
 2256 CONTINUE
C
C     IN STEPS 2260 TO 2320 THE INITIAL OXYGEN CONCENTRATIONS ARE
C     CALCULATED BY PARABOLIC INTERPOLATION. THIS IS NECESSARY DUE TO
C     THE DECREASE IN BETA THICKNESS AS THE EXTERNAL LAYERS GROW.
C
      AA(1) = AS1
C
     #AB(1) = AB(1) + 7.*AM3*(4.*AC(1)-3.*AB(1)-AD(1)) +
     #         49.0*AM4*(AD(1)+AB(1)-2.*AC(1))
C
     #AC(1) = AC(1) + 6.*AM3*(4.*AD(1)-3.*AC(1)-AE(1)) +
     #         36.0*AM4*(AE(1)+AC(1)-2.*AD(1))
C
     #AD(1) = AD(1) + 5.*AM3*(4.*AE(1)-3.*AD(1)-AF(1)) +
     #         25.0*AM4*(AF(1)+AD(1)-2.*AE(1))
C
     #AE(1) = AE(1) + 4.*AM3*(4.*AF(1)-3.*AE(1)-AG(1)) +
     #         16.0*AM4*(AG(1)+AE(1)-2.*AF(1))
C
     #AF(1) = AF(1) + 3.*AM3*(4.*AG(1)-3.*AF(1)-AH(1)) +
     #          9.0*AM4*(AH(1)+AF(1)-2.*AG(1))
C
     #AG(1) = AG(1) + 2.*AM3*(4.*AH(1)-3.*AG(1)-AI(1)) +
     #          4.0*AM4*(AI(1)+AG(1)-2.*AH(1))
```

TABLE B-14.IV (continued)

```
C
      AH(1) = AH(1) + 1.*AM3*(4.*AI(1)-3.*AH(1)-AH(1)) +
     #          1.0*AM4*(AH(1)+AH(1)-2.*AI(1))
C
      DO 2535 J = 2,6
C
      AA(J) = AS1
      AB(J) = (AA(J-1) + (AM1-2.)*AB(J-1) + AC(J-1))/(AM1)
      AC(J) = (AB(J-1) + (AM1-2.)*AC(J-1) + AD(J-1))/(AM1)
      AD(J) = (AC(J-1) + (AM1-2.)*AD(J-1) + AE(J-1))/(AM1)
      AE(J) = (AD(J-1) + (AM1-2.)*AE(J-1) + AF(J-1))/(AM1)
      AF(J) = (AE(J-1) + (AM1-2.)*AF(J-1) + AG(J-1))/(AM1)
      AG(J) = (AF(J-1) + (AM1-2.)*AG(J-1) + AH(J-1))/(AM1)
      AH(J) = (AG(J-1) + (AM1-2.)*AH(J-1) + AI(J-1))/(AM1)
      AI(J) = ((AM1-2.)*AI(J-1)+2.*AH(J-1))/AM1
C
 2535 CONTINUE
      AO2 = (6.49*AL6)/300.0
      AO2 = AO2*(AA(6) + AI(6) + 2.*(AC(6) + AE(6) + AG(6))
     #          +4.*(AB(6) + AD(6) + AF(6) + AH(6)))
C     AO2 IS THE OXYGEN IN THE BETA,GM/CM**2,(BY SIMPSON'S RULE).
C
      AA1 = AA(6)/100.
      AB1 = AB(6)/100.
      AC1 = AC(6)/100.
      AD1 = AD(6)/100.
      AE1 = AE(6)/100.
      AF1 = AF(6)/100.
      AG1 = AG(6)/100.
      AH1 = AH(6)/100.
      AI1 = AI(6)/100.
C     REASSIGNS CONC'S AT END OF THIS TIME INT TO START VALUES FOR NEXT
C
      Y88 = 10.0*W1/(0.26*5820.0)
C     Y88 = EFFECTIVE OXIDE THICKNESS IN METERS USED TO CALCULATE POWER
C           GENERATED BY ZR-H2O REACTION. THIS ASSUMES THAT ALL THE
C           OXYGEN UPTAKE MAKES ZRO2, THUS COMPENSATING FOR NEGLECTING
C           THE HEAT OF SOLUTION OF OXYGEN.
      P = ((6490.)*(6.45E06)*(2.10)*DRCO*(Y88-Y880))/DT
C
      BWTFRO = ((AO2)/(6.49*AL8)) - .0012
      IF(BWTFRO .LT. 0.0) BWTFRO = 0.0
C
      AWTFRO = (W1 - (AO2-.0012*6.49*AL8) - (5.82*.26*Y8))/(6.49*Y9)
      IF(AWTFRO .LT. 0.0) AWTFRO = 0.0
C
C     CONVERSION TO SI UNITS:
      W1  = 10.*W1
      Y8  = Y8/100.
      Y9  = Y9/100.
      AL8 = AL8/100.
      AM5 = AM5/100.
C
      GO TO 3100
 2770 CONTINUE
      WRITE(6,2771) DT
 2771 FORMAT(//20X,*DELTA BETA IS TOO LARGE FOR*,E15.5,*SEC INCREMENTS
     # - SORRY*)
      GO TO 3100
C
 2785 WRITE(6,5020)
 5020 FORMAT(//2CX,*DIFFUSION IS OCCURRING TOO RAPIDLY FOR THIS ROUTINE
     # TO ACCURATELY CALCULATE OXYGEN CONCENTRATIONS - SORRY*)
C
 3100 CONTINUE
      RETURN
      END
```

B-14.15. K. Videm, "Properties of Zirconium Base Cladding Materials Corrosion and Hydrogen Pickup," *Advanced Course on Limiting Aspects of Fuel Element Performance in Water Cooled Power Reactors at the Institute for Antomenergi in Kjeller, Norway, August 24 – 28, 1970.*

B-14.16. F. H. Megerth, C. P. Ruiz, U. E. Wolff, *Zircaloy-Clad UO_2 Fuel Rod Evaluation Program,* GEAP-10371 (June 1971).

B-14.17. H. E. Williamson et al, *AEC Fuel Cycle Program Examination of UO_2 Fuel Rods Operated in the VBWR to 10,000 MWD/TU,* GEAP-4597 (1965).

B-14.18. E. Hillner, "Corrosion and Hydriding Performance in Zircaloy Tubing after Extended Exposure in the Shippingport PWR," *Zirconium in Nuclear Applications,* ASTM-STP-551 (1974) pp 449-462.

B-14.19. W. R. Smalley, *Saxton Core II Fuel Performance Evaluation, Part I: Materials,* WCAP-3385-56 (1971).

B-14.20. W. R. Smalley, *Saxton Core III Fuel Materials Performance,* WCAP-3385-57 (1974).

B-14.21. J. V. Cathcart, *Quarterly Progress Report on the Zirconium Metal-Water Oxidation Kinetics Program Sponsored by the NRC Division of Reactor Safety Research for July – September 1975,* ORNL-5148 (December 1975).

B-14.22. J. V. Cathcart, *Quarterly Progress Report on the Zirconium Metal-Water Oxidation Kinetics Program Sponsored by the NRC Division of Reactor Safety Research for October – December 1975,* ORNL/TM-5248 (March 1976).

B-14.23. J. V. Cathcart, *Quarterly Progress Report on the Zirconium Metal-Water Oxidation Kinetics Progam Sponsored by the NRC Division of Reactor Safety Research for January – March 1976,* ORNL/NUREG/TM-17, NRC-3 (May 1976).

B-14.24. J. V. Cathcart, *Quarterly Progress Report on the Zirconium Metal-Water Oxidation Kinetics Program Sponsored by the NRC Division of Reactor Safety Research for October – December 1976,* ORNL/NUREG/TM-87 (February 1977).

B-14.25. R. R. Biederman and W. G. Dobson, "A Study of Zircaloy – Steam Oxidation Reaction Kinetics," *Fourth Interim Progress Report,* Worchester Polytechnic Institute (October 1, 1975 – January 15, 1976).

B-14.26. R. G. Ballinger, W. G. Dobson, R. R. Biederman, "Oxidation Reaction Kinetics of Zircaloy-4 in an Unlimited Steam Environment," *Journal of Nuclear Materials, 62* (November 1976) pp 213-220.

B-14.27. V. F. Urbanic, "Method for Estimating the Exposure Time and Temperature for Zircaloy Oxidation in Steam," *Journal of Nuclear Materials, 59* (1976) pp 90-94.

B-14.28. G. Schanz and S. Leistikow, "Anwnedung und Experimentelle Überprüfung des Codes SIMTRAN-1 zur Beschreibung der Zircaloy/Wasserdampf-HT-Oxidation," *Atomwirtschaft* (August 1976) pp 409-410.

B-14.29. S. Leistikow et al, "Untersuchen zur Hochtemperatur-Wasserdampf-Oxidation von Zircaloy-4 Hüllrohren," *PBS Halbjahresbericht 1976/2*, KFK 2435 (Feburary 1977).

B-14.30. S. Kawasaki et al, *Reaction of Zircaloy Cladding with Steam Under Simulated Loss-of-Coolant Accident Conditions*, JAERI-M-6181 (July 1975).

B-14.31. D. L. Douglass, "Oxide Plasticity in the Oxidation Mechanism of Zirconium and its Alloys," *Corrosion Science, 5* (1965).

B-14.32. R. A. Perkins, *Zirconium Metal-Water Oxidation Kinetics II. Oxygen-18 Diffusion in β-Zircaloy*, ORNL/NUREG/TM-19 (1976) p 33.

B-14.33. S. Malang, *SIMTRAN I – A Computer Code for the Simultaneous Calculation of Oxygen Distributions and Temperature Profiles in Zircaloy During Exposure to High Temperature Oxidizing Environments*, ORNL-5083 (November 1975).

B-14.34. L. Baker and L. C. Just, *Studies of Metal-Water Reactions at High Temperatures – III. Experimental and Theoretical Studies of the Zirconium-Water Reaction*, ANL-6548, (May 1962).

B-14.35. J. V. Cathcart, *Quarterly Progress Report on the Zirconium Metal-Water Oxidation Kinetics Program Sponsored by the NRC Division of Reactor Safety Research for July – September 1976*, ORNL/NUREG/TM-62 (December 1976).

B-14.36. S. L. Seiffert and T. F. Cook, *Power-Cooling-Mismatch Test Series Test PCM-4 Postirradiation Examination*, NUREG/CR-02381 TREE-1230 (July 1978).

14.6 Bibliography

The following references also contain information pertinent to high temperature zircaloy oxidation and have been cited in previous versions of MATPRO but not in this latest update. They are included for completeness.

(1) A. W. Lemmon, *Studies Relating to the Reaction Between Zirconium and Water at High Temperatures*, BMI-1154 (1957).

(2) D. H. Bradhurst and P. M. Heuer, "The Influence of Oxide Stress on the Breakaway Oxidation of Zircaloy-2," *Journal of Nuclear Materials, 37* (1970) pp 35-47.

(3) D. O. Hobson and P. L. Rittenhouse, *Embrittlement of Zircaloy-Clad Fuel Rods by Steam During LOCA Transients*, ORNL-4758 (January 1972).

(4) R. E. Pawel, "Oxygen Diffusion in Beta Zircaloy During Steam Oxidation," *Journal of Nuclear Materials, 50* (1974) pp 247-258.

(5) R. R. Biederman and W. G. Dobson, "A Study of Zircaloy-Steam Oxidation Reaction Kinetics," *Fifth Interim Progress Report,* Worchester Polytechnic Institute (January 16, – April 15, 1976).

(6) T. G. Odekirk, *Detailed Test Plan Report for PBF Test Series PCM-20: The Behavior of Unirradiated PWR Fuel Rods Under Power-Cooling-Mismatch Conditions,* ANCR-1095 (April 1974).

(7) A. W. Urquhart and D. A. Vermilyea, "Characterization of Zircaloy Oxidation Films," *Zirconium in Nuclear Applications,* ASTM-STP-551 (1974) pp 463-478.

(8) R. E. Pawel, *Zirconium Metal-Water Oxidation Kinetics III. Oxygen Diffusion in Oxide and Alpha Zircaloy Phases,* ORNL/NUREG-5 (October 1976).

15. CLADDING HYDROGEN UPTAKE (CHUPTK)

(D. L. Hagrman)

This subroutine calculates the average weight fraction of hydrogen in zircaloy cladding during typical reactor operation at temperatures of 523 to 650 K. Required inputs are: as-received hydrogen concentration in the cladding, initial fuel water content, fuel pellet diameter, type of cladding (zircaloy-2 or zircaloy-4), cladding inside and outside diameters, type of reactor (BWR or PWR), oxide thickness at the start and end of the current time step, temperature at the oxide-coolant interface, heat flux, zirconium oxide thermal conductivity, and the average weight fraction of hydrogen in the cladding at the start of the current time step.

15.1 Summary

The average weight fraction of hydrogen in zircaloy cladding during steady state conditions is

$$H = H_o + H_1 + H_c \qquad \text{(B-15.1)}$$

where

H = net weight fraction of hydrogen in the cladding (ppm).

H_o = initial concentration of hydrogen in the cladding due to impurities introduced during manufacturing and autoclaving (ppm). Typical values are 8 to 30 ppm[B-15.1, B-15.2]

H_1 = concentration of hydrogen in the cladding due to internal outgassing of water absorbed by the fuel (ppm).

H_c = concentration of hydrogen in the cladding due to absorption of hydrogen from the coolant (ppm).

H_o is an input parameter. H_1 is calculated by the routine using the input values for parts per million water vapor in the fuel, the input cladding dimensions, and the input fuel pellet diameter. CHUPTK assumes that all the hydrogen from the water vapor in the fuel is picked up by the cladding.

The primary consideration in determining H is the determination of H_c. Analytical expressions for H_c are divided into three parts; Equation (B-15.2a) for oxide films thinner than the transition thickness[a], Equation (B-15.2b) for oxide films equal to the transition thickness at some point in the current time step, and Equation (B-15.2c) for oxide films greater than the transition thickness during the current time step. In these equations, the variable H_c has been converted from a fraction of the oxide's oxygen increase to units of average parts per million by weight in the cladding.

$$H_{cf} = \left[\frac{(9 \times 10^5)d_o}{d_o^2 - d_i^2}\right]\left[\frac{B}{8A}\right][X_f - X_i] + H_{ci} \qquad \text{(B-15.2a)}$$

$$H_{cf} = \left[\frac{(9 \times 10^5)d_o}{d_o^2 - d_i^2}\right]\left[\left(\frac{B}{8A}\right)(X_{TRAN} - X_i) + \left(\frac{C}{8A}\right)(X_F - X_{TRAN})\right] + H_{ci} \qquad \text{(B-15.2b)}$$

$$H_{cf} = \left[\frac{(9 \times 10^5)d_o}{d_o^2 - d_i^2}\right]\left[\frac{C}{8A}\right][X_f - X_i] + H_{ci} \qquad \text{(B-15.2c)}$$

where

H_{cf} = weight fraction of hydrogen added to the cladding from the coolant at the end of the current time step (ppm by weight).

H_{ci} = weight fraction of hydrogen added to the cladding from the coolant at the start of the current time step (ppm by weight).

---

[a] Oxide film growth is discussed in conjunction with the description of the cladding oxidation subcode, CORROS. The terms pre- and posttransition refer to two different stages in the growth of the oxide film. A transition between the two stages occurs when the oxide film has added approximately 30 mg of oxide per dm^2 of oxide surface.

d_o = cladding outside diameter (m).

d_i = cladding inside diameter (m).

B = fraction of hydrogen liberated by the reaction with the coolant which is absorbed by the cladding during pretransition oxidation. The value of B is a function of the input parameters ICOR (BWR or PWR chemistry) and ICM (zircaloy-2 or zircaloy-4). Values of B for zircaloy-2 are 0.48 in a PWR environment and 0.29 in a BWR environment. For zircaloy-4, B = 0.12.

C = fraction of hydrogen liberated by the reaction with the coolant which is absorbed by the cladding during posttransition oxidation. The value of C is a function of the input parameter ICM (zircaloy-2 or zircaloy-4). The value of C for zircaloy-2 is 1.0. For zircaloy-4, C = 0.12.

A = a parameter describing the enhancement of the oxidation rate of the cladding in the reactor environment. The parameter is discussed in conjunction with the description of the cladding oxidation subcode, CORROS. The value for A is determined in the subcode by user specification of BWR and PWR chemistry with the input parameter ICOR.

X_i = oxide layer thickness at the start of the current time step (m).

X_f = oxide layer thickness at the end of the current time step (m).

X_{TRAN} = oxide layer thickness at the transition point (m). Typically 2×10^{-6} meters. The value of X_{TRAN} is calculated by the CHUPTK subcode using the expression developed for CORROS (Section B-14, this appendix) and the input information.

The approach and general physical picture used to model hydrogen uptake are summarized in Section B-15.2. Section B-15.3 develops the basic out-of-pile model, and Section B-15.4 generalizes the basic model so that it describes in-pile hydrogen uptake.

15.2 Background and Approach

It is generally agreed[B-15.3, B-15.4] that oxidation of zirconium alloys by water in the temperature range from 523 to 673 K proceeds by the migration of oxygen vacancies in the oxide layer. Charge and physical size considerations imply that the mechanism of introduction of hydrogen into the zirconium metal through an oxide film is by entry of neutral hydrogen atoms into oxygen vacancies in the lattice (H_2 is too large and H^+ is too positive). The constant ratio of absorbed hydrogen to oxygen taken up by the cladding (the "pickup fraction") is explained as having been determined by the competition between possible subsequent reactions of the atomic hydrogen created by corrosion (the atomic hydrogen can combine to form a gas or enter a surface vacancy in the oxide lattice).

In this approach, the close relationship between the hydrogen weight gain and the oxygen weight gain from the coolant is viewed as a consequence of the fact that the oxygen and hydrogen usually come from a common source (the water molecule) and are transported to the metal by a common carrier (oxygen vacancies). The hydrogen pickup fraction is determined by the composition of the coolant-oxide surface. In particular, it is suspected that nickel oxide from the nickel in zircaloy-2 absorbs atomic hydrogen at the surface of the oxide and thereby enhances the fractional hydrogen uptake for zircaloy-2.

15.3 Out-of-Pile Basis for the Model

The in-pile model is based primarily on out-of-pile data because well characterized data on hydrogen uptake as a function of time and temperature have been published only for out-of-pile corrosion. At least two plausible suggestions for a hydrogen uptake model can be presented from the approach discussed in Section B-15.2. According to both of these suggestions, the dependent variable is the ratio of the corrosion-liberated hydrogen to oxygen which is absorbed by the metal, although the independent variables differ. A brief summary of the two models, and a third less probable model follows.

15.3.1 Simple Probabilistic Hydrogen Pickup Model. In this model, the fraction of released hydrogen absorbed by the oxide surface is assumed to be proportional to the rate of appearance of oxide vacancies at the oxide-coolant interface. In the discussion of the cladding oxidation model, CORROS, it is shown that the vacancies appear at a rate proportional to the inverse of the square of the oxygen weight gain during the pretransition phase of oxidation. During the posttransition phase of oxidation, the surface averaged rate of appearance of oxide vacancies is constant and proportional to three times the inverse of the square of the weight of the oxide layer at transition. This model ignores any details of the surface chemistry involved in the absorption of atomic hydrogen by the oxide vacancies.

15.3.2 Surface-Controlled Hydrogen Pickup Model. In this model, the fraction of released hydrogen absorbed by the oxide surface is a constant determined by the metallurgy of the oxide surface. The picture assumes that the effect of absorption of atomic hydrogen is dominant in the capture of hydrogen by the oxide film's outer surface.

15.3.3 Diffusion-Controlled Hydrogen Pickup Model. It is also conceivable that the time rate of hydrogen input into the metal is controlled by some as yet unconsidered independent diffusion process. In the case of diffusion-controlled hydrogen uptake, the net time rate of hydrogen pickup is proportional to the inverse thickness of the oxide layer.

The rate equations implied by the three alternate pictures are summarized in Table B-15.I. Pretransition expressions were formulated simply by writing down the mathematical equivalent of the descriptions above. Posttransition expressions for the hydrogen pickup fraction were derived by replacing powers of X (proportional to the oxide thickness) in the pretransition expressions with powers of X averaged over a rate-determining oxide thickness

TABLE B-15.I

RATE EQUATIONS FOR HYDROGEN UPTAKE

	Pretransition Rates	Posttransition
(1) Simple Probabilisitic Pickup Fraction Determination	$\frac{dH}{dX} = \frac{G}{X^2}$	$\frac{dH}{dX} = G/\overline{X^2} = \frac{3G}{X_{TRAN}^2}$
(2) Surface-Controlled Pickup Fraction Determination	$\frac{dH}{dX} = P$	$\frac{dH}{dX} = P$
(3) Diffusion-Controlled Time Rate	$\frac{dH}{dX} = \left(\frac{Q}{X}\right)$	$\frac{dH}{dX} = Q/\overline{X} = \frac{2Q}{X_{TRAN}}$

where

H = hydrogen weight gain (mg/dm^2)

X = oxygen weight gain (mg/dm^2, corresponds to oxide thickness)

t = time at temperature

X_{TRAN} = the transition weight of the oxide layer (mg/dm^2)

$\overline{X^2}$ = the average of X^2 with values of X distributed at random between 0 and the transition thickness, X_{TRAN} (mg/dm^2)

$\overline{X}$ = the space average of X with values of X distributed at random between 0 and the transition thickness (mg/dm^2)

G, P, Q = constants

that randomly varies from zero to the transition thickness of the oxide film. A discussion of the posttransition oxide film and this approach to describing posttransition rates is included in the description of the cladding oxidation subcode CORROS in Section B-14.

When the three very different expressions for hydrogen uptake obtained with these models were integrated and compared with the pretransition data of Tables 7 and 9 of Reference B-15.3, the pretransition data for zircaloy-2 and zircaloy-4 were found to conform best to the assumption that the rate is surface-controlled. The surface-controlled model is therefore used.

Comparison of experimental pretransition and posttransition hydrogen pickup fractions[B-15.3] for zircaloy-2 show that the posttransition rate is about twice the pretransition rate. For zircaloy-4, the pre- and posttransition rates are similar. The reason for this difference between zircaloy-2 and -4 is not well understood but may be related to the presence of nickel which absorbs atomic hydrogen in zircaloy-2.

The simple surface-controlled hydrogen pickup model of Table B-15.I has therefore been modified slightly

for pretransition

$$\frac{dH}{dX} = \frac{B}{8} \qquad \text{(B-15.3a)}$$

for posttransition

$$\frac{dH}{dX} = \frac{C}{8} \qquad \text{(B-15.3b)}$$

where B and C are determined by the oxide surface metallurgy of the particular alloy and 8 accounts for the different weights of hydrogen and oxygen in water so that $\frac{dH}{dx} = \frac{1}{8}$ for complete "pickup."

15.4 Generalization to an In-pile Model

Prediction of in-pile corrosion is complicated because important variables (local temperature and reactor chemistry) are not always reported and because data on the time dependence of corrosion are limited. Enhancement of the hydrogen uptake factors by the reactor environment is treated by determining the value of the pickup fractions B and C for each reactor environment. Changes in the rate of hydrogen picked up caused by changes in the oxidation rate are described with the parameter A which is discussed in conjunction with the oxidation model, CORROS. Thus separate parameters are specified to describe the separate processes involved in determining the total rate of hydrogen uptake.

The basic equations for the fraction of hydrogen pickup with respect to the amount of oxygen pickup (dH/dX) are discussed at the end of Section B-15.3 [Equation (B-15.3a)

and (B-15.3b)]. Those equations reference out-of-pile oxidation. For in-pile pickup, the enhancement factor A must again be used. It is presumed that the effect which enhances the oxidation rate in the reactor does not enhance the rate of hydrogen uptake. Thus the enhancement of the oxidation rate by a factor A will decrease the fractional hydrogen uptake by a factor $\frac{1}{A}$.

The rate equations for in-pile oxidation and for fractional pickup of hydrogen are summarized in Equations (B-15.4a) and (B-15.4b) for both pre- and posttransition regimes

for the pretransition in-pile regime

$$\frac{dH}{dX} = \frac{B}{\delta A} \qquad \text{(B-15.4a)}$$

for the posttransition in-pile regime

$$\frac{dH}{dX} = \frac{C}{\delta A} \cdot \qquad \text{(B-15.4b)}$$

Integration of Equation (B-15.4a) and (B-15.4b) and conversion of the integrated forms from weight gains to oxide thickness and parts per million hydrogen by weight leads to Equations (B-15.2a) to (B-15.2c).

An out-of-pile value of the parameter B has been determined in Reference B-15.4 (from unpublished data) to be B = 0.33 for zircaloy-2. For zircaloy-4, a value of B = 0.12 was obtained from Figure 12 of Reference B-15.3. The result is consistent with a value of 10% recommended by Reference B-15.4.

When values of B were fit to the average hydrogen pickup values for the zircaloy-4 rods of the Saxton reactor[B-15.5, B-15.6], an average value of B = 0.104 ± 0.04 was obtained. Thus the out-of-pile determined value of B = 0.12 is apparently adequate for zircaloy-4 rods in PWRs. Since no data on zircaloy-4 cladding in a BWR are available, the PWR value, B = 0.12, is returned for the unlikely case of zircaloy-4 in a BWR. Values of B obtained by fitting the zircaloy-2 PWR hydrogen pickup reported in Reference B-15.2 were B = 0.48 ± 0.07 while a fit to the BWR hydrogen pickup data on the zircaloy-2 rods of Reference B-15.7 produced B = 0.29 ± 0.06. Since the PWR environment has an over-pressure of hydrogen and it is known that hydrogen overpressures enhance the out-of-pile pickup fraction[B-15.3], it is suggested that difference in PWR and BWR values for B with zircaloy-2 is an effect of the different environments.

15.5 Cladding Hydrogen Uptake Subcode CHUPTK Listing

A listing of the FORTRAN subcode CHUPTK is presented in Table B-15.II.

TABLE B-15.II

LISTING OF THE CHUPTK SUBCODE

```
C
C
      SUBROUTINE CHUPTK(CHORG ,PPMH2O,DP    ,ICM   ,DCO   ,DCI   ,
     #  ICOR  ,ZRO2AI,ZRO2BI,TCOI  ,QCI   ,ZOXKI ,CHYDAI,CHYDBI,
     #  CHCONC)
C
CCC   CHUPTK CALCULATES AVERAGE CONCENTRATION OF HYDROGEN IN ZIRCALOY
CCC   CLADDING
CCC
CCC   CHCONC = OUTPUT AVERAGE CONCENTRATION OF
CCC            HYDROGEN IN CLADDING AT END OF TIME STEP (PPM)
CCC   CHYDBI = OUTPUT HYDROGEN FROM COOLANT IN CLADDING AT END
CCC            OF TIME STEP (PPM)
CCC
CCC   CHORG  = INPUT INITIAL HYDROGEN IN CLADDING (PPM)
CCC   PPMH2O = INPUT INITIAL FUEL WATER CONTENT (PPM)
CCC   DP     = INPUT FUEL PELLET DIAMETER (M)
CCC   ICM    = INPUT CLADDING MATERIAL FLAG (ICM = 2 FOR ZIRCALOY 2,
CCC                                          ICM = 4 FOR ZIRCALOY 4)
CCC   DCO    = INPUT CLADDING OUTSIDE DIAMETER (M)
CCC   DCI    = INPUT CLADDING INSIDE DIAMETER (M)
CCC   ICOR   = INPUT REACTOR CHEMISTRY .GE. 2 FOR PWR, .LT. 2 FOR BWR
CCC   ZRO2AI = INPUT OXIDE THICKNESS AT START OF CURRENT TIME STEP (M)
CCC   ZRO2BI = INPUT OXIDE THICKNESS AT END OF CURRENT TIME STEP (M)
CCC   TCOI   = INPUT ZRO2-COOLANT INTERFACE TEMPERATURE (K)
CCC   QCI    = INPUT AXIAL INCREMENT HEAT FLUX (WATT/METER**2)
CCC   ZOXKI  = INPUT ZIRCALOY OXIDE THERMAL CONDUCTIVITY (W/(M-K))
CCC   CHYDAI = INPUT HYDROGEN FROM COOLANT IN CLADDING AT START
CCC            OF TIME STEP (PPM)
CCC
CCC   THE EQUATIONS USED IN THIS SUBROUTINE ARE BASED ON DATA FROM
CCC   (1) E. HILLNER, HYDROGEN ABSORPTION IN ZIRCALOY DURING ACQUEOUS
CCC   CORROSION, EFFECT OF ENVIORNMENT, WESTINGHOUSE REPORT WAPD-TM-411
CCC   (1964)
CCC   (2) A. VAN DER LINDE, CALCULATION OF THE SAFE LIFETIME EXPECTANCY
CCC   OF ZIRCONIUM ALLOY CANNING IN THE FUEL ELEMENTS OF THE NERO
CCC   REACTOR, REPORT RCN-41(1965)
CCC   (3) F. H. MEGERTH, C. P. RUIZ, U. E. WOLFF, ZIRCALOY-CLAD UO2
CCC   FUEL ROD EVALUATION PROGRAM FINAL REPORT, GENERAL ELECTRIC
CCC   REPORT GEAP 10371 (1971)
CCC   (4) W. R. SMALLEY, SAXTON CORE II FUEL PERFORMANCE EVALUATION
CCC   PART I MATERIALS, WESTINGHOUSE REPORT WCAP-3385-56 (1971)
CCC   (5) W. R. SMALLEY, EVALUATION OF SAXTON CORE III FUEL
CCC   MATERIALS PERFORMANCE, WESTINGHOUSE REPORT WCAP-3385-57 (1974)
CCC   (6) E. HILLNER, CORROSION AND HYDRIDING PERFORMANCE OF ZIRCALOY
CCC   TUBING AFTER EXTENDED EXPOSURE IN THE SHIPPINGPORT PWR,
C     SYMPOSIUM ON ZIRCONIUM IN NUCLEAR APPLICATIONS, ASTM STP 551
C     (1974)
C
CCC   THIS MODEL SHOULD NOT BE USED OUTSIDE THE THE TEMPERATURE RANGE
CCC   523.15 - 673.15 (250 - 400 C).
CCC
C     CHUPTK CODED BY D. L. HAGRMAN FEBRUARY 1977
C     MODIFIED BY D. L. HAGRMAN JUNE 1978
C
      IF(TCOI .LE. 366.5) GO TO 40
      IF(ZRO2AI .LE. 0.0) ZRO2AI = 1.0 E-10
      TCOIC = TCOI + QCI * ZRO2AI/ZOXKI
      WIRAN = 7.7490E-06 * EXP(-7.90E02/TCOIC)
      IF(ICOR.GE.2) GO TO 10
C
C     BWR ENVIRONMENT
      A = 4.840E05*  EXP(-1.945E-02* TCOI)
      IF(TCOI.LE.500.) A = 28.92887
      B = 0.12
      IF(ICM .LE. 2) B = 0.29
      GO TO 15
C
C     PWR ENVIRONMENT
   10 A = 1.203E02*  EXP(-7.118E-03* TCOI)
      IF(TCOI.LE.500.) A = 3.424614
      B = 0.12
      IF(ICM .LE. 2) B = 0.48
   15 IF(TCOI .GT. 673.) A = 1.0
      C = 1.0
      IF(ICM .LE. 2) C = 1.0/8
C
```

TABLE B-15.II (continued)

```
C     FIND HYDROGEN UPTAKE FROM COOLANT DURING CURRENT TIME STEP
C
      D = (9.0E+05)*DCO/(DCO**2-DCI**2)
      IF(ZRO2AI .GT. WTRAN) GO TO 30
      IF(ZRO2BI .GE. WTRAN) GO TO 25
C
C     ALL OXIDATION PRETRANSITION
      CHUPC = D * (B/(8 * A)) * (ZRO2BI - ZRO2AI)
      GO TO 50
C
C     PART OF OXIDATION PRETRANSITION
   25 CHUPC = D * ((B/(8 * A)) * (WTRAN  - ZRO2AI) +
     #        (C *   B/(8 * A)) * (ZRO2BI - WTRAN))
      GO TO 50
C
C     ALL OXIDATION POST - TRANSITION
   30 CHUPC = D * (C*B/(8 * A))*(ZRO2BI - ZRO2AI)
      GO TO 50
C
   40 CHUPC  = 0.0
C
C     SUM HYDROGEN FROM COOLANT
   50 CHYDBI = CHYDAI + CHUPC
C
C     SUM HYDROGEN FROM ALLOY, FUEL MOISTURE AND COOLANT
      CHCONC = CHCKG + 0.186 *PPMH2O*((DP**2)/(DCO**2 - DCI**2)) +
     #         CHYDBI
C
      RETURN
      END
```

15.6 References

B-15.1. F. H. Megerth, C. P. Ruiz, U. E. Wolff, *Zircaloy-Clad UO_2 Fuel Rod Evaluation Program,* GEAP-10371 (June 1971).

B-15.2. E. Hillner, "Corrosion and Hydriding Performance of Zircaloy Tubing after Extended Exposure in the Shippingport PWR," *Zirconium in Nuclear Applications,* ASTM-STP-551 (1974) pp 449-462.

B-15.3. E. Hillner, *Hydrogen Absorption in Zircaloy During Aqueous Corrosion, Effect of Environment,* WAPD-TM-411 (November 1964).

B-15.4. A. Van der Linde, *Calculation of the Safe Life Time Expectancy of Zirconium Alloy Canning in the Fuel-Elements of the Nero Reactor,* RCN-41 (July 1965).

B-15.5. W. R. Smalley, *Saxton Core II Fuel Performace Evaluation, Part I: Materials,* WCAP-3385-56 (July 1971).

B-15.6. W. R. Smalley, *Saxton Core III Fuel Materials Performance,* WCAP-3385-57 (July 1974).

B-15.7. H. E. Williamson et al, *AEC Fuel Cycle Program Examination of UO_2 Fuel Rods Operated in the VBWR to 10,000 MWD/TU,* GEAP-4597 (1965).

16. CLADDING MEYER HARDNESS (CMHARD)

(M. A. Morgan)

The routine CMHARD calculates Meyer hardness as a function of cladding temperature.

16.1 Summary

One of the parameters required for calculating fuel-to-cladding contact conductance is hardness. As the contact pressure between the two surfaces increases, the points of contact enlarge due to localized plastic deformation, and the solid-to-solid thermal conductance is improved. The Meyer hardness is used by Ross and Stoute[B-16.1] in their heat transfer correlation as an indication of the hardness of resistance to deformation of the softer (zircaloy) material.

The Meyer hardness number is a measure of indentation hardness and is defined in conjunction with Meyer's law, $L = ad^n$ where L is the load, d is the diameter of impression at the surface of a specimen in a static ball test, n is the Meyer work hardening coefficient, and a is a material constant. The Meyer hardness number (MH) is defined as $(4L/\pi d^2)$. Other hardness numbers are available (Brinell, Rockwell, etc.), and conversion from one to another is possible. However, the routine CMHARD was created to provide information required by the Ross and Stoute gap conductance model.

Meyer hardness numbers for temperatures from 298 to 877 K were taken from Peggs and Godin[B-16.2]. A regression analysis of the reciprocal of the Meyer hardness values versus the log of temperature was used to obtain the analytical expression used in CMHARD. The correlation used is given by Equation (B-16.1).

$$MH = \exp\left[2.6034 \times 10^{1} + T\left[-2.6394 \times 10^{-2} + T\left[4.3502 \times 10^{-5} + T\,(2.5621 \times 10^{-8})\right]\right]\right] \qquad \text{(B-16.1)}$$

where

MH = Meyer hardness (N/m^2)

T = temperature (K).

Figure B-16.1 illustrates the correlation and its data base. The Meyer hardness decreases rapidly with increasing temperature, beginning at 2×10^9 MPa at room temperature and decreasing to 2×10^8 MPa at 875 K. The hardness is presumed to continue its rapid rate of decrease at temperatures above 875 K.

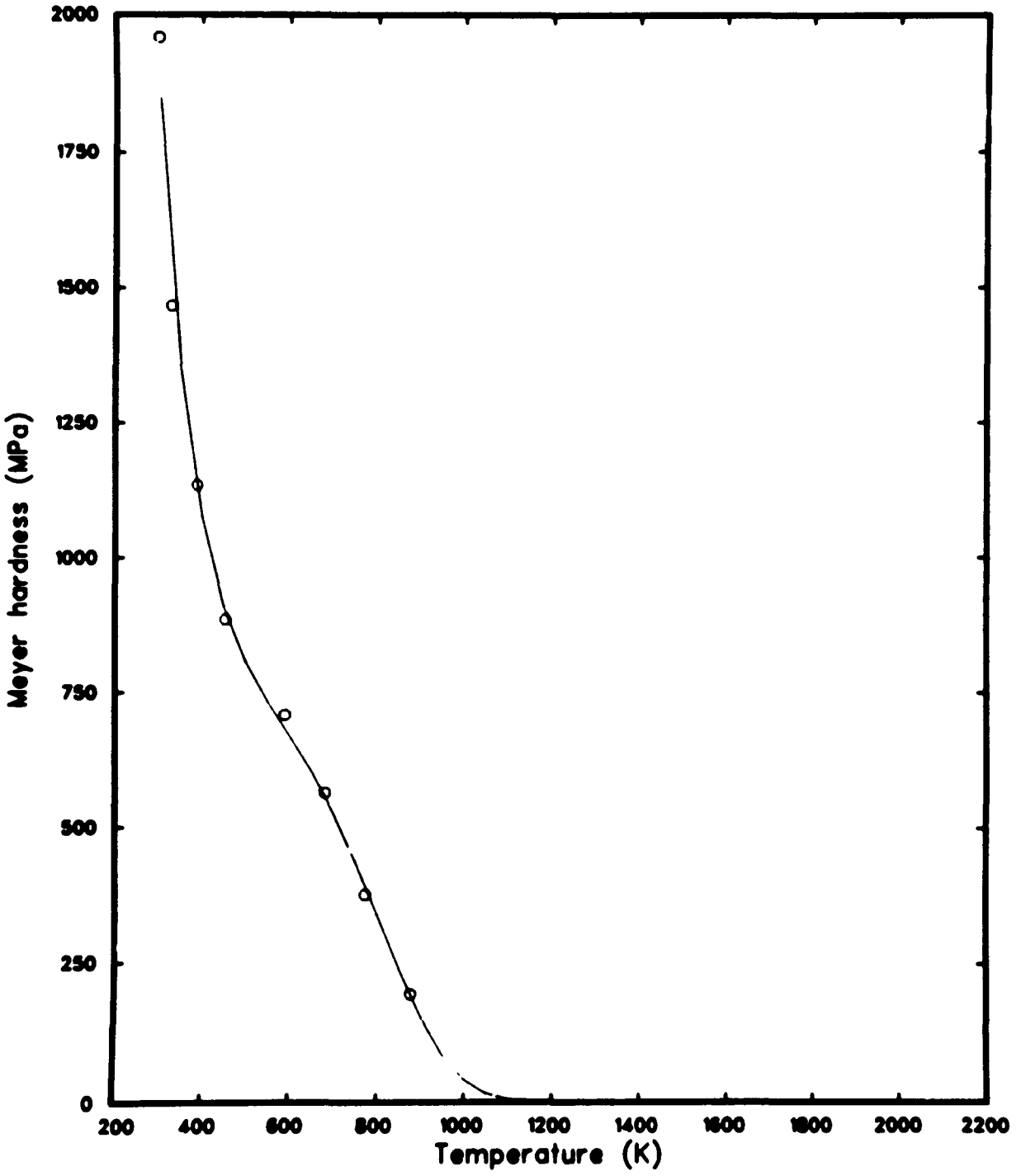

Fig. B-16.1 Values of the CMHARD correlation and its data base.

16.2 Cladding Meyer Hardness Subcode CMHARD Listing

A listing of the FORTRAN subcode CMHARD is presented in Table B-16.I.

TABLE B-16.I

LISTING OF THE CMHARD SUBCODE

```
      C
      C     FUNCTION CMHARD(CTEMP)
      C
      C     THE ROUTINE CMHARD CALCULATES MEYER HARDNESS AS A FUNCTION OF
      C     CLADDING TEMPERATURE.
      C
      C     CMHARD = OUTPUT MEYER HARDNESS OF ZIRCALOY CLADDING (N/M**2)
      C
      C     CTEMP = INPUT CLADDING TEMPERATURE (K)
      C
      C     THE EQUATIONS USED IN THIS FUNCTION ARE BASED ON DATA FROM
      C     (1) A. M. ROSS AND R. L. STOUTE, HEAT TRANSFER COEFFICIENT
      C         BETWEEN UO2 AND ZIRCALOY - 2, AECL - 1552 (JUNE 1962)
      C     (2) I. D. PEGGS AND D. P. GODIN, THE YIELD STRENGTH - HOT
      C         HARDNESS RELATIONSHIP OF ZIRCALOY - 4, JOURNAL OF NUCLEAR
      C         MATERIALS 57 PP 246 - 248 (1975)
      C
      C     CMHARD WAS CODED BY V.F.BASTON IN MAY 1974.
      C     MODIFIED BY M. A. MORGAN JUNE 1978
      C
            T = CTEMP
            CMHARD = EXP(2.6034E 01 - 2.6394E-02 * T + 4.3502E-05 * T**2 -
           #           2.5621E-08 * T**3)
            RETURN
            END
```

16.3 References

B-16.1. A. M. Ross and R. L. Stoute, *Heat Transfer Coefficient Between UO_2 and Zircaloy-2*, AECL-1552 (June 1962).

B-16.2. I. D. Peggs and D. P. Godin, "The Yield Strength – Hot Hardness Relationship of Zircaloy-4," *Journal of Nuclear Materials, 57* (1975) pp 246-248.

APPENDIX C

GAS MATERIAL PROPERTIES

APPENDIX C

GAS MATERIAL PROPERTIES

Two properties of the internal gas of light water reactor fuel rods have been included in MATPRO – Version 11. The thermal conductivity of seven gases (and their mixture in any combination) is modeled, as is gas viscosity. Gas viscosity and thermal conductivity are modeled as functions of temperature and composition.

1. GAS THERMAL CONDUCTIVITY (GTHCON)

(P. E. MacDonald)

The cladding-fuel gap conductance is, in part, dependent on the thermal conductivity of the gap gas mixture. Thermal conductivity relations for seven gases have been taken from the literature as has a scheme for calculating the conductivity of mixtures of those gases. The thermal conductivities of the light gases, hydrogen and helium, have been adjusted to allow for imperfect energy transfer between solids and gas in the Knudsen flow regime.

1.1 Conductivity of Gases and Gas Mixtures

The relationship for calculating the thermal conductivity of a monatomic gas mixture is based on the work of Brokaw[C-1.1]:

$$k_{mix} = \sum_{i=1}^{n} \left(\frac{k_i}{1 + \sum_{\substack{j=i \\ j \neq i}}^{n} \psi_{ij} \frac{x_j}{x_i}} \right) \tag{C-1.1}$$

where

$$\psi_{ij} = \phi_{ij} \left[1 + 2.41 \frac{(M_i - M_j)(M_i - 0.142\, M_j)}{(M_i + M_j)^2} \right] \tag{C-1.2}$$

and

$$\phi_{ij} = \frac{\left[1 + \left(\frac{k_i}{k_j}\right)^{1/2} \left(\frac{M_i}{M_j}\right)^{1/4}\right]^2}{2^{3/2} \left(1 + \frac{M_i}{M_j}\right)^{1/2}} \qquad \text{(C-1.3)}$$

and

n = number of components in mixture

M_i = molecular weight of the chemical species i

x_i = mole fraction of the chemical species i

k_i = thermal conductivity of the chemical species i.

The thermal conductivity equations of the individual rare gases are based on the correlative work of Gandhi and Saxena[C-1.2]. The resulting expressions are[C-1.3]

$$k_{helium} = 3.366 \times 10^{-3} T^{0.668} \qquad \text{(C-1.4)}$$

$$k_{argon} = 3.421 \times 10^{-4} T^{0.701} \qquad \text{(C-1.5)}$$

$$k_{xenon} = 4.0288 \times 10^{-5} T^{0.872} \qquad \text{(C-1.6)}$$

$$k_{krypton} = 4.726 \times 10^{-5} T^{0.923} \qquad \text{(C-1.7)}$$

where

k = thermal conductivity (W/m·K)

T = gas temperature (K).

In addition, the following conductivity equations for nitrogen, hydrogen, and steam[C-1.3,C-1.4] are used:

$$k_{N_2} = 2.091 \times 10^{-4} T^{0.846} \qquad \text{(C-1.8)}$$

$$k_{H_2} = 1.6355 \times 10^{-3} T^{0.8213} \qquad \text{(C-1.9)}$$

$$k_{steam} = (-2.8516 \times 10^{-8} + 9.424 \times 10^{-10} T - 6.004 \times 10^{-14} T^2) \frac{P}{T} + \frac{1.009\ P^2}{T^2\ (T-273)^{4.2}} - 8.4083 \times 10^{-3} - 1.19998 \times 10^{-5}\ T - 6.706 \times 10^{-8}\ T^2 - 4.51 \times 10^{-11}\ T^3 \qquad \text{(C-1.10)}$$

where

P = gas pressure (N/m^2).

The thermal conductivity of monatomic gases has been measured by a large number of workers. Gandhi and Saxena, through the facilities of the Thermophysical Properties Research Center of Purdue University, developed a consistent, correlated set of thermal conductivity data for each rare gas through careful evaluation of experimental techniques, review of viscosity data and kinetic theory, and intercomparison of various data. The data on which the Gandhi and Saxena analysis were based are: helium (References C-1.5 – C-1.22), argon (References C-1.5, C-1.9 – C-1.12, C-1.17 – C-1.21, C-1.23 – C-1.34), krypton (References C-1.9, C-1.14, C-1.17 – C-1.19, C-1.25 – C-1.28, C-1.30, and C-1.35), and xenon (References C-1.9, C-1.10, C-1.13, C-1.14, C-1.17 – C-1.19, C-1.27, C-1.35, and C-1.36).

The equations based on the correlative work of Gandhi and Saxena have also been compared with the results of the review of experimental and theoretical rare gas conductivities published by Andrew and Calvert[C-1.37]. Little difference was noted.

Figure C-1.1 compares the conductivities of the xenon-helium mixture at 520°C (as a function of mole fraction) calculated by GTHCON with those measured and calculated by other investigators (References C-1.1, C-1.38 – C-1.42 as summarized in Reference C-1.37). The GTHCON values compare well with other published theoretical and experimental values.

1.2 Conductivities in the Knudsen Domain

The thermal conductivity of the gas mixture plays an important role in determining so-called "contact" gap conductance as well as "open" gap conductance in a fuel rod. When the mean free path of the gas molecules is greater than 0.01 times the characteristic dimension (gap), normal heat flow formulas become inaccurate. Heat transfer from a solid to a gas in this Knudsen domain is then dependent on an accommodation coefficient which is defined as the ratio of the actual energy interchange to the maximum possible energy interchange between a surface and a gas. Generally, the accommodation coefficient of a

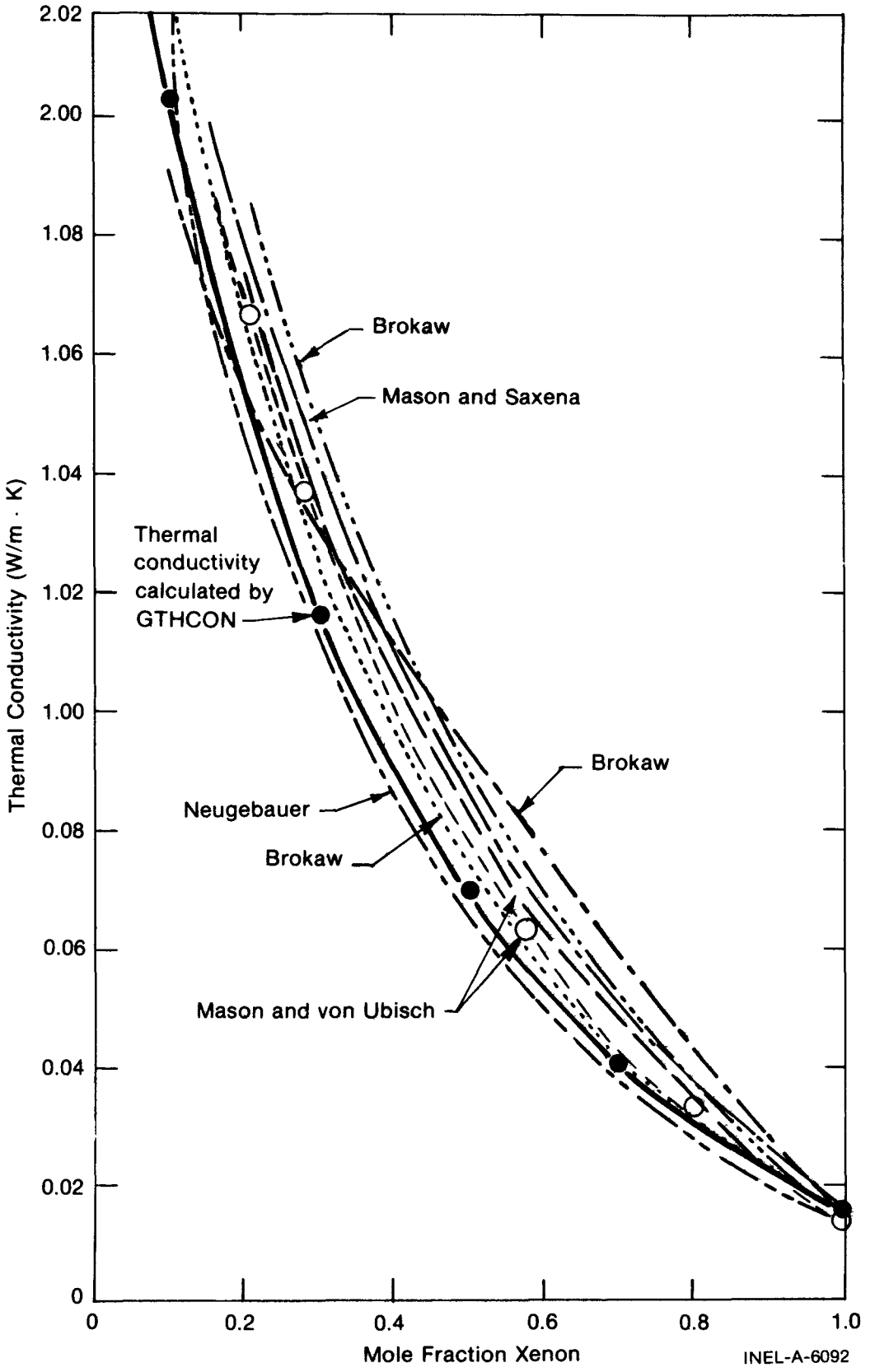

Fig. C-1.1 Thermal conductivity of xenon-helium mixtures at 520°C.

heavy gas such as argon or xenon is near unity and this effect can be neglected. But the effect cannot be neglected when the gap is filled with a light gas such as helium. Dean[C-1.43] has presented the following factor by which the bulk thermal conductivity of the light gases, helium and hydrogen, should be divided when temperature drops are calculated in the Knudsen domain:

$$f = 1 + \frac{\alpha_1 + \alpha_2 - \alpha_1 \alpha_2}{\alpha_1 \alpha_2} \frac{4}{c_p + c_v} \frac{k}{\mu} \frac{\lambda}{\zeta} \qquad \text{(C-1.11)}$$

where

α_1 = accommodation coefficient of the fuel (J/J)

α_2 = accommodation coefficient of the cladding (J/J)

c_p = constant pressure heat capacity (J/kg·K)

c_v = constant volume heat capacity (J/kg·K)

k = gas thermal conductivity (W/m·K)

μ = gas viscosity (N·s/m^2)

λ = mean path (m)

ζ = characteristic dimension (gap) (m).

The mean path (λ) can be written as

$$\lambda = \frac{3\mu}{\rho} \left[\frac{\pi M}{8kT}\right]^{1/2} \qquad \text{(C-1.12)}$$

where

μ = gas viscosity (N·s/m^2)

T = gas temperature (K)

M = mass of the molecule (kg)

k = Boltzman constant (1.38 x 10^{-23} J/K)

ρ = density of gas (kg/m^3).

If λ is substituted in Equation (C-1.11) and c_p and c_v are assumed to be temperature independent, then Equation (C-1.11) can be rewritten using the ideal gas law and the fact that $\rho = nM/V$ as

$$f = 1 + C \frac{k\sqrt{T}}{P\zeta} \qquad \text{(C-1.13)}$$

where

k = thermal conductivity (W/m·K)

T = temperature (K)

P = pressure (Pa)

ζ = characteristic dimension (m)

C = empirical constant.

The characteristic dimension, ζ, is essentially equal to the gap dimension and during pellet-to-cladding contact should be equal to the root mean square of the surface roughness, approximately 4.389×10^{-6} meters in most commercial fuel rods. A value for C of approximately 0.2103 $N\text{-}K^{1/2}/W$ was determined. C was determined by comparing fuel centerline temperature predictions with thermocouple measurements of centerline temperatures in helium-filled test rods with strong pellet-cladding mechanical interaction and high contract pressure.

Values for the thermal accommodation coefficients of the uranium oxide fuel and zircaloy cladding, α_1 and α_2, of approximately 0.3 and 0.07, respectively, are obtained by equating Equations (C-1.11) and (C-1.13). Eckert and Drake[C-1.44] have published thermal accommodation coefficients for glass (a ceramic) and helium of approximately 0.3, as well as coefficients ranging from 0.011 to approximately 0.2 for tungsten or nickel and helium. Thus the accommodation coefficients determined by comparison of measured and predicted in-pile temperatures compare favorably with the limited thermal accommodation coefficient data published for similar materials.

The effect of heat transfer in the Knudsen domain on fuel temperatures is indicated in Figure C-1.2. Campbell and DesHaies[C-1.45] performed an experiment in which the fuel rod internal gas pressure was reduced from about 15.2 MPa during irradiation thereby allowing the cladding to collapse onto the fuel. Fuel temperatures near the pellet surface and cladding circumferential strain were continuously monitored. As the internal pressure was decreased, the gap width became smaller (as indicated in Figure C-1.2), the gap conductance increased, and the fuel surface temperature decreased. Further pressure reduction from about 1 MPa results in increasingly imperfect energy exchange between the fill gas and the fuel and cladding, however. This effect more than compensates for the decreased gap width and the fuel temperature, and then the fuel radius is seen to increase.

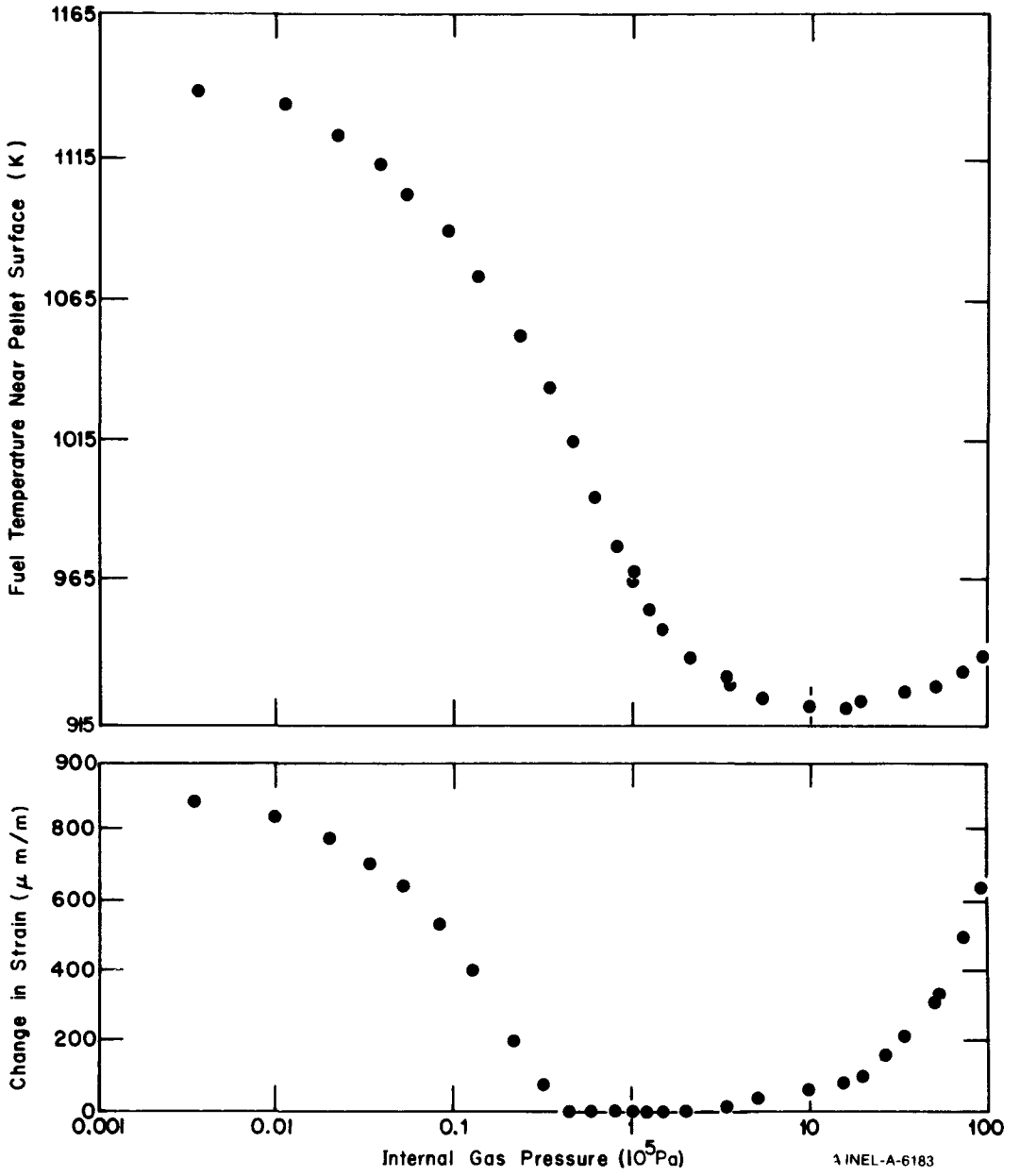

Fig. C-1.2 Effect of measured internal gas pressure on fuel temperatures near the pellet surface.

Continued reduction in fill gas pressure increased fuel temperatures until heat transfer through mating asperity points became dominant. At pressures below approximately 1000 Pa, the heat transfer was primarily through contact conductance, and the temperatures stabilized.

1.3 Gas Thermal Conductivity Subcode GTHCON Listing

A listing of the FORTRAN subcode GTHCON is presented in Table C-1.I.

TABLE C-1.I

LISTING OF THE GTHCON SUBCODE

```
C
      FUNCTION GTHCON(GMIX, GTEMP, GPRES, GPTHK)
C
CCCCCC GTHCON CALCULATES GAS THERMAL CONDUCTIVITY AS A FUNCTION OF
CCCCCC TEMPERATURE AND GAS FRACTION FOR SEVEN GASES:
CCCCCC
CCCCCC GTHCON  = OUTPUT GAS THERMAL CONDUCTIVITY (W/M-K).
CCCCCC
CCCCCC GMIX(I) = INPUT MOLE FRACTIONS OF THE GAS MIXTURE
CCCCCC THE SEVEN ELEMENTS OF GMIX MUST SUM TO 1.0
CCCCCC     CONSTITUENT GAS NUMBER KEY
CCCCCC         1 HELIUM
CCCCCC         2 ARGON
CCCCCC         3 KRYPTON
CCCCCC         4 XENON
CCCCCC         5 HYDROGEN
CCCCCC         6 NITROGEN
CCCCCC         7 WATER VAPOR
CCCCCC
CCCCCC GTEMP   = INPUT GAS TEMPERATURE (K)
CCCCCC GPRES   = INPUT GAS PRESSURE (PA)
CCCCCC           USED FOR KNUDSEN DOMAIN CORRECTION AND FOR STEAM
CCCCCC           NOT USED IF 0.
CCCCCC GPTHK   = INPUT EFFECTIVE GAP THICKNESS FOR KNUDSEN DOMAIN (M)
CCCCCC           (MAXIMUM OF GAP DIMENSION OR SURFACE ROUGHNESS)
CCCCCC           NOT USED IF 0.
CCCCCC
C FORMULA FOR GAS MIXTURES IS FROM  R.S.BROKAW, REPORT NASA TR R-81
C (1960). CONDUCTIVITY OF RARE GASES IS BASED ON  J.M.GANDHI AND
C S.C.SAXENA, JOUR. CHEM. AND ENG. DATA, VOL.13, NO.3 (1968)
C ALSO: WISCONSIN ELECTRIC POWER CO., DOCKET NO. 50-301 (JAN 1973)
C THE ACCOMMODATION FACTOR IS FROM  R.A.DEAN, CVNA-127 (1962)
C     STEAM EQUATION IS FROM  MEYER, ET.AL., "THERMODYNAMIC AND
C     TRANSPORT PROPERTIES OF STEAM", THE AMERICAN SOCIETY OF
C     MECHANICAL ENGINEERS (1967)
CCCCCC
CCCCCC GTHCON CODED BY R.C.YOUNG  MARCH 1975
CCCCCC ADAPTED FROM ROUTINE CMIX BY P.E.MACDONALD
C
      COMMON       / LACEMDL   / MAXIDX, EMFLAG
      DIMENSION EMFLAG(1)
C
      DIMENSION GMIX(7), A(7), C(7), R(7), AA(6), BB(6)
      DATA A  /4.003   , 39.944  ,83.80   ,131.30    , 2.016   ,28.8   ,
     #        18.016  /
C     R = SQRT(A)
      DATA R  /2.00075 ,  6.3201 , 9.1542  ,11.4586  , 1.41986 ,
     #         5.3666  ,  4.2445 /
C
      DATA AA /1.314E-3,  1.31E-4, 1.588E-5, 1.395E-5, 5.834E-4,7.35E-5/
      DATA BB /0.668   ,  0.701  , 0.92331 , 0.872   , 0.8213  ,0.846  /
      DATA EPS/1.E-9   /
C
      DATA       ON     /  2HON   /,
     #           OFF    /  3HOFF  /,
     #           LOCIDX /   16    /
C
      IF(EMFLAG(LOCIDX) .EQ. ON )
     #           GTHCON = EMGTON(GMIX  ,GTEMP ,GPRES ,GPTHK       )
      IF(EMFLAG(LOCIDX) .EQ. ON )  GO TO 40
C
C     CONVERT TEMP TO RANKINE
      TR = GTEMP * 1.8
      IF (TR.GT.10000.) GO TO 90
      IF (TR.GT.0.) GO TO 5
   90 WRITE (6,95)    GTEMP, GMIX
   95 FORMAT(25H1GTHCON INPUT BAD. GTEMP=,1PE12.4,2H K,/
     #       10HOFRACTIONS, (10E12.4))
      STOP
    5 L = 0
C     CALCULATE SMALL GAP CORRECTION
      FACC = GPRES * GPTHK
      IF(FACC .GT. EPS) FACC = SQRT(TR) * 1.7863 / FACC
```

TABLE C-1.I (continued)

```
C
      DO 10 I = 1,6
      IF (GMIX(I) .LE. EPS) GO TO 10
      L = I
      C(I) = AA(I) * TR**BB(I)
      IF (FACC .LE. 0.) GO TO 10
      IF (I.EQ.1 .OR. I.EQ.5) C(I) = C(I) / (1.0 + C(I) * FACC)
   10 CONTINUE
C
      IF (GMIX(7) .LE. EPS) GO TO 15
      L = 7
C                              STEAM
      TC = GTEMP - 273.15
      C(7) = 17.6E-3 + TC*( 5.87E-5 + TC*( 1.04E-7 - 4.51E-11*TC))
      IF (GPRES.LE.1.E5) GO TO 8
C     USE IDEAL GAS LAW FOR DENSITY - OK FOR CORRECTION AT HIGH TEMP.
      DEN = 2.1668E-6 * GPRES / GTEMP
      C(7) = C(7) + DEN*( 103.51E-3 + TC*(0.4198E-3 - 2.771E-8*TC)
     #                   + 2.1482E11 * DEN/TC**4.2)
    8 C(7) = C(7)/1.73073467
   15 IF (L.LE.0) GO TO 90
C
      GTHCON = 0.
      DO 30 I = 1,L
      IF (GMIX(I) .LE. EPS) GO TO 30
      SUM = 0.
      DO 25 J=1,L
      IF (J .EQ. I) GO TO 25
      IF (GMIX(J) .LE. EPS) GO TO 25
      RC  = C(I) / C(J)
      RA  = A(I) / A(J)
      FIJ =  1. + 2.41 * (RA-1.) * (RA-.142) / (1.+RA)**2
      GIJ = (1. +  SQRT(RC*R(I)/R(J)) )**2 /  SQRT(8.*(1.+RA))
      SUM = SUM + FIJ * GIJ * GMIX(J)
   25 CONTINUE
      GTHCON = GTHCON + C(I) * GMIX(I) / (GMIX(I) + SUM)
   30 CONTINUE
C     CONVERT FROM BTU/HR.FT.F  TO  W/M.K
      GTHCON = GTHCON * 1.73073467
   40 CONTINUE
C
      RETURN
      END
```

1.4 References

C-1.1. R. S. Brokaw, *Alignment Charts for Transport Properties, Viscosity, Thermal Conductivity, and Diffusion Coefficients for Nonpolar Gases and Gas Mixtures at Low Density,* Lewis Research Center, NASA-TR-R-81 (1960).

C-1.2. J. M. Gandhi and S. C. Saxena, "Correlated Thermal Conductivity Data of Rare Gases and Their Binary Mixtures at Ordinary Pressures," *Journal of Chemical and Engineering Data, 13,* 3 (1968).

C-1.3. Wisconsin Electric Power Company, "Fuel Densification," Point Beach Nuclear Plant, Unit 2, Docket 50301-78 (December 1972).

C-1.4. *Thermodynamic and Transport Properties of Steam,* New York: American Society of Mechanical Engineers, 1968.

C-1.5. H. Cheung, L. A. Bromley, C. R. Wilke, "Thermal Conductivity of Gas Mixtures," *AIChE Journal 8* (1962) pp 221-228.

C-1.6. J. M. Davidson and J. F. Music, *Experimental Thermal Conductivities of Gases and Gaseous Mixtures at Zero Degrees Centigrade,* HW-29021 (July 1953).

C-1.7. R. S. Hansen, R. R. Frost, J. A. Murphy, "The Thermal Conductivity of Hydrogen-Helium Mixtures," *Journal of Physical Chemistry, 68,* 7 (1964) pp 2028-2029.

C-1.8. H. L. Johnston and E. R. Grilly, "The Thermal Conductivities of Eight Common Gases Between 80^{o} and 380^{o} K," *Journal of Chemical Physics, 14* (1946) pp 233-238.

C-1.9. W. G. Kannuluik and E. H. Carman, "The Thermal Conductivity of Rare Gases," *Proceedings Physics Society London, B, 65* (September 1952) pp 701-709.

C-1.10. W. G. Kannuluik and L. H. Martin, "Thermal Conductivity of Gases at 0^{o}C," *Proceedings of the Royal Society London, 144* (May 1934) pp 496-513.

C-1.11. F. G. Keyes, *Project Squid,* Massachusetts Institute of Technology, Cambridge, Technical Report, 37 (April 1, 1952) (as referenced in C-1.2).

C-1.12. J. M. Lenoir and E. W. Comings, "Thermal Conductivity of Gases. Measurement at High Pressure," *Chemical Engineering Progress, 47* (1951) pp 223-231.

C-1.13. S. C. Saxena and J. P. Agrawal, "Thermal Conductivity of Polyatomic Gases and Relaxation Phenomena," *Journal of Chemical Physics, 35* (1961) pp 2107-2113.

C-1.14. B. N. Srivastava and A. K. Barua, "Thermal Conductivity of Binary Mixtures of Diatomic and Monatomic Gases," *Journal of Chemical Physics, 32* (1960) pp 427-435.

C-1.15. Y. S. Touloukian (ed.), "Thermal Conductivity," *Thermophysical Properties Research Center, Data Book,* Volume 2, Chapter 1, Purdue University (1966).

C-1.16. L. B. Thomas and R. C. Golike, "A Comparative Study of Accommodation Coefficients by the Temperature-Jump and Low-Pressure Methods and Thermal Conductivities of Helium, Neon, and Carbon Dioxide," *Journal of Chemical Physics, 22* (1954) pp 300-305.

C-1.17. E. Thornton, "Viscosity and Thermal Conductivity of Binary Gas Mixtures: Xenon-Krypton, Xenon-Argon, Xenon-Neon, and Xenon-Helium," *Proceedings of the Physics Society London, 76* (1960) pp 104-112; "Viscosity and Thermal Conductivity of Binary Gas Mixtures: Krypton-Argon, Krypton-Neon, and Krypton-Helium," *Ibid., 77* (1961) pp 1166-1169.

C-1.18. E. Thornton and W. A. D. Baker, "Viscosity and Thermal Conductivity of Binary Gas Mixtures: Argon-Neon, Argon-Helium, and Neon-Helium," *Proceedings of the Physics Society London, 80* (1962) pp 1171-1175.

C-1.19. H. von Ubisch, "The Thermal Conductivities of Mixtures of Rare Gases at 29°C and at 520°C," *Arkiv foer Fysik, 16* 7 (1959) pp 93-100.

C-1.20. J. Wachsmuth, "Conduction of Heat in Mixtures of Argon and Helium," *Physikalische Zeitschrift, 9* (April 1908) pp 235-240.

C-1.21. F. G. Waelbroech and P. Zucherbrodt, "Thermal Conductivities of Gases at Low Pressures. I. Monatomic Gases, Helium, and Argon," *Journal of Chemical Physics, 28* (1958) pp 523-524.

C-1.22. R. E. Walker, N. deHaas, A. A. Westenberg, "New Method of Measuring Gas Thermal Conductivity," *Physics of Fluids, 3* (May-June 1960) pp 482-483.

C-1.23. B. G. Dickins, "Effect of Accommodation on Heat Conduction through Gases," *Proceedings of the Royal Society London, 143* (February 1934) pp 517-540.

C-1.24. W. C. Gardiner and K. L. Schafer, "Transport Phenomena in Gases and Intermolecular Forces," *Zeitschrift fur Elektrochemie, 60* (1956) pp 588-594.

C-1.25. F. G. Keyes, "Thermal Conductivity of Gases," *Transactions of the American Society of Mechanical Engineers, 76* (1954) pp 809-816.

C-1.26. F. G. Keyes, "Thermal Conductivity of Gases," *Transactions of the American Society of Mechanical Engineers, 77* (1955) pp 899-906.

C-1.27. K. L. Schafer and K. H. Grundler, "The Heat Transport in Quartz Power-Gas Mixtures, A Method for the Determination of the Thermal Conductivity of Gases at High Temperatures," *Zeitschrift fur Elektrochemie, 63,* 4 (1959) pp 449-453.

C-1.28. K. L. Schafer and F. W. Reiter, "Method for the Measurement of Heat Conductivity at 1100°C," *Zeitschrift fur Elektrochemie, 61* (1957) pp 1230-1235.

C-1.29. J. V. Sengers, PhD Dissertation, Amsterdam (1962) (as referenced in C-1.2).

C-1.30. B. N. Srivastava and S. C. Saxena, "Thermal Conductivity of Binary and Ternary Rare Gas Mixtures," *Proceedings of the Physics Society of London, B, 70,* 4 (April 1957) pp 369-378.

C-1.31. S. Weber, "Experimental Researches on the Thermal Conductivity of Gases," *Annalen de Physik, 54,* 4 (March 1917) pp 325-356.

C-1.32. S. Weber, "Heat Conductivity of Gases," *Annalen de Physik, 82,* (February 1927) pp 479-503.

C-1.33. L. S. Zaitseva, "An Experimental Investigation of the Heat Conductivity of Monatomic Gases Over Wide Temperature Intervals," *Zhurnal Technicheskai Fisziki, 29,* 4 (April 1959) pp 497-505.

C-1.34. L. S. Zaitseva, "An Experimental Investigation of the Heat Conductivity of Monatomic Gases Over Wide Temperature Intervals," *Soviet Physics – Technical Physics, 4,* (April 1959) pp 444-450.

C-1.35. H. H. Landolt, *Landolt-Bornstein Physikalisch-Chemische Tabellen,* Berlin: J. Springer, 1912.

C-1.36. A. K. Barua, "Thermal Conductivity of Eucken-Type Factor for the Binary Mixtures H-He, H-Ne, H-Kr and H-Xe," *Indian Journal of Physics, 34,* 4 (1960) pp 169-183.

C-1.37. A. D. Andrew and C. S. Calvert, *Thermal Conductivity and Viscosity of Neon, Helium, Argon, Xenon, and Their Binary Mixtures,* General Electric Company, TID-24636 (April 1966).

C-1.38. R. S. Brokaw, *Approximate Formulas for Viscosity and Thermal Conductivity of Gas Mixtures,* Lewis Research Center, NASA-TN-D-2502 (November 1964).

C-1.39. E. A. Mason and S. C. Saxena, "Approximate Formula for the Thermal Conductivity of Gas Mixtures," *Physics of Fluids, 1,* 5 (September-October 1958) pp 361-369.

C-1.40. F. J. Neugebauer, *Collection of Heat-Transfer Properties of Gases at Moderate Pressures and Rules for Rapid Estimation of Missing Data,* General Electric Company, 62 GL 54 (April 1962).

C-1.41. R. S. Brokaw, "Estimating Thermal Conductivities for Nonpolar Gas Mixtures – Simple Empirical Method," *Indian Journal of Engineering Chemistry, 47* (1955) pp 2398-2400.

C-1.42. E. A. Mason and H. von Ubisch, "Thermal Conductivities of Rare Gas Mixtures," *Physics of Fluids, 3,* 3 (May-June 1960) pp 355-361.

C-1.43. R. A. Dean, *Thermal Contact Conductance Between UO_2 and Zircaloy-2,* Westinghouse Electric Company, CVNA-127 (May 1962).

C-1.44. E. R. G. Eckert and R. M. Drake, *Analysis of Heat & Mass Transfer,* New York: McGraw-Hill Book Company, Inc., 1972.

C-1.45. F. R. Campbell and R. DesHaies, "The Effect of Gas Pressure on Fuel/Sheath Heat Transfer," *Transactions of the American Nuclear Society, 21* (June 1975) p 380.

2. GAS VISCOSITY (GVISCO)

(G. A. Reymann)

Viscosity is important in describing the dynamic behavior of fluids. According to kinetic theory for a gas having a net mass motion, molecules tend to lose forward momentum due to proximity of stationary surfaces. This loss is described in terms of a viscosity, and it is pertinent to the flow of gas in a fuel-cladding gap as well as through a cladding rupture. In particular, the rate at which gas flows into the ballooning section of a fuel rod is inversely proportional to the fill gas viscosity for narrow gaps, becoming less dependent on the gas viscosity as the gap widens and flow becomes turbulent.

Bretsznajder[C-2.1], Bird et al[C-2.2], and Hirschfelder et al[C-2.3] have discussed in detail the functional relationships for viscosity, which in summary showed dependence on temperature, pressure, and gas composition. The formulation used in the routine GVISCO was taken from Bird et al and is

$$\mu_{mix} = \sum_{i=1}^{n} \frac{X_i \mu_i}{\sum_{j=1}^{n} X_j \Phi_{ij}} \qquad \text{(C-2.1)}$$

where

μ_{mix} = viscosity of gas mixture (kg/m·s)

n = number of chemical species in the mixture

X_i, X_j = the mole fractions of species i and j

μ_i, μ_j = the viscosities of species i and j (kg/m·s)

and Φ_{ij} is a dimensionless parameter defined as

$$\Phi_{ij} = \frac{1}{\sqrt{8}} \left(1 + \frac{M_i}{M_j}\right)^{-1/2} \left[1 + \left(\frac{\mu_i}{\mu_j}\right)^{1/2} \left(\frac{M_j}{M_i}\right)^{1/4}\right]^2 \qquad \text{(C-2.2)}$$

where

M_i, M_j = the molecular weights of species i and j (kg/mol).

The viscosity of a pure monatomic species may be expressed as

$$\mu_i = 8.4411 \times 10^{-24} \frac{\sqrt{MT}}{\sigma^2 k T/\epsilon} \quad \text{(C-2.3)}$$

where

μ_i = viscosity of species i (kg/m·s)

M = molecular weight of species (kg/mol)

σ = the collision diameter (m)

T = absolute temperature (K)

ϵ = the maximum energy of attraction between a pair of molecules (J/molecule)

k = Boltzmann's constant = 1.38×10^{-23} (J/K).

Bird et al state that Equations (C-2.1) through (C-2.3) are useful for computing viscosities of nonpolar gases and gas mixtures at low density from their tabulated values of the intermolecular force parameters σ and ϵ. Figure C-2.1 shows the viscosities for three different cases calculated from Equation (C-2.1): (a) helium only, (b) an equal molar mixture of helium and xenon, and (c) an equal molar mixture of helium, argon, krypton, and xenon. The routine GVISCO currently allows seven gases to be considered: helium, argon, krypton, xenon, hydrogen, nitrogen, and steam. Additional nonpolar gases may be readily added to GVISCO if desired.

The viscosity of steam, μ_s, is taken from Meyer et al[C-2.4]:

$$\mu_s = (0.407T - 30.8) \times 10^{-7} \quad \text{(C-2.4)}$$

where

μ_s = viscosity of steam (kg/m·s)

T = temperature (K).

A density correction could be applied, but examination of tabular data indicates the correction is small at typical fuel rod temperatures.

2.1 Gas Viscosity Subcode GVISCO Listing

The listing of the FORTRAN subcode GVISCO used for calculating gas viscosity is presented in Table C-2.I.

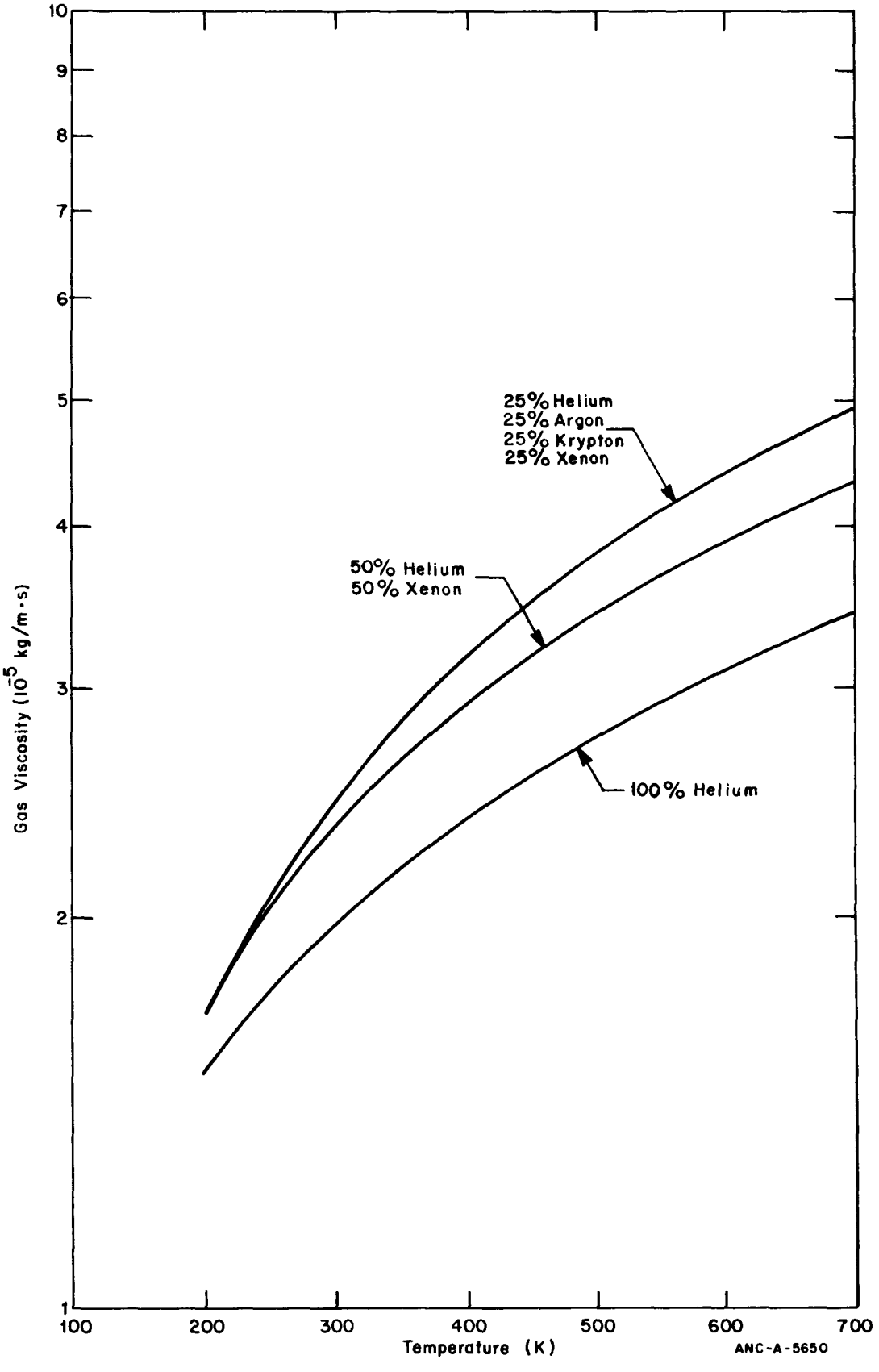

Fig. C-2.1 Gas viscosity as a function of temperature for pure helium, a binary mixture of helium and xenon, and for an equal molar mixture of helium, argon, krypton, and xenon.

TABLE C-2.I

LISTING OF THE GVISCO SUBCODE

```
C
C     FUNCTION GVISCO(GMIX, GTEMP)
C
CCCCC GVISCO CALCULATES THE GAS VISCOSITY AS A FUNCTION OF
CCCCC TEMPERATURE AND GAS MOLE FRACTIONS.
CCCCC
CCCCC GVISCO  = OUTPUT GAS VISCOSITY (KG/M-S)
CCCCC
CCCCC GMIX(I) = INPUT ARRAY OF GAS MOLAR FRACTIONS
CCCCC THE SEVEN ELEMENTS OF GMIX MUST SUM TO 1.0
CCCCC    I = 1  HELIUM
CCCCC    I = 2  ARGON
CCCCC    I = 3  KRYPTON
CCCCC    I = 4  XENON
CCCCC    I = 5  HYDROGEN
CCCCC    I = 6  NITROGEN
CCCCC    I = 7  STEAM - FROM 1967 ASME AT 1 BAR PRESSURE
CCCCC GTEMP=INPUT GAS TEMPERATURE (K).
CCCCC
CCCCC THE GAS VISCOSITY RELATIONSHIPS USED IN THIS FUNCTION
CCCCC ARE THOSE STATED BY BIRD,STEWART,AND LIGHTFOOT,
CCCCC "TRANSPORT PHENOMENA",P 26 AND P 258 (1954).
CCCCC BIRD, HIRSCHFELDER, CURTISS, TRANS. ASME 76(1954)1011-1038,
CCCCC    OR   HANDBOOK OF PHYSICS, SECTION 5.5 (MCGRAW-HILL) 1954.
CCCCC
CCCCC STEAM EQUATION IS FROM  MAYER, ET AL, "THERMODYNAMIC AND
CCCCC TRANSPORT PROPERTIES OF STEAM", THE AMERICAN SOCIETY OF
CCCCC MECHANICAL ENGINEERS (1967)
CCCCC
CCCCC     CODED BY R.C.YOUNG  MARCH 1975
C
      DIMENSION SIGMA2(6), EOK(6), IM(6)
      DIMENSION A(7), R(7), VIS(7), GMIX(7)
      DIMENSION TABLE(164)
      DATA EPS, NT, IM / 1.E-8, 82, 6*1 /
C
C     DATA SIGMA / 2.576, 3.418, 3.498, 4.055, 2.915, 3.617/
      DATA SIGMA2 / 6.635776, 11.682724, 12.236004, 16.443025,
     #              8.497225, 13.082689/
      DATA  EOK  / 10.2,  124.,  225.,  229.,  38.0,  97.0/
      DATA   A   / 4.003,39.944, 83.80, 131.3, 2.016, 28.97, 18.016/
C     R = SQRT(A)
      DATA R / 2.00075  , 6.3201  , 9.1542  , 11.4586  , 1.41986  ,
     #         5.3666   , 4.2445  /
C
      DATA TABLE / 2.785,.30, 2.628,.35, 2.492,.40, 2.368,.45, 2.257,.5,
     A2.156,.55, 2.065,.60, 1.982,.65, 1.908,.70, 1.841,.75, 1.780,.80,
     B1.725,.85, 1.675,.90, 1.629,.95, 1.587,1.0, 1.549,1.05,1.514,1.1,
     C1.482,1.15,1.452,1.2, 1.424,1.25,1.399,1.3, 1.375,1.35,1.353,1.4,
     D1.333,1.45,1.314,1.5, 1.296,1.55,1.279,1.6, 1.264,1.65,1.248,1.7,
     E1.234,1.75,1.221,1.8, 1.209,1.85,1.197,1.9, 1.186,1.95,1.175,2.0,
     F1.156,2.1, 1.138,2.2, 1.122,2.3, 1.107,2.4, 1.093,2.5, 1.081,2.6,
     G1.069,2.7, 1.058,2.8, 1.048,2.9, 1.039,3.0, 1.030,3.1, 1.022,3.2,
     H1.014,3.3, 1.007,3.4, .9999,3.5, .9932,3.6, .9870,3.7, .9811,3.8,
     I.9755,3.9, .9700,4.0, .9649,4.1, .9600,4.2, .9553,4.3, .9507,4.4,
     J.9464,4.5, .9422,4.6, .9382,4.7, .9343,4.8, .9305,4.9, .9269,5.0,
     K.8963,6.0, .8727,7.0, .8538,8.0, .8379,9.0, .8242,10., .7432,20.,
     L.7005,30., .6716,40., .6504,50., .6335,60., .6194,70., .6076,80.,
     M.5973,90., .5882,100., .5320,200., .5016,300., .4811,400./
C
      L = 0
      DO 10 I = 1,6
      IF (GMIX(I) .LE. EPS) GO TO 10
      L = I
      TKOE   = GTEMP / EOK(I)
      IF (TKOE.GT.400.) TKOE=400.
      OMEGA  = POLATE(TABLE, TKOE, NT, IM(I) )
      VIS(I) = 2.6693E-6 *  SQRT(A(I)*GTEMP) / (SIGMA2(I)*OMEGA)
   10 CONTINUE
      IF (GMIX(7) .LE. EPS) GO TO 15
      L      = 7
C     VIS(7) = 1.E-7 * ( 0.407*(GTEMP-273.15) + 80.4 )
      VIS(7) = 0.407E-7 * GTEMP - 30.77 E-7
```

TABLE C-2.I (continued)

```
C
   15 IF(L.LE. 0 ) WRITE(6,25) GMIX, GTEMP
   25 FORMAT(28H ERROR IN GVISCO WITH GMIX= ,7(E10.4,3X),/,
     #       12H AND GTEMP= ,E10.4                      )
      IF(L.LE. 0 ) STOP
      GVISCO = 0.0
C
      DO 30 I = 1,L
      IF (GMIX(I) .LE. EPS) GO TO 30
      SUM = 0.
      DO 20 J = 1,L
      IF (J .EQ. I) GO TO 20
      IF (GMIX(J) .LE. EPS) GO TO 20
      RV  = VIS(I) / VIS(J)
      PHI = (1. + SQRT(RV*R(J)/R(I)))**2 / SQRT(8.*(1.+A(I)/A(J)))
      SUM = SUM + GMIX(J) * PHI
   20 CONTINUE
      GVISCO = GVISCO + GMIX(I) * VIS(I) / (GMIX(I) + SUM)
   30 CONTINUE
C
      RETURN
      END
```

2.2 References

C-2.1. S. Bretsznajder, *Prediction of Transport and Other Physical Properties of Fluids,* New York: Pergamon Press, 1971.

C-2.2. R. B. Bird, W. E. Stewart, E. N. Lightfoot, *Transport Phenomena,* New York: John Wiley & Sons, Inc. 1954.

C-2.3. J. O. Hirschfelder, C. F. Curtiss, R. B. Bird, *Molecular Theory of Gases and Liquids,* New York: John Wiley & Sons, Inc., 1954.

C-2.4. C. A. Meyer et al, *Thermodynamic and Transport Properties of Steam,* New York: The American Society of Mechanical Engineers, 1967.

APPENDIX D

SUPPORTING MATERIAL FOR MATPRO

APPENDIX D

SUPPORTING MATERIAL FOR MATPRO

This appendix contains two subcodes often called by other subcodes in MATPRO. The first is the physical property subroutine PHYPRO. It provides melting temperatures and heats of fusion for light water reactor fuels and cladding, and also includes the phase transformation temperatures for zircaloy cladding. The fuel melting temperature is a function of burnup and plutonia content. The second routine is the linear interpolation code POLATE. This is used in a few models where analytical forms for the material property being described are inconvenient or unjustified. It interpolates between values listed in a table.

In addition, this appendix contains a list of the SI units used in MATPRO and a few conversion factors to enable users to readily convert from units with which they may be more accustomed.

1. PHYSICAL PROPERTIES (PHYPRO)

(C. S. Olsen and R. L. Miller)

The routine PHYPRO returns melting temperatures and heats of fusion for UO_2, (U, Pu)O_2, and zircaloy as well as α to β transformation temperatures for zirconium and zircaloy. The fuel melting temperatures are modeled as a function of burnup and plutonia content.

1.1 UO_2 and (U, Pu)O_2 Melting Point

The melting point of unirradiated UO_2 has been measured by several investigators with varying results. Brassfield et al[D-1.1] and Lyons et al[D-1.2] have published compilations and discussions of several recent experimental results and have listed "best" value UO_2 melting points of 3113 and 3133 ± 15 K, respectively, for burnups less than 10 000 MWd/MtU. The routine PHYPRO uses Brassfield's et al recommendation of 3113 K for the melting temperature of unirradiated UO_2.

Lyon and Baily[D-1.3] determined the phase diagram for stoichiometric (U, Pu)O_2 mixed oxides. The temperature data for the solidus and for the liquidus boundaries were fit by least-squares techniques to parabolic equations. The results are given by Equations (D-1.1) and (D-1.2).

$$T\ (\text{solidus}) = 3113 - 5.414\ C + 7.468 \times 10^{-3}\ C^2 \qquad \text{(D-1.1)}$$

$$T\ (\text{liquidus}) = 3113 - 3.219\ C - 1.449 \times 10^{-2}\ C^2 \qquad \text{(D-1.2)}$$

where

C = the mole percent of PuO_2

T = temperature (K).

The solidus curve is used for the melting point of mixed oxides and the difference between the liquidus and solidus boundaries defines the temperature range in which solid and liquid coexist. Figure D-1.1 shows the solidus and liquidus boundaries.

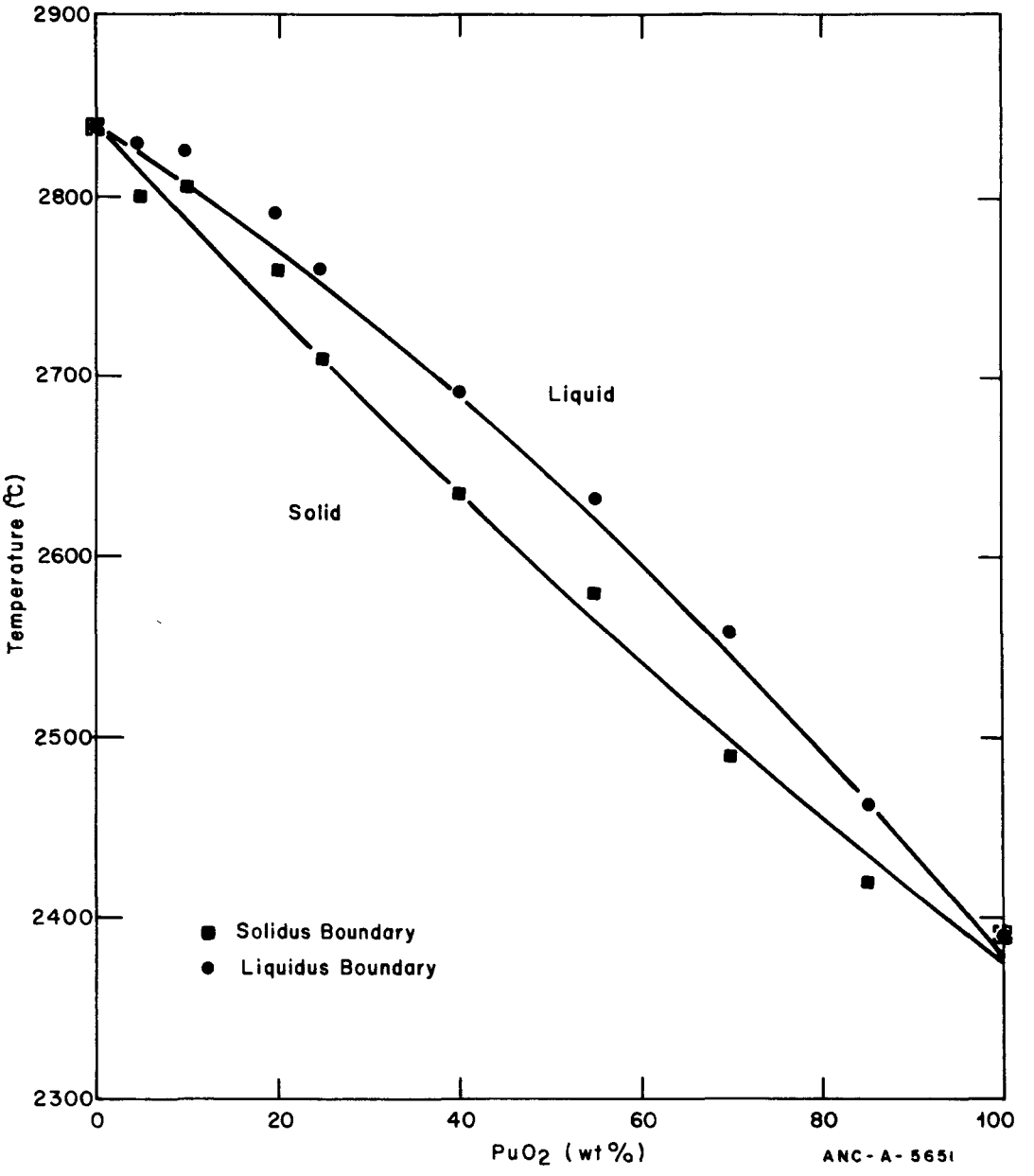

Fig. D-1.1 Phase diagram for stoichiometric uranium-plutonium oxides.

Christensen[D-1.4, D-1.5] established that the melting point of his UO_2 samples decreased with fuel burnup. The largest decrease measured by Christensen was about 32 K per 10 000 MWd/MtM. Krankota and Craig[D-1.6] have also reported a 50 to 100 K decrease in the melting point of irradiated mixed oxide test samples for burnups between 55 000 and 85 000 MWd/MtM. However, these results are not in accord with those of Reavis and Green[D-1.7] who reported no significant reduction in the melting point of UO_2 due to irradiation. Since a fission event results in the accumulation of cationic fission products together with some liberation of oxygen, a lowering of the melting point of UO_2 during irradiation is expected. Therefore following Christensen, the melting point of UO_2 and mixed oxides is decreased 32 K per 10 000 MWd/MtM in PHYPRO.

1.2 UO_2 and (U, Pu)O_2 Heat of Fusion

The two calorimetrically determined values for the heat of fusion of unirradiated UO_2 are in good agreement. Specifically, Hein and Flagella[D-1.8] found 76 ± 2 kJ/mol and Leibowitz et al[D-1.9] reported a value of 74 kJ/mol. These results suggest that the heat of fusion of unirradiated UO_2 is adequately known from present analyses. The routine PHYPRO uses Leibowitz's et al calorimetry value of 2.74×10^5 J/kg for the heat of fusion of UO_2.

Leibowitz et al[D-1.10] determined a heat of fusion for mixed oxides of 67 kJ/mol from three tests. This 10% agreement between UO_2 and mixed oxide values for the heat of fusion is reasonable because of the similarity in crystal structure and atomic bonding. Therefore, unless conflicting data become available, the UO_2 value will be used for the heat of fusion of mixed oxides.

1.3 Zircaloy Melting Point and Transformation Temperatures

The reported melting point of zircaloy is below that reported for unalloyed zirconium. The addition of tin lowers the zirconium melting point[D-1.11], and small amounts of iron, nickel, or chromium decrease the solidus temperatures of a binary mixture about 70 K for each 0.1% addition of solute[D-1.12]. These results are for the binary mixtures of zirconium and one solute: tin, iron, chromium, or nickel. In the five component zircaloy system, the effect of each solute may not be additive, and therefore a separate determination is required. The zircaloy-2 melting point has been measured to be about 2098 K, and this value is returned by PHYPRO.

Pure zirconium isothermally transforms from the α phase to the β phase at 1135 K[D-1.13]. The routine PHYPRO returns 1135.15 K for the zirconium transformation temperature when the variable CTRANZ is called. Zircaloy, however, undergoes the same transformation over a range of temperatures. PHYPRO returns the variable CTRANB for the beginning of the α-β transformation (1083.15 K) And the variable CTRANE for the end of the α-β transformation (1243.15 K)[D-1.14].

1.4 Zircaloy Heat of Fusion

The heat of fusion of zircaloy depends to some extent on its composition and the extent of oxidization. Brassfield et al have suggested that the heat of fusion of zircaloy-4 differs little from that of zirconium and lists the heat of fusion of zirconium as 20.5 kJ/mol. However, Quill[D-1.15] lists the heat of fusion of zirconium as 23 kJ/mol with uncertainty. The routine PHYPRO returns Brassfield's et al listed heat of fusion for zirconium of 2.25×10^5 J/kg.

1.5 Physical Properties Subcode PHYPRO Listing

The FORTRAN subcode PHYPRO is listed in Table D-1.I.

1.6 References

D-1.1. H. C. Brassfield et al, *Recommended Property and Reactor Kinetics Data for Use in Evaluating a Light-Water-Cooled Reactor Loss-of-Coolant Incident Involving Zircaloy-4 or 304-SS-Clad UO_2,* GEMP-482 (April 1968).

D-1.2. M. F. Lyons et al, "UO_2 Properties Affecting Performance," *Nuclear Engineering and Design, 21* (1972) p 167.

D-1.3. W. L. Lyon and W. E. Baily, "The Solid-Liquid Phase Diagram for the UO_2-PuO_2 System," *Journal of Nuclear Materials, 22,* 332 (1967).

D-1.4. J. A. Christensen, *Radiation Effects on UO_2 Melting,* HW-69234 (March 1962).

D-1.5. J. A. Christensen, R. J. Allio, A. Biancheria, *Melting Point of Irradiated Uranium Dioxide,* WCAP-6065 (1965).

D-1.6. J. L. Krankota and C. N. Craig, "Melting Point of High Burnup PuO_2-UO_2," *Transactions of the American Nuclear Society, 11,* 132 (1968)

D-1.7. J. G. Reavis and J. L. Green, "Transformation Temperatures of Irradiated UO_2-PuO_2 Fast Reactor Fuels," *Transactions of the American Nuclear Society, 14* 593 (1971).

D-1.8. R. A. Hein and P. N. Flagella, *Enthalpy Measurements of UO_2 and Tungsten to 3,260°K,* GE-NMPO-578 (February 1968).

D-1.9. L. Leibowitz, M. G. Chasanov, L. W. Mishler, D. F. Fischer, "Enthalpy of Liquid Uranium Dioxide to 3,500°K," *Journal of Nuclear Materials, 39* (1971) p 115.

D-1.10. L. Leibowitz, D. F. Fischer, M. G. Chasanov, *Enthalpy of Molten Uranium-Plutonium Oxide,* ANL-8082, (February 1975).

TABLE D-1.I

LISTING OF THE PHYPRO SUBCODE

```
C
C
      SUBROUTINE PHYPRO
C
CCC   PHYPRO RETURNS UO2, (U,PU)O2, AND ZIRCALOY MELTING POINTS
CCC   AND HEATS OF FUSION, AND ZIRCONIUM AND ZIRCALOY ALPHA TO BETA
CCC   TRANSITION TEMPERATURES.
C
      COMMON /PHYPRO / FTMELT,FHEFUS,CTMELT,CHEFUS,CTRANB,
     #                 CTRANE,CTRANZ,FDELTA,BU    ,COMP
C
CCC   FTMELT = OUTPUT UO2 OR MIXED OXIDE FUEL MELTING POINTS (K)
CCC   FHEFUS = OUTPUT UO2 OR MIXED OXIDE FUEL HEAT OF FUSION (J/KG)
CCC   CTMELT = OUTPUT ZR CLAD MELTING POINT (K)
CCC   CHEFUS = OUTPUT ZR CLAD HEAT OF FUSION (J/KG).
CCC   CTRANB = OUTPUT BEGIN OF ZR-4 ALPHA-BETA TRANSUS TEMPERATURE (K)
CCC   CTRANE = OUTPUT END OF ZR-4 ALPHA-BETA TRANSUS TEMPERATURE (K)
CCC   CTRANZ = OUTPUT ZR ISOTHERMAL ALPHA-BETA TRANSUS TEMPERATURE (K)
CCC   FDELTA = OUTPUT LIQUID-SOLID COEXISTENCE TEMPERATURE RANGE (K)
CCC
CCC   BU     = INPUT BURNUP (MW-S/KG-U)
CCC   COMP   = INPUT PUO2 CONTENT (WT%)
CCC
CCC   THE UO2 AND ZR CLADDING MELTING POINTS AND HEATS OF FUSION ARE
CCC   TAKEN FROM THE FOLLOWING REFERENCES. UO2 FUEL MELTING POINT OF
CCC   3113K FROM H.C.BRASSFIELD ET AL GEMP-482. UO2 HEAT OF FUSION
CCC   OF 17.7 KCAL/MOLE FROM L.LEIBOWITZ ET AL, J.NUC.MAT., VOL39 P 115
CCC   (1971). CLADDING MELTING POINT OF 2098 K FROM M.L. PICKLESIMER
CCC   PRIVATE COMMUNICATION. CLADDING HEAT OF FUSION OF 4.9 KCAL/MOL
CCC   FROM BRASSFIELD ET AL, GEMP-482.
CCC
CCC   BEGINNING OF ZIRCALOY ALPHA-BETA TRANSUS TEMPERATURE IS 1083K
CCC   DATA TAKEN FROM M.L. PICKLESIMER, U. S. PATENT 2,894,866
CCC   END OF ZIRCALOY ALPHA-BETA TRANSUS TEMPERATURE IS 1244 K
CCC   DATA TAKEN FROM M.L. PICKLESIMER, U. S. PATENT 2,894,866
CCC   ISOTHERMAL ZIRCONIUM ALPHA-BETA TRANSUS TEMPERATURE IS 1135 K
CCC   DATA TAKEN FROM  B.LUSTMAN&F.KERZE "THE METALLURGY OF ZIRCONIUM"
CCC   MCGRAW-HILL BOOK CO., NEW YORK, 1955
CCC   MIXED OXIDE MELTING POINT  WAS OBTAINED FROM LYON ET AL, J. NUC.
CCC   MAT., 22 (1967) P 332
C
CCC   PHYPRO WAS CODED BY V.F. BASTON IN MAY 1974
CCC   MODIFIED BY C.S. OLSEN IN FEB. 1975
CCC   MODIFIED BY B.W. BURNHAM IN NOV. 1977
C
      COMMON      / LACEMDL   / MAXIDX, EMFLAG
      DIMENSION   EMFLAG(1)
      DATA        ON          / 2HON    /,
     #            OFF         / 3HOFF   /,
     #            LCCIDX      / 2       /
C
      SLDUS(C)   = 2840.0 - 5.41395*C + 7.46839E-3*C*C
      LIQDUS(C)  = 2840.0 - 3.2186*C - 1.448518E-2*C*C
      FBU = BU/86.4
      IF (COMP .GT. 0.0) GO TO 10
C
      FTMELT=3113.15 - 32.0*FBU/10000.0
      FDELTA = 1.0E-10
      GO TO 20
C
   10 C1     = COMP
      FTMELT = SLDUS(C1) + 273.15 - 32.0*FBU/10000.0
      FDELTA = LIQDUS(C1) - SLDUS(C1)- 32.0*FBU/10000.0
C
   20 FHEFUS = 27.4E+4
      CTMELT = 2098.15
      CHEFUS = 22.5E+04
      CTRANB = 1083.15
      CTRANE = 1243.15
      CTRANZ = 1135.15
      RETURN
      END
```

D-1.11. D. J. McPherson and M. Hansen, "The System Zirconium-Tin," *Transactions of the American Society for Metals, 45,* 915 (1953).

D-1.12. E. T. Hayes, A. H. Roberson, O. G. Paasche, "The Zirconium-Nickel Phase Diagram," *Transactions of the American Society for Metals, 45,* 893 (1953).

D-1.13. B. Lustman and F. Kerze, *The Metallurgy of Zirconium,* New York: McGraw-Hill Book Company, Inc., 1955.

D-1.14. M. L. Picklesimer, "Method of Annealing and Rolling Zirconium-Base Alloys," U.S. Patent 2,894,866 (July 14, 1959).

D-1.15. L. L. Quill, *Chemistry and Metallurgy of Miscellaneous Materials, Thermodynamic, National Nuclear Energy Series,* IV, 19B, New York: McGraw-Hill Book Company, Inc., 1950.

2. LINEAR INTERPOLATION ROUTINE (POLATE)

A number of the MATPRO subcodes contain tables of data for a property rather than analytical expressions. Examples are cladding axial and radial thermal expansion in the region of 1073 to 1273 K and cladding specific heat capacity. In these cases discontinuities exist in the temperature range of the α and β phase transformation. POLATE is used when analytical expressions based on theory are not available and interpolation of reported data is simpler than use of an empirical equation.

A listing of the subcode POLATE is given in Table D-2.I.

TABLE D-2.I

LISTING OF POLATE SUBCODE

```
      FUNCTION POLATE (XY,XX,NN,KK)
C
      DIMENSION XY(2)
C
C     XY IS A TABLE OF Y(1), X(1), Y(2), X(2), ... Y(NN), X(NN)
C     XX IS THE GIVEN VALUE FOR X
C     NN IS THE NUMBER OF PAIRS OF ENTRIES IN XY
C     KK IS BOTH THE POSITION GUESS AND THE FINAL VALUE
C
      DATA ZERO , DM10 / 0.   ,  1.E-10 /
C
    1 X = XX
    2 N = NN
    3 M = IABS(N)
    4 K = KK
C     IF (K .LE. 0) K = 1
C     IF (K .GT. N) K = N
C
C     IS CONSTANT WANTED
      IF (M-1) 5,6,10
    5 POLATE = ZERO
      RETURN
    6 POLATE = XY(1)
      RETURN
```

TABLE D-2.1 (continued)

```
C
C       LOOP TO DECREASE INDEX
   10   IF (XY(2*K)-X) 20,20,11
   11   K = K - 1
   12   IF (K) 30,30,10
C
C       LOOP TO INCREASE INDEX
   20   IF(X-XY(2*K+2)-DM10)100,100,21
   21   K = K + 1
   22   IF(K-M)20,20,40
C
C       TEST FOR EXTRAPOLATION
   30   IF (N) 31,5,180
   31   K = 1
        GO TO 100
   40   IF (N) 41,5,190
   41   K = M - 1
C
C       EVERYTHING OK, GET ANSWER
  100   KK = K
  101   POLATE = XY(2*K-1) + (X-XY(2*K)) * (XY(2*K+1)-XY(2*K-1))
     1                                   / (XY(2*K+2)-XY(2*K))
  102   RETURN
C
C       POLATE FAILURE, SEARCH OUT OF BOUNDS
  180   POLATE = XY(1)
        GO TO 200
  190   POLATE = XY(2*M-1)
  200   CONTINUE
C 200   WRITE (6,210) KK, K, N, X, (XY(2*I),I=1,N)
C 201   CALL FAIL
  202   RETURN
  210   FORMAT(16H ERROR IN POLATE / 16HOINITIAL INDEX =, I6, 10X,
       113HFINAL INDEX =, I6, 10X, 14HARRAY LENGTH =, I6, 10X,
       210HARGUMENT =, E14.6 / 20HOTABLE OF X VALUES = / (8E15.6))
C
        END
```

3. SI UNITS USED IN MATPRO

The intent of materials properties work for MATPRO has been to code correlations in the Standard International System (SI) of Units. However, in some cases relationships are other units as taken directly from the literature. Table D-3.I indicates the SI units employed in MATPRO subcodes; Table D-3.II indicates some conversion factors that may be useful in interpreting other units.

TABLE D-3.I

SI UNITS FOR USE IN MATPRO

Quantity	Unit	SI Symbol	Formula
Base Units			
length	meter	m	
time	second	s	
mass	kilogram	kg	
thermodynamic temperature	kelvin	K	
amount of substance	mole	mol	
Derived Units			
area	square meter	m^2	
density	kilogram per cubic meter	kg/m^3	
energy	joule	J	N·m
force	newton	N	$kg \cdot m/s^2$
power	watt	W	J/s
pressure	pascal	Pa	N/m^2
specific heat	joule per kilogram kelvin	J/kg·K	
stress	newton per square meter	Pa	N/m^2
thermal conductivity	watt per meter kelvin	W/m·K	
velocity	meter per second	m/s	
viscosity (dynamic)	newton second per square meter	$N \cdot s/m^2$	
volume	cubic meter	m^3	

TABLE D-3.II

CONVERSION FACTORS

To Convert From	To	Multiply By
$foot^2$	$meter^2$ (m^2)	9.29030E-02
$pound\text{-}mass/foot^3$	$kilogram/meter^3$ (kg/m^3)	1.60185E+01
pound-force-foot	joule (J)	1.35582E+00
pound-force	newton (N)	4.44822E+00
pound-force-foot/s	watt (W)	1.35582E+00
$pound\text{-}force/foot^2$	pascal (Pa)	4.78803E+01
$pound\text{-}force/inch^2$ (psi)	pascal (Pa)	6.89476E+03
British thermal unit/ pound mass-^{o}Fahrenheit	joule/kilogram-kelvin (J/kg·K)	4.18400E+03
calorie/gram-^{o}Celsius (thermochemical)	joule/kilogram-kelvin (J/kg·K)	4.18400E+03
British thermal unit-inch/hour-$foot^2$-^{o}Fahrenheit	watt/meter kelvin (W/m·K)	1.44131E-01
foot/second	meter/second (m/s)	3.04800E-01
$foot^3$	$meter^3$ (m^3)	2.83168E-02

DISTRIBUTION RECORD FOR NUREG/CR-0497

(TREE-1280)

Internal Distribution

1 - Chicago Patent Group - DOE
9800 South Cass
Argonne, IL 60439

2 - R. L. Blackledge
Idaho Operations Office - DOE
Idaho Falls, ID 83401

3 - R. J. Beers, ID

4 - P. E. Litteneker, ID

5 - R. E. Tiller, ID

6 - H. P. Pearson
Information Processing, EG&G

7-12 - INEL Technical Library

13-32 - Authors

33-120 - Special Internal

External Distribution

121-122 - Saul Levine, Director
Office of Nuclear Regulatory Research, NRC
Washington, D.C. 20555

123-124 - Technical Information Center - DOE
Box 62
Oak Ridge, TN 37830

125-442 - Distribution under R3, Water Reactor Safety Research - Fuel Behavior